IRON SPECIATION CONTROL ON MINERAL-BIOCHAR COMPOSITES FOR ENVIRONMENT DECONTAMINATION

ZIBO XU

PhD

The Hong Kong Polytechnic University

2023

The Hong Kong Polytechnic University

Department of Civil and Environmental Engineering

Iron Speciation Control on Mineral-Biochar Composites for Environment Decontamination

Zibo XU

A thesis submitted in partial fulfilment of the requirements for the degree
of Doctor of Philosophy

March 2023

CERTIFICATE OF ORIGINALITY

I hereby declare that this thesis is my own work and that, to the best of my knowledge and belief, it reproduces no material previously published or written, nor material that has been accepted for the award of any other degree or diploma, except where due acknowledgement has been made in the text.

Zibo XU

ABSTRACT

Biochar, a carbon-rich material produced from the thermal treatment of biomass wastes with limited oxygen, was highlighted as a negative emission technology. Engineered biochar with a fit-for-purpose production can solve multiple environmental problems with the achievement of the circular economy. Among different modification technologies, impregnating iron (Fe) with the formation of Fe-biochar has been widely investigated owing to its high reactivity, natural abundance, facile synthesis, and environmental benignancy, while the precise control of Fe species on Fe-biochar for target pollutants immobilization is still unclear. This thesis focused on the precise control of Fe-species on Fe-biochar for the toxic metals immobilization process, and the key findings include: (i) Pyrolysis temperature affected the redox activity of the produced Fe-biochar. Increasing pyrolysis temperature altered the Fe-biochar from reductive to oxidative for the pollutants immobilization; (ii) The content of different carbon species in biochar led to distinct reductive-Fe and amorphous-Fe contents in the resulting Fe-biochar composites, and thus affected its immobilization mechanisms for arsenic; (iii) The crystallinity of Fe mineral affected the electron transfer routine with biochar during the Cr(VI) reduction process; (iv) Reductive transformation of Fe within the Fe-Mn binary oxide on Fe-Mn biochar was found during the pyrolysis process, forming embedded Fe(0) clusters within $FeMnO_2$ with a high Fe efficiency for the Cr(VI) immobilization; and (v) The hydrothermal pretreatment affects the mineral species on the Fe-Mn biochar. Higher hydrothermal temperature with co-existing urea led to the formation of nano-sized Fe(0) surrounded by the lattice-expanded MnO and cotton-like graphitic carbon, providing a high immobilization capacity for the frequently-appeared toxic metals in electroplating water. Results from this study could serve as the guideline for efficient Fe-biochar production for toxic metal immobilization. Based on the current finding, future studies about particle size control, metal-carbon framework design, production standard of Fe-biochar, carbon emission of modified biochar, and overall economic concern are suggested to promote the engineered biochar for industrial-level application.

PUBLICATION ARISING FROM PHD STUDY

First author Journal Papers

Xu, Z.; Wan, Z.; Sun, Y.; Cao, X.; Hou, D.; Alessi. D.; Ok, Y. S.; Tsang, D.*, Unraveling Iron Speciation on Fe-biochar with Distinct Arsenic Removal Mechanisms and Depth Distributions of As and Fe. ***Chemical Engineering Journal*** 2021, 425, 131489

Xu, Z.; Wan, Z.; Sun, Y.; Gao, B.; Hou, D.; Cao, X.; Komárek. M.; Ok, Y. S.; Tsang, D.*, Electroactive Fe-biochar for Redox-related Remediation of Arsenic and Chromium: Distinct Redox Nature with Varying Iron/carbon Speciation. ***Journal of Hazardous Materials***. 2022, 430, 128479

Xu, Z.; Yu, Y.; Xu, X.*; Tsang, D.; Yao, C.; Fan, J.; Zhao, L.; Qiu, H.; Cao, X., Direct and Indirect Electron Transfer Routes of Chromium(VI) Reduction with Different Crystalline Ferric Oxyhydroxides in the Presence of Pyrogenic Carbon. ***Environmental Science & Technology*** 2022, *56* (3), 1724–1735

Xu, Z.; Sun, M.; Xu, X.; Cao, X.*; Ippolito, J.; Mohanty, S.; Ni, B.; Xu, S.; Tsang, D.*; Efficient Electron-donating of Fe-Mn Biochar for Chromium(VI) Immobilization: Key Role of Embedded Zero-Valent Iron Clusters within Iron-Manganese Oxide. ***Journal of Hazardous Materials.*** 2023, 456, 131632

Xu, Z.; He, M.; Xu, X.; Cao, X.; Tsang, D.*. Impacts of Different Activation Processes on the Carbon Stability of Biochar for Oxidation Resistance. ***Bioresource Technology*** 2021, 338, 125555

Xu, Z.; Xu, X.*; Yu, Y.; Yao, C.; Tsang, D.*; Cao, X., Evolution of Redox Activity of Biochar during Interaction with Soil Minerals: Effect on the Electron Donating and Mediating Capacities for Cr(VI) Reduction. ***Journal of Hazardous Materials***. 2021, 414, 125483

He, M.[#]; **Xu, Z.**[#]; Hou, D.; Gao, B.; Cao, X.; Ok, Y. S.; Rinklebe J.; Bolan N., Tsang, D.*, Waste-derived Biochar for Water Pollution Control and Sustainable Development. ***Nature Reviews Earth & Environment*** 2022, 3, 444-460 (**[#]Co-first Author**)

Xu, Z.; Tsang, D.*. Redox-induced Transformation of Potentially Toxic Elements with Organic Carbon in Soil. ***Carbon Research*** 2022, 1, 9

Other Journal Papers

Yang, F.; **Xu, Z.**; Huang, Y.; Tsang, D.; Ok, Y. S.; Zhao, L.; Qiu, H.; Xu, X.; Cao, X*., Stabilization of Dissolvable Biochar by Soil Minerals: Release Reduction and Organo-mineral Complexes Formation. ***Journal of Hazardous Materials***. 2021, 412, 125213

Yu, Y.; **Xu, Z.**; Xu, X.*; Zhao, L.; Qiu, H.; Cao, X., Synergistic role of bulk carbon and iron minerals inherent in the sludge-derived biochar for As(V) immobilization. ***Chemical Engineering Journal*** 2021, 417, 129183

Wan, Z.; **Xu, Z**.; Sun, Y.; He, M.; Hou, D.; Cao, X.; Tsang, D.*, Critical Impact of Nitrogen Vacancies in Nonradical Carbocatalysis on Nitrogen-Doped Graphitic Biochar. ***Environmental Science & Technology*** 2021, *55* (10), 1724–1735

Feng, K.; **Xu, Z.**; Gao, B.; Xu, X.*; Zhao, L.; Qiu, H.; Cao, X.Mesoporous ball-milling iron-loaded biochar for enhanced sorption of reactive red: Performance and mechanisms. ***Environmental Pollution*** 2021, 290, 117992

He, M.; **Xu, Z**.;Sun, Y.; Chan, P.; Liu, I.; Tsang, D.*, Critical impacts of pyrolysis conditions and activation methods on application-oriented production of wood waste-derived biochar**.** ***Bioresource Technology*** 2021, 341, 125811

Zhu, X.; **Xu, Z.**; You, S.; Komárek. M.; Alessi. D.; Yuan, X.; Palansooriya, K. N.; Ok, Y. S.; Tsang, D.*, Machine learning exploration of the direct and indirect roles of Fe impregnation on Cr(VI) removal by engineered biochar. ***Chemical Engineering Journal*** 2021, 428, 131967

Wan, Z.; **Xu, Z**.; Sun, Y.; Zhang, Q.; Hou, D.;Gao, B.; Khan, E.; Graham, N.; Tsang, D.*,Stoichiometric Carbocatalysis via Epoxide-like C−S−O Configuration on Sulfur-Doped Biochar for Environmental Remediation. ***Journal of Hazardous Materials***. 2022, 428, 128223

Zhu, X.; He, M.; **Xu, Z**.; Luo, Z.; Gao, B.; Ruan, R.; Wang, C.; Wong, K.; Tsang, D.*, Combined acid pretreatment and co-hydrothermal carbonization to enhance energy recovery from food waste digestate. ***Energy Conversion and Management.*** 2022, 266, 115855

He, M.; Cao, Y.; **Xu, Z**.;You, S.; Ruan, R.; Gao, B.; Wong, K.; Tsang, D.*, Process water recirculation for catalytic hydrothermal carbonization of anaerobic digestate: Water-Energy-Nutrient Nexus. ***Bioresource Technology*** 2022, 361, 127694

Wan, Z.; Cao, Y.; **Xu, Z**.; Duan, X.; Xu, S.; Hou, D.; Wang, S.; Tsang, D.; Revealing Intrinsic Relations Between Cu Scales and Radical/Nonradical Oxidations to Regulate Nucleophilic/Electrophilic Catalysis. Advanced Functional Materials 2023

Wang, M.; Liu, K.; **Xu, Z.**; Dutata, S.; Valix, M.; Alessi, D.; Zimmerman, J.; Tsang, D.; Selective Extraction of Critical Metals from Spent Lithium-Ion Batteries. ***Environmental Science & Technology*** 2023

ACKNOWLEDGEMENTS

First and foremost, I would like to thank my supervisor, Prof. Dan Tsang, for all the opportunities from which I progressively learned skills. He is passionate about sharing his immense knowledge and thoughtful insight, which always inspires and improves my research. During each discussion, he gave me chances to train my research abilities and tried his best to improve my taste in the academy. It is my great honour to have three years of PhD study with him, which will benefit my lifetime.

Special thanks are to Prof. Xinde Cao, my supervisor for my master's study, and Prof. Xiaoyun Xu. They bring me across the threshold of research and give unconditional support to my research. I also want to thank all my co-authors for their insightful thoughts on my research.

My gratitude goes to our kind and wise lab technicians, Mr Lam, Celine, Jonathan, and Dorothy, who always provide efficient and professional technical assistance, which greatly smoothed my experimental work. Without them, the ideas on paper and my mind cannot come into reality safely and efficiently. I want to thank my previous and current groupmates for the time we experienced together. I am not naming them here but in my heart. Also, I am grateful to have the support from my friends in Mainland and Hong Kong during my doctoral study these years, especially Yu, Jie, Yulu, Yewen, Wangrui, Chengbo, Xiangan, Yueyang, Wenying, Xue, Yijia, Lele, Lei, Jerry, Bo, Grace, Qiaozhi, Yuying, Jingyi, and Mengdi. The happy moments we spent together revitalized me to move on. I also want to thank the opportunities given by the Hong Kong PhD Fellowship Scheme for my incredible doctoral journey.

Lastly, I want to express my profound appreciation for my family. Their endless love is always my backup. Having them is the luckiest thing in my life.

TABLE OF CONTENTS

List of Figures

List of Tables

Chapter 1- Introduction

1.1 Background

Owing to rapid urbanization and growing demand for natural resources, the stability and functionality of the environment have been severely threatened by various environmental degradation processes, such as degradation of soil quality, depletion of clean water, and loss of biodiversity. In this context, the United Nations' Sustainable Development Goals (SDGs) for 2030 were framed to tackle various environmental, social, and economic issues at a global scale. To turn promises into reality, biochar has been highlighted as a negative emission technology (NET) by the Intergovernmental Panel on Climate Change (IPCC 2019), which can be used to mitigate climate change and limit global temperature increases to 1.5 °C.

For more than thousands of years, biochar has been widely adopted for traditional agricultural practices as a pyrogenic carbonaceous material, such as Amazonian Dark Earths, which offers high fertility to the soil (Lehmann and Joseph 2015). The concept of biochar as a potential NET strategy was first introduced in 2006 (Lehmann et al., 2006) as a carbon-enriched material produced from the thermochemical treatment of various biomass wastes in an oxygen-limited environment for soil amendment (IBI 2015a). The global biochar marker has had a significant increase in the last decade; according to the biochar industry report from IBI (IBI 2015b), the sales volume of biochar from reported producers (~25% of all the industry) was 85 kilotons in 2015; while the actual volume should be higher as this data was significantly underrepresented for the Asian market (especially in China and Southeast Asia). Currently, most biochar is applied for soil amendment, while biochar for other applications such as soil and wastewater treatment still has a great growing potential (IBI 2015b) due to the easily tuneable properties, outstanding performance, and economic benefits of biochar (He et al., 2021a).

Controlling the biochar properties, which are highly dependent on the production conditions (Cai et al., 2021), was the key to its application, and biochar with a fit-for-purpose design has been shown to address environmental challenges with the simultaneous attainment of a circular economy (Chen et al., 2021a, Lehmann et al., 2021, Shaheen et al., 2019a, Yang et al., 2021a). Recently, various modification approaches, including physical activation, mineral addition, and element doping, have been applied to obtain enhanced performance of biochar for various applications and maximize the values of biochar application (Gong et al., 2022, Medeiros et al., 2021, Wang and Wang 2019). Among different technologies, impregnating iron (Fe) with the formation of Fe-biochar composites has been widely investigated owing to its high reactivity, natural abundance, facile synthesis, and environmental benignancy (Liang et al., 2021c, Xu et al., 2022a, Xu et al., 2021f, Yu et al., 2021).

The critical process in the tailored design of Fe-biochar composites is to manipulate the desirable iron speciation during the pyrolysis process. It is generally acknowledged that reductive gases such as carbon monoxide and methane formed during biomass pyrolysis (Chen et al., 2021b) through the dehydration and decomposition of organic components (Xiao et al., 2018b), and these gas intermediates reciprocally reduce the co-present iron species from the +3 state (Fe_2O_3/$Fe(OH)_3$) to +8/3 (Fe_3O_4), +2 (FeO), and even 0 (ZVI) (Feng et al., 2020, Qiu et al., 2020, Shen 2015, Xu et al., 2022a). In addition, the labile carbon fraction could also directly participate in the thermal reduction of iron oxide with the formation of metallic iron, which was highly related to the pyrolysis temperature (Shen 2015, Xu et al., 2021f). In addition to the reduction process, the elevated pyrolysis temperature may facilitate the crystallization of iron minerals (Arinchtein et al., 2020, Yu et al., 2021), and higher pyrolysis temperature will also provide excess energy to cover the surface energy of particles for spontaneous agglomeration (Li et al., 2021c, Li et al., 2020e). The combination of Fe and other elements was also found with higher energy under high-temperature pyrolysis, which further affects the Fe mineral speciation, especially considering the rich impurities in biochar due to the biomass feedstock. However, the current study about the precise Fe speciation control (considering valence state, crystallinity, and particle size) on Fe-biochar still lacks.

Moreover, the different environmental applications usually require varying Fe speciation on the Fe-biochar (Liu et al., 2023, Zhu et al., 2022b). Iron is widely recognized as the overarching active moiety in Fe-biochar for the redox-related decontamination process, and different iron speciations can support various redox-related remediation processes. The low-valent (*e.g.*, zero-valent iron (ZVI) and Fe(II)) and high-valent iron (*e.g.,* Fe(III) and Fe(IV)) would preferably drive reduction (Xu et al., 2022a, Yang et al., 2022a) and oxidation (Liang et al., 2021c) reactions, respectively. The electron-donating capacity of Fe could support the reductive immobilization of pollutants (*e.g.,* Cr(VI) reduction) (Xu et al., 2022a) or drive the activation of O_2 or oxidant for Fenton-like reactions (Mazarji et al., 2021, Zhou et al., 2022b). Meanwhile, high-valent speciation of Fe resulted in the oxidation of pollutants (*e.g.,* As(III) or organic pollutants) (Gubler and ThomasArrigo 2021, Liang et al., 2021c, Zhao et al., 2022b). In addition to the redox process, varying iron speciation might dominate different pollutants' immobilization routes. For instance, immobilization of As by ZVI is usually realized by the reduction of As on the surface of ZVI with the formation of the Fe-As complex shell (Fan et al., 2020). However, co-precipitation of As with released Fe and the direct sorption/complexation was the main immobilization routine of amorphous ferric/ferrous minerals (Gubler and ThomasArrigo 2021). Besides, iron minerals' crystallinity and particle size will significantly affect their reactivity (Aeppli et al., 2019a, Aeppli et al., 2019b, Xu et al., 2022b, Yu et al., 2021), which also needs more consideration during the application process. Crystal iron mineral usually has higher stability with less combination potential with the pollutants, while the amorphous iron phase could form an intense chemical combination with pollutants with a highly variable iron valence (Xu et al., 2022b). Notably, the surface functionalities and graphitic structure in the biochar phase could affect the immobilization reactions, which might support the remediation process of Fe-biochar (Xu et al., 2022a, Xu et al., 2020e). At the moment, we still lack consistent framework to assess the needed Fe-biochar when focused on the targeted application.

In addition to the sole Fe-modified biochar, binary oxide modification with Fe and other metals has recently become a research hot spot (Gholami et al., 2020, Liang et al., 2021a, Qi et al., 2022, Xing et al., 2022, Yin et al., 2020b). Among different metals, Mn was the widely selected element to form the binary oxide with Fe due to their similar radius, properties, valence states, and outstanding redox reactivity (Liu et al., 2021a, Wen et al., 2020, Zhang et al., 2014). It was found that Fe-Mn biochar showed a higher reactivity than Fe-biochar and Mn-biochar with a similar metal amount, and it is customarily related to the unique Fe/Mn species with a strong synergy impact (Chen et al., 2020b, Xu et al., 2023b). The precise mineral speciation control within the Fe-contained binary metal-modified biochar is still limited currently due to the complexity of the potential transformation process. For example, both binary oxide (e.g.,

$FeMn_2O_4$) (Chen et al., 2020b, Hao et al., 2020, Yang et al., 2022b) or separated Fe and Mn minerals (Zoroufchi Benis et al., 2022) can be formed on biochar, and they were shown contrasting removal capacity and mechanisms. Moreover, the underlying mechanisms for the pollutants' immobilization still lack solid evidence to support, especially considering the synergy impact of Fe and other metals.

1.2 Scope and Objectives

The tailored manipulation of iron speciation is crucial yet still challenging for further developing Fe-biochar for environmental application. The current studies overlook the well-planned design of Fe-biochar synthesis, and there is still a lack of corresponding evidence about the iron speciation control on the Fe-biochar. In this study, we would like to figure out the Fe speciation control mechanisms during Fe-biochar preparation and reveal the needed Fe speciation when targeting different environmental applications. Toxic metals, including chromium (Cr) and arsenic (As), were selected as the target pollutants since immobilization normally needs the combined redox and sorption/complexation.

Details objectives of this study include:

- To understand the speciation transformation of iron minerals on the Fe-biochar during the fabrication process
- To explore the redox capacity of Fe-biochar with different Fe species when targeting the redox-induced immobilization of Cr(VI) and As(III)
- To investigate the As removal mechanisms of Fe-biochar with varying Fe species through the combined redox and complexation process

- To reveal the impact of Fe crystallinity on the electron transfer routine of Fe-biochar for Cr(VI) reduction
- To evaluate the Fe mineral transformation within the binary Fe-Mn oxide on biochar and its impact on the toxic metals immobilization
- To validate the higher removal performance of as-prepared mineral-biochar composites for pollutants immobilization compared to the commercial zero-valent iron (ZVI)
- To provide strategies for desired iron speciation on Fe-biochar when targeting different environmental applications

1.3 Thesis overview

The thesis contains eight chapters in total. Following **Chapter 1** as the introduction, **Chapter 2** is the literature review which reviews the Fe-biochar production technologies and the relevant immobilization mechanisms for the toxic metals. The current research gap is also summarized at the end of this chapter.

Chapters 3-5 studied the control of Fe-speciation on Fe-biochar composites and its impact on the toxic metal's immobilization. **Chapter 3** focused on the redox reactivity of Fe-biochar with different Fe species. Electrochemical approaches are used to evaluate redox reactivity and determine its relationship with the Cr(VI) reduction and As(III) oxidation. Based on the different redox reactivity of Fe-biochar, the redox-related immobilization routine of As by different Fe-biochar was further revealed (**Chapter 4**). To further evaluate the contribution of mineral crystallinity on the electron transfer routine, **Chapter 5** focused on the impact of iron minerals with different crystallinity and revealed the different electron transfer mechanisms during the Cr(VI) immobilization by biochar and iron mineral.

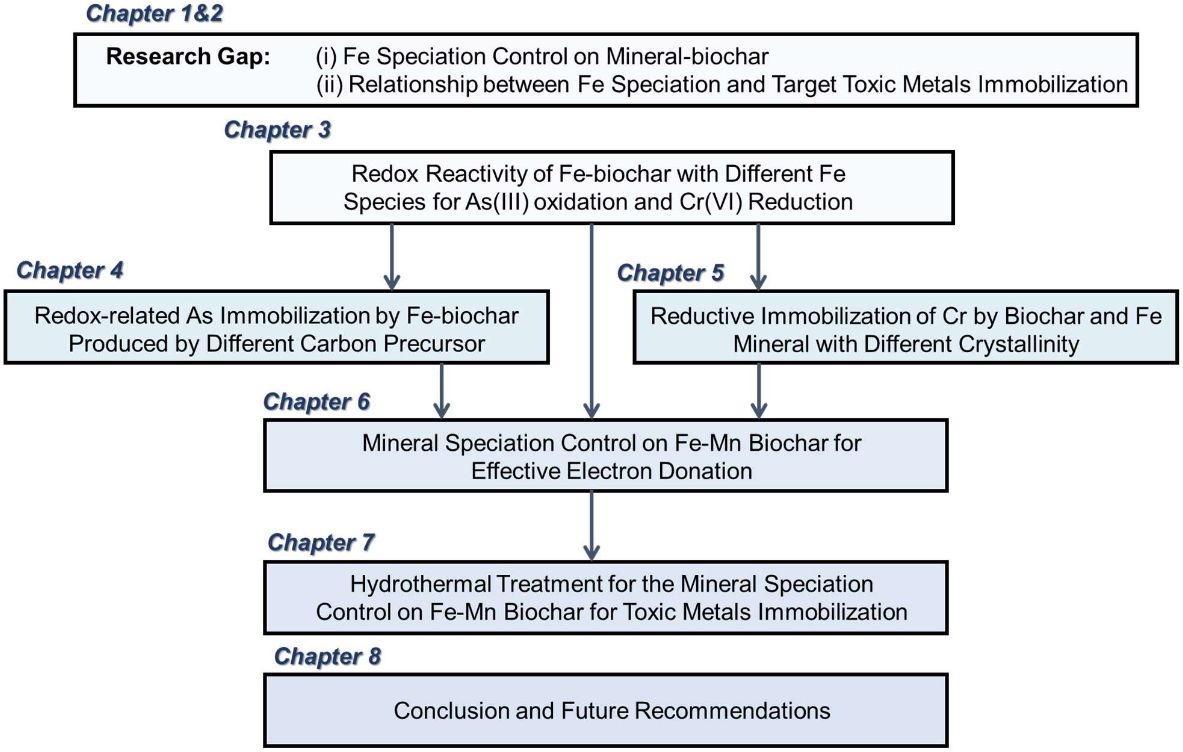

Figure 1-1 Thesis Overview

With one step forward for better Fe efficiency and removal performance, Fe and Mn are co-impregnated into the mineral biochar system in **Chapter 6** and **Chapter 7**. **Chapter 6** reveals the complex Fe mineral transformation in the Fe-Mn biochar under the pyrolysis condition and investigates its electron transfer efficiency and mechanisms. The reduction immobilization of Cr(VI) was selected as the targeted application to evaluate the electron donating efficiency. Hydrothermal modification is further introduced into the Fe-Mn biochar preparation in **Chapter 7** to maximize the efficiency of the toxic metals immobilization in the electroplating wastewater. The impacts of hydrothermal conditions on the Fe mineral transformation are evaluated, and the as-prepared Fe-Mn biochar showed a higher efficiency than the commercial and modified ZVI, indicating the potential industrialization as a high-value material.

Chapter 8 concludes the critical findings in this thesis and suggests the next-stage research for preparing science-based, high-value, and eco-friendly mineral-biochar composites to achieve carbon neutrality and environmental remediation.

Chapter 2 Literature Review

2.1 Biochar Production

Biochar can be produced across varying scales from large industrial down to small domestic level, making it applicable to various socioeconomic situations (Whitman and Lehmann 2009, Woolf et al., 2010). Biochar production is usually accompanied by bioenergy products, such as bio-oil and syngas (Yang et al., 2021b), which can be used for electricity production, chemical substitution, heating, and diesel substitution after extra treatment (Woolf et al., 2010). Diverse strategies, including conventional thermal pyrolysis (300–900 °C and residence time >1 h), gasification (> 700 °C), and microwave pyrolysis (0.3–300 GHz), have been used to produce biochar (Chen et al., 2020c). Among different methods, thermal pyrolysis methods have the highest economic feasibility, potential for climate change mitigation, and technological maturity, thus becoming the dominant technologies for biochar production(Chen et al., 2019b). Pyrolysis conditions, feedstocks, and various modification methods determined the properties of produced biochar (Cai et al., 2021).

2.1.1 Feedstock

The nature of the feedstock plays a critical role in the resultant biochar's elemental composition. The feedstock type ranges from lignin-rich and cellulose-rich biomass (e.g., crop residues and wood waste) to mineral-rich biomass (e.g., animal litter and municipal solid waste) (Xiao et al., 2018b, Xu et al., 2017). The formed biomass usually produced biochar with abundant C, H, and O content and rich aliphatic or aromatic structure, while the latter biomass produced biochar with higher inorganic composition, including Ca, P, Fe, S, and Mg (Xiao et al., 2018b, Xu et al., 2017). Therefore, selecting suitable feedstock could produce biochar with the desirable elements, which has been proven for various feedstock, including Si-rich rice straw (Xiao et al., 2014), N-rich algae, shrimp shell (Nan et al., 2020), or water hyacinth (Liang et al., 2018), P-rich cow manure (Cao et al., 2009, Cao et al., 2011), Fe-rich sludge (Tao et al., 2020, Yu et al., 2021), and K-rich crop residue (Xu et al., 2017). Moreover, some elements, such as Ca and Fe, significantly shape carbon speciation during the pyrolysis, which needs further consideration during biochar production (Nan et al., 2020, Xiao et al., 2017).

2.1.2 Pyrolysis condition

Pyrolysis temperature is a vital controller for the properties of biochar. With increasing pyrolysis temperature, the organic phase in the feedstock undergoes dehydration, organic components disruption, and subsequent aromatization, which results in the increase of C content and decline of H and O content in the biochar (Keiluweit et al., 2010, Lehmann and Joseph 2012). The increasing pyrolysis temperature will also cause the transformation of the carbon from aliphatic and amorphous to aromatic and graphitic (Xiao and Chen 2017a). Due to the loss of organic composition during pyrolysis, inorganic elements like P, Ca, and Fe will be concentrated at a high pyrolysis temperature. Speciation of these elements also varies with the increasing pyrolysis temperature from the high valence state to the low valence state, from mineral salt to mineral oxide or even elementary substance, and from amorphous speciation to crystal speciation due to the thermal synthesis process (Qiu et al., 2020, Xiao et al., 2018b). In addition to the element speciation and concentration, morphological and physical properties will change with the increasing pyrolysis temperature. A higher pyrolysis temperature will cause an increased surface area with a porous pore structure due to thermal condensation (Li et al., 2019).

2.1.3 Modification

Various modification methods were also applied to improve the properties of biochar for target environmental applications (Wang and Wang 2019). Loading of endogenous materials was widely used to modify biochar for the targeted application, and elements, including Fe (Qiu et al., 2020), Ca (Liu et al., 2019), Mg (Liu et al., 2013b), Cu (Wan et al., 2019), and N (Wan et al., 2020a, Xiao et al., 2018b), were the commonly studied elements for modification. Mixing biomass or biochar with selected chemicals or wastes can form the modified biochar with enriched elements and high performance to treat stubborn pollutants. Additionally, ball-milling, physical activation by steam or CO_2, and chemical activation by acid, alkalinity, or oxidizing agent were also used to improve the reactivity of biochar for the target application (Anto et al., 2021, Wang and Wang 2019, Yuan et al., 2021). Considering pollutants immobilization mechanisms, the following strategy was widely used for biochar modification (**Figure 2-1**).

Sorption: Physical activation (He et al., 2021a) (steam or CO_2 activation) and chemical activation (acid (Nzediegwu et al., 2021), alkaline treatment (Li et al., 2017a), mineral impregnation (Yu et al., 2021), and oxidation (Sanford et al., 2019)) are widely used to improve the surface area, porosity and surface functionality of biochar, leading to a higher sorption performance (Sizmur et al., 2017). Some specific modification methods are also used to improve the removal capacities of target pollutants, such as Fe impregnation for As removal

(Yu et al., 2021).

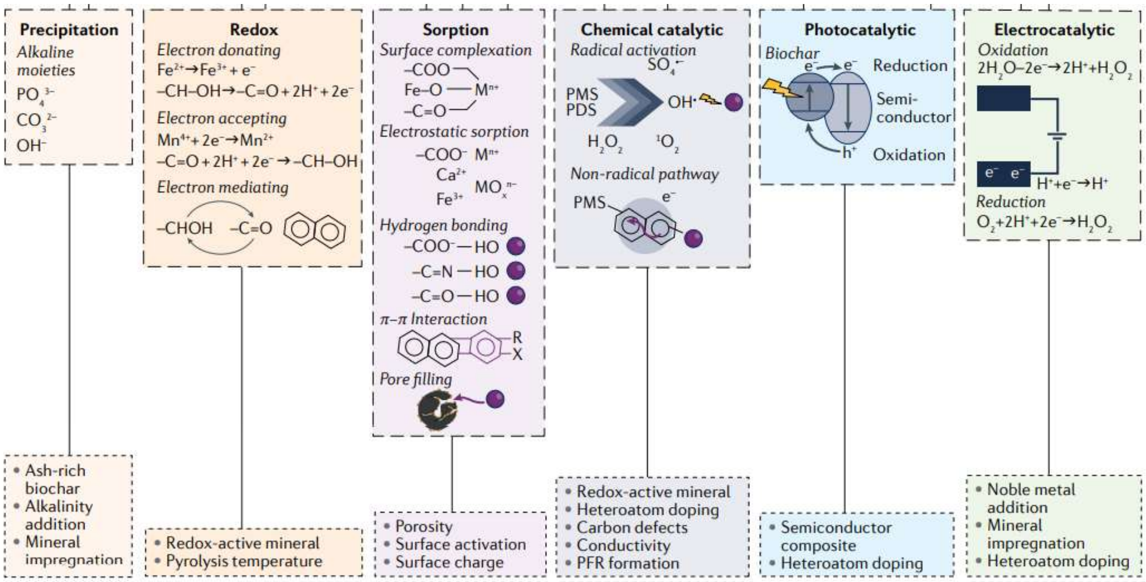

Figure 2-1 Biochar modification for the required immobilization strategy (He et al., 2022)

Precipitation: Increasing the alkalinity and ash content, such as phosphate, is the widely used strategy for precipitation enhancement (Zhao et al., 2016a).

Redox reaction: Adding redox-active minerals, such as Fe-minerals (Xu et al., 2021f) or Mn-minerals (Cuong et al., 2021), could substantially enhance the redox reactivity of formed biochar. The pyrolysis temperature is also critical for the redox reactivity of biochar because both the carbon and mineral phases undergo the redox-related transformation during pyrolysis (Xu et al., 2022a).

Chemical catalytic: Impregnation of redox-active elements is widely used to enhance the electron transfer process with oxidants, facilitating ROS formation, as the higher valence elements cause direct oxygen transfer for the degradation of pollutants (Liang et al., 2021c). Doping elements inside carbon structures (Wan et al., 2021) or defect formation (Liu et al., 2022) lead to a charge difference in biochar, facilitating the combination of pollutants and oxidants and thus enhancing the catalytic degradation process. Other potential strategies to improve the degradation capacity of biochar include the generation of PFRs during metal loading or designed thermal processes (Ruan et al., 2019) and enhancing the conductivity by forming a graphitic structure (Sun et al., 2017).

Electrocatalytic: Heteroatom doping (such as N) (Zhou et al., 2015), novel metal impregnation (such as Pt) (Yao et al., 2020), redox-active mineral addition (such as Fe and Mn) (Zhang et al., 2022c) were used to facilitate the reduction process on the biochar cathode. Besides, a similar modification strategy, including both heteroatom doping (Chen et al., 2014b) and mineral impregnation (Zhang et al., 2020c), was used for enhanced oxidation on the biochar anode.

In short, various types of biochar with different properties can be precisely fabricated by controlling the nature of the feedstock, the pyrolysis condition, and the modification methods. Different environmental applications need distinct biochar properties, and the designed synthesis of biochar for target environmental applications can remarkably improve its performance and value. Fe modification is the most used method when targeting pollutants immobilization, and the preparation of Fe-biochar composites and their capacity will be reviewed in the following sections.

2.2 Fe-biochar Production

Several methods are used to prepare Fe-biochar with different species, including co-pyrolysis, post-impregnation, hydrothermal treatment, and ball milling (**Figure 2-2**).

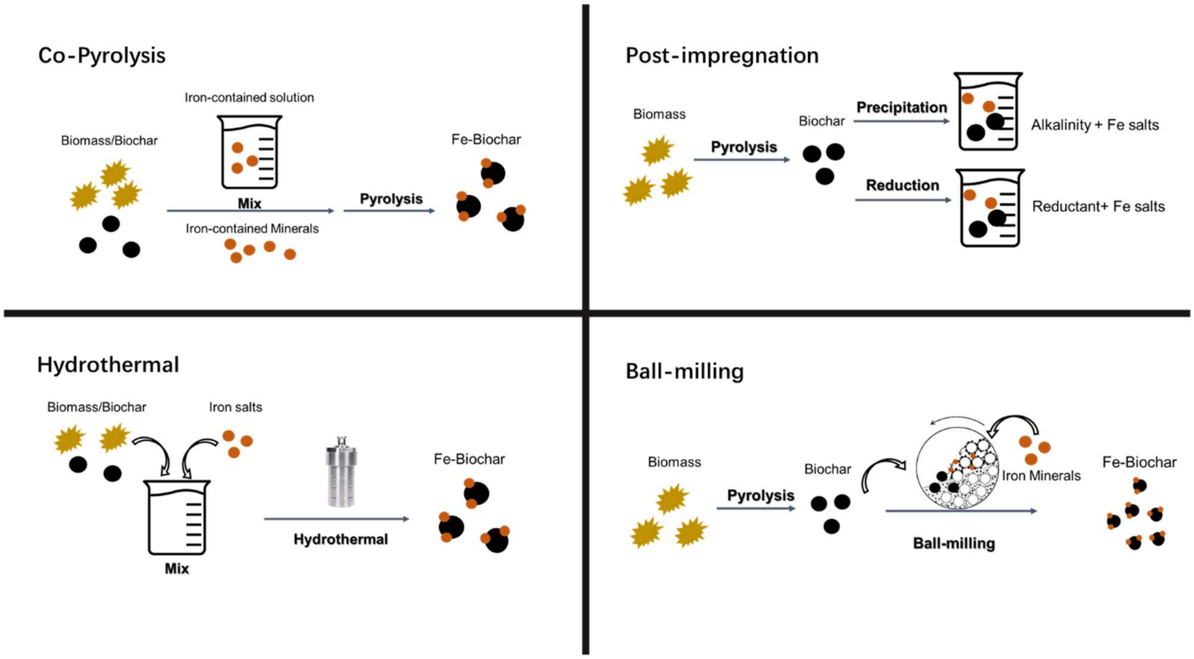

Figure 2-2 Production approach for Fe-biochar

2.2.1 Co-pyrolysis

Fe-biochar composites can be formed by co-pyrolysis with iron salts/minerals and biochar/biomass under an oxygen-limited environment (Gillingham et al., 2022, Lyu et al., 2020). The biomass or formed biochar was first impregnated with a solution containing iron or dry mixed with iron salt/minerals and then underwent pyrolysis. The advantage of the co-pyrolysis method is that it can form Fe-biochar with a one-step pyrolysis process, saving energy (Fan et al., 2020). In addition, adding Fe could catalyze the biomass pyrolysis process (Zhao et al., 2020), implying the potential advantage of forming bio-oil and syngas. Fe speciation on the formed Fe-biochar was mainly controlled by the pyrolysis condition, and a higher pyrolysis temperature leads to a reductive transition of the iron minerals from hematite, magnetite, wustite, to zero-valent iron and iron carbide (Gan et al., 2020, Qiu et al., 2020, Xu et al., 2022a, Yan et al., 2013). Due to the higher thermal stability of Fe_3O_4, it was the widely found iron mineral on Fe-biochar with a relatively lower temperature (<600°C), while ZVI became the primary speciation under a high pyrolysis temperature with rich reducing moieties (Xu et al., 2022a, Xu et al., 2021f). Various iron minerals/salts, including $FeCl_3$, Fe_2O_3, and $FeSO_4$, were selected as the iron source during the Fe-biochar production (Chen et al., 2019a, Park et al., 2019, Qiu et al., 2020, Xu et al., 2022a), and iron-rich waste such as red mud and sludge was also selected as the potential iron sources to improve the waste recycling benefits (Kang et al., 2023, Liang et al., 2023, Qin et al., 2022). However, the precise control of mineral speciation and repeatability is still questionable when introducing iron-rich waste as feedstock. Besides, co-pyrolysis processes are limited by high energy consumption, especially for biomass with high water content.

2.2.2 Post-impregnation

Post-impregnation was also widely used for Fe-biochar preparation. During the post-impregnation process, pristine biochar was first produced by pyrolysis, and then iron was loaded on the formed biochar with additional precipitation or reduction process. Although extra efforts and chemicals were used for the Fe loading, it can offer a more controllable and precise Fe speciation on the biochar. Moreover, post-impregnation could regulate the shape and size of the Fe particles attached to the biochar due to the mild and controllable formation condition (Li et al., 2021e).

The most common post-impregnation method was the coprecipitation process, achieved by the Fe precipitation under a mild or alkalinity environment. By choosing the suitable Fe^{2+}/Fe^{3+} ratios and the reaction pH, the wanted Fe particles could be precisely formed and attached to the biochar surface. For instance, magnetite or maghemite particles were formed by co-precipitating Fe^{3+} and Fe^{2+} with dropwise added NaOH (Han et al., 2015). In addition, the liquid-phase reduction was used to load reductive iron on the biochar, and the strong reducing agents, e.g., sodium borohydride ($NaBH_4$) or potassium borohydride (KBH_4), were mixed with Fe^{3+} for the formation of zero-valent iron (ZVI) particles on biochar (Huang et al., 2022, Jiang et al., 2020, Zhang et al., 2019b). Based on the reductive formation of ZVI, extra chemical agents can be further added to the reaction system to obtain a higher reactivity. For instance, sulfur was introduced during the reductive transformation of ZVI on the biochar by Gao et al., (2023), and the sulfidated nanoscale ZVI showed higher reactivity than the pure ZVI attached to the biochar. Although the surface functionality on biochar could serve as the fixing site to stabilize the nano-sized ZVI particles (Huang et al., 2022), the stabilizing agent, such as carboxymethyl cellulose, can also be introduced during the reduction process for higher stability with less aggregation (Zhang et al., 2019b). Some studies have demonstrated that the adsorption capacity of Fe-biochar produced by the post-impregnation methods showed a higher capacity for pollutants immobilization than the Fe-biochar prepared by co-pyrolysis (Wang et al., 2015a), which might overcome the high chemical input and complex fabrication process.

2.2.3 Hydrothermal treatment

Hydrothermal treatment is cost-effective with a relatively low temperature (100–300 °C) and self-generated pressure, which have been widely used for material synthesis. The hydrothermal process can be directly used for biomass carbonization by forming so-called hydrochar, and thus the one-pot synthesis of Fe-(hydrothermal)-biochar was conducted by the co-hydrothermal of biomass and iron minerals (Cai et al., 2019, Rong et al., 2019). For instance, magnetic bamboo-based biochar could be produced by the 200°C hydrothermal of bamboo waste, $FeCl_3$, and CH_3COONa. Nano-sized Fe_3O_4 was formed and strictly attached to the biochar surface, and a high removal capacity for the toxic U(VI) in the solution was found (Chen et al., 2023). Alkalinity was normally added during the hydrothermal process to ensure the precipitation of iron particles, and a reducing agent (*e.g.,* organic carbon or inorganic reducing moiety) was used to manipulate the iron speciation (Zhang et al., 2020a, Zhang and Hay 2020). For instance, reducing $Na_2S_2O_4$ was added into the hydrothermal system for the reductive transformation of iron, and sulfidated Fe was successfully formed on biochar. In addition to the one-pot synthesis, hydrothermal of biochar and different iron minerals was also conducted to control the Fe speciation precisely. For example, Yu et al., (2022) conducted 120° C hydrothermal of $FeSO_4$ with NH_4OH and biochar, and Fe_3O_4-loaded biochar was successfully formed. The doping elements, such as nitrogen, could also be introduced into the Fe-biochar by adding a suitable co-hydrothermal agent (Ahmad et al., 2023). According to the studies from Chen et al., (2023), different ratios of urea and $FeCl_3$ were added together with biochar during the hydrothermal process, and a series of Fe-biochar with Fe-N bonding was thus formed, which showed a higher reactivity for the pollutants removal.

Normally, hydrothermal treatment provides a smaller size of Fe particles and a better distribution compared to pyrolysis and post-impregnation due to the repeated dissolution and precipitation during the hydrothermal treatment. Therefore, Fe-biochar prepared by hydrothermal treatment had a higher removal capacity for Cr(VI) (142.9 mg g^{-1}), compared to the Fe-biochar prepared by reductive formation (58.82 mg g^{-1}), co-pyrolysis (43.122 mg g^{-1}), or coprecipitation (23.85 ± 0.23 mg g^{-1}) (Cai et al., 2019, Li et al., 2021e, Rong et al., 2019).

However, the hydrothermal itself cannot provide a strong reducing condition for the formation of ZVI if no potent reducing agent is added, and high pressure during the treatment leads to a potential risk during the real application.

2.2.4 Ball-milling

Ball milling, as a mechanochemical technique, has attracted increasing attention for biochar modification and biochar-mineral impregnation in recent years due to its operational simplicity (Kumar et al., 2020). During the high-energy process, chemical bonding within the iron minerals and biochar will be destroyed and reformed (Zhuang et al., 2016), and the particle size of both biochar and iron minerals will be decreased. Different iron minerals were used for the Fe-biochar production through ball milling. Shan et al., (2016) mixed biochar with ZVI, hematite, or magnetite under 550 rpm ball-milling and ultrafine Fe-biochar, and results showed that Fe_3O_4-biochar showed the best pollutants sorption performance. Although the ball-milling normally provided a robust oxidation environment with high energy input, Fe(0) could still be preserved due to the protection of biochar after ball-milling with a good distribution and small size of the biochar (Wang et al., 2020c). In addition to the smaller size, ball milling will also decrease the crystallinity of iron minerals with a higher surface area, leading to a higher sorption potential (Feng et al., 2021).

In short, Fe speciation on the Fe-biochar can be fabricated through various approaches for the targeted application. Due to the complex Fe speciation on the Fe-biochar, the precise control of Fe speciation is challenging, and the relevant mechanisms are unknown. Besides, different Fe-speciation might lead to distinct properties and removal mechanisms, and its relationship with the production methods and conditions is also unclear.

2.3 Mechanisms Involved in the Removal of Pollutants by Fe-biochar

Fe-biochar has been developed to deal with contaminants (inorganic metals and organic pollutants) in different environmental matrices according to their unique properties (Lyu et al., 2020). The immobilization process was driven by a combined redox reaction and sorption process, which is highly related to the Fe/C species on the Fe-biochar.

2.3.1 Sorption

Fe-biochar has shown an excellent capacity for the sorption removal of various toxic metals, including As, Cr, Ni, Cu, and Pb, due to the electrostatic interaction, surface complexation, ion exchange, and precipitation (Lyu et al., 2020). Both Fe-phase and biochar-phase can contribute to the sorption of pollutants. For instance, oxygen-containing functional groups on the biochar and the surface Fe–OH on iron minerals can form stable complexation with the toxic metals, leading to efficient removal. Besides, precipitation with the alkalinity released from the biochar (e.g., $Cd(OH)_2$ precipitation) and the coprecipitation with released iron (e.g., Fe-As coprecipitation) both occurred during the removal of toxic metals. Moreover, in some cases, Fe mineral and biochar might complement each other during the removal process. Iron oxides usually contain a positive charge on the surface, attracting the anionic pollutants during removal, while a negative charge was widely found in biochar. Therefore, iron impregnation could facilitate the removal of anionic pollutants, such as arsenic, through electrostatic attraction. This reciprocal process helped overcome the drawbacks of using biochar or iron minerals alone as the sorption materials, such as the limited As removal capacity of biochar.

2.3.2 Reduction

The reducing capacity, or electron-donating capacity, of Fe-biochar, was the dominant property in some remediation processes, such as Cr(VI) reduction and immobilization. Similar to the sorption process, both biochar and iron minerals with suitable species could serve as the electron-donating moiety for the reduction process. For biochar, it has been widely proved that its reducing capacity mainly came from the surface reductive functionality such as phenol and hydroxyl, and the reducing capacity decreased with the increasing pyrolysis temperature due to the change of surface functionality (Klüpfel et al., 2014). However, the iron species normally changed from oxidative to reductive phase with the increasing temperature during the co-pyrolysis process, and the latter, especially the ZVI, showed a higher reducing capacity (Qiu et al., 2020, Xu et al., 2022a). Therefore, producing the Fe-biochar with reductive Fe and C phases might be difficult through a simple co-pyrolysis process. Focusing on the higher reducing capacity of Fe phase on Fe-biochar is the typical approach, usually for ZVI with the highest electron donating potential, and biochar mainly serves as the supporting matrix. For example, Qian et al. (2019) prepared the nZVI-loaded biochar by the liquid-phase reduction approach of $FeSO_4$ with KBH_4, and a high reducing capacity for the Cr(VI) was found. They also tested the effects of BC pyrolysis temperatures on the effectiveness and stability of the supported nZVI, and BC400 showed the highest ability to support the nZVI due to the rich carboxyl. The sulfur introduction is the primary approach for an enhanced reducing capacity of ZVI-biochar composites (Pang et al., 2019), while phosphate doping is also reported to facilitate the electron transfer of ZVI on biochar recently (Huang et al., 2023). Other reducing Fe species, such as FeS and FeO, were studied as the potential loading moiety on biochar for the reduction process (Lyu et al., 2020, Lyu et al., 2017, Yang et al., 2017). Although they principally provided fewer electrons than ZVI, the accessibility of releasable Fe^{2+} might lead to a faster reduction and immobilization process.

2.3.3 Oxidation

The oxidation of pollutants by Fe-biochar could be achieved by either direct oxidation or mediated oxidation with oxidants. Due to the electron-rich nature of Fe-biochar, it can also serve as the catalysis for the mediated oxidation process for the pollutants immobilization. Reactive oxygen species, including $OH^{\cdot}$, $O_2^{-\cdot}$, $SO_4^{-\cdot}$, and $^1O_2$, can be generated based on the catalytic impact of Fe-biochar with oxidants (O_2, H_2O_2, persulfate), leading to the oxidative transformation and degradation of pollutants (Mao et al., 2019, Wang et al., 2020b, Zhang et al., 2020d). The mediated oxidation started from the electron donation from Fe-biochar to the oxidants, and thus, the contributing moiety was similar to the reduction process (i.e., surface oxygen-containing functional groups and defects on biochar and reduced-state iron) (Li et al., 2020f, Mao et al., 2019). For example, Wang et al. (2017a) produced Fe-biochar from sewage sludge, and the electron from Fe(II) on iron and hydroxyl on biochar dominated the catalytic degradation process. A similar contradiction in the pyrolysis condition of Fe-biochar was also found for the mediated oxidation process, *i.e.,* the oxidative transformation of carbon and reductive transformation of iron, and some studies indicated that a mild temperature might benefit the mediated oxidation process (Yi et al., 2020). In addition, the electron-shuttling capacity of Fe-biochar also contributed to the electron transfer from pollutants to oxidants, leading to the facilitated degradation process (Liang et al., 2021b).

Fe-biochar might also directly oxidize the pollutants through an electron-accepting process. Biochar itself could act as the oxidant during the reaction, and higher pyrolysis temperature facilitates the formation of oxidative quinone on the biochar surface (Zhang et al., 2019d). High valence Fe (Fe(IV)) on the Fe-biochar might also contribute to the direct oxidation with the co-existed oxidants, and the low pyrolysis temperature of Fe-biochar led to this oxidation pathway (Liang et al., 2021c).

In summary, different targeted applications required different Fe-species based on the immobilization mechanisms. The sorption, reduction, and oxidation process can be caused by various Fe species, while the controlling approach for the wanted immobilization route with precise Fe species control is still questionable. Moreover, the combined redox reaction with the sorption or immobilization process by each specific Fe species during the pollutants removal process remained cloudy.

2.4 Fe-contained Binary Metal-modified Biochar

The binary oxide-modified biochar, such as Fe-Mn biochar, has become a research hot spot in recent years. Fe and Mn were the widely selected binary oxide among different metals due to their similar radius, properties, valence states, and outstanding redox reactivity (Liu et al., 2021a, Wen et al., 2020, Zhang et al., 2014). Similar preparation methods, including co-pyrolysis (Ding et al., 2022, Yin et al., 2020a, Zoroufchi Benis et al., 2022) and post-impregnation (Chu et al., 2022, Qu et al., 2023), were used to prepare Fe-Mn biochar. The main mineral species were binary oxide (e.g., $FeMn_2O_4$) (Chen et al., 2020b, Hao et al., 2020, Yang et al., 2022b) or separated Fe and Mn minerals (Zoroufchi Benis et al., 2022), according to the different preparation approaches. One-step impregnation usually leads to a high possibility of the formation of binary oxide, while the separated loaded process causes the formation of separated oxide (Zoroufchi Benis et al., 2022).

It was found that Fe-Mn biochar showed a higher reactivity than Fe-biochar and Mn-biochar with a similar metal amount(Xu et al., 2023b). The synergistic effect between Fe and Mn through the valence transformation was the key to the higher redox reactivity of Fe-Mn biochar (Chen et al., 2020b), and the higher sorption affinity with the Mn doping also contributed to the immobilization process (Sun et al., 2023, Yang et al., 2022b). In addition, the formation of the Mn-metal complex was widely found during the immobilization of heavy metals(Tan et al., 2023), and thus, less Fe-metal complex was formed on the Fe surface, causing efficient electron exchange with pollutants and Fe. Besides, Lin et al. (2017) indicated that the strong oxidation capacity of the Mn oxide might contribute to the direct oxidative transformation of pollutants (As(III)) and facilitate its afterwards immobilization with the Fe phase.

Other Fe-contained binary metal-modified biochar, including Fe-Cu biochar (Gholami et al., 2020, Liang et al., 2021a, Qi et al., 2022), Fe-Ni biochar (Xing et al., 2022, Yin et al., 2020b), and Fe-Ca biochar (Zhang et al., 2023), was also studied. The synergistic effect mainly came from the higher charge transfer efficiency, regulated electronic structure, enhanced electron exchange, and the selectivity to targeted pollutants of Fe-metal structure (Hou et al., 2021, Qi et al., 2022, Xing et al., 2022). However, the research progress of this Fe-metal biochar is still limited and far less than Fe-Mn biochar

The precise mineral speciation control within the Fe-contained binary metal-modified biochar is still limited currently due to the complexity of the potential transformation process. Moreover, the underlying mechanisms for the pollutants' immobilization still lack solid evidence to support, especially considering the synergy impact of Fe and other metals. More studies about the formation species and related immobilization mechanisms are highly recommended.

2.5 Research Gap

Based on the literature review, sustainable research had been conducted on Fe-biochar production and evaluated its potential capacity for the remediation process. However, some crucial problems for precise Fe-biochar fabrication and the related immobilization mechanisms are still unclear.

Firstly, precise control of Fe speciation on Fe-biochar is still questionable. Fe on the Fe-biochar contained varying valence states, crystal structure, binding parameters, and particle size based on the production process. How to precisely control the Fe speciation on biochar will be critical to maximizing its value during environmental decontamination. Secondly, the relationship between the redox reactivity and Fe speciation on the Fe-biochar is unknown, and the redox reactivity of Fe-biochar will be vital for the redox-related immobilization, including Cr(VI) and As(III) immobilization. Thirdly, the combined redox and immobilization mechanisms during toxic metals removal by Fe-biochar need further evaluation, especially considering different Fe speciation. Fourthly, the impact of the Fe mineral crystallinity on its redox and immobilization performance with biochar remains unclear since current studies widely overlooked the potential impact of the crystallinity on the electron transfer mechanisms. Above the sole Fe control on Fe-biochar, binary metal-modified biochar has obtained an increasing interest in recent years, while the control of the Fe speciation on the binary metal-modified biochar is limited in the existing literature, and its impact on pollutants removal is also uncertain. Moreover, the impact of hydrothermal treatment on Fe speciation also needs a more detailed study, especially within the Fe-contained binary mineral-modified biochar. The impact of introduced hydrothermal treatment on Fe speciation needs further investigation. Last but not least, Fe-biochar's potential economic benefits and removal efficiency compared to the commercial/modified ZVI also needs a systematical evaluation to evidence the advantage and large-scale application potential of Fe-biochar.

This cutting-edge research aims to inform next-generation engineered Fe-biochar production for sustainable environmental remediation and carbon neutrality. The objective is to unravel the precise Fe speciation control on the Fe-biochar for the target pollutants immobilization process *via* addressing the above-mentioned research gaps.

Chapter 3 Impact of Fe Species on the Electroactive Nature of Fe-Biochar for the Redox-induced Pollutants Immobilization

3.1 Introduction

Toxic element contamination in the water matrix is recognized as a global environmental problem (Miranda et al., 2022, Yin et al., 2019). Among different toxic elements, the anionic metal(loid)s, including both chromium (Cr) and arsenic (As), have attracted more attention due to the varying speciation, high toxicity, carcinogenicity, and mobility (Smedley and Kinniburgh 2002, Xu et al., 2020e). Cr and As predominately exist in two oxidation states, Cr(VI)/Cr(III) and As(V)/As(III), and one valence state (Cr(VI) and As(III)) has higher mobility, solubility, and toxicity than the other one (Fei et al., 2022, Wang et al., 2022b). Therefore, driving the redox reaction (*i.e.,* reduction and oxidation) to change the speciation of Cr/As becomes a promising strategy. Various approaches, such as electrochemical, photo-electrochemical, biological treatment, and redox processes accelerated by electroactive materials, have been employed (Ghoreishian et al., 2021, Yin et al., 2019, Zuo et al., 2021). Among these technologies, Fe-biochar, an electroactive material produced *via* scalable pyrolysis of naturally occurring Fe-rich biomass waste, has been widely investigated (Kamali et al., 2021, Yu et al., 2021). Due to its facile synthesis, wide availability of raw materials, the advantage for circular bioeconomy, and a spectrum of iron speciation (Tian et al., 2021b, Zeng et al., 2020, Zhou et al., 2021), Fe-biochar can be a sustainable and practical alternative for the redox-related remediation of As- and Cr-containing wastewater.

Iron is widely recognized as the overarching redox-active moiety in Fe-biochar. Different iron speciations, which can be affected by the temperature-dependent carbothermal reduction process, can support various redox-related remediation processes (Feng et al., 2020, Qiu et al., 2020). The low-valent (*e.g.*, Fe(0) and Fe(II)) and high-valent iron (*e.g.,* Fe(III) and Fe(IV)) would preferably drive reduction (Wei et al., 2021) and oxidation (Liang et al., 2021d, Tian et al., 2020) reactions, respectively. The carbon phase (biochar) in Fe-biochar is generally considered as the support substrate to disperse iron particles or additives to fabricate the iron speciation, but it could also provide considerable electron reactivity (Li et al., 2020a). The electron-donating (*e.g.*, phenolic −OH) and electron-withdrawing (*e.g.*, quinoid and carbonyl) functionalities on the biochar surface could mediate the reducing or oxidizing reactions depending on the physicochemical characteristics (Xu et al., 2020f, Zhong et al., 2019), while they have been largely overlooked in the existing literature. For instance, recent studies have claimed that As(III) oxidation by Fe-biochar can be attributed to newly formed $^{\bullet}$OH radicals with electrons donated from Fe(0), whereas the possible role of oxidative biochar produced at a high temperature (700 °C) has not been elucidated (Liu et al., 2020b, Yang et al., 2020a). Based on a recent machine learning study about Cr(VI) immobilization by Fe-biochar, the surface functionality of carbon is believed to play a more significant role than iron in determining the overall effectiveness (Zhu et al., 2022b), while there is a lack of supportive evidence and mechanisms from experimental investigations.

The holistic redox state of the Fe-biochar, determined by the reactivity from both iron and carbon phases, is crucial to the preferred redox reaction. Only considering one composition of Fe-biochar (*i.e.,* iron or carbon) might misunderstand the integral redox state, leading to limited efficiency and even a potential risk (*e.g.,* As(V) reduction to more toxic As(III)). However, the current research failed to articulate the integral redox state of Fe-biochar in view of the contrasting transformation of iron and carbon's speciation. With a rising temperature, reductive phenolic and hydroxyl may evolve into oxidative quinoid and carbonyl (Klüpfel et al., 2014), while oxidative ferric may transform into reductive ferrous (Qiu et al., 2020). Meanwhile, the redox reaction between biochar and iron would also be responsible for the variable redox state of Fe/C sites (Xu et al., 2020e, Xu et al., 2021e). Besides, it is often overlooked that the disparity of crystallinity/aromaticity may change the redox performance of Fe/C (Aeppli et al., 2019a, Sun et al., 2018b). Little information is available for scrutinizing the impact of the crystallization/graphitization process on Fe-biochar's holistic redox state and performance.

In addition to the inherent redox properties of the Fe-biochar, the redox condition of the polluted water matrix also affect the transformation of As/Cr. The introduction of the O_2 might generate the reactive oxygen species (ROS), especially hydroxyl radical ($^\bullet$OH), with the support of carbon material (Fang et al., 2015) or Fe(II) (Zhang et al., 2020b). The formed ROS can cause either oxidation or reduction process, thus altering the redox transformation of As/Cr (Zhong et al., 2019). Water matrix normally contains a wide range of the O_2 from anoxic to oxic (Stein et al., 2021, Zhang et al., 2020b, Zhong et al., 2021a), while there is still no sufficient study evaluated the performance of Fe-biochar under different water redox conditions. Moreover, the relationship between the inherent redox properties of Fe-biochar and the redox condition of the water matrix during the pollutants transformation is also unknown.

In this study, I hypothesize that the redox transformation of As/Cr was controlled by the inherent redox properties of Fe-biochar and the redox condition of the water matrix, and the former was mainly governed by Fe/C speciation and crystallinity. To testify this hypothesis, a series of Fe-biochar with tuneable Fe/C speciation were designed and fabricated *via* a novel two-step pyrolysis at different temperatures to adjust the integral redox reactivity. Batch redox reactions were performed under both anoxic and oxic conditions in simulated wastewater to obtain insight into the transformation mechanisms of Cr/As with Fe-biochar. Through multiple advanced characterization, electrochemical analyses, and experimental techniques, we deliberated the vital roles of Fe/C in the rational design of Fe-biochar with high redox reactivity for environmental remediation.

3.2 Materials and Methods

3.2.1 Preparation of Fe-biochar

Raw biomass, the local yard waste collected from the EcoPark in Hong Kong, was crushed to pass through a 120-mesh sieve (particle size < 0.125 mm) before pyrolysis. Yard waste was selected as the biomass feedstock based on its low ash content with limited impact on the Fe speciation transformation. The first pyrolysis process of biomass without iron could regulate the redox moiety and graphitization degree of formed biochar (Sun et al., 2018b, Zhang et al., 2018b, Zhang et al., 2019d), and different biochar properties could alter the iron properties during the second pyrolysis process with iron (Xu et al., 2021d). Four temperatures (*i.e.,* 400, 550, 700, and 850 °C) were first used to prepare the pristine biochar (*i.e.,* BC400, BC550, BC700, and BC850) through slow pyrolysis of the yard waste in a N_2 atmosphere for 1 h with a ramping rate of 10 °C min^{-1} (Xu et al., 2021d). The suspension of biochar and Fe^{3+} was obtained by mixing 10 g of the biochar with a 100-mL $FeCl_3$ solution in a glass beaker (Fe concentration of 10 g L^{-1}, Fe-to-biochar ratio of 1:10 based on the Fe concentration prepared from natural Fe-rich biomass) (Yu et al., 2021), which was then stirred at 200 rpm for 24 h. The mixtures were dried at 60 °C for over 72 h, ground and sieved again for homogeneity, and then stored in a dry container before its second pyrolysis. These mixtures were named as BC400-Fe, BC550-Fe, BC700-Fe, and BC850-Fe, respectively.

Two temperatures, 400 °C and 850 °C, were selected as the second pyrolysis temperature to produce the Fe-biochar with different Fe/C speciation and redox reactivity. A high temperature (850 °C) could support the formation of low-valent iron (*e.g.,* Fe(0)), while low temperature (400 °C) would probably result in high-valent iron (*e.g.,* Fe_2O_3) (Qiu et al., 2020). Meanwhile, distinct crystallinity of both carbon and iron phases was expected to be formed at low and high temperatures, considering that a higher temperature could facilitate the iron crystallization and carbon graphitization process (Sun et al., 2018b). It is worth noting that the surface moieties on the biochar could be further changed due to the iron-carbon interactions and pyrolysis reactions, especially at a high temperature. The ramping rate was set as 10 °C min^{-1} and the pyrolysis duration was 1 h. The resultant Fe-biochar were denoted as BCX-Fe-Y, where X and Y are the first pyrolysis temperature (400–850 °C) and second pyrolysis temperature (400 or 850 °C), respectively. Chemicals used in this study were of analytical grade (**Appendix A**).

3.2.2 Redox-related transformation and immobilization of pollutants with Fe-biochar

Batch experiments of Cr(VI) reduction and As(III) oxidation were carried out in simulated wastewater to evaluate the redox-related transformation and immobilization of both As(III) and Cr(VI) by Fe-biochar. Briefly, 0.1 g of Fe-biochar sample was added into a 100-mL solution containing Cr(VI) or As(III) at an initial concentration of 30 mg L^{-1}, which was prepared by dissolving a pre-determined amount of $NaAsO_2$ or K_2CrO_4 in simulated wastewater (44 mg L^{-1} KH_2PO_4, 23 mg L^{-1} NH_4Cl, 14 mg L^{-1} $CaCl_2$, 90 mg L^{-1} $MgSO_4 \cdot 7H_2O$, 1.3 g L^{-1} NaAc, and 0.3 mL L^{-1} trace element solution, see **Appendix A**) (He et al., 2019). The concentration of pollutants was based on the possible concentration in wastewater (Fu et al., 2021b, He et al., 2019). The solution pH was set as ~6.5 by adding an appropriate HCl or NaOH. Both anoxic and oxic situations were conducted to simulate different redox conditions in the water matrix. For the anoxic reaction, all solutions were purged with ultrapure nitrogen (99.999%) for over two hours first (dissolved oxygen concentration below 0.3 mg L^{-1}), and the biochar samples were also deoxygenated under vacuum. The reactors were sealed after adding all solutions and Fe-biochars, and the mixtures were mechanically shaken at 250 rpm for 48 h until apparent equilibrium was reached. For the oxic reaction, a wide-mouth reactor was used to ensure the interaction with O_2 (dissolved oxygen concentration over 8.0 mg L^{-1}), and the reaction time and the shaking speed were similar to the anoxic reaction. Both anoxic and oxic reactions were conducted at 25 °C and covered with aluminium foil to avoid the possibility of a photochemical reaction. All the experiments were performed in triplicate, and the total Cr(VI) reduction amount and As(III) oxidation amount by Fe-biochar were calculated based on the newly formed Cr(III) and As(V), respectively. After the 48 h redox reaction between the Fe-biochar and pollutants (*i.e.,* Cr(VI) or As(III)), these mixtures were filtered through a 0.45-μm membrane filter to collect the filtrates and solids.

For Cr(VI) reduction, a part of the collected filtrates was immediately analyzed for the concentration of total Cr (Cr(Total)) by an inductively coupled plasma optical emission spectroscopy (ICP-OES, SPECTROBLUE) after acidic digestion with concentrated HNO_3. Cr(VI) concentration was determined by the diphenyl-carbohydrazide spectrophotometric method (Xu et al., 2020f). The concentration of Cr(III) in the solution was calculated by the difference between the total Cr and Cr(VI) concentrations in the solution. Given that both Cr(VI) and Cr(III) existed on the solid, XPS analysis was used to classify Cr(VI) and Cr(III) proportion on the solids. Cr2p was divided into $2p_{3/2}$ orbitals of Cr(III) (~575.5 eV), $2p_{3/2}$ orbitals of Cr(VI) (~582 eV), $2p_{1/2}$ orbitals of Cr(III) (~587.5 eV), and $2p_{1/2}$ orbitals of Cr(VI) (~591 eV), respectively, to obtain the proportion of Cr(III) and Cr(VI) on the solids (results were shown in **Table C1**)(Xu et al., 2021e, Xu et al., 2020f). The total Cr(VI) reduction amount was calculated based on the Cr(III) amount in both the solution and the solid (**Eq. 3.1**).

$$C_{Red} = \frac{\mathrm{Cr(III)}_e + \alpha[\mathrm{Cr(Total)}_0 - \mathrm{Cr(Total)}_e]}{m_{Fe-biocha}} \qquad \textbf{Eq. 3.1}$$

where $\mathrm{Cr(Total)}_0$ was the initial concentration of Cr(Total), all in Cr(VI) speciation, 60 mg L^{-1}; $\mathrm{Cr(Total)}_e$ and $\mathrm{Cr(III)}_e$ were the concentrations of Cr(Total) and Cr(III) after 48-h redox reaction, respectively; α was the proportion of Cr(III) on the solid phase obtained from XPS analysis; $m_{Fe\text{-}biochar}$ was the concentration of the Fe-biochar, 1 g L^{-1}. C_{Red} was the total reduction amount of Cr(VI) by the Fe- biochar, mg g^{-1}.

Similarly, the As(III) oxidation amount was determined by the As(V) concentration in both the solution and the solid. Arsenic speciation in the solution (*i.e.*, As(III) and As(V)) was determined by the combined use of arsenic speciation cartridge (Metal Soft) and ICP-OES (Chen et al., 2017, Meng et al., 2000). Theoretically, arsenate (As(V)) in the samples was removed by the cartridge at controlled pH (4–9), while arsenite (As(III)) remained in the filtered water. Therefore, the As(III) concentration was directly detected by ICP-OES, and the proportion of As(V) was determined by the difference between the total As and As(III). The proportion of As(V) and As(III) on the solid was determined by XPS analysis for the As 3d spectra, which was divided into As(V) (45.2–45.8 eV) and As(III) (44.0–44.8 eV), respectively (Yu et al., 2021). The total As(III) oxidation amount was calculated based on the As(V) amount in both the solution and solid (**Eq. 3.2**).

$$C_{Ox} = \frac{\mathrm{As(V)}_e + \beta[\mathrm{As(Total)}_0 - \mathrm{As(Total)}_e]}{m_{Fe-biochar}} \qquad \textbf{Eq. 3.2}$$

where As(Total)$_0$ was the initial concentration of As(Total), all in As(III) speciation, 60 mg L^{-1}; As(Total)$_e$ and As(V)$_e$ were the concentrations of As(Total) and As(V) after 48-h redox reaction, respectively; β was the proportion of As(V) on the solid phase obtained from XPS analysis; m$_{\text{Fe-biochar}}$ was the concentration of the Fe- biochar, 1 g L^{-1}. C$_{\text{Ox}}$ was the total oxidation amount of As(III) by the Fe- biochar, mg g^{-1}.

3.2.3 Electrochemical analysis

The redox capacity of the pristine biochar and Fe-biochar was quantified by the mediated electrochemical reduction (MER) and oxidation (MEO) methods (Klüpfel et al., 2014). All the electrochemical analysis was performed in an anoxic glove box, and all the Fe-biochar were placed under a vacuum in the antechamber to remove the adsorbed O$_2$. The Fe-biochar (1 g L^{-1}) was suspended in glass vials containing a neutral (pH= ~6.5−7.0) anoxic buffer solution (0.1 mol KCl and 0.01 mol 3-morpholinopropane-1-sulfonic acid). For the MEO test, a 9-mL glassy carbon cylinder served both as the working electrode and electrochemical reaction vessel. The Ag/AgCl electrode served as the reference electrode, and the counter electrode was a coiled platinum wire with porous glass wrapped outside. The working potential was set at 0.61 V, and

ABTS (2, 2′-azino-bis (3-ethyl-benzthiazoline-6-sulfonic acid) diammonium salt) was selected as the mediator for the MEO reaction. The Fe-biochar suspensions were spiked into the cells, and the electron-donating capacity (EDC) of the composites was determined by integrating the current peak response with triplicates (**Eq. 3.3**). For the MER test, Ziv (Zwitterionic viologen 4,4′-bipyridinium-1,1′-bis(2-ethylsulfonate)) was chosen as the mediator, and the working potential was set at -0.49 V. Electron-accepting capacity (EAC) of the composites was determined by the triplicated MER test (**Eq. 3.4**) with a similar testing procedure as the MEO test. The detailed procedures can be found in previous publications (Zhang et al., 2018b, Zhang et al., 2019d).

$$EDC = \frac{\int \frac{I_{Ox}}{F} dt}{m_{Fe-biochar}} \qquad \textbf{Eq. 3.3}$$

$$EAC = \frac{\int \frac{I_{Red}}{F} dt}{m_{Fe-biochar}} \qquad \textbf{Eq. 3.4}$$

where I_{Red} and I_{Ox} [A] are the corrected electrochemical currents in the MER and MEO tests, respectively; F [s A (mol e^-)$^{-1}$] is the Faraday constant; and $m_{Fe\text{-}biochar}$ [g] is the mass of the Fe-biochar sample. Electron exchange capacity (EEC = EAC + EDC) [mmol e^- (g Fe-biochar)$^{-1}$] was calculated to evaluate its total capacity to accept and donate electrons. The ratios of EDC/EEC and EAC/EEC were determined to identify the redox state of the Fe-biochar. The relationship between the EDC/EAC and the related pollutants transformation amount under either oxic or anoxic environment were also evaluated to study the electron transfer mechanisms during the redox process of Cr(VI) and As(III) with Fe-biochar.

3.2.4 Characterization for Fe-biochar

Iron speciation in the different Fe-biochar was characterized by quantitative X-ray diffraction (Q-XRD), and crystallinity of iron minerals was determined by an XRD pattern as well as a transmission electron microscopy (TEM) with selected area electron diffraction patterns (SAED) and energy-dispersive X-ray spectroscopy (EDX). A Fourier transform infrared spectrometer (FTIR) and an X-ray photoelectron spectroscopy (XPS) was used to identify the surface functionality of the Fe-biochar. Meanwhile, the carbon structure was evaluated through XRD, Raman spectroscopy, and XPS analysis. Elemental analysis and surface area analysis was also conducted. Moreover, the electron paramagnetic resonance (EPR) analysis was also performed with 5,5-dimethyl-1-pyrrolidine N−Oxide (DMPO) under the oxic environment to evaluate the formation of radicals by different Fe-biochars. Details of the characterization methods were available in **Appendix B**.

3.3 Results and Discussion

3.3.1 Redox-related transformation of Cr(VI) and As(III) in simulated wastewater

Distinct redox transformation of Cr(VI) and As(III) was found by different Fe-biochars under both oxic and anoxic environments (**Table 3-1**). For the Cr(VI) reduction and immobilization process, Fe-biochar showed a more potent Cr(VI) reducing capacity than pristine biochar in both anoxic (4.93−20.51 > 2.41−4.11 mg g^{-1}) and oxic environments (5.27−22.40 > 2.70−4.42 mg g^{-1}). Due to the enhanced reductive transformation, Fe-biochars also performed a better total Cr removal capacity than pristine biochar (4.94−21.02 > 3.05−4.09 mg g^{-1}, **Table C1** and **Figure C1, Appendix C**). In particular, the BCX-Fe-400 with a lower second-step pyrolysis temperature obtained a higher amount of Cr(VI) reduction (7.50−22.40 mg g^{-1}, 0.43−1.29 mmol e^{-} g^{-1}) than the BCX-Fe-850 produced by a higher temperature

(4.93−6.58 mg g^{-1}, 0.28−0.38 mmol e^{-} g^{-1}). Interestingly, a slightly higher reduction amount of Cr(VI) by low-temperature BCX-Fe-400 was found in the oxic environment than the anoxic environment, while no apparent difference can be detected for pristine biochar and high-temperature BCX-Fe-850. The introduction of O_2 might lead to the formation of ROS with either carbon or iron, which would affect the redox transformation of Cr(VI) by Fe-biochars.

Table 3-1 Redox performance of Fe-biochar for pollutants transformation in simulated wastewater

Biochar	Cr(VI) reduction amount (mg g^{-1})		As(III) oxidation amount (mg g^{-1})	
	Anoxic	Oxic	Anoxic	Oxic
BC400	4.11 ± 0.38	4.41 ± 0.34	0.88 ± 0.26	1.44 ± 0.25
BC550	3.51 ± 0.33	3.82 ± 0.19	2.06 ± 0.43	2.10 ± 0.31
BC700	2.41 ± 0.21	2.70 ± 0.14	1.66 ± 0.35	1.95 ± 0.11
BC850	2.67 ± 0.28	3.34 ± 0.05	1.73 ± 0.06	2.03 ± 0.17
BC400-Fe-400	14.78 ± 0.44	15.20 ± 0.70	6.95 ± 0.18	9.51 ± 0.14
BC550-Fe-400	20.51 ± 0.45	22.40 ± 0.07	7.49 ± 0.17	10.46 ± 0.22
BC700-Fe-400	12.33 ± 0.43	13.96 ± 0.41	5.72 ± 0.31	7.63 ± 0.40
BC850-Fe-400	7.49 ± 0.37	7.89 ± 0.22	5.82 ± 0.19	7.69 ± 0.59
BC400-Fe-850	6.58 ± 0.15	5.44 ± 0.12	8.75 ± 0.36	10.52 ± 0.19
BC550-Fe-850	5.51 ± 0.62	5.47 ± 0.13	7.98 ± 0.15	9.77 ± 0.05
BC700-Fe-850	4.93 ± 0.17	5.27 ± 0.12	7.29 ± 0.20	8.54 ± 0.43
BC850-Fe-850	6.45 ± 0.29	5.96 ± 0.13	5.54 ± 0.28	6.65 ± 0.29

A contrasting performance was found for the As(III) oxidation and immobilization process (**Table 3-1** and **Figure C-2, Appendix C**). More effective As(III) oxidation was achieved by the BCX-Fe-850 compared with the BCX-Fe-400 (5.54−8.75 mg g^{-1} > 5.72−7.49 mg g^{-1}) under the anoxic situation, while a similar or even higher oxidation performance can be found for BCX-Fe-400 under oxic status (7.63−10.46 mg g^{-1}) compared with BCX-Fe-850 (6.65−10.52 mg g^{-1}). The As(III) oxidation process resulted in the effective As removal by Fe-biochar in both oxic and anoxic environment (up to 9.44 mg g^{-1}), and the pristine biochar showed limited As removal capacity with a lower As(III) oxidation amount (0.89−2.10 mg g^{-1}, **Figure C2, Appendix C**). The existence of O_2 had a noticeable impact on the increase of As(III) oxidation by all Fe-biochar, and a higher raise was found with low-temperature BCX-Fe-400 (1.87−2.97 mg g^{-1}, 0.05−0.08 mmol e^- g^{-1}) than BCX-Fe-850 (1.11−1.79 mg g^{-1}, 0.03−0.05 mmol e^- g^{-1}), which might be related to the effective formation of ROS with BXC-Fe-400 (Liang et al., 2021). EPR analysis supported this statement because a more apparent characteristic pattern of DMPO-OH adduct could be found on BCX-Fe-400 compared with BCX-Fe-850 and BCX (**Figure 3-1**).

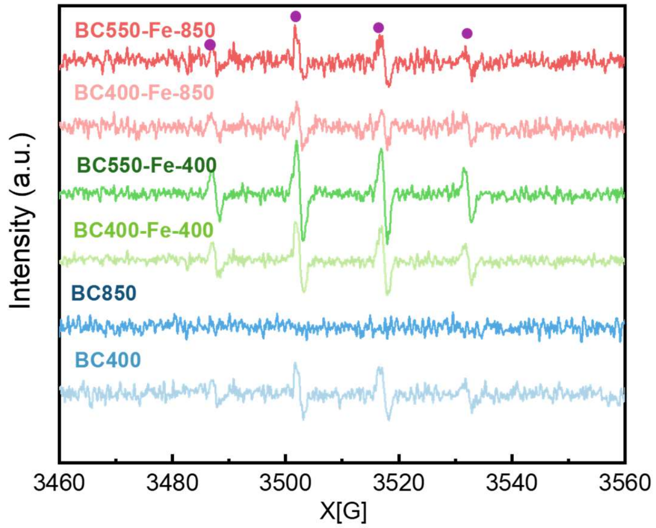

Figure 3-1 EPR spectra of DMPO-OH adducts at the initial 2 min

In short, the BCX-Fe-400 was most effective for Cr(VI) reduction, while the BCX-Fe-850 was most suitable for As(III) oxidation in the anoxic conditions. Under the oxic conditions, BCX-Fe-400 was more sensitive to activate O_2 with the formation of ROS compared with

BCX-Fe-850, and an enhanced As(III) oxidation and Cr(VI) reduction was thus found with BCX-Fe-400. The elevated redox-related transformation process led to the enhanced immobilization performance by Fe-biochar, and distinct redox transformation should be related to the redox moiety of Fe-biochar for either donating or accepting process.

3.3.2 Redox reactivity of Fe-biochar determined the pollutant's transformation

According to the electrochemical analysis, the Fe-biochar showed a high EEC of 0.87−1.82 mmol g^{-1} compared with the pristine biochar (0.56−1.04 mmol g^{-1}) (**Figure 3-2**). Reducing activity (EDC of 0.43−1.28 mmol g^{-1} and EDC/EEC up to 70.6%, **Figure 3-3**) was dominant for the Fe-biochar (BCX-Fe-400) produced at a lower second-step pyrolysis temperature. By contrast, a higher pyrolysis temperature (BCX-Fe-850) resulted in a strong oxidization potential (EAC of 0.71−1.39 mmol g^{-1} and EAC/EEC of 63.7−76.2%). The varying holistic redox state determined the redox performance during the transformation of pollutants. The higher direct electron-donating capacity of low-temperature BCX-Fe-400 caused a potent Cr(VI) reducing capacity, while As(III) oxidation was more effective by the oxidative BCX-Fe-850. Moreover, the higher electron-donating capacity of BCX-Fe-400 might facilitate the reductive formation of $^{\bullet}HO_2$, H_2O_2, and $^{\bullet}OH$ with the O_2 (**Eqs. 3.5 − 3.7**), and these ROS would cause the enhanced redox transformation of either As(III) (**Eqs. 3.8 − 3.10**) or Cr(VI) (**Eqs. 3.11**) with a successive single/double-electron transfer process (Dehghani et al., 2016, Kim et al., 2015, Zhong et al., 2019). The elevated formation of $^{\cdot}OH$ by BCX-Fe-400 further evidenced this mediated electron transfer process under the oxic environment (**Figure 3-1**).

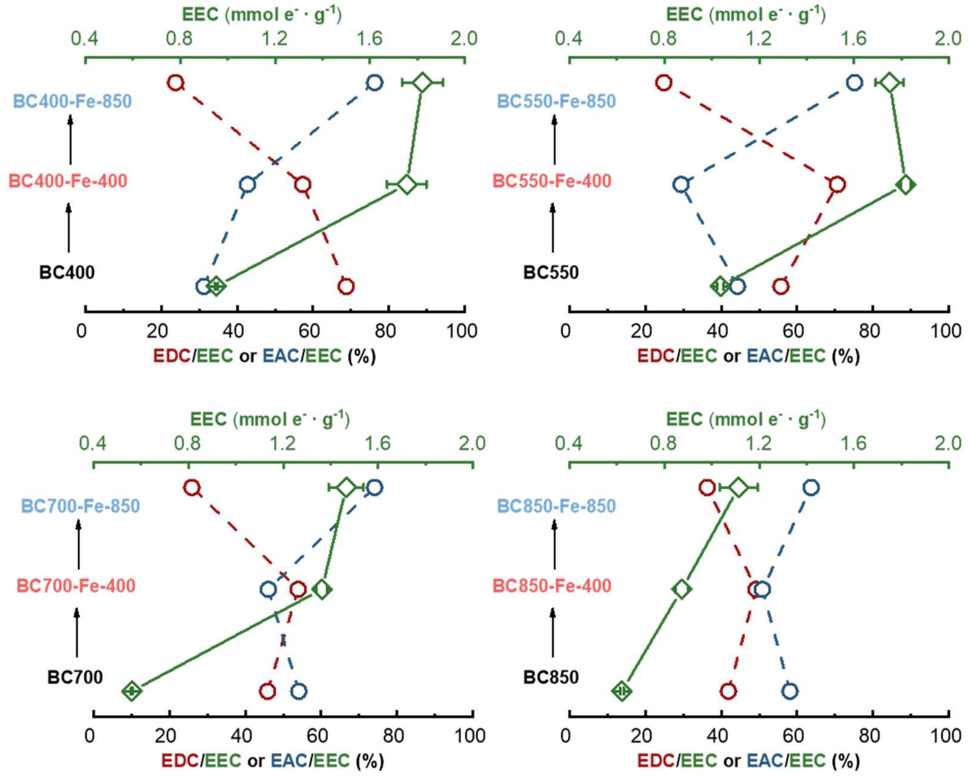

Figure 3-2 Changes of electron exchange capacity (EEC) (green) and relative contributions of EAC (blue) or EDC (red) to the total EEC

$$O_2 + H^+ + e^- \rightarrow \cdot HO_2 \qquad \textbf{Eq. 3.5}$$

$$\cdot HO_2 + H^+ + e^- \rightarrow H_2O_2 \qquad \textbf{Eq. 3.6}$$

$$e^- + H_2O_2 \rightarrow OH^- + \cdot OH \qquad \textbf{Eq. 3.7}$$

$$As(III) + H^+ + {}^{\bullet}OH \rightarrow As(IV) + H_2O \qquad \textbf{Eq. 3.8}$$

$$As(IV) + H^+ + {}^{\bullet}OH \rightarrow As(V) + H_2O \qquad \textbf{Eq. 3.9}$$

$$As(III) + 2H^+ + H_2O_2 \rightarrow As(V) + 2H_2O \qquad \textbf{Eq. 3.10}$$

$$2Cr(VI) + 3H_2O_2 \rightarrow 2Cr(III) + 6H^+ + 3O_2 \qquad \textbf{Eq. 3.11}$$

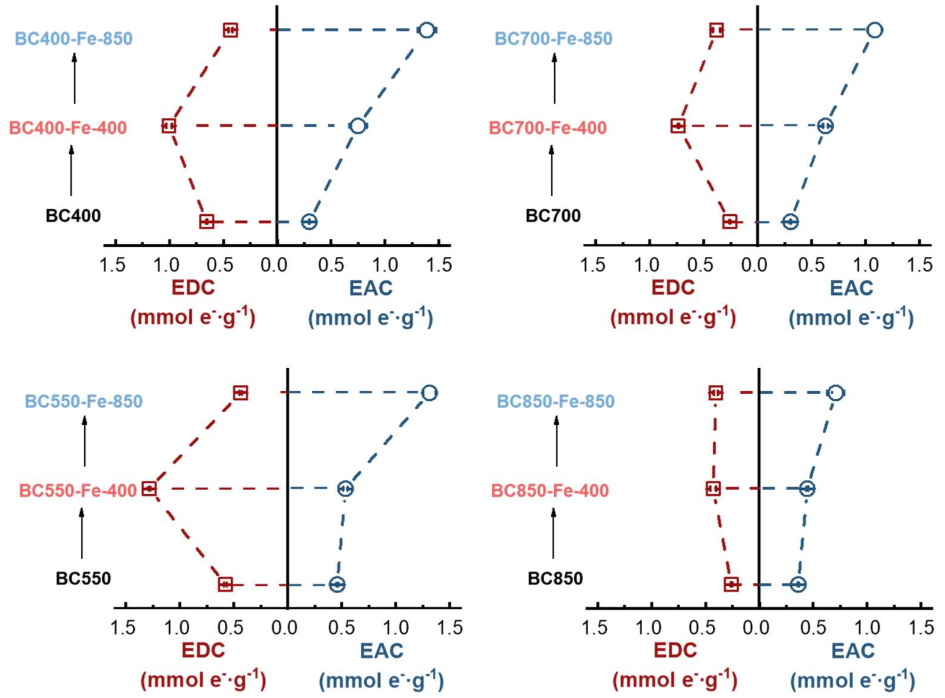

Figure 3-3 The electron-accepting capacity (EAC) (blue) and electron-donating capacity (EDC) (red) of the Fe-biochar produced from various pyrolysis temperatures

Overall, the transition of a reducing state (BCX-Fe-400) to an oxidizing state (BCX-Fe-850) of Fe-biochar can be ascribed to the transformation of both iron and carbon phases during the second-step pyrolysis. The production temperature of the carbon substrate could affect its redox activity. The Fe-biochar derived from the low-temperature biochar (BC400 and BC550, in the first-step pyrolysis) exhibited a much higher EEC (1.74−1.82 mmol g^{-1}) compared with that of high-temperature biochar (0.87−1.47 mmol g^{-1}). These results indicated that the redox reactivity of the Fe-biochar could be a function of the properties of biochar support through the regulation of Fe-speciation or its intrinsic redox reactivity. The roles of different moieties during the redox transformation on Fe-biochar were discussed separately in the following section.

3.3.3 Amorphous ferrous mineral determined the EDC of Fe-biochar

The iron minerals are customarily considered as the primary factor to the varied redox reactivity in Fe-biochar, and thus the transformation of Fe was first evaluated. The Fe content increased from 74.6–81.4 mg g^{-1} (BCX-Fe-400) to 84.6–90.0 mg g^{-1} (BCX-Fe-850) with an increasing pyrolysis temperature, probably due to the thermal decomposition of biochar under a high temperature (**Table C2, Appendix C**) (Qiu et al., 2020). Meanwhile, the Fe-speciation changed with the pyrolysis temperature based on the Q-XRD analysis of the Fe-biochar (**Figure 3-4** and **C3**). Amorphous-Fe (68.5–100%) and low-crystalline akaganeite (0–31.5%) were the primary Fe speciation on the Fe-biochar (BCX-Fe) after the wet-impregnation process. These iron minerals transformed into low-crystalline $FeCl_2$ (9.4–35.6%) and hematite (Fe_2O_3, 24.0–33.1%) under 400 °C, and then further converted into crystal magnetite (Fe_3O_4, 70.1–79.7%), wustite (FeO, 8.5–18.7%), and metallic-Fe (3.6–12.1%) at 850 °C (**Figure 3-4**). The TG-DTG analysis (**Figure C4**) identified that pyrolysis over 800 °C induced a carbothermal reduction process with a quick mass loss of the Fe-biochar (**Eqs. 3.12−3.14**), causing the formation of low-valent iron minerals.

$$6\ Fe_2O_3 + {\equiv}C \rightarrow 4\ Fe_3O_4 + CO_2 \uparrow \qquad \textbf{Eq. 3.12}$$

$$2\ Fe_3O_4 + {\equiv}C \rightarrow 6\ FeO + CO_2 \uparrow \qquad \textbf{Eq. 3.13}$$

$$2\ FeO + {\equiv}C \rightarrow 2\ Fe + CO_2 \uparrow \qquad \textbf{Eq. 3.14}$$

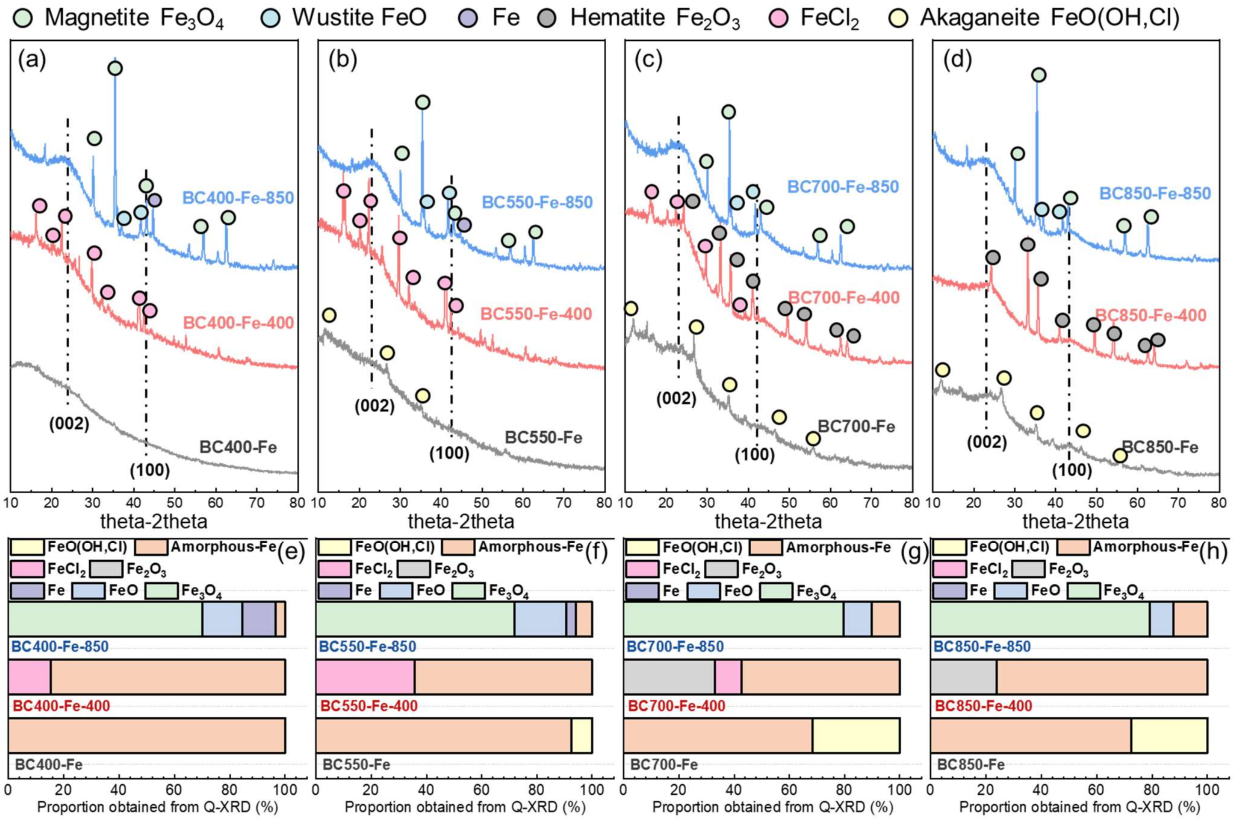

Figure 3-4 XRD patterns of the different Fe-biochar (a−d) and their Fe speciation obtained from Q-XRD analysis (e−f)

It should be noted that different carbon substrates also changed the composition of Fe minerals. About 15.2–35.6% $FeCl_2$ with no Fe_2O_3 was formed on the BC400-Fe-400 and BC550-Fe-400, while Fe_2O_3 (24.0%) was the only crystal iron mineral on the BC850-Fe-400. Under the high pyrolysis temperature of 850 °C, a higher amount of metallic-Fe(0) (3.6–12.1%) was formed in the BC400-Fe-850 and BC550-Fe-850, while there was no Fe(0) in the BC700-Fe-850 and BC850-Fe-850. This difference in speciation could be ascribed to the distinct properties of the carbon substrate produced by the first-step pyrolysis. Strong reducing capacity with higher EDC in the BC400 and BC550 was observed to induce the reduction of iron to a lower valence state, and the higher amount of volatile carbon in the low-temperature biochar might also facilitate iron reduction during the pyrolysis process (Shen 2015, Sun et al., 2019).

There was inconsistent variation in the reductive transformation of iron minerals and the reducing capacity of Fe-biochar. For instance, the BC400-Fe-850 contained the largest fraction of metallic Fe(0) and FeO, but it showed a limited EDC with a lower reducing capacity for Cr(VI). Meanwhile, the BC550-Fe-400 with no metallic Fe(0) showed the best electron-donating capacity for either direct Cr(VI) reduction or mediated As(III) oxidation with O_2. It has been widely recognized that the metallic Fe(0) can theoretically offer more electrons than other iron minerals under similar conditions; however, it failed to act as the primary electron-donating moiety in this study. The transition of iron morphology and crystallinity might contribute to the unexpected changes in the reducing capacity of the Fe-biochar.

Homogeneous distribution of Fe element was found on the surface of the BCX-Fe before pyrolysis, and it would gradually transform to the mineral grains during the second-step pyrolysis (**Figure 3-5a** and **Figure C5, Appendix C**). A lower temperature of 400 °C turned the iron minerals into spherical particles with a small diameter (1–5 μm), which further transformed into a crystal phase with an enlarged diameter (10–20 μm), possibly due to the mineral aggregation under a high temperature of 850 °C (**Figure 3-5**). The TEM-EDX mapping with SAED patterns (**Figure 3-5b** and **Figure C6, Appendix C**) illustrated that amorphous/low-crystalline iron grains (ring-structure without light spots in the SAED patterns) with an average length lower than 50 nm attached on the carbon edge of the BCX-Fe-400 (Nadejde et al., 2015). With the increase in pyrolysis temperature, crystal iron particles (light spots in the SAED patterns) (Nadejde et al., 2015) with a longer length (0.5–1 μm) aggregated and attached on the BCX-Fe-850, collaborating with the SEM results and Q-XRD analysis (**Figure 3-5**). Meanwhile, the average crystallite size in the BCX-Fe-850 (27.7–30.4 nm) was larger than that in the BXC-Fe-400 (3.0–9.0 nm) based on the Scherrer formula and XRD analysis (**Table C3, Appendix C**).

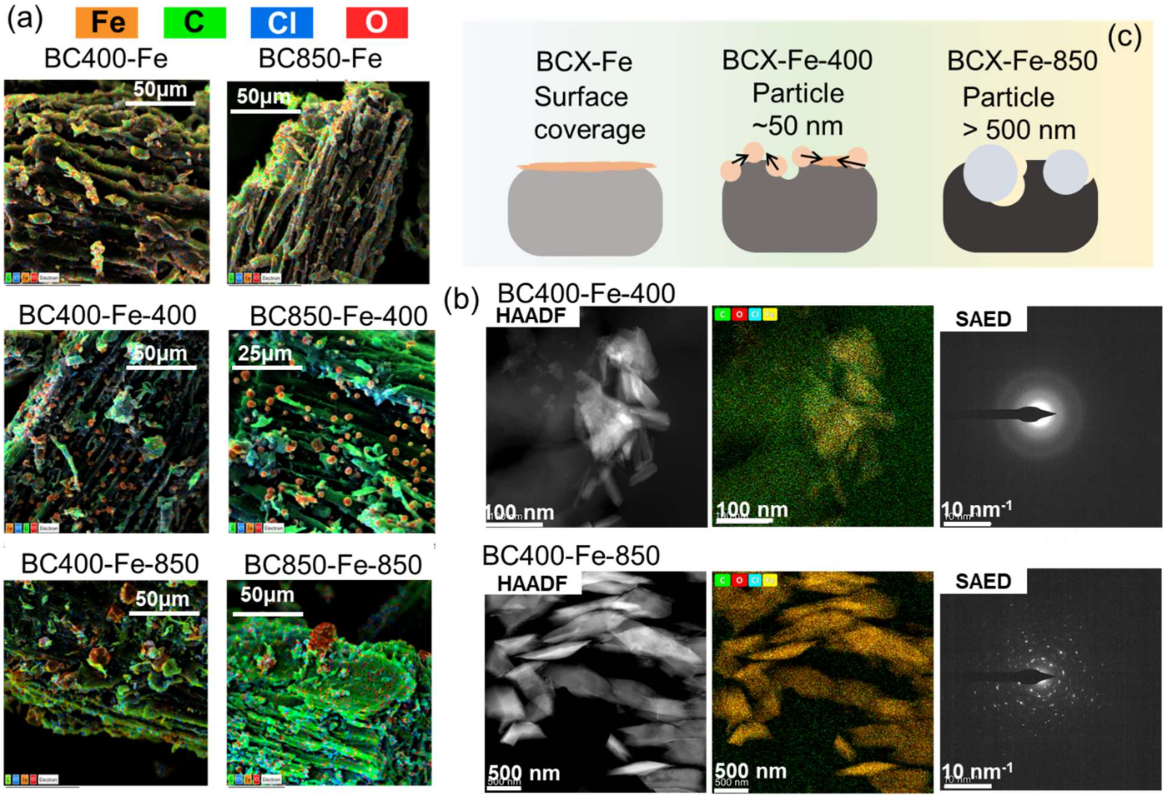

Figure 3-5 SEM-EDX images (a) and TEM-EDX images with corresponding SAED patterns (b) of the selected Fe-biochar. Transformation of the iron particles during the impregnation and pyrolysis processes (c)

The small particle sizes and high iron solubility of these amorphous ferrous minerals could facilitate electron delivery through released Fe ions or interfacial reactions (Aeppli et al., 2018, Heinrich et al., 2021, Xie et al., 2020), accounting for the potent reducing capacity of low-temperature Fe-biochar (*i.e.,* BCX-Fe-400), especially for BC400-Fe-400 and BC550-Fe-400 with a high amount of amorphous/low crystalline ferrous minerals. In contrast, fewer electrons could be offered by large-size crystal iron minerals on the high-temperature Fe-biochar (*i.e.,* BCX-Fe-850), probably due to limited surface contact with the reactant and a highly stable crystal structure (Aeppli et al., 2019a, Aeppli et al., 2018). XPS analysis revealed that a higher decrease of Fe(II) was found in BC400-Fe-400 (8.8%) than BCX-Fe-850 after Cr(VI) removal (3.6−5.9%) (**Figure C7**), evidencing the higher availability of Fe(II) with smaller particle size and lower crystallinity for the electron-donating process (Xu et al., 2022b). To further evaluate the critical role of amorphous ferrous minerals on EDC, seven additional Fe-biochar were produced *via* pyrolysis of the BC850-Fe at 400–700 °C (**Figure C8**). High-temperature carbon substrate (BC850) might contain a limited degree of reductive functionality (*e.g.,* hydroxyl), while pyrolysis under 700 °C might only allow the limited formation of crystal iron minerals through carbothermal reduction based on the TG analysis (**Figure C4**). A positive linear relationship between the EDC and amorphous Fe content was observed, corroborating the importance of amorphous ferrous minerals on the electron-donating process (**Figure C8**).

Consequently, the amorphous ferrous mineral in BCX-Fe-400 dominated the electron-donating process, which was related to the direct Cr(VI) reduction (**Eq. 3.15**) and mediated As(III) oxidation with O_2 (**Eqs. 3.16-3.20**). However, the oxidation capability of Fe-biochar for pollutants cannot be fully justified by the transition of Fe speciation and crystallinity. The strongest direct oxidation capability for As(III) was found in the BC400-Fe-850 with abundant metallic Fe(0) and FeO but a limited amount of ferric oxide. Besides, the BC850-Fe-400 with the largest fraction of ferric oxide (hematite, Fe_2O_3) only exhibited a slightly higher EAC compared with its carbon substrate (BC850) (**Figure 3-2**). It was, thus, speculated that carbon/oxygen moieties were mainly responsible for the differences of oxidizing capability among Fe-biochar.

$$\text{Cr(VI)} + 3{\equiv}\text{Fe(II)} \rightarrow \text{Cr(III)} + 3{\equiv}\text{Fe(III)} \qquad \textbf{Eq. 3.15}$$

$$O_2 + H^+ + \equiv Fe(II) \rightarrow {}^{\bullet}HO_2 + \equiv Fe(III)$$ **Eq. 3.16**

$$\cdot HO_2 + H^+ + \equiv Fe(II) \rightarrow H_2O_2 + \equiv Fe(III)$$ **Eq. 3.17**

$$\equiv Fe(II) + H_2O_2 \rightarrow OH^- + {}^{\bullet}OH + \equiv Fe(III)$$ **Eq. 3.18**

$${}^{\bullet}HO_2 + \equiv Fe(III) \rightarrow O_2 + \equiv Fe(II) + H^+$$ **Eq. 3.19**

$$\equiv Fe(III) + H_2O_2 \rightarrow {}^{\bullet}HO_2 + H^+ + \equiv Fe(II)$$ **Eq. 3.20**

3.3.4 Critical role of O-functionality for the redox reactivity of Fe-biochar

The biochar surface functionality was extensively altered following the pyrolysis with Fe at different temperatures. The FTIR spectra (**Figure 3-6a** and **Figure C9, Appendix C**) described a rich surface functionality in the BC400-Fe-400, including carboxyl (−COO, 1376 and 1453 cm^{-1}), hydroxyl (−OH, ~3400 cm^{-1}), quinoid (1614 cm^{-1}), and carbon-oxygen bonding (C−O, ~1255 cm^{-1}) (Clurman et al., 2020, Rajabi et al., 2021, Tian et al., 2019, Zhong et al., 2019). Compared with the pristine BC400, a narrowed gap between the peaks within 1300−1500 cm^{-1} (*i.e.*, symmetric and asymmetric vibrations of $-COO^-$) in the BC400-Fe-400 might indicate bidentate chelation between the carboxyl groups and iron ions (Deng et al., 2021, Sutton et al., 2015). A substantial amount of hydroxyl groups (−OH, ~3400 cm^{-1}) was found in the BC400-Fe-400 compared with the BC400, ascribed to biochar oxidation by ferric minerals (**Eq. 3.21**) and hydroxyl groups in amorphous iron minerals (Xu et al., 2020e). With further pyrolysis at a high temperature (850 °C), an apparent decrease of hydroxyl groups on the BC400-Fe-850 was observed due to the decomposition of iron hydroxides and −OH groups at high temperatures (Xu et al., 2020f, Zhang et al., 2019d). However, a noticeable boost of symmetric and asymmetric vibrations of carboxyl (1376 and 1459 cm^{-1}) was shown on the

BC400-Fe-850, indicating the enhanced oxidation of surface functionality associated with the reduction of Fe under a high pyrolysis temperature (**Eqs. 3.22−3.23**).

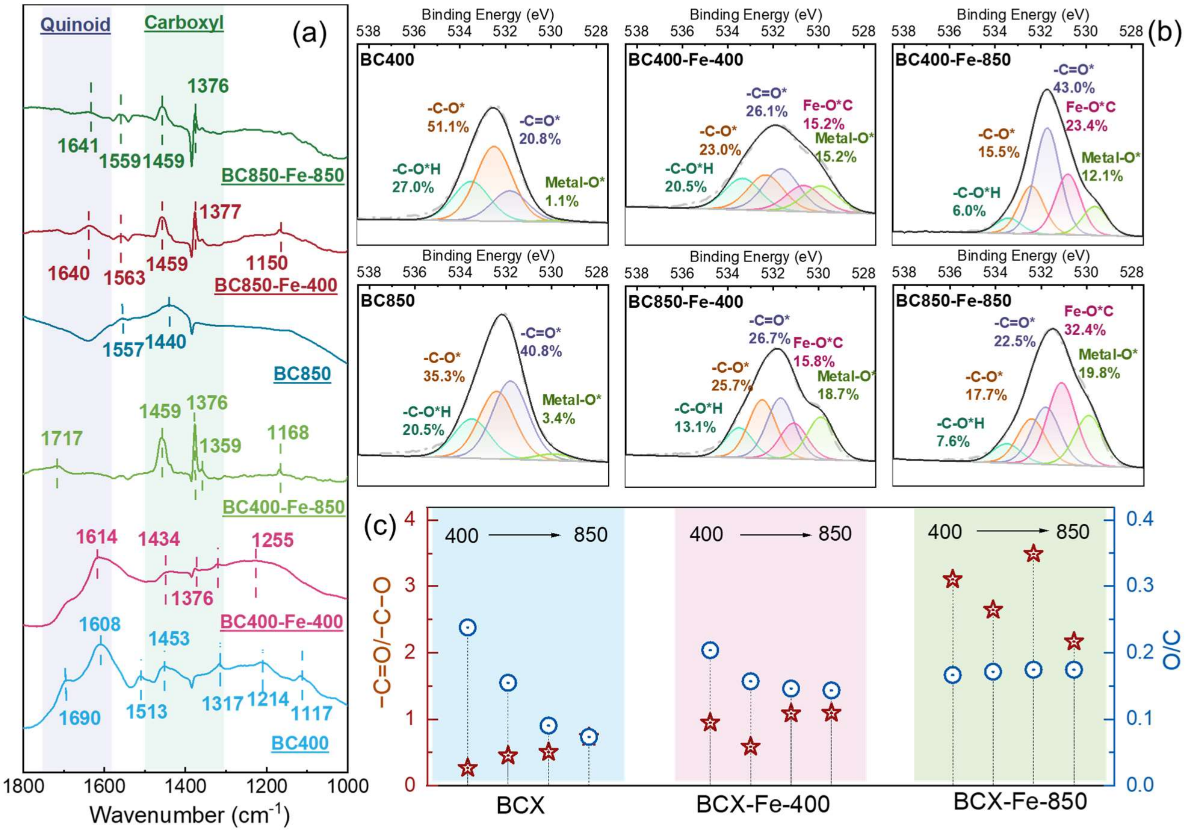

Figure 3-6 FTIR patterns (a), XPS spectrum of O1s (b), −C=O/−C−O ratio obtained from XPS analysis, and O/C ratio from EA analysis of Fe-biochar (c) (X = 400, 550, 700, and 850 with the order shown in the figures)

$$2Fe(OH)_3 + -CH_3 \rightarrow 2Fe(OH)_2 + -CH_2-OH + H_2O \qquad \textbf{Eq. 3.21}$$

$$4Fe(OH)_3 + -CH_2-OH \rightarrow 4Fe(OH)_2 + -COOH + 3H_2O \qquad \textbf{Eq. 3.22}$$

$$2Fe(OH)_2 + -CH_2-OH \rightarrow 2Fe + -COOH + 3H_2O \qquad \textbf{Eq. 3.23}$$

$$2Fe(OH)_3 + >CH_2 \rightarrow 2Fe(OH)_2 + >CH-OH + H_2O \qquad \textbf{Eq. 3.24}$$

$$2Fe(OH)_3 + >CH-OH \rightarrow 2Fe(OH)_2 + >C=O + H_2O \qquad \textbf{Eq. 3.25}$$

Although the pristine BC700 and BC850 contained limited O-moieties, peaks of hydroxyl (~3400 cm^{-1}), quinoid (1634−1640 cm^{-1}), and carboxyl (1458−1459 cm^{-1}) were still detected on the BC700-Fe-400 and BC850-Fe-400 (**Figure 3-6a** and **Figure C9, Appendix C**). The redox reactions between iron and carbon might facilitate the formation of O-moieties on the biochar surface (**Eqs. 3.24−3.25**) (Xu et al., 2020e), as evidenced by higher O/C ratios of the BC700-Fe-400 and BC850-Fe-400 (0.14−0.15) than the pristine biochar (0.07−0.09 for BC700 and BC850) (**Table S2** and **Figure 3-6c**). Compared with the pristine biochar produced at 850 °C (BC850), a larger amount of carboxyl (1376−1460 cm^{-1}) and quinoid (1638−1641 cm^{-1}) groups were formed on the BCX-Fe-850 (**Figure 3-6a** and **Figure C9, Appendix C**) with a higher O/C ratio (0.17 > 0.07, **Figure 3-6c**) due to the oxidation induced by iron. Moreover, semiquinone-type persistent free radicals (PFRs) with higher redox reactivity might be formed on the biochar with rich O-functional groups (**Eq. 3.26**) (Zhong et al., 2019). These surface functionalities could serve as the primary electron-accepting moieties, contributing to the higher oxidizing capacity of the BCX-Fe-850.

The redox state of the carbon was further scrutinized based on quantitative analysis of the O-moieties. The deconvoluted O1s XPS spectra (**Figure 3-6b** and **Figure C10, Appendix C)** demonstrated a decline of hydroxyl content in the BCX-Fe-400 (11.2−20.5%) and a further decrease to 6.0−18.0% on the BCX-Fe-850 in comparison to the pristine biochar (19.9−27.0%). Meanwhile, Fe−OC (12.3−37.1%, iron chelation with O-moiety) and metal−O (10.9−21.2%, mainly Fe−O) were newly formed on the Fe-biochar. The pristine biochar exhibited a limited oxidizing potential (−C=O/−C−O of 0.26−0.73), which was significantly improved (0.59−1.09 for BCX-Fe-400 and 2.12−3.49 for BCX-Fe-850) (**Figure 3-6c**) after pyrolysis with Fe at higher temperatures. In conclusion, the direct oxidation by the surface quinoid, carboxyl, or semiquinone-type PFRs was responsible for the higher As(III) oxidation by BCX-Fe-850 (**Eqs.**

3.27−3.29).

The transition of surface functionalities also indicated the limited contribution of the reductive O-moieties (*i.e.,* −OH or −C−O) for the direct reduction of Cr(VI) by Fe-biochar. However, the PFRs might be responsible for the electron-donating processes of Fe-biochar (**Eqs. 3.30−3.33**) (Zhao et al., 2018b, Zhong et al., 2019, Zhong et al., 2021b, Zhong et al., 2018), especially for BCX-Fe-850 with rich surface functionality. It was worth mentioning that the transition of the O-functionalities determined the redox performance of pristine biochar. The decrease of reductive O-moieties with the increase of oxidative functionalities (**Figure C10, Appendix C**) resulted in the decline of electron-donating performance (both Cr(VI) reduction and $^{\bullet}$OH formation, **Figure 3-1**) with an increase in As(III) oxidation amount.

$$2{>}C{=}O + {>}C{-}OH \rightarrow 2{>}C{-}O^{\bullet} + H^{+} + {>}C{-}O^{-}$$ **Eq. 3.26**

$$As(III) + 2H^{+} + {>}C{=}O \rightarrow As(V) + {>}CHOH$$ **Eq. 3.27**

$$2As(III) + 4H^{+} + {-}COOH \rightarrow 2As(V) + {-}CH_2{-}OH + H_2O$$ **Eq. 3.28**

$$As(III) + 4H^{+} + 2{>}C{-}O^{\bullet} + 2{>}C{-}O^{-} \rightarrow As(V) + 4{>}C{-}OH$$ **Eq. 3.29**

$$Cr(VI) + 3{>}C{-}O^{\bullet} + 3{>}C{-}O^{-} \rightarrow Cr(III) + 6{>}C{=}O$$ **Eq. 3.30**

$$O_2 + H^{+} {>}C{-}O^{\bullet} + {>}C{-}O^{-} \rightarrow {}^{\bullet}HO_2 + 2{>}C{=}O$$ **Eq. 3.31**

$${}^{\bullet}HO_2 + H^{+} + {>}C{-}O^{\bullet} + {>}C{-}O^{-} \rightarrow H_2O_2 + 2{>}C{=}O$$ **Eq. 3.32**

$$H_2O_2 + {>}C{-}O^{\bullet} + {>}C{-}O^{-} \rightarrow OH^{-} + {}^{\bullet}OH + 2{>}C{=}O$$ **Eq. 3.33**

3.3.5 Enhanced electron transfer by the graphitic carbon structure

By comparison of the relationship between the oxidative surface functionality and oxidizing capacity of biochars, a significant linear relationship with a steep slope of 6.1 (**Figure**

3-7a) between EAC and the carbon-oxygen double bond (*i.e.,* −C=O and chelated carboxyl /carbonyl /quinoid as C−OFe) was only observed for the BCX-Fe-850. This implied that the enhanced oxidation potential of the BCX-Fe-850 was possibly related to the graphitic crystallite, rich defects, and porous structure formed at a high temperature. Moreover, higher electron efficiency was also found on BCX-Fe-850 for the mediated oxidation of As(III) with O_2 compared with BC400-Fe-400 and BC550-Fe-400. Although the EDC of BCX-Fe-850 (0.38−0.44 mmol g^{-1}) was much lower than BC400-Fe-400 and BC550-Fe-400 (1.01−1.28 mmol g^{-1}), it can cause an approximate mediated oxidation amount (0.03−0.05 mmol g^{-1} *vs.* 0.07−0.08 mmol g^{-1}) with a higher electron efficiency (*i.e.,* percentage of the electron used for the mediating process, 7.3−11.0% > 6.2−6.8%), which might also relate to the properties of high-temperature-formed carbon.

A higher graphitization degree of Fe-biochar was found under a higher pyrolysis temperature with the emergence of typical graphite at $2\theta = 23°$ (002) and 43° (100) (**Figure 3-4a**) (Sun et al., 2018b). The XPS analysis (**Figure C11, Appendix C**) proved a higher −sp^2 C level on the BCX-Fe-850 (54.8−64.2%) compared with the BCX-Fe-400 (24.8−49.2%), again indicating the formation of a more graphitic structure after high-temperature pyrolysis. Both L_a (in-plane coherence length) and L_c (perpendicular size of the turbostratically stacked crystallites) (Sun et al., 2018b, Wang et al., 2021b) were elevated with increasing pyrolysis temperature (**Figure 3-7b**, and **Table C4, Appendix C**), reaffirming a high graphitization degree of the BCX-Fe-850. This would enhance the carbon conductivity for faster electron transfer and better expression of active redox sites (Sun et al., 2017, Sun et al., 2018b, Xu et al., 2019b). It should be noted that the −sp^2 C level, L_c, and L_a of the BCX-Fe-850 were even higher than those of the BC850 or BC850-Fe (46.6%, 1.10 nm, and 4.89 nm, **Figure 3-7b**), suggesting that co-pyrolysis with iron could further enhance the graphitization process of biochar.

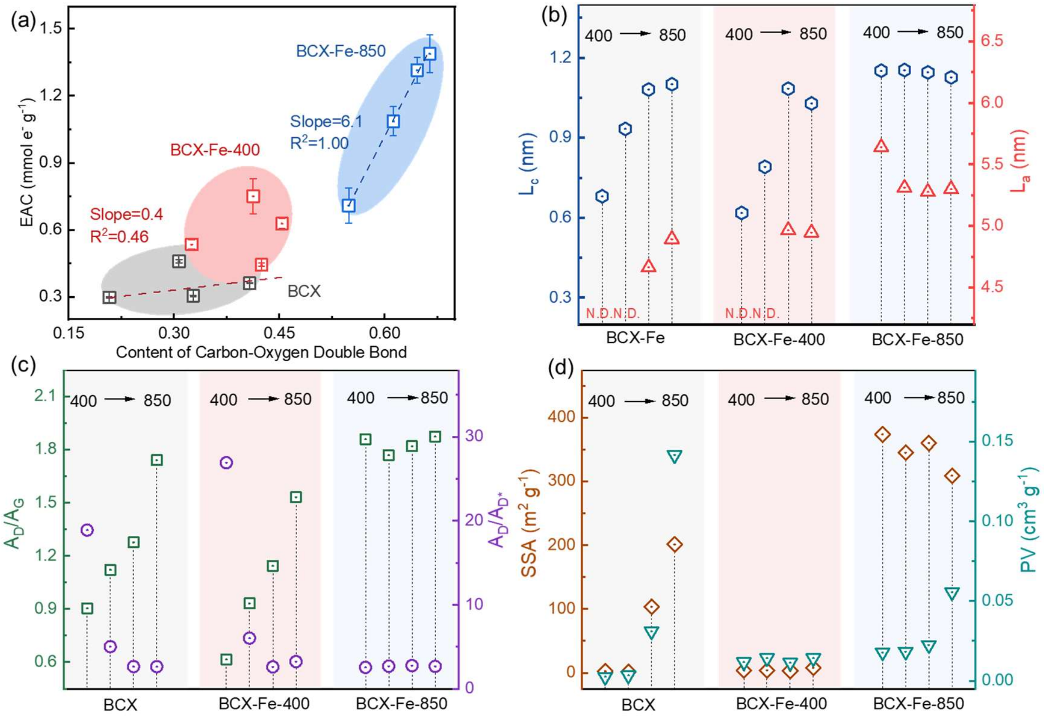

Figure 3-7 Relationship between the EAC and the content of carbon-oxygen double bond obtained from XPS analysis (a); the size of graphite crystallites (b); the ratios of A_D/A_G and A_D/A_{D^*} obtained from Raman spectra (c); or the textile properties including SSA and PV (d) of the different Fe-biochar (X = 400, 550, 700, and 850 with the order shown in figures)

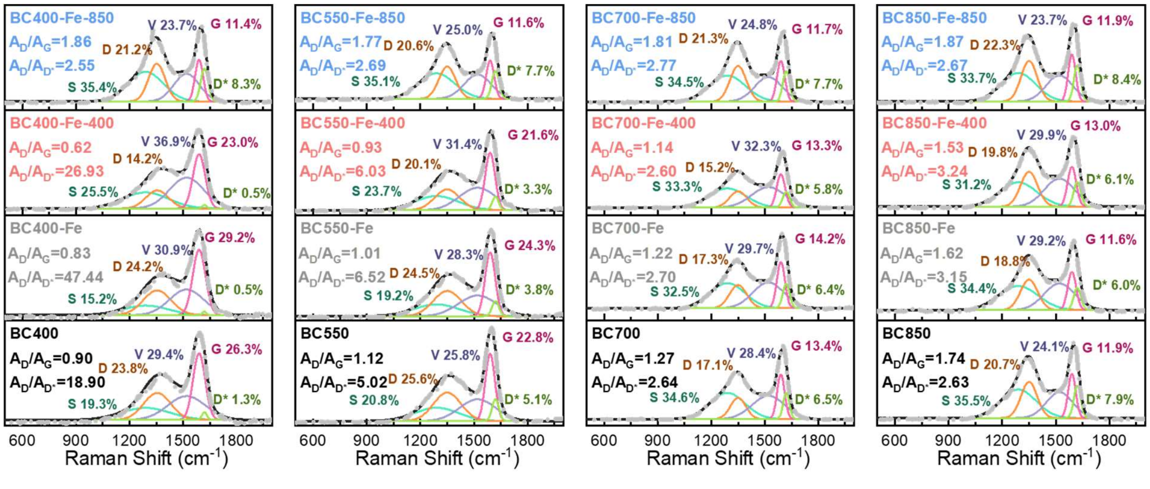

Figure 3-8 Raman spectra of the different Fe-biochar

Besides, more carbon defects were formed with higher pyrolysis temperatures based on the Raman spectra. Two prominent peaks, D-band at ~1350 cm^{-1} representing a disordered graphitic carbon structure and G-band at ~1560 cm^{-1} assigned to graphitic carbon with aromatic rings, were highlighted in all Fe-biochars, and the ratios of A_D/A_G were higher in the BCX-Fe-850 (**Figure 3-7c**) due to disorientation and corrugation of graphitic basal planes during co-pyrolysis with Fe (McDonald-Wharry et al., 2013). Similar A_D/A_G ratios of the BCX-Fe-400 and BCX-Fe suggested a limited change of carbon defects during low-temperature pyrolysis (**Figure 3-7c** and **3-8**). The S-band (~1290 cm^{-1}, transformation of sp^2 to sp^3 hybridization), V-band (~1510 cm^{-1}, amorphous carbon phase), and D^*-band (~1620 cm^{-1}, related to defect features) were also obtained after peak deconvolution (Yang et al., 2020b), and the ratios of A_D/A_{D^*} were used to evaluate the specific defect types (*e.g.*, boundaries, vacancies, or sp^3 carbon) of the different Fe-biochar (Xue et al., 2021, Yang et al., 2020b). Edge-type defects with a low A_D/A_{D^*} (2.59−2.77) were dominant on the BCX-Fe-850 (**Figure 3-7c**), which would enhance the electronic affiliation and mediating process, accounting for a more substantial oxidation potential. In contrast, the low-temperature Fe-biochar contained a higher A_D/A_{D^*}, inferring a different type of carbon defect (**Figure 3-8**). For instance, the BC400-Fe-400 (high A_D/A_{D^*} of 26.9) presented a distinct defect type of sp^3 hybridization or vacancies, which generally manifest a lower redox reactivity than edge-type defects (Eckmann et al., 2012, Yang et al., 2020b).

The porous structure affecting the accessibility of redox-active sites on the Fe-biochar (Li et al., 2020a) was also changed by the graphitization of different carbon substrates during co-pyrolysis with Fe. A low specific surface area (SSA) of 3.14−7.83 $m^2\ g^{-1}$ with a small pore volume (PV) of 0.011−0.014 $cm^3\ g^{-1}$ was found on the BCX-Fe-400 (**Figure 3-7d** and **Figures C12−C13, Appendix C**). An inferior porosity of the BC400 and BC550 (SSA of 1.53−2.43 $m^2\ g^{-1}$ and PV of 0.002−0.004 $cm^3\ g^{-1}$) corresponded to a low SSA of their respective Fe-biochar (BC400-Fe-400 and BC550-Fe-400). Nevertheless, pore blockage by newly formed iron minerals on a well-developed carbon structure (BC700 and BC850, with SSA of 104−201 $m^2\ g^{-1}$ and PV of 0.031−0.141 $cm^3\ g^{-1}$) also resulted in a lower SSA and PV for the BC700-Fe-400 and BC850-Fe-400. The BCX-Fe-400 was featured with macropores (> 50 nm) (30.8−55.7% of the total PV) (**Table C5**) as micropores and mesopores (< 50 nm) might be blocked by the small nano-sized iron grains according to the TEM images. Unlike the low-temperature produced Fe-biochar, a well-developed porous structure (SSA of 308−373 $m^2\ g^{-1}$ and PV of 0.018−0.056 $cm^3\ g^{-1}$) was formed on the BCX-Fe-850 (**Figure 3-7d**) with enriched small mesopore (2−10 nm) (60.0−68.2% of total PV) (**Table C5**). This structure might facilitate the exposure of redox-active sites and contribute to elevated electron transfer of BCX-Fe-850 than BCX-Fe-400 during either direct electron donating/accepting or mediated electron transfer with O_2.

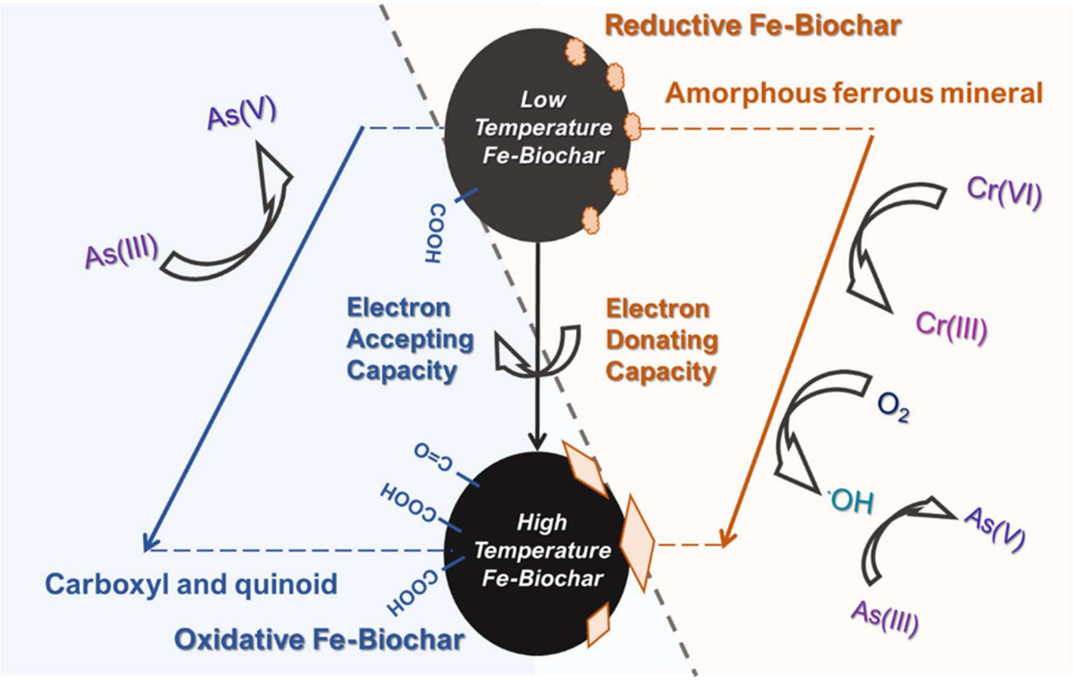

Figure 3-9 Graphical summarization of Chapter 3

3.4 Conclusions

Turning the iron mineral and biomass waste into remediation materials brings the "win-win" effect (*i.e.,* waste reuse and environmental remediation), making Fe-biochar a sustainable alternation for the electroactive materials for redox-related wastewater treatment. The results demonstrated that low-temperature Fe-biochar had a higher reducing capacity for Cr(VI) due to its higher EDC, predominantly offered by the amorphous/low-crystalline ferrous minerals. Besides, effective generation of ROS (*e.g.,* $^{\bullet}$OH) by the electron-donating moiety of low-temperature Fe-biochar was found, leading to the mediated redox-related transformation of pollutants under the oxic environment. By contrast, the oxidative surface functionalities on the high-temperature Fe-biochar caused the potent As(III) oxidation, but it failed to generate ROS sufficiently with O_2. Moreover, graphitic structure, edge-type defects, and the porous structure formed in high-temperature Fe-biochar could facilitate the electron transfer, leading to higher electron efficiency. The shift of primary redox moieties of Fe-biochar and the critical impact of carbon substrate on the overall redox reactivity should be considered during the production-design stage for effective wastewater treatment. Oxidative Fe-biochar can be directly used for the oxidation process during the pollutants control, while reductive Fe-biochar might be desirable for direct reduction or mediated electron transfer with O_2 (**Figure 3-9**).

Chapter 4 Impact of Fe Species on the Arsenic Immobilization and Redox-induced Transformation

4.1 Introduction

Arsenic (As) has been recognized as a global environmental concern due to its high toxicity towards human health and ecosystems (Shi et al., 2017, Song et al., 2020). Various decontamination methods, including bioremediation, sorption, precipitation, phytoremediation, and electro-coagulation, have been explored to control As pollution in recent years (Alka et al., 2021, Amen et al., 2020, Liu et al., 2020a, Weerasundara et al., 2021). Among these methods, iron-based materials (*e.g.*, ferric hydroxide (Guan et al., 2008), zero-valent iron (ZVI) (Das and Bezbaruah 2021, Sun et al., 2011, Yan et al., 2012a), nano-sized iron/iron oxide (Brockgreitens et al., 2020, Otero-González et al., 2020), and sulfide-modified ZVI (Singh et al., 2021)) have advantages in the immobilization of As *via* several mechanisms (*i.e.*, electrostatic interaction, monodentate/bidentate complexation, co-precipitation, and redox interactions). In particular, Fe-biochar composites prepared through the pyrolysis of iron-rich biomass or mixture of iron sources and selected biomass waste have attracted growing interest as an effective material for As decontamination (Bakshi et al., 2018, Sun et al., 2019, Zou et al., 2016). This low-cost and eco-friendly procedure can simultaneously realize environmental remediation along with carbon sequestration (Lehmann 2007a, b, Rawal et al., 2016, Shaheen et al., 2019b, Wang et al., 2020d).

The key process in the tailored design of Fe-biochar composites is to manipulate the desirable iron speciation during the pyrolysis process to achieve an optimal As immobilization capacity. It is generally acknowledged that reductive gases such as CO and CH_4 are formed during biomass pyrolysis (Chen et al., 2021b) due to the dehydration and decomposition of organic components (Xiao et al., 2018a), and these gas intermediates reciprocally reduce the co-present iron species from the +3 state (Fe_2O_3/$Fe(OH)_3$) to +8/3 (Fe_3O_4), +2 (FeO), and 0 (ZVI) (Shen 2015, Yang et al., 2008). The labile carbon fraction could also directly participate in the thermal reduction of iron oxide (Cazetta et al., 2016, Shen 2015, Sun et al., 2019). Furthermore, the elevated pyrolysis temperature may facilitate the transformation of amorphous/low-crystallinity iron hydroxides to crystalline iron minerals, even without the participation of carbon (Arinchtein et al., 2020, Francis et al., 2009, Yu et al., 2021). We speculate that labile-/amorphous-carbon with a higher degree of volatile compounds possibly induces the formation of lower-state iron, while stable-/graphitic-carbon may primarily change the crystallinity of newly formed iron species with limited change in the chemical state of iron. Both the reductive-Fe amount (*e.g.,* ZVI) (Bakshi et al., 2018, Fan et al., 2020) (related to the former process) and the crystallinity of Fe (Yu et al., 2021) (associated with the latter process) may have repercussions on the As removal capacity and mechanisms by the Fe-biochar composites. Therefore, controlling the fractions of amorphous-/labile-carbon and graphitic-/stable-carbon for the manipulation of iron speciation is probably conducive to fabricating fit-for-purpose Fe-biochar composites for As decontamination. However, current research often overlooks the well-planned design of Fe-biochar synthesis and there is still a lack of corresponding evidence about the influence of carbon species on iron speciation.

Iron species on the biochar govern the immobilization mechanisms and redox reactions of As. For reductive iron species such as ZVI, As(V) and As(III) reduction occurred on the surface of ZVI accompanied by the oxidation of iron (Ling and Zhang 2017), where the newly formed ferric oxide could also stabilize As (Ling and Zhang 2014, Yan et al., 2012b). Meanwhile, As(III) oxidation was found to be triggered by the intermediates formed through interactions between ZVI and O_2 (*e.g.*, Fe(IV) species or hydroxyl radicals (Pang et al., 2011)) at the solid-liquid interface. The resultant As(V) was subsequently immobilized through electrostatic interaction, complexation, and co-precipitation on the surface of iron minerals (Gubler and ThomasArrigo 2021, McCann et al., 2018, Yoon et al., 2016). Other Fe species (*e.g.*, amorphous ferric hydroxide) contributed to As immobilization *via* direct sorption and co-precipitation (Luo et al., 2018, Luong et al., 2018, Sowers et al., 2017, Yu et al., 2021), although As(III) oxidation may happen on the ferric mineral surface in the presence of Fe(II) (Gubler and ThomasArrigo 2021, Ona-Nguema et al., 2010). Moreover, redox-active moieties (*e.g.*, phenolic −OH and quinoid −C═O) on biochar may drive the redox transformation of As (Amen et al., 2020, Yuan et al., 2017). Direct oxidation of As(III) by the quinoid −C═O on the surface of biochar was reported (Niazi et al., 2018, Zhong et al., 2019), and electron-donating moieties could indirectly oxidize As(III) together with intermediates (*e.g.*, hydroxyl radicals) produced at the solid-liquid interface (Wang et al., 2021c, Zhong et al., 2019). The resultant As(V) was fixed on the iron phases through sorption and complexation (Alkurdi et al., 2019, Amen et al., 2020, Zhang et al., 2016a). The variations in both reaction sites and reaction sequence of redox and sorption may cause a “layered distribution” of As and Fe with different valence states. In this study, the unprecedented revealing of this hierarchical distribution of Fe-biochar composites with amorphous-Fe or reductive-Fe can provide insightful details about the As immobilization mechanisms.

Herein, a series of Fe-biochar composites with varying iron speciations was fabricated by controlling the co-pyrolyzed carbon phases (*i.e.,* ranging from labile-/amorphous-C to stable-/graphitic-C) and pyrolysis conditions. Immobilization capacities and mechanisms of these Fe-biochar composites for As(V) and As(III) were analyzed. The main objectives of this study were to scrutinize (i) the roles of different carbon fractions on regulating the Fe speciation in the Fe-biochar composites and (ii) the hierarchical depth distributions of As and Fe on the Fe-biochar composites after As immobilization. Using multiple characterization methods, including semi-quantitative Q-XRD, depth-profiling XPS analysis, Raman spectroscopy, and Pearson correlation coefficient (PCC) analysis, we unveiled the vital roles of carbon structures in manipulating the resultant Fe speciation and the distinct depth distributions of Fe and As provided direct evidence for the underlying mechanisms of As immobilization with the Fe-biochar composites.

4.2 Materials and Methods

4.2.1 Preparation of Fe-biochars

Detailed information about used chemicals is provided in **Appendix A**. A mixture of locally available light yard waste (LYW), collected from EcoPark in Hong Kong, was selected as the raw biomass. This biomass was crushed to pass through a 120-mesh sieve (particle size < 0.125 mm) and dried at 60 °C for 24 h before pyrolysis. Four biochars (BC400, BC550, BC700, and BC850) pyrolyzed at different temperatures (*i.e.,* 400, 550, 700, and 850 °C) were first prepared through the slow pyrolysis of LYW under N_2 atmosphere for 1 h with a ramping rate of 10 °C min^{-1}. These temperatures were selected to obtain biochars with varying carbon structures, including transition char, amorphous char, composite char, and graphitic char (Keiluweit et al., 2010).

The basic properties of the resulting biochars are summarized in **Figure D1** (**Appendix D**). Then, 20 g of each biochar was added into 200 mL $FeCl_3$ solution (10 g Fe L^{-1}) (biochar-to-Fe mass ratio as 10:1). Each mixture was stirred with a magnetic stirrer at 200 rpm for 24 h, dried at 60 °C for over 72 h, and then crushed to pass a 120-mesh sieve and stored in a dry container before its second pyrolysis. The resulting Fe-biochar composites were denoted as BCX-Fe, where X indicates the first pyrolysis temperature.

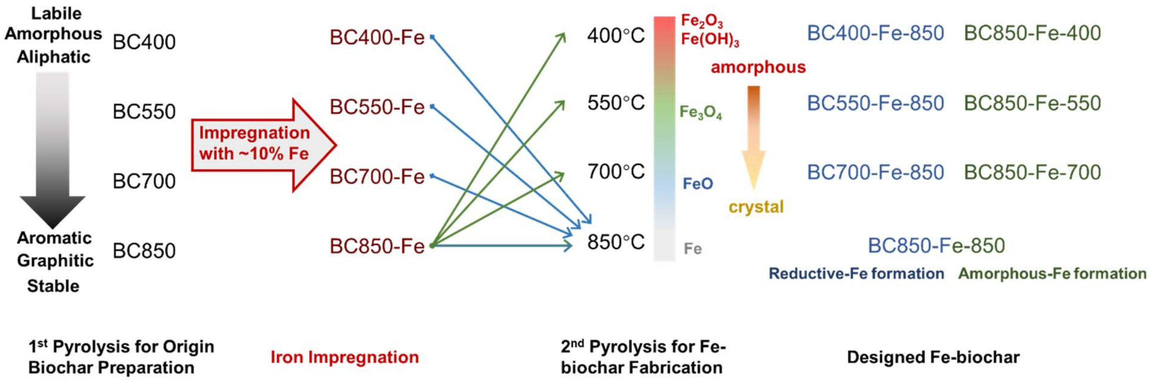

Figure 4-1 Designed procedures to fabricate the Fe-biochars

Two series of Fe-biochars (a total of 7) were designed. Firstly, four Fe-biochar composites (BC400-Fe, BC550-Fe, BC700-Fe, and BC850-Fe) were pyrolyzed at 850 °C for 1 h to evaluate the potential of varied carbon structures to form a diverse spectrum of reduced Fe species. A higher pyrolysis temperature over 800 °C can lead to the formation of ZVI with the reduction by biochar matrix (Sun et al., 2019). These four Fe-biochar composites with rich reductive-Fe were named BCX-Fe-850, where X indicates the first pyrolysis temperature. Secondly, to study the variations in the Fe species with initially stable-/graphitic-carbon, only BC850-Fe was used to fabricate the second series of Fe-biochars through pyrolysis at 400 °C, 550 °C, and 700 °C for 1 h. Due to the high stability of BC850, these three pyrolytic temperatures might result in relatively high contents of amorphous-Fe on the Fe-biochar composites with limited Fe valence transformation. This series of Fe-biochar composites with high amorphous-Fe contents were named BC850-Fe-X, where X was the second pyrolysis temperature. The design and preparation procedures for all seven Fe-biochar composites are summarized in **Figure 4-1**, and all these Fe-biochar composites were stored in a sealed container before further use.

4.2.2 Characterization

Detailed information about XRD, XPS, Raman spectrometer, Quantitative X-ray diffraction (Q-XRD), and other characterization methods can be found in **Appendix B**. Various Fe extraction methods were also conducted to quantify the Fe-speciation in the Fe-biochar composites, including the soluble-, reducible-, and extractable-Fe, which are explained in **Appendix B**.

4.2.3 As Immobilization mechanisms and hierarchical depth distributions

The immobilization capacities of all Fe-biochar composites for both As(V) and As(III) were evaluated through batch experiments. Briefly, 0.1 g of selected Fe-biochar composite was added into a 50 mL centrifuge tube containing 50 mL of 60 mg L^{-1} As(III) or As(V) solution, which was prepared by dissolving an appropriate amount of $NaAsO_2$ or $Na_2HAsO_4 \cdot 7H_2O$, respectively, in a 20 mM NaCl background solution. The resulting concentrations of As(III) or As(V) were within the maximum concentrations of As wastewater generated by smelting, metallurgical plant, or soil washing (Kim and Baek 2019, Li et al., 2021f, Tang et al., 2017). The above mixtures were shaken at 250 rpm under 25 ± 1 °C without light irradiation until equilibrium was reached (48 h). All experiments were conducted in triplicate, and the detection methods were similar to the **section 3.2.2**. The filtrates was analyzed for the concentration of As and Fe by ICP analysis, and the Fe(II) concentration was detected by UV-Vis at 510 nm wavelength after phenanthroline complexation (Luan et al., 2012, Xu et al., 2019c). The solids fractions after filtration were collected carefully and freeze-dried before further characterization, including Q-XRD, SEM-EDX, and XPS analysis with depth profiling.

The Pearson correlation coefficient (PCC) was calculated to assess the vector similarity between the physicochemical properties, Fe-speciation, and As removal capacities of Fe-biochars with the supplement of extra 11 Fe-biochar composites as elaborated in **Appendix D**. Depth profiling XPS analysis was used to evaluate the hierarchical depth distributions of As and Fe on typical Fe-biochar composites after As(III) or As(V) removal from the solution. An argon gun was used to etch the surface of Fe-biochar composites with a standard sputter rate before XPS analysis, and thus the distributions and chemical properties of As and Fe under the different depths of Fe-biochar composites could be evaluated. Detailed information about the depth profiling XPS can be found in **Appendix B**.

4.3 Results and Discussion

4.3.1 Manipulation of iron speciation in Fe-biochar

After the designed fabrication (**Figure 4-1**), the total Fe contents of the resulting seven Fe-biochar composites ranged between 81.4–90.0 mg g^{-1} (**Table D1, Appendix D**), and various Fe speciations were observed according to the XRD analysis (**Figure 4-2**). The use of a second pyrolysis temperature of 850 °C induced the formation of wustite (FeO) and magnetite (Fe_3O_4), while ZVI was only formed on BC400-Fe-850 and BC550-Fe-850 that contained abundant labile-C. Based on semi-quantitative Q-XRD analysis, the highest ZVI content of 10.9 mg g^{-1} was found in the BC400-Fe-850, which also had the lowest amorphous-Fe content (3.11 mg g^{-1}) (**Figure 4-2b**, **Figure D2**, and **Table D2, Appendix D**). These results implied that labile carbon in the low-temperature biochars promoted reductive-Fe formation (e.g., ZVI), whereas stable/graphitic carbon in the high-temperature biochars failed to act similarly an effective reducing agent.

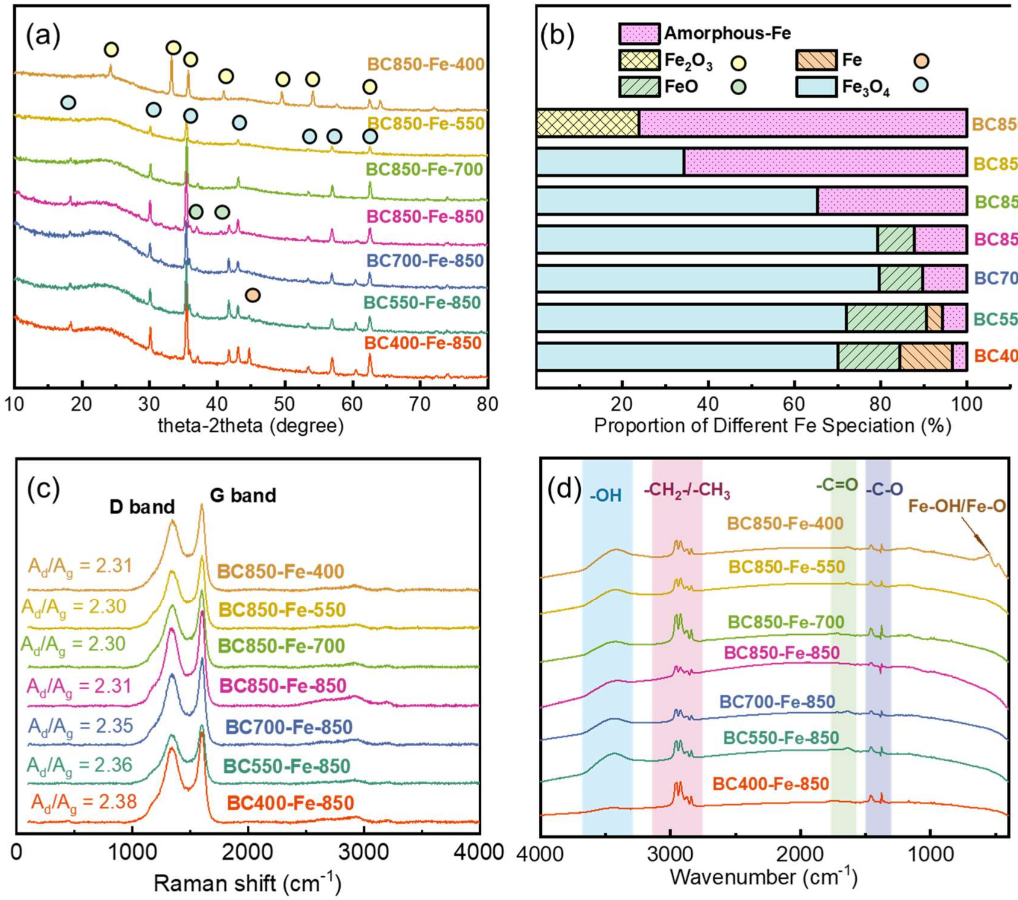

Figure 4-2 XRD patterns (a), semi-quantitative Q-XRD analysis (b), Raman spectra (c), and FTIR spectra (d) of different Fe-biochars (Hematite: Fe_2O_3; Magnetite: Fe_3O_4; Wustite: FeO; Metallic Fe: Fe).

For the Fe-biochar composites produced *via* pyrolysis of BC850-Fe at a lower pyrolysis temperature, only magnetite (Fe_3O_4) (BC850-Fe-700 and BC850-Fe-550) and hematite (Fe_2O_3)

(BC850-Fe-400) were formed, and no completely reductive-Fe species (*i.e.,* ZVI and FeO) were observed (**Figure 4-2a**). XPS analysis showed that these three Fe-biochar composites exhibited slightly higher Fe(III) proportion (28.0-30.2%) than those produced at 850 °C (25.5-27.6%) (**Figure D3**), further suggesting the limited Fe reduction process. According to the Q-XRD analysis, amorphous-Fe was the dominant Fe-species in BC850-Fe-400, and its amount decreased from 61.9 mg g^{-1} to 28.9 mg g^{-1} with the increase of second pyrolysis temperature to 700 °C (**Figures 4-2b**, **D2**, and **Table D2, Appendix D**). The amorphous-Fe contents in these Fe-biochar composites were much higher than those produced at second pyrolysis temperature of 850 °C (< 10.3 mg g^{-1}). These results indicated that graphitic-C only promoted the formation of high-valence Fe minerals and amorphous-Fe during the co-pyrolysis, which was supported by other recent findings (Qiu et al., 2020). SEM-EDX analysis revealed that similar and spherical Fe particles were attached on the biochar surface in all Fe-biochar composites despite the difference in Fe speciations (**Figure D4**), indicating that the surface morphology of these composites might play a less significant role in the As decontamination compared with Fe-species.

The driving role of carbon structures in tuning the Fe speciation was further verified using Raman spectroscopy, Fourier transform infrared spectroscopy (FTIR), and elemental analysis (EA). An increased value of A_d/A_g (*i.e.,* area ratio between D-band and G-band from Raman spectroscopy) from 1.62–1.82 to 2.36–2.38 (**Figure 4-2c** and **Figure D1**), a decreased surface functionality (**Figures 4-2d** and **Figure D1**), and a reduced O/C atomic ratio from 0.24 to 0.17 (**Figure D1** and **D5, Appendix D**) were observed after the pyrolysis of BC400-Fe/BC550-Fe at 850 °C. This corresponded to the transformation from labile-/aliphatic-C to stable-/aromatic-

C during the second pyrolysis at a higher temperature (Xiao et al., 2018a, Zhang et al., 2019d). This carbon transformation would facilitate the carbothermal reduction process (Shen 2015), leading to a higher content of reductive-Fe in the resulting Fe-biochar composites (**Figures 4-2a** and **b**). However, limited carbon transformation occurred on the graphitic-C (BC850-Fe) during its second pyrolysis, as indicated by the negligible changes in the A_d/A_g ratio and H/C atomic ratio (**Figures 4-2c**, **D1**, **D5**, and **D6**, **Appendix D**). The higher stability of BC850-Fe accounted for the limited carbon transformation and the high proportion of amorphous-Fe on BC850-Fe-700/550/400 with a limited reducing process. A peak of Fe–OH/Fe–O (~557 cm^{-1}) was observed on BC850-Fe-400 (**Figure 4-2d**), which could be attributed to amorphous iron hydroxide (Shi et al., 2019, Zhu et al., 2017b), further confirming its high content of amorphous iron. Despite their distinct carbon structures before the second pyrolysis process, all seven Fe-biochar composites displayed similar final carbon properties (*i.e.,* surface functionality) after variable carbon transformation processes (**Table D1**, **Figures 4-2c-d**, **D5**, and **D6**, **Appendix D**). This suggested that the impact of the carbon matrix may be secondary and indirect when comparing the As immobilization capacities of these Fe-biochar composites.

The porosity change of Fe-biochar composites also supported the different carbon transformations with Fe (**Table D1** and **Figures D7-D8)**. There was an apparent increase of the specific surface area (SSA) from 2.62–5.74 m^2 g^{-1} (BC400/550/700/850-Fe) to 308–373 m^2 g^{-1} (BC400/550/700/850-Fe-850) with an increased pore volume (PV) from 0.007–0.018 cm^3 g^{-1} to 0.018–0.056 cm^3 g^{-1} after the second pyrolysis at 850 °C. The carbothermal reduction process of Fe appeared to consume the labile fraction in the carbon matrix and thus formed a more porous structure in the resulting Fe-biochar composites. By contrast, there were limited transitions of SSA from 5.74 $m^2 g^{-1}$ (BC850-Fe) to 7.83–10.7 $m^2 g^{-1}$ (BC850-Fe-400/550/700) and PV from 0.018 $cm^3 g^{-1}$ to 0.014–0.020 $cm^3 g^{-1}$ on graphitic-C (BC850-Fe) after the second pyrolysis at lower temperatures, confirming the negligible transformation of stable/graphitic carbon with Fe. Overall, labile-/amorphous-C under a higher temperature in the second pyrolysis resulted in a Fe-biochar composite containing more reductive-Fe species (*e.g.*, ZVI), while stable-/graphitic-C substrate (BC850) produced more amorphous-Fe species after the second pyrolysis. This remarkable difference of Fe-speciation in these Fe-biochar composites would play a key role in governing variable As immobilization capacities.

4.3.2 Arsenic immobilization capacities

The immobilization capacities of the two series of Fe-biochar composites for both As(V) and As(III) were explored (**Figures 4-3a** and **4-3b**). Among those Fe-biochar composites containing more reductive-Fe (*i.e.,* BC400/550/700/850-Fe-850), BC400-Fe-850 showed the highest immobilization capacities for both As(V) (4.34 mg g^{-1}) and As(III) (7.72 mg g^{-1}). The As(V) and As(III) removal capacity declined markedly to 0.29 mg g^{-1} and 1.18 mg g^{-1}, respectively, when the first pyrolysis temperature was raised to 850 °C (BC850-Fe-850) (**Table 4-1**). Interestingly, Fe-biochar composites with more amorphous-Fe species (*i.e.,* BC850-Fe-400/550/700) also showed considerable removal capacities for both As(V) and As(III) despite the absence of ZVI. About 1.68–1.82 mg g^{-1} As(V) and 2.97–2.98 mg g^{-1} As(III) were removed by BC850-Fe-550 and BC850-Fe-700 after 48-h immobilization, and BC850-Fe-400 effectively immobilized 11.0 mg g^{-1} As(V) and 7.70 mg g^{-1} As(III) (**Table 4-1**). BC850-Fe-400 could provide an even higher As immobilization capacity than BC400-Fe-850 (4.34 mg g⁻

^{1} for As(V) and 7.72 mg g^{-1} for As(III)), which had the highest ZVI content. It is worth noting that pristine BC850 with high SSA (201 m^2 g^{-1}, **Figure D8**) and similar carbon properties (**Figure D1**) showed a limited immobilization capacity for both As(V) and As(III), indicating that the Fe species instead of carbon properties primarily determined the As removal performance.

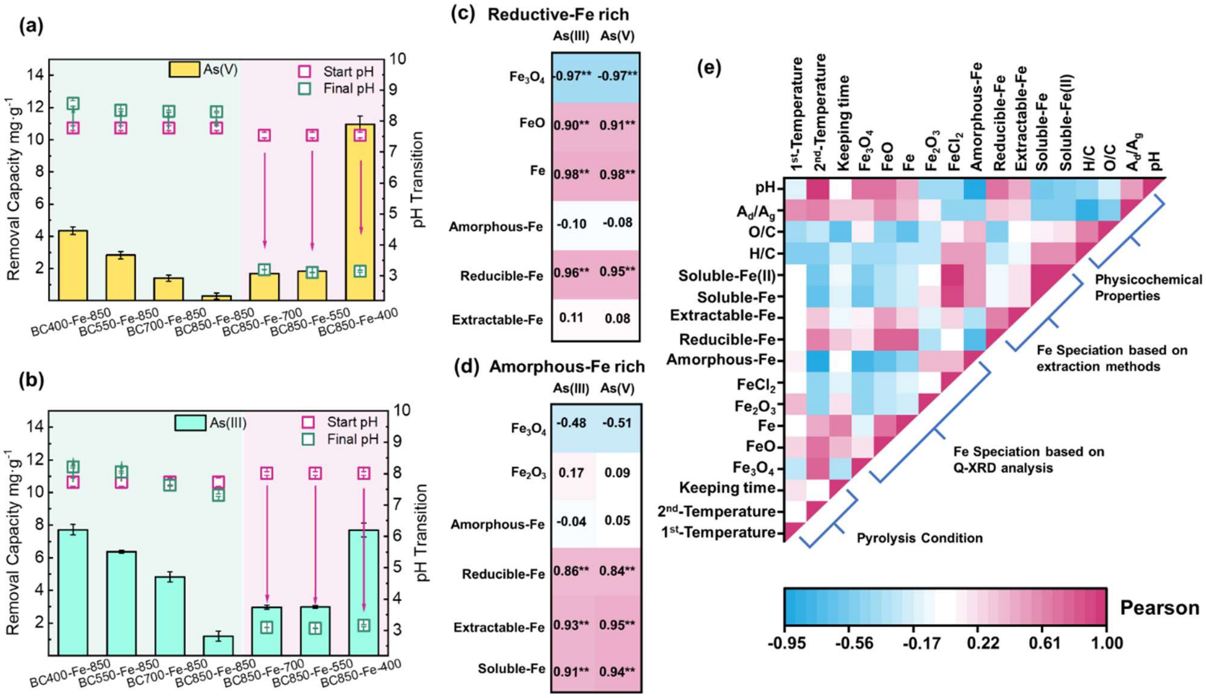

Figure 4-3 Removal capacities for As(V) (a) and As(III) (b) of the Fe-biochars and the change of solution pH after the reaction. Pearson correlation coefficient analysis of the As(III)/(V) removal capacities and Fe-speciation in the Fe-biochars containing abundant reductive-Fe (c) or abundant amorphous-Fe (d) (**$p < 0.01$, *$p < 0.05$). Pearson correlation matrix of the pyrolysis conditions, Fe speciation, and physicochemical properties of all Fe-biochars (e).

Both series of Fe-biochar composites with variable Fe species (*i.e.,* reductive-Fe and amorphous-Fe) could accomplish considerable As decontamination, which was close to those in relevant studies with similar Fe speciation and Fe loading (**Table D3**); however, the dominant immobilization mechanisms would be distinct. For instance, the ZVI content may contribute to As(V) and As(III) removal by Fe(0)-biochar (Bakshi et al., 2018, Fan et al., 2020), while direct sorption and co-precipitation might dominate As immobilization for the Fe-biochar possessing abundant amorphous Fe (Yu et al., 2021).

Table 4-1 Arsenic removal capacities of different Fe-biochars

Fe-biochar	As(V) removal capacity (mg g^{-1})	As(III) removal capacity (mg g^{-1})
BC400-Fe-850	4.34±0.23	7.72±0.32
BC550-Fe-850	2.83±0.23	6.37±0.08
BC700-Fe-850	1.39±0.19	4.83±0.31
BC850-Fe-850	0.29±0.19	1.19±0.30
BC850-Fe-700	1.68±0.02	2.97±0.12
BC850-Fe-550	1.82±0.24	2.98±0.08
BC850-Fe-400	11.0±0.5	7.70±0.41

4.3.3 Role of ZVI on the As immobilization by reductive-Fe rich biochar

A slight increase in the pH value from ~7.8 to 8.3–8.6 was found in the As(V) solution after the addition of Fe-biochar composites containing high proportion of reductive-Fe (BCX-Fe-850) (**Figure 4-3a**). As the intrinsic pH of these Fe-biochar composites (7.3–7.5, **Table D1**) was lower than that of the solution, the increased solution pH may be attributed to the consumption of H^+ during the As(V) reduction by reductive-Fe (**Eq. 4.1**) (Bakshi et al., 2018). No Fe dissolution and only limited soluble As(III) were detected (< 0.15 mg g^{-1}) after the As immobilization (**Figure D9**, **Appendix D**), indicating that this reaction might be an interfacial process instead of a solution reaction (Yan et al., 2012a). As(V) was reduced on the ZVI surface and then directly immobilized as the Fe-As surface complex (Bakshi et al., 2018, Hu et al., 2015), which could be evidenced by a well-overlapping distribution of Fe and As observed in the SEM-EDX mapping (**Figure 4-4**).

$$HAsO_4^{2-}\ (As(V)) + 2e^- + 3H^+ \rightarrow H_2AsO_3^-\ (As(III)) + H_2O \qquad \textbf{Eq.4.1}$$

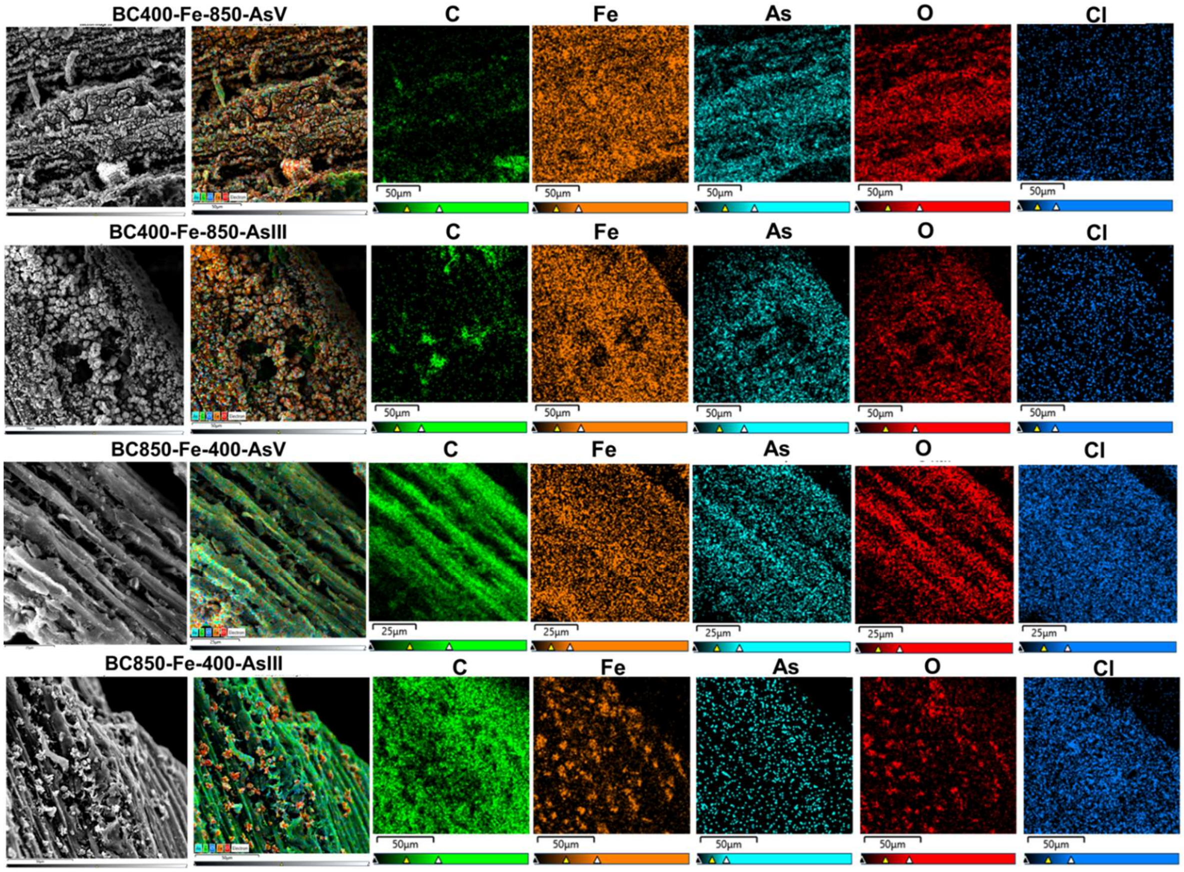

Figure 4-4 SEM images with EDX elemental (C, Fe, As, O, and Cl) distribution of the different Fe-biochars after arsenic removal.

A slight increase in the solution pH from 7.7 to 8.1–8.2 was detected after As(III) immobilization by BC400-Fe-850 and BC550-Fe-850, while a marginally increased or even a decreased pH occurred for BC700-Fe-850 and BC850-Fe-850 (**Figure 4-3b**). This phenomenon could be attributed to As(III) oxidation with simultaneous H^+ generation (**Eq. 4.2**). About 0.65–5.48 mg g^{-1} of As(V) was formed after adding these four Fe-biochar composites (**Figure D9**), and BC700-Fe-850 and BC850-Fe-850 reached relatively high soluble As(V) concentrations of 3.34 mg g^{-1} and 5.48 mg g^{-1}, respectively. The carbon phase in Fe-biochar may be the primary oxidizing moieties for As(III) (Zhong et al., 2019) in view of the remarkable electron-accepting capacity of high-temperature biochar (Kluepfel et al., 2014, Zhang et al., 2019d). As(III) oxidation by ZVI-derived intermediates, such as Fe(IV) and hydroxyl radicals (Pang et al., 2011, Zhang et al., 2021), was possibly less critical considering relatively low As(V) concentrations in BC400/550-Fe-850 (*i.e.*, high ZVI content) as compared with BC700/850-Fe-850 (*i.e.*, low ZVI content). An overlapping elemental distribution of Fe and As was also observed on BC400-Fe-850 after As(III) removal (**Figure 4-4**), corroborating the indispensable role of Fe-As combination in As(III) immobilization. Both the redox reaction with carbon fraction and the sorption onto Fe-phases contributed to the As(III) removal by the Fe-biochar enriched with reductive-Fe.

$$H_2AsO_3^{-} \text{ (As(III)) - } 2e^{-} + H_2O \rightarrow HAsO_4^{2-} \text{ (As(V))} + 3H^{+} \qquad \textbf{Eq.4.2}$$

To verify the critical role of ZVI, several Fe-biochar composites with different reductive-Fe loadings (*i.e.,* ZVI and FeO) and similar pH values were designed (**Appendix D**). PCC analysis between the As removal capacities and Fe speciation of these Fe-biochars showed that the As(V) and As(III) removal capacities were positively related to the contents of ZVI (r = 0.98) and FeO (r = 0.90–0.91), but negatively associated with the amount of Fe_3O_4 (r = -0.97) (**Figure 4-3c** and **Figure D10, Appendix D**). In addition, the As removal capacities were highly correlated with the reducible-Fe content (r = 0.95–0.96), as determined by the hydroxylamine-HCl extraction method (Poulton and Canfield 2005, Slotznick et al., 2018). A nearly linear relationship (R^2= 0.90–0.92, **Figure D11**) could be well established between As removal capacity and reducible-Fe fraction, reinforcing the importance of ZVI (PCC of 0.80 between ZVI and reducible-Fe, **Figure 4-3e** and **Table D4**). Moreover, Q-XRD revealed a decrease of

ZVI from 10.91 mg g^{-1} to 6.51–7.91 mg g^{-1} on BC400-Fe-850 with a concomitant increase of amorphous-Fe from 3.11 mg g^{-1} to 11.4–16.9 mg g^{-1} during the As immobilization process (**Figure 4-5**). Overall, the formation of ZVI related to the labile-C was the critical component for an efficient As removal by Fe-biochar composites with rich reductive-Fe.

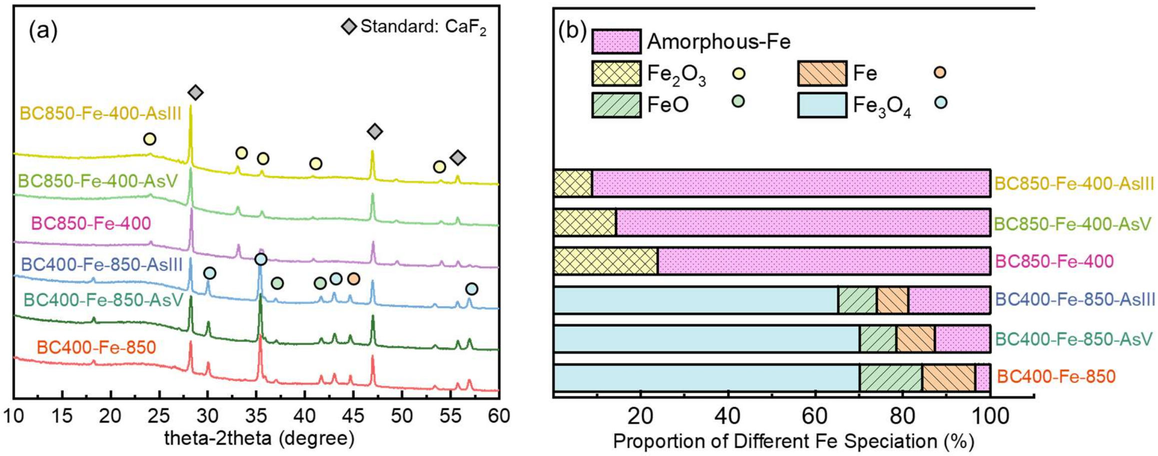

Figure 4-5 Q-XRD patterns (a) and semi-quantitative analysis (b) of the different Fe-biochars before and after arsenic immobilization with the addition of CaF_2 standard (Hematite: Fe_2O_3; Magnetite: Fe_3O_4; Wustite: FeO; Metallic Fe: Fe).

4.3.4 Core-shell structure generated by redox reactions between arsenic and ZVI

To explore the As immobilization mechanisms of Fe-biochar composites, an advanced depth profiling XPS analysis was conducted on BC400-Fe-850, which was the typical reductive-Fe rich biochar. Results showed that BC400-Fe-850 was covered by an iron-oxide layer (~10–20 nm) after the reaction with As(V) or As(III) with no Fe(0) (**Figure 4-6** and **Figure D12**). Fe(0) could only be detected at the depths of 20–50 nm, and its proportion increased to 6.2% and 9.9% at the 200 nm depth after As(V) and As(III) removal, respectively. The atomic ratio of O/Fe also suggested the formation of an oxide shell on the ZVI surface (**Figures 4-6** and **D13**). Higher O/Fe atomic ratios of 3.8–6.5 were found on Fe-biochar composites after As(V) decontamination within the first ~20 nm from the surface, and they decreased to 2.8–3.4 in the depth range between 20 to 200 nm. A similar transition was found after As(III) immobilization that the O/Fe atomic ratios as 3.4–8.1 were found within the ~20 nm from the surface, and then declined to 2.6–2.8 from 20 nm to 200 nm.

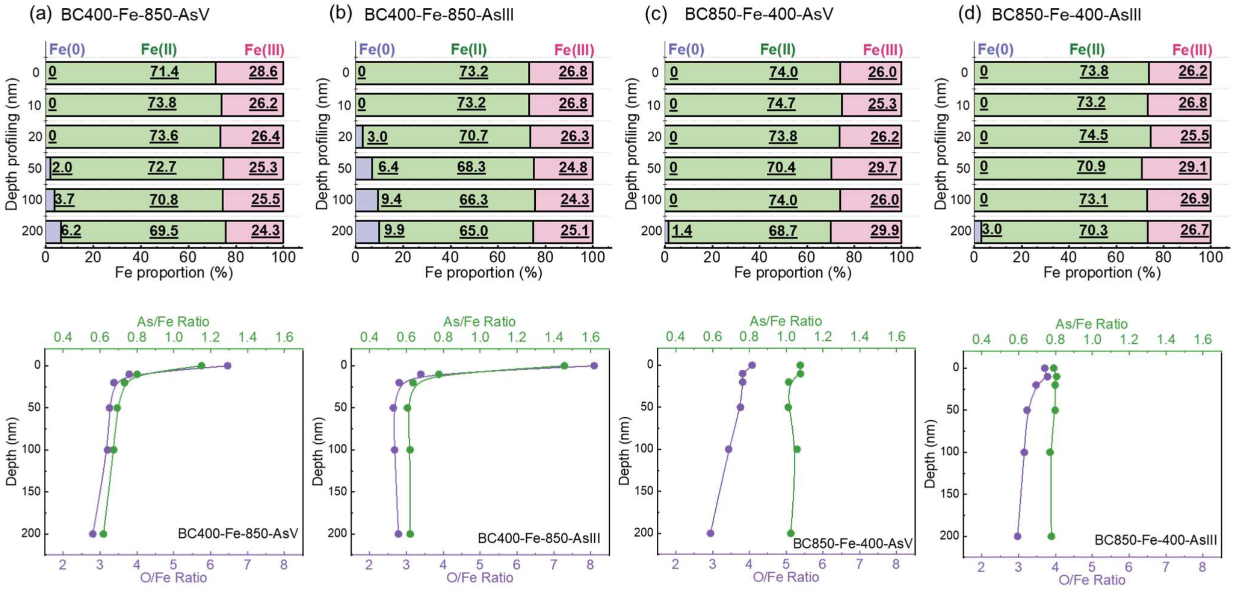

Figure 4-6 Depth-profiling XPS analysis of the Fe speciation (upper part) and atomic elemental ratio (O/Fe and As/Fe) (down part) on the typical Fe-biochars after As removal.

Besides, As accumulation also varied over depth. High As/Fe atomic ratios were observed within 0–10 nm of the surface of BC400-Fe-850 (0.8–1.2 for As(V) and 0.7–1.5 for As(III)), and the ratios decreased to 0.6–0.7 when depth approached below 20 nm. No apparent change of As/Fe atomic ratios could be observed between a depth range of 20-200 nm (0.6–0.7 for As(V) and 0.6 for As(III)) (**Figure 4-6**).

The proportion of different As species (*i.e.*, As(V), As(III), and As(0)) varied in different layers of BC400-Fe-850 (**Figure 4-7**). For As(V) immobilization, As(V) was the primary As species on the surface (92.7%, **Figure 4-7a**), and its proportion gradually decreased to 42.8% with an increasing depth (**Figure 4-8**). Meanwhile, the proportion of As(III) and As(0) showed a noticeable increase to ~37.8% and 19.4% (**Figure 4-7a**), respectively. These results provided credible evidence for the critical role of ZVI in As(V) immobilization (**Figure 4-7c**).

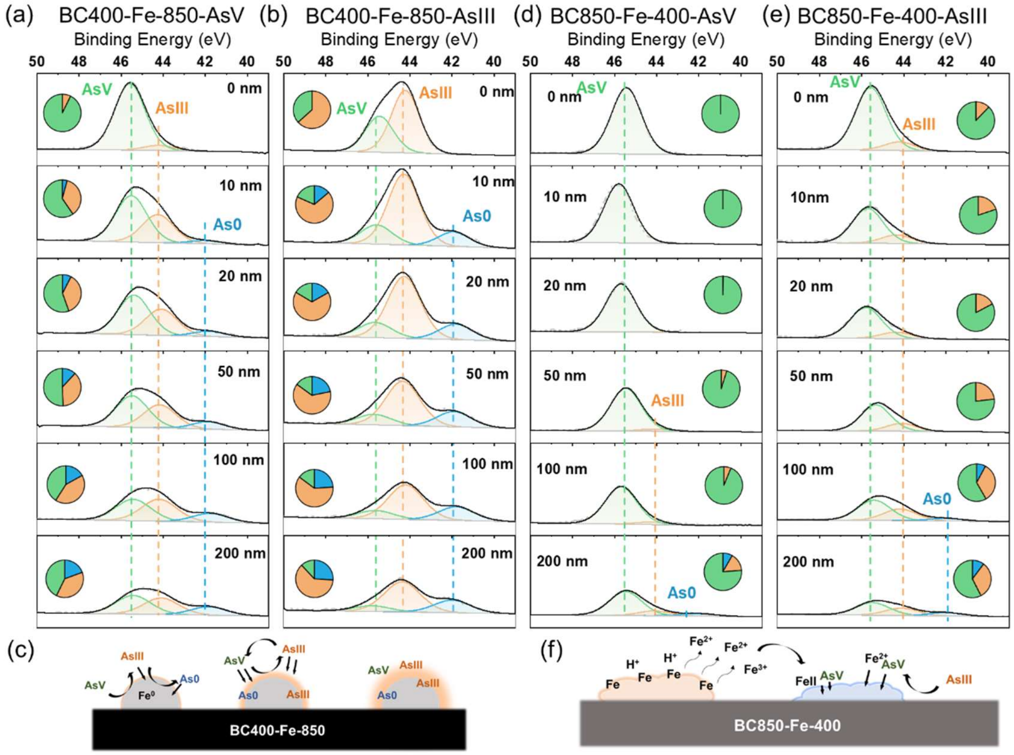

Figure 4-7 Depth-profiling XPS analysis of As 3d binding state on the typical Fe-biochars after As removal (a, b, d, e). The schematic diagram of As immobilization mechanisms by the Fe-biochars (c, f).

Specifically, the reduction of As(V) to As(III) and even As(0) through As–Fe binding happened after the intraparticle diffusion of As into the ZVI layer. The As(V) reduction led to the formation of the iron-oxide on the surface of ZVI, and this newly formed iron oxide could effectively attract As(V) and As(III) through electrostatic interactions and surface complexation with Fe (≡Fe–O–As(III/V)) (Ling et al., 2017, Ling and Zhang 2017). A core-shell structure was formed during the As removal process, *i.e.,* ZVI coordinating with As(0)/As(III) acted as the core, and amorphous iron oxide complexing with As(V)/As(III) was the outside-shell (**Figure 4-7c**). The higher As/Fe atomic ratios (0.8–1.2) within the first ~10 nm from the surface indicated the preferable As immobilization onto the surface oxide shell compared with the inner reduction and adjoint complexation with ZVI core. For As(III) removal by BC400-Fe-850 (**Figure 4-7b** and **Figure 4-8**), the appearance of As(0) (13.9–26.0%) below 10 nm suggested a similar As intraparticle diffusion and reduction process by Fe(0). As(V) was mainly observed on the outside layer of BC400-Fe-850 (36.6%) during the As(III) immobilization and decreased to 12.0–18.4% at 10–200 nm depth (**Figures 4-7b** and **Figure 4-8**), indicating that As(III) was probably oxidized by the surface functional groups of biochar (Zhong et al., 2019, Zhong et al., 2020) or intermediates (*e.g.*, Fe(IV) and hydroxyl radicals (Pang et al., 2011, Zhang et al., 2021)) and then stabilized on the iron-oxide shell.

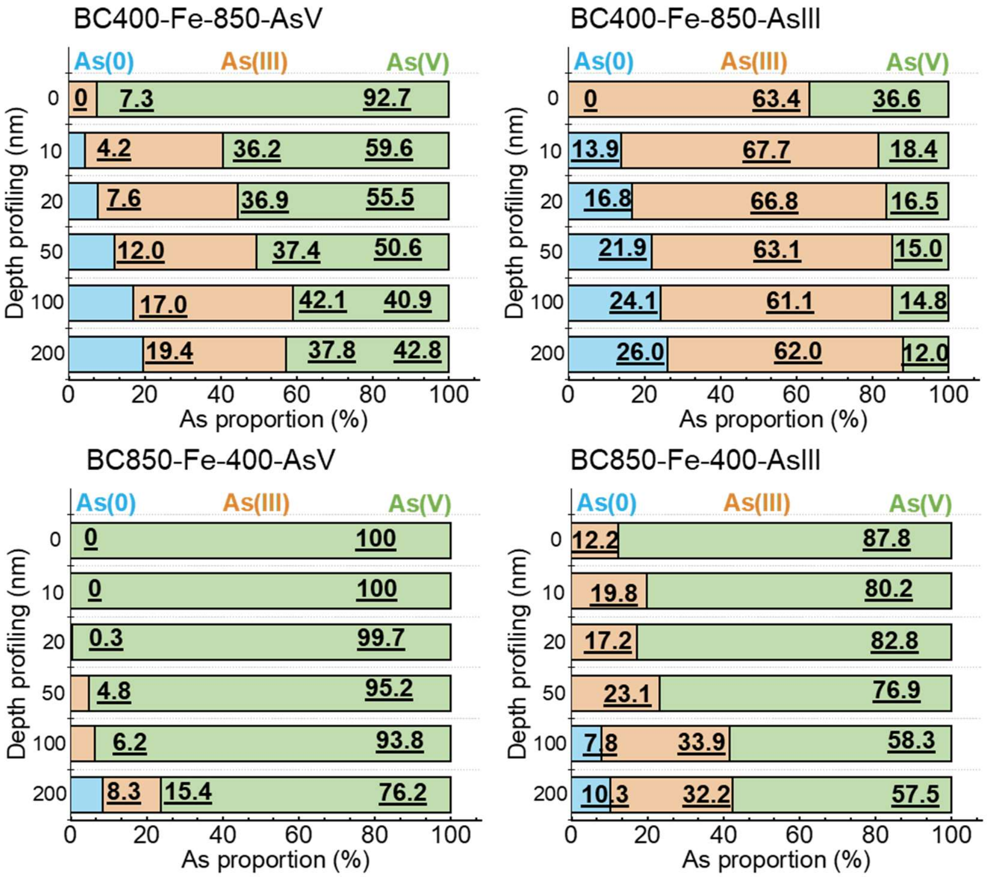

Figure 4-8 As speciation on the selected Fe-biochars after As removal based on the XPS depth profiling analysis.

4.3.5 Acidity from amorphous-Fe rich biochar facilitated arsenic decontamination

Unlike the Fe-biochar composites rich in reductive-Fe (*i.e.*, BC400/550/700/850-Fe-850), an apparent decrease in solution pH was found after the addition of Fe-biochar composites containing a higher fraction of amorphous-Fe (BC850-Fe-400/550/700) during both As(V) (from 7.6 to 3.1–3.2) and As(III) (from 8.0 to 3.1–3.2) immobilization. This phenomenon was plausibly due to the high acidity of these Fe-biochar composites (pH = 2.9–3.1, **Table D1**). The hydrolysis process of amorphous-Fe (Pan et al., 2021) was evidenced by the negative relationship between pH and amorphous-Fe content (PCC of -0.92, **Figure 4-3e** and **Table D4**).

To identify the role of acidity from amorphous-Fe, the initial solution pH was adjusted to 10.2–10.4 before the addition of amorphous-Fe-rich composites (**Figure D14, Appendix D**). Compared with the unadjusted experiments, the pH after As immobilization by Fe-biochar composites increased to 3.4–3.8, and the immobilization capacities slightly changed to 1.73–10.1 mg g^{-1} for As(V) and 2.50–7.10 mg g^{-1} for As(III). The lower As immobilization capacity of BC850-Fe-400 at a higher pH confirmed the importance of acidity during the As immobilization process. The acidic condition could facilitate Fe dissolution and enhance electrostatic interactions between Fe-biochar and As (Amen et al., 2020, Wen et al., 2021), thus improving their As immobilization capacities. Results from the adjusted pH experiments also indicated that the amorphous-Fe could effectively buffer the solution's alkalinity and maintain an acidic environment, leading to a considerable immobilization capacity for As even at a high initial pH. In addition, a low initial pH (3.2–3.3) was also set for the Fe-biochar composites containing reductive-Fe to test the As immobilization capacities, where improved removal was found for both As(V) (0.85–12.1 mg g^{-1} > 0.29–4.34 mg g^{-1}) and As(III) (1.24–9.78 mg g^{-1} > 1.19–7.72 mg g^{-1}) (**Figure D14**). These results indicated that the As immobilization capacity of Fe-biochar would be inhibited by the limited acidity due to the less amorphous-Fe content.

4.3.6 Arsenic removal *via* co-precipitation with the Fe released from amorphous-Fe rich biochar

Despite the strengthened As immobilization by the acidity, the soluble Fe released from these amorphous-Fe-rich composites might determine the As removal. There was no significant correlation between different iron minerals (*i.e.*, amorphous-Fe, Fe_2O_3, and Fe_3O_4) and As removal capacities (r=-0.51–0.17, p>0.05, **Figures 4-3d** and **D15**) based on the PCC analysis of these Fe-biochar composites. In contrast, the As removal capacities were highly relevant to extractable-Fe (r = 0.93–0.95), soluble-Fe (r = 0.91–0.94), and reducible-Fe (r = 0.84–0.86) (**Figures 4-3d** and **D15**), determined through different extraction methods. These Fe fractions represented the active Fe in the amorphous-phase that could be readily released into the solution through chelation by dissolved organic carbon from biochar (Kim et al., 2020) or reduction to soluble Fe(II) by reductive biochar moieties (Xu et al., 2020e). There was a linear relationship (R^2 = 0.71–0.90) between the As removal amount and the Fe content of Fe-biochar composites (**Figure D16**). The released Fe ions can co-precipitate with As to form As-Fe amorphous complexes on carbon (Daenzer et al., 2014, Yu et al., 2021), which was corroborated by the homogeneous distribution of As on the biochar surface (**Figure 4-4**), the increase in amorphous-Fe content (**Figure 4-5**), and the decline in the soluble Fe concentration after As immobilization (**Figure D17**). Limited As(V) reduction was induced (< 0.5 mg g^{-1},

Figure D9) by amorphous-Fe-rich biochar composites, but As(III) oxidation could possibly be achieved due to oxidizing capacity of both biochar (Zhong et al., 2020) and ferric minerals (Alkurdi et al., 2019, Amstaetter et al., 2010, Ona-Nguema et al., 2010) during the co-precipitation process. More soluble Fe(II) was formed after As(III) removal compared with As(V) removal, evidencing the oxidation of As(III) along with Fe(III) reduction (**Figure D17**). In short, Fe released from the amorphous-Fe was a critical factor for As removal by Fe-biochar with abundant amorphous-Fe.

4.3.7 Fixed layered composition of arsenic and rron by the co-precipitation process

BC850-Fe-400 was selected as the representative Fe-biochar composites with rich amorphous-Fe to evaluate the depth distribution of As and Fe generated through the co-precipitation process. There was no noticeable change of O/Fe atomic ratio at different depths of BC850-Fe-400 after As(V) (2.9–4.1) or As(III) (3.0–3.8) removal, and the Fe valence remained constant at different layers (**Figures 4-6c**, **4-6d,** and **Figure D13**). The As/Fe atomic ratios also kept stable in BC850-Fe-400 after As(V) (~1.0–1.1) or As(III) (~0.8) immobilization, and As(V) was the dominant form on BC850-Fe-400 in both systems (76.2–100% for As(V) immobilization and 57.5–87.8% for As(III) immobilization) (**Figures 4-7d**, **4-7e** and **4-8**). The fairly stable ratio and speciation of As/Fe indicated the possible formation of an amorphous scorodite-like mineral ($FeAsO_4$, Fe/As ~1) or ferrous arsenate ($FeHAsO_4$, Fe/As ~1) on BC850-Fe-400, reaffirming the As removal by the co-precipitation process (**Figure 4-7f**). Accordingly, lower As/Fe atomic ratios were found after As(III) removal as the As(III) should be oxidized to As(V) with the consumption of extra Fe before co-precipitation.

4.3.8 Comparison between the reductive-Fe-biochar and amorphous-Fe-biochar

Various primary Fe species on Fe-biochar caused the different immobilization processes, leading to a distinct hierarchical distribution of As and Fe in the biochar composites. Core-shell structure on the reductive-Fe-biochar after As immobilization offered plausible evidence of combined redox and sorption process for As in the presence of ZVI. By contrast, a marginally changed As/Fe ratio and steady compositions of As and Fe were found in the amorphous-Fe-biochar after As removal, corresponding to the co-precipitation process.

The intrinsic advantages/disadvantages of reductive-Fe-biochar and amorphous-Fe-biochar for As immobilization can be inferred in light of the varying removal mechanisms and hierarchical depth distributions. For reductive-Fe-biochar, highly toxic As(III) was encapsulated inside the iron oxide shell during the immobilization process; however, the stability of this iron oxide shell remained uncertain. Dissolution of the amorphous oxide layer might represent a potential risk of As(III) remobilization into the environment. The fate of elemental As combined with Fe(0) was also unclear. Thus, future studies are required to prove the long-term stability of As fixed on the reductive-Fe-biochars under seasonally changeable field-relevant conditions. For the amorphous-Fe-biochars, the oxidative transformation of As(III) to low toxicity As(V) and the high As removal capacity offered apparent advantages, especially considering the lower energy input for biochar composites production. However, the unintended environmental risk of the indigenous acidity associated with released Fe ions and the competition of coexisting anions (*e.g.,* PO_4^{3-}) during the co-precipitation process still mandate further investigation.

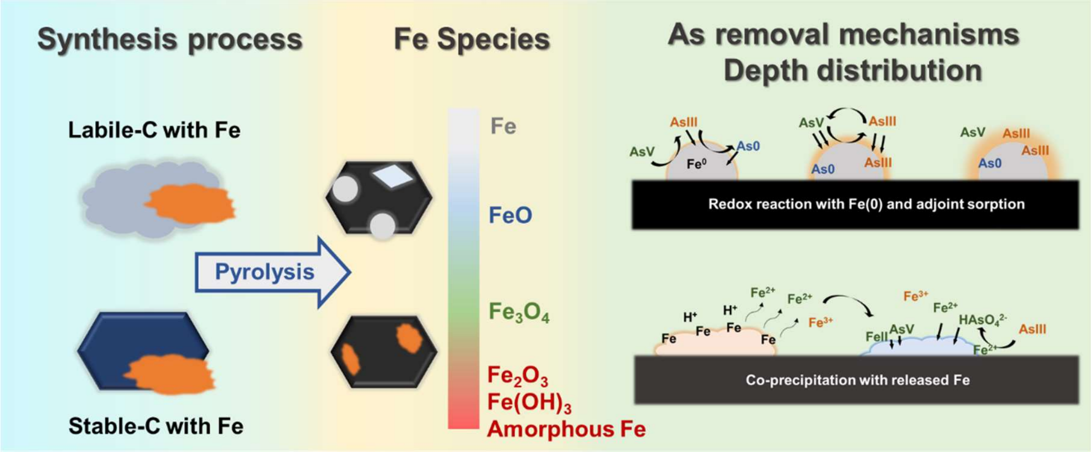

Figure 4-9 Graphical summarization of Chapter 4

4.4 Conclusions

We proposed a hypothesis-driven manipulation of Fe speciation in the design of Fe-biochar composites, and the underlying mechanisms and hierarchical depth distributions of Fe and As were scrutinized **(Figure 4-9**). Our results evidenced that reductive-Fe species, which mainly immobilized As through redox reaction and sorption/complexation, were formed at a high pyrolysis temperature with co-pyrolyzed labile-/amorphous-C. In contrast, amorphous-Fe species were primarily produced with stable-/graphitic-C, and they removed As through co-precipitation with released Fe. Our study highlighted the key roles of carbon structures in regulating Fe species in biochar composites. Labile-/amorphous-C and stable/graphitic-C led to distinct ZVI and amorphous-Fe contents in the resulting Fe-biochar composites during the pyrolysis process. Therefore, understanding and customizing the carbon structures is a prerequisite for fabricating biochar composites with the targeted Fe species. The hierarchical distributions analyzed in this study offered unprecedented high-resolution details on the As removal mechanisms by different Fe-biochar composites, thus providing direct evidence about

As immobilization through co-precipitation and/or sorption with redox reaction. Overall, these findings can guide our rational design of multifunctional Fe-biochar composites for broader and fit-for-purpose applications, which are indispensable for actualizing sustainable environmental remediation together with global decarbonization.

Chapter 5 Impact of Fe Mineral Crystallinity on the Electron Transfer Routine during Cr(VI) Reduction by Biochar

5.1 Introduction

Iron, which is widely existed as ferric oxyhydroxide mineral in nature, plays a vital role in the dynamics of toxic metal(loid)s in the environment (Boland et al., 2014, Borch et al., 2010, Kawamoto et al., 2021). Specifically, redox cycling of Fe(III)/Fe(II) (Bishop et al., 2019) and the adjoint sorption-desorption of toxic elements (Mamun et al., 2017) are crucial processes that eventually influence the mobility and toxicity of metal(loid)s. Redox processes of iron minerals often involve organic matter as an electron donor due to its high reducing capability and binding affinity (Herndon et al., 2017, Poggenburg et al., 2018). Recently, biochar was recognized as a potential electron-donating moiety for various environmental applications (Bowman et al., 2009, Lehmann 2007b). This particular organic carbon shows a unique character due to its rich functional groups and aromatic structure (Kluepfel et al., 2014). The phenol-like groups within the pyrogenic carbon can influence the biogeochemical cycling of contaminants due to the high redox reactivity (Huang et al., 2019), and the superior conductivity of pyrogenic carbon related to the aromatic conjugated carbon structure may facilitate the electron transfer with iron mineral (Sun et al., 2017). These specific properties of pyrogenic carbon might provide different interaction mechanisms with iron minerals and pollutants.

The high reducing capacity of the pyrogenic carbon/biochar has been highlighted for the pollutant reduction-immobilization in the past few years. Biochar could directly reduce high toxic Cr(VI) (Mandal et al., 2017) and immobilize the generated Cr(III) through sorption and precipitation (Li et al., 2017b). Recent studies mainly focused on the direct electron transfer process between biochar and Cr(VI) (Xu et al., 2019a, Xu et al., 2020f). The fate of Cr(VI) might be further affected by the existence of iron minerals due to the interaction between iron minerals and biochar. Such a process will oxidize the surface functional group of biochar (Yang et al., 2016), and the resulting Fe-biochar complex may inhibit the direct Cr(VI) reduction process by biochar (Xu et al., 2020e, Xu et al., 2021e). On the other hand, this interaction process might also cause the indirect electron transfer from biochar to Cr(VI) through iron minerals. That is, Fe(III) from iron minerals might be reduced to Fe(II) through interaction with biochar, and the generated Fe(II) might subsequently reduce the Cr(VI). The indirect electron transfer process is crucial to explain the fate of chromium since the chromium have a high sorption affinity on the positive iron minerals (Moreira et al., 2018). Until now, there is still no sufficient evidence regarding the indirect electron transfer route from biochar to Cr(VI) through the transformation of iron.

Moreover, the crystallinity of iron minerals might greatly affect the redox routine with Cr(VI). In general, amorphous ferric hydroxide or ferrihydrite, which usually acts as a dominant sink for numerous metals (Hajji et al., 2019, Taylor et al., 2009), could be formed through rapid Fe(II) oxidation (Cismasu et al., 2016) or hydrolysis of Fe(III) (Wu et al., 2020). These ferric oxyhydroxides are thermodynamically unstable (Chen et al., 2015a, Cornell and Schwertmann 2003) and generally transform into more crystalline iron phases, through ageing or thermal incubation (Cismasu et al., 2016, Hu et al., 2018, Li et al., 2020d). Therefore, different crystalline iron minerals with various redox capacities and sorption capabilities can be formed (Aeppli et al., 2019b, Sun et al., 2018a). Aeppli et al. found that the redox capacity of iron minerals decreased through the transformation from poorly crystalline ferrihydrite to thermodynamically more stable goethite by mediated electrochemical reduction test (Aeppli et al., 2019a). Therefore, it can be speculated that the fate of Cr(VI) will be affected by iron minerals with different crystallinity in the presence of biochar.

Overall, research regarding the electron transfer route for Cr(VI) reduction in soil by iron minerals and biochar is limited. Especially, it remains unclear what impacts the crystallinity of ferric oxyhydroxide exert on such an electron transfer process with biochar. Therefore, this study was conducted (1) to determine the direct and indirect reduction of Cr(VI) with different crystalline ferric oxyhydroxides in the presence of biochar by kinetics experiment, alkalinity extraction, XPS analysis, *etc.*; and (2) to elucidate the electron transfer mechanism of Cr(VI) reduction with different crystalline ferric oxyhydroxides and biochar through multiple advanced analysis including transmission electron microscopy with electron energy loss spectroscopy (TEM-EELS), TEM-EDS, XPS, and Raman imaging combined with Emission Scanning Electron Microscope (Raman-SEM).

5.2 Materials and Methods

5.2.1 Preparation of ferric oxyhydroxides with different crystallinity

Ferric oxyhydroxides with different degrees of crystallinity were prepared using a modified method by Villalobos and Leckie(2000). Specifically, 0.5 L of 2 M NaOH solution was added into 0.5 L of 0.5 M $FeCl_3$ solution to form ferric oxyhydroxides (goethite) above the required stoichiometric ratio (*i.e.,* 3:1 for Fe^{3+} and OH^- to form $Fe(OH)_3$ precipitation). In order to simulate the change of ferric oxyhydroxides from low-crystallinity to high-crystallinity (Aeppli et al., 2019a), we incubated the precipitated ferric oxyhydroxide at 60 °C in the oven for 6 h or 72 h, and the resulting product could be considered as low- and high-crystallinity ferric oxyhydroxides, respectively, since ageing at 60 °C for over 24 h ensured the formation of crystal ferric oxyhydroxide (Matta et al., 2007). These two ferric oxyhydroxides were filtered, washed with distilled water, freeze-dried, and denoted as Fe-L and Fe-H, respectively. XRD and SEM were used to confirm the different crystallinity degrees of these ferric oxyhydroxides. Basic properties such as surface area and zeta potential were determined, and detailed information can be found in **Appendix B**.

5.2.2 Preparation and characterization of biochar

Biochar samples were produced under O_2-limited pyrolysis of peanut shells based on the previous study (Xu et al., 2019c). Peanut shell was selected as the feedstock since the produced biochar has a high reducing capacity (Xu et al., 2019c), which can offer more electrons for the Cr(VI) reduction with iron mineral. Biochar was produced at 400 °C and 700 °C with a holding time of 4 h, denoted as BC400 and BC700, respectively. These two biochars were selected as the representative pyrogenic carbon since they contained different reducing moieties for Cr(VI) reduction, *i.e.*, surface O-moiety or carbon defects with aromatic conjugated clusters, based on our previous research (Xu et al., 2022a, Xu et al., 2020f). The produced biochar was ball-milled and then passed through a 200-mesh (0.074 mm) sieve. Basic characterizations of biochar, including elements content, Raman spectra, XPS analysis, *etc.,* were described in **Appendix B**.

5.2.3 Immobilization of soil Cr(VI) with ferric oxyhydroxides and biochar

The Cr-contaminated soils were prepared from the standard OECD (Organization for Economic Cooperation and Development) soils (Pontoni et al., 2016), which contained 68.5% quartz sand, 13.6% kaolin clay, and 10.0% sphagnum peat, with the addition of 0.5% K_2CrO_4 and ~6.4% ferric oxyhydroxide (Fe-L or Fe-H) (pH= ~7.0). The OECD soil was used to precisely control the crystallinity of ferric oxyhydroxides and exclude the possible impact from other active soil components. The detailed preparation procedures, references, and composition of these Cr(VI) polluted soils are shown in **Appendix E**. The Cr-contaminated soils were mixed with 1% (w/w) BC400 or BC700 and then equilibrated for 3-month in triplicates. Water content was kept as ~70% WHC (water holding capacity) with daily addition referred to the soil condition in the previous study (Xu et al., 2018b). The Cr-contaminated soils without any biochar addition were set as control. These soil samples were freeze-dried after incubation and then evaluated for Cr(VI) immobilization by toxicity characteristic leaching procedure (TCLP) extraction with triplicates. TCLP extraction was conducted through 0.1 M acetic acid with a sample-to-fluid ratio of 1:20 according to the USEPA Method 1311 (EPA 1992), which has been widely applied to evaluate the immobilization effectiveness of heavy metals in contaminated soil receiving the treatment. The concentration of Cr(VI) in the extraction solution was detected with the diphenyl-carbohydrazide spectrophotometric method at 540 nm (Xu et al., 2020f). Cr(VI) immobilization amount in different soil was calculated by the difference between the extracted Cr(VI) concentration with and without biochar addition.

5.2.4 Reduction and conversion of aqueous Cr(VI) with ferric oxyhydroxide and biochar

To elucidate Cr(VI) reduction process in soil, an ideal solution system was set to determine Cr(VI) reduction and conversion process with different ferric oxyhydroxide and biochar. Briefly, 2 g Fe-L or Fe-H were added into 1 L of 100 mg L^{-1} Cr(VI) solution (K_2CrO_4 with 0.1 M KCl) to form the ferric oxyhydroxide-associated Cr(VI) that commonly exists in the Cr-contaminated soil system. These mixtures were mechanically shaken at 200 rpm for 7-day to ensure the thorough mixing and equilibrium of Cr(VI) sorption on ferric oxyhydroxides. Then 2 g biochar (BC400 or BC700) was added into the solution above for another 7-day reaction to simulate the appearance of pyrogenic carbon. The pH was controlled at 6.5 during the whole reaction process by 1 M NaOH or HCl. Detailed setting reference, sampling methods, and control experiments, including biochar, ferric oxyhydroxide, dissolved biochar (released dissolved organic carbon from biochar) with ferric oxyhydroxide, and carbonaceous material comparison (*i.e.,* graphite and activated carbon) with or without ferric oxyhydroxide were all described in **Appendix E**.

Filtrates collected at the selected time interval were immediately analyzed for the concentration of total Cr (Cr_{Total}) and Cr(VI), and the concentration of Cr(III) in solution was calculated by the difference between the total Cr and Cr(VI) concentration. Besides, the amount of Cr sorbed on biochar and ferric oxyhydroxide was calculated from the difference between the initial and measured concentrations of Cr_{Total} in the solution. Given that both Cr(VI) and Cr(III) existed on the solid, alkalinity extraction experiment (Zhao et al., 2016c), XPS, and TEM-EELS were used to clarify the Cr(VI) and Cr(III) distribution on the solid after the 14-day reaction. Details for these characterizations are described in **Appendix E**.

5.2.5 Exploration of electron transfer mechanisms for Cr(VI) reduction by ferric oxyhydroxides and biochar

There could be two ways of electron transfer for Cr(VI) reduction: (i) direct electron transfer from biochar to Cr(VI) and (ii) indirect electron transfer from first biochar to iron mineral and then to Cr(VI) with Fe(III)/Fe(II) transformation. Aqueous Cr(VI) can be directly reduced by biochar with the participation of the surface-reducing functional groups. The direct transfer of electrons from biochar for Cr(VI) reduction was studied by detecting electron-donating moieties on biochar and Cr existing forms after Cr(VI) reduction by XPS and TEM-EELS. The Cr(VI) sorbed on the iron mineral might also be reduced indirectly through the biochar-induced transformation of Fe(II)/Fe(III) on iron minerals. To determine this indirect electron transfer route, firstly, TEM-EDS and Raman-SEM were used to determine the association and electron transfer through surface functionality and carbon defects between biochar and iron mineral. Besides, the reduction of pristine Fe-L/Fe-H by biochar without Cr(VI) was also conducted, and the transformation of Fe(III)/Fe(II) was determined by XPS and TEM-EELS analysis to verify the electron transfer from biochar to iron mineral. Secondly, the amount and distribution of Fe and Cr with different valence states on iron minerals after biochar reduction were detected by XPS analysis and TEM-EELS to evidence the electron transfer from Fe to Cr. The Cr(VI) reduction performance and mechanisms by biochar and biochar-reduced ferric oxyhydroxide were compared to further evaluate this electron transfer routine. Details of EELS analysis, XPS analysis, Raman-SEM analysis, and redox reaction between iron minerals and biochar were described in **Appendix E**.

5.3 Results and Discussion

5.3.1 Different crystallinity ferric oxyhydroxides, biochar, and their effects on soil Cr(VI) immobilization

The XRD analysis showed the dominance of goethite in iron minerals with different crystallinity (**Figure 5-1**). The Fe-L, which was incubated within a short time of 6 h, showed broader and shorter characteristic peaks of goethite with an average crystalline diameter of 17.6 nm (**Table E1, Appendix E**), while it also had the broad peaks of ferrihydrite between 35° and 63° (inserted **Figure 5-1a**), indicating the formation of a poor crystallinity ferrihydrite in Fe-L (Zhu et al., 2019a). When the iron mineral was incubated for 72 h, only sharp peaks of goethite were found in the XRD pattern (**Figure 5-1a**), indicating the formation of crystalline goethite (crystalline size as 29.8 nm, **Table E1**) in Fe-H. Results from XRD confirmed our assumption that Fe-L was mainly a low-crystallinity ferric oxyhydroxide, while high-crystallinity ferric oxyhydroxide was dominant in Fe-H. This result was further evidenced by the SEM image in which the mineral in Fe-L was mainly in an amorphous irregular shape (**Figure 5-1b**) while that in Fe-H was acicular crystal (**Figure 5-1c**) (Aeppli et al., 2019a). Besides, Fe-L had a higher specific surface area (~118 m^2 g^{-1}) than Fe-H (~32 m^2 g^{-1}), with a similar surface zeta potential (pH_{pzc} = 8.0–8.4, **Table E1**). The higher crystallinity with the decreased specific surface area of Fe-H might lead to the lower sorption capacity for Cr(VI) compared with Fe-L (Hajji et al., 2019).

Biochar produced at two temperatures also showed different properties (**Table E2, Appendix E**). Compared to BC700, BC400 had a higher O content (16.6% *vs.* 5.4%) and H content (3.5% *vs.* 1.1%), but with a lower I_D/I_G ratio (*i.e.,* intensity ratio between D-band and G-band obtained from Raman spectrum, 1.15 *vs.* 1.55) and surface area (19.8 m^2 g^{-1} *vs.* 283 m^2 g^{-1}), indicating the richness of aliphatic carbon with limited pore structure in BC400, while BC700 contained fewer O-moieties with rich aromatic conjugated clusters. The difference between BC400 and BC700 was given by the "percolation" temperature at about 700 °C, which could enhance the expansion of aromatic cluster size with loss of O moiety (Pignatello et al., 2017).

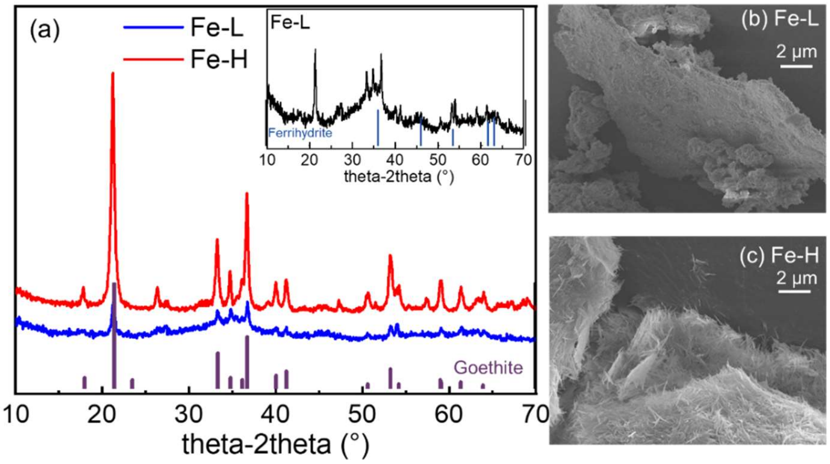

Figure 5-1 XRD patterns of iron minerals with different crystallinity (a); SEM image of iron minerals with different crystallinity (b-c). Fe-L: iron mineral with low crystallinity; and Fe-H: iron mineral with high crystallinity.

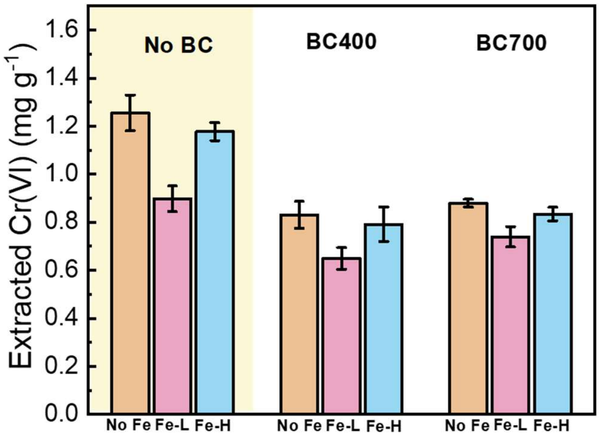

Figure 5-2 Concentrations of Cr(VI) extracted by TCLP from different crystallinity iron mineral soil with the presence of pyrogenic carbon biochar

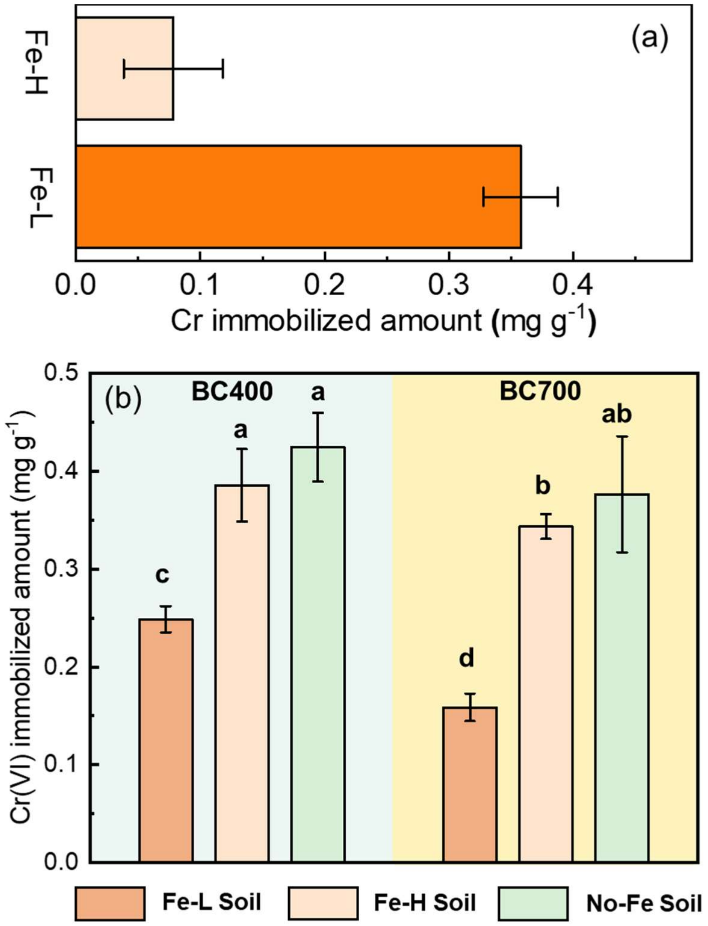

Figure 5-3 Cr(VI) immobilization amount by Fe-L or Fe-H alone (a), and immobilization amount of Cr(VI) by biochar in soil with different iron minerals after the 3-months incubation. (mean values in each experiment followed by the same letters are not significantly different using Tukey's HSD test at $p < 0.05$);

The existence of Fe-L and Fe-H reduced the extracted Cr(VI) amount from 1.26 mg g^{-1} to 0.90 mg g^{-1} and 1.18 mg g^{-1} in the soil, respectively (**Figure 5-2**). A higher decline of Cr(VI) with Fe-L (0.36 mg g^{-1}) was found compared to that with Fe-H (0.08 mg g^{-1}) (**Figure 5-3**), which was probably due to the higher surface area of the Fe-L (**Table E1, Appendix E**). With the addition of biochar, a further decrease of the extracted Cr(VI) concentration was found in soils with both Fe-L and Fe-H. BC400 and BC700 declined the extracted Cr(VI) from 0.90–

1.18 mg g^{-1} to 0.65–0.79 mg g^{-1} and 0.74–0.83 mg g^{-1}, respectively, after 3-month incubation (**Figure 5-3**), and BC400 offered a relatively higher immobilization capacity than BC700. About 0.16–0.25 mg g^{-1} Cr(VI) was further immobilized with biochar addition in Fe-L soil after 3-month incubation (**Figure 5-3**), and a higher Cr(VI) immobilization amount (0.34–0.39 mg g^{-1}) was found in Fe-H soil with biochar (**Figure 5-3**). These results indicated that biochar could enhance the Cr(VI) immobilization with iron minerals in the soil, but the underlying mechanisms might be varied with the crystallinity of existing iron minerals in the soil.

5.3.2 Pyrogenic carbon-induced reduction of Cr(VI) with ferric oxyhydroxides

To explore the underlying mechanism of Cr immobilization in the soil, the solution experiment was conducted. Similar to the soil system, both Fe-L and Fe-H significantly decreased the Cr(VI) concentration in the ideal solution system from 100 mg L^{-1} to 63.2 mg L^{-1} and 91.6 mg L^{-1}, respectively, after 7-day co-existence (**Figure E1, Appendix E**). The total Cr (Cr_{Total}) had a similar decline (**Figure E1**), and the alkalinity extraction showed that over 96.5% of Cr on the ferric oxyhydroxide was Cr(VI) after 7-day sorption (**Table E3**). These observations indicated the limited occurrence of Cr(VI) reduction into Cr(III). Furthermore, TEM-EELS analysis showed that the main form of Fe on the Cr-Fe complex was still Fe(III) (EELS peak at 706.4–706.8eV (Archanjo et al., 2017), **Figure E1**), further indicating the negligible electron transfer during the decontamination process. These results proved that sorption rather than reduction was responsible for Cr(VI) removal by both Fe-L and Fe-H. The electrostatic adsorption and surface complexation could be the main sorption mechanisms (Johnston and Chrysochoou 2012, Veselská et al., 2016), and Fe-L provided an elevated Cr(VI) sorption capacity with a higher proportion of inner-sphere complexation (56.4%) than Fe-H (25.6%) (**Figures E2–E3**, **Appendix E**).

Table 5-1. Relative distribution of Cr in both aqueous and solid phase (biochar and iron mineral alone or in combination) after 14-day Cr(VI) removal in solution system (Total Cr concentration was 100 mg L^{-1})

	Solution (%)		Solid (%)		Total Cr(VI) reduced or Cr(III) generated proportion (%)
	Cr(VI)	Cr(III)	Cr(VI)	Cr(III)	
Fe-L	61.7	0.9	36.4	1.1	1.9
Fe-H	87.3	0.3	11.6	0.8	1.1
BC400	62.8	7.6	0.9	28.7	36.3
BC400 + Fe-L	49.5	8.5	20.6	21.4	29.9
BC400 + Fe-H	61.8	13.8	1.7	22.8	36.6
BC700	58.0	7.3	0.7	34.0	41.3
BC700 + Fe-L	42.8	14.4	21.4	21.4	35.8
BC700 + Fe-H	52.2	19.5	3.8	24.5	43.9

After a 7-day reaction of Cr(VI) with ferric oxyhydroxides, biochar was added, and a further decrease in aqueous Cr(VI) concentration was found (**Figure 5-4** and **Table 5-1**). BC400 and BC700 reduced aqueous Cr(VI) concentrations from 63.2–91.6 mg L^{-1} to 49.5–61.7 mg L^{-1} and 42.8–52.2 mg L^{-1}, respectively, after another 7-day reaction (**Figure 5-4a** and **Figure 5-4b**). The Cr_{Total} concentration also decreased from 63.1–91.3 mg L^{-1} to 58.0–75.6 mg L^{-1} and 57.2–71.7 mg L^{-1} for BC400 and BC700, respectively (**Figure E4**), meanwhile Cr(III) was formed in solution with a concentration of 8.5–13.8 mg L^{-1} and 14.4–20.0 mg L^{-1} for BC400 and BC700, respectively (**Figure 5-4d** and **Figure 5-4e**). The considerable amount of soluble Cr(III) in the solution might relate to the complexation with dissolved organic matter from biochar.[51] Biochar increased the reduction rate of Cr(VI) by Fe-L and Fe-H to 1.5–2.0×10^{-3} h^{-1} and 1.8–2.7×10^{-3} h^{-1}, respectively (**Figure 5-4g**). It is worth noting that no further change in Cr_{Total}, Cr(VI), and Cr(III) was found with ferric oxyhydroxide alone (*i.e.,* without biochar addition) during the further 7-day reaction (**Figure 5-4** and **Figure E1, Appendix E**), and the decrease of Cr(VI) and increase of Cr(III) with no Fe presence only happened after biochar addition **(Figure 5-4c** and **Figure 5-4f)**. These results indicated that the reduction process happened after biochar addition and became the main Cr(VI) abatement process (Xu et al., 2019a, Xu et al., 2020f). As carbonaceous materials, activated carbon and graphite gave a slight decrease of Cr(VI), and no Cr(III) generation was observed due to their limited reducing capacity (**Figure E5**), reaffirming the high reducing ability of biochar was responsible for the reduction reaction of Cr(VI).

As a fact, biochar alone can decrease about 37.2–42.0 mg L^{-1} aqueous Cr(VI) **(Figure 5-4c)**, higher than the reduction amount (13.5–39.4 mg L^{-1}) of biochar with ferric oxyhydroxides **(Figure 5-4a** and **Figure 5-4b)**. Correspondingly, the reduction rates of aqueous Cr(VI) by biochar alone (2.4–2.8 $\times 10^{-3}$ h^{-1}) were higher than that by biochar with Fe-L (1.5–2.0 $\times 10^{-3}$ h^{-1}) and Fe-H (1.8–2.7 $\times 10^{-3}$ h^{-1}) (**Figure 5-4g**). These results indicated that iron minerals, especially the Fe-L, inhibited the direct reduction rate and amount of aqueous Cr(VI) by biochar. One possible reason might be the lower initial Cr(VI) concentration in the Fe-L system (63.2 mg L^{-1}) compared with Fe-H (91.6 mg L^{-1}) and no Fe system (100 mg L^{-1}) when biochar was added. To exclude the possible impact from the initial concentration on the Cr(VI) reduction rate by biochar, different initial Cr(VI) concentrations from 60–100 mg L^{-1} were set for biochar reaction (**Figure E6** and **Figure E7**, **Appendix E**). Interestingly, no noticeable difference in the reduction rate constant was found with various initial concentrations for both BC400 and BC700 (**Figure E6** and **Figure E7**, **Appendix E**), indicating the initial Cr(VI) concentration was not the rate-limited step for biochar reduction within this concentration range. Instead, the consumption of electron by Cr(VI)-ferric oxyhydroxides complex (*i.e.,* electron for reduction of Cr(VI) sorbed on ferric oxyhydroxides or Fe(III) on ferric oxyhydroxide) should be the primary reason for the decrease of reduction constant and amount with Fe-L, which was explained detailedly in the following section.

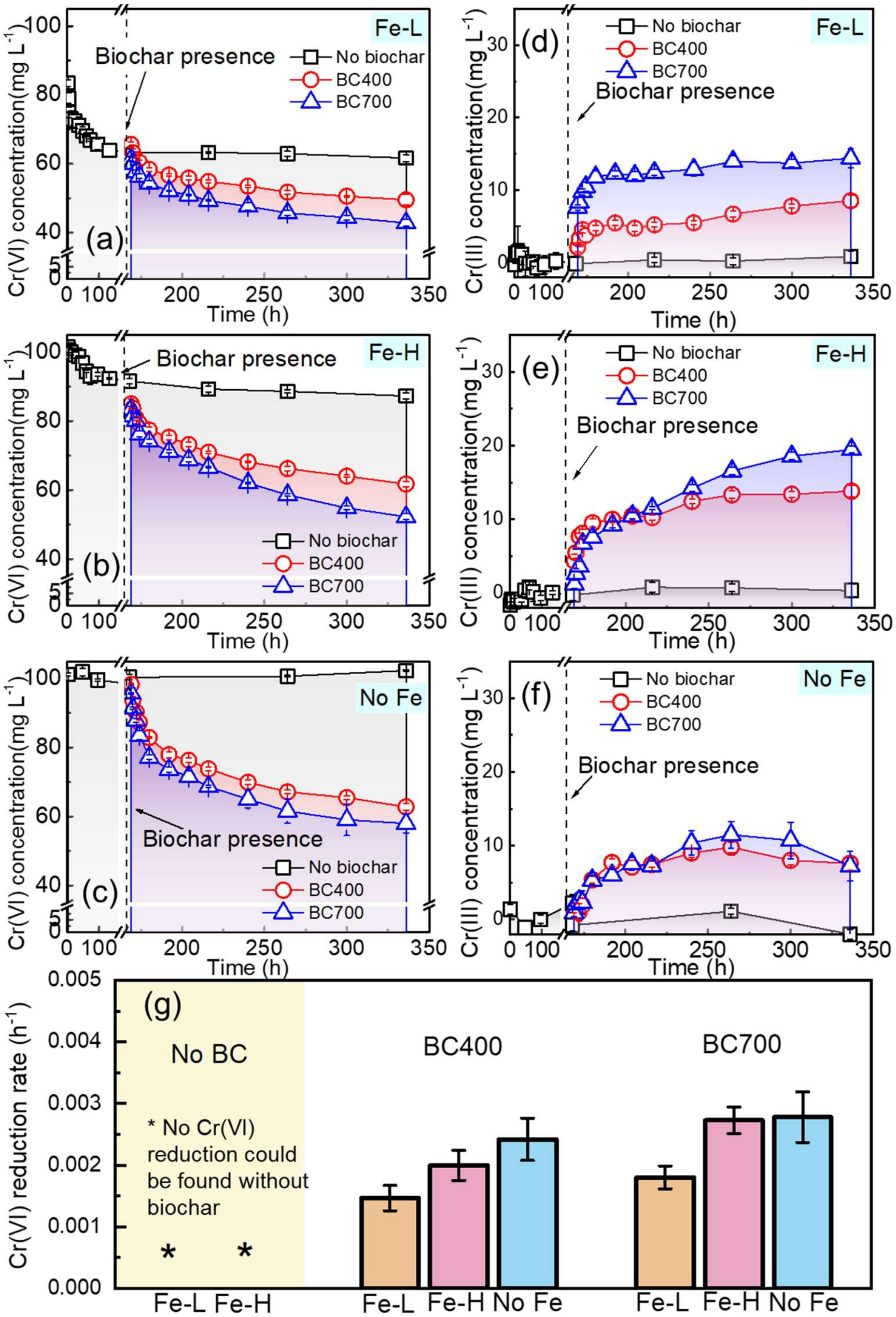

Figure 5-4 Changes in the concentration of Cr(VI) (a, b, c) and Cr(III) (d, e, f) in solution with biochar and iron minerals (biochar+Fe-L: a&d; biochar+Fe-H: b&e; biochar alone: c&f); reduction rates of Cr(VI) in solution (g).

Looking at the solid phase of the ferric oxyhydroxide-biochar mixture, we found that the proportion of Cr(VI) in the solids decreased from 97.2% to 49.0–49.9% for Fe-L and from 93.8% to 6.90–13.5% for Fe-H, with the increase of solid Cr(III) to 50.1–93.1% (**Table E3**). XPS analysis further confirmed the change of dominant Cr form from Cr(VI) to Cr(III) after reaction with biochar (**Figure E8, Appendix E**), again evidencing the occurrence of Cr(VI) reduction on the solid surface. TEM-EELS analysis on the iron mineral region also showed that the primary forms of Cr and Fe might be the Cr(III) (~578.8 eV) (Daulton and Little 2006) and Fe(III) (~706.0 eV) (Archanjo et al., 2017), respectively after biochar addition (**Figure 5-5**). The areas of Fe and Cr were highly associated, indicating the possible formation of iron-chromium minerals on iron minerals (*e.g.,* $Fe_{2-x}Cr_xO_3$ (Bishop et al., 2014, Mullet et al., 2007), **Figure 5-5f** and **Figure 5-5h**). Besides, sorption of the generated Cr(III) on the carbon area might also increase the Cr(III) proportion on the solid phase, which caused the formation of 10-nm Cr(III) spherical particles according to the EELS peak of Cr L3 edge at ~575.2 eV (Bishop et al., 2019, Daulton and Little 2006) (**Figure 5-5d** and Figure 5-5**e**). It should be noted that Cr L3 edge (~578.8 eV) on the iron mineral area (**Figure 5-5g**) was larger than Cr L3 edge (~575.2 eV) on the carbon area (**Figure 5-5e**) since more Cr(VI) with higher L3 edge (Arevalo-Lopez and Alario-Franco 2009, Daulton and Little 2006) were left on the iron minerals, which was consistent with XPS analysis (**Figure E8**).

Considering the reduction proportion of Cr(VI) in both solid and aqueous phases (**Table 5-1**), biochar with high crystallinity Fe-H showed a similar Cr(VI) reduction to biochar alone (36.6–43.9% *vs.* 36.3–41.3%). However, the Cr(VI) reduction proportion decreased from 36.3% in biochar alone to 29.9% and from 41.3% in biochar alone to 35.8% for BC400 and BC700 with lower crystallinity Fe-L, respectively (**Table 5-1**). Similar results were found in the soil system that the Cr(VI) immobilized amount by biochar in Fe-L soil (0.16–0.25 mg g^{-1}) was lower than its amount in the No-Fe soil (0.38–0.42 mg g^{-1}), while no significant differences were found between No-Fe soil (0.38–0.42 mg g^{-1}) and Fe-H soil (0.34-0.39 mg g^{-1}) with biochar (**Figure 5-3**). The discrepancy in the impact of Fe-L and Fe-H on the total Cr(VI) reduction amount was probably due to the different electron transfer routines and mechanisms among biochar-iron minerals-Cr(VI). It is worth noting that two pyrogenic carbon (BC400 and BC700) underwent a similar impact from iron minerals, implying that the different electron transfer processes might occur for a wide range of pyrogenic carbon.

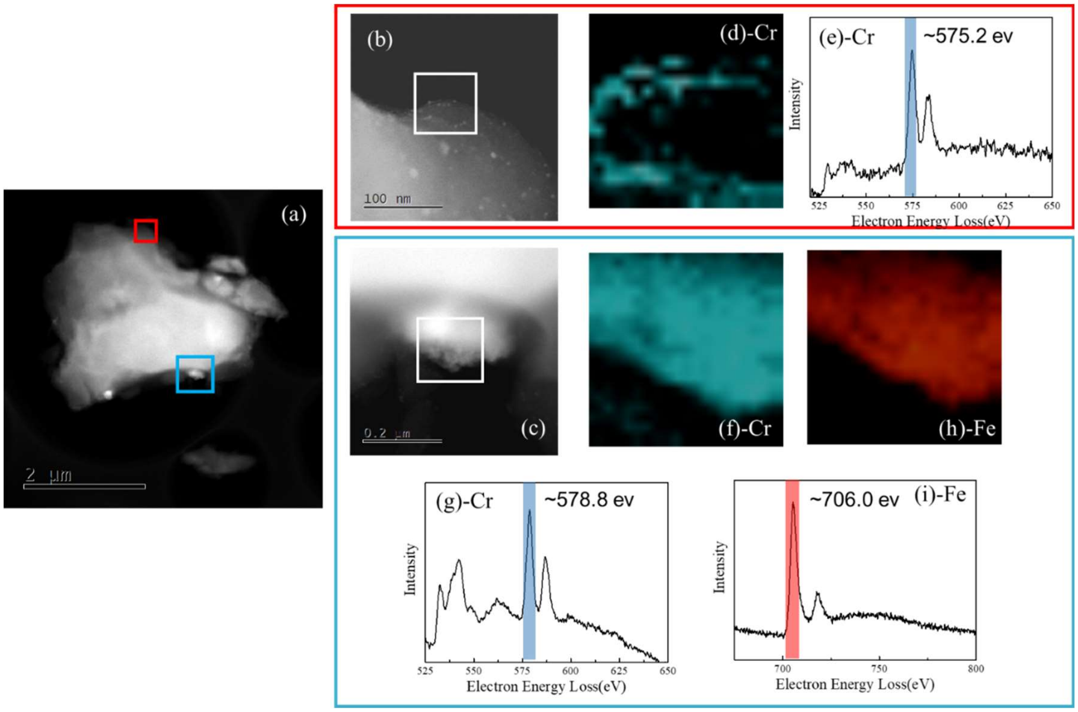

Figure 5-5 TEM image of BC400-Fe-L-Cr complex (a); TEM-EELS mapping (d) and EELS pattern (e) of Cr on carbon region (b, red); TEM-EELS mapping (f & h) and EELS pattern (g & i) of Cr and Fe on the iron region (c, blue).

5.3.3 Indirect electron transfer routine for Cr(VI) reduction with low-crystallinity ferric oxyhydroxides and pyrogenic carbon

Even if the reduction amount of Cr(VI) on the solid phase was considered, less reduction amount of Cr(VI) was observed for biochar with Fe-L than biochar alone or biochar with Fe-H. In addition to the direct reduction of Cr(VI) by biochar, low-crystallinity Fe-L could easily complex with biochar particles and thus caused the indirect electron transfer from biochar to Cr(VI) through iron mineral, leading to the lower Cr(VI) reduction amount.

Step one for indirect electron transfer routine: chemical bonding between biochar and Fe.

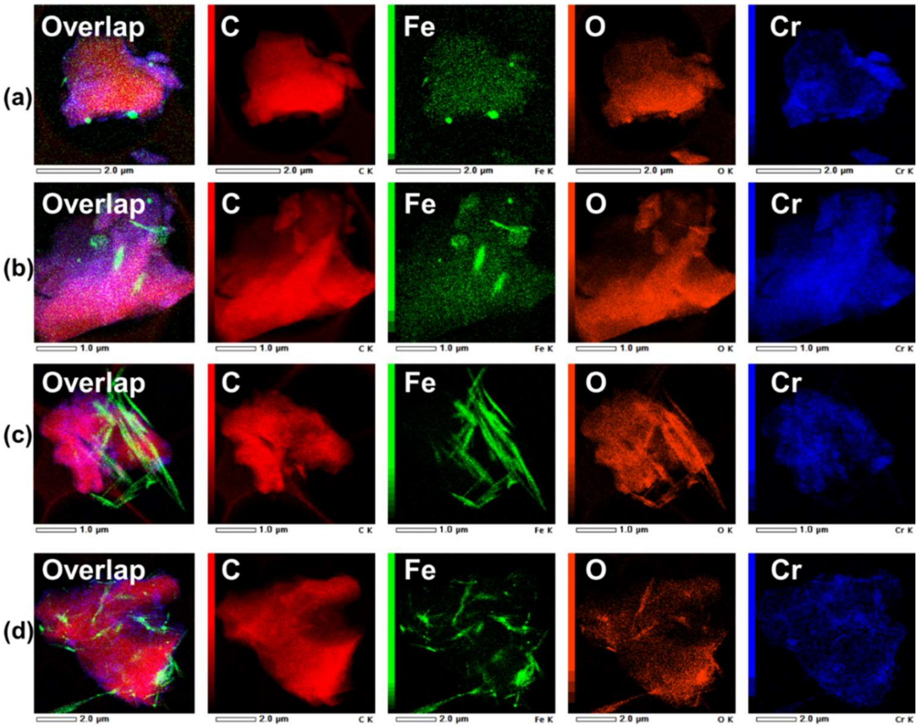

Figure 5-6 Element mapping of the complex of BC400-Fe-L-Cr(a), BC700-Fe-L-Cr (b), BC400-Fe-H-Cr (c), and BC700-Fe-H-Cr (d) formed by reaction between biochar and Cr-laden Fe-L/Fe-H.

TEM-EDS (**Figure 5-6**) showed a well-proportioned distribution of Fe on the biochar with Fe-L (*i.e.,* Fe almost covered the biochar surface, **Figure 5-6a** and **Figure 5-6b**) compared with Fe-H (*i.e.,* Fe still kept its acicular shape, **Figure 5-6c** and **Figure 5-6d**), indicating a stronger association of Fe-L on biochar surface. Higher solubility and complex potential of low-crystallinity iron led to this strong and homogeneous aggregation with biochar via electrostatic interaction and surface complexation (Bonneville et al., 2009, Lian et al., 2019). Besides, the change in the crystalline size of Fe-L was also higher than that in Fe-H after reaction with biochar (**Figure E9**), further suggesting the potent interaction between Fe-L and biochar. In fact, the aggregation of organic matter with iron minerals (*e.g.,* ferric hydroxide) widely occurs in the natural environment through adsorption, co-precipitation, or chemical bonding (Bahureksa et al., 2021, Fritzsche et al., 2021, Joseph et al., 2010).

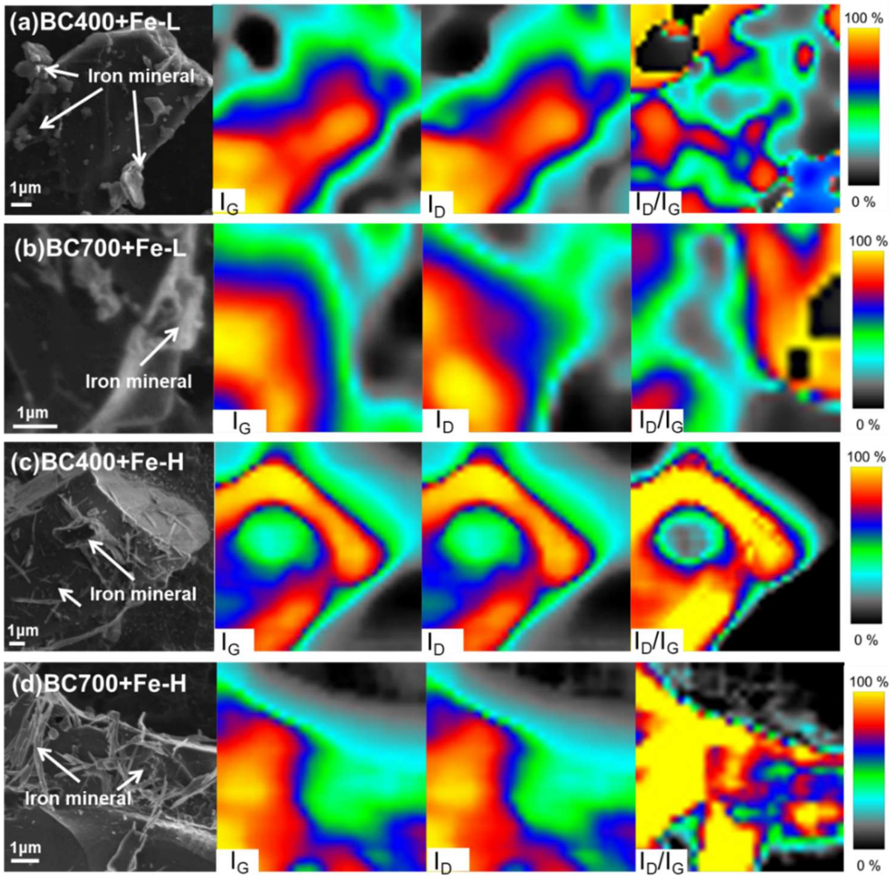

Figure 5-7 SEM images and Raman spectra mapping of I_D, I_G, and I_D/I_G for BC400-Fe-L-Cr complex (a), BC700-Fe-L-Cr complex (b), BC400-Fe-H-Cr complex (c), and BC700-Fe-H-Cr (d); Raman spectra and selected mapping area were shown in Figure E10

Raman-SEM and XPS analysis revealed the chemical combination between Fe-L and biochar. As detected by Raman-SEM (**Figure 5-7** and **Figure E10, Appendix E**), the ratios of I_D/I_G, which represents the amount of carbon defects, were higher near the joints of Fe-L for both BC400 and BC700 (**Figure 5-7a** and **Figure 5-7b**) compared with the other area. The higher carbon defects might be attributed to the combination between ferric oxyhydroxides and biochar surface (Sun et al., 2019) through chemical bonding such as C–O–Fe, introducing the metal-atom sites and -sp^3 hybridization defects (Xue et al., 2020) on the biochar surface (**Figure E10**). XPS analysis (**Figure 5-8** and **Table E4**) further evidenced this chemical bonding that a new peak centered at ~532.5–533 eV (ether-type-O of C–O–Fe bonding (Qian et al., 2017, Zhou et al., 2007)) was found on the Fe-L-biochar complex. Besides, oxidation of the biochar surface by Fe(III) might also result in the doping of O atoms on biochar (*e.g.,* oxidative formation of carbonyl or carboxyl (Xu et al., 2020e, Xu et al., 2021e)), leading to the increase of defects on the joint area (**Figure E10**). The high defect level around the joint area indicated the intense combination through chemical bonding (*i.e.,* C–O–Fe) between biochar and Fe-L, which might be the premise for the electron transfer from biochar to Fe-L (Zeng et al., 2020). Besides, this chemical combination might block the reactive sites on the biochar, alleviating the probability of direct interaction between biochar and Cr(VI) during the reduction process.

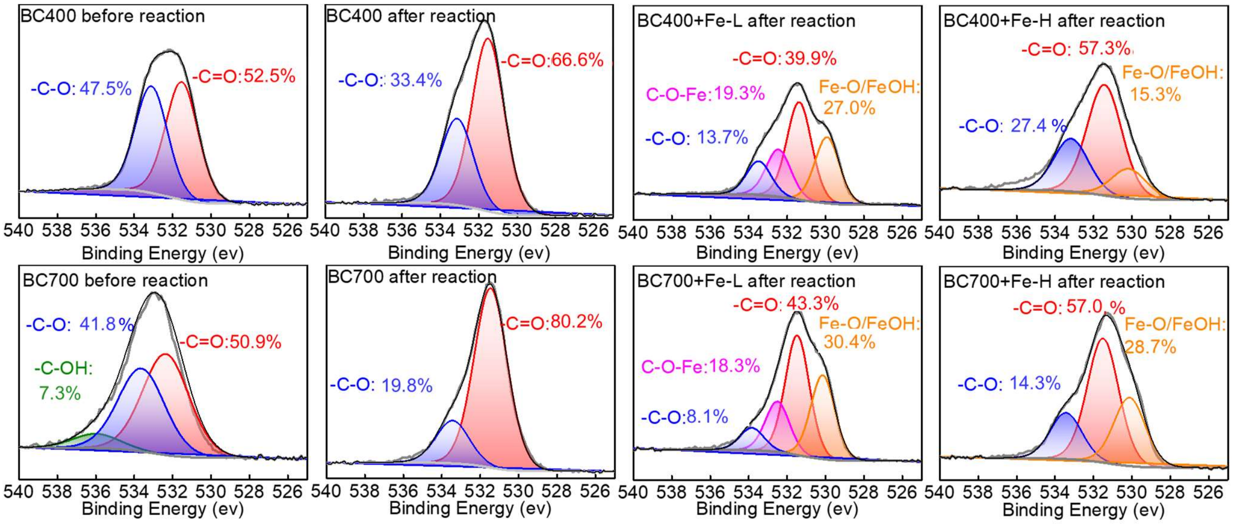

Figure 5-8 XPS spectra of O1s for biochar (BC400 and BC700), iron mineral (Fe-L and Fe-H)-biochar complex before and after Cr(VI) removal.

Step two for indirect electron transfer routine: electron from biochar to Fe-L

The electron transfer process from biochar to Fe-L was investigated by TEM-EELS analysis. Fe(II) could be found in the middle of Fe-L, which was near the combined region of biochar (**Figure 5-9a**), indicating the Fe(III) reduction on Fe-L by biochar. Besides, less reductive phenol was found on biochar near the region of Fe-L, again evidencing the consumption of electrons on biochar (**Figure 5-9a**). XPS further supported that Fe(II) was formed on Fe-L with about 30.1–30.5% Fe(II) as detected by XPS analysis (**Figure E11** and **Table E5**). Moreover, the redox reaction between biochar and Fe-L without Cr(VI) also showed the reductive formation of Fe(II) on Fe-L with the oxidative transformation of the surface functional group (*i.e.,* –C–O to –C=O) on biochar according to both XPS (**Figure 5-8, Figure E12**, and **Figure E13**, **Appendix E**) and TEM-EELS analysis (**Figure E14**), reaffirming this second step of indirect electron transfer, *i.e.,* electron transfer from biochar to Fe-L.

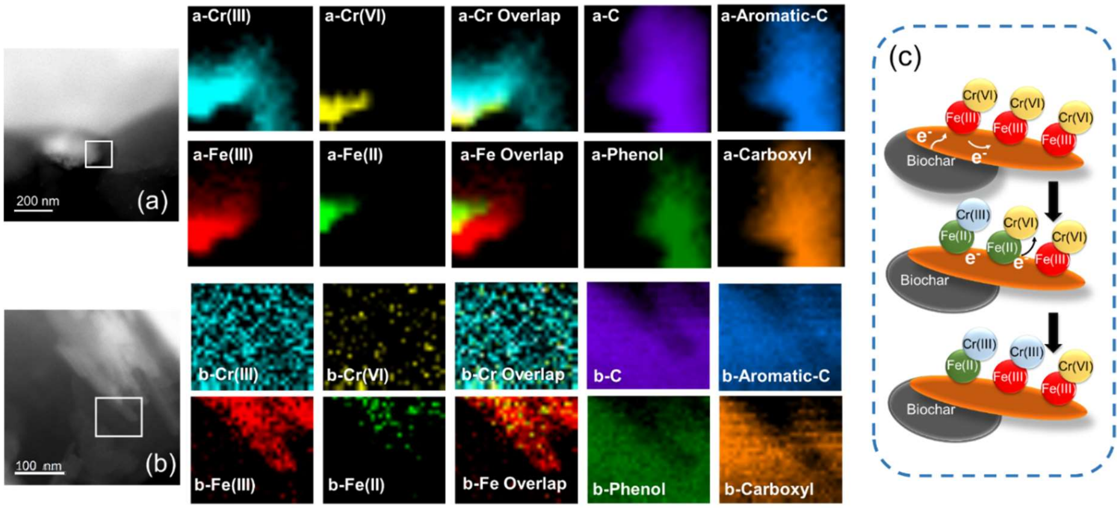

Figure 5-9 TEM-EELS mapping of C, Cr, and Fe with speciation on the selected area of biochar-Fe-L-Cr complex (a) and biochar-Fe-H-Cr complex (b); Schematic diagram for the electron transfer route between biochar and low crystallinity Fe-L (c). EELS spectrum can be found in Figure E15;

Step three for indirect electron transfer routine: electron from Fe(II) to Cr(VI).

TEM-EELS also revealed the formation of Cr(III) in the middle of the iron mineral with Fe(II), while Cr(VI) was only found at the bottom of the iron particle with Fe(III), which was far away from the combination region (**Figures 5-9a** and **E15**). Several electron transfer processes might contribute to this unique and representative distribution of Cr(VI)/Cr(III) and Fe(III)/Fe(II) on the biochar-mineral surface (**Figure 5-9** and **Figure E16**). The first and most possible one was the indirect electron transfer through the valence transformation of the iron (**Figure 5-9c**), *i.e.,* the electron on Fe(II) further transferred to Cr(VI). Since electrons on the biochar failed to transfer to Fe(III) at the bottom of ferric oxyhydroxide, which was relatively far from carbon particles, limited Cr(VI) reduction was found on these iron areas (**Figure 5-9a**). The Fe(II) proportion on the biochar-reduced Fe-L (*i.e.,* Fe-L after reduction by biochar) decreased from 31.5–32.9% to 21.6–23.9% after 7-day Cr(VI) reduction (**Figure E13, Appendix E**), further evidencing the existence of this electron transfer process. Another possibility was that biochar might directly reduce Cr(VI) on the approached ferric oxyhydroxide. However, this process might be less crucial compared with the first indirect routine due to the following reason: (1) the reduction rate of the formed Fe(II) on Fe-L was faster than biochar (**Figures E17–18, Appendix E**); (2) Reducing moiety (*e.g.,* –C–O) on biochar would be oxidized by Fe(III) quickly, which inhibited the reducing capacity of biochar alone (Xu et al., 2020e, Xu et al., 2021e) (**Figure 5-8** and **Figure E12**). (3) Transition of Fe(II) to Fe(III) was much more apparent than the transition of –C–O to –C=O during the Cr(VI) reduction by biochar-Fe-L complex (**Figure 5-8**, **Figure E12**, and **Figure E13**); (4) Cr(VI) was combined on Fe-L mainly through inner-sphere complexation (**Figure E2** and **Figure E3**), limiting its potential to release and reduced by biochar; (5) chemical combination between Fe-L and biochar might cause the attenuation of direct Cr(VI) reduction by biochar due to the block of reactive sites. Besides, released organic carbon from bulk pyrogenic carbon might also have a considerable reducing capacity (Xu et al., 2021a), which might be sorbed on the iron surface and then reduce the Cr(VI). However, the dissolved organic carbon from BC400 had a limited effect on the Cr(VI) reduction and even inhibited the sorption of Cr(VI) on ferric oxyhydroxides (**Figure E19**), which might be attributed to its low concentration and competition of sorption sites with Cr(VI).

In summary, the electron transfer from biochar to Cr(VI) combined with Fe-L occurred mainly through the indirect pathway (**Figure 5-9c**); that is, biochar combined with iron mineral (step 1) and reduced the Fe(III) to Fe(II) (step 2) before the Cr(VI) reduction by Fe(II) (step 3). During this electron transfer routine, Fe(III) on Fe-L "catches" the electron from biochar, which was stored as Fe(II) even after Cr(VI) reduction, as evidenced by XPS and TEM-EELS. These electrons could not "reach" Cr(VI) and thus caused the decrease of Cr(VI) reduction amount compared to the direct reduction of Cr(VI) by biochar. In fact, the electron-donating capacity (EDC) of biochar also showed an apparent decrease with the co-existence of Fe-L (0.66–0.96

mmol e⁻ g^{-1}) compared with biochar alone (0.84–1.12 mmol e⁻ g^{-1}) or with Fe-H (0.81–1.06 mmol e⁻ g^{-1}, **Figure 5-10**). Higher electron accepting capacity (EAC) of Fe-L might cause this decrease due to the electron transfer from biochar to Fe-L. These electrochemical results further evidenced the indirect electron transfer process and the "capture" of electrons within the biochar-Fe-L complex.

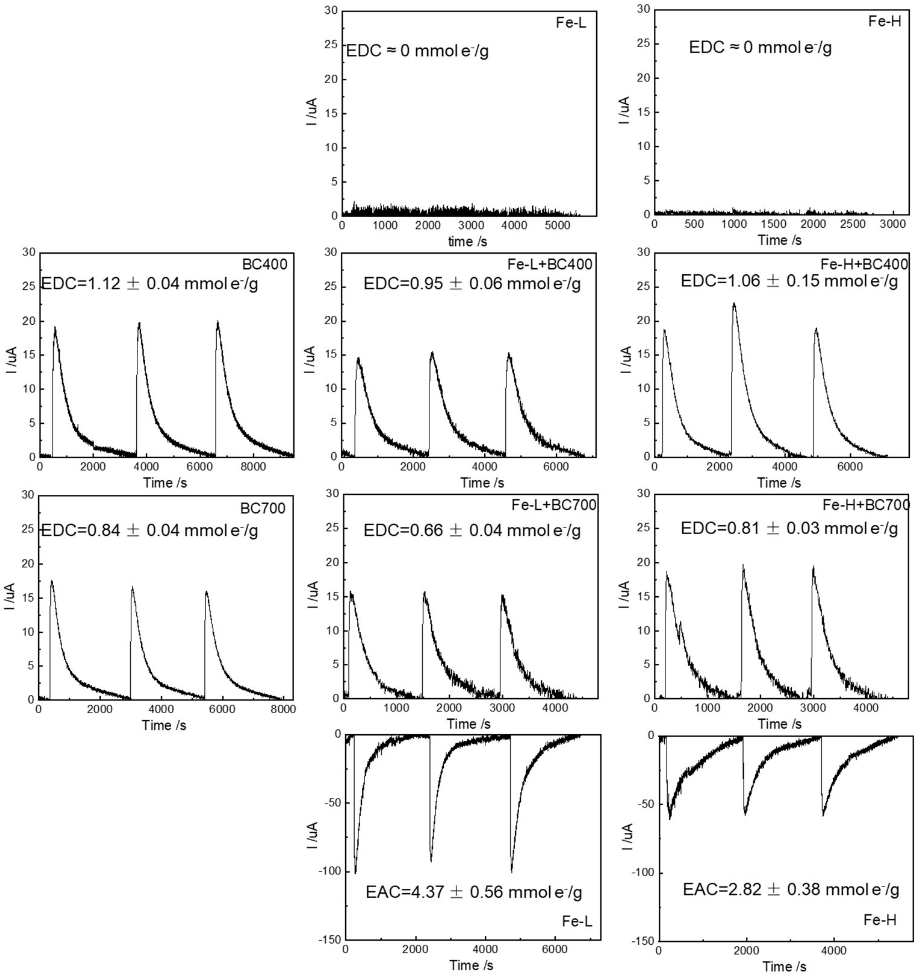

Figure 5-10 EDC and EAC of biochar and iron mineral in the separated or combined system

It is worth mentioning that the direct electron transfer between biochar and Cr(VI) also occurred with the formation of Cr(III) on the biochar surface (**Figure 5-5**), but its contribution might be lower than the indirect one. To evaluate the potential contribution of these two electron transfer routines, the remained Cr(VI)-containing solution was replaced by the background solution without any Cr(VI) after 7-day sorption of Cr(VI) by Fe-L. Then biochar was added to launch the indirect electron transfer, and about 21.8–23.9 mg L^{-1} Cr(VI) on the Fe-L was reduced, representing 66.6–73.0% of the Cr(VI) reduction amount in the system with the solution Cr(VI) (**Figure E20**). Therefore, we could conclude that the majority of Cr(VI) was reduced via the indirect electron transfer routine with Fe-L and biochar.

5.3.4 Direct electron transfer routine for Cr(VI) reduction by high-crystallinity ferric oxyhydroxides and pyrogenic carbon

Compared to Fe-L (**Figure 5-6a** and **Figure 5-6b**), limited complexation between biochar and high-crystallinity iron mineral Fe-H was found, and Fe-H was physically attached to the biochar surface since it kept its original acicular morphology **(Figure 5-6c** and **Figure 5-6d)**. No significant change in I_D/I_G was found near the joint area of Fe-H and biochar, and a similar strength of I_D/I_G was found on the whole biochar surface (**Figure 5-7c** and **Figure 5-7d**), again evidencing the limited combination and reaction between biochar and Fe-H. Only Fe-O/Fe(O)OH bound could be detected on the biochar-Fe-H complex (**Figure 5-8**), and a slight change of the crystalline size was found on Fe-H after the interaction of biochar (**Figure E9**), further verifying that only physical attachment was formed between biochar and Fe-H. Limited chemical combination and higher stability of the crystal iron mineral (Chen et al., 2015a, Cornell and Schwertmann 2003) would inhibit the electron transfer between biochar and Fe-H, contributing to the low Fe(II) proportion on Fe-H (14.4–17.0%, **Figure E11** and **Table E5**). Thus, only Fe(III) and Cr(III) could be detected by TEM-EELS (**Figure 5-9b** and **Figure E15**) on the Fe-H with inconspicuous signal and distribution of Cr(VI) and Fe(II). These observations indicated that the indirect electron transfer between the high-crystallinity ferric oxyhydroxide (Fe-H) and biochar might be more laboursome than the low-crystallinity ferric oxyhydroxide (Fe-L). Besides, less sorption amount (**Figure 5-3**) and limited inner-sphere complexation (**Figure E1** and **Figure E2**) of Cr(VI) on the Fe-H would also alleviate the indirect electron transfer through the iron mineral. Instead, the direct electron transfer process between biochar and aqueous Cr(VI) should be dominant for Fe-H.

Rich surface functional groups on pyrogenic carbon can directly serve as the moiety for Cr(VI) reduction (Xu et al., 2020f). The ratio of –C–O to –C=O for BC400 and BC700 decreased from 0.91 to 0.34-0.50 and from 0.96 to 0.19-0.25, respectively, after Cr(VI) reduction based on the XPS analysis of O1s (**Table E2** and **E4**). XPS analysis about the C1s showed similar results that more oxidative O-containing functional groups, such as the –COO group, were formed on the biochar surface (**Table E6**) after Cr(VI) reduction.

The occurrence of Fe^{3+} might inhibit the direct reduction of aqueous Cr(VI) by biochar since the interaction with Fe(III) would oxidize the surface functional groups of biochar, which might result in the decrease of aqueous Cr(VI) reduction amount (Xu et al., 2020e, Xu et al., 2021e). A similar phenomenon was found on Fe-L in this study with an apparent decrease of biochar's surface –C–O (–C–O/–C=O ratio as 0.19-0.34) and higher Fe(II) amount (30.1–30.5%). However, no apparent change of O-moiety was found on the biochar with Fe-H, which only altered the –C–O/–C=O ratio from 0.25-0.50 to 0.25-0.48, compared with the biochar alone after Cr(VI) reduction. The higher stability of iron and limited chemical combination between Fe-H and biochar might block the oxidation of O-moiety on biochar by Fe(III).

In summary, direct electron transfer from the reductive C-O functional group on biochar to Cr(VI) was the main electron transfer route for Cr(VI) reduction with high-crystallinity ferric oxyhydroxides. The similar EDC of biochar with and without Fe-H also evidenced that the direct electron transfer was dominant for Cr(VI) reduction process by biochar with Fe-H (**Figure 5-10**). The indirect electron transfer from biochar to Fe-H for reducing Cr(VI) was alleviated due to the weak combination between Fe-H with biochar, high iron stability, lower EAC, and negligible Cr complexation on Fe-H.

5.4 Conclusions

This study demonstrated that the crystallinity of ferric oxyhydroxide minerals affected the immobilization/reduction capacity and electron transfer routes of Cr(VI) in the presence of biochar (**Figure 5-11**). The reduction of Cr(VI) in the low-crystallinity ferric oxyhydroxide system was mainly caused by the indirect electron transfer, *i.e.,* biochar firstly donated the electron to Fe(III) on the iron minerals for Fe(II) generation, which further reduced the Cr(VI) sorbed on iron minerals afterwards. Parts of the electrons from biochar were consumed for Fe(II) formation even after Cr(VI) reduction during the indirect electron transfer, leading to a decreased reduction amount of Cr(VI) compared with the direct electron transfer from biochar to Cr(VI). For the high-crystallinity ferric oxyhydroxides, the indirect electron transfer pathway was alleviated due to its limited combination with biochar, less sorption amount of Cr(VI), and higher Fe(III) stability of the iron crystalline. Direct electron transfer from biochar to Cr(VI) became the main electron transport for Cr(VI) reduction. Our results indicated that electron transfer mechanisms involving iron minerals would change with the iron crystallization process, which was critical for the immobilization of contaminants with biochar.

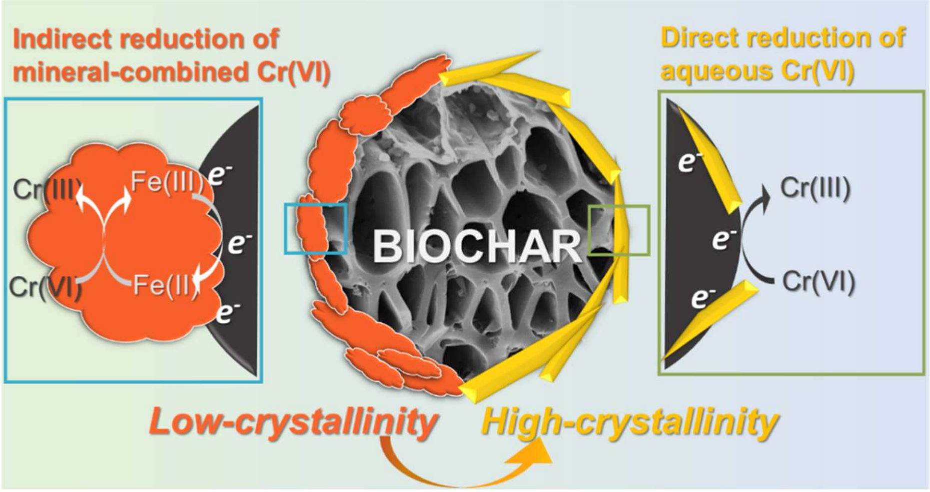

Figure 5-11 Graphical summarization of Chapter 5

Chapter 6 Fe species in Fe-Mn Biochar for Effective Cr(VI) Reduction: Key Role of the Embedded Zero-valent Iron Clusters within Fe-Mn Oxide

6.1 Introduction

The global environmental concern is increasing due to the growing demand for clean water and population expansion. Practical, affordable, and environmentally benign treatment technologies for water decontamination are urgently needed (Kümmerer et al., 2018, Shannon et al., 2008, Zhang et al., 2022b). Zero-valent iron (ZVI) is one of the most critical multifunctional materials for water purification due to its unique properties, including high reactivity, natural abundance, facile synthesis, the broad spectrum of pollutants immobilization, and environmental benignancy (Bae et al., 2018, Zhao et al., 2016b).

One of the main bottlenecks in practical applications of ZVI-based materials in water is the low Fe efficiency caused by self-aggregation (Zhou et al., 2022b). Controlling the particle size to the nano-level and stabilizing the ZVI particles with carbon materials, such as biochar, a carbon-rich product from biomass-waste pyrolysis with rich porous structure and surface functionality (He et al., 2022, Lehmann et al., 2021, Xiao et al., 2018a), can be a promising strategy to prevent ZVI self-aggregation (Xu et al., 2020c). The nature of waste utilization and carbon sequestration of biochar also bring the environmental and sustainable advantage of as-formed ZVI-biochar composites (Lehmann et al., 2021, Wan et al., 2020c). Moreover, pyrolysis with biochar can directly reduce the iron oxides to ZVI, simplifying the preparation process of ZVI-biochar composites with no extra chemicals (Fan et al., 2020, Xu et al., 2022a).

However, surface passivation during the storage and decontamination process has been a major concern for the efficiency of ZVI (Bae et al., 2018, Gu et al., 2019, Guan et al., 2015). Surface passivation is caused either by the interactions of ZVI with O_2 and H_2O that results in the surface iron oxide layer (mainly amorphous Fe (hydro)oxide) (Bae et al., 2018) or by the formation of the iron-pollutant complexes and precipitates during the pollutant removal (Fan et al., 2020, Zhang et al., 2018a). Although the passivation layer could assist in removing contaminants through sorption and complexation (Mu et al., 2017, Xu et al., 2021c), it significantly inhibits the electron-donating potential and efficiency of the ZVI for the redox-related process since the electron transfer between core ZVI and surface iron oxide was the rate-limited step (Hu et al., 2019, Li et al., 2021b, Vogt and Weckhuysen 2022). In the latest studies, even the integration of ZVI with supporting carbon typically had a limited effect on the de-passivation (Zhang et al., 2022a), and the strong oxidation capacity of high-temperature biochar might enhance the oxidation of ZVI (Xu et al., 2022a, Zhong et al., 2021b).

To improve the efficiency of the core-ZVI during the application, different strategies, including de-passivation (acid treatment or chemical reduction) and surface modification (Bae et al., 2018, Garcia et al., 2021, Ling et al., 2022) were used. For example, Wei and co-workers (2022) exert tensile strain on ZVI by boron introduction, thereby populating the oxide shell with abundant electrons for pollutant immobilization. However, the de-passivation approach normally requires a high amount of chemicals (mainly acid and reducing agent) before usage, and the de-passivated ZVI will quickly react with O_2 or H_2O to form the dense oxide layer again, leading to lower stability and high cost. Besides, surface passivation might still happen on modified ZVI during the interaction with pollutants during the utilization, accounting for the commonly found decreased reactivity and efficiency. Therefore, developing a better strategy and designing an active ZVI-containing composite with higher passivation-resistance stability, electron/iron efficiency, and economic benefits is crucial.

Inhibiting the Fe atom diffusion and restricting its coordination with O_2, H_2O, impurities, and pollutants can be the key to the passivation resistance of ZVI-based material(Bae et al., 2018, Li et al., 2021d). Using binary oxide as the precursor may be a potential strategy to separate and stabilize the ZVI. In particular, Fe and Mn can form a series of binary oxides, including $MnFeO_3$, $MnFe_2O_4$, and $MnFeO_2$, with chemical binding (Fe−O−Mn), due to the similar radius, properties, and valence states (Liu et al., 2021a, Wen et al., 2020, Zhang et al., 2014). The Fe atoms can be separated by Mn in the binary oxides when Fe and Mn ions are homogeneously dispersed and mixed on the supporting material (biochar). After forming the binary oxides, Fe oxides can be reduced to metallic Fe via a suitable reducing condition (*i.e.,* thermal reduction with biochar) (Xu et al., 2022a, Xu et al., 2021f). This process may resemble oxygen-vacancy formation within the binary oxides (Wu et al., 2021), but a more strongly reductive state would be needed to construct ZVI with the complete removal of oxygen (Zhou et al., 2022a).

Chromium, a commonly encountered toxic metal, was selected as the target to evaluate the electron-donating potential of different ZVI species. The current remediation technologies still face low removal performance for highly toxic Cr(VI), and the reduction of Cr(VI) to less toxic Cr(III) is the key to effective Cr removal from wastewater. This study proposes biochar as an appropriate supporting material for anchoring Fe-Mn oxide and customizing its transformation, owing to its rich surface area, oxygen functionality, and inherent alkalinity (Xia et al., 2019).

Through this tailored process, Fe(0) is hypothesized to be formed, embedded, and stabilized in the Fe-Mn oxide structure during biochar pyrolysis, which can impart a higher Fe efficiency for electron donating. To testify the hypothesis, a series of Fe-Mn biochar with different embedded ZVI contents were fabricated, and the mineral speciation and valence state were characterized to evidence the in-situ formation of embedded ZVI clusters. The Fe utilization efficiency of the embedded ZVI clusters was evaluated and compared with commercial and modified ZVI. The theoretical calculation was conducted to evidence the underlying mechanisms, and the economic benefits were accordingly assessed. Accordingly, we proposed a brand-new strategy for preparing active and low-cost ZVI-based material for water decontamination.

6.2 Material and Methods

6.2.1 Preparation of Fe-Mn biochar

All reagents used in the synthesis process were analytical grade unless noted, with the detailed information provided in **Appendix A**. The biochar used in this study was produced from the locally abundant woody yard waste at the EcoPark in Hong Kong (He et al., 2021b). To understand the impact of biochar properties on the Fe-Mn mineral transformation and embedded ZVI clusters formation, we produced two pristine biochar by pyrolysis at 550 and 850°C for 2 h under the N_2 atmosphere with a ramping rate of 10 °C min^{-1}, based on the before results. The as-prepared biochar was ground by mortar and sealed in a dry container. Next, Fe and Mn salts (2% each by mass of biochar) were co-dissolved in a beaker with DI water (200 mL) and biochar (2 g). The mixture was stirred at 200 rpm for 24 h and dried at 60°C for at least 72 h. The biochar-mineral complex was ground for homogeneity, passed through a 120-mesh sieve, and then pyrolyzed under 850 °C for 2 h for ZVI formation. The formed biochar composites were denoted as BC550-FeMn-850 and BC850-FeMn-850 (Fe-Mn biochar).

To better understand the potential transformation of mineral clusters during the pyrolysis with biochar, different holding times ranging from 1−8 h were selected to treat Fe-Mn precursors with BC850. In addition, optimized Mn amounts (0.5−8%) were used to prepare different Fe-Mn precursors with BC850 and 2% Fe to evaluate the potential role of Mn on the efficiency of formed ZVI. Fe-Mn biochar with higher Fe and Mn amounts (2−4%) was also produced. For comparison, Fe biochar and Mn biochar were produced with a similar process (2 h pyrolysis at 850°C). Fe biochar served as the control to compare the reactivity of the ZVI alone on biochar, while the potential impact from Mn oxides was evaluated by Mn biochar. Pristine biochar without any mineral addition was also prepared under a similar procedure, and it was washed with HCl and water to ensure a similar acidity compared with Fe-Mn biochar. All the samples were stored in the container under a dry N_2 atmosphere until their characterization and use.

6.2.2 Cr(VI) removal efficiency

We conducted batch experiments for the Cr(VI) removal in simulated wastewater open to the atmosphere at 25 °C. Typically, 0.1 g of the Fe-Mn biochar composite was mixed at 250 rpm in 100 mL solution containing 15 mg L^{-1} Cr(VI). The solution pH was maintained at ~6.5 by adding an appropriate amount of HCl or NaOH, and the ionic strength was controlled by adding 10 mmol of NaCl. During the 24-h reaction, ~1 mL of solution was collected and separated to detect Cr concentration and speciation at the selected time intervals. The concentration of Cr(VI) was determined by the colourimetric method at 540 nm using diphenyl-carbohydrazide, and the total Cr concentration was determined by the ICP-OES (Xu et al., 2019b). The Cr(VI) removal kinetics by different Fe-Mn biochar was calculated based on the Cr(VI) concentrations at different times. All kinetics experiments were conducted in triplicate.

After the 24-h reaction, the solids were collected through filtration (0.45 μm) and freeze-dried to evaluate the Cr speciation (similar to section 3.2.4). The Cr(VI) removal efficiencies of Fe biochar and Mn biochar were assessed for comparison under a similar procedure. We also conducted batch experiments for the Cr(VI) removal efficiency under co-existed anions and simulated wastewater (**Appendix F**). Commercial-ZVI, reduced ZVI, S-ZVI, and Ni-ZVI were also prepared as the widely used ZVI-based materials (Tian et al., 2021a, Xu et al., 2020b, Zhou et al., 2022b) (**Appendix F**), aand the removal efficiency was tested to compare Cr(VI) removal performance and Fe efficiency. The Fe utilization efficiency (Fe efficiency), i.e., the proportion of Fe used for the Cr(VI) reduction by offering electron, was calculated (**Eq.6.1**) based on the electron transfer between Fe(0) and Cr(VI) (1:1) (**Eq.6.2**).

$$\text{Fe efficiency for Cr(VI) reduction (mol/mol)} = \frac{Cr(VI)\ removed\ (mol)}{\text{Fe added (mol)}} \qquad \textbf{Eq.6.1}$$

$$\text{Fe(0)} + \text{Cr(VI)} \rightarrow \text{Fe(III)} + \text{Cr(III)} \qquad \textbf{Eq.6.2}$$

6.2.3 Passivation-resistance stability

Passivation caused by the oxidation of Fe(0) by water or oxidants might lead to fewer electrons received by the Cr(VI). To assess the stability of as-prepared Fe-Mn biochar during the interactions with H_2O and O_2, Fe-Mn biochar was oxidized by natural oxidation (room conditions for 1 and 3 months), wet oxidation (water with O_2, 10 g L^{-1}), water interaction (water without O_2 by N_2 purging, 10 g L^{-1}), or accelerated oxidation with H_2O_2 (0.5, 1, and 5%, 10 g L^{-1}). The change in ZVI proportion was estimated, and the reducing capacity for Cr(VI) removal after the oxidation process was determined by batch experiments. Fe-biochar was set as the control to compare the passivation-resistance stability of ZVI without Mn. Reduced ZVI by $NaBH_4$ (**Appendix F**) was also used as the control for the oxidation stability of ZVI particles alone.

6.2.4 Characterization

To evidence the speciation and morphology of embedded ZVI in Fe-Mn oxides, different Fe-Mn biochar composites were characterized by XRD, AC-STEM with selected area electron diffraction patterns (SAED), and HR-TEM with EDX. An XPS with depth etching was used to identify the Fe(0) contents and Mn states over varying depths within the Fe-Mn biochar, which is critical for evaluating the surface passivation of ZVI and the potential formation of ZVI clusters without a crystal lattice (Hu et al., 2019, Li et al., 2021d). Hydrogen temperature-programmed reduction (H_2-TPR) and Raman analyses were conducted to evaluate the construction of embedded ZVI clusters associated with biochar pyrolysis. Details for the characterization methods was shown in **Appendix B**. Besides, DFT calculations were performed to assess the transformation process of Fe-Mn minerals with biochar and the combination energy during the immobilization and passivation process (**Appendix F**). An economic comparison of as-prepared Fe-Mn biochar and ZVI was conducted based on the costs of the feedstock only (**Appendix F**).

6.3 Results and Discussion

6.3.1 Cr(VI) removal performance

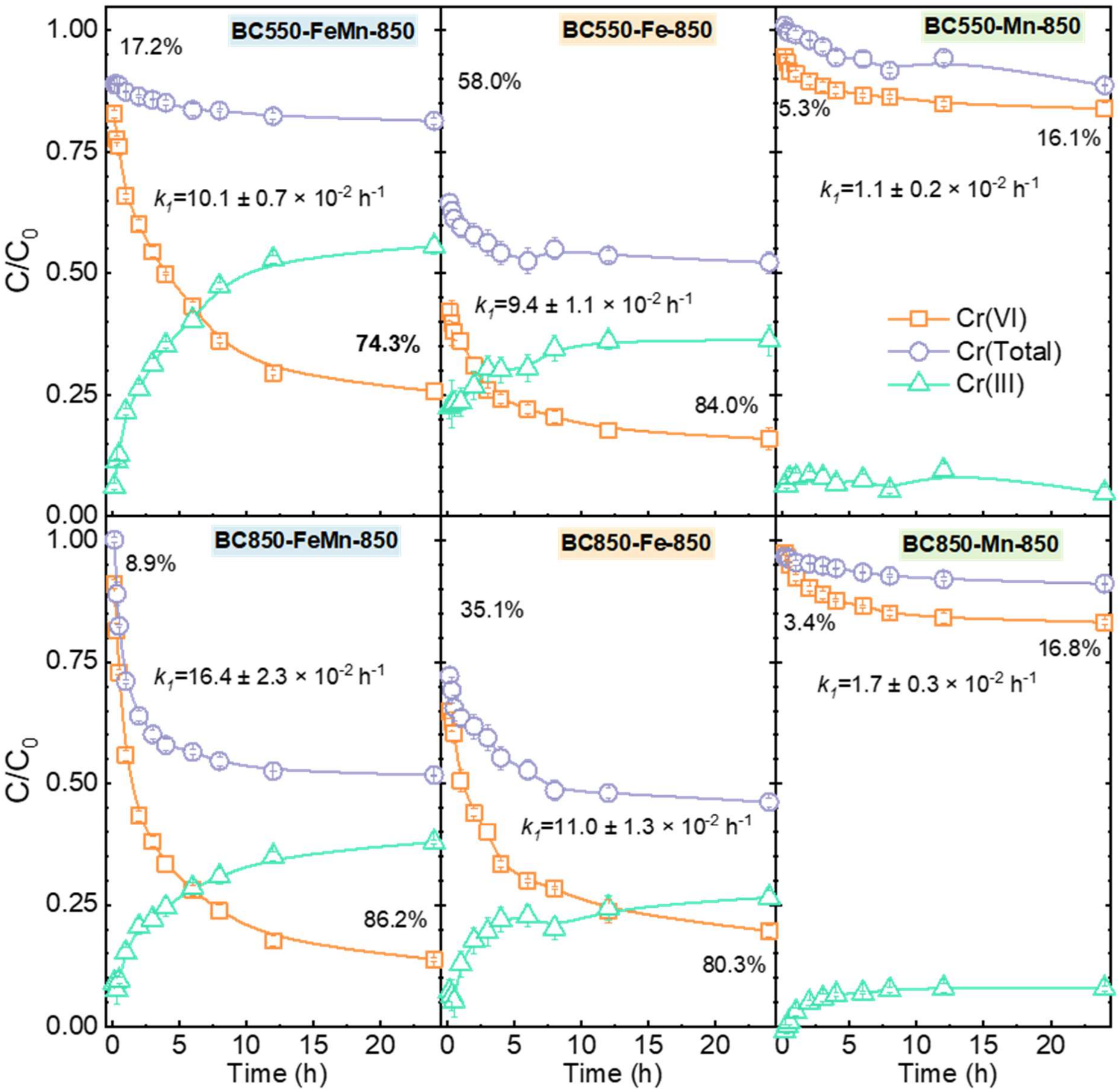

Figure 6-1 Change of chromium concentration with different biochars; The numbers showed the removal proportion of Cr(VI) after 0.25 h or 24 h and the removal kinetics constants.

Approximately 74.3−86.2% of Cr(VI) was removed by the Fe-Mn biochar after the 24-h reaction (**Figure 6-1**), and the removal kinetics (rate coefficients) were estimated to be 10.1−16.4 × 10^{-2} h^{-1}. Compared with the unary metal-modified and pristine biochar with the same holding time (2 h) and total metal content (2% + 2% *vs* 4%), the removal capacity of Fe-

Mn biochar (~74.3−86.2%) was slightly higher than that of Fe biochar (~80.3−84.0%) but much larger than that of Mn biochar (~16.1−16.8%) and pristine biochar (12.8−14.6%, **Figure F1, Appendix F**). These results indicated that Fe was the key to the Cr(VI) reduction and immobilization by the Fe-Mn biochar, while the Mn minerals and carbon phases had only limited contributions. The XPS analysis revealed that the main Cr species was Cr(III), with a binding energy of 577.0−577.4 eV after the immobilization process (**Figure 6-2**), implying the reduction of Cr(VI) by ZVI was the key to the Cr(VI) decontamination. It is noted that a higher amount of Cr(III) remained in the solution after 24-h reaction, which required further treatment by precipitation for the entire removal process. In this study, we primarily focused on the Cr(VI) reduction process to evaluate the Fe utilization efficiency in Fe-Mn biochar.

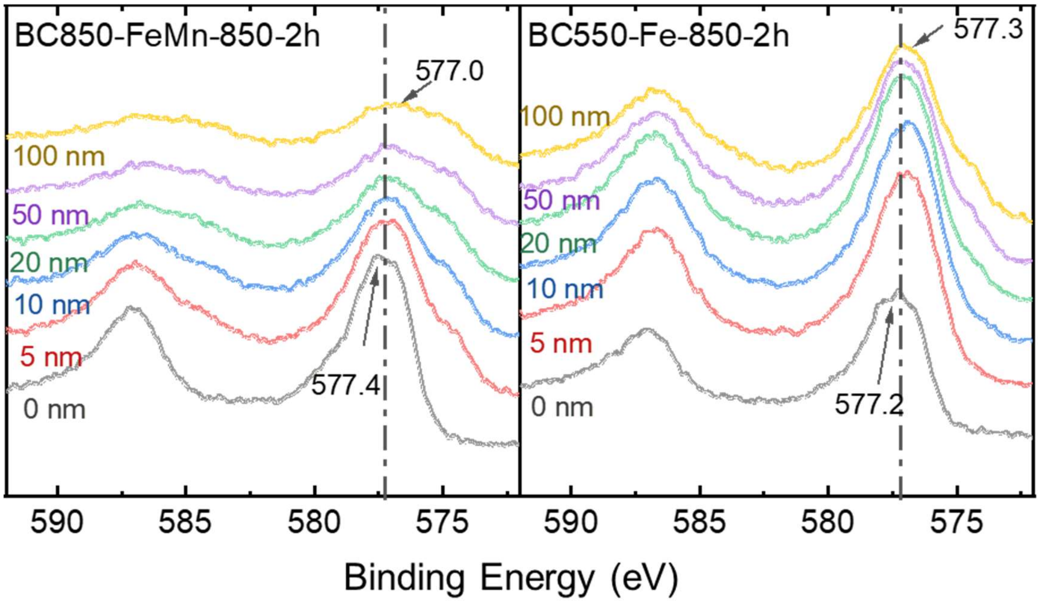

Figure 6-2 XPS depth profiling analysis of the Cr 2p binding state in the BC850-Fe-Mn-850-2h and BC550-Fe-850-2h after Cr(VI) removal.

6.3.2 Fe efficiency of Fe-Mn biochar for Cr(VI) removal

Theoretically, each Fe(0) atom could reduce one Cr(VI) to Cr(III) by offering electrons (**Eq.6-2**), and the Fe efficiency for the Cr(VI) reduction of different Fe-Mn biochar and Fe-biochar was calculated accordingly. The efficiency of Fe-Mn biochar was much higher than the Fe biochar containing the same Fe content (0.55−0.71 > 0.51−0.52 for 2% Fe; 0.41 > 0.33−0.34 for 4% Fe) (**Figure 6-3**).

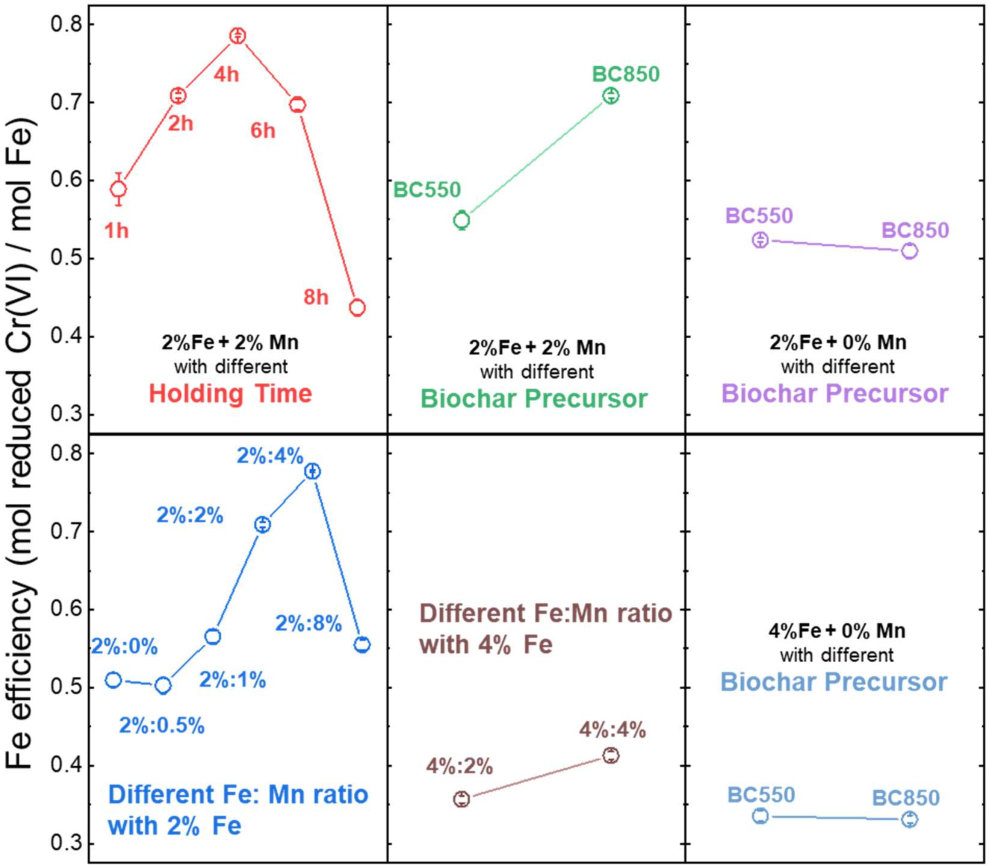

Figure 6-3. Fe efficiency of different Fe-Mn biochar and Fe biochar during the Cr(VI) removal, all Fe-Mn biochar was prepared with BC850 to compare holding time and ratio if it was not specified.

Considering the different preparation conditions, the Fe-Mn biochar produced with BC550 as the precursor showed lower Fe efficiency for Cr(VI) removal than BC850-FeMn-850, and the Fe efficiency increased first (1−4 h) and then decreased with the increasing holding time

(**Figure 6-3** and **Figure F2**). Besides, reducing Cr(VI) by the Fe-Mn biochar was sensitive to a critical concentration of Mn (0.5−8%). That is, increasing the Mn content to 4% in the composites facilitated the Cr removal, while a further increase in the Mn content caused a net decrease in the Cr removal (**Figure 6-3** and **Figure F2**). Moreover, Fe-Mn biochar produced with BC850 showed a higher efficiency than that produced with BC550, while different results was found for Fe biochar (**Figure 6-3)**. This contrasting phenomenon indicates the different Fe species in Fe-Mn biochar and Fe biochar. Suitable preparation conditions determined the high Fe efficiency related to the suitable species, and varying Fe efficiency also indicated the complicated mineral transformation process in Fe-Mn biochar.

6.3.3 Comparison of Fe efficiency between Fe-Mn biochar, Fe-biochar, and ZVI

All Fe-Mn biochar showed a noticeably higher Fe efficiency for the Cr(VI) immobilization than ZVI alone. Either commercial ZVI (0.47×10^{-2}) or modified ZVI ($0.94-1.3 \times 10^{-2}$) showed a low Fe efficiency for Cr(VI) immobilization with a considerable amount of Cr(VI) left in the solution (4.3−10.6 mg L^{-1}), indicating the inhibited reduction process was related to the surface passivation of ZVI instead of the low remaining Cr(VI) concentration. In addition, the Cr(VI) reduction by ZVI might be achieved by the electron transfer between Cr(VI) and Fe(II) after the oxidative generation of Fe(II) during Fe(0) passivation, leading to lower Fe efficiency (0.33 in theory). These results confirmed that the unique Fe speciation in the Fe-Mn biochar (especially for that with 4h holding and 2% : 4% Fe : Mn ratio) might inhibit the ZVI passivation and aggregation, causing the direct electron transfer between Fe(0) and Cr(VI) with a high Fe efficiency. It is noted that the carbon and Mn phase might also contribute to the Cr(VI) reduction (<16.8%). After excluding this contribution, all Fe-Mn biochar could still show higher efficiency (0.27−0.64) than the ZVI or modified ZVI (0.47−1.3 × 10-2).

Table 6-1 Fe efficiency of Fe-Mn biochar, Fe-biochar, commercial ZVI, and reduced ZVI for the Cr(VI) immobilization in different wastewater.

Material	Electroplating Wastewater		Mining Wastewater		Textile Wastewater	
	Immobilized Cr(VI) (mg g^{-1})	Fe efficiency (mol mol^{-1})	Immobilized Cr(VI) (mg g^{-1})	Fe efficiency (mol mol^{-1})	Immobilized Cr(VI) (mg g^{-1})	Fe efficiency (mol mol^{-1})
BC850-FeMn-850-1h	320.2±5.7	0.34±0.01	250.7±31.4	0.40±0.03	312.7±22.1	0.34±0.02
BC850-FeMn-850-2h	606.9±12.4	0.65±0.01	483.4±29.0	0.66±0.03	528.3±22.1	0.57±0.02
BC850-FeMn-850-4h	765.5±13.0	0.82±0.01	707.0±14.9	0.90±0.02	619.1±5.3	0.67±0.01
BC850-FeMn-850-6h	752.6±19.3	0.81±0.02	545.7±27.9	0.72±0.03	593.7±11.4	0.64±0.01
BC850-FeMn-850-8h	367.2±3.4	0.40±0.00	197.6±59.3	0.35±0.06	22.2±12.4	0.24±0.01
BC550-Fe-850-2h	250.9±8.6	0.27±0.01	250.1±2.8	0.27±0.01	174.9±4.2	0.19±0.00
Reduced ZVI	15.4±0.4	0.02±0.00	19.2±0.5	0.02±0.00	13.8±0.1	0.01±0.00
Commercial ZVI	6.3±0.5	0.01±0.00	5.3±0.4	0.01±0.00	6.4±0.0	0.00±0.00

Moreover, we found that the Fe-Mn biochar could still keep high efficiency of 0.34−0.90 in simulated wastewater from electroplating, mining, and textile industry, especially for the BC850-FeMn-850-4h with a Fe efficiency of 0.67−0.90 (**Table 6-1**). A similar trend of Fe-Mn biochar's efficiency with the increasing holding time was found in the wastewater matrix; that is, it increased first (1−4 h) and then decreased (4−8 h). A much lower Fe efficiency was found for Fe-biochar (0.19−0.27), commercial ZVI (0.00−0.01), and reduced ZVI (0.01−0.02) (**Table 6-1**), further evidencing the outstanding Fe efficiency in Fe-Mn biochar.

The widely co-existed impurities in the wastewater might participate in forming the passivation layer of ZVI through complexation or co-precipitation and thus decrease the Fe efficiency. As shown in **Figure 6-4**, Cl^- and SO_4^{2-} have a limited impact on the Fe efficiency under either low (1:1) or high (10:1) concentration, while the existence of phosphate alleviated the Cr(VI) reduction process due to the competitive complexation (Xu et al., 2022b). Commercial ZVI and modified ZVI showed a significant decline in Fe efficiency from 0.47×10^{-2} to 0.31×10^{-2} and from $0.94{-}1.3\times 10^{-2}$ to $0.62{-}0.77\times 10^{-2}$, respectively, with the existence of 1:1 phosphate. The efficiency further decreased to $0.10{-}0.33 \times 10^{-2}$ in the presence of a 10-times higher phosphate (71.7−81.1 % decrease compared to the origin efficiency). However, Fe in the Fe-Mn biochar showed higher stability with only 35.9−46.7% decrease in the presence of phosphate, while limited stability improvement was demonstrated in the Fe biochar (80.7% decrease). This result indicated that the higher stability for the co-existed phosphate should mainly come from the unique properties of Fe in the Fe-Mn oxide instead of the biochar.

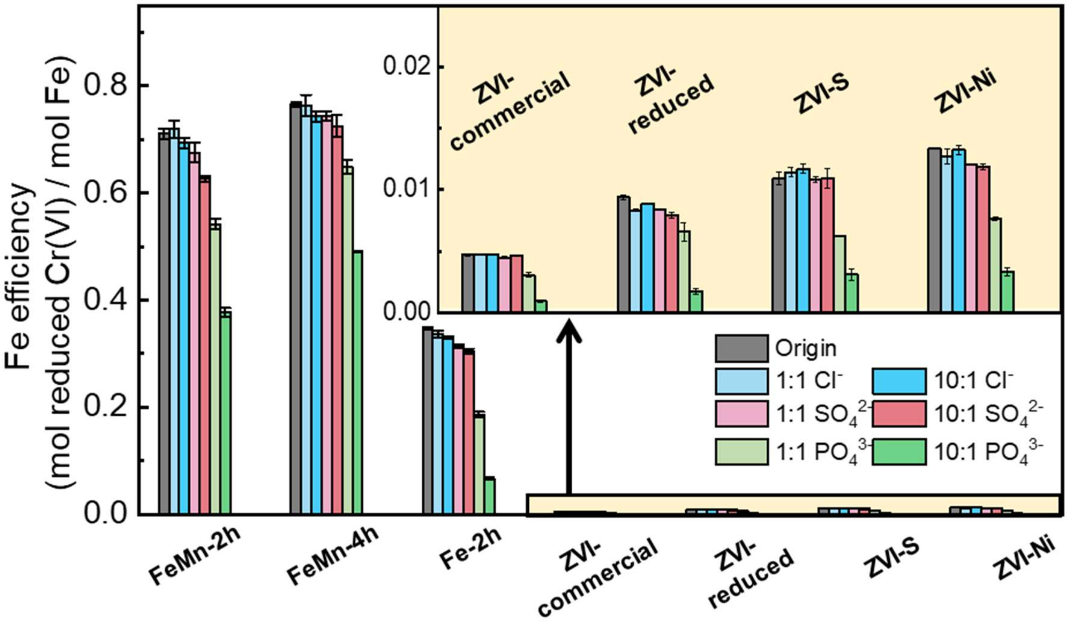

Figure 6-4 Fe efficiency of Fe-Mn biochar, Fe biochar, and commercial/modified ZVI for Cr(VI) immobilization with/without co-existing impurities. The insert figure was the enlarged version to show the difference between ZVI

6.3.4 Preserved Fe efficiency of Fe-Mn biochar with oxidants.

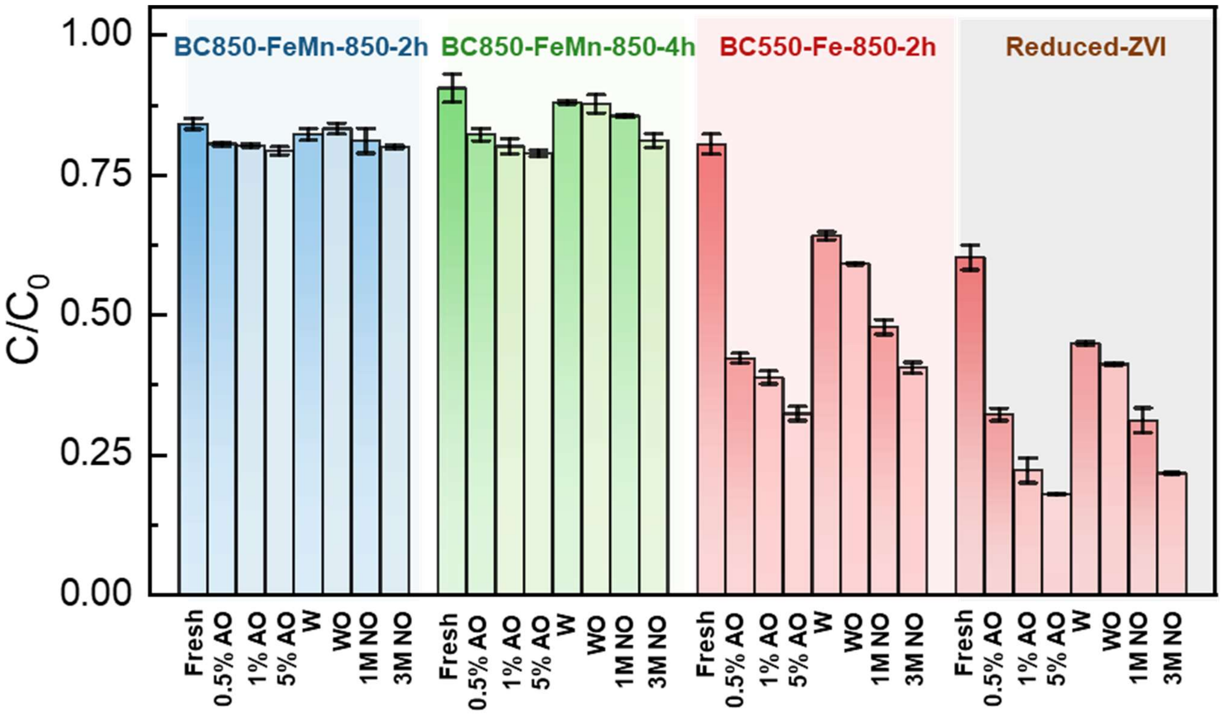

Figure 6-5 Cr(VI) removal efficiency of Fe-Mn biochar, Fe-biochar, and reduced-ZVI after natural oxidation (NO), accelerated oxidation (AO), interaction with water only (N_2 purged to remove O_2) (W), and interaction with O_2-contained water (WO). 0.5, 1, and 5% indicated the concentration of the used H2O2 for the accelerated oxidation process. 1M and 3M represent the natural oxidation with 1 and 3 months.

Interaction between the oxidants with ZVI during the storage (O_2 in air) and application (O_2 or H_2O in wastewater) might also decline the electron efficiency of ZVI for the targeted pollutants. The Cr(VI) removal proportion of BC850-FeMn-850-2h could still achieve 79.3−83.3% after the proposed oxidation process (**Figure 6-5**), comparable to the initial efficiency of 84.2%. A greater decrease in Cr(VI) immobilization was found in BC850-FeMn-850-4h after the oxidation processes, yet it could maintain an efficiency of over 78.9%. By contrast, the reactivity of Fe-biochar (BC550-Fe-850) significantly decreased to 32.3−42.2% (accelerated oxidation), 64.1% (water interaction), 59.1% (wet oxidation), and 40.5−47.8%

(natural oxidation) after the interaction with oxidants, and reduced ZVI also showed a similar decrease from 60.2% to 17.8−44.8%. Promising stability with preserved efficiency of Fe-Mn biochar was found after interaction with O_2, water, or strong oxidants (H_2O_2), and it should be oriented from the unique Fe species. Moreover, the stable efficiency also indicated the potential advantage of Fe-Mn biochar during long-term utilization or storage.

6.3.5 Mineral species in Fe-Mn biochar

According to the HR-TEM with EDX analysis (**Figure 6-6a**), Fe, Mn, and O fitted on the carbon phase of Fe-Mn biochar, evidencing the formation of Fe-Mn binary oxide. XRD analysis confirmed that $FeMnO_2$ was the primary mineral speciation in the Fe-Mn biochar with 2-6 h holding time (**Figure 6-6b**), and the (111) plane of $FeMnO_2$ was also detected with HR-TEM (**Figure F3**). These results indicated the formation of binary oxide with Fe-O-Mn bond in the lattice instead of the physical mixture of FeO and MnO, and the formation of the solid solution under high-temperature pyrolysis is the key to the transformation process.

Interestingly, the peak position of $FeMnO_2$ slightly left-shifted with the increasing holding time (**Figure 6-6b**) and Fe-Mn ratio (**Figure F4**) due to the evolution of the FeO/MnO ratio in the formed $FeMnO_2$. Based on the peak positions of Fe-Mn biochar over varying Fe/Mn ratios and those of standard $FeMnO_2$ in the database, we concluded that the FeO proportion in $FeMnO_2$ decreased with the increase of holding time from 2h to 6h (**Figure 6-6b** and **Figure F4**) due to the reductive transformation of FeO structure in $FeMnO_2$ to ZVI cluster without a crystal structure. It is worth noting that crystal ZVI could be found on Fe-Mn biochar with 1h and 8h pyrolysis. It might be caused by the limited combination of Fe and Mn minerals under a short interaction time (1h) or spontaneous agglomeration of Fe particles with excess energy under a longer pyrolysis duration (8h) (Li et al., 2021c, Li et al., 2020e).

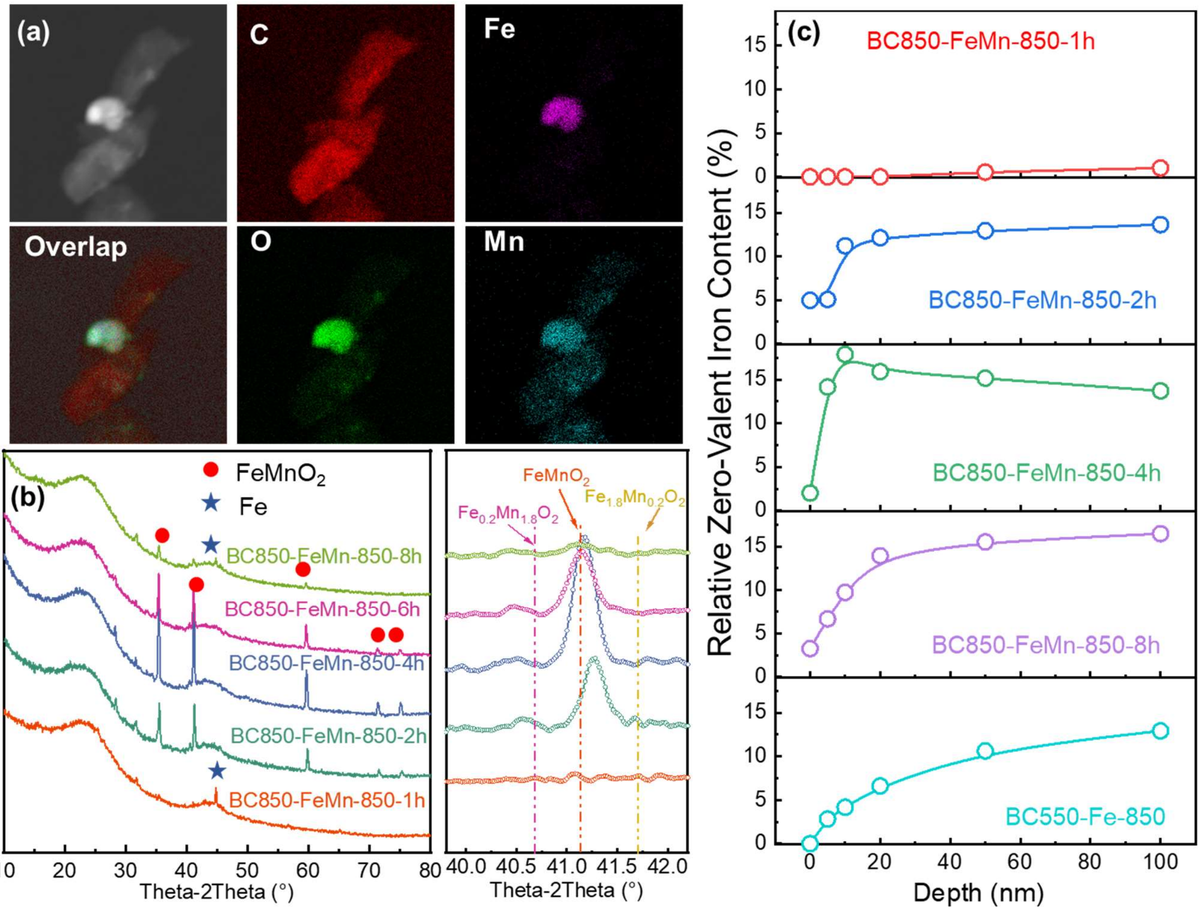

Figure 6-6 TEM-EDX analysis of the Fe-Mn biochar (**a**); XRD pattern of Fe-Mn biochar and the (200) peak position (**b**); ZVI proportion (**c**) under the different depths of Fe biochar and Fe-Mn biochar

The AC-STEM with SAED analysis revealed the formation of nano-sized ZVI clusters with the specific plane surrounding the $FeMnO_2$ and MnO_2 (2.0 Å, (110) lattice of Fe(0), **Figure F5**, **Appendix F**). The XPS analysis with depth profiling confirmed the ZVI cluster formation during the high-temperature pyrolysis of the Fe-Mn biochar (BC850-FeMn-850). Fe(0) content increased during the first 2 h of pyrolysis, attained its largest content at 4 h, and then maintained during the subsequent pyrolysis (4−8 h, **Figure 6-6c**). The ZVI might exist in the form of nano-sized ZVI clusters without forming the lattice structure because no XRD peaks of ZVI were found, manifesting the excellent dispersion and embedment of ZVI clusters in the oxide support(Zhou et al., 2022a). Compared with the Fe-biochar with ZVI alone (evidenced by XRD BC550-Fe-850, **Figure F3**), the Fe(0) proportion of Fe-Mn biochar was higher at all depths (5.0−13.6% > 0.0−12.9%, **Figure F6** and **Table F1**, **Appendix F**), leading to the higher reduction capacity and efficiency. A considerable amount of Fe(0) was formed on the surface (0 nm) of Fe-Mn biochar, while no Fe(0) was detected on Fe-biochar, evidencing that the ZVI cluster on Fe-Mn biochar might undergo limited surface passivation and keep its high efficiency.

Moreover, H_2-TPR analysis confirmed the formation of the ZVI cluster on the Fe-Mn biochar (**Figure F7**). The intensity of the H_2 reduction peaks of Fe-O decreased with the increase of holding time (BC850-FeMn-850-4h < BC850-FeMn-850-2h), pointing the formation of ZVI clusters with the decrease of FeO under longer pyrolysis. Besides, the Raman spectrum supported the in-situ formation of embedded ZVI clusters (**Figure F7**). The characteristic peaks of iron oxides (~700 and 540 cm^{-1}) (Achola et al., 2020, Gong et al., 2021) disappeared, and only characteristic peaks of the Mn−O bonding (~640 cm^{-1}) (Li et al., 2020b, Portillo-Vélez and Zanella 2020) can be found in Fe-Mn biochar with 2h and 4h pyrolysis time.

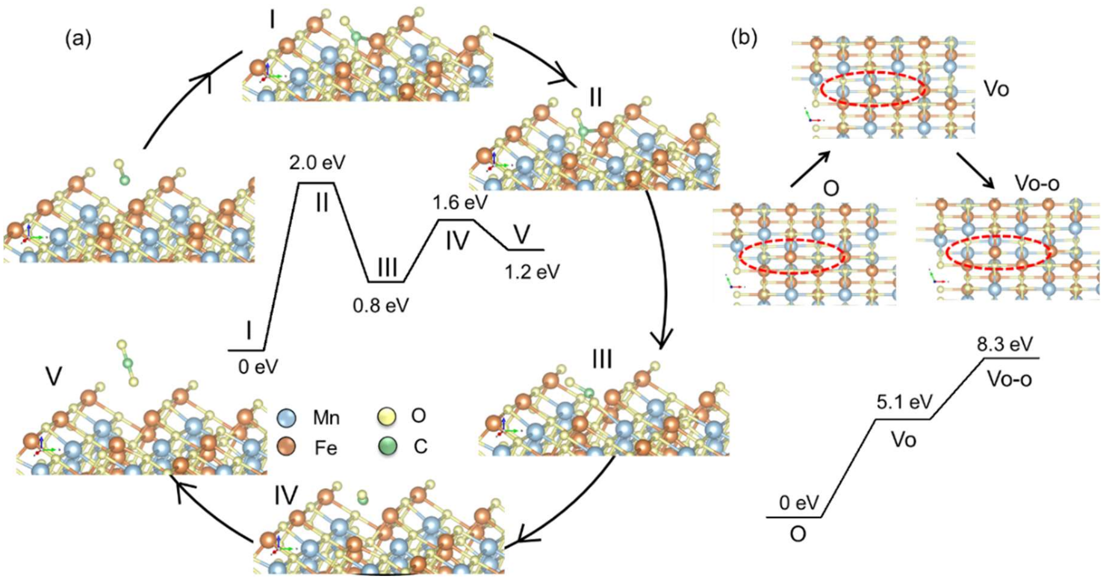

Figure 6-7 Proposed reaction mechanism for O vacancy formation on the $FeMnO_2$ with CO reduction (**a**). The inset shows the calculated energy profiles; The structures of intermediates and transition states are shown in the reaction route; Comparison of energy required for the first (V_O) and second ($V_{O\text{-}O}$) O-vacancy formation on the $FeMnO_2$ (**b**)

The reduction of Fe with the formation of ZVI cluster on Fe-Mn oxide might be caused by surface functionality on biochar (Xiao et al., 2018a, Xu et al., 2021f). The DFT calculations unveiled the potential reaction route for the O removal with the CO generated by biochar's surface functionality (**Figure 6-7a**). Based on the calculations, CO is first adsorbed on the $FeMnO_2$ by forming Fe−C and O−C bonds. After overcoming the energy barriers of 2.0 and 0.8 eV, the Fe−C bonding and O−Metal bonds were broken in sequence with the formation of oxygen vacancy and the release of CO_2. In this case, the Fe-C bond cleavage was the rate-limited step due to the higher energy barrier (2.0 eV), requiring a high pyrolysis temperature. We also found that the energy demand for the further removal of the O was lower than the first O linked with the same Fe atom (**Figure 6-7b**), implying the potential construction of ZVI. Both increased O/C ratio and oxidative conversion of the O-functional group on biochar (**Table F2**, **Table F3**, and **Figure F8**, **Appendix F**) with rising holding time can directly evidence this reduction process.

The valence transformation of M occurred during the reductive formation of ZVI (**Table F4, Appendix F**). Based on XPS analysis, different Mn speciation, including Mn(IV), Mn(III), and Mn(II), were formed on the Fe-Mn biochar (**Figure F9**). The average Mn state significantly increased from 2.5−3.4 (1 h) to 3.2−3.6 (2−4 h) with the rising pyrolysis duration and kept steady later 3.4−3.9 (8 h) (**Figure F9**). The increase in the Mn state indicated the generation of Mn(III) and Mn(IV) in the Fe-Mn biochar during the in-situ formation of Fe(0), and more Mn(IV) and Mn(III) were formed on Fe-Mn biochar surface with a longer holding time as 4 h. The AC-STEM-SAED revealed the potential formation of MnO_2 on the Fe-Mn biochar with a specific lattice distance of 4.0 Å (101) and 3.1 Å (110) (**Figure F5**), and the metallic iron (2.0 Å (110) lattice) was formed surrounding the MnO_2 structure. These results suggested a potential formation pathway for ZVI clusters via the oxygen transfer from the FeO to the MnO structure, along with the formation of ZVI clusters and MnO_2.

6.3.6 Transformation route of Fe during the pyrolysis

Motivated by the characterizations and calculation, a possible in-situ formation mechanism of embedded ZVI clusters within Fe-Mn oxide was proposed (**Figure 6-8**). We found that crystal ZVI with amorphous Mn mineral was first formed within a short pyrolysis time and then gradually transformed into crystal $FeMnO_2$ with increasing pyrolysis time (step 1 in **Figure 6-8**). The Mn in the amorphous mineral might combine with the iron and iron oxides to construct $FeMnO_2$ during pyrolysis (1-h ripening stage). The reductive formation of ZVI clusters occurred with further pyrolysis, and the formed ZVI would be embedded into the

$FeMnO_2$ skeleton. The generated CO molecules during biochar pyrolysis may first remove the skeleton oxygen and promote the formation of oxygen vacancies with FeO (step 2 in **Figure 6-8**), and the concomitant O removal would result in the construction of ZVI (step 3 in **Figure 6-8**). The DFT calculations unveiled the potential reaction route for the O vacancy formation during the biochar pyrolysis, indicating the potential formation of ZVI (2−6 h reduction).

Interestingly, the characteristic peaks of ZVI appeared again when the holding time reached 8 h based on the XRD analysis, and the possible reason was the agglomeration and crystallization of the formed ZVI clusters with the excessive pyrolysis duration (step 4 in **Figure 6-8**). A longer pyrolysis duration could provide excess energy to promote sufficiently fast surface diffusion and supply the surface energy of particles for spontaneous agglomeration (Li et al., 2021c, Li et al., 2020e). Hence, the spontaneous agglomeration of ZVI clusters, along with the formation of the lattice structure, was the primary process for the longer duration of pyrolysis.

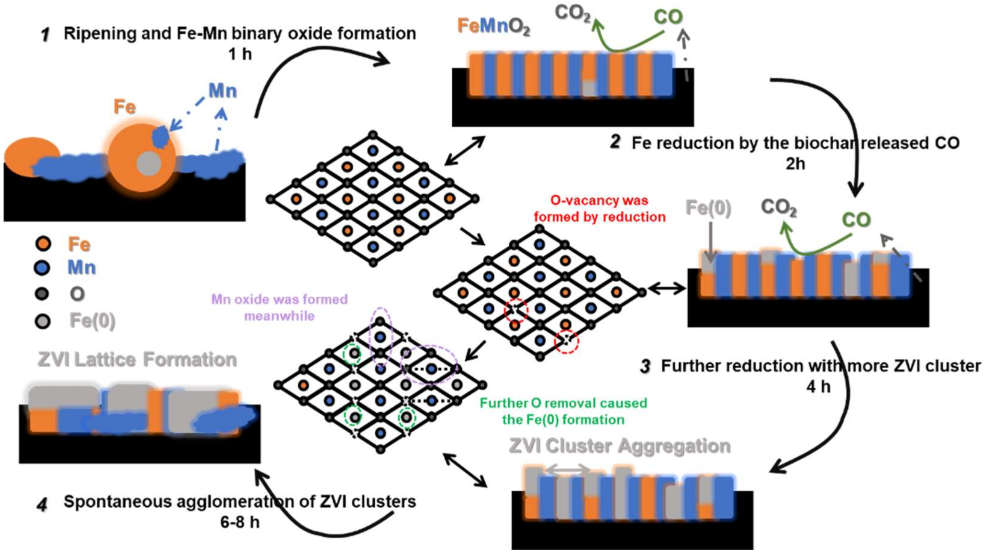

Figure 6-8. $FeMnO_2$ transformation with embedded ZVI cluster formation on the Fe-Mn biochar during the pyrolysis with increased holding time.

6.3.7 Mechanism for the hhigh Fe efficiency of embedded ZVI cluster.

Based on the XPS analysis (**Figure F10** and **Table F5, Appendix F**), over 100 nm depth of Fe(0) on the Fe-Mn biochar was consumed for the Cr(VI) reduction with the formation of Fe(III)/Fe(II) (**Figure 6-9a**). These results indicated that electrons in the core area of the embedded ZVI clusters on Fe-Mn biochar were fully utilized, which could be the key to efficient electron-donating of Fe-Mn biochar. By contrast, a considerable amount of Fe(0) was left after the Cr(VI) immobilization process by Fe-biochar, and only the surface 20 nm-deep ZVI was used for Cr(VI) reduction (**Figure 6-9b**) (Li et al., 2021b). The ZVI/electron in the deeper depth was normally hard to be used due to surface passivation since the electron/ZVI diffusion through the passivation layer was the rate-limited step (Li et al., 2021d).

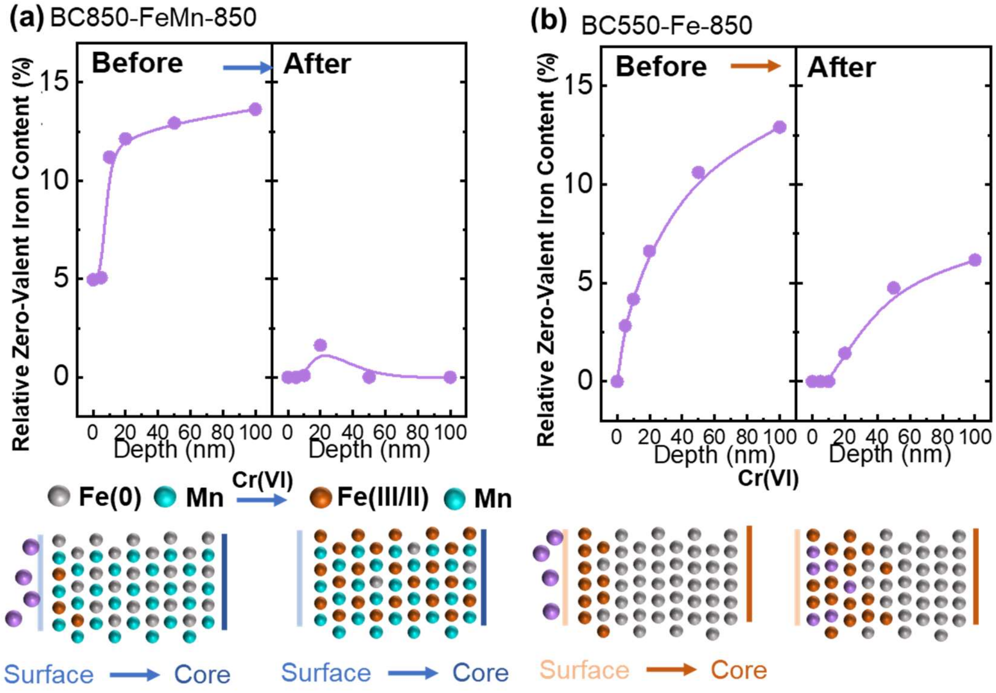

Figure 6-9 The ZVI content under the different depths of Fe-Mn biochar (**a**) and Fe biochar (**b**) before and after Cr(VI) removal. The schematic below shows the Fe(0) variation for Cr(VI) reduction from surface to depth.

The following process might contribute to the high Fe efficiency of embedded ZVI cluster during the immobilization process:

(i) Limited Fe-Cr Complexation with Fe-Mn Oxide. Different combination processes during the Cr(VI) immobilization by Fe-Mn biochar and Fe biochar might determine electron utilization. For ZVI alone on Fe-biochar, a dense passivation layer was formed by the accompanied reduction and sorption processes of chromium (Mu et al., 2017, Zhao et al., 2022a), evidenced by the highly fitted distribution of Fe and Cr after immobilization (**Figure 6-10a**), and it will restrict the further electron transfer between core ZVI and Cr(VI). By contrast, the embedded ZVI clusters in the Fe-Mn biochar did not fix the formed Cr(III) after reduction, and the Cr(III) was mainly sorbed and precipitated on the carbon surface (Xu et al., 2019e) afterwards (**Figure 6-10b**). In other words, no Fe-Cr passivation layer was formed on the ZVI clusters on Fe-Mn biochar due to the potent combination between Fe and Mn, leading to the facilitated electron transfer between core-ZVI and Cr(VI). In addition, the intense binding between Fe and Mn might lead to the limited passivation of ZVI with impurities like phosphate, causing the preserved efficiency (**Figure 6-4**).

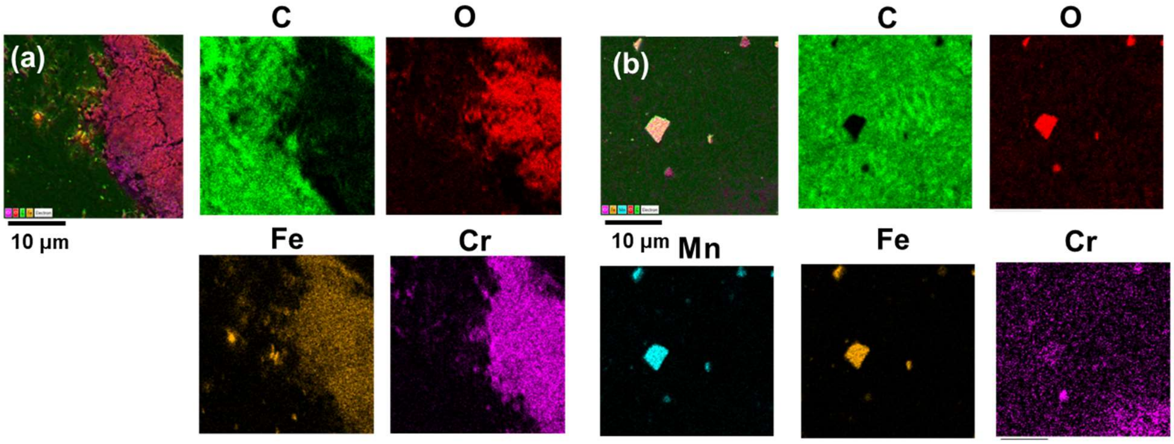

Figure 6-10 The distribution of different elements on Fe biochar (**a**) and Fe-Mn biochar (**b**)

(ii) High Cr(VI) Affinity of the Surface Fe-Mn Oxide. In addition to the limited passivation of ZVI clusters on Fe-Mn biochar, the surface Fe-Mn oxide has an active affinity with Cr(VI), which is also critical for efficient electron-donating. The DFT calculations revealed that $FeMnO_2$ had a higher $HCrO_4^-$ adsorption potential than $FeCrO_3$ and Fe_2CrO_4 (the model mineral for the Fe−Cr complex covered on the ZVI) due to the lower adsorption energy (-3.9 eV < 2.0−2.1 eV, **Figure 6-11**). The potent coordination of $FeMnO_2$ with $HCrO_4^-$ could facilitate the reduction of Cr(VI) by the Fe(0) at a deeper depth, while the surface coverage with the Fe−Cr complex inhibited this electron transfer. In short, the separated processes of reduction and immobilization by the embedded ZVI clusters in the Fe-Mn oxide could ensure a high Fe efficiency by forming an "activated" layer (Fe-Mn oxide) instead of a passivation layer (Fe-Cr complex).

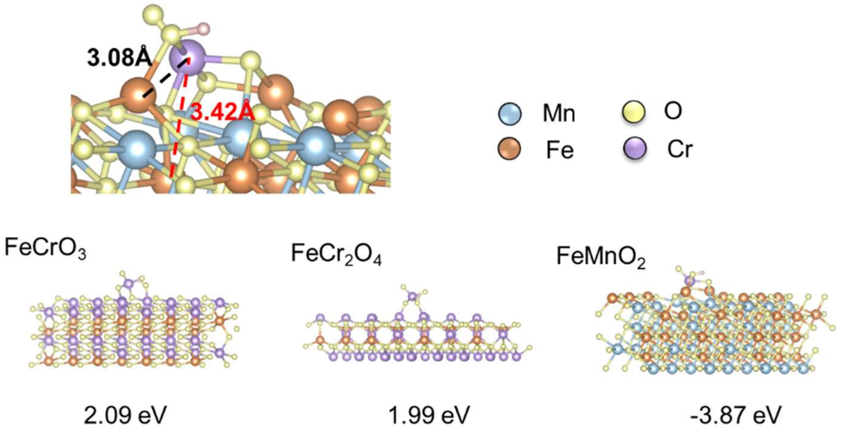

Figure 6-11 The combined energy and pattern of $HCrO_4^-$ on the $FeCrO_3$, $FeCr_2O_4$, and $FeMnO_2$. $FeCrO_3$ and $FeCr_2O_4$ were selected as the model mineral for the Fe-Cr complex formed during the Cr(VI) removal by Fe biochar

(iii) Oxidation Resistance of Embedded ZVI Clusters on Fe-Mn Biochar. The oxidation of Fe(0) by water or oxidants also leads to the less electron received by the Cr(VI), which also causes the low efficiency of ZVI. The formation of surface Fe-Mn oxide protected the inner ZVI cluster during its interaction with impurities/oxidants, leading to a higher efficiency for Cr(VI) removal. A thinner layer of oxidized Fe was formed on Fe-Mn biochar than Fe biochar (ZVI alone) **(Figure 6-12**, **Figure F11**, and **Table F6, Appendix F**), indicating less electron consumption with oxidants (oxidants and water). Using 10% Fe(0) content as the benchmark to evaluate the iron oxide layer, the passivation layer of ZVI alone could reach over 100 nm after the oxidation, while the surface oxide layer of the embedded ZVI clusters only increased from ~10 nm to ~50 nm (accelerated oxidation) and ~20 nm (natural oxidation) (**Figure 6-12**). The oxidation resistance stability was further confirmed by the preserved reducing capacity of Fe-Mn biochar and the significant decline of Fe-biochar/ZVI after interacting with different oxidants (**Figure 6-5**).

According to the DFT calculation, the surface of $FeMnO_2$ had a lower potential to trap O_2 than Fe_2O_3 and FeO (model minerals for the surface passivation layer of ZVI) with higher energy demand (-0.4 eV > -1.4−-1.0 eV, **Figure 6-13**), leading to the protection impact for ZVI clusters. In addition, forming the $FeMnO_2$ layer with Fe−O−Mn bonding (~10−20 nm) might alleviate the Fe oxidation since the rate-limiting step of surface passivation was the diffusion of Fe ions in the oxide layer (Bae et al., 2018). We found that the valence state of Mn, especially at the 5−20 nm depth, decreased during the oxidation process (**Figure F12** and **Table F4**), which might be related to the formation of $FeMnO_2$. Moreover, higher reductive surface functionality on the BC850-FeMn-850 than BC550-Fe-850 (**Figure F8**) could also alleviate the Fe oxidation (Xu et al., 2020e, Xu et al., 2022b), and the noticeable increase in the O/C ratio across the entire depth of BC850-FeMn-850 after the oxidation process further supported this conclusion (**Table F7**).

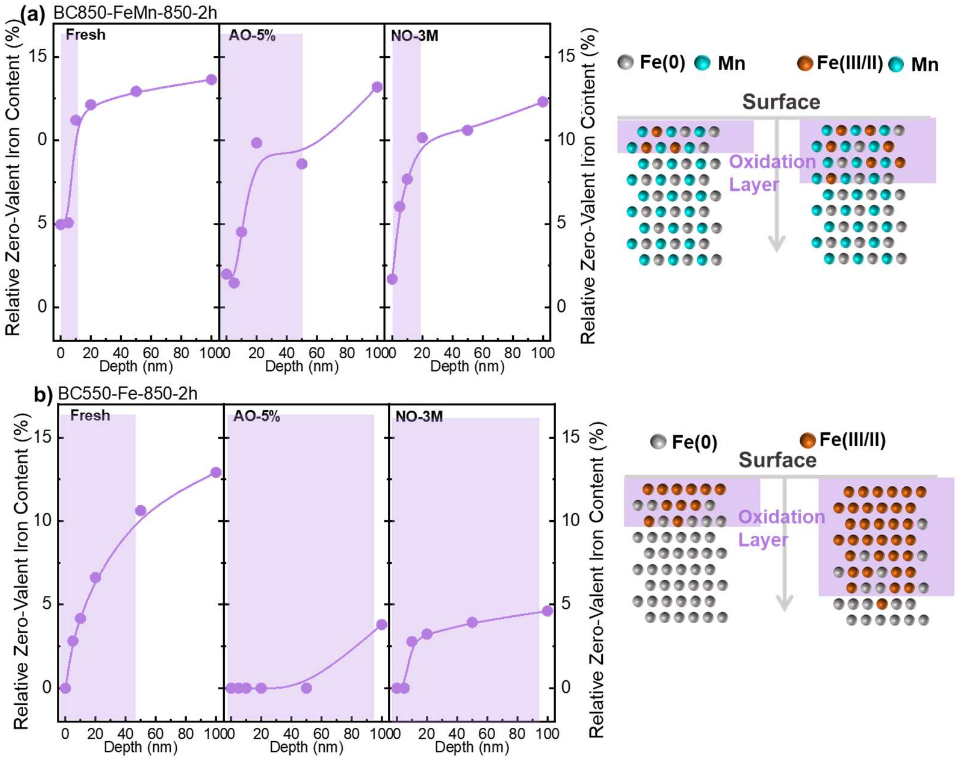

Figure 6-12 The Fe(0) content under different depths of Fe biochar (**a**) or Fe-Mn biochar (**b**) before and after the oxidation process. The schematic diagram shows the oxidation of ZVI to iron oxide from the surface during the interaction with O_2. Less Fe(0) was oxidized on Fe-Mn biochar during the interaction with O_2, water, and strong oxidant, leading to more electron transfer with Cr(VI);

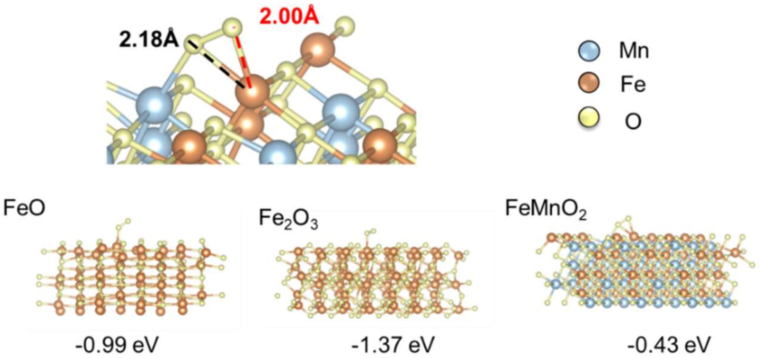

Figure 6-13 The combination energy and pattern of O_2 on the $FeCrO_3$, $FeCr_2O_4$, and $FeMnO_2$. Fe_2O_3 and FeO were selected as the model iron oxide for the passivation layer of the ZVI on Fe biochar.

(iv) Electron Transfer by Mn. The valence state of Mn increased after the Cr(VI) removal process (**Figure F13**), implying that the Mn electron might partially contribute to the Cr(VI) reduction process directly or through the electron mediating (Xu et al., 2021e). The contribution of the Mn electron might mainly be achieved with the embedded ZVI clusters since Fe-Mn biochar only showed a higher efficiency by forming embedded ZVI clusters within Fe-Mn oxide (Fe-Mn biochar with 2-6 h holding) instead of the separated ZVI and Mn minerals (Fe-Mn biochar with 1 or 8 h holding) (**Figure 6-3** and **Table 6-1**). In addition, the variation of Fe efficiency with different Fe: Mn ratios (**Figure 6-3**) also supported this conclusion since increasing Mn content at a higher Mn amount decreased the Fe efficiency.

In short, the $FeMnO_2$ coverage inhibited the interactions between inner ZVI and oxidants but facilitated its binding with Cr(VI). The limited formation of the Fe-Cr complex also alleviated the passivation of ZVI during Cr(VI) reduction, and the Mn might further support the electron transfer between ZVI and Cr(VI). All of these processes could account for higher efficiency of the embedded ZVI clusters on Fe-Mn oxide, resulting in efficient Cr(VI) removal by Fe-Mn biochar.

6.3.8 Economic analysis of Fe-Mn biochar

The feedstock costs of different Fe-Mn biochar, Fe-biochar, and ZVI has been calculated accordingly (**Table 6-2** and **Appendix F**). The cost of commercial ZVI particles was 6.3 times higher than the Fe-Mn biochar, and a much higher cost (63.3−75.4 times higher) was found for the modified ZVI (reduced ZVI, S-ZVI, and Ni-ZVI). Even considering the potential cost of the pyrolysis process, the price of preparing Fe-Mn biochar is still lower than the commercial and modified ZVI (**Table 6-2**). Based on the cost and the Fe efficiency in simulated wastewater, using Fe-Mn biochar to treat the concentrated industry wastewater had up to 6.4−8.0 and 20.6−26.9 times higher economic benefits than commercial ZVI and modified ZVI, respectively. It is noted that potential degeneration of the performance during storage and transportation of Fe-based materials was not considered, which might also be crucial for the actual application of Fe-based materials. Due to the higher stability for oxidation-resistance of Fe-Mn biochar (**Figure 6-5**), it should have a much higher economic benefit because of storage and transportation during field-scale applications.

Table 6-2 Cost and Performance Balance of Different Fe-based Materials

Materials	Material Cost (USD Kg^{-1})	Electroplating		Mining		Textile	
		Needed amount ($\times 10^{-2}$ $Kg\ L^{-1}$)	Cost for treating (USD L^{-1})	Needed amount ($\times 10^{-2}$ $Kg\ L^{-1}$)	Cost for treating (USD L^{-1})	Needed amount ($\times 10^{-2}$ $Kg\ L^{-1}$)	Cost for treating (USD L^{-1})
BC850-FeMn-850-1h	67.3	3.1	2.1	10.0	6.7	2.0	1.4
BC850-FeMn-850-2h	78.4	1.6	1.3	6.2	4.8	1.2	0.9
BC850-FeMn-850-4h	100.6	1.3	1.3	4.5	4.5	1.0	1.0
BC850-FeMn-850-6h	122.9	1.3	1.6	5.6	6.9	1.0	1.3
BC850-FeMn-850-8h	145.1	2.7	4.0	11.6	16.9	2.3	3.3
BC550-Fe-850-2h	82.4	2.0	1.6	7.5	6.2	1.7	1.4
Reduced ZVI	2501.3	1.3	32.4	3.9	97.8	1.0	25.5
Commercial ZVI	289.1	3.2	9.2	14.2	40.9	2.3	6.7

6.4 Conclusions

A dense surface passivation layer restricts the efficiency of ZVI for environmental applications, which was the main bottleneck of ZVI-based materials for wastewater treatment. Our solution, the Fe-Mn biochar with embedded ZVI clusters, presented a higher Fe efficiency with outstanding stability for water decontamination with potential economic benefits. According to the Cr(VI) removal efficiency, the embedded ZVI cluster could perform up to 80.5-161.7 times higher efficiency than the commercial/modified ZVI in the (waste)water matrix with lower cost (**Figure 6-14**). The unique embedded ZVI clusters contributed to the high Fe efficiency due to the less formation of the passivation layer and enhanced affinity with Cr(VI). This work provides a new direction for developing future ZVI-based materials with a high atom efficiency, while further analysis is needed to unveil and quantify the long-term interactions. Our findings advocate the customized production of high-value engineered biochar, which will benefit the biochar industry and end-users in different fields.

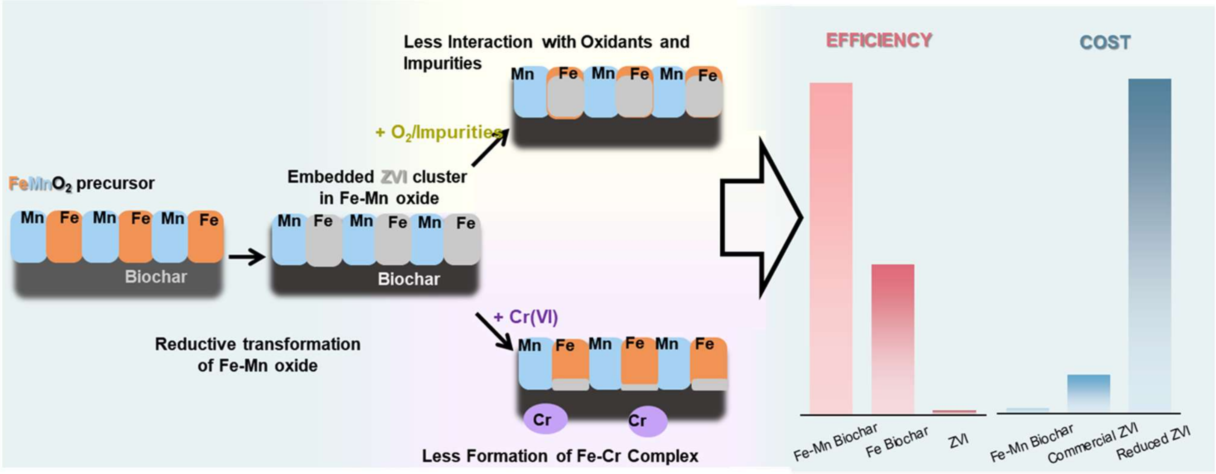

Figure 6-14 Graphical summarization of Chapter 6

Chapter 7 Hydrothermal Treatment for the Fe-Mn Minerals Speciation Control on Biochar: Targeted the Toxic Metals Immobilization

7.1 Introduction

Due to growing industrialization, toxic metals are being released into the environment from various industries (e.g., electroplating and mining) at an ever-growing amount (De Beni et al., 2022). For instance, about 2–20% of the chemicals used in the electroplating industry contain toxic metals and would be discharged (Costa et al., 2022). Based on the estimation, approximately 2 million tons of industrial wastewater with high toxic metal content are discharged daily, causing severe toxic metal pollution in the water matrix (Bolisetty et al., 2019, Rajoria et al., 2021). Toxic metal pollution is one of the foremost global risk factors for illness and diseases and contributes to reducing the available drinkable water worldwide (Bolisetty et al., 2019). Therefore, a suitable approach for toxic metal immobilization is urgently needed.

Engineered biochar has attracted growing attention for the toxic metals removals from wastewater due to the facile synthesis, wide availability of raw materials, high efficiency and the potential advantage of circular bioeconomy (He et al., 2022, Shaheen et al., 2022, Wang and Wang 2019). Among different modification methods, Fe-Mn co-modified biochar was the recent research hot spot due to the following reason: (1) Both Fe and Mn oxides have multiple valence states, which might bring extra redox reactivity (Qi et al., 2012, Xu et al., 2023a); (2) Fe and Mn are relatively cheap, less toxic, and easy to acquire from nature; (3) the introduction of Fe and Mn can further affect the properties of carbon phase during the production process, leading to the enhanced performance (Tian et al., 2021b, Wang et al., 2022a, Xu et al., 2022a); (4) Similar atomic radius of Fe and Mn atoms enable the formation of binary oxide with different valence state during the fabrication process; (5) biochar with rich surface functionality can improve the stability of the mineral particles by the firmly anchoring process (Wan et al., 2020b, Wan et al., 2023); and (6) the magnetic properties of Fe-Mn mineral improves the separability of catalysts (Xie et al., 2022, Xu et al., 2020d).

However, the current study mainly produced Fe-Mn biochar through simple impregnation methods without precise control of the Fe-Mn mineral speciation. Due to the variety of Fe (0, +2, +3) and Mn valence states (+2, +3, +4, +7), a complex mineral speciation with different Fe/Mn species might exist on the Fe-Mn biochar according to the preparation condition. Besides, Fe and Mn can be either combined as binary oxide or separated as single Fe oxide and Mn oxide on the biochar, and the different mineral combinations might also affect the reactivity of the Fe-Mn biochar (Chen et al., 2020b, Zoroufchi Benis et al., 2022). Therefore, unveiling the mineral transformation mechanisms during the Fe-Mn biochar production is highly needed. Besides, the underlying mechanism during the toxic metal immobilization by Fe-Mn biochar is also unclear. Most studies used the synergy impact from Fe and Mn to explain the enhanced immobilization impact without convincing evidence. The specific role of each moiety (i.e., Fe, Mn, and C) during the pollutants immobilization needs further clarification for the on-demand Fe-Mn biochar production.

Moreover, the settlement of the spent engineered biochar after the toxic metals removal is another problem for real industrial-level applications. If the toxic metals on the spent Fe-Mn biochar could keep stable, applying the Fe-Mn biochar might be a promising approach since biochar will benefit the soil properties as the amendment (Cai et al., 2021, Hagemann et al., 2017, Lehmann et al., 2021, Qian et al., 2023), and thus a win-win impact, i.e., pollutants immobilization and soil improvement, can be achieved. Moreover, it simplifies traditional wastewater treatment, *i.e.,* removing pollutants from water to solids and stabilizing them with further treatment, to a simple one-step approach (removing and stabilizing the toxic metals in one step). Therefore, the stability of the toxic metals on the spent engineered biochar is another focus of this study.

In this chapter, we focus on the Fe-Mn mineral transformation during the production of Fe-Mn biochar with hydrothermal treatment, which is widely reported as an impregnation approach for mineral loading (Guo et al., 2019, Nandagudi et al., 2022), and the role of each moiety was scrutinized during the toxic metals immobilization. The electroplating wastewater with varying properties is selected as the target wastewater in this chapter, which contains numerous toxic metals (Costa et al., 2022, Martín-Lara et al., 2014). Moreover, the stability of the toxic metals on spent Fe-Mn biochar after incubation with soil was also evaluated to evidence the feasibility of direct settlement in soil.

7.2 Materials and Methods

7.2.1 Preparation of Fe-Mn Biochar with hydrothermal pretreatment

All reagents used in the synthesis process were analytical grade, and the detailed information was summarized in **Appendix A.** The biochar used in this study was produced from the locally abundant woody waste at the EcoPark in Hong Kong, and pristine biochar was first produced at 550°C for 2 h under the N_2 atmosphere (BC550) before further treatment.

Fe and Mn impregnation was achieved by a hydrothermal process. $FeCl_3$ and $MnCl_2$ (2 mmol each) were co-dissolved in a beaker with DI water (50 mL). Biochar (BC550, 3g) was added with afterwards 30 min stirring, and then alkalinity (NaOH or Urea, 15 mmol in 15 ml DI water) was dropwise added with stirring. After another 30 mins stirring, the mixture was transferred into the hydrothermal autoclave and heated at 120 or 180°C for 12 h. After cooling to the ambient temperature, the composite was washed with DI water and ethanol and dried in a freeze-dryer. A second pyrolysis at 850°C with 4 h holding time was then conducted on the as-prepared biochar-mineral complex, and the formed biochar composites were denoted as 120-OH, 120-U, 180-OH, and 180-U according to the hydrothermal temperature and co-hydrothermal alkalinity.

To better evaluate the mineral transformation during the hydrothermal and pyrolysis, 150°C was also set as the hydrothermal temperature to study the mineral speciation on the as-prepared Fe-Mn biochar. In addition, since the carbon properties normally affect the mineral transformation during the pyrolysis process, we also produced different biochar precursors, i.e., biochar produced under 850°C under N_2 atmosphere (BC850) and biochar produced under 850°C with CO_2 activation (BC850C), for the Fe-Mn mineral loading and studied the impact of biochar properties on the mineral speciation after hydrothermal and pyrolysis process. For comparison, Fe biochar and Mn biochar were produced with a similar hydrothermal (120 and 180°C with NaOH or urea) and pyrolysis (850°C for 4h). All these samples were stored in the container under a dry N_2 atmosphere until their characterization and use.

7.2.2 Decontamination of the simulated electroplating wastewater

The properties of the real electroplating wastewater were first collected from the published literature, and relevant information about the used literature and results are shown in **Appendix G** and **Figure 7-1.** According to the collected properties, batch experiments were conducted to remove toxic metals. Typically, 0.2 g of the Fe-Mn biochar composite was mixed at 250 rpm in the 100 mL solution containing toxic metals, including Cr(VI), Cu(II), Ni(II), and Zn(II), and the concentration and ratio between each toxic metals was determined based on the literature (**Appendix G**). The solution pH was adjusted to ~2-6.5 by dropwise adding HCl or NaOH, and the ionic strength was controlled by adding ten mmol of NaCl. The batch experiment was conducted for 24 h to ensure the completed removal of pollutants by Fe-Mn biochar, and the solution was collected and separated to detect metals concentration and speciation. ICP-OES and colourimetric methods were used for the detection, and detailed information was described in the previous chapter and **Appendix B**. Kinetics experiments were also conducted for 24 h to evaluate the removal constant of different Fe-Mn biochar. All experiments were conducted in triplicate. Commercial ZVI, reduced ZVI, S-ZVI, and Ni-ZVI were also set as the comparison for the removal efficiency evaluation (Tian et al., 2021a, Xu et al., 2020b, Zhou et al., 2022b) (details in **Appendix G**).

7.2.3 Stability of the immobilized toxic metals on the Fe-Mn biochar

Two extraction methods, acid extraction and $CaCl_2$ extraction, were used to extract the toxic metals from spent Fe-Mn biochar. The acid extraction was set based on the HJ-299-2007 and similar to the synthetic precipitation leaching procedure (SPLP) procedure, which simulated the leaching that originates from acidic rain (Pandey et al., 2012). The extracting fluid was prepared by adding a mixture of sulfuric acid/nitric acid (2/1, w/w) to deionized water until the pH was 3.2 ± 0.05. The samples were mixed with the solution with the liquid-to-solid ratio of 10:1, agitated for 18 ± 2 h at 30 rpm, and then separated through filtration. 0.01 M $CaCl_2$ solution was also used to extract the spent Fe-Mn biochar (the liquid-to-solid ratio of 10:1) (Xu et al., 2018c) since the extraction amount is highly related to the bioavailability of toxic metals in soil (Meers et al., 2007). The mixed solution was shaken at 150 rpm for 24 h and then filtered for further detection. The concentration of toxic metals in the solution was evaluated by the ICP-OES, and the spent reduced ZVI was also set as the control for the comparison.

A potential approach to settle the spent Fe-Mn biochar was applied to the soil, and the stability of the toxic metals on the Fe-Mn biochar will be the determining property of this process. Therefore, we mixed the spent Fe-Mn biochar and soil (1% mixing ratio) and incubated for 1 month under 70% water content, and similar extraction methods were then conducted to evaluate the release of toxic metals after the incubation process.

7.2.4 Characterization

To evidence the mineral transformation of Fe-Mn oxides during the hydrothermal and pyrolysis process, Fe-Mn biochar composites were characterized by XPS, XRD, and AC-STEM with SAED and EDX (**Appendix B**). Besides, Raman analysis was conducted to evaluate the properties of carbon during the modification process. An XPS with depth profiling was conducted to identify the valence states of toxic metals on Fe-Mn biochar after immobilization. Besides, STEM with EDX analysis was also conducted to evidence the toxic metals distribution on Fe-Mn biochar after the immobilization. DFT calculations compared the metal sorption capacity of different Fe/Mn minerals for the targeted toxic metals. H_2-TPR was used to support the redox reaction during the immobilization process. Details for the characterization methods are shown in **Appendix B**.

7.3 Results and Discussion

7.3.1 Pollutants removal capacity of Fe-Mn biochar under typical electroplating wastewater

The typical condition of electroplating wastewater was summarized in **Figure 7-1a** and **Figure 7-1b** according to the reported data in the literature. Seven metals commonly exist in the electroplating wastewater with varying concentrations from 0 to over 600 mg L^{-1} **(Figure 7-1a)**. Chromium (Cr), nickel (Ni), zinc (Zn), and copper (Cu) show a relatively higher concentration in the electroplating wastewater, and its average value could reach 366.9 mg L^{-1} (Cr), 233.7 mg L^{-1} (Ni), 143.9 mg L^{-1} (Zn), and 604.1 mg L^{-1} (Cu). The concentration of toxic metals is highly variable, but the most common concentration exists in the range of 0-200 mgL^{-1}. The total organic carbon in these wastewaters is also highly variable, and its average amount could reach 135 mg L^{-1}. High acidity is widely found in the electroplating wastewater (**Figure 7-1b**) with a widely reported pH of around 2–3. The co-existed anion metals (Cr) and cation metals (Ni, Zn, and Cu) under an acidic situation might be the key to the efficient immobilization of the electroplating wastewater.

According to the reported ratio between anion and cation in the real electroplating wastewater (**Figure 7-1b**), we first evaluated the Cr(VI) reduction capacity of Fe-Mn biochar and ZVI under the different ratios of anion and cation pollutants. A high reduction amount can be found in both Fe-Mn biochars, and it was significantly higher than the commercial and modified ZVI (**Figure 7-1c**). Considering the impact of the increasing co-existed cations, a much more apparent decrease in the removal amount was found for ZVI, and a preserved capacity was shown for Fe-Mn biochar. Similarly, Fe-Mn biochar could keep a high reducing efficiency with varying pH, while a significant decrease was found in ZVI with the increasing pH in the wastewater (**Figure 7-1d**).

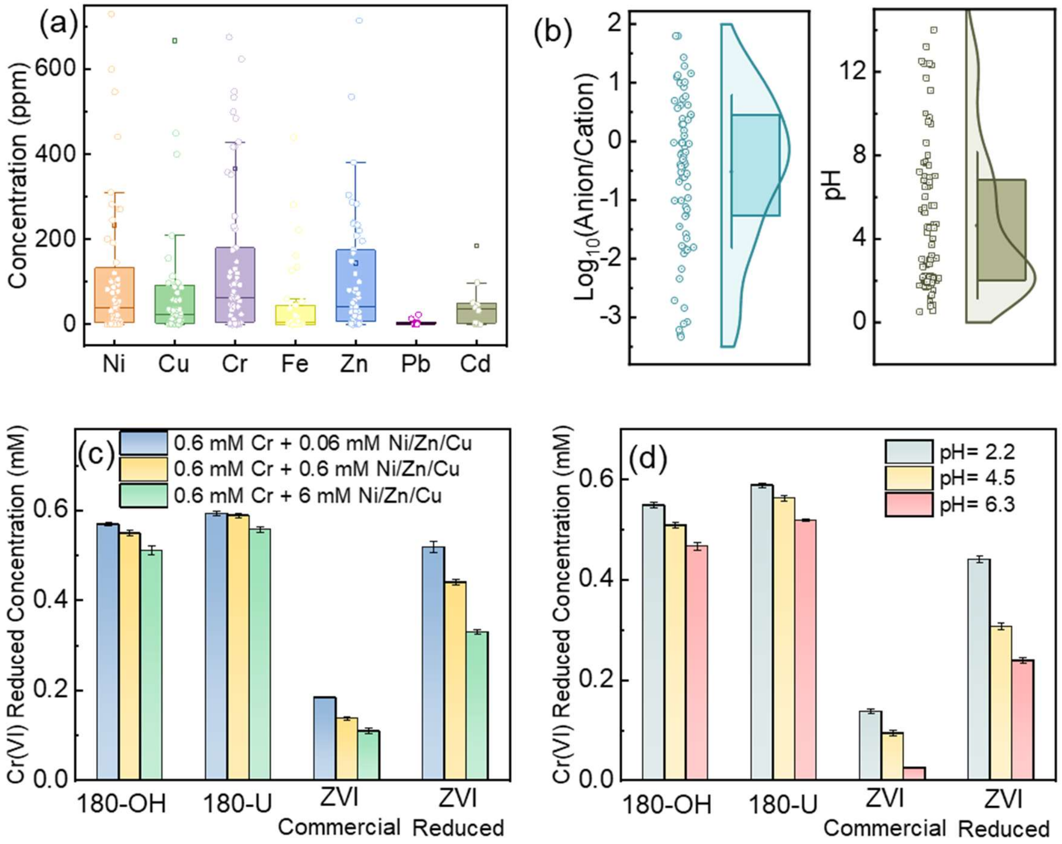

Figure 7-1 Box chart for the metal concentration in the electroplating wastewater (**a**); Violin with box chart for the anion/cation ratio and pH of the electroplating wastewater (**b**); Cr(VI) reduction concentration under different anion/cation ratio (**c**) and pH (**d**).

The removal capacity of different toxic metals was then evaluated under the selected condition (pH=~2.5 and Anion/Cation=~1). A higher hydrothermal temperature and co-hydrothermal with urea benefited the metals removal capacity of Fe-Mn biochar. The highest removal capacity for Cr, Cu, Ni, and Zn was found for the Fe-Mn biochar produced with 180°C hydrothermal and urea, and its removal capacity reached 12.1 mg g^{-1} (Cr), 5.0 mg g^{-1} (Cu), 4.7 mg g^{-1} (Ni), and 4.9 mg g^{-1} (Zn) (**Figure 7-2a**). The removal capacity was higher than the widely-used commercial ZVI and modified ZVI, which only performed a moderate removal capacity of 4.4–9.0 mg g^{-1} (Cr), 3.4–5.0 mg g^{-1} (Cu), 1.0–3.4 mg g^{-1} (Ni), and 1.6–4.0 mg g^{-1} (Zn). Using the emission standard of pollutants for the electroplating industry (GB 21900-2008), only Fe-Mn biochar produced with 180°C hydrothermal treatment and urea could reach the standard requirement with remained metal concentration of 0.3 mg L^{-1} (Cr (Total)), 0.1 mg L^{-1} (Cr (VI)), 0.0 mg L^{-1} (Cu), 0.4 mg L^{-1} (Ni), and 0.5 mg L^{-1} (Zn) (**Figure 7-2b**, **Figure 7-2c**, and **Figure 7-2d**). By contrast, the commercial/modified ZVI failed to reach the emission standard, especially for the chromium emission, which might be caused by the inhibition from the co-existed cations (**Figure 7-1c**).

Comparing with the Fe-Mn biochar without hydrothermal treatment (**Figure G1, Appendix G**), hydrothermal treatment, especially the high-temperature treatment with urea, significantly improved the removal performance for Cr(VI), Zn, and Ni, while Cu can be totally immobilized even without hydrothermal treatment. Moreover, Fe-Mn biochar produced with hydrothermal treatment also showed a higher removal capacity than Fe-biochar (**Figure G2**) or Mn biochar (**Figure G3**) with similar hydrothermal treatment, further evidencing the importance of binary oxide modification with biochar.

Removal kinetics was also evaluated for the Fe-Mn biochar and reduced ZVI (**Figure 7-3**). All toxic metals can be removed within 5h for either Fe-Mn biochar or ZVI. The reduction of Cr(VI) was faster than the immobilization of total Cr, causing the accumulation of Cr(III) under a shorter reaction time (< 5h) with Fe-Mn biochar. More toxic metals were moved by Fe-Mn biochar compared with the ZVI during the 24h reaction, which is consistent with the batch experiment (**Figure 7-2**).

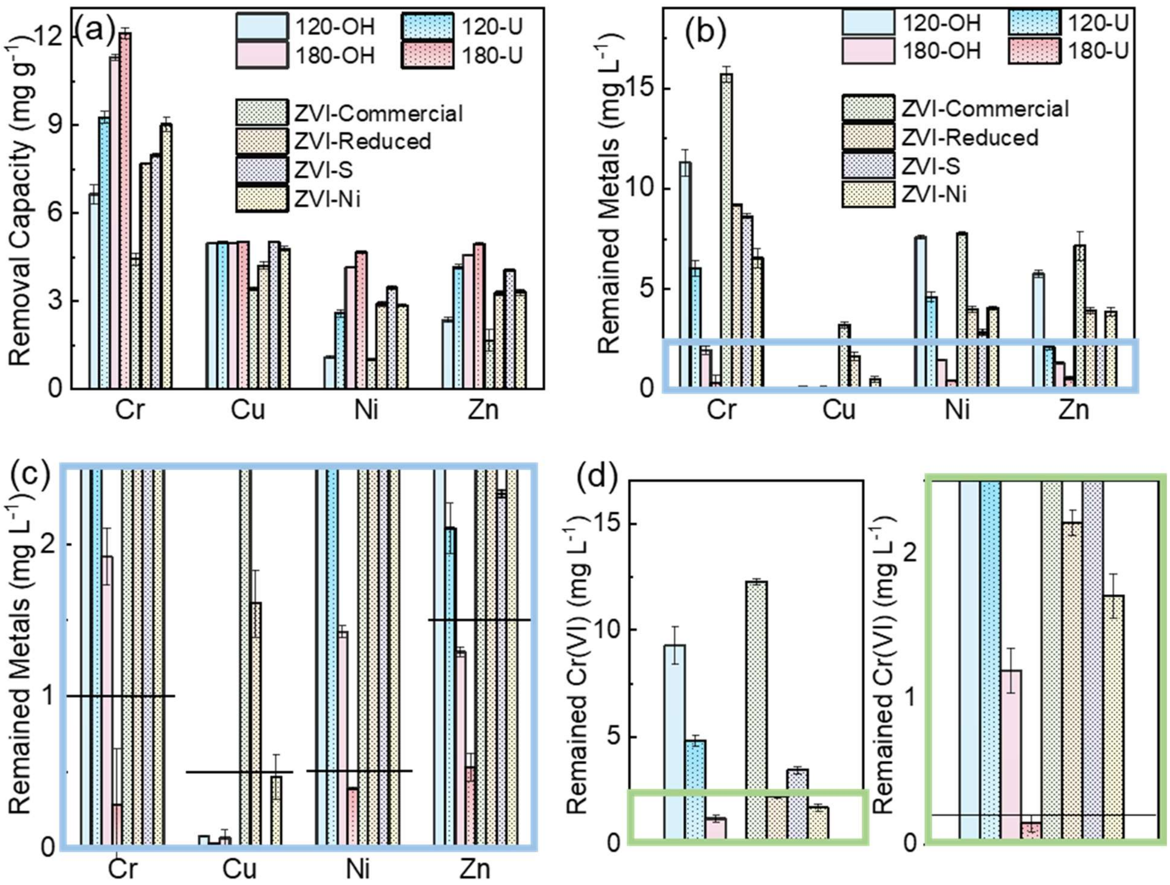

Figure 7-2 Toxic metal removal capacity of different Fe-Mn biochar and ZVI (**a**); Remaining total metal concentration after treatment (**b**) and enlarged version of the blue box in the **b** (**c**); Remaining Cr(VI) concentration after treatment and enlarged version of the green box (**d**). pH was set as ~2.5, and the concentration of Cr(VI), Cu, Ni, and Zn was set as 25 mg L^{-1}, 10 mg L^{-1}, 10 mg L^{-1}, and 10 mg L^{-1}, respectively. The added amount of Fe-Mn biochar or modified ZVI was 2 g L^{-1}, and the reaction time was 24h. The black line in the **c** and **d** represent the emission standard of pollutants for the electroplating industry

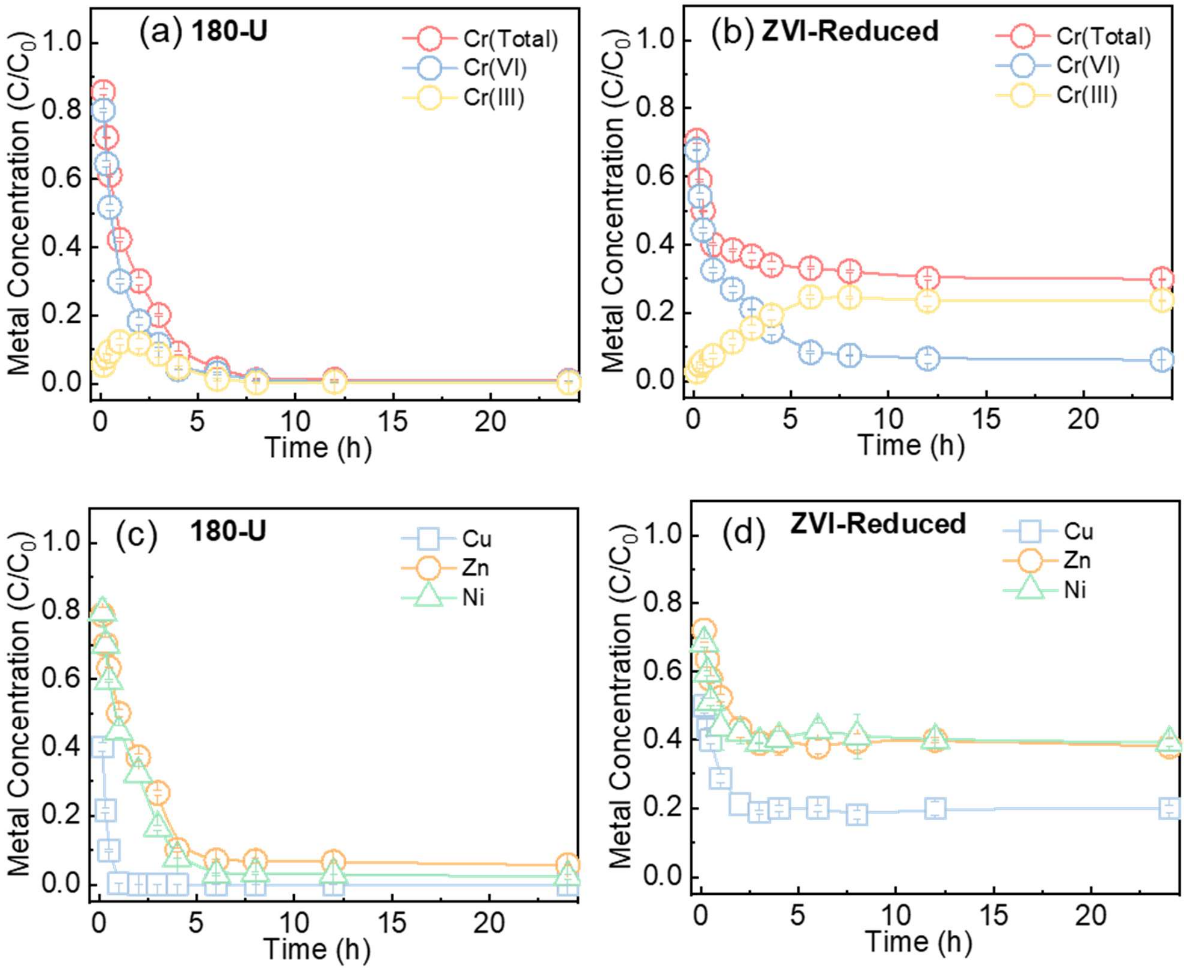

Figure 7-3 Change of the Cr(Total), Cr(VI), and Cr(III) during the 24 h reaction with Fe-Mn biochar produced with urea and 180°C hydrothermal temperature (**a**) or reduced ZVI (**b**); Change of the Cu, Ni, and Zn during the 24 h reaction with Fe-Mn biochar produced with urea and 180°C hydrothermal temperature (**c**) or reduced ZVI (**d**); Setting condition was similar to the Figure 7-2.

In short, Fe-Mn biochar produced with the 180°C hydrothermal treatment with urea showed a higher removal capacity for different toxic metals in the electroplating wastewater compared to the commercial/modified ZVI). It also showed a preserved efficiency under varying acidity and anion/cations ratio conditions in the electroplating wastewater, indicating the potential target as the varying electroplating plants. The unique Fe species with the Mn mineral fabrication under this hydrothermal condition might bring this advantage.

6.3.2 Stability of the immobilized toxic metals on the Fe-Mn biochar

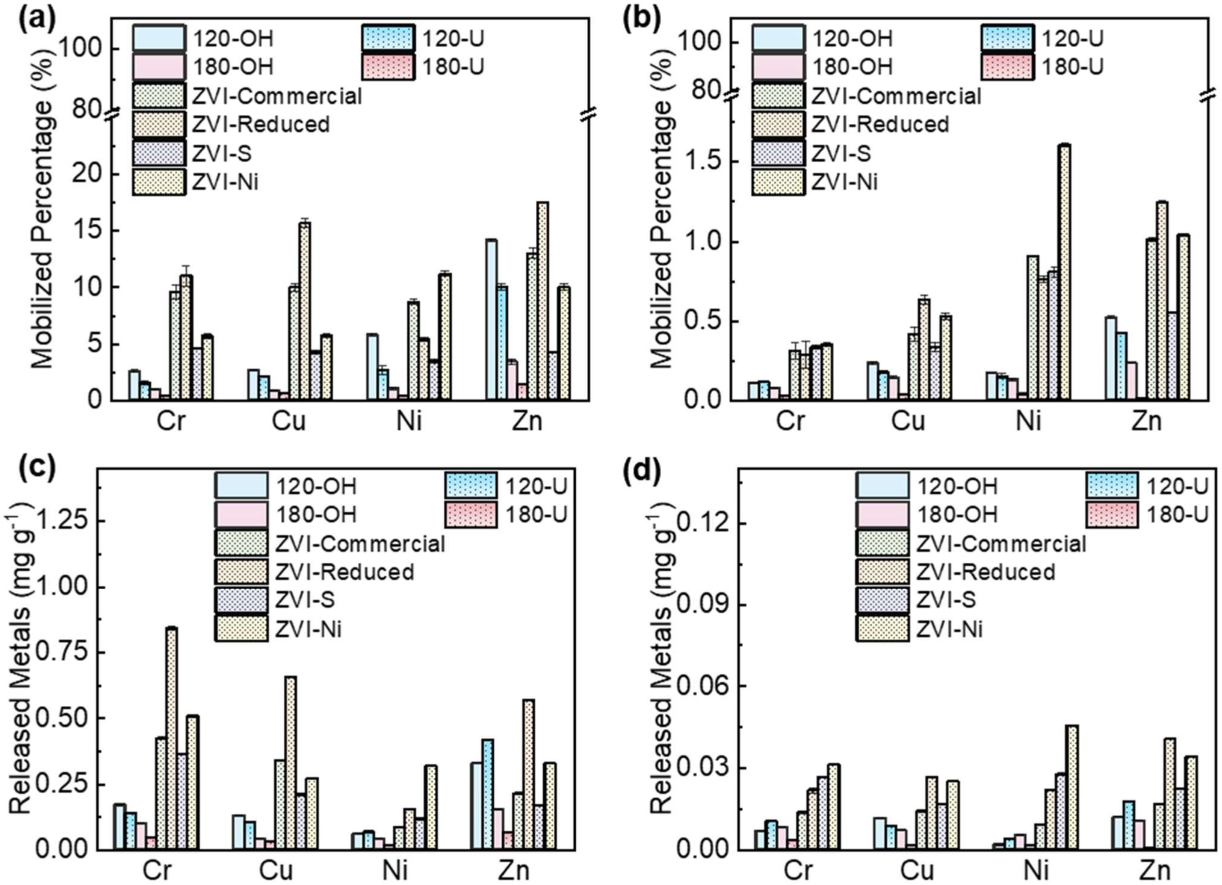

Figure 7-4 The mobilized percentage from spent Fe-Mn biochar or modified/commercial ZVI by acid (**a**) or $CaCl_2$ extraction (**b**); Released metals from spent Fe-Mn biochar or modified/commercial ZVI by acid (**c**) or $CaCl_2$ extraction (**d**)

Two extraction methods were used to evaluate the released potential of toxic metals (**Figure 7-4**). Fe-Mn biochar produced with 180°C hydrothermal treatment and urea (180-U) showed the best stability with only 0.32–1.35% and 0.01–0.03% toxic metals released after aicd and $CaCl_2$ extraction, respectively. More toxic metals were released with Fe-Mn biochar produced with lower hydrothermal temperature and NaOH (up to 2.56–14.08% (acid) and 0.10–0.52% ($CaCl_2$)), indicating the key role of the hydrothermal treatment condition. Moreover, a significantly higher proportion of all toxic metals was extracted from ZVI than the

Fe-Mn biochar by either $CaCl_2$ or acid extraction. The released proportion could reach up to 8.65–17.39% (acid) and 0.35–1.60% ($CaCl_2$) with a high released amount of 0.32–0.84 mg g^{-1} material (acid) and 0.01–0.05 mg g^{-1} material ($CaCl_2$). This again confirms the advantage of the Fe-Mn biochar, the outstanding stability during the extraction.

Table 7-1 Extraction amount and proportion of toxic metals from spent Fe-Mn biochar and ZVI after one month's incubation in soil

Materials	Toxic Metals	$CaCl_2$ extraction		Acid extraction	
		Released amount ($\times 10^{-3}$ mg g^{-1})	Proportion (%)	Released amount ($\times 10^{-3}$ mg g^{-1})	Proportion (%)
Fe-Mn biochar (U-180)	Cr	2.1	0.02	23.3	0.19
	Cu	1.0	0.02	13.9	0.28
	Ni	0.6	0.01	11.0	0.24
	Zn	2.2	0.05	46.7	0.95
Reduced ZVI	Cr	16.7	0.22	498.6	6.50
	Cu	14.0	0.33	374.2	8.91
	Ni	11.9	0.41	97.7	3.39
	Zn	23.4	0.72	374.7	11.51

According to the high stability of the fixed metals on the Fe-Mn biochar during the extraction process, it has a high potential for long-term stability after the settlement of the spent Fe-Mn biochar. Therefore, we further evaluate the stability of spent Fe-Mn biochar after long-term incubation in the soil through similar extraction methods (**Table 7-1**). Fe-Mn biochar (U-180) still showed higher stability than reduced ZVI after 1 month of soil incubation. Only 23.3×10^{-3} mg g^{-1} Cr, 13.9×10^{-3} mg g^{-1} Cu, 11.0×10^{-3} mg g^{-1} Ni, and 46.7×10^{-3} mg g^{-1} Zn can be extracted from spent Fe-Mn biochar through acid extraction, and an even lower extraction amount was found through $CaCl_2$ extraction (0.6–2.2×10^{-3} mg g^{-1}). A higher proportion of toxic metals was extracted from spent reduced ZVI by both acid (3.39–11.52 % > 0.24–0.95%) and $CaCl_2$ extraction (0.21–0.72% > 0.01–0.05%).

The promising stability of Fe-Mn biochar might mainly come from the fixation of biochar on immobilized metals, as biochar is widely reported as immobilizing agent for toxic metals through surface functionality or porous structure. More importantly, the unique Fe species with Mn oxide on the Fe-Mn biochar prepared under suitable conditions (180°C hydrothermal and urea) might also bring the advantage of immobilizing toxic metals.

6.3.3 Mineral species controlled by the hydrothermal process

Co-hydrothermal alkalinity significantly affected the mineral speciation during the hydrothermal process, leading to the different reactivity of the Fe-Mn biochar (**Figure 7-2** and **Figure 7-4**). Based on the XRD analysis, co-hydrothermal alkaline agents affected the Fe-Mn speciation on the Fe-Mn biochar. For the hydrothermal process with NaOH, $MnFe_2O_4$ was the main mineral speciation on the Fe-Mn biochar after the hydrothermal process, while $MnCO_3$ and Fe_2O_3 were found on Fe-Mn produced with urea (**Figure 7-5a**). The hydrothermal decomposition of urea might be the main reason for the separated formation of Fe and Mn minerals. It is worth noting that no apparent difference can be found when comparing different hydrothermal temperatures, indicating the completed reaction under a lower hydrothermal temperature (120°C).

Urea was trended to be decomposed under a higher temperature (>80°C) with the formation of CO_2 and NH_3 (Goel et al., 2022, Li et al., 2021a) **Eq.7.1**), and the formed NH_3 will further react with water for the formation of OH^- during the hydrothermal process (**Eq.7.2**).

Then, the alkalinity will then cause the precipitation of Fe^{3+} with hydroxide formation and then further transformed into oxide with the high-temperature hydrothermal process (**Eq.7.3**). Meanwhile, the formed CO_2 might directly react with the Mn^{2+} and OH^- in the solution with the formation of $MnCO_3$ (**Eq.7.4**). In short, the decomposition of urea caused the formation of separated Fe_2O_3 and $MnCO_3$. For NaOH, it will immediately react with Fe^{3+} and Mn^{2+} during the mixing process with the formation of Fe-Mn hydroxide. The binary mineral precursor will then transform to the binary oxide ($MnFe_2O_4$) during the further hydrothermal process (**Eq.7.5**)

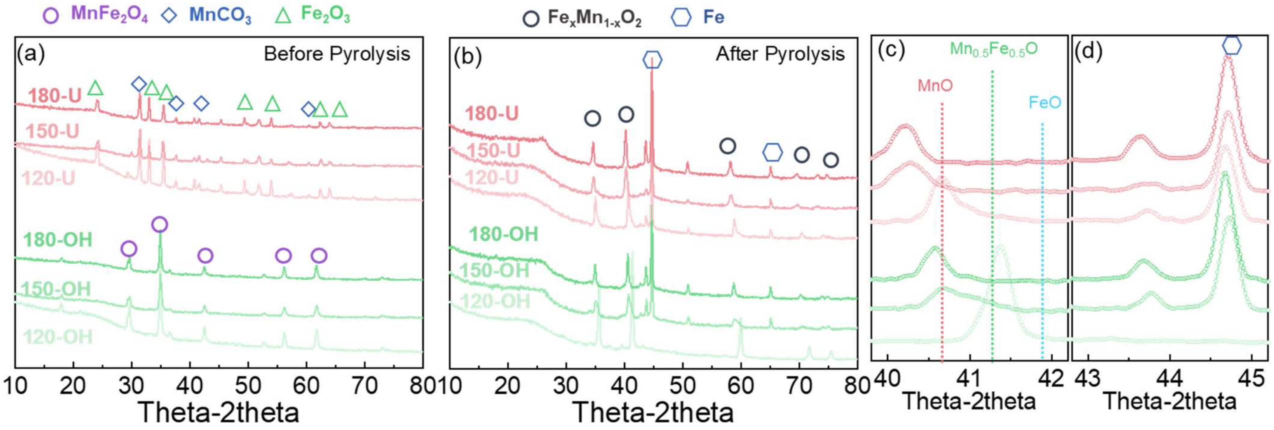

Figure 7-5 XRD pattern of Fe-Mn biochar after the hydrothermal process (**a**) and after hydrothermal and further pyrolysis process (**b**); The enlarged XRD pattern for the Fe-Mn biochar after hydrothermal and pyrolysis process (**c&d**).

$CO(NH_2)_2 + H_2O \rightarrow CO_2 + 2NH_3$ **Eq.7.1**

$NH_3 + H_2O \rightarrow NH_4^+ + OH^-$ **Eq.7.2**

$6OH^- + 2Fe^{3+} \rightarrow Fe_2O_3 + 3H_2O$ **Eq.7.3**

$Mn^{2+} + CO_2 + 2OH^- \rightarrow MnCO_3 + H_2O$ **Eq.7.4**

$Mn^{2+} + 2Fe^{3+} + 8OH^- \rightarrow MnFe_2O_4 + 4H_2O$ **Eq.7.5**

$MnFe_2O_4 + CO \rightarrow MnFe_2O_3\ ((MnO)_{1/3}(FeO)_{2/3}) + CO_2$ **Eq.7.6**

$MnFe_2O_3\ ((MnO)_{1/3}(FeO)_{2/3}) + CO \rightarrow MnFeO_2\ ((MnO)_{1/2}(FeO)_{1/2}) + Fe + CO_2$ **Eq.7.7**

$$MnFeO_2 + CO \rightarrow MnO + Fe + CO_2 \quad \textbf{Eq.7.8}$$

$$Fe_2O_3 + 3CO \rightarrow 2Fe + 3CO_2 \quad \textbf{Eq.7.9}$$

Different mineral species after the hydrothermal process will further affect the final mineral speciation after the second pyrolysis process. As shown in **Figure 7-5b**, Fe(0) can be found in all Fe-Mn biochar except the 120-OH (120°C hydrothermal with NaOH), and the $Fe_xMn_{1-x}O_2$ was formed in all Fe-Mn biochar with a varying peak position. The thermal reduction process with the biochar-formed CO could be the main reason for the formation of these minerals (Feng et al., 2020, Qiu et al., 2020, Shen 2015, Xu et al., 2022a) (**Eq.7.6–Eq.7.9**). With an enlarged version **(Figure 7-5c** and **Figure 7-5d**), a left shift was shown in the Fe-Mn biochar with the increasing hydrothermal temperature, and urea-produced samples also showed a minor peak position than the NaOH sample.

To further evidence the impact of hydrothermal treatment on mineral speciation, different biochar precursor was also involved in studying the mineral speciation transformation. Results showed that the biochar precursor has less impact on mineral speciation before (**Figure G4**, **Appendix G**) or after pyrolysis (**Figure G5, Appendix G**) compared to the hydrothermal conditions, evidencing the determined role of hydrothermal conditions on the mineral regulation. $MnFe_2O_4$ and $Fe_2O_3/MnCO_3$ were still the main minerals after the hydrothermal treatment (**Figure G4**), and they will transform to Fe and $Fe_xMn_{1-x}O_2$ after the pyrolysis process (**Figure G5**). More Fe(0) was formed on the Fe-Mn biochar with the BC550 as the precursor than BC850 and BC850C due to the rich reductive potential on low-temperature-produced biochar (Xu et al., 2021f).

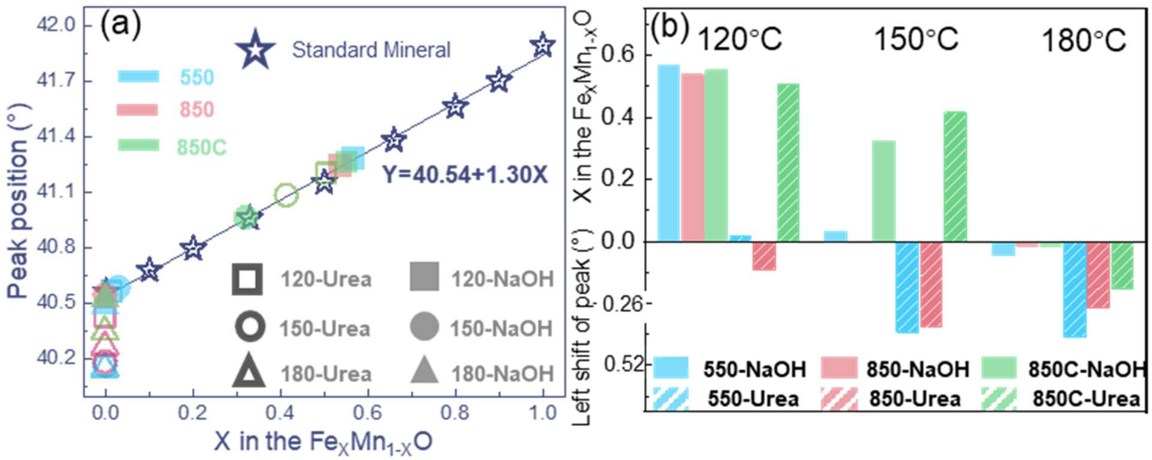

Figure 7-6 Relationship of peak position and X in the $Fe_XMn_{1-X}O_2$ (**a**); The calculated ratio of different Fe-Mn biochar (upper part, **b**), and the left shift of peak caused by the expansion of MnO lattice (down part, **b**)

According to the standard peak position of $FeMnO_2$ with different Fe to Mn ratios (**Figure 7.6**), we can conclude that the Fe content in the binary oxide decrease with the increasing hydrothermal temperature with NaOH due to the reductive formation of Fe(0) (**Eq.7.7** and **Eq.7.8**), and binary oxide with limited Fe(0) was the primary mineral speciation in the Fe-Mn biochar produced with 120°C hydrothermal. A high hydrothermal temperature might form a loose structure of the minerals with smaller particle sizes (Numpilai et al., 2022, Zeng et al., 2021), thus leading to an easy reductive transformation. For the urea-treated sample, less binary oxide was formed even under 120°C hydrothermal temperature, indicating the more straightforward Fe reduction from Fe_2O_3 than the $MnFe_2O_4$. Besides, the higher hydrothermal temperature (over 150°C) might lead to the further left shift of peaks of MnO. The potential reason is the expansion of the Mn-O lattice in the crystal structure due to the high-pressure treatment during the hydrothermal process. The decomposition of urea with high pressure due to the gas generation (**Eq.7.1**) and the decomposition of $MnCO_3$ during the thermal treatment might also cause the expansion of the crystal lattice. This unique Mn species with the completed Fe(0) formation could be the key to the high reactivity of the Fe-Mn biochar produced with urea and 180°C hydrothermal temperature. It is worth noting that biochar precursors also affect the mineral speciation of the produced Fe-Mn biochar; that is, the reductive transformation of Fe was inhibited with the biochar produced at 850°C and CO_2 (850-C), and it might be caused by the limited CO formation with higher thermal stability.

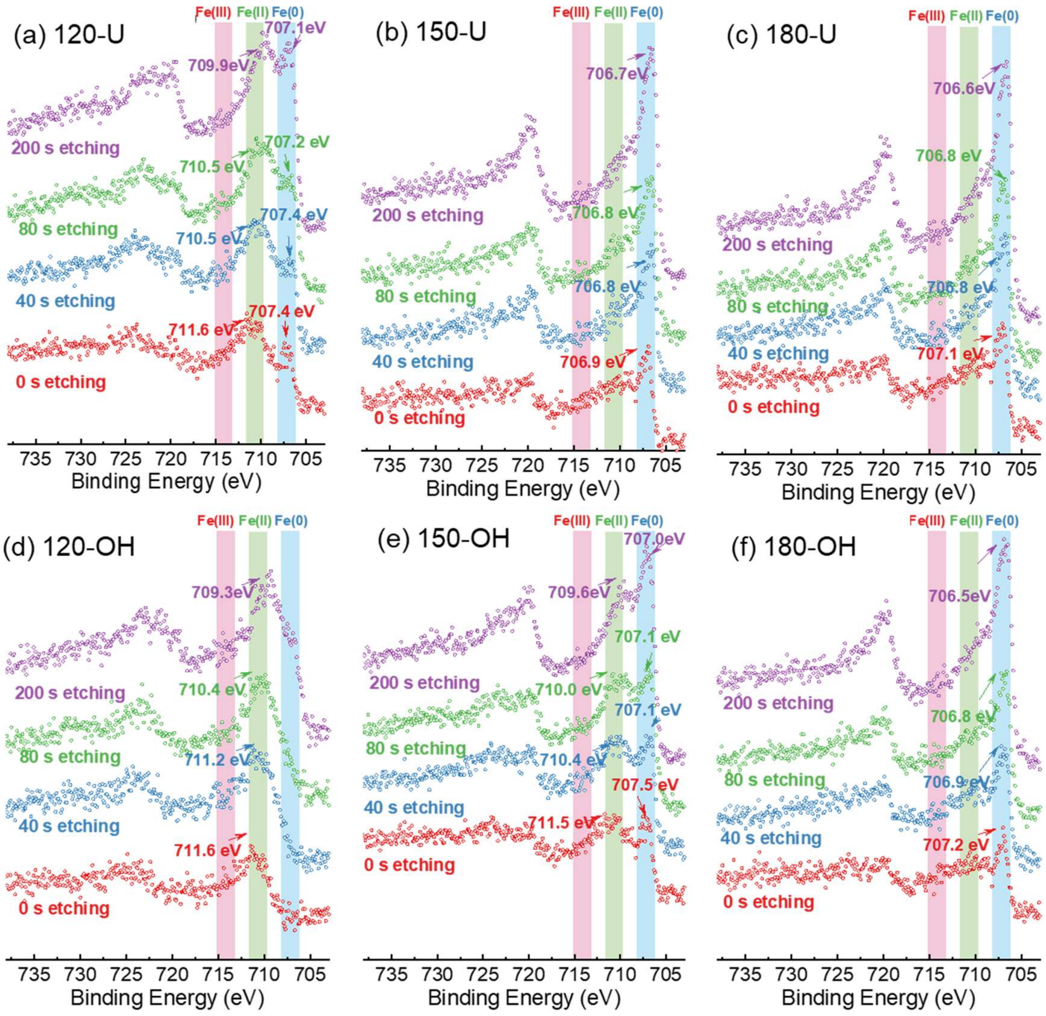

Figure 7-7 XPS analysis for the Fe 2p spectrum of different Fe-Mn biochar; Different etching was conducted to evaluate Fe species under different depths of Fe-Mn biochar

XPS analysis with depth profiling was then conducted to further evaluate the mineral speciation of the produced Fe-Mn biochar. Consistent with the XRD results, the Fe(0) peak can be found in all Fe-Mn biochar after pyrolysis except the 120-OH (**Figure 7-7**). Besides, the Fe(0) peak was more apparent under a higher hydrothermal temperature and with the addition of urea. It is worth mentioning that a high proportion of Fe(0) can be found even on the surface of the Fe-Mn biochar, especially for the U-180, indicating the limited passivation of the Fe(0) with the protection of biochar and Mn oxide, which might contribute to the higher reactivity. Similarly, Mn(II) was the main Mn species in all Fe-Mn biochar, suggesting the limited valence transformation of Mn with different hydrothermal conditions (**Figure G6**). However, a slight red shift was found with increasing hydrothermal temperature, which might manifest the Mn oxide's lattice expansion.

7.3.4 Impact of hydrothermal condition on the Fe-Mn mineral distribution on the biochar

TEM-EDX and SAED analysis were used to confirm the mineral distribution of the Fe-Mn biochar (**Figure 7-8**). A highly fitted distribution of Fe and Mn minerals was found on the low-hydrothermal-temperature produced biochar (120°C), while a slight separation was shown with a high hydrothermal temperature. This result indicated that the higher energy with pressure during hydrothermal processes could affect the mineral distribution on carbon. Normally, the high hydrothermal temperature will accelerate the formation of crystal nuclei with enhanced anisotropy (Zeng et al., 2021), thus leading to the separated distribution of mineral particles with smaller sizes. For the low hydrothermal temperature Fe-Mn biochar, binary oxide ($FeMnO_2$ for 120-OH) and cooperative Fe and Mn oxide (Fe/FeO and MnO for 120-U) were the existing primary forms. With the increasing hydrothermal temperature, separated Fe(0) and

MnO became the main existing mineral forms in biochar. In addition, SAED analysis confirmed the formation of Fe(0) with the lattice as 1.99-2.00 Å on 120-U, 180-OH, and 180-U, while only $Fe_XMn_{1-X}O_2$ was found on 120-OH, which is consistent with the XRD and XPS analysis. Moreover, the lattice expansion of the MnO was also confirmed by the SAED analysis that the lattice of MnO increased from 1.53–1.54 Å to 1.58–1.60 Å with a higher hydrothermal temperature.

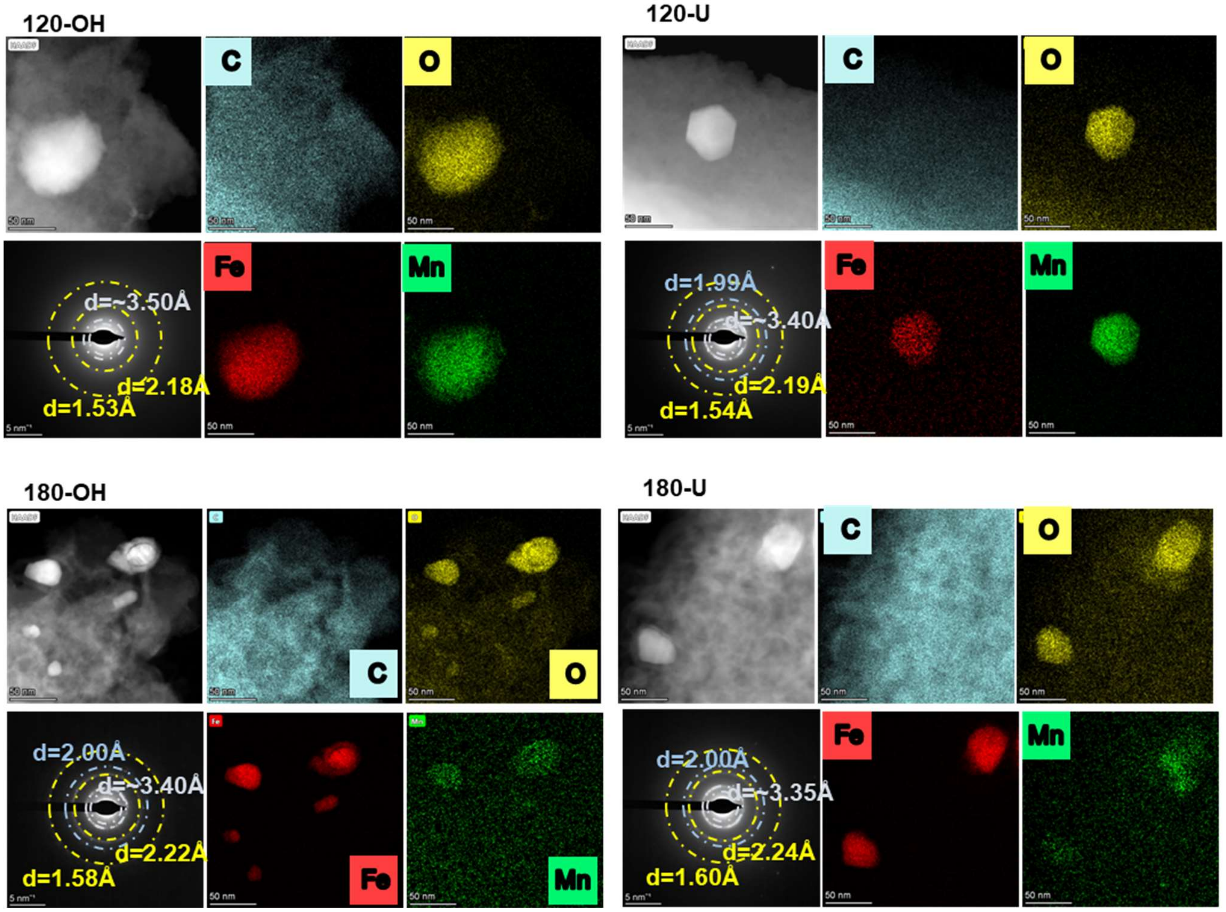

Figure 7-8 TEM-EDX-SAED analysis for the Fe-Mn biochar produced under different hydrothermal conditions.

With a high-resolution TEM analysis, the existence of $Fe_XMn_{1-X}O_2$ and Fe was further confirmed with the specific lattice of 1.99–2.01 Å (110) of Fe(0) and 2.50–2.59 Å of $Fe_XMn_{1-X}O_2$ (**Figure G7** and **Figure 7-9**). Moreover, the separation of Fe and Mn minerals with a higher hydrothermal temperature was also confirmed by the HR-TEM analysis. We could find the formation of Fe(0) (1.98 Å) from the surrounding MnO (2.50 Å) on 180-U (**Figure 7-9b**), evidencing the potential separation process with the reductive transformation. By contrast, the existence of Fe (2.00 Å) and $FeMnO_2$ was highly fitted in 120-U (**Figure 7-9a**), indicating cooperative growth.

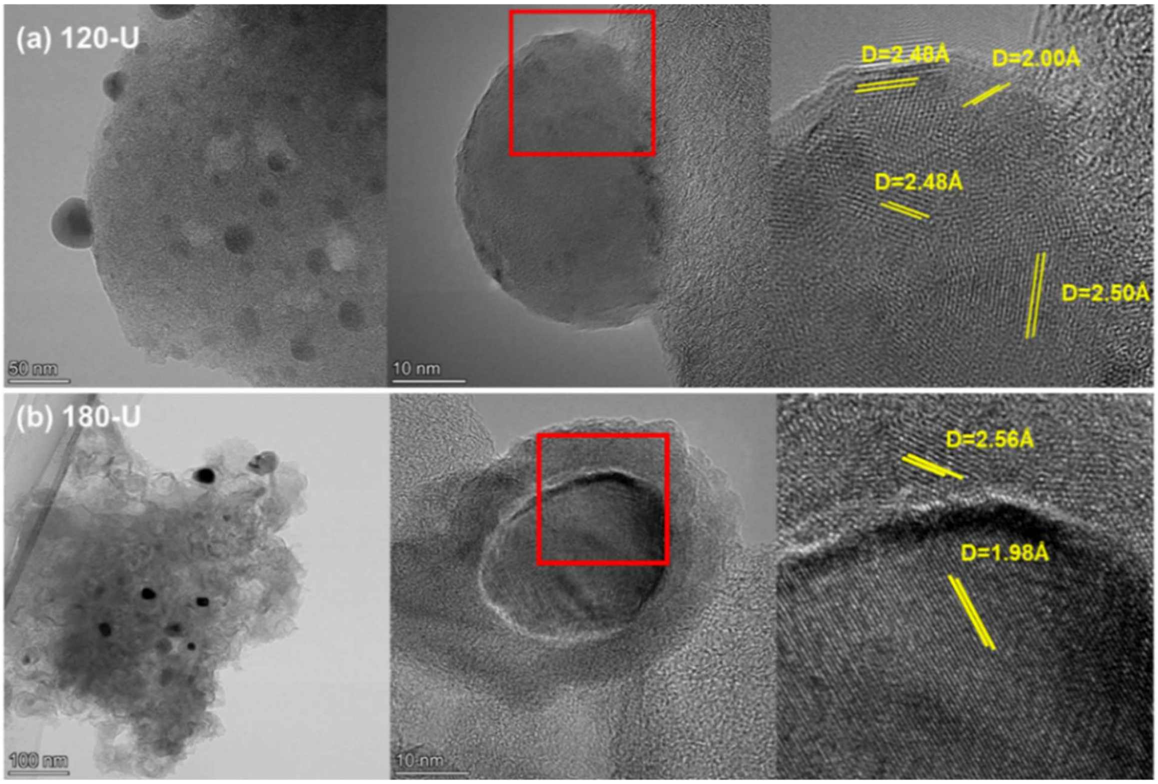

Figure 7-9 HR-TEM analysis of Fe-Mn biochar (a:120-U, b:180-U). The right figure was the enlarged version of the red square in the middle figure.

7.3.5 Change of the carbon properties during the hydrothermal process

A broad peak around 23–25° can be found on the XRD pattern of Fe-Mn biochar produced under 180°C hydrothermal and urea (**Figure 7-5** and **Figure G5, Appendix G**) and a lattice of 3.35–3.50 Å was shown in the SAED pattern (**Figure 7-8**). All these characterizations indicate the potential formation of the graphite structure on the Fe-Mn biochar; thus, Raman analysis was conducted to evaluate the difference with varying hydrothermal conditions. Five peaks, including S-band (~1290 cm^{-1}, the transformation of sp^2 to sp^3 hybridization), D-band (~1350 cm^{-1} representing a disordered graphitic carbon structure), A-band (~1500 cm^{-1}, amorphous carbon phase), G-band (~1560 cm^{-1} assigned to graphitic carbon with aromatic rings), and D^*-band (~1620 cm^{-1}, related to defect features) were obtained after peak deconvolution (McDonald-Wharry et al., 2013, Yang et al., 2020b) (**Figure 7-10**, **Figure G8**, and **Figure G9**, **Appendix G**). The indicators, including I_D/I_G (representing the formation of disorder structure) and I_A/I_G (representing the amorphous carbon content) (Xue et al., 2021, Yang et al., 2020b), were calculated to compare the change in the graphitic structure during the production of Fe-Mn biochar (**Figure 7-10**).

The hydrothermal process has a limited impact on the disordered structure and carbon defects on the graphitic carbon, except the 180°C hydrothermal treatment increased the disorder degree of the BC550 (**Figure 7-10d**). The lower stability of low-temperature-produced biochar (Leng and Huang 2018, Xu et al., 2021b) and the higher energy provided by the 180°C hydrothermal process might cause the aromatization of biochar with the increase of disorder carbon structure (Zhang et al., 2019c), especially under the catalyze by co-existed Fe (Wang et al., 2022a). Besides, the hydrothermal process increased the amorphous carbon content of BC550, while little change was found in BC850 and BC850C (**Figure 7-10e**), which might still be caused by the lower stability of BC550. All these results confirmed that the high-temperature hydrothermal process mainly affected the carbon structure of BC550 instead of the high-temperature produced biochar, and the potential affecting process might be the dehydration and decarboxylate process (Xie et al., 2023).

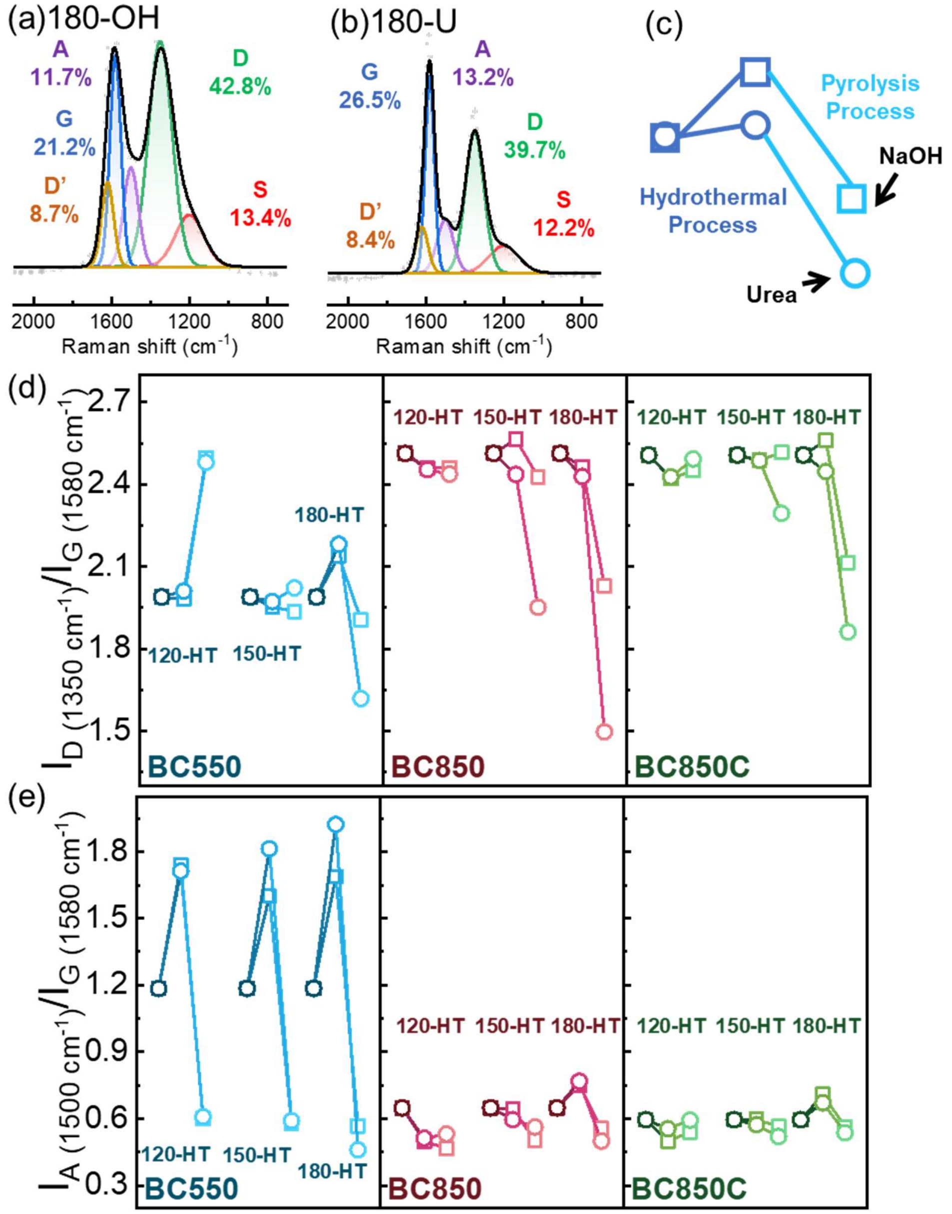

Figure 7-10 Raman peaks deconvolution of Fe-Mn biochar (**a**:180-OH; **b**:180-U); Symbol explanation (**c**) for the comparison of ID/IG (**d**) and IA/IG (**e**) ratio during the preparation of Fe-Mn biochar; The Raman peaks deconvolution of other Fe-Mn biochar was shown in the **Figure G8** and **Figure G9**, Appendix **G**.

During the further pyrolysis after the hydrothermal treatment, the amorphous carbon content in BC550 is deceased (**Figure 7-10e**), and the amorphous carbon might participate in the thermal reduction process, leading to the high reductive formation of Fe on the BC550 even with a lower hydrothermal temperature (**Figure 7-6** and **Figure G5**). The disorder degree also decreased after the pyrolysis process, implying graphitization of the carbon structure (**Figure 7-10d**). Compared to the biochar precursor, a more ordered graphitic structure was formed after the hydrothermal and pyrolysis (**Figure 7-10d**), which might facilitate the immobilization process due to the enhanced electron transfer from Fe with graphitic carbon (Xu et al., 2022a). The higher hydrothermal temperature and co-hydrothermal with urea showed a higher decrease in disorder degree and amorphous content, contributing to the higher immobilization capacity of Fe-Mn biochar produced with 180°C hydrothermal and urea. Notably, an increase in disorder degree was found on BC550 after 120°C hydrothermal and pyrolysis. The potential reason might be the limited impact of 120°C hydrothermal on the carbon structure of BC550, and thus it increased to a similar disorder degree of BC850 after the pyrolysis process due to the disorientation and corrugation of graphitic basal at high temperature.

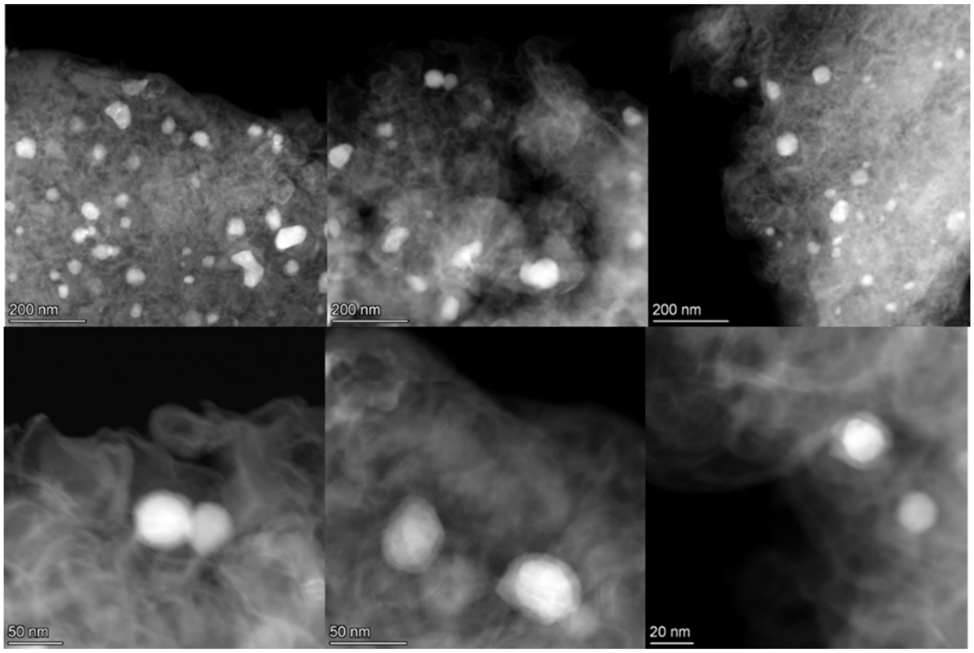

Figure 7-11 TEM analysis of Fe-Mn biochar (U-180) produced with 180°C hydrothermal and urea under different scales

In conclusion, more graphitic carbon was formed on the Fe-Mn biochar after the 180°C hydrothermal process with urea. TEM analysis revealed the nature of the graphitic carbon phase on the Fe-Mn biochar; it was a cotton/sponge-like structure supporting the nano-sized mineral particles (**Figure 7-11**). This kind of structure could support the dispersibility of the mineral particles with a higher reactivity and stability. Similar results were also found in the literature that a high-temperature hydrothermal process caused the formation of a sponge-like supporter with a high stabilization impact for the attached nanoparticles (Numpilai et al., 2022). Besides, due to the high conductivity of the graphitic carbon, it might also facilitate the fast electron transfer between Fe(0) and the pollutants (Xu et al., 2022a, Xu et al., 2019b, Xu et al., 2020f), thus causing an efficient immobilization of toxic metals.

7.3.6 Role of Fe: fast electron transfer for the toxic metals reduction

XPS analysis with depth profiling was conducted to evaluate the metal valence state of the Fe-Mn biochar after the immobilization process. Ni(II), Cr(III), Cu(II), and Zn(II) were the main existing forms of toxic metals on the spent Fe-Mn biochar (180-U and 120-U), with the existence of Fe(III) and Mn(II) (**Figure 7-12**). With the increasing etching depth, Ni(0) and Cu(0) appeared, becoming the primary forms of Ni and Cu on the spent Fe-Mn biochar. By contrast, Mn(II), Fe(III), and Zn(II) remain unchanged in the overall 200s etching depth. The existing nature of toxic metals indicated the existence of the redox reactions between Fe(0) and toxic metals during the immobilization process (**Eq.7-10**, **Eq.7-11**, and **Eq.7-12**), and it could be the key to the toxic metals immobilization and its long-term stability. Moreover, the H_2-TPR analysis also confirmed this redox reaction due to the increase of iron oxide peaks after the immobilization (**Figure G10**).

$$\mathrm{Fe(0) + Cr(VI) \rightarrow Fe(III) + Cr(III)} \qquad \textbf{Eq.7-10}$$

$$\mathrm{2Fe(0) + 3Cu(II) \rightarrow 2Fe(III) + 3Cu(0)} \qquad \textbf{Eq.7-11}$$

$$\mathrm{2Fe(0) + 3Ni(II) \rightarrow 2Fe(III) + 3Ni(0)} \qquad \textbf{Eq.7-12}$$

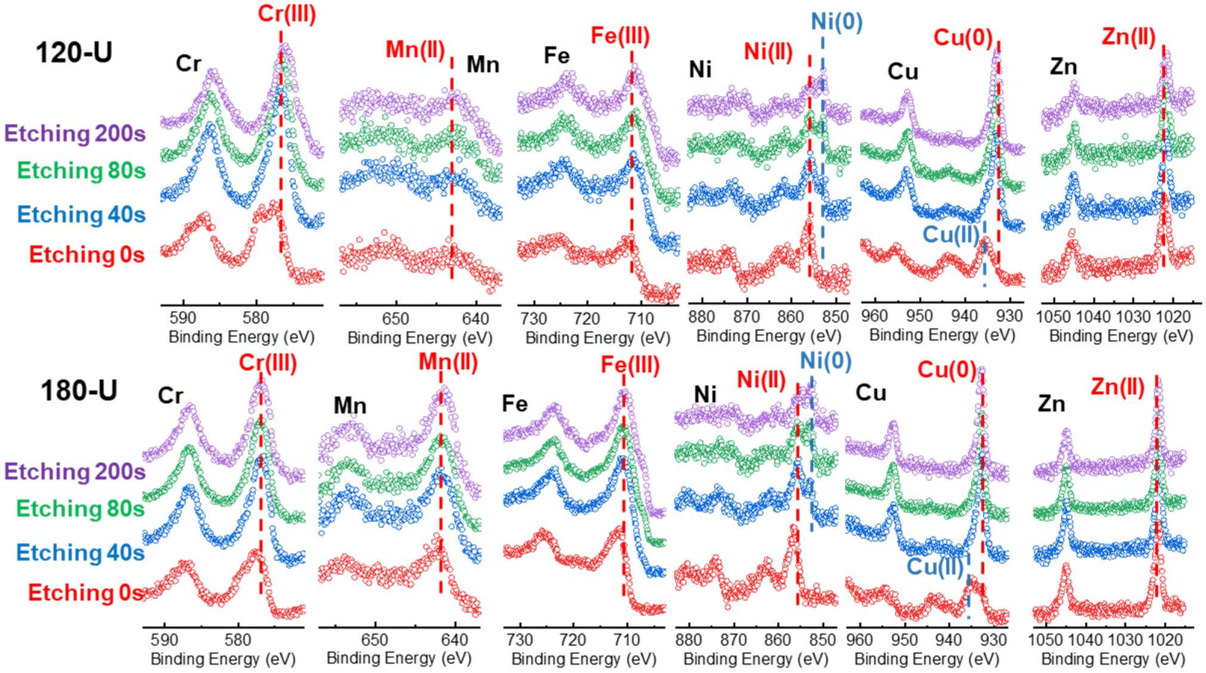

Figure 7-12 XPS analysis for the Cr, Mn, Fe, Ni, Cu, and Zn of different Fe-Mn biochar after the toxic metals immobilization process; Different etching was conducted to evaluate to Fe species under different depths of Fe-Mn biochar

The reduction of Cr(VI) was normally the determining step for the Cr immobilization since Cr(III) has a higher potential for precipitation and sorption (Liu et al., 2020c). The Cr(III) usually have higher stability than the Cr(VI) due to the positive nature and lower mobility in the environment matrix. Besides, the redox reaction might directly combine with the growth of the Fe-Cr/Mn-Cr complex, serving as the direct immobilization approach. Although the reduction reaction was not the premise of the immobilization process for Cu and Ni immobilization, forming a zero-valent metal state might also bring the advantage of its stability in the environment matrix, which could be the main reason for the less leachability during the extraction process.

Comparing the valence state between 120-U and 180-U (**Figure 7-12**), we found that Cr(VI) can be formed on the surface of 120-U, while only Cr(III) was formed on 180-U. The lower Fe(0) content of the Fe-Mn biochar produced with the low hydrothermal temperature might be the main reason for the limited reduction process. The maintained Cr(VI) on the 120-U also led to its lower stability with a higher releasing amount during the extraction process.

7.3.7 Role of Mn: Fixation site for the toxic metals after the reduction

According to the TEM-EDX analysis for the spent Fe-Mn biochar, a highly fitted distribution of Mn and toxic metals (Cr, Cu, Ni, and Zn) was found on both 120-U and 180-U (**Figure 7-13** and **Figure G11, Appendix G**). For 120-U, since the Fe and Mn were still combined due to the lower hydrothermal process, the complex of Mn and toxic metals was formed surrounding the iron minerals. Meanwhile, a clear separation between Mn-toxic metals and Fe was found on the 180-U, implying Mn mainly contributed to the fixation of toxic metals after the reductive transformation.

The separated reduction and immobilization process might bring the following advantages to the removal process. Firstly, no Fe-metals passivation layer was formed on the Fe surface, facilitating its electron transfer process (Bae et al., 2018, Zhang et al., 2018a). This might also explain the better reducing capacity of 180-U than 120-U since still surface complex was formed on the Fe surface of 120-U. Secondly, the surrounding Mn-toxic metal complex around the Fe might also stabilize the iron particles, leading to less passivation with impurities and long-term stability (evidenced by the less iron release with the co-existed Mn, **Figure G12**, **Appendix G**). Thirdly, oxygen on the MnO usually showed a better sorption affinity to cationic metals than the Fe oxide, leading to higher stability. DFT calculation revealed that MnO showed a stronger combination affinity to Cr and Ni than $FeMnO_2$ or FeO, while higher sorption affinity was found on FeO when targeting as the Cr(VI) (existed as $HCrO_4$). The calculation results confirmed the existence of the separated reduction and immobilization process, especially targeting the Cr immobilization; that is, Cr(VI) was sorbed and reduced by iron, and the formed Cr(III) was fixed on the MnO afterwards. We also set a mineral model to study the combining affinity of MnO with an expanded lattice (MnO*) based on the XRD results (**Figure 7-5**), and a higher sorption affinity was found for both Cr and Ni. The more robust combination of toxic metals on MnO with the expanded lattice might contribute to the higher stability of metals sorbed on 180-U.

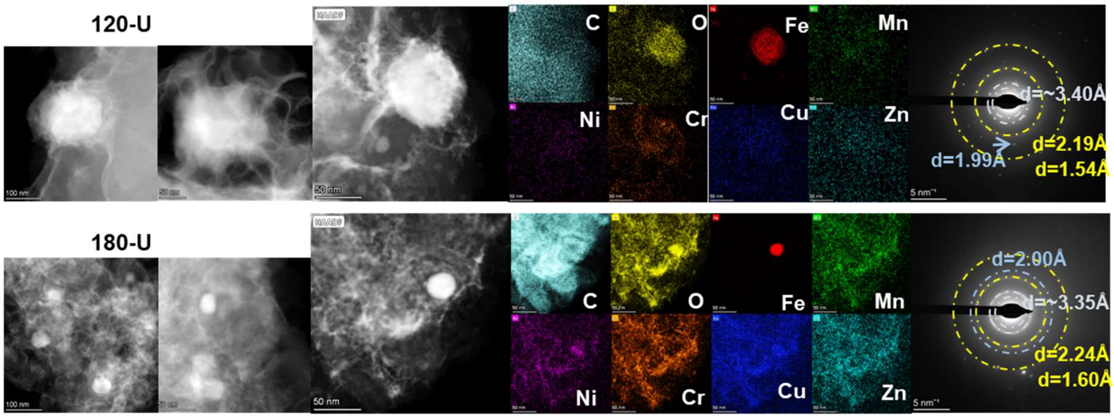

Figure 7-13 TEM-EDX analysis of Fe-Mn biochar after the toxic metals removal

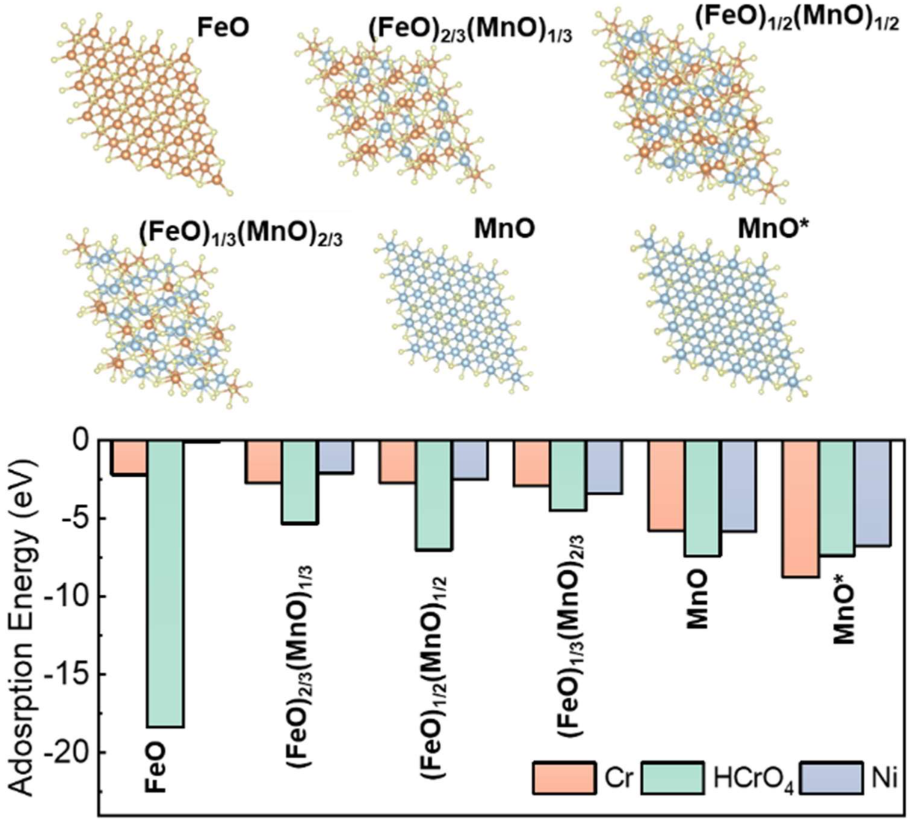

Figure 7-14 DFT calculation of different Fe/Mn oxides and the sorption capacity for different speciation of the toxic metals

7.3.9 Role of C: Stabilization of the mineral particles and electron transfer

As shown in **Figure 7-13** and **Figure G13**, cotton-like graphitic carbon still existed after the proposed immobilization process, and this carbon supported the long-term stability of mineral particles even under an acidic environment (**Figure 7-4**, acid extraction). The lower release potential of Fe from the Fe-Mn biochar also supported this conclusion (**Figure G12**, **Appendix G**).

Notably, the conductivity from the well-grown graphitic structure might also support the reduction and immobilization process (Xu et al., 2022a, Xu et al., 2019b, Xu et al., 2020f). The conductivity from the graphitic carbon might facilitate the electron transfer among Fe, Mn, and different toxic metals. Since the cationic metals (*i.e.,* Ni and Cu) have a higher potential to be immobilized on the MnO surface, they might accept the electron from the Fe(0) through the carbon mediating, i.e., the electron from Fe(0) mediated through the graphitic carbon and reached the toxic metals sorbed on the MnO afterwards. In short, the highly graphitic carbon might greatly support the separate reduction and immobilization process, leading to higher efficiency.

7.4 Conclusion

We studied the impact of hydrothermal conditions on the Fe/Mn speciation on the Fe-Mn biochar and its capacity for toxic metals immobilization in the electroplating wastewater. A higher hydrothermal temperature with co-existing urea (U-180) provided the best immobilization capacity for the frequently-appeared toxic metals in electroplating water, and the outstanding removal efficiency of Fe-Mn biochar (U-180) kept constant under varying conditions in electroplating wastewater. Besides, higher stability of the immobilized metals on U-180 was found, implying the possibility of direct settlement of spent Fe-Mm biochar without treatment. The Fe(0) surrounded by the lattice-expanded MnO and cotton-like graphitic carbon was formed on Fe-Mn biochar after the hydrothermal and pyrolysis process, and the separated reduction and immobilization process, *i.e.,* toxic metals were reduced by Fe(0) and immobilized on the MnO, was the primary decontamination mechanism, leading to the high immobilization capacity. Our result could support the efficient electroplating wastewater treatment and provide a guideline for the hydrothermal treatment of the binary oxide-modified biochar.

Chapter 8 Conclusions and Recommendation

8.1 Conclusions

Precise control of Fe speciation in Fe-biochar composites was studied, and the relevant immobilization mechanisms for the targeted application were evaluated. The key findings are summarized below:

- Pyrolysis temperature affected the redox activity of the produced Fe-biochar. Low-temperature produced Fe-biochar had a higher reducing capacity (Cr(VI) reduction), predominantly offered by the amorphous/low-crystalline ferrous minerals. By contrast, the oxidative surface functionalities on the high-temperature Fe-biochar dominated its oxidizing capacity (As(III) oxidation). The shift of primary redox moieties of Fe-biochar should be taken into account during the production-design stage for effective wastewater treatment. (**Chapter 3**)
- Carbon species of biochar, labile-/amorphous-C and stable/graphitic-C, led to distinct reductive-Fe and amorphous-Fe contents in the resulting Fe-biochar composites during the pyrolysis process. The reductive-Fe species, mainly immobilized As through redox reaction and sorption/complexation, were formed at a high pyrolysis temperature with co-pyrolyzed labile-/amorphous-C. In contrast, amorphous-Fe species were primarily produced with stable-/graphitic-C, and they removed As through co-precipitation with released Fe. A deep understanding of the role of carbon species on the Fe-biochar species can guide our rational design of multifunctional Fe-biochar composites for broader and fit-for-purpose applications. (**Chapter 4**)
- The crystallinity of Fe mineral greatly affects the electron transfer routine with biochar.

The reduction of Cr(VI) by biochar with the low-crystallinity ferric oxyhydroxide was mainly caused by the indirect electron transfer, *i.e.,* biochar firstly donated the electron to Fe(III) on the iron minerals for Fe(II) generation, which further reduced the Cr(VI) sorbed on iron minerals afterwards. For the high-crystallinity ferric oxyhydroxides, the indirect electron transfer pathway was alleviated due to its limited combination with biochar, less sorption amount of Cr(VI), and higher Fe(III) stability of the iron crystalline. Direct electron transfer from biochar to Cr(VI) became the main electron transport for Cr(VI) reduction. Considering the reactivity of Fe-mineral with different crystallinity is needed for the immobilization of contaminants by Fe-biochar. (**Chapter 5**)

- Reductive transformation of Fe within the Fe-Mn binary oxide on biochar was found during the co-pyrolysis process, forming embedded ZVI clusters within $FeMnO_2$ on Fe-Mn biochar. An up to 80.5-161.7 times higher Cr(VI) removal efficiency was found for the embedded ZVI cluster compared to the commercial/modified ZVI due to the less formation of the passivation layer and enhanced affinity with Cr(VI). This work provides a new direction for developing future Fe-biochar with high atom efficiency and stability. (**Chapter 6**)
- The hydrothermal pretreatment affects the mineral transformation of the Fe-Mn biochar. A higher hydrothermal temperature with co-existing urea provided a high immobilization capacity for the frequently-appeared toxic metals in electroplating water, and outstanding stability of the immobilized metals was also found on the as-prepared Fe-Mn biochar. The Fe(0) surrounded by the lattice-expanded MnO and cotton-like graphitic carbon was formed on Fe-Mn biochar after the hydrothermal and pyrolysis process, and the separated

reduction and immobilization process led to the high decontamination capacity. Hydrothermal pretreatment could produce a more efficient Fe-Mn biochar for wastewater decontamination. (**Chapter 7**)

8.2 Recommendations and future work

Precise control of Fe species on the Fe-biochar for the targeted remediation process can help us to provide efficient engineered biochar. Future work can be conducted in the following aspects based on the current progress.

- The Fe mineral transformation during the pyrolysis and hydrothermal with biochar has been studied. However, this study mainly focused on the mineral forms and crystallinity control of Fe mineral, and the size control of the attached Fe-mineral is overlooked. Simple pyrolysis and hydrothermal might not provide precise control of the mineral particle size on the biochar, and future studies are needed by involving more external stabilizers to control the particle size of the mineral. Besides, adjusting the pore on biochar with the control of mineral formation inside the pore can also be a possible approach for mineral size control.
- In addition to the mineral-biochar composites, the metal-carbon framework can be a future direction for engineered biochar materials. Fe atoms can be fixed on the biochar through Fe-O-C or Fe-N-C bonding, i.e., atomic-level dispersed Fe on biochar, and the formed modified biochar should have higher atomic efficiency and activity for the degradation of the pollutants. Compared with the current single-atom catalyst, biochar's economic benefits and easily tuneable properties bring a higher industrialization potential.

- The properties of modified biochar are highly variable due to the inconsistency of the feedstock and production conditions. Different studies reported variable biochar/modified biochar performances, which will mislead the selection and production of biochar. The production guideline and standard of Fe-biochar are needed based on its properties and capacities, which will benefit the industrialization of engineered biochar production.
- Lignin and cellulose-based feedstock with limited ash content (*i.e.,* woody yard waste and peanut shell) were selected to produce biochar in this study. Other feedstock, such as rice straw, cow manure, sludge, and crop residue with rich and different ash content, might lead to a different Fe transformation and performance during Fe-biochar production, which also needs further evaluation. Involving more biomass waste for producing biochar and engineered biochar with environmental benefits is crucial for the large-scale promotion of the biochar industry.
- Biochar production has been considered the negative-emission technology due to its carbon stability and bioenergy generation, while the potential carbon emission of modified biochar is unclear. Introducing iron and the modification process could cause a potential carbon emission; thus, future study about carbon emission is needed to confirm the carbon sequestration nature of modified biochar technology.
- The overall economic concern of the Fe-modified biochar and its life cycle assessment during the industrial-scale application needs more studies. Current studies only focused on the efficiency of a well-controlled Fe-biochar, while the higher production cost might alleviate its industrial application. The balance between high efficiency and low cost

needs further research. Moreover, the current studies mainly used pure chemicals for biochar modification, which might impose additional financial burdens. Thus, finding suitable sources for biochar modification, such as waste-based feedstock, and evaluating the capacities of the as-prepared modified biochar are needed.

Appendix A Chemicals

Ultrapure water (UW, 18.2 MΩ cm) obtained from a Millipore Milli-Q water purification system (Milford, USA) was adopted to configure all the aqueous solutions. Sodium chloride ($NaCl$), manganese chloride ($MnCl_2$), 1,10-phenanthroline, sodium arsenite ($NaAsO_2$), and potassium chromate (K_2CrO_4) were obtained from AccuChem Co. Ltd. Ferric chloride hexahydrate ($FeCl_3{\cdot}6H_2O$), magnesium sulfate ($MgSO_4{\cdot}7H_2O$), potassium bromide (KBr, FTIR-spectrum grade), sodium hydroxide ($NaOH$), ferrous sulfate heptahydrate ($FeSO_4{\cdot}7H_2O$), metallic Fe (Fe, >99.9%), ammonium acetate ($CH_3CO_2NH_4$), 3-morpholinopropane-1-sulfonic acid (MOPs), 1,5-diphenylcarbazide ($((C_6H_5)NHNH)_2CO$), calcium chloride ($CaCl_2$), and calcium fluoride (CaF_2) were purchased from Sigma-Aldrich Chemical Co. Ltd. Ethanol (C_2H_5OH), hydrochloric acid (HCl, 37%), and acetone ($(CH_3)_2CO$) were obtained from Anaqua Global International Inc. Ltd. Nitric acid (HNO_3), phosphoric acid (H_3PO_4, 85%), potassium phosphate monobasic (KH_2PO_4), 5,5-dimethy-l-1-pyrroline-N-oxide, magnetite (Fe_3O_4), maghemite (Fe_2O_3), and oxalic acid ($H_2C_2O_4{\cdot}2H_2O$), and sulfuric acid (H_2SO_4) were purchased from Aladdin Chemical Co. Ltd. Plasma Emission Standard (ICP) (PE-CAL2-ASL-1) was purchased from AccuStandard. The trace element solution contained 30 mg L^{-1} $CuSO_4{\cdot}5H_2O$, 120 mg L^{-1} $ZnSO_4{\cdot}7H_2O$, 150 mg L^{-1} $CoCl_2{\cdot}6H_2O$, 150 mg L^{-1} H_3BO_3, 180 mg L^{-1} KI, and 10 g L^{-1} EDTA-2Na, and the chemical used was obtained from Sigma-Aldrich Chemical Co. Ltd and Aladdin Chemical Co. Ltd.

Appendix B Characterization Methods

Raman Spectrometer. Raman spectrometer (Renishaw, UK) was used to reveal the defective level and graphitization degree of the samples at 532 nm edge excitation. All the related deconvolution and calculation were conducted using the Origin2019 software.

Fourier Transform Infrared Spectroscopy (FTIR). The FTIR (PerkinElmer UATR Two) was adopted to investigate surface functional groups with the wavelength range of 400–4000 cm^{-1} after tabletting with KBr.

Elemental Analysis. Ultimate elemental analysis (EA, Vario EL cube, Germany) was implemented to estimate CHONS elemental content in the samples.

Textual Properties. Textural characteristics of the different Fe-biochar and pristine biochar were determined by using N_2 adsorption-desorption isotherms obtained from a surface area analyzer (Quantachrome Autosorb, USA) for Brunauer-Emmett-Teller (BET) surface area and Barrett-Joyner-Halenda (BJH) porosity analyses at 77 K.

Thermogravimetric Analysis. Weight loss associated with thermal pyrolysis of the Fe-biochar mixtures (BCX-Fe) was detected through thermogravimetry-derivative thermogravimetry analysis (TG/DTG). The thermal analysis started at 30 °C with a ramping rate of 10 °C min^{-1} to 900 °C in a N_2 environment to simulate the pyrolysis process.

Metal Content. The metal content on the biochar was characterized by ICP-OES or Atomic Absorption Spectrometry (AAS, Agilent 240 AA) analysis after total digestion with HNO_3.

Electron Paramagnetic Resonance (EPR). The EPR spectra were obtained using an EMX10/12 spectrometer (EMX10/12, Bruker, Germany). In the sample vials, 150 mM 5,5-

dimethyl-1-pyrroline-N-oxide (DMPO) was added as the spin-trapping agent into the solution with biochar (1 g L^{-1}) and air purging. Peak intensities of the DMPO–OH signals at 2 min were applied as indexes of the generated ROS.

X-ray Photoelectron Spectroscopy (XPS). An XPS (Thermo Scientific Nexsa) with Al Kα radiation was used to study the chemical state of oxygen on the sample surfaces. The binding energy of all the characteristic peaks was calibrated before devolution. Devolution of the XPS data was conducted using the CasaXPS software with the Gaussian-Lorentzian model, and the component peaks were identified by comparing their binding energies with the values reported in the literature. The C1s spectra were divided into aromatic carbon (C–C sp^2 284.4–284.6 eV), aliphatic carbon (C–C sp^3, 285.0–285.1 eV), hydroxyl (C–OH, 285.6–285.8 eV), epoxy (C–O–C, 286.7–286.9 eV), carbonyl (C=O, 288.0–288.1 eV), and carboxyl (O–C=O, 289.1–289.3 eV) (Kovtun et al., 2019, Wang et al., 2021b). The O1s spectra were divided into peaks of –C–OH (533.5eV), –C–OC (532.4–532.6 eV), –C=O (531.5–531.8 eV), –Fe–OC (530.8–531.2 eV), and Metal–O (~529.8 eV) (Arrigo et al., 2010, Qian et al., 2017, Xu et al., 2021e, Zhou et al., 2007). The ratio of the carbon-oxygen double bond and carbon-oxygen single bond was calculated based on **Eq.B–1**, where A represents the area ratio of different speciation. The Fe2p was divided into peaks of $2p_{3/2}$ orbitals of Fe^{2+} (711.0–712.0 eV), $2p_{3/2}$ orbitals of Fe^{3+} (712.5–713.5 eV), Fe satellite (715.7–720.0 eV), $2p_{1/2}$ orbitals of Fe^{2+} (724.1–725.6 eV), and $2p_{1/2}$ orbitals of Fe^{3+} (727.0–728.5 eV), respectively (Sun et al., 2019, Wu et al., 2012, Xu et al., 2016, Xu et al., 2020e, Xu et al., 2021e).

$$-\mathrm{C}=\mathrm{O}/_{-\mathrm{C}-\mathrm{O}}=\frac{A_{-\mathrm{C=O}}+A_{-\mathrm{Fe-OC}}}{A_{-\mathrm{C-OC}}+A_{-\mathrm{C-OH}}} \quad \textbf{Eq. B–1}$$

X-ray Diffraction Pattern (XRD). XRD (Rigaku SmartLab-9kW-advance) was used to examine crystal iron speciation on the Fe-biochar. The scanning rate was set at 10° min^{-1}, and the 2θ collection range was 10–80°. The MDI Jade 6.0 was employed to identify diffraction peaks and crystalline iron speciation based on the Joint Committee on Powder Diffraction Standards (JCPDS) database and Crystallography Open Database. The following mineral information from the database was used in this study: hematite (PDF33-0664, CIF9000139), magnetite (PDF19-0629, CIF1539747), wustite (PDF06-0615, CIF1011168), metal-iron (PDF06-0696, CIF1100108), iron chloride hydrate (PDF16-0123, CIF1532206), and calcium fluoride (PDF48-1298, CIF1000043). Quantitative X-ray diffraction (Q-XRD) with CaF_2 as a standard internal material was performed to evaluate the content of each crystal iron speciation in the Fe-biochar. A certain amount of CaF_2 (5–8 *wt.*%) was mixed with each Fe-biochar before the XRD analysis, and the scan speed was set at 5° min^{-1} with a scanning range of 10–60°. Amorphous-Fe content was calculated by the gap between total Fe content (detected by total digestion) and the sum of each crystal Fe mineral.

Morphology Analysis. A scanning electron microscopy (SEM, TESCAN VEGA3) and a transmission electron microscopy (TEM, FEI Talos F200X) equipped with the Oxford energy-dispersive X-ray spectroscopy (EDX) detector was conducted to study the morphology of iron minerals on the Fe-biochar. Selected area electron diffraction patterns (SAED) images were also acquired using an FEI Tecnai T-12 operated at 120 kV to evaluate the crystallinity of iron minerals on the Fe-biochar. The spherical aberration-corrected scanning transmission electron microscopy (AC-STEM, JEM-ARM200F) was also conducted to evaluate the morphology and speciation of formed minerals.

H_2-TPR analysis. The H_2-TPR experiments were performed on a Chemisorp TPx 290 instrument; the samples were degassed at 200 °C for three hours under an Ar atmosphere before the tests, and the reducing gas was 10% H_2/Ar (Li et al., 2021c).

Particle Size of Crystal Iron Minerals. The particle size of the different Fe-minerals was calculated by the Scherrer formulas (**Eq. B–2**) (Scherrer 1912). The baseline deduction and peak fitting were conducted by the MDI Jade 6.0 and Origin 2019. The particle size obtained from different facets was comparable, and thus the particle size calculated by the main characteristic peak was selected to represent the particle size of the iron minerals (**Table S3**).

$$L_{Fe} = \frac{k \times \lambda}{\beta \times \cos\theta} \qquad \textbf{Eq. B–2}$$

$$L_{ave} = \frac{\sum_{i=1}^{n} L_n \times M_n}{\sum_{i=1}^{n} M_n} \times 100\% \qquad \textbf{Eq. B–3}$$

where k was 0.89, and λ was 0.15406 nm, the wavelength of Cu Kα radiation. Besides, the β and θ were the half-peak width (FWHM) and diffraction angle of the corresponding diffraction peak, respectively. The average crystal particle size of the iron minerals was also calculated based on the proportion (M_n) and particle size (L_n) of each iron mineral in the Fe-biochar (**Eq. B–3**). It was worth mentioning that the crystalline size of amorphous-Fe was set as 0 nm during calculating the average crystal particle size.

L_a and L_c of Graphite Crystallite. Since the peaks of iron minerals and graphitic carbon might be overlapped, the Lorentz-Gaussian curve was used to fit the peaks of (002) and (100) crystal face with Origin 2019 after deducting the baseline to exclude the peaks of iron mineral. The obtained peak position and FWHM were used to calculate the graphite crystallite size L_a (in-plane coherence length) and L_c (perpendicular size of the turbostratically stacked crystallites) (Sun et al., 2018b, Wang et al., 2021b). The Warren formula was used to calculate L_a (**Eq. B–4**), and the Scherrer formula is used to calculate L_c (**Eq. B–5**) (Scherrer 1912, Wang et al., 2021b, Warren 1941).

$$L_a = \frac{1.84 \times \lambda}{\beta_1 \times \cos\theta_1} \qquad \textbf{Eq. B–4}$$

$$L_c = \frac{0.89 \times \lambda}{\beta_2 \times \cos\theta_2} \qquad \textbf{Eq. B–5}$$

where λ was the wavelength of Cu Kα radiation, and the β and θ were the FWHM and diffraction angle of the corresponding diffraction peak, respectively.

Quantitative X-ray diffraction (Q-XRD). Q-XRD with CaF_2 as an internal standard material was performed to evaluate the content of each crystal iron speciation in Fe-biochar. A certain amount of CaF_2 (5–8 *wt.*%) was mixed with each Fe-biochar before the XRD analysis, and the scan speed was set at 5° min^{-1} with a scanning range of 10–60 °. Rigaku's PDXL software was applied to analyze the quantitative X-ray diffraction (QXRD) using whole powder pattern fitting. Amorphous Fe content was calculated by the difference between the total Fe content and the sum of each crystal iron mineral content obtained by Q-XRD analysis.

Pure iron minerals, including maghemite (Fe_2O_3), magnetite (Fe_3O_4), and metal Fe were set as quality control to test the accuracy of the Q-XRD analysis for iron minerals. Five mass ratios of iron mineral to CaF_2 were set within 0.4–0.8 (*i.e.,* 40–80%) were set between iron mineral and (**Figure B1**), and the difference between the actual content and the calculated content was within 10% for Fe_3O_4 and Fe_2O_3 (**Figure B1d–e**). For metallic-Fe, a relatively higher gap (10–20%) was found (insert **Figure B1f**), which was possibly attributed to the surface oxidation of metallic-Fe with the formation of Fe_3O_4 as detected by Q-XRD (**Figure B1c**). Therefore, the metallic Fe content was re-calculated by adding the Fe amount in Fe_3O_4 to the calculated content. Then the difference between the actual and calculated content was lower than 10% (**Figure B1f**). Overall, these results proved that Q-XRD analysis could serve as a semi-quantitative method to detect crystal and amorphous Fe speciation.

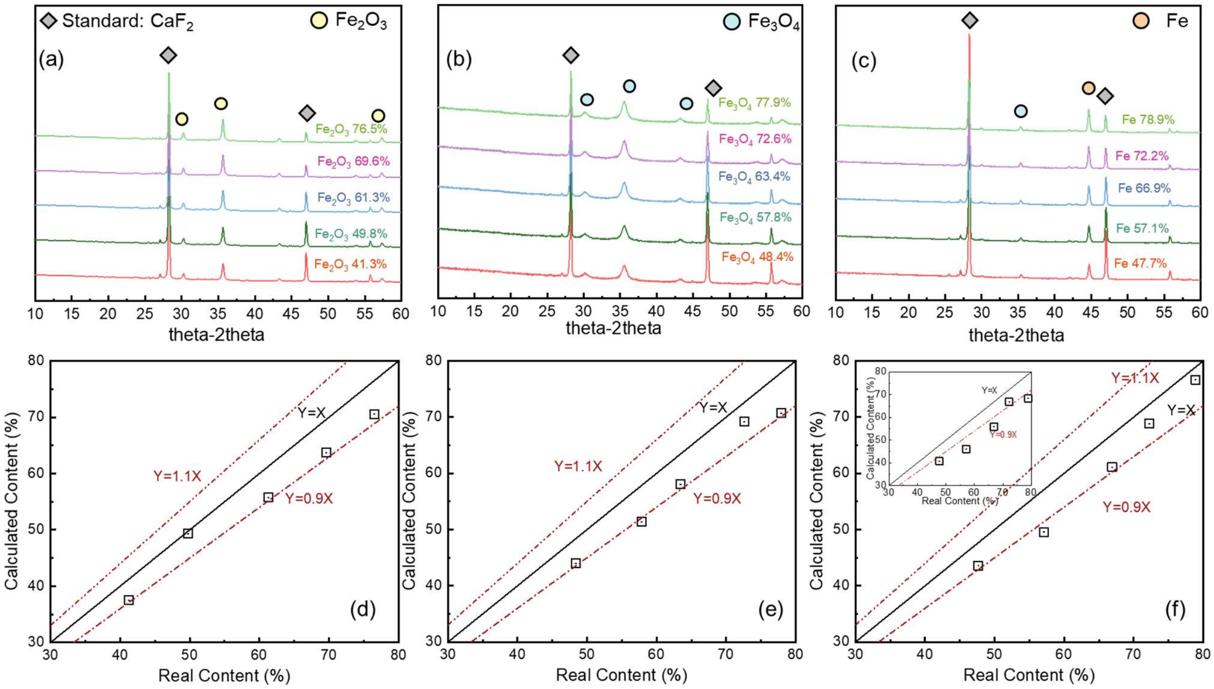

Figure B1 Q-XRD analysis of the typical iron minerals, including Fe_2O_3 (a), Fe_3O_4 (b), and Fe (c). Comparison of the actual Fe content and the calculated Fe content by Q-XRD analysis for Fe_2O_3 (d), Fe_3O_4 (e), and Fe after correcting the oxidized Fe amount (f) (insert f is the comparison using the un-corrected Fe content)

Zeta Potential. The Zeta potential was determined by TR-DLS (Malvern Zetasizer Nano ZS90, Malvern, Worcestershire, UK) under different pH.

Fe Extraction. Different extraction methods were also conducted in triplicate to analyze the iron speciation of each Fe-biochars, including (1) *Soluble Fe*, also considered as exchangeable Fe or release Fe(Poulton and Canfield 2005), which was directly extracted by mixing 2 g L^{-1} Fe-biochar with 20 mM NaCl for 48 h (in accordance with the reaction time of the As immobilization experiment); (2) *Reducible Fe* was extracted by a mixed reagent of 1 M hydroxylamine–HCl solution in 25% (*v/v*) acetic acid (Poulton and Canfield 2005, Slotznick et al., 2018). A mass of ~100 mg samples was mixed with 10 mL hydroxylamine–HCl solution, and this mixture was then shaken for 48 hours to complete the extraction; and (3) *Extractable Fe* was determined using a mixed solution (pH = 3.2) of 0.2 M ammonium oxalate and 0.17 M oxalic acid solution (Slotznick et al., 2018). The strong chelating capacity of oxalic acid could provide extraction of labile iron minerals (Hammond et al., 2020, Yu et al., 2021). An aliquot of 100 mg sample was added into 10 mL mixed solution, and the extraction process was conducted without light for 6 h at 200 rpm. The extracted Fe concentrations from different extraction methods were all determined by AAS. The Fe(II) content in the soluble Fe was also determined photo-metrically using the UV-Vis at 510 nm wavelength (Luan et al., 2012, Xu et al., 2019c) after complexation with phenanthroline.

Depth-profiling XPS analysis. The distribution of As and Fe in different depths below the surface of the selected Fe-biochar samples was examined by XPS with an argon gun (1 eV) for depth profiling. The XPS depth profile spectra were collected using an argon ion gun (1000 eV energy, 1.00 mm raster size). These conditions lead to a sputter rate of 0.34 nm s^{-1} for Ta_2O_5. The diameter of the analyzed area was 200 × 200 μm, and the average atomic concentration of the tested elements *(i.e.,* Fe, As, C, O) was presented. Sputtering under a vacuum may result in the reduction of Fe(III) and Fe(II), according to previous studies (Lewin et al., 2009, Xu et al., 2016). However, this process might be negligible in this study since no Fe(0) was found within a 100 nm depth of the materials. Deconvolution methods were similar to the normal XPS analysis mentioned before. The Fe2p was divided into $2p_{3/2}$ orbitals of Fe^0 (707.0–708.0 eV), Fe^{2+} (711.0–712.0 eV), $2p_{3/2}$ orbitals of Fe^{3+} (712.5–713.5 eV), Fe satellite (715.7–720.0 eV), $2p_{1/2}$ orbitals of Fe^0 (720.0–721.0 eV), Fe^{2+} (724.1–725.6 eV), and $2p_{1/2}$ orbitals of Fe^{3+} (727.0–728.5 eV), respectively (Sun et al., 2019, Wu et al., 2012, Xu et al., 2016, Xu et al., 2020e, Xu et al., 2021e). The As 3d spectra were divided into As(V) (45.2–45.8eV), As(III) (44.0–44.8 eV), and As(0) (40.0–42.0eV), respectively (Liao et al., 2021, Ramos et al., 2009, Xi et al., 2019, Zhang et al., 2016b). Mn 2p spectra can be divided into Mn(II) (~641.5 eV), Mn(III) (~643 eV), and Mn(IV) (~644.1 eV) (Xu et al., 2021e), respectively. The average valence state of Mn was also calculated based on the proportion.

Appendix C

Table C1. The proportion of Cr(VI)/Cr(III) and As(V)/As(III) on the Fe-biochar surface after the redox-related immobilization process

Fe- biochar	Cr-Anoxic (%)		As-Anoxic (%)		Cr-Oxic (%)		As-Oxic (%)	
	Cr(VI)	Cr(III)	As(V)	As(III)	Cr(VI)	Cr(III)	As(V)	As(III)
BC400	83.6	16.4	N.D.	N.D.	84.1	15.9	N.D.	N.D.
BC550	84.9	15.1	N.D.	N.D.	86.9	13.1	N.D.	N.D.
BC700	82.6	17.4	N.D.	N.D.	82.8	17.2	N.D.	N.D.
BC850	82.5	17.5	N.D.	N.D.	84.9	15.2	N.D.	N.D.
BC400-Fe-400	84.1	15.9	92.6	7.4	83.2	16.8	96.5	3.5
BC550-Fe-400	83.9	16.1	88.1	11.9	83.5	16.6	100.0	0
BC700-Fe-400	81.2	18.8	79.4	20.6	85.9	14.1	91.3	8.7
BC850-Fe-400	80.4	19.6	86.3	13.8	86.4	13.6	99.1	0.9
BC400-Fe-850	78.1	22.0	85.7	14.3	73.7	26.4	95.9	4.1
BC550-Fe-850	77.9	22.1	95.1	4.9	84.8	15.2	100.0	0
BC700-Fe-850	75.9	24.1	95.6	4.4	85.4	14.6	93.8	6.2
BC850-Fe-850	82.2	17.9	100.0	0	85.3	14.7	100.0	0

Table C2. Basic physicochemical properties of the pristine biochar and Fe-biochar.

Fe-biochar	Yield (%)	Element content (%) [a]				H/C [b]	O/C [b]	Ash (*wt.* %)	Total Fe content (mg g^{-1})[c]
		C	H	N	O				
BC400	37.1 [d]	70.5	4.8	0.8	22.4	0.81	0.24	1.5	N.D.[f]
BC550	26.4 [d]	77.3	3.2	1.0	15.9	0.49	0.15	2.6	N.D.[f]
BC700	23.8 [d]	83.8	1.9	0.9	10.1	0.27	0.09	3.3	N.D.[f]
BC850	21.4 [d]	85.6	1.2	0.9	8.4	0.16	0.07	4.0	N.D.[f]
BC400-Fe	/	64.4	3.8	0.8	21.5	0.70	0.25	9.5	57.3
BC550-Fe	/	68.6	2.9	0.9	18.1	0.50	0.20	9.6	58.2
BC700-Fe	/	70.4	1.6	0.7	15.9	0.27	0.17	11.3	62.3
BC850-Fe	/	71.0	1.0	0.7	15.1	0.17	0.16	12.2	66.2
BC400-Fe-400	74.2 [e]	63.8	3.2	0.8	17.3	0.60	0.20	15.0	74.6
BC550-Fe-400	74.3 [e]	67.0	2.4	0.8	14.0	0.43	0.16	15.8	76.9
BC700-Fe-400	83.5 [e]	68.8	1.0	0.6	13.4	0.17	0.15	16.1	76.7
BC850-Fe-400	87.3 [e]	69.3	0.8	1.2	13.2	0.14	0.14	15.5	81.4
BC400-Fe-850	70.8 [e]	66.5	0.9	1.3	14.8	0.16	0.17	16.5	90.0
BC550-Fe-850	72.2 [e]	66.7	0.9	1.3	15.2	0.16	0.17	15.8	86.9
BC700-Fe-850	76.2 [e]	66.7	0.9	1.7	15.5	0.17	0.17	15.2	85.0
BC850-Fe-850	80.3 [e]	66.5	0.9	1.4	15.5	0.15	0.17	15.8	84.6

[a] mass content; [b] atomic ratio; [c] detected by total digestion; [d] yield of the first-step pyrolysis; [e] yield of second-step pyrolysis; [f] Not detectable

Table C3. The particle size of different iron minerals in the Fe-biochar.

Fe-biochar	Characteristic Peaks												Average size (nm)
BCX-Fe	(3 0 -1)Akaganeite			(2 1 -1) Akaganeite [a]			(2 1 -5) Akaganeite						
	2θ (°)	FWHM	L_{Fe} (nm)	2θ (°)	FWHM	L_{Fe} (nm)	2θ (°)	FWHM	L_{Fe} (nm)				
X=400		N.D.			N.D.			N.D.					0
X=550	26.66	0.66	13.30	35.12	0.52	18.47	55.82	0.80	17.46				1.38
X=700	26.72	0.38	23.27	35.16	0.57	16.95	55.86	0.88	17.07				5.34
X=850	36.88	0.82	10.75	35.18	0.52	18.38	55.86	0.67	21.02				5.05
BCX-Fe-400	(0 0 1) $FeCl_2$ [a]			(-2 0 1) $FeCl_2$			(0 1 2) Fe_2O_3			(1 1 0) Fe_2O_3 [a]			
	2θ (°)	FWHM	L_{Fe} (nm)	2θ (°)	FWHM	L_{Fe} (nm)	2θ (°)	FWHM	L_{Fe} (nm)	2θ (°)	FWHM	L_{Fe} (nm)	
X=400	16.20	0.42	19.39	22.46	0.34	24.86		N.D.			N.D.		2.95
X=550	16.50	0.66	12.49	22.34	0.33	25.74		N.D.			N.D.		4.45
X=700	16.12	0.56	14.68	22.34	0.32	26.63	24.02	0.60	14.38	35.62	0.42	22.85	8.95
X=850		N.D.			N.D.		24.22	0.38	22.73	35.70	0.38	25.80	6.18
BCX-Fe-850	(2 2 0) Fe_3O_4			(3 1 1) Fe_3O_4 [a]			(2 0 0) FeO			(1 1 0) Fe			
	2θ (°)	FWHM	L_{Fe} (nm)	2θ (°)	FWHM	L_{Fe} (nm)	2θ (°)	FWHM	L_{Fe} (nm)	2θ (°)	FWHM	L_{Fe} (nm)	
X=400	30.18	0.29	31.77	35.44	0.29	33.02	41.78	0.40	26.08	44.76	0.39	28.59	30.35
X=550	30.08	0.23	40.17	35.40	0.29	33.70	41.68	0.38	27.68	44.76	0.40	27.45	30.41
X=700	30.04	0.25	36.59	35.40	0.30	31.91	41.68	0.32	32.46		N.D.		28.71
X=850	30.06	0.28	32.07	35.42	0.31	31.40	41.76	0.32	33.12		N.D.		27.72

[a] Only the prominent characteristic peaks of akaganeite, $FeCl_2$, Fe_3O_4, and Fe_2O_3 was used to represent the mineral size of specific minerals

Table C4. Peak position, FWHM, and size of graphitic carbon in the Fe-biochar.

Fe- biochar	Peak position (2 Theta)		FWHM		L_c (nm)	L_a (nm)
	(002)	(100)	(002)	(100)		
BC400-Fe	20.61	N.D.	12.34	N.D.	0.68	N.D. [a]
BC550-Fe	24.36	N.D.	9.24	N.D.	0.93	N.D.
BC700-Fe	24.20	44.26	7.97	4.86	1.08	4.66
BC850-Fe	24.82	43.61	7.86	4.58	1.10	4.89
BC400-Fe-400	21.44	N.D.	13.66	N.D.	0.62	N.D.
BC550-Fe-400	22.31	N.D.	10.74	N.D.	0.79	N.D.
BC700-Fe-400	24.21	44.20	7.95	4.56	1.08	4.97
BC850-Fe-400	23.15	43.95	8.31	4.56	1.03	4.95
BC400-Fe-850	23.85	43.65	7.46	3.98	1.15	5.64
BC550-Fe-850	23.77	43.91	7.44	4.25	1.15	5.31
BC700-Fe-850	23.48	44.60	7.48	4.32	1.15	5.28
BC850-Fe-850	23.73	43.55	7.62	4.23	1.13	5.30

[a] peaks of La was not detected based on the XRD pattern.

Table C5. Pore distribution of the different Fe-biochar.

Fe- biochar	Pore volume (cm^3 g^{-1})				Pore proportion (%)			
	Micro <2 nm	Small-meso 2-10 nm	Large-meso 10-50 nm	Macro >50 nm	Micro <2 nm	Small-meso 2-10 nm	Large-meso 10-50 nm	Macro >50 nm
BC400	0.0000	0.0007	0.0002	0.0016	0.0	27.5	8.3	64.2
BC400-Fe	0.0002	0.0013	0.0014	0.0043	3.7	18.2	19.0	59.2
BC400-Fe-400	0.0001	0.0029	0.0028	0.0059	0.9	24.6	24.3	50.2
BC400-Fe-850	0.0021	0.0118	0.0009	0.0030	12.1	66.0	5.2	16.7
BC550	0.0000	0.0002	0.0006	0.0025	2.2	6.7	18.5	72.6
BC550-Fe	0.0002	0.0013	0.0035	0.0030	2.5	15.6	44.2	37.7
BC550-Fe-400	0.0001	0.0022	0.0052	0.0067	0.9	15.1	36.8	47.1
BC550-Fe-850	0.0021	0.0119	0.0013	0.0030	11.5	65.1	7.0	16.4
BC700	0.0013	0.0198	0.0047	0.0052	4.3	63.8	15.0	16.8
BC700-Fe	0.0000	0.0009	0.0029	0.0029	0.6	13.3	43.4	42.8
BC700-Fe-400	0.0000	0.0013	0.0037	0.0063	0.1	11.7	32.5	55.7
BC700-Fe-850	0.0028	0.0153	0.0012	0.0031	12.3	68.2	5.5	14.0
BC850	0.0031	0.0752	0.0564	0.0067	2.2	53.2	39.8	4.8
BC850-Fe	0.0000	0.0040	0.0057	0.0079	0.0	22.9	32.3	44.8
BC850-Fe-400	0.0002	0.0040	0.0056	0.0044	1.4	28.4	39.4	30.8
BC850-Fe-850	0.0031	0.0333	0.0143	0.0048	5.6	60.0	27.8	8.7

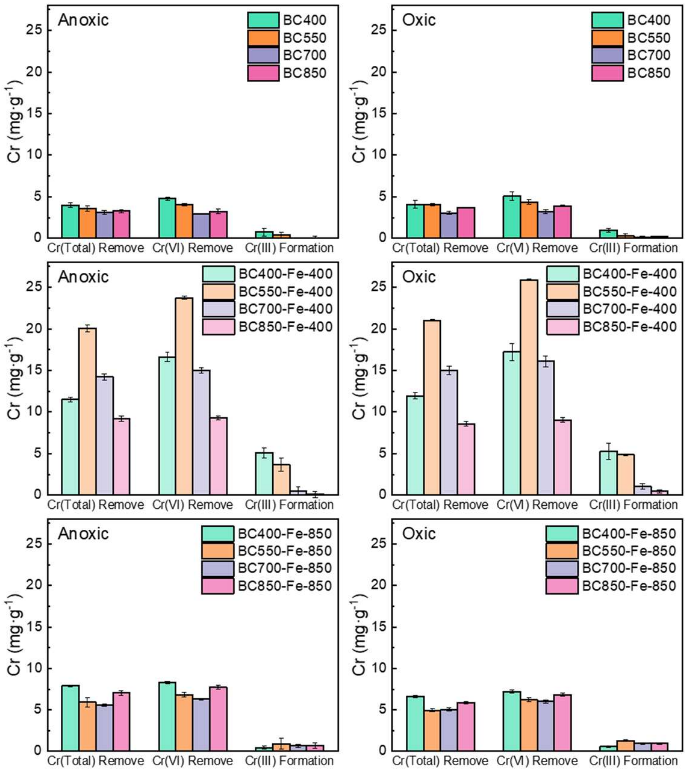

Figure C1. Cr(Total) removal, Cr(VI) removal, and Cr(III) formation amount of the different Fe-biochar or pristine biochar under the oxic or anoxic environment.

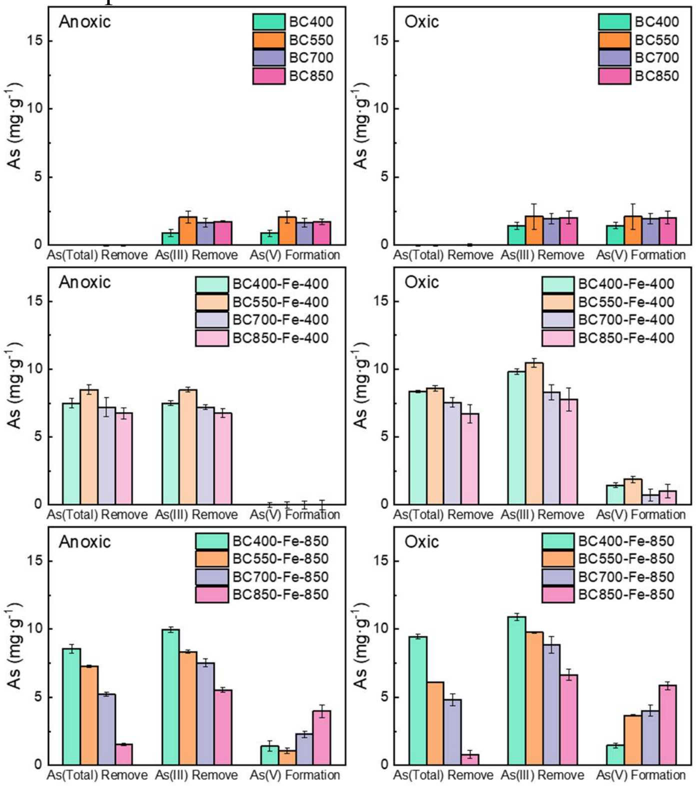

Figure C2. As(Total) removal, As(III) removal, and As(V) formation amount of the different Fe-biochar or pristine biochar under the oxic or anoxic environment.

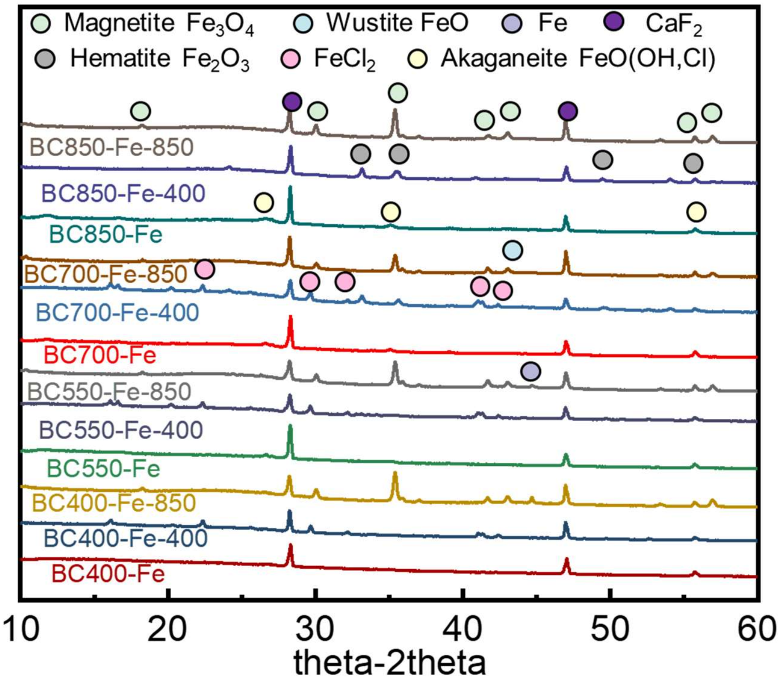

Figure C3. Q-XRD patterns of the different Fe-biochar with the addition of CaF_2 as the standard.

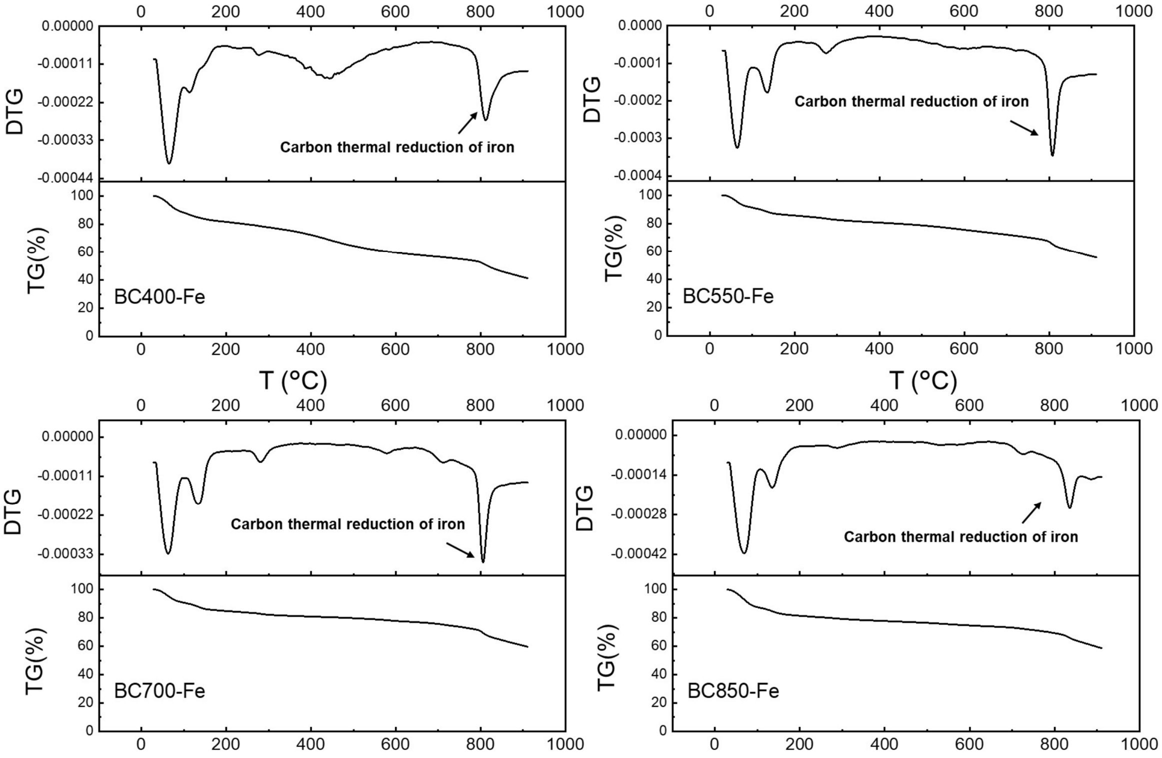

Figure C4. TG-DTG analysis of the different Fe-biochar.

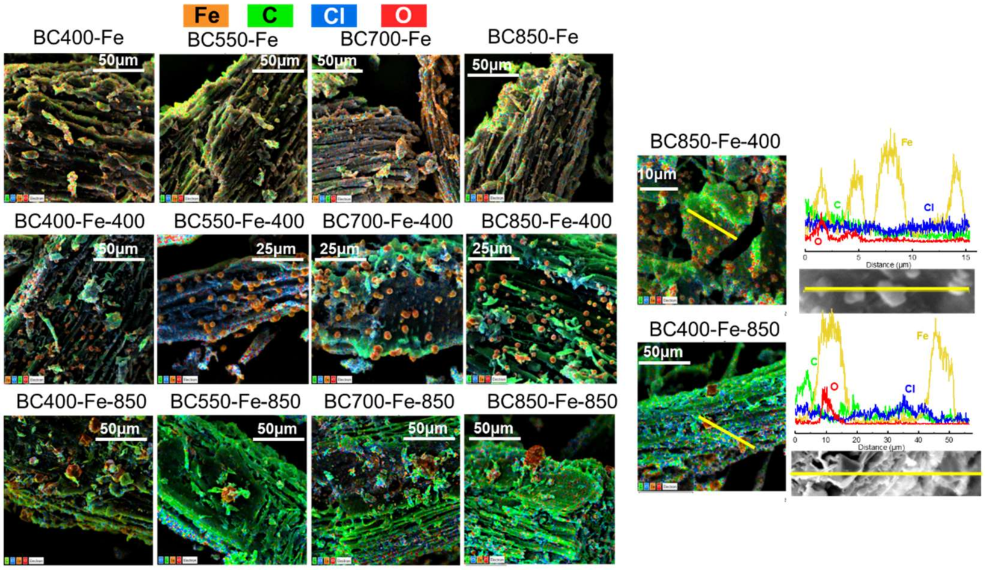

Figure C5. SEM-EDX images of all the Fe-biochar (BCX-Fe, BCX-Fe-400, and BCX-Fe-850) (right) and line scanning of element content on the Fe-biochar (left).

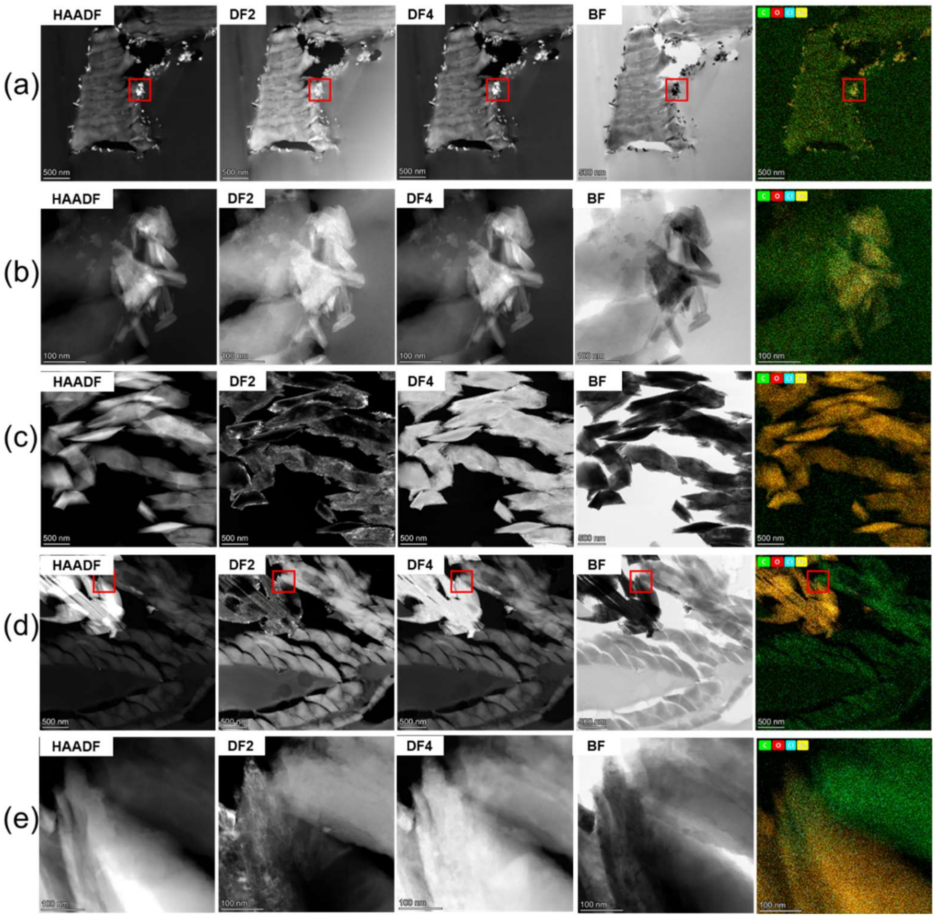

Figure C6. TEM-EDX images of the BC400-Fe-400 (**a–b**) and BC400-Fe-850 (**c–e**). b and e were the high magnification images of the marked area in a and d

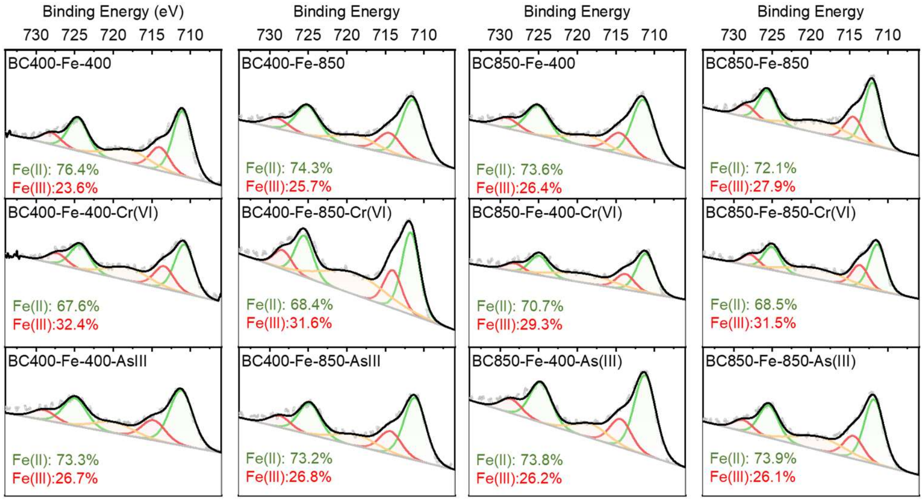

Figure C7. Fe2p XPS spectra of the different Fe-biochar or pristine biochar before and after pollutants removal.

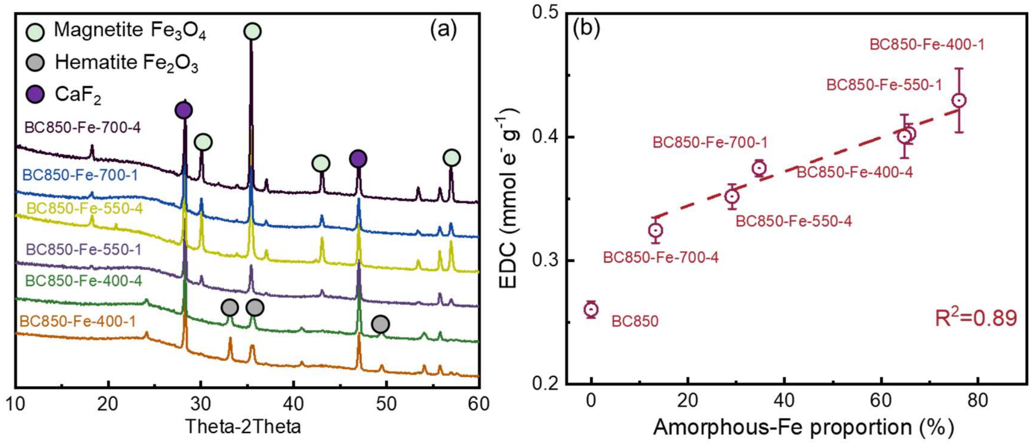

Figure C8. Q-XRD analysis of the Fe-biochar with different amorphous-Fe content (a); Relationship between the amorphous-Fe proportion and EDC of these Fe-biochar (b).

A series of Fe-biochar was designed to exclude the possible effect from the aliphatic composition of the biochar. The BC850-Fe was pyrolyzed at 400−700 °C with a keeping time of 1 or 4 h. These Fe-biochar were named BC850-Fe-X-Y, where X was the pyrolysis temperature, and Y was the keeping time. Only the amorphous-Fe content in the Fe-biochar might be altered with limited valence transformation. EDC of these Fe-biochar was detected and compared with the proportion of amorphous-Fe obtained from the Q-XRD analysis. A positive linear relationship ($R^2 = 0.89$) between the EDC and amorphous Fe proportion can be found, evidencing the importance of amorphous ferrous minerals for EDC of the Fe-biochar.

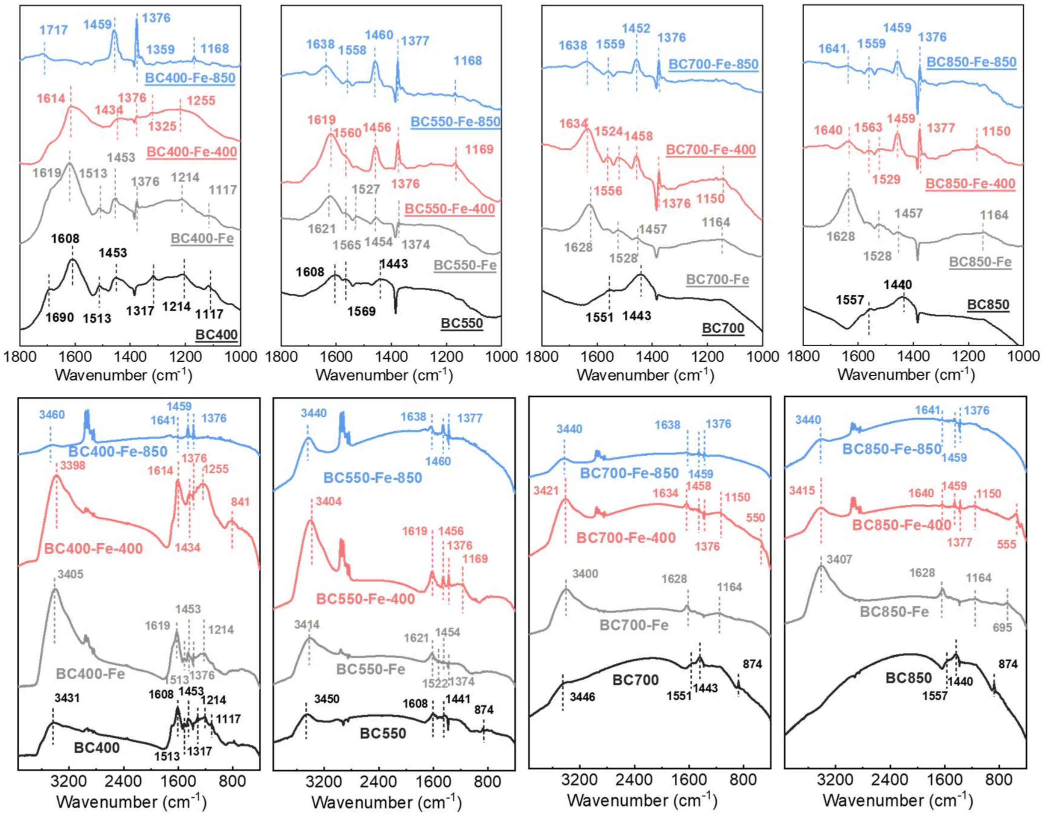

Figure C9. FTIR patterns of the different Fe-biochar with a wavelength of 1000−1800 cm^{-1} (up part) and 400−4000 cm^{-1} (down part)

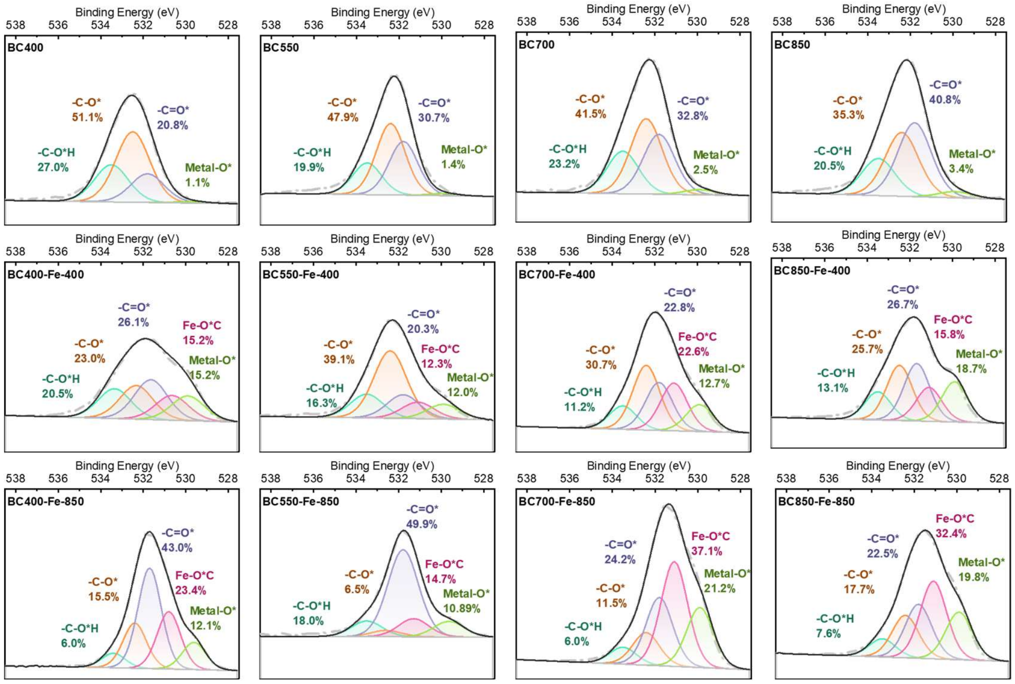

Figure C10. O1s XPS spectra of the different Fe-biochar or pristine biochar.

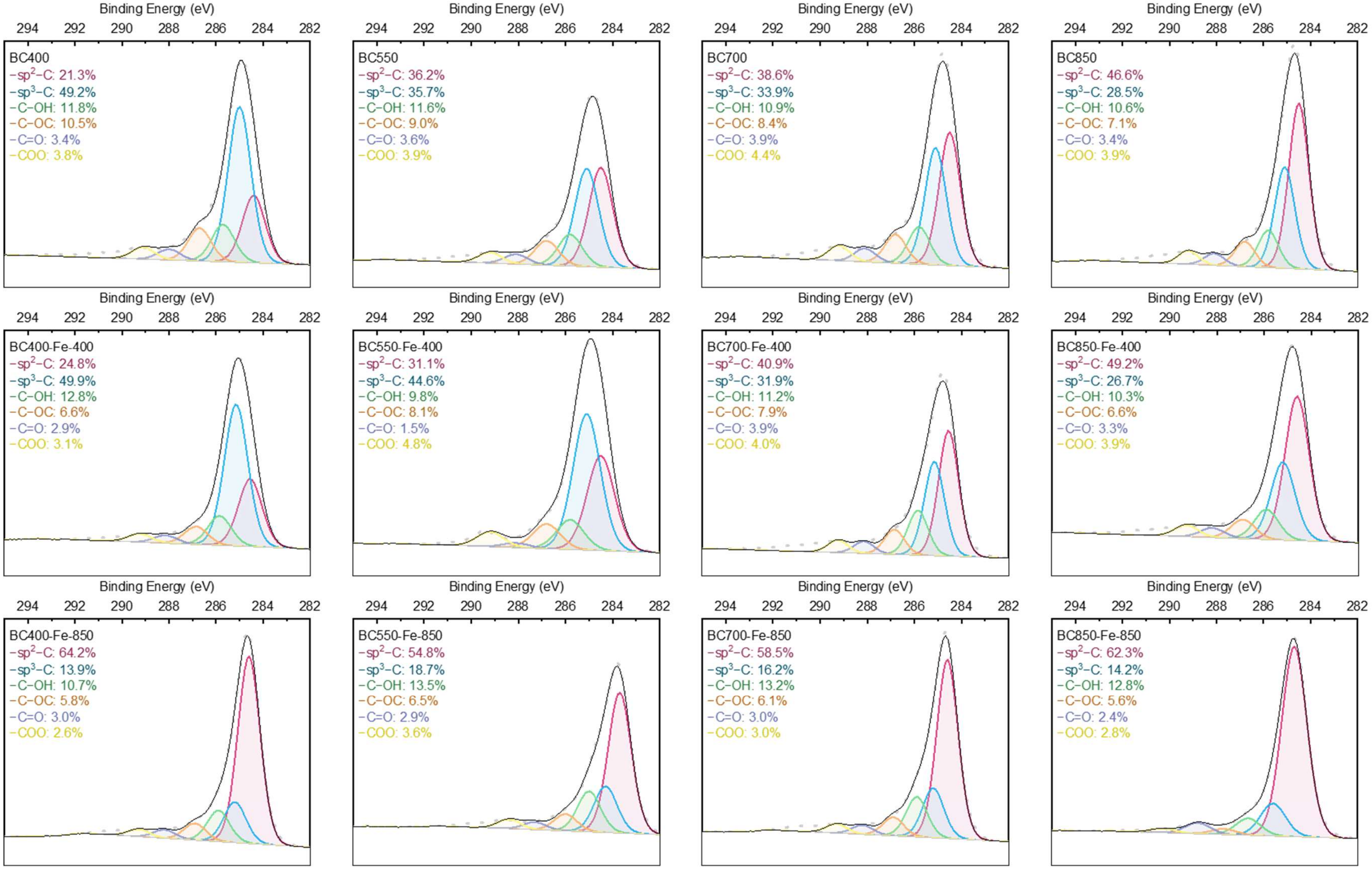

Figure C11. C1s XPS spectra of the different Fe-biochar or pristine biochar.

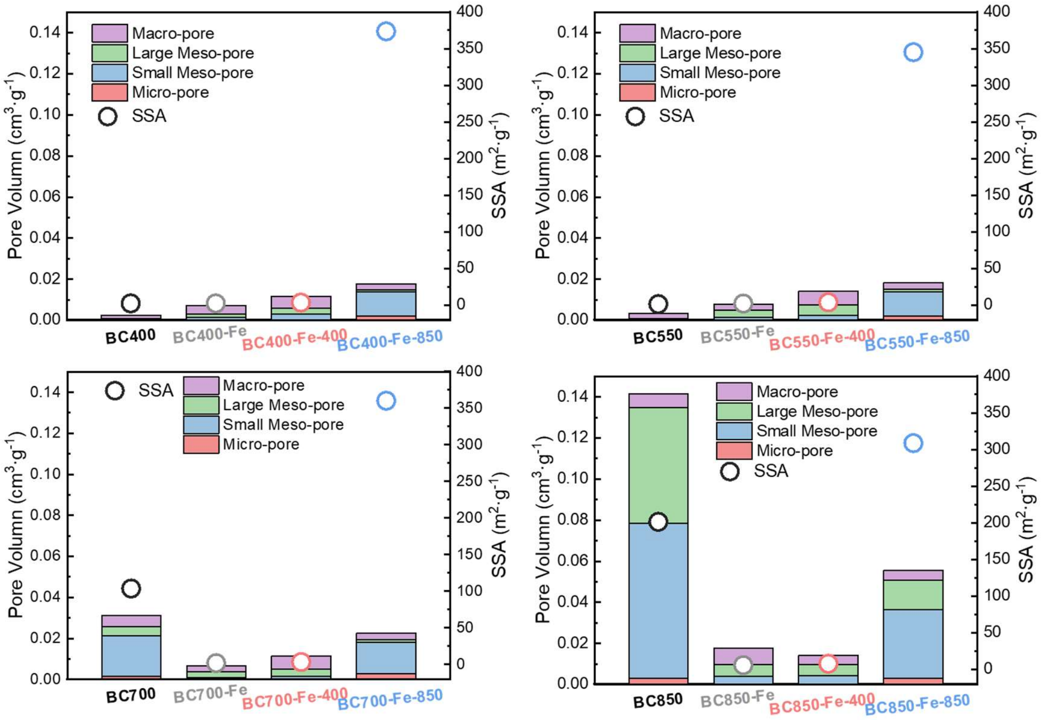

Figure C12. Specific surface area (SSA) and pore volume (PV) of the different Fe-biochar.

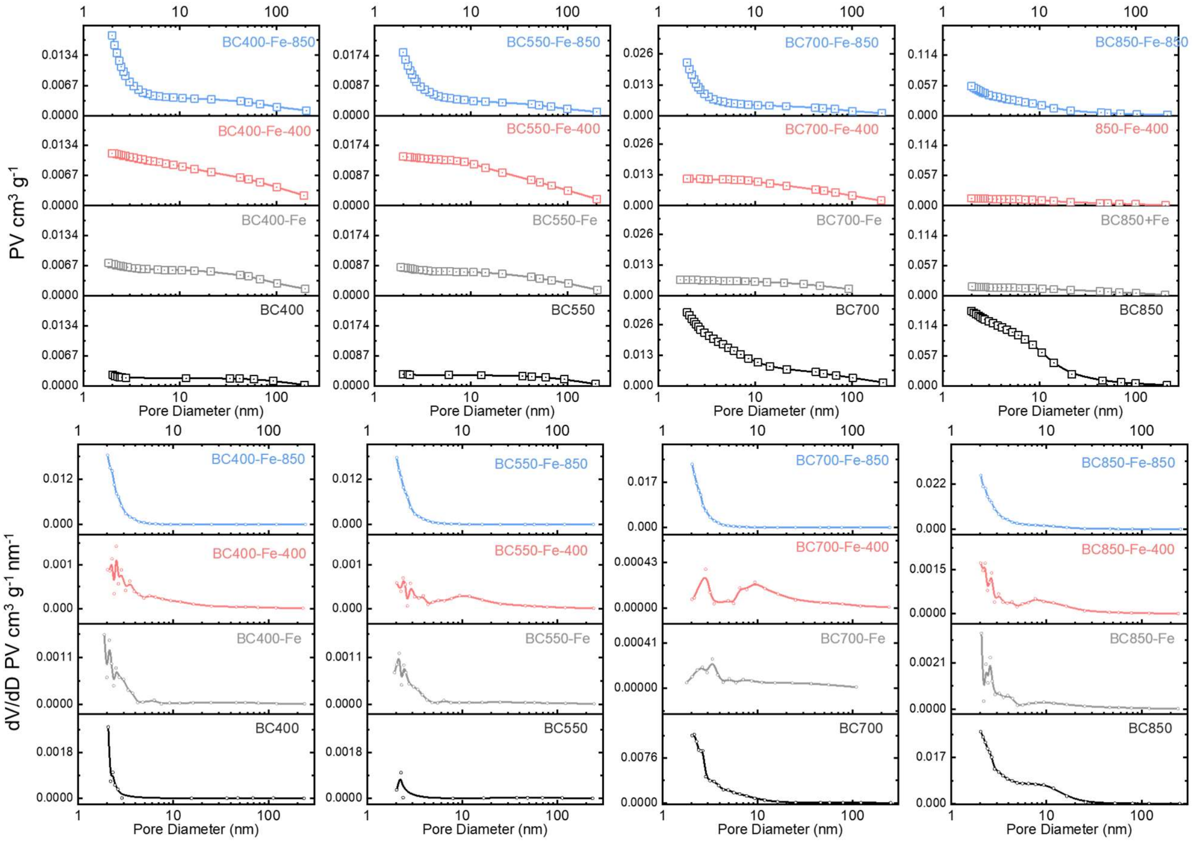

Figure C13. The pore distribution of the different Fe-biochar.

Appendix D

Pearson Correlation Analysis for Fe-speciation and As Removal Performance. To enlarge the database of the As removal performance by different Fe-biochar with designed Fe-speciation, several Fe-biochars were designed as follows:

(i) The BC400-Fe and BC850-Fe were pyrolyzed at 850 °C with a longer keeping time of 4 h, which offered a more reducing environment and a complete formation of reductive Fe (Sun et al., 2019). The obtained Fe-biochars were named as BC400-Fe-850-4 and BC850-Fe-850-4, respectively;

(ii) The BC400-Fe and BC850-Fe were also pyrolyzed at 400 °C for 4 h to thoroughly transform amorphous-Fe to crystal-Fe. These two composites were denoted as BC400-Fe-400-4 and BC850-Fe-400-4, respectively;

(iii) The BC400-Fe, BC550-Fe, and BC700-Fe also undergo the second pyrolysis at 400 °C for 1 h. A varied amount of amorphous-Fe content with limited iron reduction would be formed due to the different carbon speciation. These Fe-biochars were named as BC400-Fe-400-1, BC550-Fe-400-1, and BC700-Fe-400-1 (or BC400-Fe-400, BC550-Fe-400, and BC700-Fe-400 in short);

(iv) The $FeCl_3$-pretreated biomass was directly pyrolyzed at 400, 550, 700, and 850 °C, respectively, for 1 h with a ramping rate of 10 °C min^{-1}. The mass ratio between biomass and Fe was set as 30:1 to ensure a similar Fe content (~10% *wt.*%) in the produced Fe-biochars. Briefly, 60 g of biomass was added into 200 mL $FeCl_3$ solution with the iron concentration of 10 g L^{-1}. This mixture was stirred for 24 h at 200 rpm, dried at 60 °C for over 72 h, crushed to pass a 120-mesh sieve, and stored in a dry container before the second pyrolysis. The produced Fe-biochars were named as BCFe-400-1, BCFe-550-1, BCFe-700-1, and BCFe-850-1 (or BCFe-400, BCFe-550, BCFe-700, and BCFe-850 in short).

Basic properties, including the Raman spectrum and element content, were determined. Fe-speciation of these 11 Fe-biochars was conducted carefully by Q-XRD and different extraction methods (see **Appendix B**). Removal capacities of these Fe-biochars for both As(V) and As(III) were also conducted with the same procedure, as shown in section **4.2.3**. The basic properties and removal performance used for the PCC analysis were summarized in **Figure D14, D18-D19**, and **Table D5-D6**.

The quantized linear dependences between any two variables were calculated by the PCC with the **Eq. D-1**(Zhu et al., 2019b, Zhu et al., 2021):

$$r = \frac{\sum_{i=1}^{n}(x_i-\bar{x})\sum_{i=1}^{n}(y_i-\bar{y})}{\sqrt{\sum_{i=1}^{n}(x_i-\bar{x})^2}\sqrt{\sum_{i=1}^{n}(y_i-\bar{y})^2}} \qquad \textbf{(Eq. D-1)}$$

where $\bar{x}$ or $\bar{y}$ indicated the mean value of variable x or y.

The significant level test (*t*) of PCC was available with **Eq. D2**, while the *p*-value was acquired through two-tailed *t* distribution with N-2 degrees of freedom.

$$t = \frac{r\sqrt{N-2}}{\sqrt{1-r^2}} \qquad \textbf{(Eq. D-2)}$$

where *N* was the number of samples and *r* was the Pearson correlation coefficient. All these statistical analyses were realized in Origin 2019.

Two databases were used to evaluate the Pearson correlation coefficient of As removal capacities and Fe speciation based on the distinct mechanisms. The first one included the BC400-Fe-850-1, BC550-Fe-850-1, BC700-Fe-850-1, BC850-Fe-850-1, BC400-Fe-850-4, BC850-Fe-850-4, and BCFe-850-1, because they contained various reductive-Fe content and similar mild pH. Besides, they mainly immobilized As by reductive Fe (e.g., ZVI) through redox reaction. The second database consisted of BC850-Fe-700-1, BC850-Fe-550-1, BC850-Fe-400-1, BC850-Fe-400-4, BC400-Fe-400-1, BC550-Fe-400-1, BC700-Fe-400-1, BC400-Fe-400-4, and BCFe-400-1. All these Fe-biochars contained high amorphous-Fe content with acidic pH. The released Fe content under low pH conditions might be the key moiety for the As immobilization.

Table D1. Basic physicochemical properties of the Fe-biochars

Fe-biochar	Element content (%) [a]				H/C [b]	O/C [b]	A_d/A_g	pH	Ash (*wt.* %)	SSA[c] ($m^2\ g^{-1}$)	Pore Volume ($cm^3\ g^{-1}$)	Total Fe content ($mg\ g^{-1}$)
	C	H	N	O								
BC400-Fe-850	66.5	0.88	1.29	14.8	0.16	0.17	2.38	7.5±0.1	16.5	373	0.018	90.0
BC550-Fe-850	66.7	0.90	1.33	15.2	0.16	0.17	2.36	7.3	15.8	345	0.018	86.9±0.1
BC700-Fe-850	66.7	0.92	1.74	15.5	0.17	0.17	2.35	7.4±0.1	15.2	360	0.022	85.0±0.2
BC850-Fe-850	66.5	0.85	1.42	15.5	0.15	0.17	2.31	7.3±0.2	15.8	308	0.056	84.6±1.4
BC850-Fe-700	67.5	0.80	1.64	14.5	0.14	0.16	2.30	3.1	15.6	10.7	0.017	83.3±0.6
BC850-Fe-550	67.9	0.78	1.82	13.7	0.14	0.15	2.30	3.1	15.8	10.2	0.020	81.5±0.9
BC850-Fe-400	69.3	0.78	1.21	13.2	0.14	0.14	2.31	2.9	15.5	7.83	0.014	81.4±0.8

[a] Mass proportion; [b] Atomic ratio; [c] specific surface area obtained from Brunauer-Emmett-Teller (BET) methods

Table D2 Iron speciation of the different Fe-biochars based on the Q-XRD analysis and Fe-different extraction methods

Fe-biochar	Q-XRD analysis (mg g^{-1})[a]					Fe-extraction methods (mg g^{-1})			
	Fe_3O_4	FeO	Fe	Fe_2O_3	Amorphous-Fe	Reducible Fe	Extractable Fe	Soluble Fe	Soluble Fe(II)
BC400-Fe-850	63.1	12.9	10.9	N.D.	3.1	67.8±1.5	89.9±5.1	N.D.	N.D.
BC550-Fe-850	62.5	16.3	3.1	N.D.	5.0	55.1±5.2	77.7±6.7	N.D.	N.D.
BC700-Fe-850	67.7	8.6	N.D.	N.D.	8.7	43.9±2.9	30.0±0.3	N.D.	N.D.
BC850-Fe-850	67.7	7.2	N.D.	N.D.	10.3	38.4±2.6	18.4±3.4	N.D.	N.D.
BC850-Fe-700	54.4	N.D.	N.D.	N.D.	28.9	12.6±0.7	4.0±0.1	0.8±0.1	0.4±0.1
BC850-Fe-550	28.0	N.D.	N.D.	N.D.	53.5	12.0±0.2	4.1±0.1	1.9±0.1	0.6±0.1
BC850-Fe-400	N.D.	N.D.	N.D.	19.5	61.9	14.7±0.4	14.8±0.6	7.4±0.8	4.2±0.9

[a] XRD pattern for the Q-XRD analysis could be found in **Figure D2**

Table D3. Comparison of the As removal capacities with published references.

Fe-biochar	Fe content (*wt.* %)	Fe speciation	As(V) removal (mg g^{-1})	As(III) removal (mg g^{-1})	Reference
ZVI-biochar complexes	55.7–59.6	Zero-valent-iron	7.9–15.6		(Bakshi et al., 2018)
Fe-impregnated biochar	6.1	Maghemite & hematite	6.8		(He et al., 2018)
Magnetic biochar	3.0	Hematite	0.4		(Wang et al., 2015b)
Iron oxide biochar	8.6	Akaganeite	8.1	6.0	(Wei et al., 2019)
magnetic biochar	2.7–8.0[a]	Magnetite & Fe_3C	8.9–13.1		(Cho et al., 2017)
bark-based magnetic iron oxide	> 50	Magnetite		13.7	(Dhoble et al., 2018)
Fe-Biochar composite	0.3–3.0[a]	Magnetite & Zero-valent-iron	5.6–7.5		(Yoon et al., 2020)
nZVI-sludge biochar	> 0.2	Fe, FeO, & Magnetite	11.3		(Liu et al., 2021b)
Magnetic biochar	10.4–14.8	Magnetite		6.1–7.0	(Wang et al., 2021d)
ZVI/biochar	10.5	Zero-valent-iron & maghemite	9.2–26.7		(Wang et al., 2017b)
Magnetic biochar	8.3–12.8	Magnetite	1.3–3.1	1.6–2.0	(Baig et al., 2014)
Reductive-Fe biochar	8.5–9.0	Fe, FeO, & Magnetite	0.3–4.3	1.2–7.7	This study
Amorphous-Fe biochar	8.1–8.3	Amorphous-Fe, hematite, & magnetite	1.7–11.0	3.0–7.7	This study

[a] Determined by the EDX results from SEM-EDX

Arsenic removal capacities of Fe-biochar with different speciation, including metallic iron (Fe(0)), FeO, magnetite (Fe_3O_4), hematite (Fe_2O_3), maghemite (Fe_2O_3), and akaganeite (FeOOH), were collected from literature. The removal capacities for both As(V) and As(III) in most literature (0.4–13.1 mg g^{-1}) were similar to this study (0.4–11.0 mg g^{-1}), while higher removal capacities (*i.e.,* 15.6–26.7 mg g^{-1}) might be attributed to the higher iron content (55.7–59.6 %), especially for the Fe speciation with high reactivity (*i.e.,* Fe(0)).

Table D4. Pearson correlation coefficient analysis of the pyrolysis condition, Fe speciation, and basic physicochemical properties of the Fe-biochars (in total 18 samples) (**$p < 0.01$, *$p < 0.05$)

	1st temperature	2nd temperature	Keeping time	Fe_3O_4	FeO	Fe	Fe_2O_3	$FeCl_2$	Amorphous-Fe	Reducible Fe	Extractable Fe	Soluble-Fe	Soluble-Fe(II)	H/C	O/C	A_d/A_g	pH
1st temperature	1	0.00	0.19	-0.27	0.24	0.05	0.39	0.02	0.13	-0.03	0.06	0.08	0.04	-0.51*	-0.37	0.56*	-0.12
2nd temperature	0.00	1	0	0.77**	0.70**	0.43	-0.49*	-0.45	-0.94**	0.66**	0.33	-0.63**	-0.58	-0.54*	-0.28	0.61**	0.94**
Keeping time	0.19	0.00	1	-0.36	0.37	0.62**	0.18	-0.16	0.00	0.30	-0.06	-0.11	-0.10	-0.21	-0.67**	0.31	0.03
Fe_3O_4	-0.27	0.77**	-0.36	1	0.17	-0.13	-0.49*	-0.43	-0.78**	0.21	0.10	-0.58*	-0.53*	-0.38	0.10	0.31	0.71**
FeO	0.24	0.70**	0.37	0.17	1	0.69**	-0.28	-0.25	-0.64**	0.79**	0.54*	-0.36	-0.33	-0.37	-0.46	0.55*	0.73**
Fe	0.05	0.43	0.62**	-0.13	0.69**	1	-0.17	-0.16	-0.43	0.80**	0.26	-0.23	-0.20	-0.25	-0.67**	0.36	0.43
Fe_2O_3	0.39	-0.49*	0.18	-0.49*	-0.28	-0.17	1	-0.01	0.39	-0.35	-0.14	0.16	0.04	-0.30	-0.25	0.13	-0.42
$FeCl_2$	0.02	-0.45	-0.16	-0.43	-0.25	-0.46	-0.01	1	0.35	0.06	0.25	0.93**	0.96**	0.52*	0.13	-0.49*	-0.40
Amorphous-Fe	0.13	-0.94**	0.00	-0.78**	-0.64**	-0.43	0.39	0.35	1	-0.72**	-0.36	0.54*	0.49*	0.52*	0.36	-0.49*	-0.92**
Reducible-Fe	-0.03	0.66**	0.30	0.21	0.79**	0.80**	-0.35	0.06	-0.72**	1	0.63**	-0.10	-0.05	-0.26	-0.52*	0.34	0.73**
Extractable-Fe	0.06	0.33	-0.06	0.10	0.54*	0.26	-0.14	0.25	-0.36	0.63**	1	0.17	0.20	-0.08	-0.02	0.28	0.44
Soluble-Fe	0.08	-0.63**	-0.11	-0.58*	-0.36	-0.23	0.16	0.93**	0.54*	-0.10	0.17	1	0.99**	0.55*	0.15	-0.52*	-0.57*
Soluble-Fe(II)	0.03	-0.58*	-0.10	-0.53*	-0.33	-0.20	0.04	0.96**	0.49*	-0.05	0.20	0.99**	1	0.59*	0.17	-0.54*	-0.51*
H/C	-0.51*	-0.54*	-0.21	-0.38	-0.37	-0.25	-0.30	0.52*	0.52*	-0.26	-0.08	0.55*	0.59*	1	0.65**	-0.85**	-0.44
O/C	-0.37	-0.28	-0.67**	0.10	-0.46	-0.67**	-0.25	0.13	0.36	-0.52*	-0.02	0.15	0.17	0.65**	1	-0.54*	-0.23
A_d/A_g	0.56*	0.61**	0.31	0.31	0.55*	0.36	0.13	-0.49*	-0.49*	0.34	0.28	-0.52*	-0.54*	-0.85**	-0.54*	1	0.53*
pH	-0.12	0.94**	0.03	0.71**	0.73**	0.43	-0.42	-0.40	-0.92**	0.73**	0.44	-0.57*	-0.51*	-0.44	-0.23	0.53*	1

Table D5. Basic physicochemical properties of the Fe-biochar prepared under different pyrolytic conditions.

Fe-biochar	Element content (%)[a]				H/C [b]	O/C [b]	A_d/A_g [c]	pH	Ash content (*wt.* %)	Total Fe content (mg g^{-1})
	C	H	N	O						
BC400-Fe-850-4	70.5	0.82	0.74	9.25	0.14	0.10	2.38	7.2±0.2	18.7	99.6±3.2
BC850-Fe-850-4	71.5	0.86	0.70	8.36	0.14	0.09	2.32	6.8	18.6	86.9±0.8
BC400-Fe-400-4	67.8	1.81	0.85	14.0	0.32	0.15	2.17	2.9	15.5	80.7±1.7
BC850-Fe-400-4	70.4	0.66	0.61	12.2	0.11	0.13	2.36	2.9	16.2	83.1±1.4
BC400-Fe-400-1	63.8	3.18	0.75	17.3	0.60	0.20	2.02	2.8	15.0	74.6±0.6
BC550-Fe-400-1	67.0	2.40	0.78	14.0	0.43	0.16	2.05	2.9	15.8	76.9±0.7
BC700-Fe-400-1	68.8	0.99	0.64	13.4	0.17	0.15	2.12	2.8	16.1	76.7±0.4
BCFe-400-1	64.3	2.87	0.62	19.2	0.54	0.22	2.00	3.1	13.0	69.6±0.4
BCFe-550-1	67.5	2.13	0.60	15.1	0.38	0.17	2.01	4.2	14.7	72.4±3.4
BCFe-700-1	68.0	1.27	0.49	14.9	0.22	0.16	2.07	6.1	15.4	84.3±5.0
BCFe-850-1	68.9	0.91	0.56	13.0	0.16	0.14	2.30	6.8±0.1	16.6	86.0±0.3

[a] Mass proportion; [b] Atomic ratio; [c] Raman spectrum could be found in **Figure D17**

Table D6. Iron speciation of other Fe-biochar based on Q-XRD analysis and different Fe-extraction methods

Fe-biochar	Q-XRD analysis (mg g^{-1})[a]						Fe-extraction methods (mg g^{-1})			
	Fe_3O_4	FeO	Fe	Fe_2O_3	$FeCl_2 \cdot 4H_2O$	Amorphous-Fe	Reducible Fe	Extractable Fe	Released Fe	Released Fe(II)
BC400-Fe-850-4	10.8	24.6	61.5	N.D.	N.D.	2.7	103.0±3.6	46.2±4.5	N.D.	N.D.
BC850-Fe-850-4	14.6	28.6	35.3	N.D.	N.D.	8.3	77.6±2.9	20.4±0.4	N.D.	N.D.
BC400-Fe-400-4	17.0	N.D.	N.D.	N.D.	2.5	61.2	17.5±1.2	18.1±1.2	12.0±0.1	11.0±0.2
BC850-Fe-400-4	N.D.	N.D.	N.D.	29.3	N.D.	53.8	6.2±0.8	7.5±0.1	2.7±0.2	1.0±0.1
BC400-Fe-400-1	N.D.	N.D.	N.D.	N.D.	11.3	63.3	24.6±3.0	30.3±0.4	23.8±0.6	22.1±0.8
BC550-Fe-400-1	N.D.	N.D.	N.D.	N.D.	27.3	49.5	52.1±0.5	49.9±0.3	34.2±0.4	32.4±0.1
700-Fe-400-1	N.D.	N.D.	N.D.	25.4	7.2	44.1	28.6±1.9	32.2±1.2	17.7±0.4	12.8±0.2
BCFe-400-1	N.D.	N.D.	N.D.	N.D.	N.D.	69.6	2.5±0.6	1.2±0.1	0.6	0.2±0.1
BCFe-550-1	51.3	N.D.	N.D.	N.D.	N.D.	21.1	25.0±2.1	9.1	N.D.	N.D.
BCFe-700-1	73.1	N.D.	N.D.	N.D.	N.D.	11.2	45.6±0.4	5.1±1.5	N.D.	N.D.
BCFe-850-1	87.4	N.D.	N.D.	N.D.	N.D.	N.D.	32.7±2.4	5.3±0.1	N.D.	N.D.

[a]: XRD pattern for the Q-XRD analysis could be found in **Figure D18**

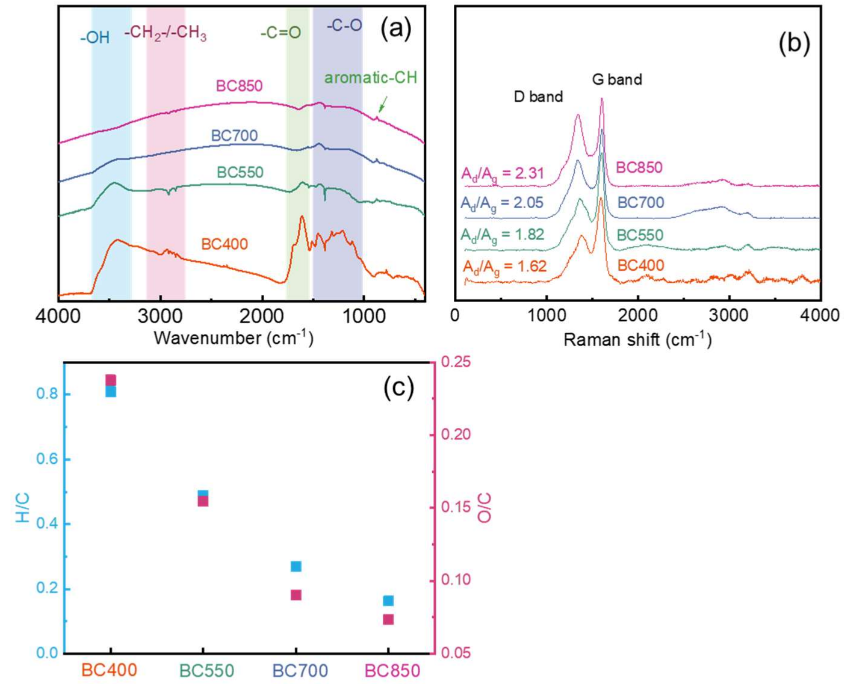

Figure D1. The FTIR spectra (a), Raman spectra (b), and element ratio (c) of the pristine biochars (BC400, BC550, BC700, and BC850).

With the increasing pyrolysis temperature, biochar undergoes dehydration, the disruption of organic components, and subsequent aromatization (Ai et al., 2020, Keiluweit et al., 2010, Xiao et al., 2018b). Different carbon phases such as (1) transition phase with the preserved character (<400 °C); (2) Amorphous phase with cracked molecules and aliphatic carbon (~450–550 °C); (3) Composite phase with the poorly ordered graphene stacks (~600–700 °C); and (4) Crystal phase (>700 °C) will be formed with the increasing pyrolysis temperature (Keiluweit et al., 2010). BC400 contained abundant surface O-functionality including –OH (~3400 cm^{-1}), –C=O (1600–1700 cm^{-1}), and –C–O (1000–1400 cm^{-1}), while relative lower O-functionality was found on BC550 with the appearance of aromatic C–H (~875 cm^{-1}) (Chen et al., 2015b, Fang et al., 2014, Xu et al., 2019a). Limit amounts of functional groups were found when the temperature reached 700 °C (*i.e.,* BC700 and BC850). Increasing A_d/A_g ratio from 1.62 to 2.31 with rising pyrolysis temperature also confirmed the formation of disordered graphitic crystallites at high temperatures (McDonald-Wharry et al., 2013, Wan et al., 2019). The decreased O/C ratio and H/C ratio further confirmed aromatization with the deoxygenating and dehydration of O-moieties with the increasing pyrolysis temperatures (Keiluweit et al., 2010, Xiao and Chen 2017b, Zhao et al., 2018a).

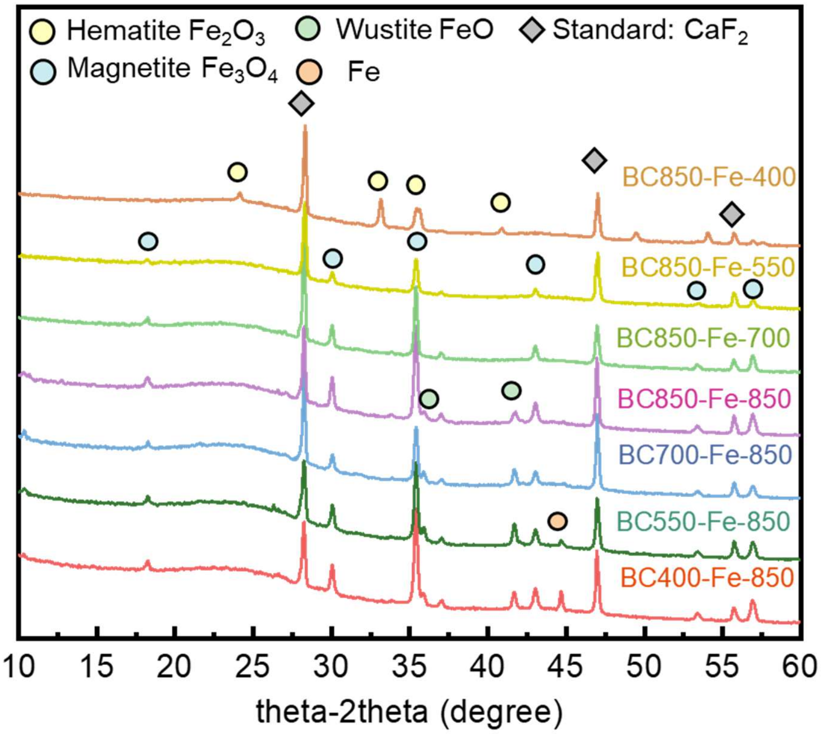

Figure D2. Q-XRD patterns of the different Fe-biochar with the addition of standard CaF_2.

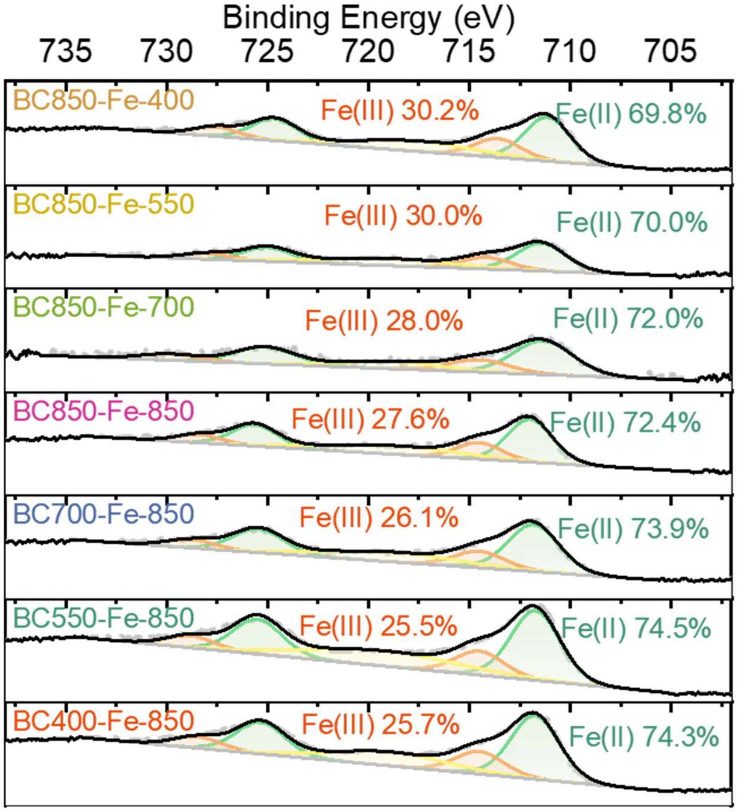

Figure D3. XPS spectra of Fe2p binding state in the different Fe-biochars.

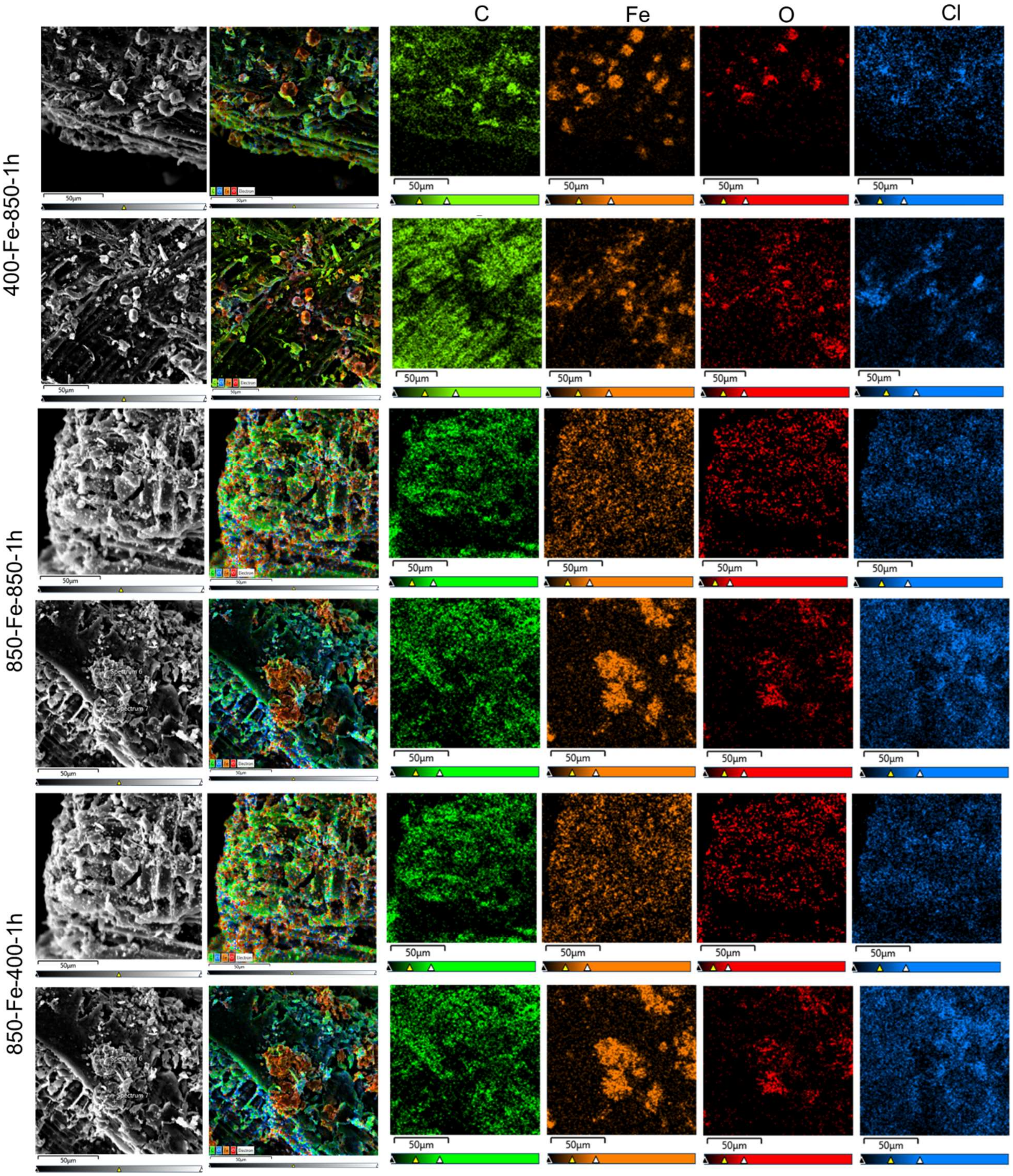

Figure D4. SEM images with EDX elemental (C, Fe, O, and Cl) distribution of the BC400-Fe-850 (up two), BC850-Fe-850 (middle two), and BC850-Fe-400 (down two).

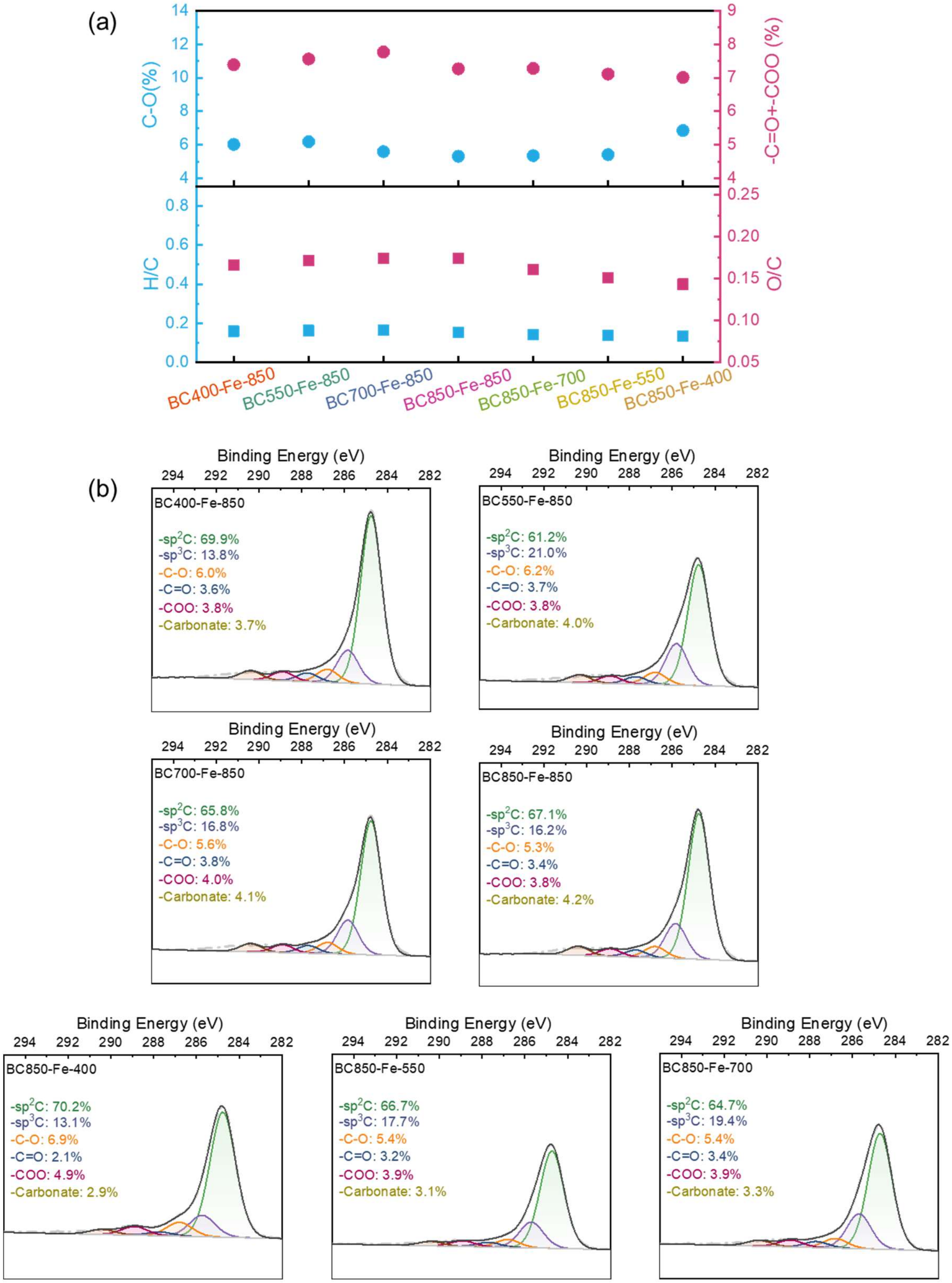

Figure D5. Elemental ratio and proportion of O-moieties of the different Fe-biochars (a); XPS deconvolution analysis of C1s binding state in the different Fe-biochars (b).

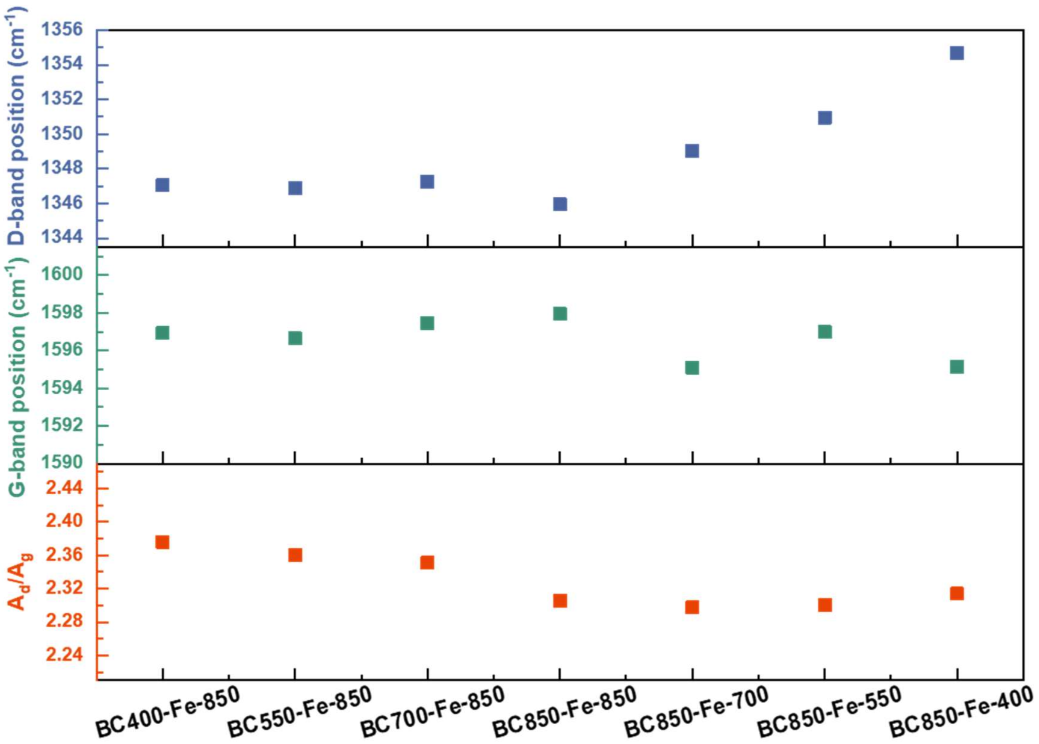

Figure D6. Raman results of the D-band position, G-band position, and A_d/A_g ratio for different Fe-biochars.

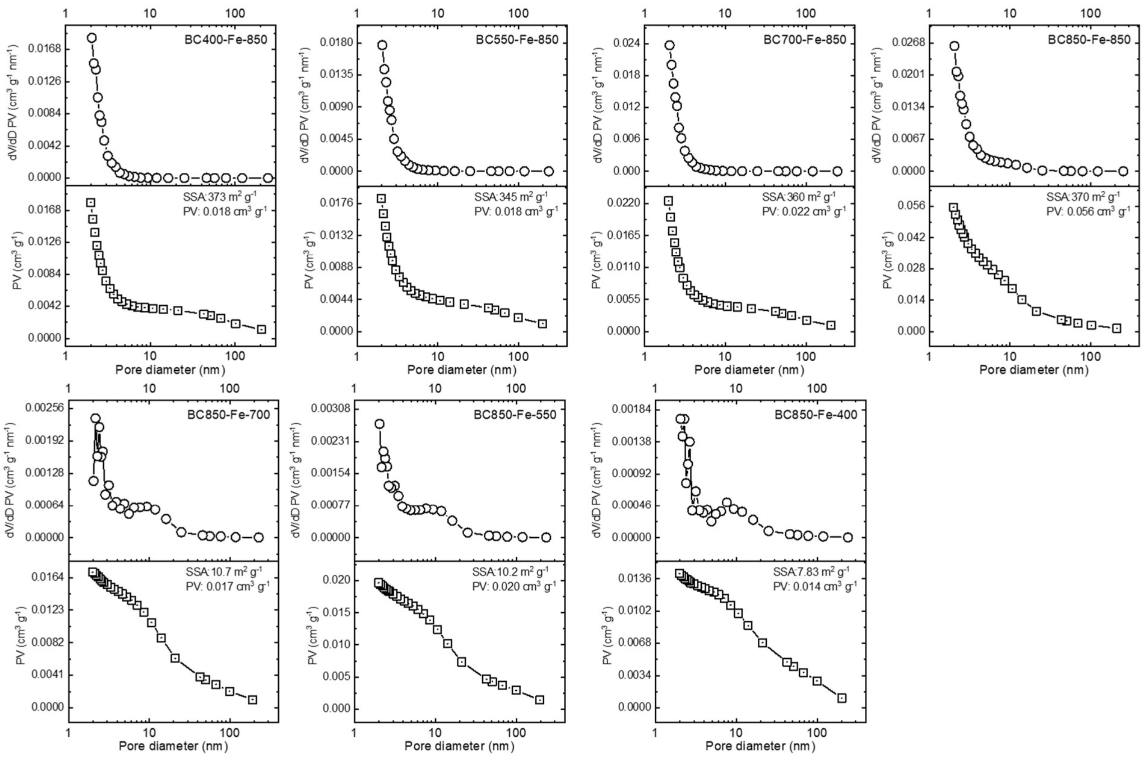

Figure D7. Pore distribution of different Fe-biochars. (SSA: specific surface area; PV: pore volume)

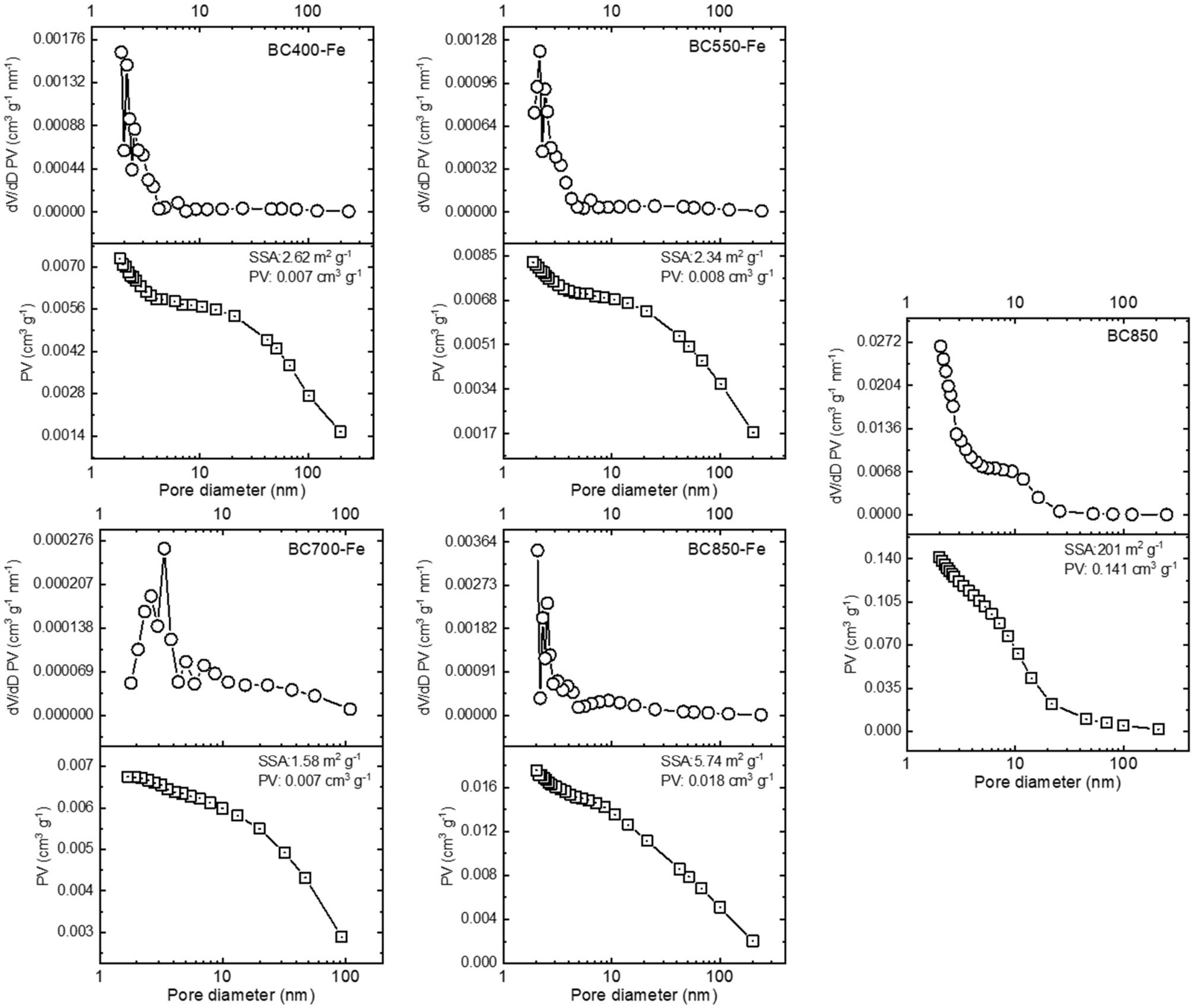

Figure D8. Pore distribution of Fe-biochar composites before pyrolysis (BC400/550/700/850-Fe) and BC850 substrate.

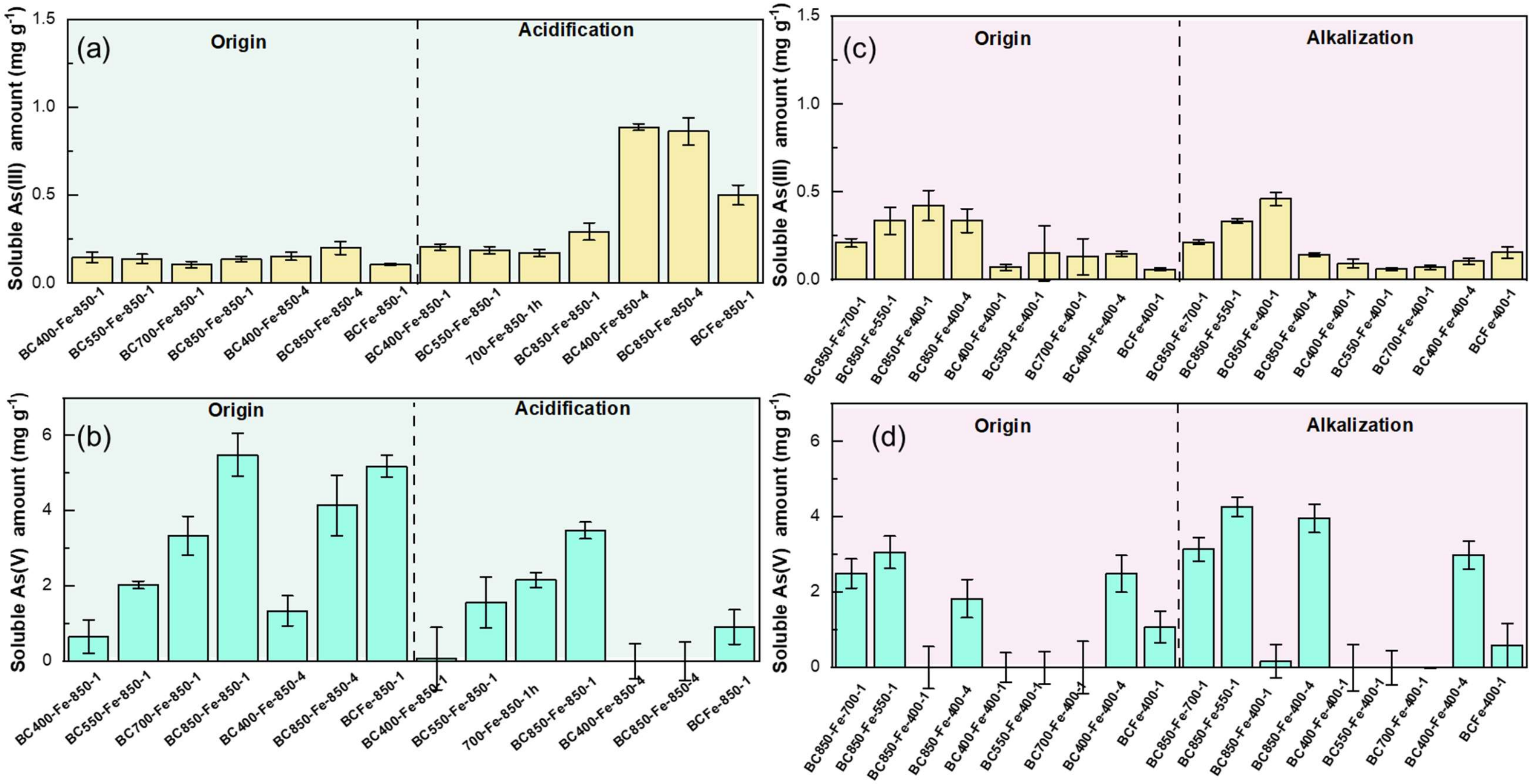

Figure D9. Amount of As(III) formation after As(V) removal (a&c) and the amount of As(V) formation after As(III) removal (b&d) by the different Fe-biochars.

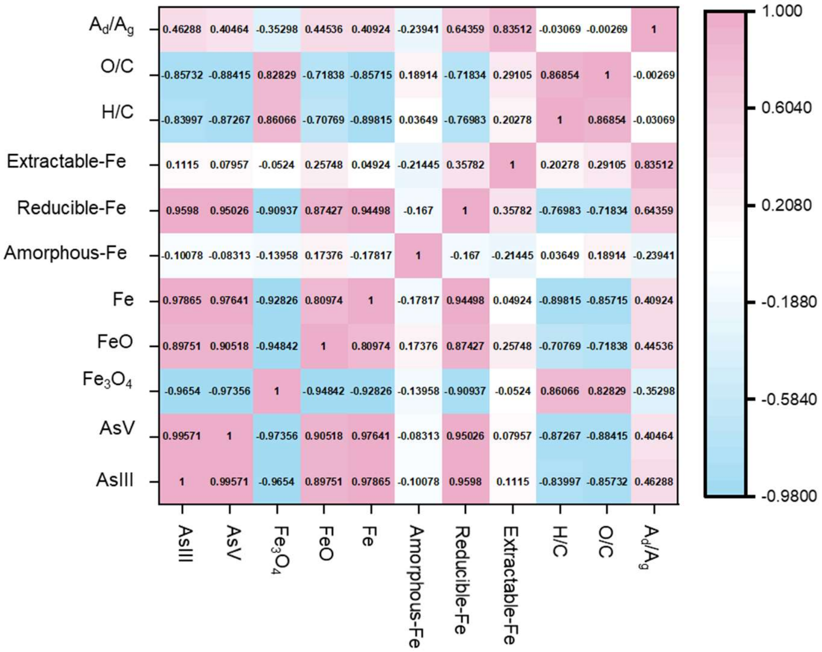

	AsIII	AsV	Fe_3O_4	FeO	Fe	Amorphous-Fe	Reducible-Fe	Extractable-Fe	H/C	O/C	A_d/A_g
A_d/A_g	0.46288	0.40464	-0.35298	0.44536	0.40924	-0.23941	0.64359	0.83512	-0.03069	-0.00269	1
O/C	-0.85732	-0.88415	0.82829	-0.71838	-0.85715	0.18914	-0.71834	0.29105	0.86854	1	-0.00269
H/C	-0.83997	-0.87267	0.86066	-0.70769	-0.89815	0.03649	-0.76983	0.20278	1	0.86854	-0.03069
Extractable-Fe	0.1115	0.07957	-0.0524	0.25748	0.04924	-0.21445	0.35782	1	0.20278	0.29105	0.83512
Reducible-Fe	0.9598	0.95026	-0.90937	0.87427	0.94498	-0.167	1	0.35782	-0.76983	-0.71834	0.64359
Amorphous-Fe	-0.10078	-0.08313	-0.13958	0.17376	-0.17817	1	-0.167	-0.21445	0.03649	0.18914	-0.23941
Fe	0.97865	0.97641	-0.92826	0.80974	1	-0.17817	0.94498	0.04924	-0.89815	-0.85715	0.40924
FeO	0.89751	0.90518	-0.94842	1	0.80974	0.17376	0.87427	0.25748	-0.70769	-0.71838	0.44536
Fe_3O_4	-0.9654	-0.97356	1	-0.94842	-0.92826	-0.13958	-0.90937	-0.0524	0.86066	0.82829	-0.35298
AsV	0.99571	1	-0.97356	0.90518	0.97641	-0.08313	0.95026	0.07957	-0.87267	-0.88415	0.40464
AsIII	1	0.99571	-0.9654	0.89751	0.97865	-0.10078	0.9598	0.1115	-0.83997	-0.85732	0.46288

Figure D10. Pearson correlation matrix of the As removal capacities, Fe speciation, and basic physicochemical properties of Fe-biochars produced at high second pyrolysis temperature (850 °C) with rich reductive-Fe content and mild-pH.

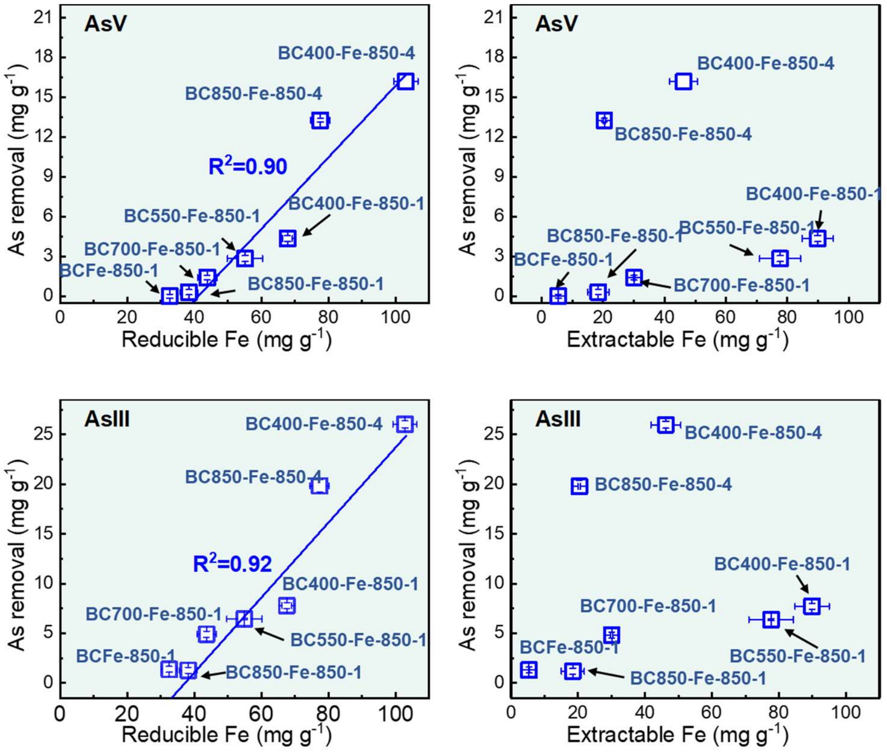

Figure D11. Linear relationship between Fe-speciation detected by different extraction methods and As removal capacities of Fe-biochars produced at high second pyrolysis temperature (850 °C) with rich reductive-Fe content and mild-pH.

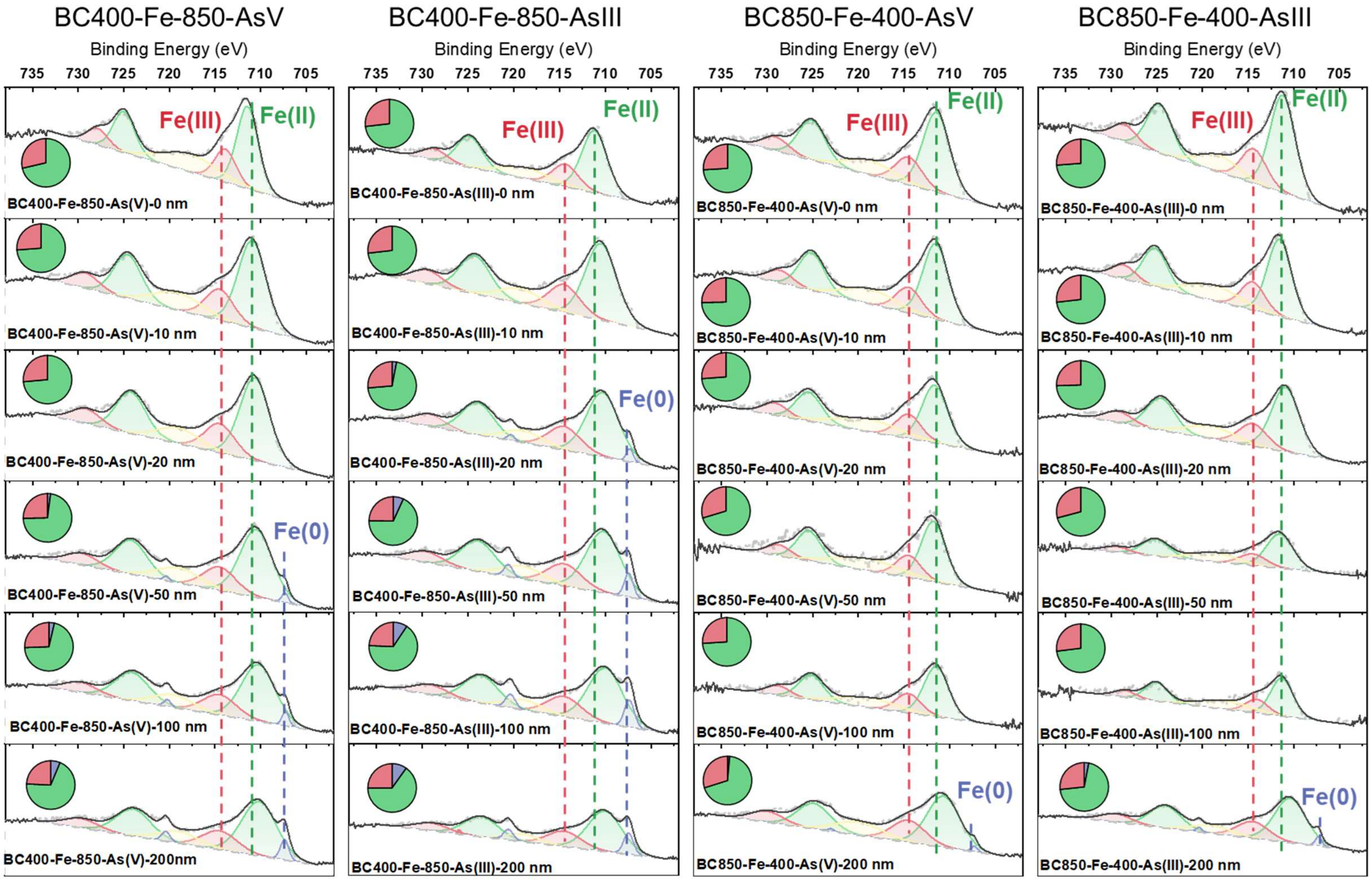

Figure D12. XPS depth profiling analysis of the Fe2p binding state in the selected Fe-biochars after As removal.

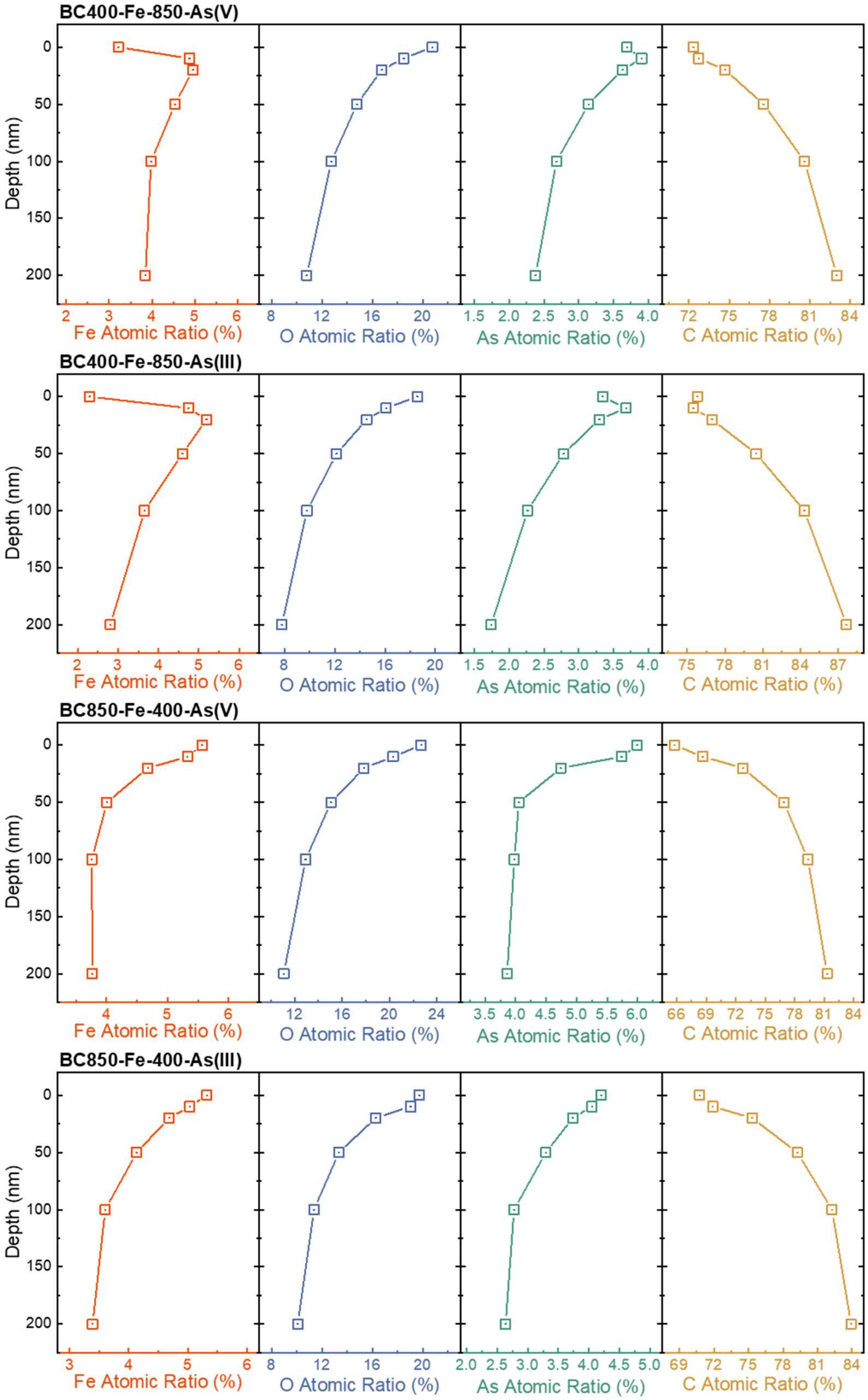

Figure D13. Atomic ratios of C, O, Fe, and As of the selected Fe-biochars after As removal based on the XPS depth profiling analysis.

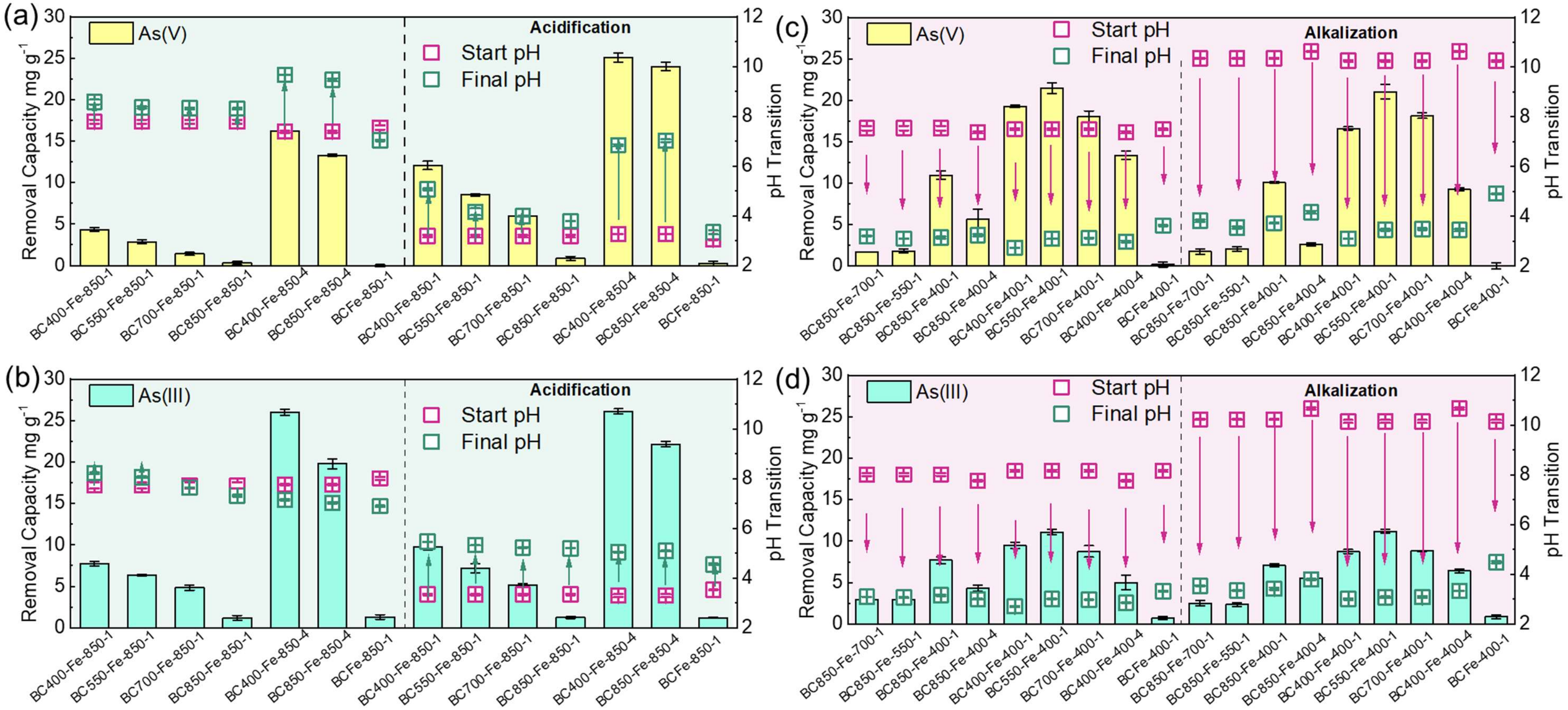

Figure D14. Removal capacities for As(V) (a&c) and As(III) (b&d) of the Fe-biochars prepared under different pyrolytic conditions and the change of solution pH before/after the reaction.

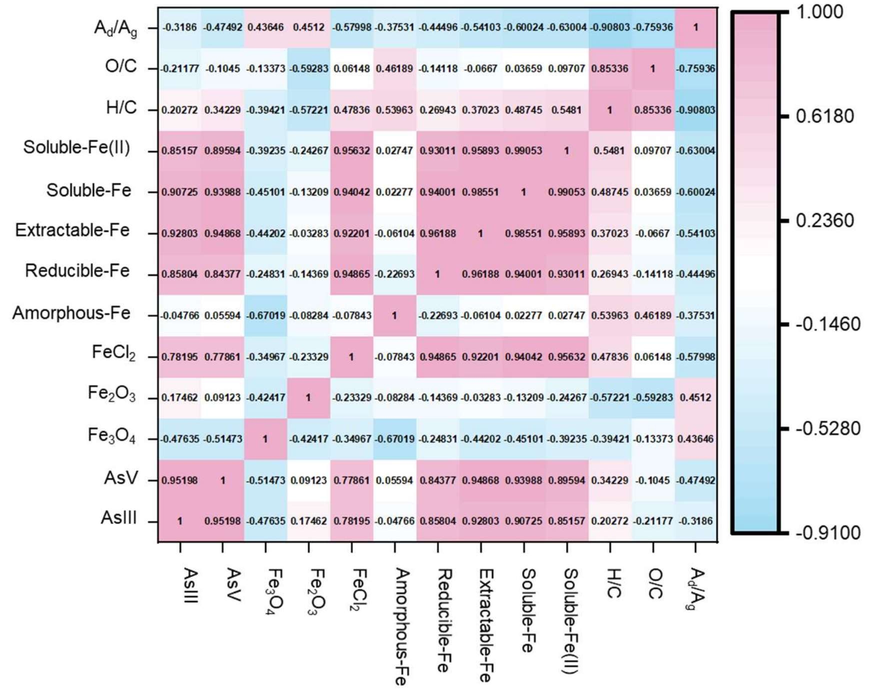

	AsIII	AsV	Fe_3O_4	Fe_2O_3	$FeCl_2$	Amorphous-Fe	Reducible-Fe	Extractable-Fe	Soluble-Fe	Soluble-Fe(II)	H/C	O/C	A_d/A_g
A_d/A_g	-0.3186	-0.47492	0.43646	0.4512	-0.57998	-0.37531	-0.44496	-0.54103	-0.60024	-0.63004	-0.90803	-0.75936	1
O/C	-0.21177	-0.1045	-0.13373	-0.59283	0.06148	0.46189	-0.14118	-0.0667	0.03659	0.09707	0.85336	1	-0.75936
H/C	0.20272	0.34229	-0.39421	-0.57221	0.47836	0.53963	0.26943	0.37023	0.48745	0.5481	1	0.85336	-0.90803
Soluble-Fe(II)	0.85157	0.89594	-0.39235	-0.24267	0.95632	0.02747	0.93011	0.95893	0.99053	1	0.5481	0.09707	-0.63004
Soluble-Fe	0.90725	0.93988	-0.45101	-0.13209	0.94042	0.02277	0.94001	0.98551	1	0.99053	0.48745	0.03659	-0.60024
Extractable-Fe	0.92803	0.94868	-0.44202	-0.03283	0.92201	-0.06104	0.96188	1	0.98551	0.95893	0.37023	-0.0667	-0.54103
Reducible-Fe	0.85804	0.84377	-0.24831	-0.14369	0.94865	-0.22693	1	0.96188	0.94001	0.93011	0.26943	-0.14118	-0.44496
Amorphous-Fe	-0.04766	0.05594	-0.67019	-0.08284	-0.07843	1	-0.22693	-0.06104	0.02277	0.02747	0.53963	0.46189	-0.37531
$FeCl_2$	0.78195	0.77861	-0.34967	-0.23329	1	-0.07843	0.94865	0.92201	0.94042	0.95632	0.47836	0.06148	-0.57998
Fe_2O_3	0.17462	0.09123	-0.42417	1	-0.23329	-0.08284	-0.14369	-0.03283	-0.13209	-0.24267	-0.57221	-0.59283	0.4512
Fe_3O_4	-0.47635	-0.51473	1	-0.42417	-0.34967	-0.67019	-0.24831	-0.44202	-0.45101	-0.39235	-0.39421	-0.13373	0.43646
AsV	0.95198	1	-0.51473	0.09123	0.77861	0.05594	0.84377	0.94868	0.93988	0.89594	0.34229	-0.1045	-0.47492
AsIII	1	0.95198	-0.47635	0.17462	0.78195	-0.04766	0.85804	0.92803	0.90725	0.85157	0.20272	-0.21177	-0.3186

Figure D15. Pearson correlation matrix of the As removal capacities, Fe speciation, and basic physicochemical properties of Fe-biochars produced at low second pyrolysis temperature (≤700 °C) with rich amorphous-Fe content and acidic pH.

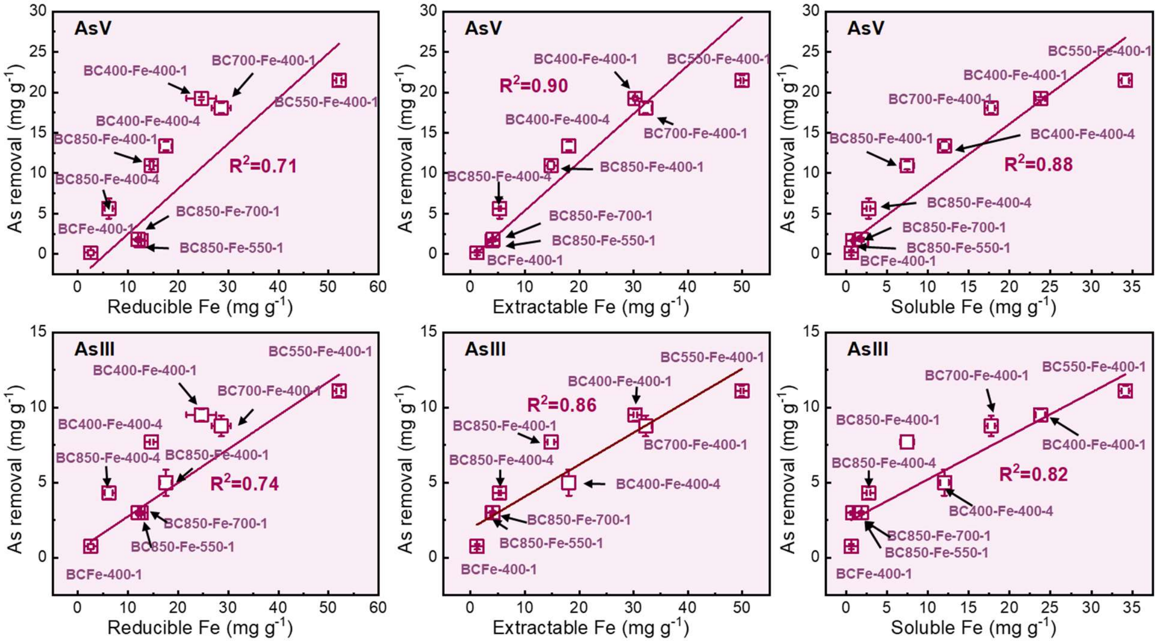

Figure D16. Linear relationship between Fe-speciation detected by different extraction methods and As removal capacities of Fe-biochars produced at low second pyrolysis temperature (≤700 °C) with rich amorphous-Fe content and acid-pH.

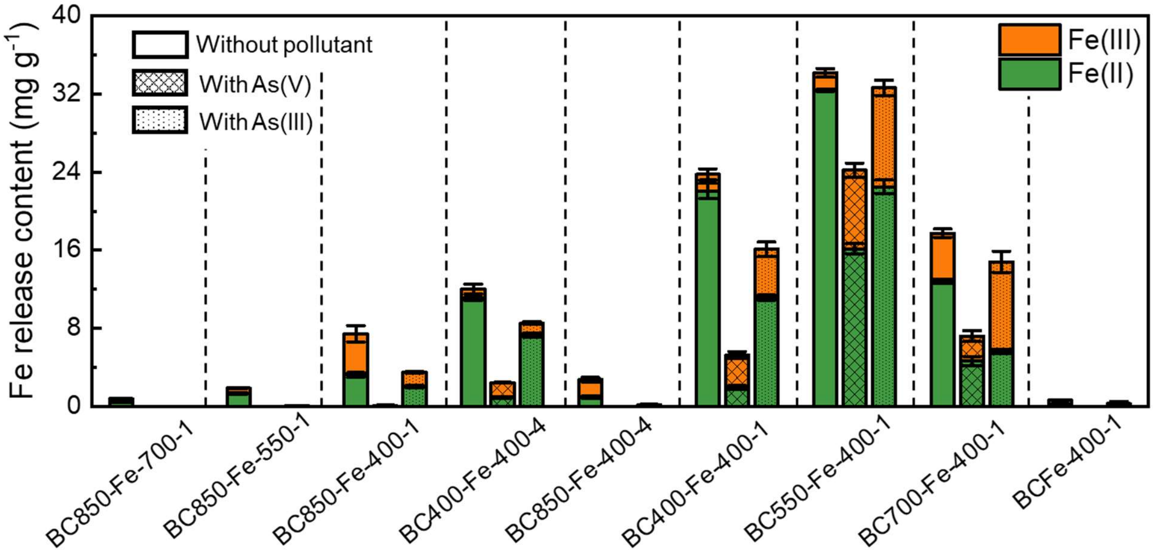

Figure D17. Amount of Fe dissolution before and after immobilization of As(V)/As(III).

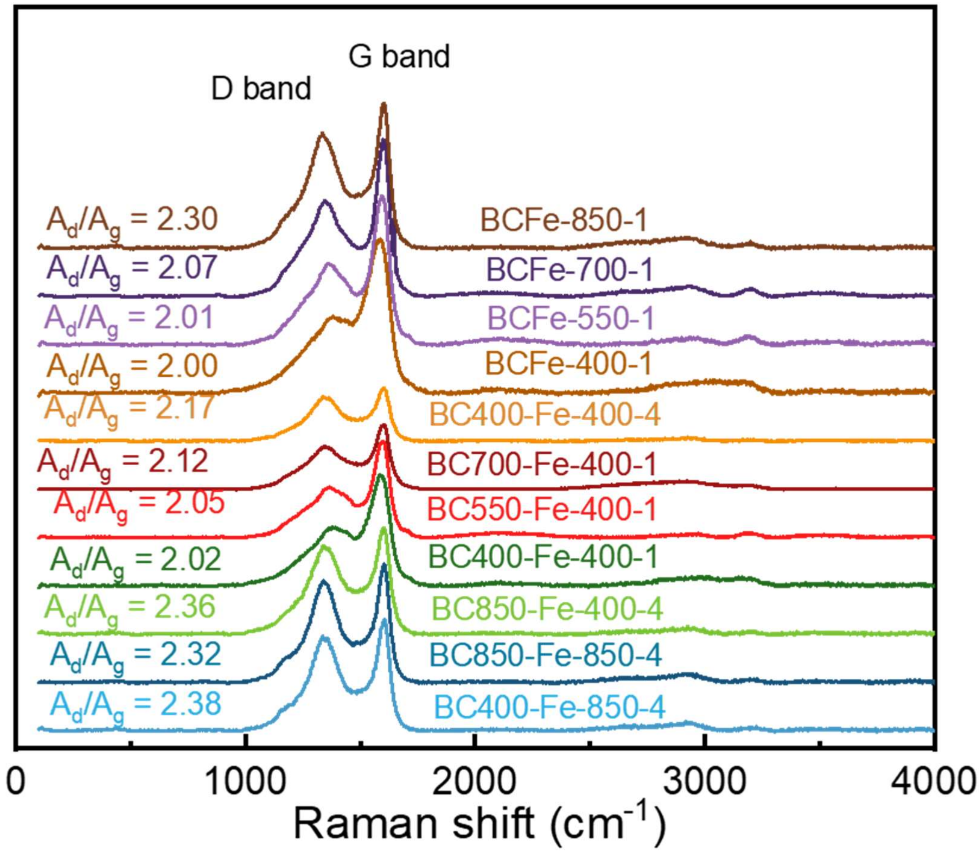

Figure D18. Raman patterns of the Fe-biochars prepared under different pyrolytic conditions.

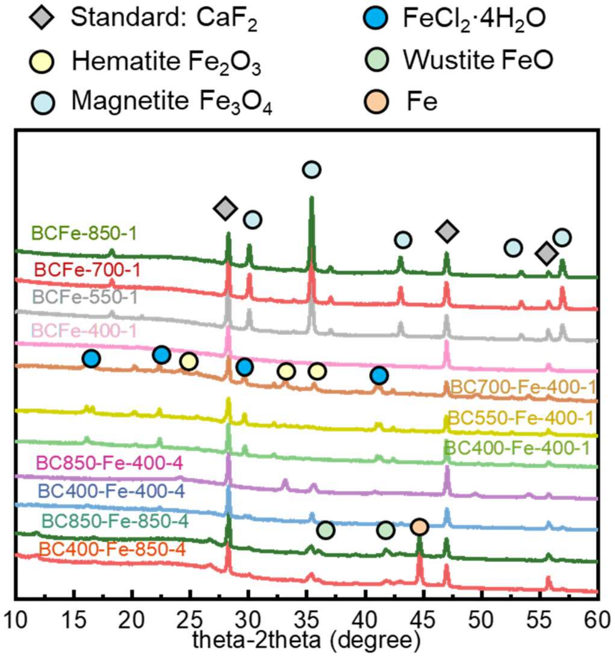

Figure D19. Q-XRD patterns of the Fe-biochars prepared under different pyrolytic conditions with the addition of standard CaF_2.

Appendix E

Preparation of Cr(VI)-contaminated OECD soils with low- and high-crystallinity ferric oxyhydroxides. Standard OECD soil, prepared according to the previous study (Pontoni et al., 2016), was selected as the basis of all test soils. Briefly, 68.5% quartz sand, 20% kaolin clay, and 10% sphagnum peat sieved at 2 mm were mixed first, and then about 1% powdered calcium carbonate was added to adjust the soil pH to 7.0 ± 0.2. About 0.5% K_2CrO_4 was added to simulate the Cr(VI) pollution, which resulted in Cr(VI) concentration of about 1340 mg kg^{-1}. This concentration was within the chromium concentration in the industrially polluted soil (Chen et al., 2021c, Yang et al., 2018b, Yang et al., 2021c). About 6.38% Fe-L or Fe-H was also added to represent kaolin clay, which targeted the iron concentration as ~4% in the soil involved in the typical iron content of red soil/swamp soil in China (Hu et al., 2021). The proportion of different components in soils was concluded below. These components were placed in glass containers, moistened distilled water, thoroughly mixed to ensure a homogeneous distribution, and then left stabilizing for 30 days. After 30 days of incubation, these soils were air-dried, passed through a 2 mm sieve, and stored in a closed container before further use.

Soil Name	Quartz Sand (%)	Kaolinite Clay (%)	Sphagnum Peat (%)	Calcium Carbonate (%)	Hexavalent Chromium (%)	Ferric Oxyhydroxide (%)
No-Fe Soil	68.50	20.00	10.00	~1.00	0.50	0.00
Fe-L Soil	68.50	13.62	10.00	~1.00	0.50	6.38 Fe-L
Fe-H Soil	68.50	13.62	10.00	~1.00	0.50	6.38 Fe-H

Sampling Process and Control Settings of Cr(VI) Immobilization Experiment in Solution System. Firstly, 2 g Fe-L or Fe-H were added into 1 L of 100 mg L^{-1} Cr(VI) solution, which was prepared by dissolving an appropriate amount of K_2CrO_4 in 0.1 M KCl background solution. The concentration ratio between ferric oxyhydroxides and chromium was set according to the possible concentration in polluted soil (Chen et al., 2021c, Yang et al., 2018b, Yang et al., 2021c). These mixtures were mechanically shaken for 7 days at 200 rpm to ensure the homogeneity of the reaction system. This process was implemented to simulate the natural sorption process of Cr(VI) on ferric oxyhydroxides and determine the Cr(VI) removal ability of ferric oxyhydroxides with different degrees of crystallinity.

After the 7-day reaction, 2 g biochar (BC400 or BC700) was added to the solution above to simulate the artificial addition of pyrogenic carbon. The mixtures were further shaken for another 7-days at 200 rpm to keep the reaction system homogenized. All experiments were done in triplicates. According to the previous study, the reaction time and the ratio between biochar and Cr(VI) were selected.(Xu et al., 2018a, Xu et al., 2019d, Xu et al., 2021e) About 3 mL mixtures were sampled and filtered using a 0.45-μm membrane filter to collect the filtrates and solids at selected time intervals during the whole 14-day process, and the pH was kept at the initial value of 6.5±0.1 by adding 1M HCl or 1M NaOH after each sampling. It is worth mentioning that the sampling process was conducted carefully and rapidly to keep the homogeneous distribution of the solid particles during the sampling process. Besides, the redox condition of the solution was not controlled during the whole reaction. Control experiments were set as follows:

(1) Graphite and activated carbon were set as the carbon material comparisons and were added

instead of biochar after the 7-day reaction between ferric oxyhydroxide and Cr(VI).

(2) Biochar without ferric oxyhydroxide existence was set as a control to reveal biochar's immobilization capacity alone. 100 mg L^{-1} Cr(VI) solution was shaken for 7-day alone without any ferric oxyhydroxide, and then biochar was added.

(3) Dissolved biochar of BC400 was set as the control to reveal the electron transfer mechanism from biochar to Cr(VI) on the ferric oxyhydroxide since the dissolved organic matter of biochar might donate electrons for Cr(VI) and Fe(III) reduction (Zhang et al., 2019a). Dissolved biochar was prepared by filtering the fresh BC400 with deionized water at a ratio of 1:100 (w/v) ratio after stirring for 48 h (Yang et al., 2018a). The dissolved organic carbon concentration was 83.4 mg L^{-1} (determined by a multi-N/C 2100 TOC (Germany) analyzer). 20 mg dissolved biochar was added into 1L 100 mg L^{-1} Cr(VI) solution with 2g ferric oxyhydroxide and shaken at 200 rpm for 7 days.

(4) Ferric oxyhydroxide without biochar addition was also set as a control to reveal the Cr(VI) immobilization ability of ferric oxyhydroxide alone. The mixture of Cr(VI) solution and ferric oxyhydroxide was shaken at 200 rpm for 14 days without biochar addition on the seventh day. The sorption process was stabilized after seven days, and little change occurred from the 7th day to the 14th day.

Alkalinity Extraction Experiment. An alkaline extraction method (Zhao et al., 2016c) was used to determine Cr species in biochar for comparison with XPS results. An appropriate amount of NaOH and Na_2CO_3 was dissolved by deionized water to make the 0.5 M NaOH + 0.28 M Na_2CO_3 extraction solution. 100 mg biochar after Cr(VI) reduction was mixed with 50 mL alkaline extraction solution. The mixtures were mechanically shaken at 160 rpm at 50°C for 24 h. The liquid phase was collected using a 0.45 μm Millipore filter for Cr(VI) measurement to determine the Cr(VI) amount on the solid surface.

Transmission Electron Microscopy (TEM) with Electron Energy Loss Spectroscopy (EELS) analysis. The biochar and ferric oxyhydroxide complex was dispersed in ethanol with sonication for 5 min. Samples were prepared by placing ten μL of the solution onto the micro carbon grid. After drying under anoxic conditions for 1 day, the samples were put directly into the TEM and analyzed by EELS for C, Fe, and Cr species. All spectra were normalized using the C K-edge integrated intensity. TEM and EELS data were processed by Gatan Digital Micrograph. EELS mapping of C was obtained using 0.5 eV window on the C edge at 285.0 eV (aromatic C), 286.75 eV (phenol), and 288.5 eV (carboxyl) (Archanjo et al., 2015, Chen et al., 2014a). A long window range among 284-292 eV was also used to evaluate the distribution of carbon in all possible speciation. EELS mapping of Cr was obtained using 2 eV wide windows on the Cr L3-edge at 575 eV(Cr(III)) and 581 eV(Cr(VI)) (Arevalo-Lopez and Alario-Franco 2009, Bishop et al., 2019, Daulton and Little 2006, Daulton et al., 2002). EELS mapping of Fe was obtained using 1 eV wide window on the Fe L-edge at 705 eV (Fe(II)) and 707 eV (Fe(III)) (Archanjo et al., 2017).

XPS Analysis. The XPS data were processed by using the CasaXPS software with the Gaussian-Lorentzian model and plotted with Origin 8.6. The C1s could be divided into sp^2-C (284.5 eV), sp^3-C (285.6eV), C-O (286.7 eV), -C=O (287.8 eV), and –COO (288.8 eV) by XPS (Fan et al., 2011). The O1s could be divided into C-O/C-OH (~533.5-534eV), -C-O-Fe(~532.5 eV), -C=O (~531-532 eV), and -Fe-O/-Fe(O)OH (~530-531 eV) by XPS according to the reference (Arrigo et al., 2010, Qian et al., 2017, Zhou et al., 2007). Fe 2p could be divided into 2p$_{3/2}$ orbitals of Fe^{2+} (711-712.5 eV), 2p$_{3/2}$ orbitals of Fe^{3+} (713-714.5 eV), Fe satellite (715-720 eV), 2p$_{1/2}$ orbitals of Fe^{2+} (724 -725.5 eV), and 2p$_{1/2}$ orbitals of Fe^{3+} (726.5-728.0 eV), respectively (Wu et al., 2012, Xu et al., 2021d, Yan et al., 2018).

Raman Imaging combined with Emission Scanning Electron Microscope (Raman-SEM) analysis. The carbon structure of biochar after Cr(VI) reduction with ferric oxyhydroxide was characterized with Raman Imaging combined with an Emission Scanning Electron Microscope system (TESCAN-MAIA3/ WITEC/MAIA3 GMU model 2016) with excitation line set to $\lambda_0 = 532$ nm. The areas were selected for mapping as the position marked as ~1320 cm^{-1} with 70 cm^{-1} wide window representing the disorder carbon defects (I_D), while ~1520 cm^{-1} with 70 cm^{-1} wide window represents the high order graphitic carbon (I_G) (Hu et al., 2017, Li et al., 2006, Wan et al., 2019). The ratio of I_D/I_G was a typical indicator to represent the disorder carbon degree (Sun et al., 2019, Wan et al., 2019), and its relevant strength was also calculated for the mapping. The Raman spectra on the ferric oxyhydroxide showed no peaks but an increase with the wavenumber due to the fluorescence.

Quantification of the contribution of direct and indirect electron transfer during the Cr(VI) reduction with Fe-L and biochar. To semi-quantified the contribution of the direct and indirect electron transfer routine during the Cr(VI) reduction with Fe-L and biochar, the remaining Cr(VI)-containing solution was replaced with the same volume of background solution without Cr(VI) after 7-day Cr(VI) sorption by Fe-L. Limited Cr(VI) concentration in the solution can inhibit the potential direct reduction of Cr(VI) by biochar. Then, 2 g L^{-1} biochar was added into the system to launch the reduction process for 7-day. The remaining Cr(VI) in both solid and solution was determined compared with the main experiment (*i.e.,* Cr(VI)-containing solution was not removed). We find that about 21.8–23.9% Cr(VI) can be reduced without the solution Cr(VI), representing the 66.6–73.0% Cr(VI) reduction amount in the system with the solution Cr(VI). Although parts of Cr(VI) were released into the solution during the reaction process, its concentration was low (< 3.3 mg L^{-1}, less than 10 %). Thus, the main electron transfer routine was indirect electron transfer for the Cr(VI) reduction with Fe-L and biochar.

Electrochemical analysis for the biochar with or without iron mineral. The electron-donating capacity (EDC) of biochar in the absence or presence of iron minerals was quantified by the mediated electrochemical oxidation (MEO) methods (Zhang et al., 2018c). All the electrochemical analysis was performed in an anoxic glovebox, and all the biochar and iron minerals were placed under a vacuum in the antechamber to remove the adsorbed O_2. The biochar (2 g L^{-1}) was suspended in glass vials containing a neutral (pH= 7.0) anoxic buffer solution (0.1 mol KCl and 0.1 mol phosphate). Iron mineral (2 g L^{-1}) was also added to study the impact of iron minerals on the electron-donating process of biochar. A 9-mL glassy carbon cylinder served both as the working electrode and electrochemical reaction vessel. The Ag/AgCl electrode served as the reference electrode, and the counter electrode was a coiled platinum wire with porous glass wrapped outside. The working potential was set at 0.61 V, and ABTS (2, 2′-azino-bis (3-ethyl-benzthiazoline-6-sulfonic acid) diammonium salt) was selected as the mediator for the MEO reaction. The biochar suspensions were spiked into the cells, and the (EDC) of the composites was determined by integrating the current peak response with triplicates (**Eq. E1**).

$$EDC = \frac{\int \frac{I_{Ox}}{F} dt}{m_{biochar}} \qquad \textbf{Eq.E1}$$

$$EAC = \frac{\int \frac{I_{Red}}{F} dt}{m_{Fe}} \qquad \textbf{Eq.E2}$$

where I_{Red} and I_{Ox} [A] are the corrected electrochemical currents in the MER and MEO tests, respectively; F [s A (mol $e^{-})^{-1}$] is the Faraday constant; and $m_{biochar}/m_{Fe}$ [g] is the mass of biochar or iron mineral sample.

EDC of Fe-L and Fe-H was also determined with a similar method. Besides, the mediated electrochemical reduction (MER) test was also conducted to evaluate the oxidizing capacity of iron minerals. Diquat (1,1′-ethylene-2,2′-bipyridyl） was chosen as the mediator, and the working potential was set at -0.35 V (Aeppli et al., 2019a, Aeppli et al., 2018, Aeppli et al., 2019b). For the MEO test, 0.01 mol MOPs (3-morpholinopropane-1-sulfonic acid) was selected as the buffering agent to control the pH as 7. Electron-accepting capacity (EAC) of iron minerals was determined by the triplicated MER test (**Eq. E2**) with a similar testing procedure as the MEO test. The co-existence of Fe-L decreased the EDC of biochar, while limit change was found with Fe-H. Iron mineral contained limited electron-donating capacity, while the high electron-accepting capacity of Fe-L might cause the decrease of biochar’s EDC.

Table E1. Selected Physicochemical Properties of Ferric oxyhydroxides

Ferric oxyhydroxides	S_{BET} ($m^2 \cdot g^{-1}$)	pH_{pzc}[a]	Crystalline size (nm)[b]
Fe-L	19.8	~8.5	17.6
Fe-H	283	~8.0	29.8

[a] detected based on the Zeta potential; [b] calculated based on the Scherrer formula

Table E2. Selected Physicochemical Properties of Biochar Derived from Peanut Shell at 400℃ and 700℃

	I_D/I_G[a]	S_{BET} ($m^2 \cdot g^{-1}$)	Element content (%)				C species (%)[b]					O species (%)[b]	
			C	H	N	O	*sp*^{2}C	*sp*^{3}C	-C-O	-C=O	-COO	-C-O	-C=O
BC400	1.15	19.8	71.4	3.49	1.39	16.6	54.0	34.0	4.98	3.74	3.25	47.5	52.5
BC700	1.55	283	83.0	1.14	0.88	5.38	63.6	26.9	3.41	3.32	2.71	49.1	50.9

[a] Determined with Raman spectrometer; [b] Determined using X-ray photoelectron spectroscopy;

Table E3. Distribution of Cr in solid phase (biochar and iron mineral alone or in combination) after 14-day Cr(VI) removal in solution system

	Cr_{Total} concentration in solid phase (mg g^{-1})	Cr(VI) concentration in solid phase (mg g^{-1})	Cr(III) concentration in solid phase (mg g^{-1})	Cr(VI) distribution in solid phase (%)	Cr(III) distribution in solid phase (%)
Fe-L	18.75 (18.45)[a]	18.22 (18.15)	0.53 (0.30)	97.15 (98.37)	2.85 (1.63)
Fe-H	6.18 (4.33)	5.80 (4.18)	0.38 (0.17)	93.75 (96.54)	6.25 (3.46)
BC400	14.85	0.45	14.35	3.03	96.97
BC400 + Fe-L	10.48	5.14	5.34	49.03	50.97
BC400 + Fe-H	6.39	0.44	5.95	6.89	93.11
BC700	16.91	0.35	16.56	2.07	97.93
BC700 + Fe-L	10.69	5.34	5.35	49.94	50.06
BC700 + Fe-H	7.02	0.95	6.07	13.53	86.47

[a] Results shown in parentheses were obtained after 7-d Cr(VI) sorption by iron mineral

Table E4. XPS Results for the O 1s Binding State and Its Relative Atomic Percentage on the Biochar Surfaces after Cr(VI) Removal in Different Reaction Systems.

Reaction System	O species (%)				
	-C-O or C-OH	-C-O-Fe	-C=O	-Fe-O or Fe(O)OH	Ratio of -C-O/-C=O
BC400 after Cr(VI) removal	33.41		66.59		0.50
BC400 + Fe-L after Cr(VI) removal	13.72	19.33	39.90	27.04	0.34
BC400 + Fe-H after Cr(VI) removal	27.36		57.31	15.33	0.48
BC700 after Cr(VI) removal	19.21		80.79		0.24
BC700 + Fe-L after Cr(VI) removal	8.05	18.25	43.32	30.38	0.19
BC700 + Fe-H after Cr(VI) removal	14.32		57.01	28.67	0.25

Table E5. XPS Results for the Fe 2p Binding State and Its Relative Atomic Percentage on the Biochar Surfaces after Cr(VI) Removal in Different Reaction Systems.

Reaction System	Fe species (%)			
	Fe(II)	Fe(III)	Fe(salt)	Ratio of Fe(II)/Fe(III)
BC400 + Fe-L after Cr(VI) removal	30.54	46.28	23.19	0.66
BC400 + Fe-H after Cr(VI) removal	17.01	55.52	27.48	0.31
BC700 + Fe-L after Cr(VI) removal	30.11	49.16	20.74	0.61
BC700 + Fe-H after Cr(VI) removal	14.37	62.94	22.69	0.23

Table E6. XPS Results for the C 1s Binding State and Its Relative Atomic Percentage on the Biochar Surfaces after Cr(VI) Removal in Different Reaction Systems.

Reaction System	C1s (%)				
	-sp^{2}C	-sp^{3}C	-C-O	-C=O	-COO
BC400	76.97	13.40	3.86	1.48	4.29
BC400 + Fe-L	73.53	15.22	4.58	1.87	4.97
BC400 + Fe-H	70.74	17.19	5.00	2.62	4.45
BC700	79.03	11.30	3.52	1.39	4.76
BC700 + Fe-L	75.17	13.70	4.11	1.92	5.10
BC700 + Fe-H	69.98	16.53	5.15	2.70	5.64

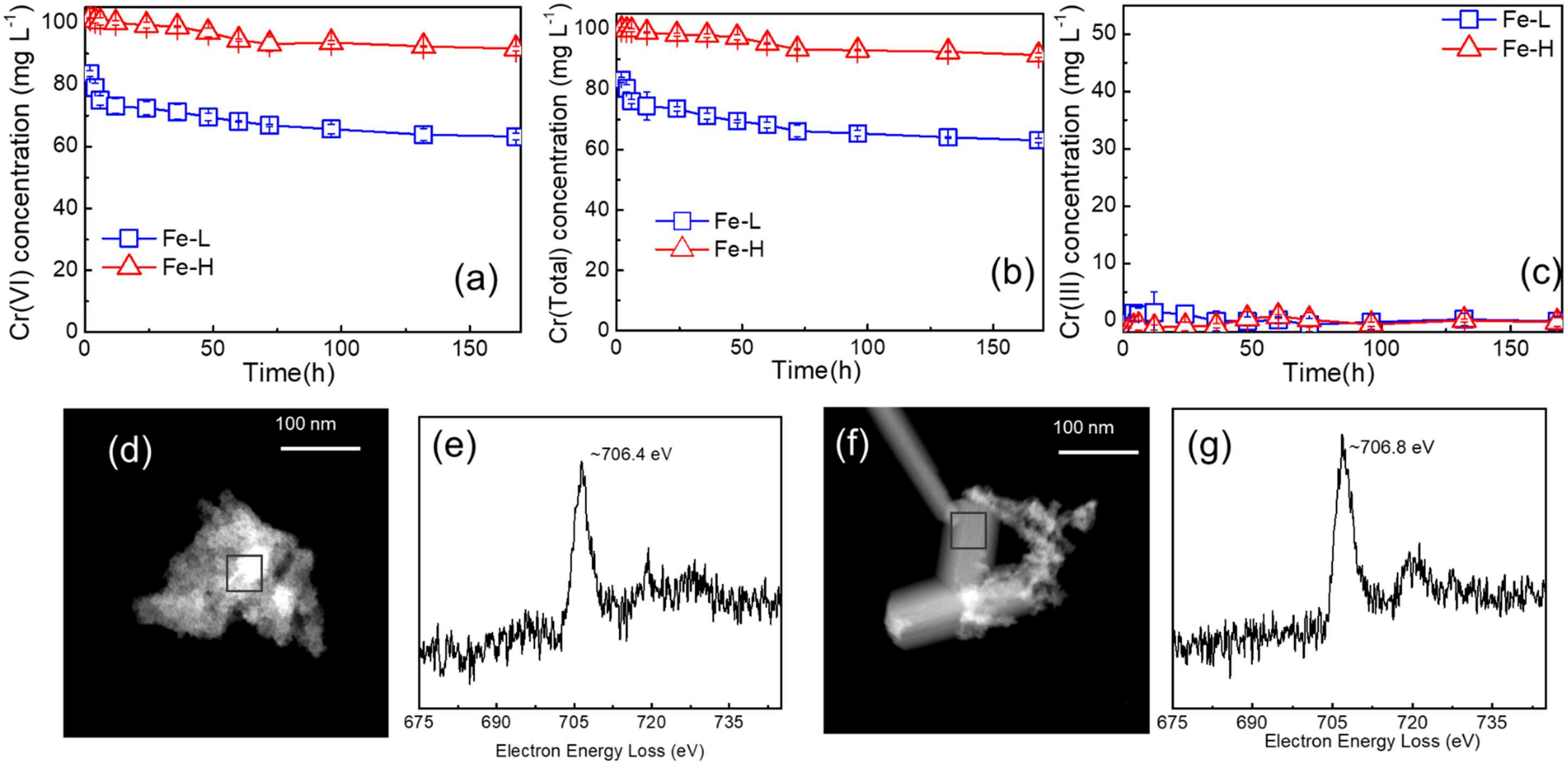

Figure E1. Changes in the concentration of Cr(VI) (a), Cr(Total) (b), and Cr(III) (c) after addition of different iron minerals for 7-day. TEM image of Fe-L (d) and Fe-H (f) after Cr(VI) sorption and its EELS spectra for Fe on the square area in d (Fe-L: e) and f (Fe-H: g).

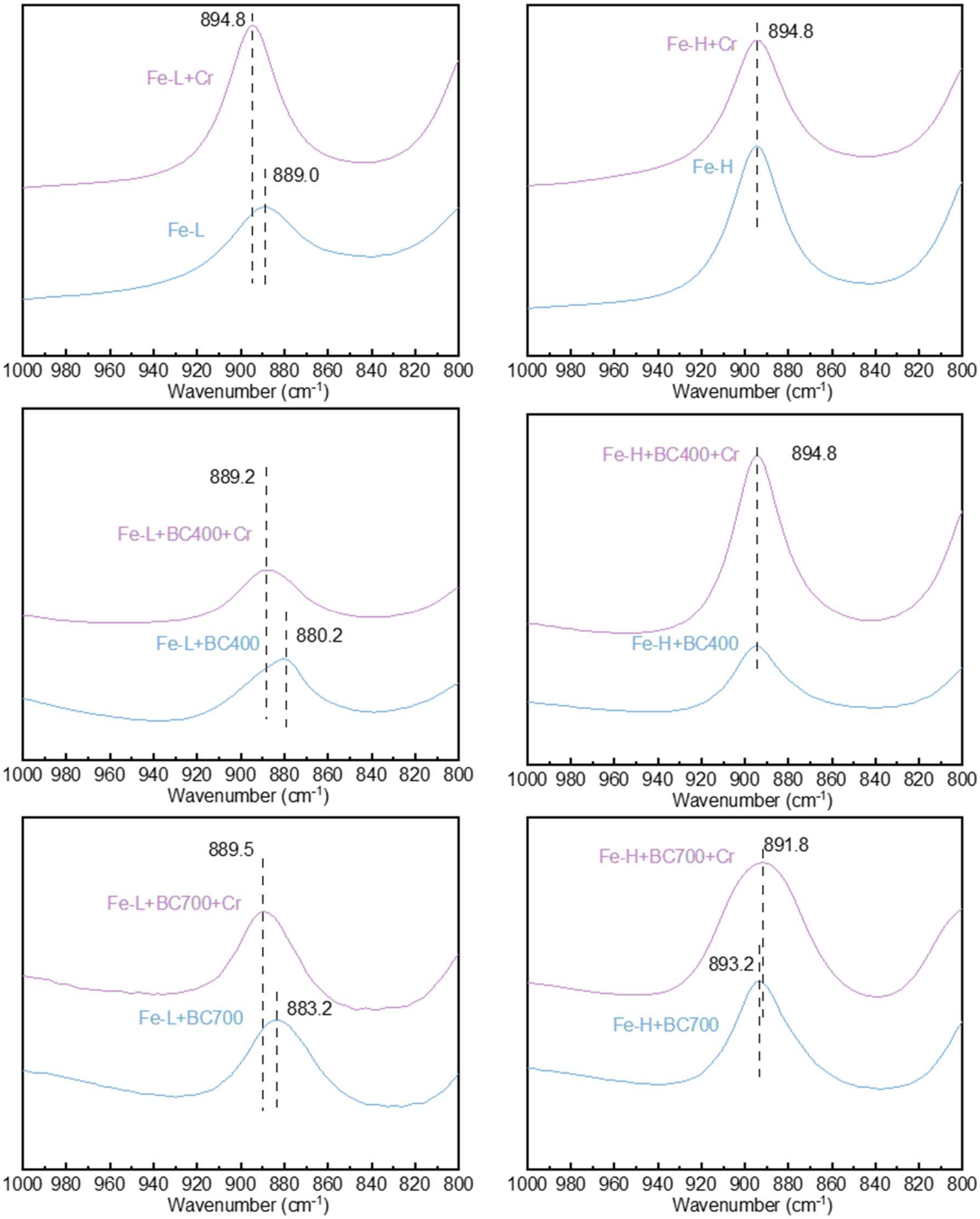

Figure E2. FTIR spectrum of different ferric oxyhydroxides before and after reaction with Cr(VI) and biochar (800-1000 cm^{-1}). The left shift of the peaks on Fe-L after Cr(VI) removal indicating the inner-sphere complexation of Cr(VI) on Fe-L, while no noticeable left shift was found on Fe-H.

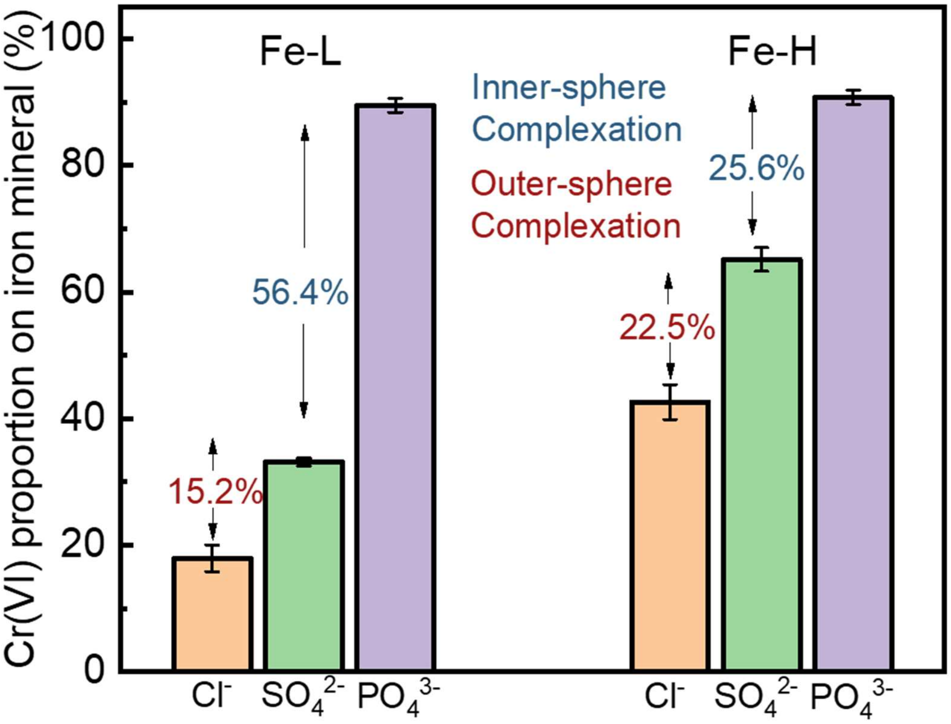

Figure E3. The proportion of inner-sphere and outer-sphere complexation of Cr(VI) is determined by different extraction agents. Phosphate can form strong inner-sphere complexation with iron minerals, which principally extracts all complexed anion ions on the iron mineral. Sulfate might only affect the outer-sphere complexed anion ions, while only free anion ions fixed through electrostatic attraction can be removed by chloride. Therefore, the proportion of inner-sphere and outer-sphere complexation of Cr(VI) can be determined by the gap of different extraction methods.

Quantification of the inner- and outer-complexation amount of Cr(VI) on the ferric oxyhydroxide. The Fourier transform infrared spectroscopy was first adopted to investigate the change of surface functional groups on ferric oxyhydroxides after Cr(VI) sorption (**Figure E2**). A shift to a high-wavenumber of the peak at ~890 cm^{-1} was found on Fe-L after Cr(VI) sorption, indicating the possible formation of inner-sphere complexation of Cr(VI) (monodentate complexation at 910 cm^{-1}) instead of out-sphere complexation (875 and 830 cm^{-1}) (Johnston and Chrysochoou 2016). In contrast, no noticeable shift can be found on Fe-H after Cr(VI) removal.

Moreover, we use different agents to extract the complexed Cr(VI) on the ferric oxyhydroxide (**Figure E3**). Phosphate can form strong inner-sphere complexation with ferric oxyhydroxide (Zhu et al., 2015), which principally extracted all complexed Cr(VI) on the ferric oxyhydroxide. Sulfate might only affect the outer-sphere complexed Cr(VI), while only free Cr(VI) fixed through electrostatic attraction can be removed by chloride (Gao et al., 2021). Therefore, we can quantify the inner-sphere Cr(VI) change during the reaction through the gap between each extraction method. The concentrations of different extraction agents were set at 0.1 M, and the pH was controlled at 6.5. Results showed that inner-sphere Cr(VI) was the primary speciation on Fe-L (56.4%), while a lower amount of inner-sphere Cr(VI) was found on Fe-H (25.6%).

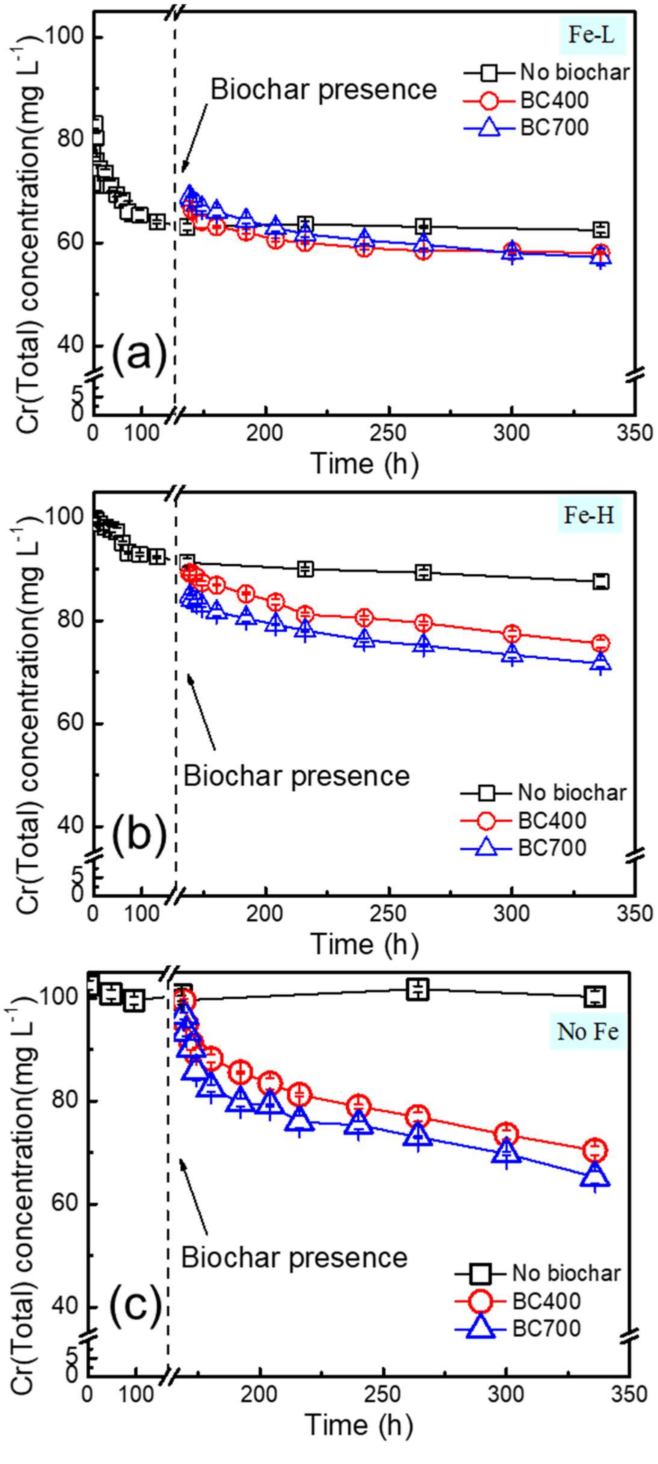

Figure E4. Changes in the concentration of Cr(Total) in solution with or without different iron minerals and biochar. Fe-L: iron mineral with low-crystallinity after 6-h aging and Fe-H: iron mineral with high-crystallinity after 72-h aging.

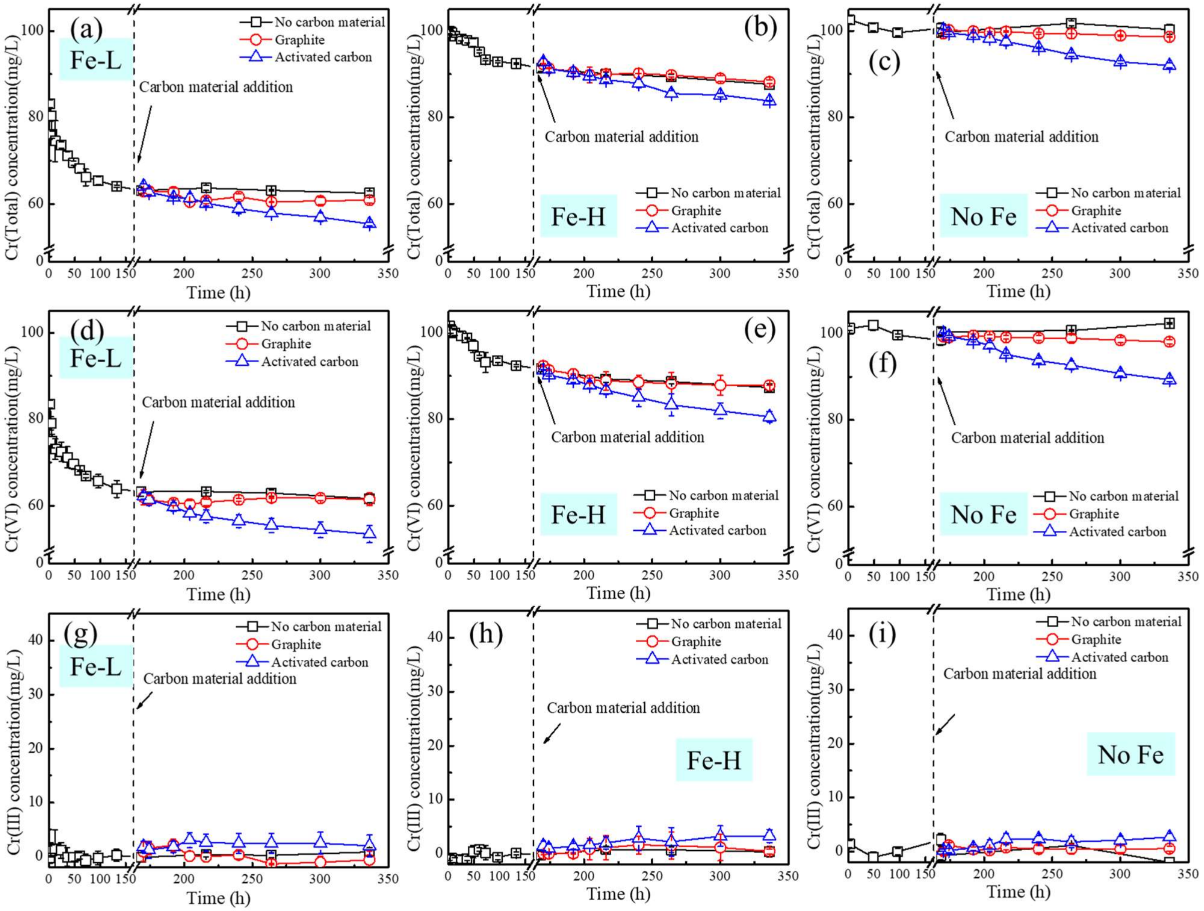

Figure E5. Changes in the concentrations of Cr(Total) (a-c), Cr(VI) (d-e) and Cr(III) (g-i) with or without different iron minerals and carbon material. Carbon materials were added at 168-h after ferric oxyhydroxide addition into Cr(VI) solution.

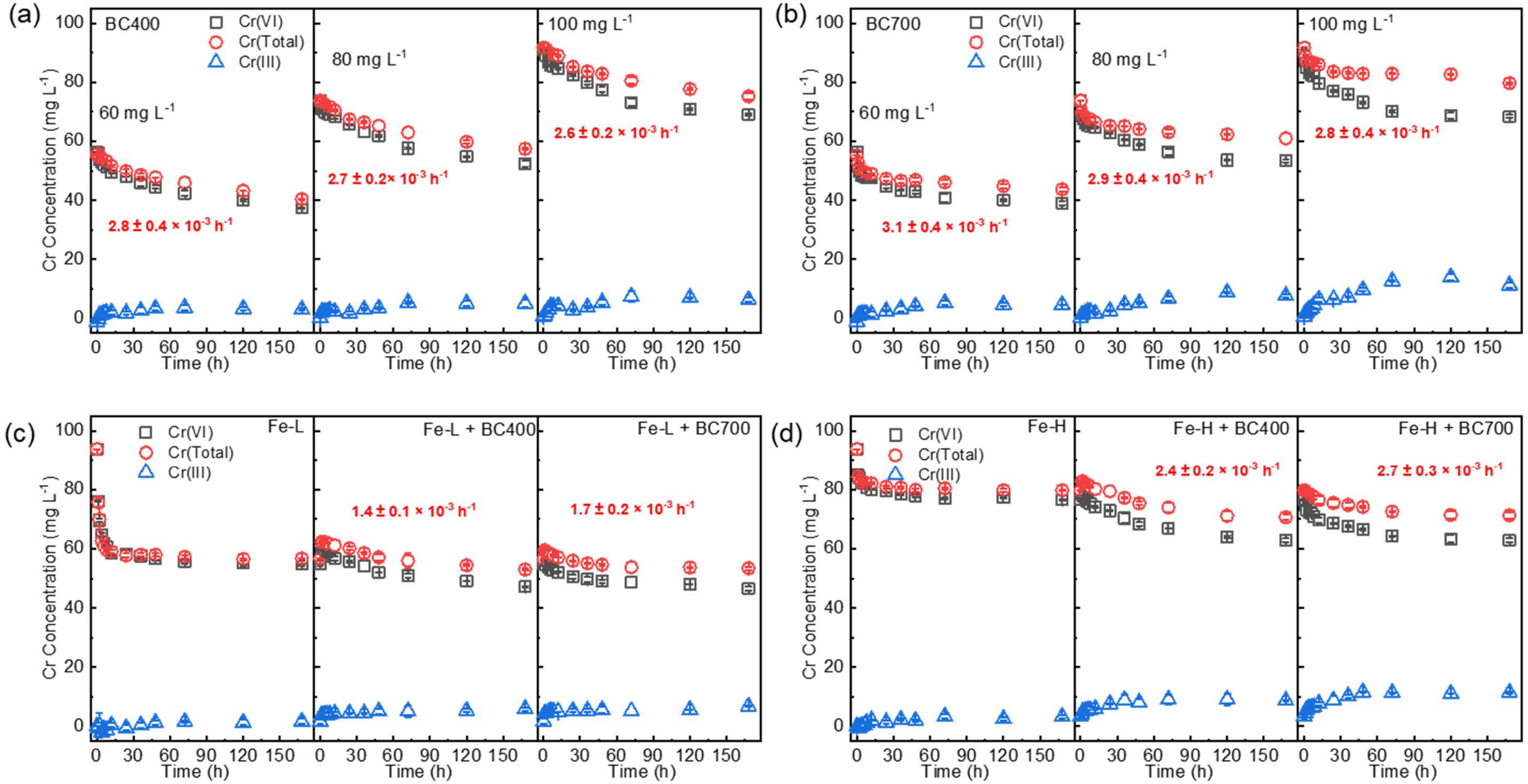

Figure E6. Changes in the concentration of Cr by adding BC400 (a) or BC700 (b) for 7-day with different initial Cr(VI) concentrations (60, 80, and 100 mg L^{-1}); Changes in the concentration of Cr by adding biochar after 7-day sorption of 100 mg L^{-1} Cr(VI) with Fe-L (c) or Fe-H (d); the Cr(VI) concentration was around 60 and 80 mg L^{-1} after 7-day sorption by Fe-L and Fe-H, respectively.

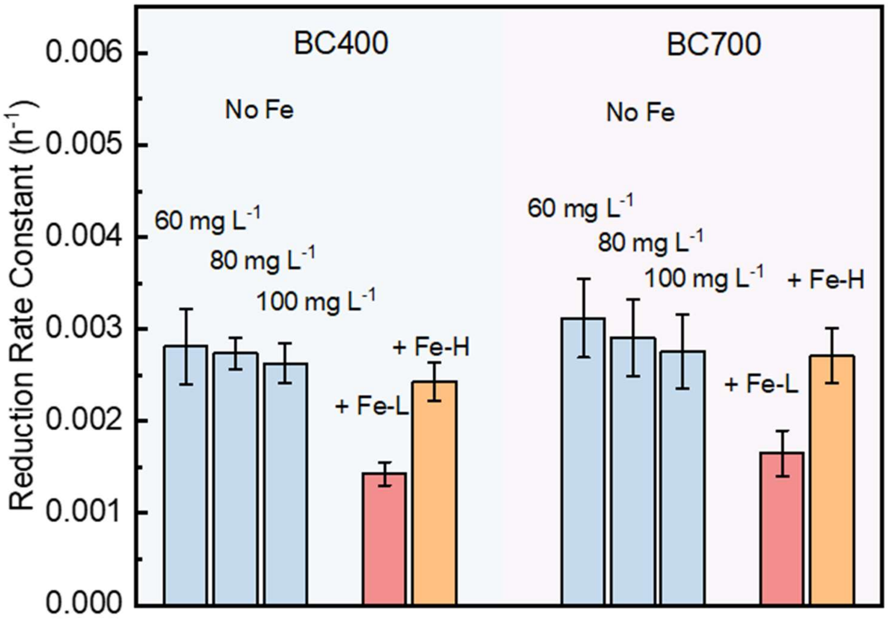

Figure E7. Comparison of the Cr(VI) reduction rate constant of biochar with different Cr(VI) initial concentrations (60, 80, and 100 mg L^{-1}) or after 7-day Cr(VI) sorption with different ferric oxyhydroxides (Fe-L or Fe-H).

Impact of the initial concentration on the Cr(VI) removal by biochar.

The impact of initial Cr(VI) concentration on the Cr(VI) removal by biochar was evaluated. Three initial concentrations of 60, 80, and 100 mg L^{-1} were set base on the Cr(VI) concentration after sorption by ferric hydroxide. No noticeable difference in the reduction rate constant was found with various initial concentrations for both BC400 and BC700, indicating the Cr(VI) concentration was not the rate-limited step for biochar reduction within this concentration range. Mass transfer from the liquid phase to the interfacial of biochar might be fast enough under this concentration. However, the reduction rate with a similar Cr(VI) concentration was still far lower than the reduction rate with Fe-L (1.8–2.0× 10^{-3} h^{-1} < 2.8–3.6 × 10^{-3} h^{-1}), evidencing the occurrence of indirect electron transfer through valence transformation of Fe on ferric oxyhydroxides should be the primary reason for the decrease of reduction rate with Fe-L.

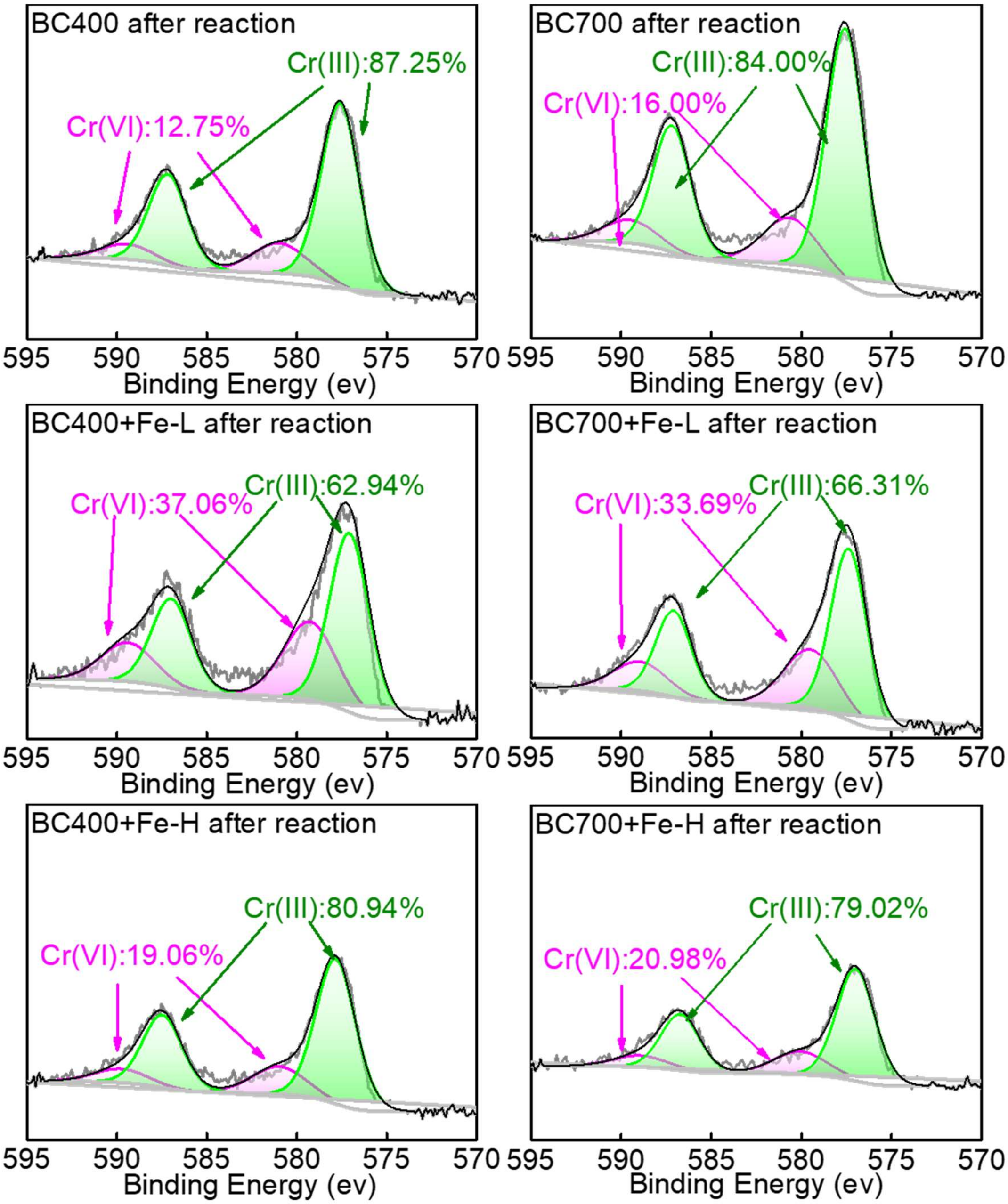

Figure E8. The proportion of Cr(VI) and Cr(III) on the solid residue of biochar and iron mineral after Cr(VI) removal as detected by XPS analysis.

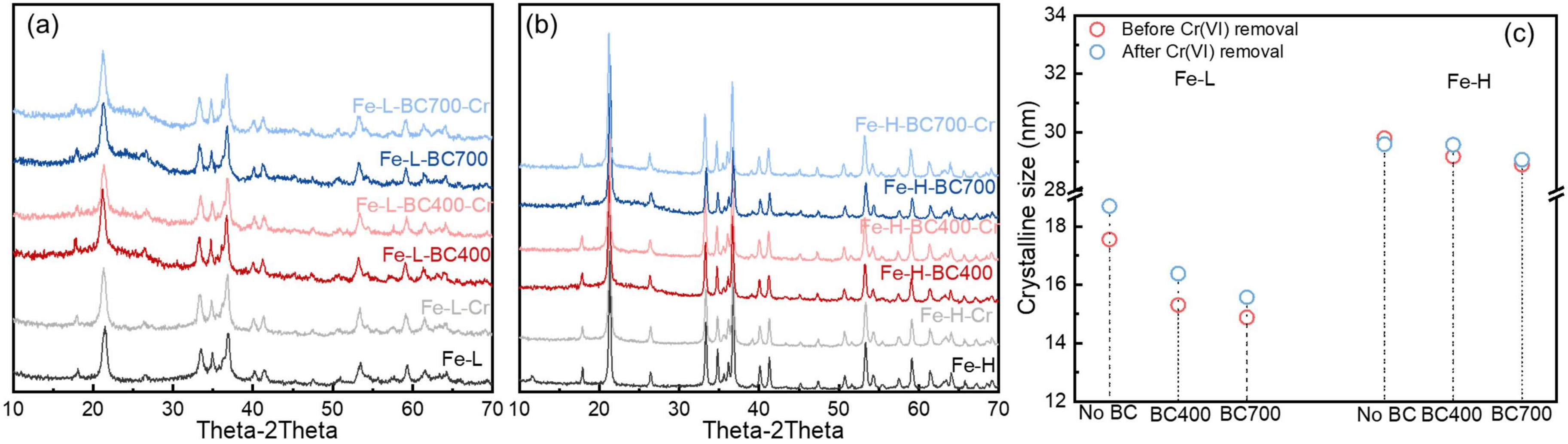

Figure E9. XRD pattern of Fe-L (a) and Fe-H (b) before and after incubation with biochar or Cr(VI); Crystalline size of the goethite in Fe-L or Fe-H (c) calculated by the XRD pattern based on the Scherrer formula.

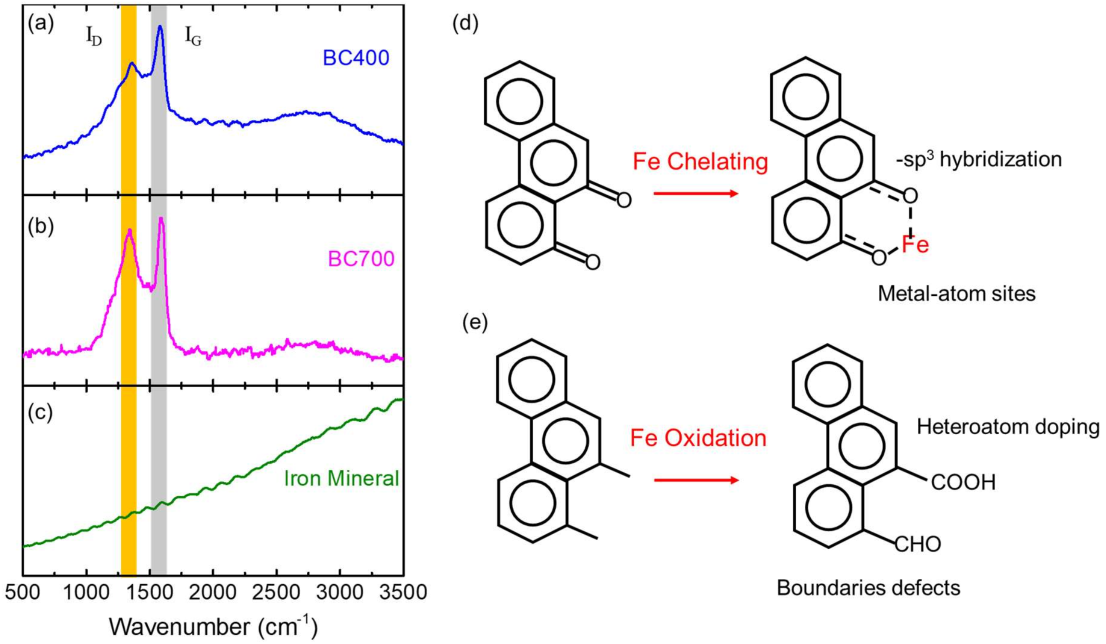

Figure E10. Raman patterns on BC400 region (a), BC700 region (b) and iron mineral region (c) and selected area of I_D and I_G for mapping as shown in Figure 5-7; possible mechanisms of the formation of defects on the biochar with Fe-chelating (d) and oxidation (e).

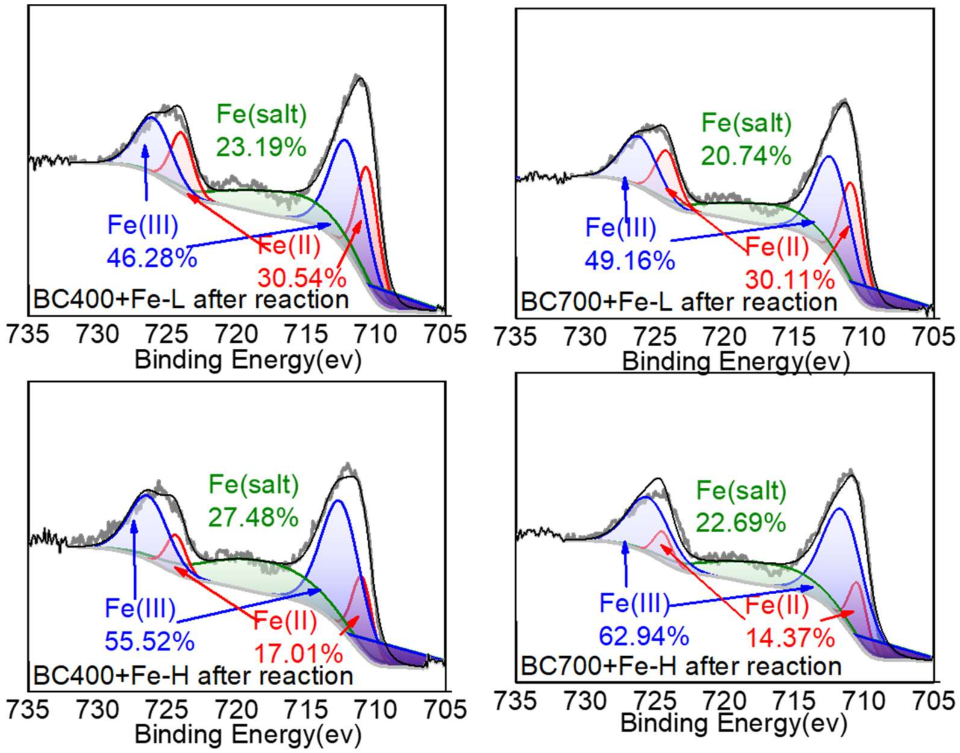

Figure E11. XPS spectra of Fe 2p for biochar-Fe mineral-Cr(VI) formed by reaction between biochar and Cr-laden Fe-L/Fe-H

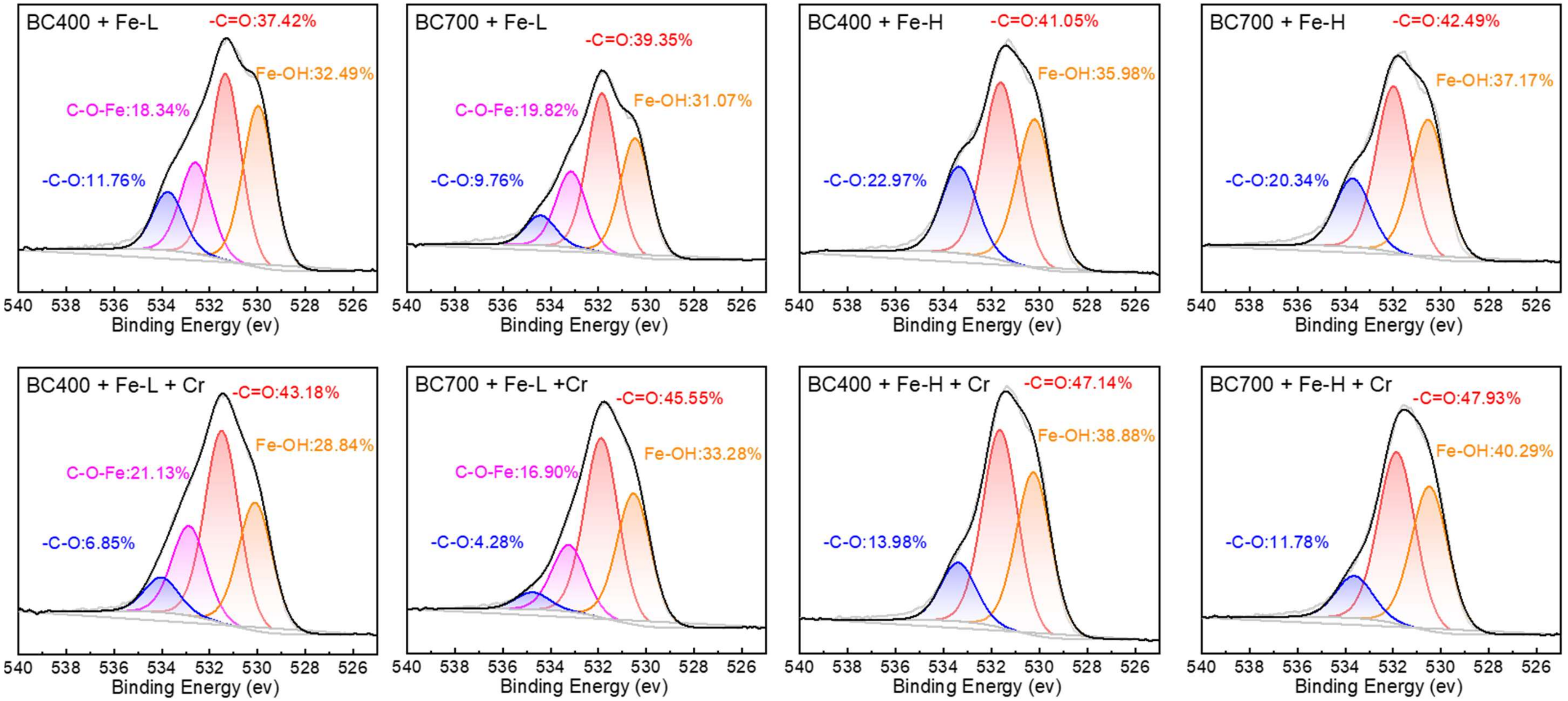

Figure E12. XPS spectra of O1s for biochar-Fe mineral complex before and after Cr(VI) removal; the biochar-Fe mineral complex was formed by incubation of biochar and Fe mineral for 7-day before the Cr(VI) removal process. A decrease of -C-O with the increase of -C=O on both BC400 and BC700 was found compared with the pristine biochar.

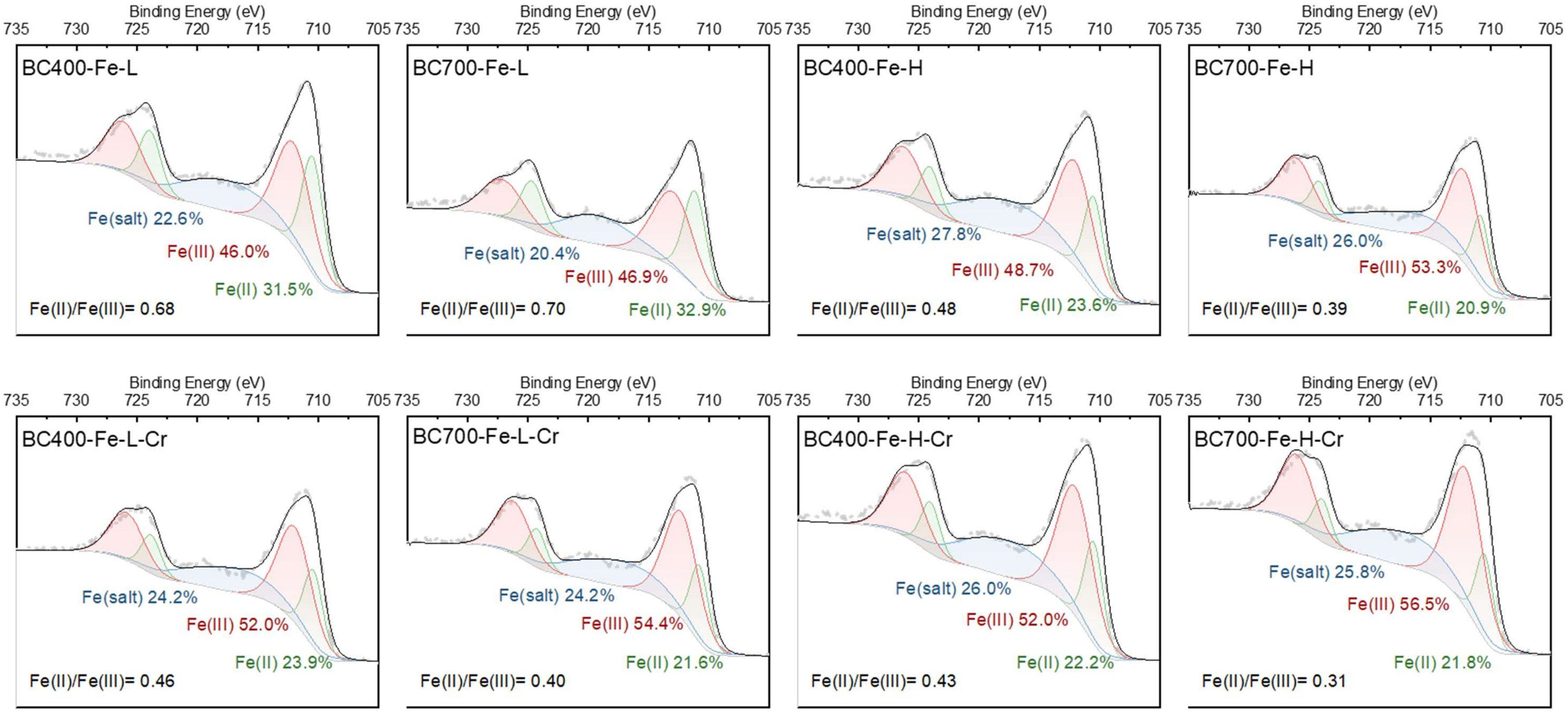

Figure E13. XPS spectra of Fe 2p for biochar-Fe mineral complex before and after Cr(VI) removal; biochar-Fe mineral complex was formed by incubation of biochar and Fe mineral for 7-day prior to the Cr(VI) removal process.

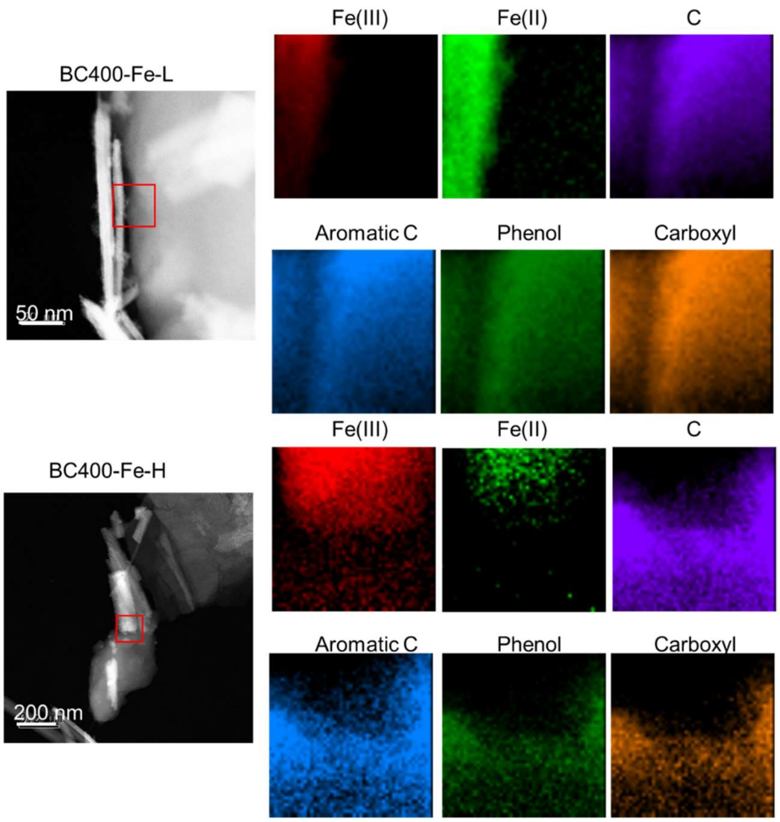

Figure E14. TEM images of the biochar-iron mineral complex region and EELS mapping of C and Fe with different states on the selected area; 704.5-705.5 eV was assigned to Fe(II); 706.5-707.5 eV was assigned to Fe(III).284.75-285.25 eV was assigned to aromatic C; 286.5-287 eV was assigned to phenol; 286.75-287.25 eV was assigned to carboxyl. A long-range from 284-292 eV was assigned to all carbon (C) speciation; an example can be found in **Figure E15**.

Redox transformation between ferric oxyhydroxide and biochar

To further evaluate the redox transformation between Fe-L/Fe-H and biochar, the ferric oxyhydroxide (2 g L^{-1}) was mixed with biochar (2 g L^{-1}) in solution (0.1 M KCl, pH=6.5), and these mixtures were mechanically shaken for 7-day at 200 rpm to ensure the homogeneity of the reaction system. After the 7-day redox reaction, XPS and TEM-EELS analyses were conducted to evaluate the formation of Fe(II) and oxidation of surface functionality. Based on the XPS analysis of the Fe speciation, a higher proportion of Fe(II) was formed on Fe-L (31.5–32.9%) compared with Fe-H (20.9–23.6%) by BC400/BC700 (**Figure E13**). Meanwhile, oxidation of the surface functional group on biochar also occurred during the interaction process, which caused the decrease of –C–O/–C=O ratio (**Figure E12**) from 0.90–0.96 to 0.25–0.31 for Fe-L and to 0.48–0.56 for Fe-H, respectively. These results strongly supported that the redox reaction happens between ferric oxyhydroxide and biochar, and Fe-L was more sensitive to be reduced. Moreover, TEM-EELS mapping confirmed Fe(II) formation on the surface of ferric oxyhydroxide, especially for the Fe-L (**Figure E14**).

The Cr(VI) removal potential of these biochar-reduced ferric oxyhydroxide was further evaluated. 100 mg L^{-1} Cr(VI) was directly added into the solution after a 7-day reaction between ferric oxyhydroxide and biochar. These mixtures will be further shaken for another 7-day at 200 rpm. About 3 mL mixtures were sampled and filtered using a 0.45-μm membrane filter to collect the filtrates and solids at selected time intervals during the 7-day reaction process, and the pH was kept at the initial value of 6.5±0.1 by adding 1 M HCl or 1 M NaOH after each sampling. The concentration of Cr(VI) in the solution was evaluated, and the proportion of Cr(VI) on the solid phase was also determined by XPS analysis and alkaline extraction. All experiments were conducted in duplicate. It was worth noting that the control group of biochar or ferric oxyhydroxide alone was also set based on a similar incubation process, *i.e.*, biochar/ ferric oxyhydroxide incubated in solution 0.1 M KCl, pH=6.5) alone for 7-day prior to the Cr(VI) addition and 7-day Cr(VI) reduction process. Results are shown in below Figure E17 and Figure E18.

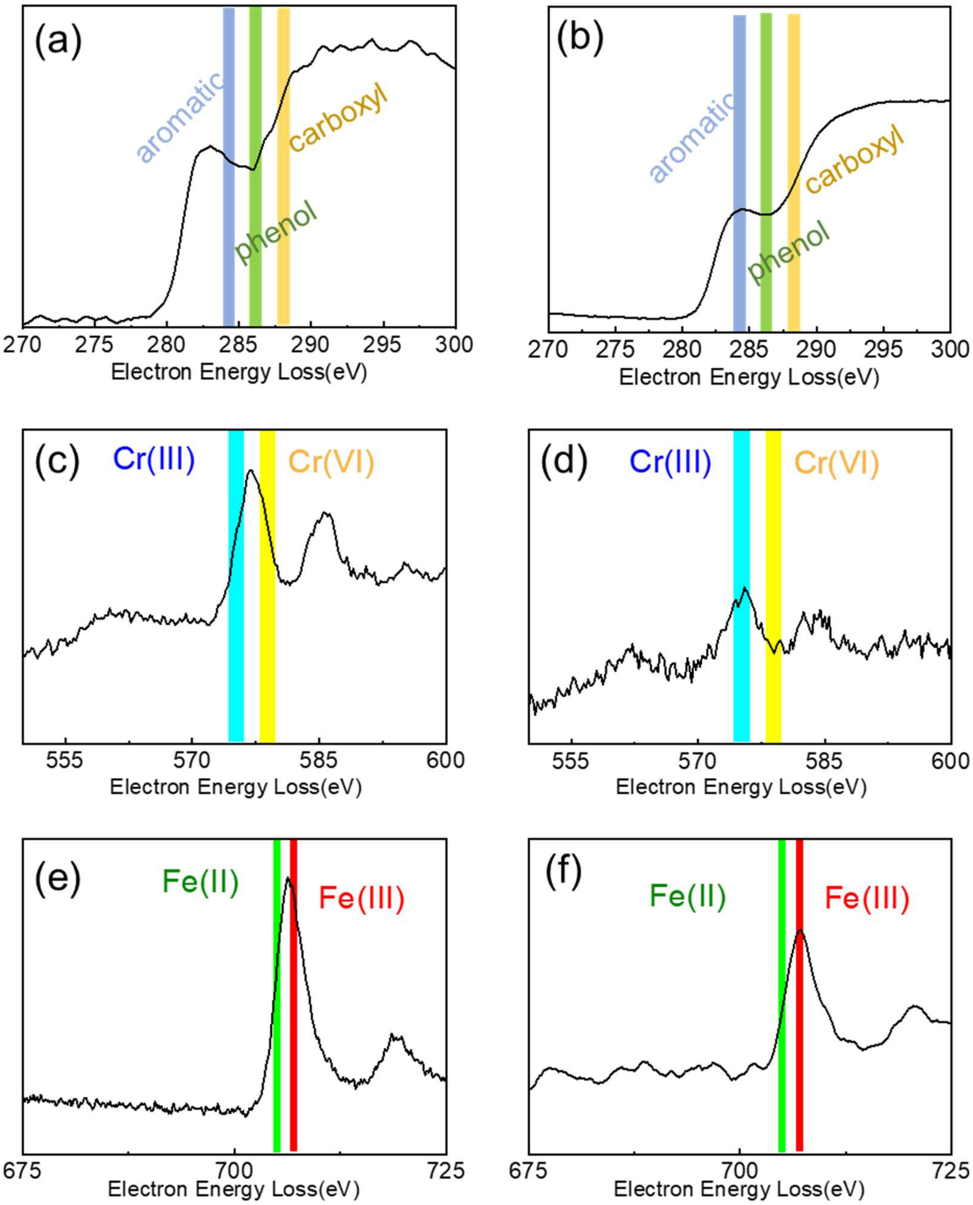

Figure E15. EELS pattern of C (a), Cr (c) and Fe (e) for biochar-Fe-L-Cr(VI) complex; EELS pattern of C (b), Cr (d) and Fe (f) for biochar-Fe-H-Cr(VI) complex. 574-576 eV was assigned to Cr(III); 580-582 eV was assigned to Cr(VI); 704.5-705.5 eV was assigned to Fe(II); 706.5-707.5 eV was assigned to Fe(III).284.75-285.25 eV was assigned to aromatic C; 286.5-287 eV was assigned to phenol; 286.75-287.25 eV was assigned to carboxyl.

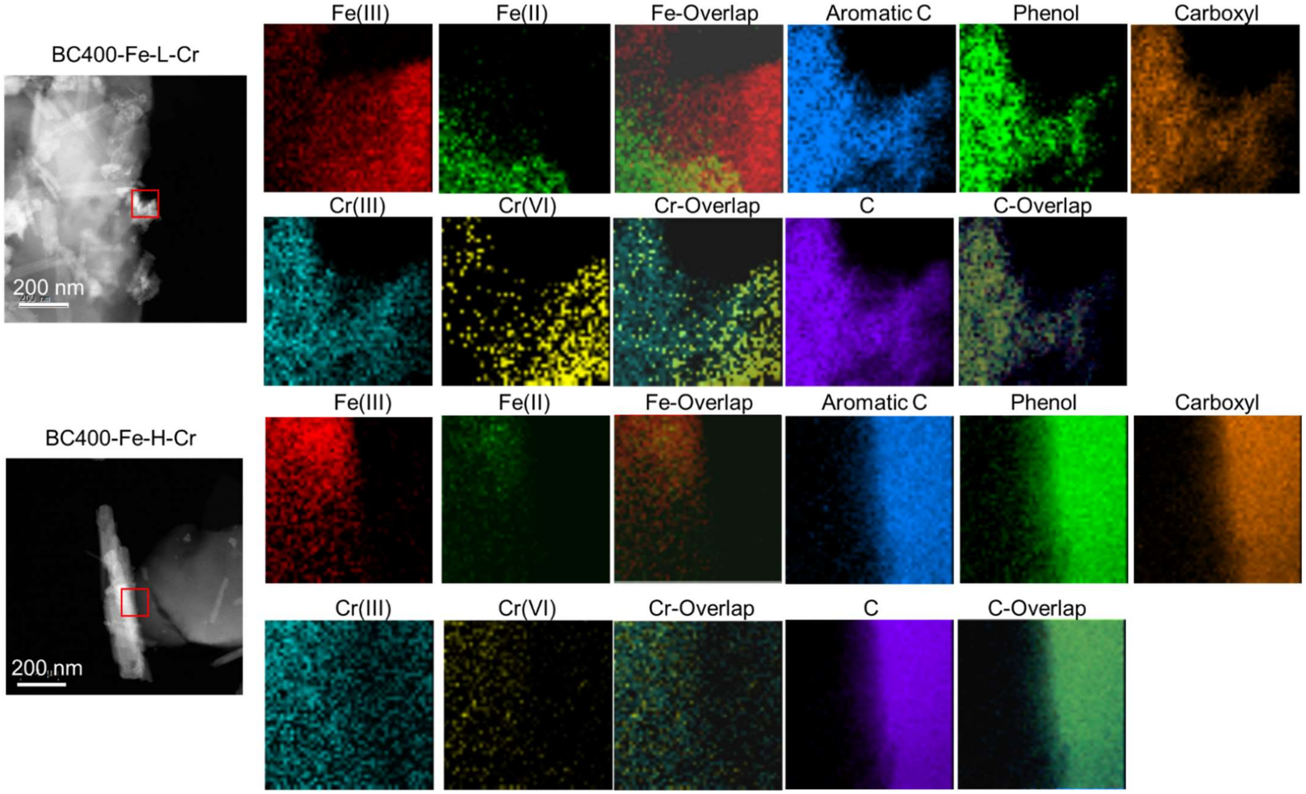

Figure E16. TEM images of the biochar-iron mineral complex after Cr(VI) reduction and EELS mapping of C, Cr, and Fe with different states on the selected area of Fe-L and Fe-H; 704.5-705.5 eV were assigned to Fe(II); 706.5-707.5 eV was assigned to Fe(III).284.75-285.25 eV was assigned to aromatic C; 286.5-287 eV was assigned to phenol; 286.75-287.25 eV was assigned to carboxyl. Long-range from 284-292 eV was assigned to all carbon (C) speciation. 574-576 eV was assigned to Cr(III); 580-582 eV was assigned to Cr(VI); Fe-overlap, Cr-overlap, and C-Overlap was the overlap figure of different speciation; The example of the selected range can be found in Figure E15.

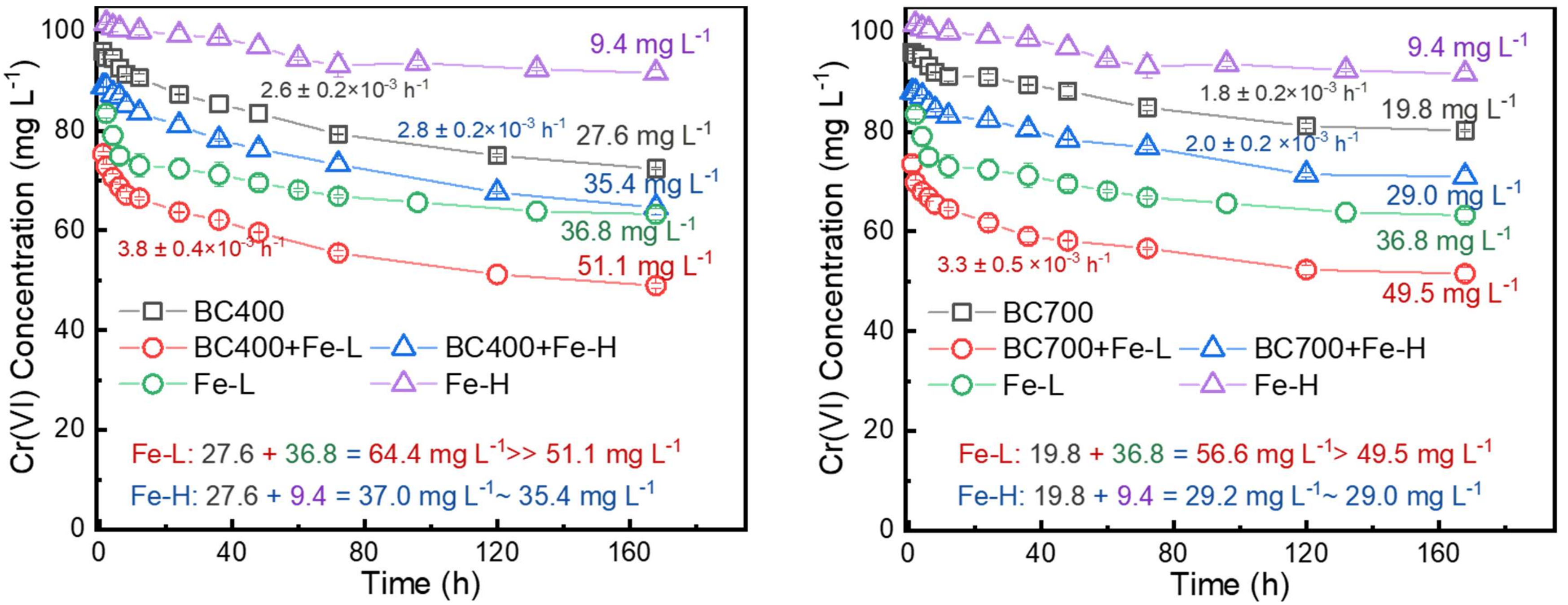

Figure E17. Comparison of the Cr(VI) reduction amount and reduction rate constant of biochar and biochar reduced iron mineral (*i.e.,* iron mineral incubated by iron mineral before the Cr(VI) reduction). Since the primary Cr speciation on the solid was Cr(III) after Cr(VI) removal (**Figure E18**), the Cr(VI) reduction was assumed to be the main immobilization for both biochar and biochar-reduced iron minerals. A higher reduction rate constant of biochar-reduced Fe-L (3.3-3.8 × 10^{-3} h^{-1}) was found compared with biochar (1.8-2.6 × 10^{-3} h^{-1}) and biochar-reduced Fe-H (2.0-2.8 × 10^{-3} h^{-1}), indicating the fast Cr(VI) reduction by Fe(II) formed on Fe-L.

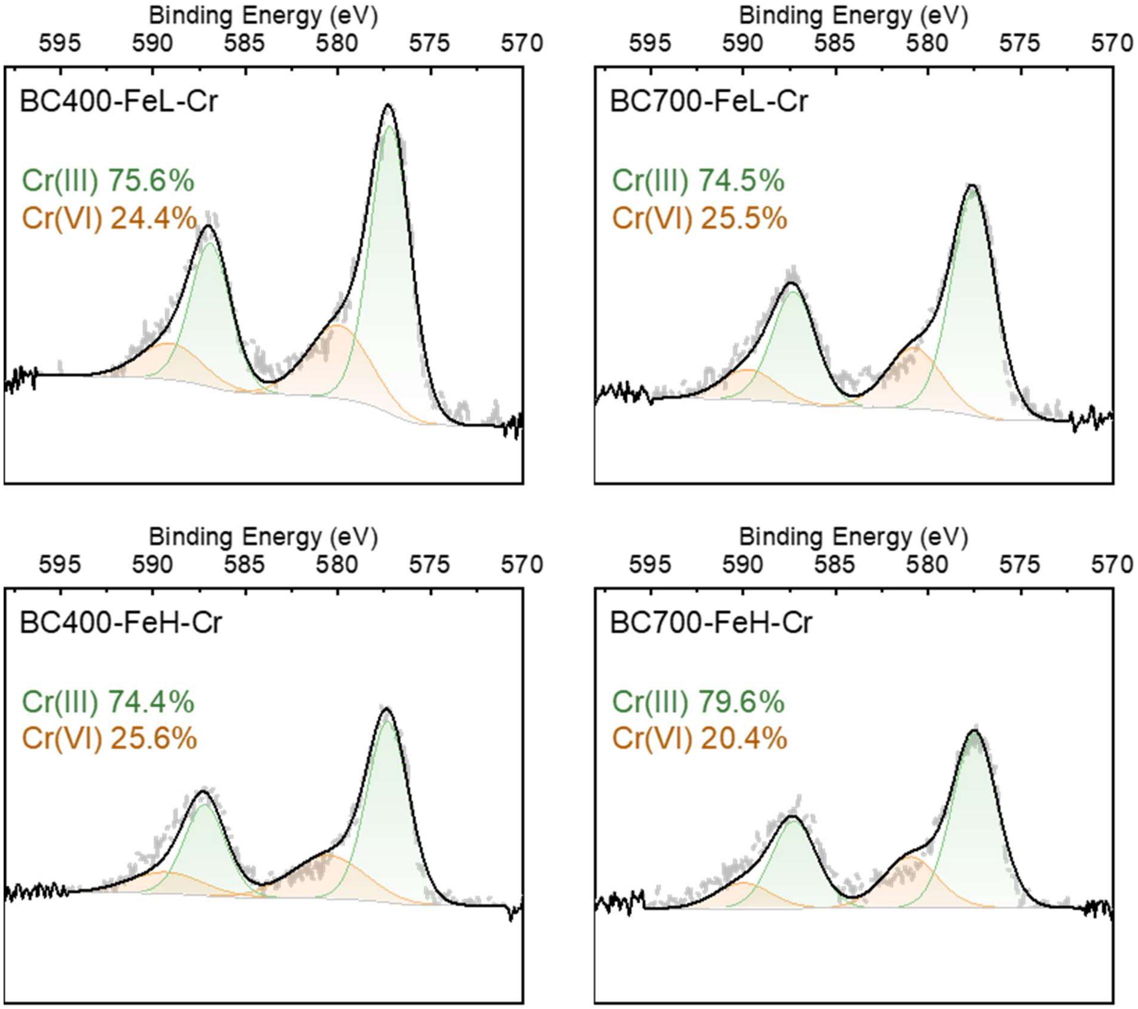

Figure E18. XPS spectra of Cr 2p for biochar reduced Fe mineral after Cr(VI) removal. Fe mineral was mixed and reduced by biochar prior to the Cr(VI) removal process.

Biochar-reduced iron mineral for Cr(VI) reduction.

Results showed that the primary speciation of Cr was Cr(III) of all biochar-ferric oxyhydroxide complex (74.4–79.6% by XPS analysis and 67.6–85.5% by alkaline extraction, **Figure E18**), indicating the reduction process was the primary immobilization mechanism for the Cr(VI) removal by biochar-reduced ferric oxyhydroxide. The higher proportion of Fe(II) on Fe-L might contribute to the reduction process, and its proportion decreases to 21.6–23.9% after Cr(VI) reduction (**Figure E13**).

Interestingly, we found that the reduction rate constant (**Figure E17**) of biochar-reduced Fe-L (3.3–3.8 × 10^{-3} h^{-1}) was much higher than biochar-reduced Fe-H (2.0–2.8 × 10^{-3} h^{-1}) and biochar alone (1.8–2.6 × 10^{-3} h^{-1}), implying the fast Cr(VI) reduction by the formed Fe(II) on ferric oxyhydroxide. This result also indicated that the indirect electron transfer routine through the valence transformation of Fe(II)/Fe(III) might have a higher opportunity than the direct electron-donating by biochar. It is worth mentioning that the total removal amount of Cr by biochar reduced Fe-L was still lower than the sum of biochar and Fe-L (**Figure E17**), indicating there is still a proportion of electron was consumed by the formation of Fe(II) on Fe-L after Cr(VI) reduction, which was also evidenced by the TEM-EELS analysis (**Figure E16**). Cr(VI) and Fe(III) were mainly found on the Fe-L far away from biochar, while Cr(III) and Fe(II) were the central speciations near the joint area of biochar and Fe-L (**Figure E16**). This distribution is similar to the biochar-Fe-L-Cr(VI) complex in the manuscript (**Figure 5-9**), which was prepared with a different addition order, *i.e.,* ferric oxyhydroxide was first mixed with Cr(VI), and then biochar was added, implying that this distribution was representative during the Cr(VI) reduction by biochar with low-crystallinity ferric oxyhydroxide. Besides, we also found that the crystalline size of the Fe-L significantly decreased from 17.6 nm to 14.9–15.3 nm after biochar reduction because of the Fe(III) reduction process and increased to 22.8–26.7 nm after Cr(VI) removal due to the Fe(II) oxidation by Cr(VI) (**Figure E9**). This transformation of the crystalline size of Fe-L also supported the valence transformation of Fe during the redox reaction with biochar and Cr(VI). In contrast, no noticeable change was shown in Fe-H during the interaction with biochar and Cr(VI) (28.9–29.8 nm).

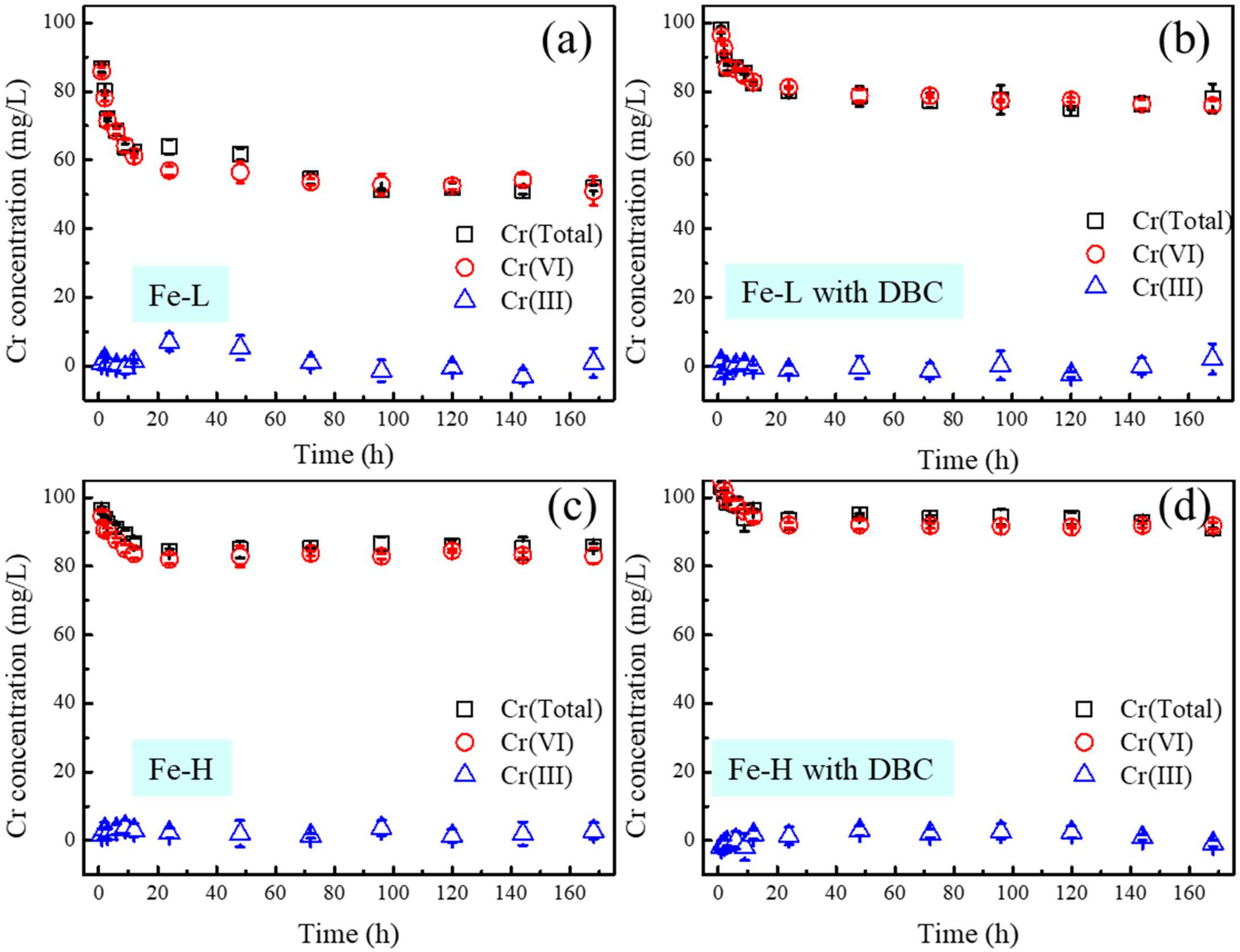

Figure E19. Changes in the concentration of Cr after addition of different iron minerals with or without dissolved biochar (DBC)

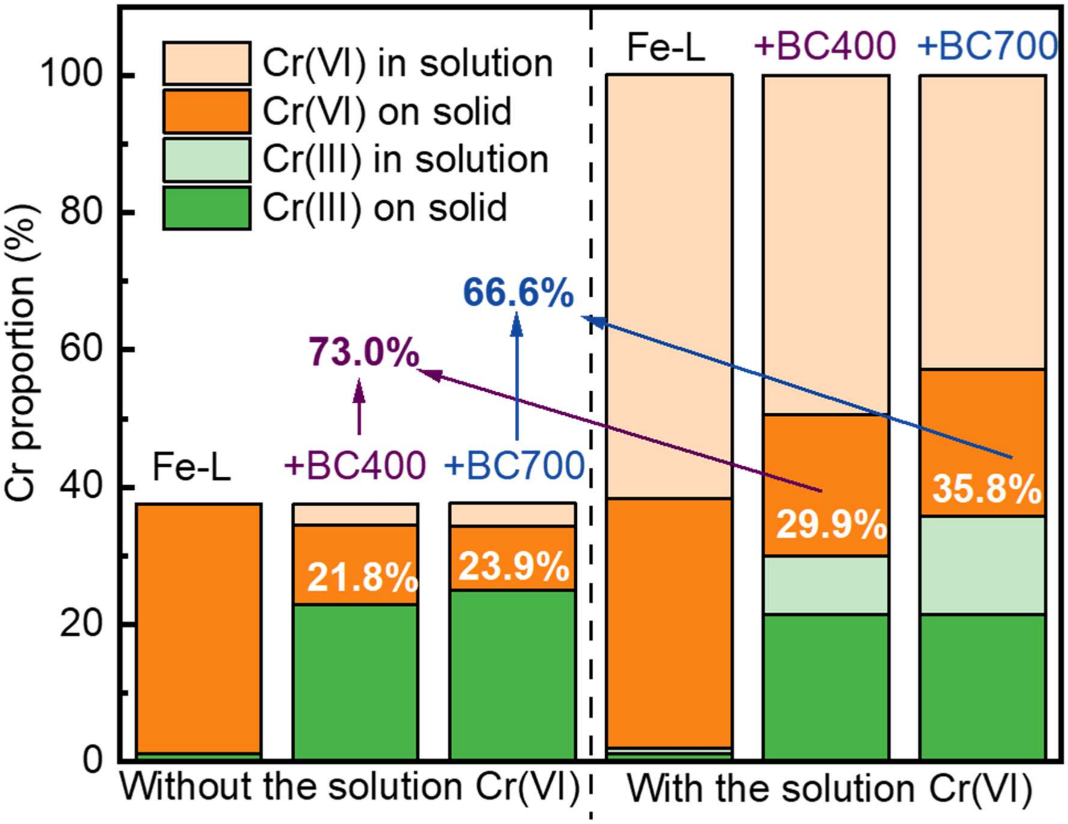

Figure E20 Comparison of the Cr(VI) reduction amount by biochar with Fe-L in the solution with/without Cr(VI). Cr(VI) in the solution was removed by replacing it with a background solution without Cr(VI) after 7-day sorption of Cr(VI) by Fe-L. The number in white represented the Cr(VI) reduction proportion launched by biochar addition. The number in blue and violet represented the contribution of the indirect electron transfer routine to the total reduction amount.

Appendix F

Batch removal of Cr(VI) in simulated wastewater or with the presence of anions

For the study about the impacts of the co-existed anions, the Cr(VI) concentration was set as 15 mg L^{-1}, and three co-existed anions (Cl^-, SO_4^{2-}, and PO_4^{3-}) with two different concentrations (molar ratio as 1:1 or 10:1) was selected. The pH was modified to around 6.5 by adding HCl or NaOH. For each setting, 0.05 g of Fe-Mn biochar, Fe biochar or commercial/modified ZVI was added into a 50-mL solution containing Cr(VI) and the co-existed ions in the wastewater, and the mixture was shaken at 250 rpm for 48 hours. Three different types of Cr(VI)-containing wastewater were also prepared according to the reported conditions in the literature: (i) electroplating wastewater (Zhu et al., 2022a): 200 mg L^{-1} Cr(VI), 125 mg L^{-1} Ca(II); 30 mg L^{-1} Al(III), 234 mg L^{-1} Zn(II), and 480 mg L^{-1} SO_4^{2-}, pH=2.84; (ii) smelting wastewater (Han et al., 2022): 750 mg L^{-1} Cr(VI), 400 mg L^{-1} Cu(II), 40 mg L^{-1} Zn(II), 20 mg L^{-1} Pb(II), and 5 mg L^{-1} Cd(II), pH=~2.0; (iii) textile wastewater (Abdel-Karim et al., 2021, Garg et al., 2022): 15 mg L^{-1} Cr(VI), 46.5 mg L^{-1} Ca(II), 0.15 mg L^{-1} Pb(II), 0.57 mg L^{-1} Ni(II), 15.6 mg L^{-1} Mg(II), 500 mg L^{-1} Na(I), and 485.6 mg L^{-1} SO_4^{2-}, 1g L^{-1} glucose, 0.2 g L^{-1} acetic acid, 0.6 g L^{-1} sucrose, and 0.1 g L^{-1} sodium dodecyl sulphate (total organic carbon was tested as 915.8 mg L^{-1}), pH=6.0. According to the maximum Fe efficiency for the Cr(VI) immobilization, different amount of materials (10 g L^{-1} for electroplating wastewater, 20 g L^{-1} for smelting wastewater, and 1 g L^{-1} for textile wastewater) was added to the simulated wastewater with 24 h (250 rpm) shaking afterwards. In addition to the different Fe-Mn biochar, modified/commercial ZVI was also selected as the adding material to evaluate ZVI's efficiency alone.

After the 24 h immobilization of Cr(VI) containing wastewater, these mixtures were filtered through a 0.45-μm membrane filter to collect the filtrates and solids. As mentioned above, the Cr(VI) concentration was analyzed through the diphenyl-carbohydrazide spectrophotometric, while ICP-OES was also used to detect the concentration of Cr(Total) and other metals in the wastewater. The Fe efficiency was also calculated accordingly.

ZVI modification

In addition to the commercial ZVI (opened within one month), three different modified ZVI were also prepared, and its potential for the Cr(VI) immobilization and Fe efficiency was analyzed. S-ZVI was modified according to the previous methods (Xu et al., 2020a); 200 mL of 37 g L^{-1} $NaBH_4$ and 2.2 g L^{-1} $Na_2S_2O_4$ solution (molar ratio, S: Fe = 0.14) was added (dropwise addition) into a continuously stirred 200 mL of 10 g L^{-1} Fe^{3+} solution under N_2 purging, followed by 10 min of stirring. The ratio and sulfur source was selected based on the previous studies, which reported that the as-prepared S-ZVI contained the best reactivity and selectivity (Xu et al., 2020a). Similarly, the Ni-ZVI was also prepared by reducing the Fe^{3+} solution and Ni^{2+} solution (molar ratio, Ni: Fe= 0.14) through the dropwise addition of $NaBH_4$ under N_2 protection (Zhu et al., 2017a). 200 mL of 37 g L^{-1} $NaBH_4$ was added into 200mL of 10 g L^{-1} Fe^{3+} and corresponding Ni^{2+} under N_2 purging, followed by 10 min of stirring. Reduced ZVI was prepared by mixing commercial ZVI particles (10 g L^{-1}) with $NaBH_4$ (37 g L^{-1}) with 30 mins stirring under N_2 protection. In all cases of modified ZVI, the formed particles were washed three times with deoxygenated DI water and freeze-dried. The vacuum was slowly released by air to stabilize the particles, which were ground and stored under anaerobic conditions before use.

First-principles calculations

All calculations in this study were performed with the Vienna ab initio Simulation Package

(VASP) within the framework of density functional theory (DFT). The exchange-correlation interactions of the electron were described via the generalized gradient approximation (GGA+U) with PBE functional, and the projector augmented wave (PAW) method was used to describe the interactions of electron and ion. The Monkhorst-Pack scheme4 with a 2x2x1 k-point mesh integrated the irreducible Brillouin zone. The kinetic energy cut-off of 500 eV was chosen for the plane wave expansion. The lattice parameters and ionic position were fully relaxed, and the total energy was converged within 10^{-5} eV per formula unit. The final forces on all ions were less than 0.02/Å.

DFT calculation was mainly conducted to analyze the formation routine of the embedded ZVI clusters on $FeMnO_2$ during the thermal reduction with biochar (reduction with the generated CO). In addition, the combination affinity of the Cr(VI) and O_2 on the $FeMnO_2$ and other iron minerals was also compared.

All the mineral model was set based on the crystal structure shown in Materials Project (https://materialsproject.org/). Details for the model of the $FeMnO_2$ (mp-1221648) are shown in **Figure F14**. The calculation model for the O vacancy was set by removing O beside the Fe-atom to simulate the partial reduction of Fe by the CO generated from biochar (**Figure F14).** Fe oxide (Fe_2O_3 (mp-19770) and FeO (mp-18905)) and Fe-Cr mineral ($FeCr_2O_4$ (mp-1104680) and $FeCrO_3$ (1078458)) were selected as the calculation model for the passivation layer of the ZVI after oxidation or complexation with Cr, respectively. The model details are also shown in **Figures F15-16**.

Economic Analysis

The feedstock cost of different materials was 39.5 USD kg^{-1} (Fe-Mn Biochar), 43.4 USD kg^{-1} (Fe Biochar), 289.1 USD kg^{-1} (Commercial ZVI), 2501.3 USD kg^{-1} (Reduced ZVI), 2975.8 USD kg^{-1} (S-ZVI), and 2860.1 USD kg^{-1} (Ni-ZVI) based on the average price from the varying companies (Innochem, Acros, Alfa, Macklin, Fisher, and Aladin; 597.9 USD kg^{-1} $NaBH_4$, 289.1 USD kg^{-1} Commerical iron powder, 204.2 USD kg^{-1} $FeCl_3 \cdot 6H_2O$, 219.1 USD kg-1 $MnCl_2 \cdot 4H_2O$, 69.7 USD kg$_{-1}$ $Na_2S_2O_4$, 185.1 USD kg^{-1} $NiCl_2 \cdot 6H_2O$). The price of biochar was set based on the price on Taobao (www.taobao.com, 4.15 USD kg^{-1} Biochar)

The feedstock cost of different materials was 39.5 USD Kg^{-1} (Fe-Mn Biochar), 43.4 USD Kg^{-1} (Fe Biochar), 289.1 USD Kg^{-1} (Commercial ZVI), 2501.3 USD Kg^{-1} (Reduced ZVI), 2975.8 USD Kg^{-1} (S-ZVI), and 2860.1 USD Kg^{-1} (Ni-ZVI) based on the chemicals from the varying companies (Innochem, Acros, Alfa, Macklin, and Aladin). After considering the cost for the pyrolysis process with different duration times, the preparation cost of different Fe-based materials is shown in **Table 6-2**. Considering the efficiency of industrial wastewater treatment, we found that Fe-Mn biochar produced with 2 and 4 h holding time offered the best economic benefits for treating all industrial wastewater (**Table 6-2**), which is significantly higher than the commercial and modified ZVI. It is also worth noting that the cost was calculated based on the lab level, and the potential cost for long-term storage and transportation was not included.

Table F1 XPS Depth-profiling results for the Fe 2p speciation and its relative atomic percentage on the Fe-Mn biochar

Biochar type	Depth (nm)	Fe(0) (%)	Fe(II) (%)	Fe(III) (%)
BC850-Fe-Mn-850-1h	0	0.0	73.5	26.5
	5	0.0	74.6	25.5
	10	0.0	78.0	22.0
	20	0.0	75.9	24.1
	50	0.6	76.0	23.5
	100	1.0	74.6	24.4
BC850-Fe-Mn-850-2h	0	5.0	69.8	25.2
	5	5.1	70.3	24.6
	10	11.2	66.5	22.3
	20	12.1	66.5	21.4
	50	12.9	66.2	20.9
	100	13.6	65.5	20.9
BC850-Fe-Mn-850-4h	0	2.0	67.7	30.3
	5	14.2	59.0	26.9
	10	17.9	58.2	24.0
	20	15.9	59.5	24.6
	50	15.2	58.9	25.9
	100	13.7	63.6	22.8
BC850-Fe-Mn-850-8h	0	3.3	74.1	22.6
	5	6.7	68.5	24.8
	10	9.7	65.4	24.9
	20	13.9	60.6	25.4
	50	15.5	60.1	24.4
	100	16.5	59.5	24.0
BC550-Fe-850-2h	0	0.0	77.1	22.9
	5	2.8	73.7	23.5
	10	4.2	71.4	24.4
	20	6.6	72.2	21.2
	50	10.6	68.4	21.0
	100	12.9	65.1	22.0

Table F2 XPS Depth-profiling results for the O 1s speciation and its relative atomic percentage on the Fe-Mn biochar

Biochar type	Depth (nm)	–C–OH (%)	–C–OC (%)	–C=O (%)	–M–OC (%)	Metal–O (%)	–C–OH + –C–OC /–C=O + –M–OC
BC850-Fe-Mn-850-1h	0	40.0	56.6	3.5	0.0	0.0	27.6
	5	37.1	55.6	5.8	1.6	0.0	12.5
	10	32.0	59.0	5.0	2.7	1.2	11.8
	20	29.2	61.8	4.6	4.4	0.1	10.1
	50	22.5	65.5	4.6	3.6	3.7	10.7
	100	22.2	62.3	6.3	4.3	4.9	8.0
BC850-Fe-Mn-850-2h	0	41.7	53.0	4.9	0.0	0.5	19.4
	5	36.0	56.1	6.8	0.0	1.1	13.6
	10	28.3	61.9	6.4	0.0	3.4	14.1
	20	23.1	66.1	7.6	0.0	3.2	11.7
	50	18.5	68.3	7.2	0.0	6.1	12.1
	100	16.2	69.5	6.1	0.0	8.1	14.1
BC850-Fe-Mn-850-4h	0	18.6	74.6	0.0	5.7	1.1	16.2
	5	27.3	51.3	14.6	2.1	4.7	4.7
	10	23.0	47.8	12.7	11.9	4.5	2.9
	20	12.4	23.2	21.1	33.0	10.3	0.7
	50	12.1	24.7	24.2	29.2	9.9	0.7
	100	11.8	24.4	20.0	33.3	10.5	0.7
BC850-Fe-Mn-850-8h	0	30.2	37.2	31.0	0.0	1.7	2.2
	5	29.4	41.4	17.9	8.1	3.1	2.5
	10	17.2	50.6	18.5	12.9	0.8	1.8
	20	14.8	50.2	23.4	9.4	2.2	2.7
	50	26.8	41.9	19.8	7.9	3.6	2.2
	100	24.7	39.3	28.9	6.9	0.1	2.0
BC550-Fe-850-2h	0	16.1	35.3	16.8	1.4	30.5	2.8
	5	15.5	30.0	18.2	1.5	34.9	2.3
	10	14.9	30.2	18.7	0.4	35.8	2.4
	20	12.7	29.2	21.5	1.0	35.8	1.9
	50	11.7	28.6	23.5	0.9	35.3	1.7
	100	9.3	27.1	27.8	1.9	34.0	1.2

Table F3 XPS Depth-profiling results for the elemental content and its atomic ratio on the Fe-Mn biochar

Biochar type	Depth (nm)	C (%)	O (%)	Mn (%)	Fe (%)	O/C	Fe/Mn	O/Fe
BC850-Fe-Mn-850-1h	0	89.1	9.7	0.7	0.5	0.11	0.78	18.31
	5	90.4	8.1	1.0	0.5	0.09	0.52	16.18
	10	91.0	7.5	0.9	0.6	0.08	0.62	13.46
	20	91.4	7.3	0.8	0.5	0.08	0.61	14.77
	50	91.9	6.6	0.9	0.6	0.07	0.70	10.94
	100	92.6	6.0	0.8	0.6	0.07	0.75	10.12
BC850-Fe-Mn-850-2h	0	87.7	11.3	0.5	0.5	0.13	1.06	21.87
	5	90.2	8.7	0.6	0.5	0.10	0.95	16.11
	10	91.1	7.9	0.6	0.5	0.09	0.81	15.95
	20	89.9	8.9	0.6	0.6	0.10	1.04	14.13
	50	90.8	7.8	0.7	0.7	0.09	0.94	11.23
	100	91.4	7.2	0.7	0.7	0.08	1.01	9.80
BC850-Fe-Mn-850-4h	0	86.7	12.3	0.5	0.6	0.14	1.20	21.73
	5	86.7	12.1	0.5	0.6	0.14	1.29	18.75
	10	88.1	11.1	0.4	0.4	0.13	1.05	27.38
	20	90.0	9.2	0.4	0.4	0.10	1.07	22.19
	50	90.9	8.2	0.4	0.4	0.09	1.08	18.50
	100	91.6	7.5	0.4	0.4	0.08	0.97	17.64
BC850-Fe-Mn-850-8h	0	87.5	11.1	1.0	0.3	0.13	0.33	32.78
	5	91.2	7.0	1.2	0.6	0.08	0.45	12.48
	10	91.7	6.7	1.2	0.4	0.07	0.33	16.75
	20	92.2	6.4	1.0	0.4	0.07	0.40	15.36
	50	92.8	5.8	0.9	0.5	0.06	0.50	12.31
	100	93.1	5.6	0.9	0.5	0.06	0.58	11.32
BC550-Fe-850-2h	0	87.8	10.8	/	1.4	0.12	/	7.83
	5	86.9	11.1		2.0	0.13		5.54
	10	86.6	11.3		2.0	0.13		5.57
	20	85.8	12.0		2.1	0.14		5.62
	50	85.2	12.1		2.7	0.14		4.57
	100	85.1	12.0		2.9	0.14		4.07

Table F4 XPS Depth-profiling results for the Mn 2p speciation and its relative atomic percentage on the Fe-Mn biochar

Biochar type	Depth (nm)	Mn(II) (%)	Mn(III) (%)	Mn(IV) (%)	Average state
BC850-Fe-Mn-850-1h	0	0.0	62.8	37.2	3.4
	5	52.8	15.9	31.2	2.8
	10	56.2	19.1	24.7	2.7
	20	71.9	0.0	28.1	2.6
	50	76.5	0.0	23.4	2.5
	100	75.1	0.0	24.9	2.5
BC850-Fe-Mn-850-2h	0	0.0	35.7	64.3	3.6
	5	0.0	60.6	39.4	3.4
	10	0.0	63.8	36.2	3.4
	20	0.0	63.8	36.2	3.4
	50	7.2	65.3	27.5	3.2
	100	3.7	63.2	33.1	3.3
BC850-Fe-Mn-850-4h	0	1.4	33.1	65.5	3.6
	5	8.7	53.6	37.8	3.3
	10	9.8	54.1	36.1	3.3
	20	9.9	59.1	31.1	3.2
	50	7.2	63.4	29.4	3.2
	100	0.0	65.3	34.7	3.3
BC850-Fe-Mn-850-8h	0	0.0	14.7	85.3	3.9
	5	0.0	19.7	80.3	3.8
	10	0.0	46.1	53.9	3.5
	20	0.0	36.3	63.7	3.6
	50	0.0	61.7	38.3	3.4
	100	3.8	56.8	39.4	3.4
BC850-Fe-Mn-850-2h after accelerated oxidation	0	19.4	71.8	8.8	2.9
	5	46.1	40.5	13.5	2.7
	10	53.6	16.4	30.0	2.8
	20	65.2	3.2	31.6	2.7
	50	23.9	42.9	33.2	3.1
	100	46.6	21.1	32.3	2.9
BC850-Fe-Mn-850-2h after natural oxidation	0	0.0	69.0	31.0	3.3
	5	13.4	10.9	75.8	3.6
	10	62.4	10.0	27.6	2.7
	20	68.7	4.8	26.5	2.6
	50	0.0	53.1	46.9	3.5
	100	19.3	14.3	66.5	3.5

Table F5 XPS Depth-profiling results for the speciation of Fe, Mn, and Cr, and the atomic content on the Fe-Mn biochar after Cr(VI) removal

Biochar type	Depth (nm)	Fe speciation			Mn speciation				Cr speciation		Atomic content (%)					Ratio		
		Fe(0) (%)	Fe(II) (%)	Fe(III) (%)	Mn(II) (%)	Mn(III) (%)	Mn(IV) (%)	Average state	Cr(III) (%)	Cr(VI) (%)	C	O	Cr	Mn	Fe	O/C	Cr/Fe	Cr/C
BC850-Fe-Mn-850-2h	0	0.0	73.3	26.7	0.0	69.1	30.9	3.3	80.7	19.3	74.8	20.7	3.4	0.6	0.5	0.28	7.06	0.05
	5	0.0	74.9	25.1	0.0	74.7	25.3	3.3	85.0	15.0	80.2	14.9	3.8	0.6	0.5	0.19	7.99	0.05
	10	0.1	76.7	23.2	0.0	59.7	40.3	3.4	83.4	16.6	83.7	12.3	3.2	0.5	0.4	0.15	8.87	0.04
	20	1.6	72.7	25.6	0.0	62.1	37.9	3.4	84.9	15.2	87.4	9.3	2.4	0.5	0.4	0.11	5.81	0.03
	50	0.0	70.5	29.5	0.0	45.7	54.3	3.5	85.3	14.7	90.3	7.2	1.7	0.4	0.4	0.08	4.79	0.02
	100	0.0	73.2	26.8	0.0	0.0	100.0	4.0	82.8	17.2	91.5	6.2	1.4	0.4	0.5	0.07	3.08	0.02
BC550-Fe-850-2h	0	0.0	73.1	26.9			/		82.8	17.2	67.9	27.2	2.9		2.0	0.40	1.43	0.04
	5	0.0	71.1	29.0					84.0	16.0	62.5	29.6	4.6		3.3	0.47	1.42	0.07
	10	0.0	74.5	25.5					83.0	17.1	63.2	28.8	5.1		3.0	0.46	1.73	0.08
	20	1.4	71.3	27.3					85.1	14.9	64.9	27.2	5.2		2.7	0.42	1.89	0.08
	50	4.8	71.6	23.6					83.4	16.6	70.6	22.1	4.7		2.7	0.31	1.79	0.07
	100	6.2	72.7	21.1					84.5	15.5	74.4	19.2	4.2		2.2	0.26	1.90	0.06

Table F6 XPS Depth-profiling results for the Fe 2p speciation and its relative atomic percentage on the Fe-Mn biochar after the oxidation process

Biochar	Depth (nm)	Fe(0) (%)	Fe(II) (%)	Fe(III) (%)
BC850-Fe-Mn-850-2h after accelerated oxidation	0	2.0	70.5	27.6
	5	1.5	72.8	25.8
	10	4.5	71.7	23.8
	20	9.8	65.5	24.7
	50	8.6	68.6	22.8
	100	13.2	64.4	22.4
BC850-Fe-Mn-850-2h after natural oxidation	0	5.0	69.8	25.2
	5	1.7	69.4	28.9
	10	6.0	69.0	25.0
	20	7.7	67.5	24.8
	50	10.2	64.6	25.2
	100	10.6	64.7	24.7
BC550-Fe-850-2h after accelerated oxidation	0	0.0	63.5	36.5
	5	0.0	73.6	26.4
	10	0.0	75.2	24.8
	20	0.0	69.8	30.2
	50	0.0	68.9	31.2
	100	3.8	65.1	31.1
BC550-Fe-850-2h after natural oxidation	0	0.0	73.4	26.6
	5	0.0	71.8	28.2
	10	2.8	69.5	27.7
	20	3.2	67.0	29.8
	50	3.9	67.0	29.0
	100	4.6	69.7	25.7

Table F7 XPS Depth-profiling results for the elemental content and its atomic ratio on the Fe-Mn biochar after the oxidation process

Biochar type	Depth (nm)	C (%)	O (%)	Mn (%)	Fe (%)	O/C	Fe/Mn	O/Fe
BC850-Fe-Mn-850-2h after acclerated oxidation	0	84.0	14.8	0.6	0.7	0.18	1.23	20.95
	5	84.8	13.8	0.6	0.8	0.16	1.33	16.88
	10	85.1	13.4	0.6	0.8	0.16	1.26	16.81
	20	86.5	12.2	0.6	0.8	0.14	1.35	15.78
	50	86.1	12.1	0.9	0.9	0.14	1.05	13.38
	100	87.4	11.1	0.9	0.8	0.13	1.11	13.23
BC850-Fe-Mn-850-2h after natural oxidation	0	83.6	15.1	0.6	0.8	0.18	1.19	20.02
	5	84.8	13.2	0.9	1.1	0.16	1.30	12.04
	10	85.6	12.3	1.0	1.0	0.14	0.97	12.09
	20	85.8	12.4	0.9	0.9	0.14	1.05	13.85
	50	86.5	11.4	0.9	1.1	0.13	1.20	10.19
	100	87.0	11.0	1.1	1.0	0.13	0.93	11.09
BC550-Fe-850-2h after acclerated oxidation	0	82.8	15.7	/	1.5	0.19	/	10.55
	5	82.8	15.9		1.3	0.19		12.44
	10	83.4	14.9		1.7	0.18		8.79
	20	84.1	14.0		1.9	0.17		7.60
	50	86.5	11.7		1.8	0.14		6.34
	100	86.1	12.0		1.9	0.14		6.30
BC550-Fe-850-2h after natural oxidation	0	81.6	16.8		1.7	0.21		10.08
	5	80.5	17.6		1.9	0.22		9.26
	10	80.5	17.1		2.4	0.21		7.26
	20	82.5	14.9		2.6	0.18		5.67
	50	85.1	12.7		2.2	0.15		5.66
	100	86.3	11.8		1.8	0.14		6.43

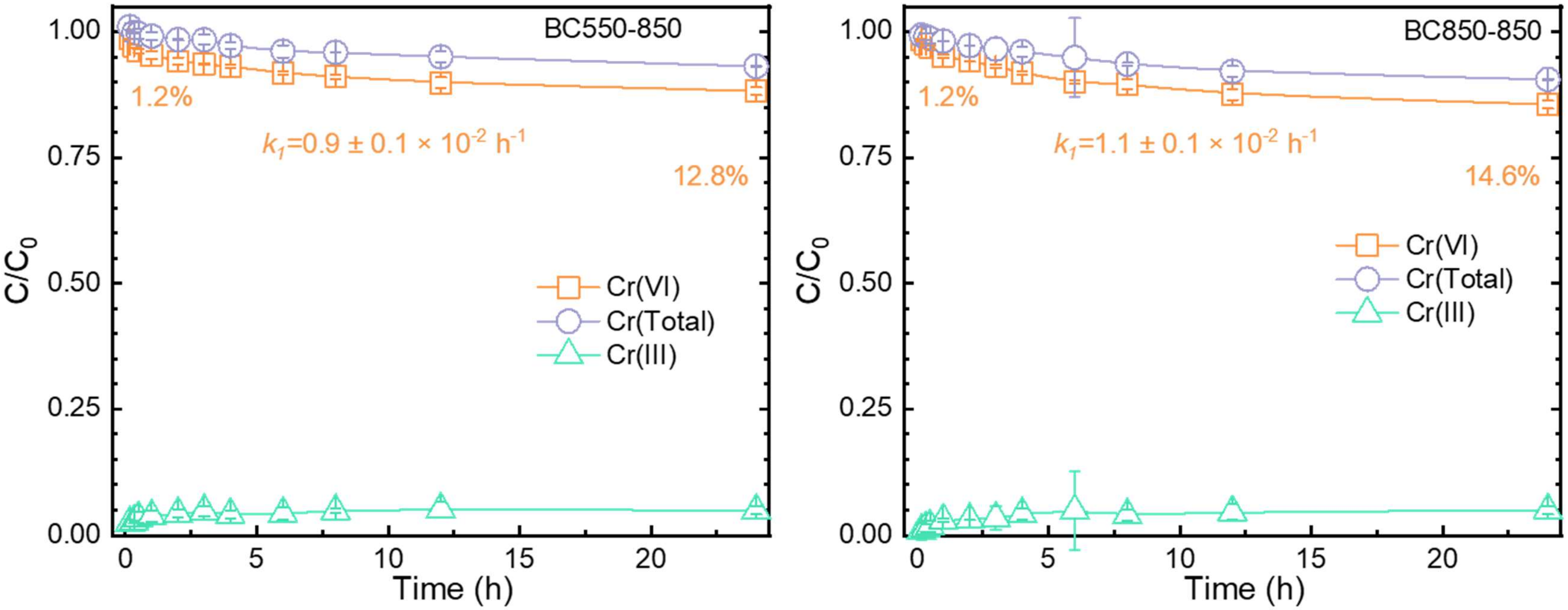

Figure F1. Cr concentration during the 24-h removal by pristine biochar. The numbers showed the removal proportion after 0.25 or 24 h reaction and the removal kinetics constants.

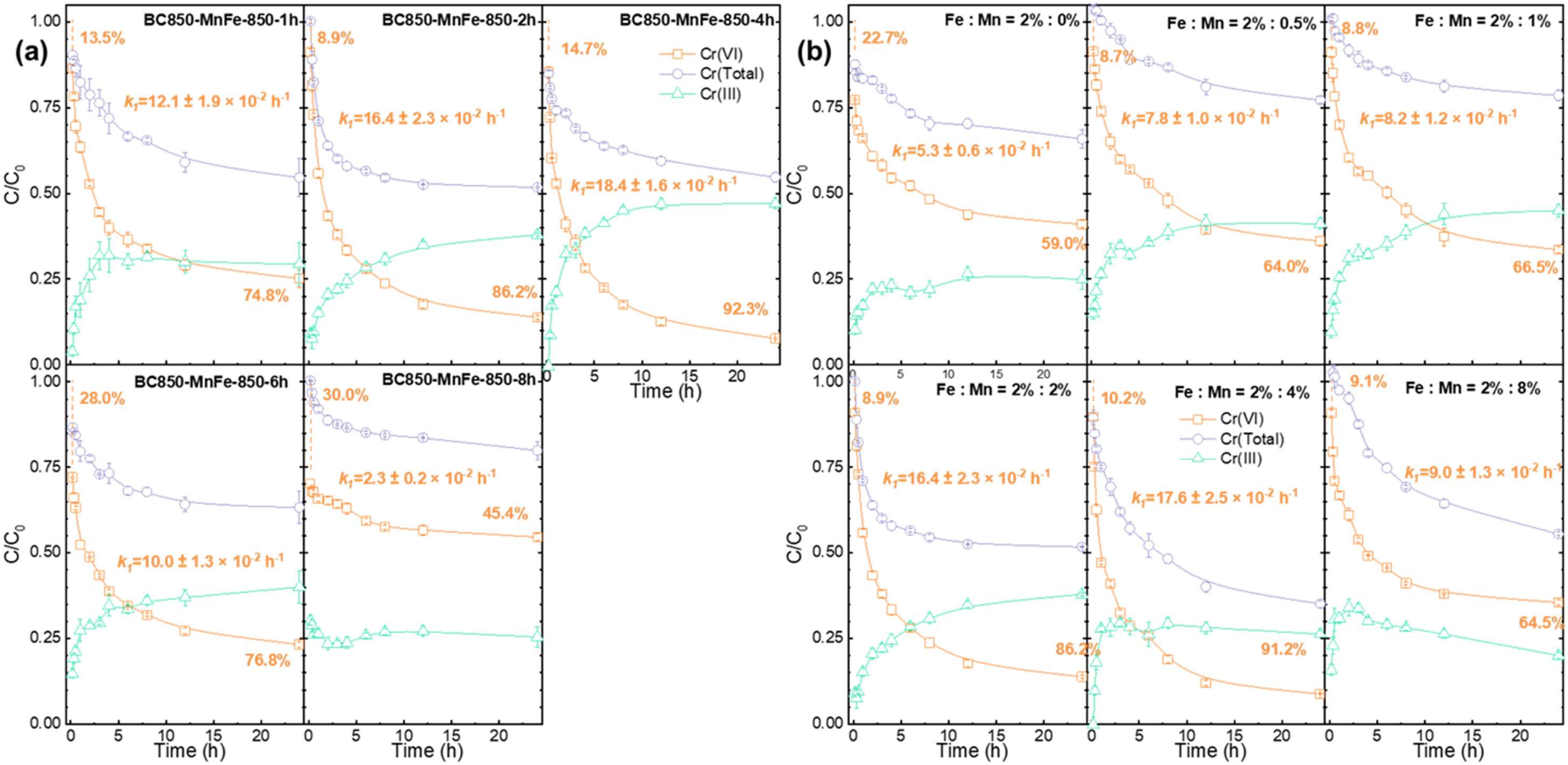

Figure F2. Cr concentration during the 24-h removal by Fe-Mn biochar with different hold times (a) or different Fe:Mn ratios (b). The numbers showed the removal proportion after 0.25 or 24 h reaction and the removal kinetics constants.

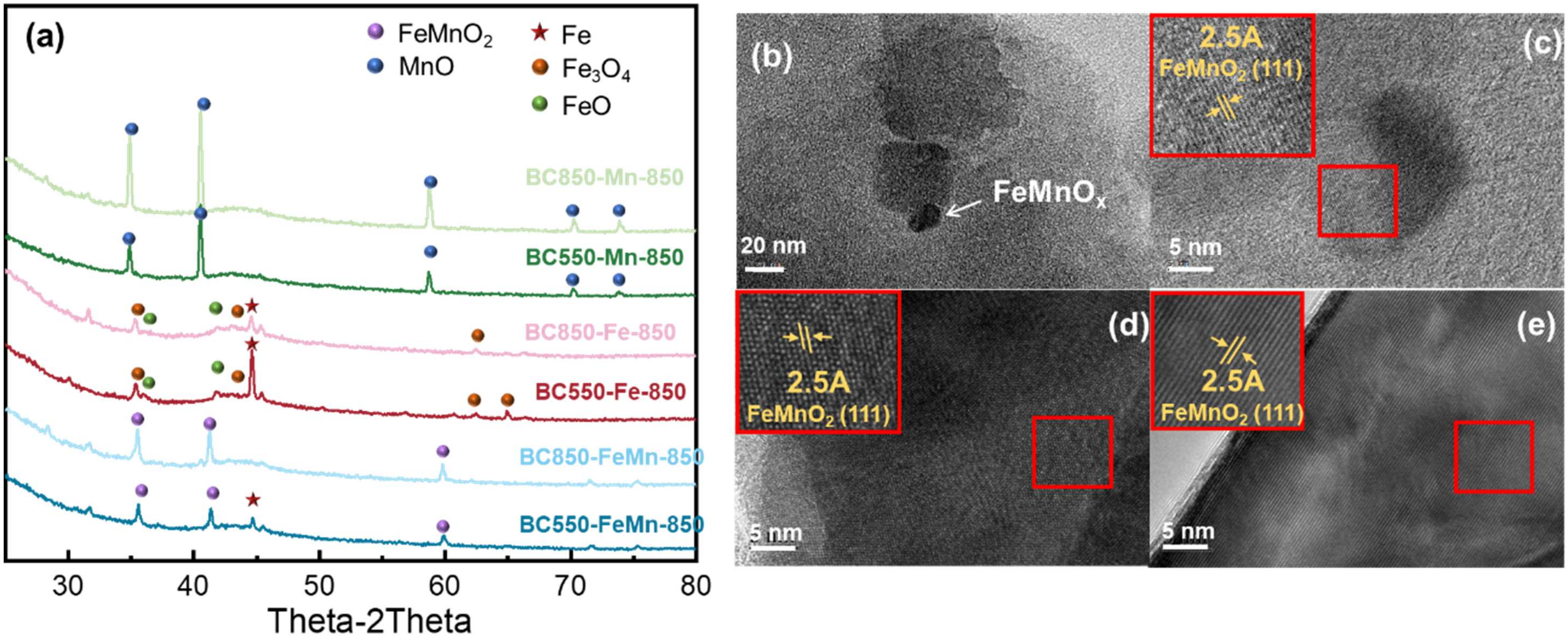

Figure F3. XRD pattern of different Fe-Mn biochars, Fe biochars, and Mn biochars (a); AC-STEM image of the BC850-FeMn-850-2h(b,c), BC850-Fe-Mn-4h (d), and BC850-FeMn-850-6h (e).

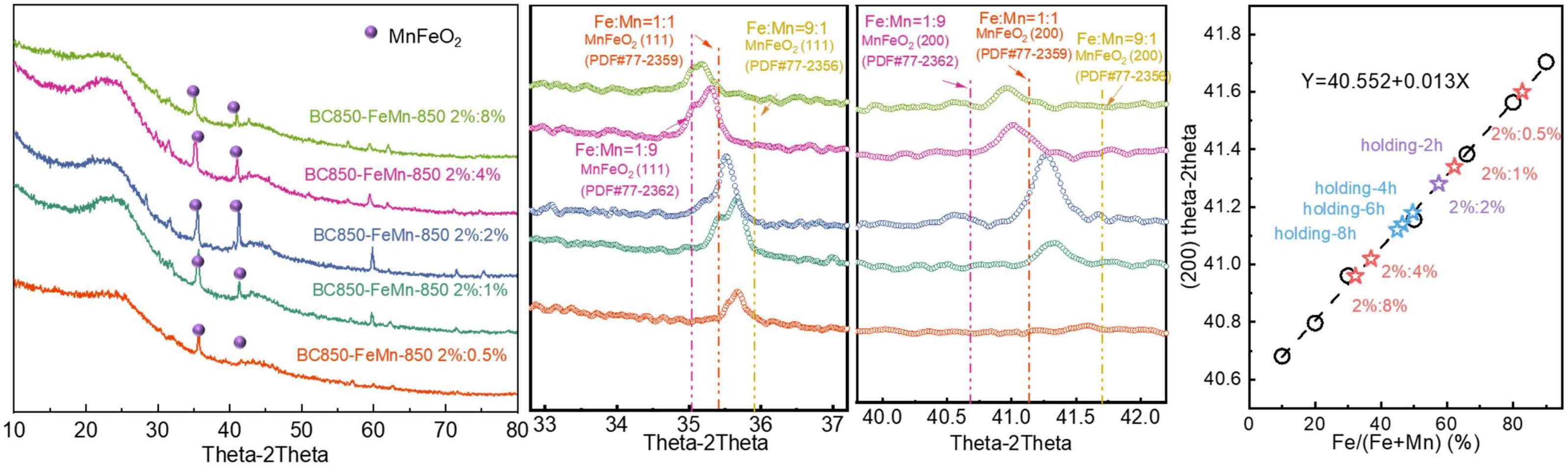

Figure F4. XRD pattern of Fe-Mn biochar with different Fe: Mn ratios (left); The comparison of the peak position of Fe-Mn biochar with MnFeO$_2$ contained different Fe: Mn ratios from the standard database (middle). Relationship between the peak position of (200) plane and Fe proportion in the FeMnO$_2$ oxide obtained from the standard minerals and Fe-Mn biochars (right).

The standard peak position of a series of FeMnO2 from the database, including $(FeO)_{0.1}(MnO)_{0.9}$ (77-2362), $(FeO)_{0.2}(MnO)_{0.8}$ (77-2361), $(FeO)_{0.33}(MnO)_{0.67}$ (77-2360), $(FeO)_{0.5}(MnO)_{0.5}$ (77-2359), $(FeO)_{0.67}(MnO)_{0.33}$ (77-2358), $(FeO)_{0.8}(MnO)_{0.2}$ (77-2357), and $(FeO)_{0.9}(MnO)_{0.1}$ (77-2356), was used to evaluate the proportion of FeO in the formed FeMnO2 on biochar. A linear relationship could be found between the peak position and the FeO proportion from the database. Based on this relationship, the proportion of FeO in the FeMnO$_2$ of Fe-Mn biochar produced with different ratios and hold times was calculated.

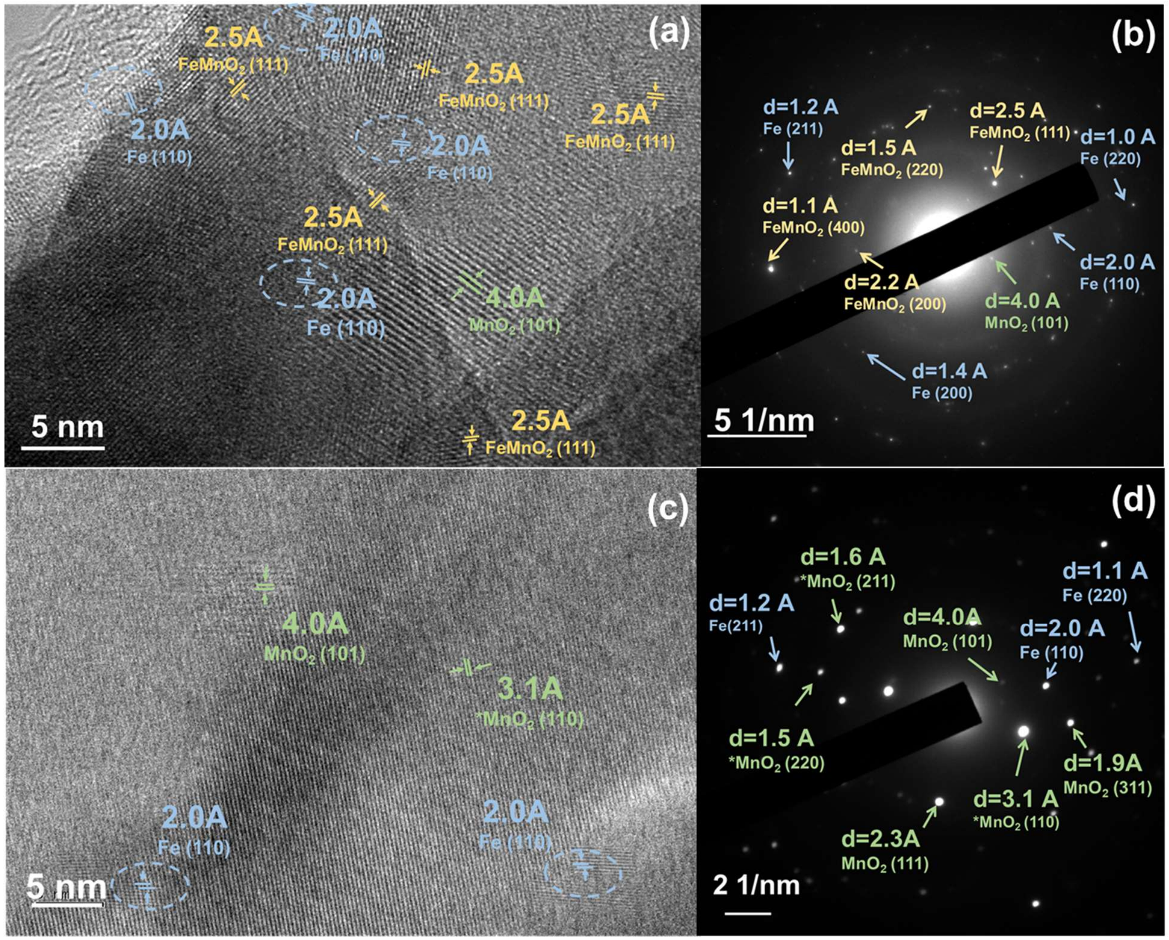

Figure F5. AC-STEM with SAED analysis for the representative area of BC850-FeMn-850-2h (a-b) and BC850-FeMn-850-4h (c-d) with Fe(0) (PDF#06-0696), FeMnO$_2$ (PDF#77-2359) and MnO$_2$ (PDF#24-0735 and PDF#44-0142) formation.

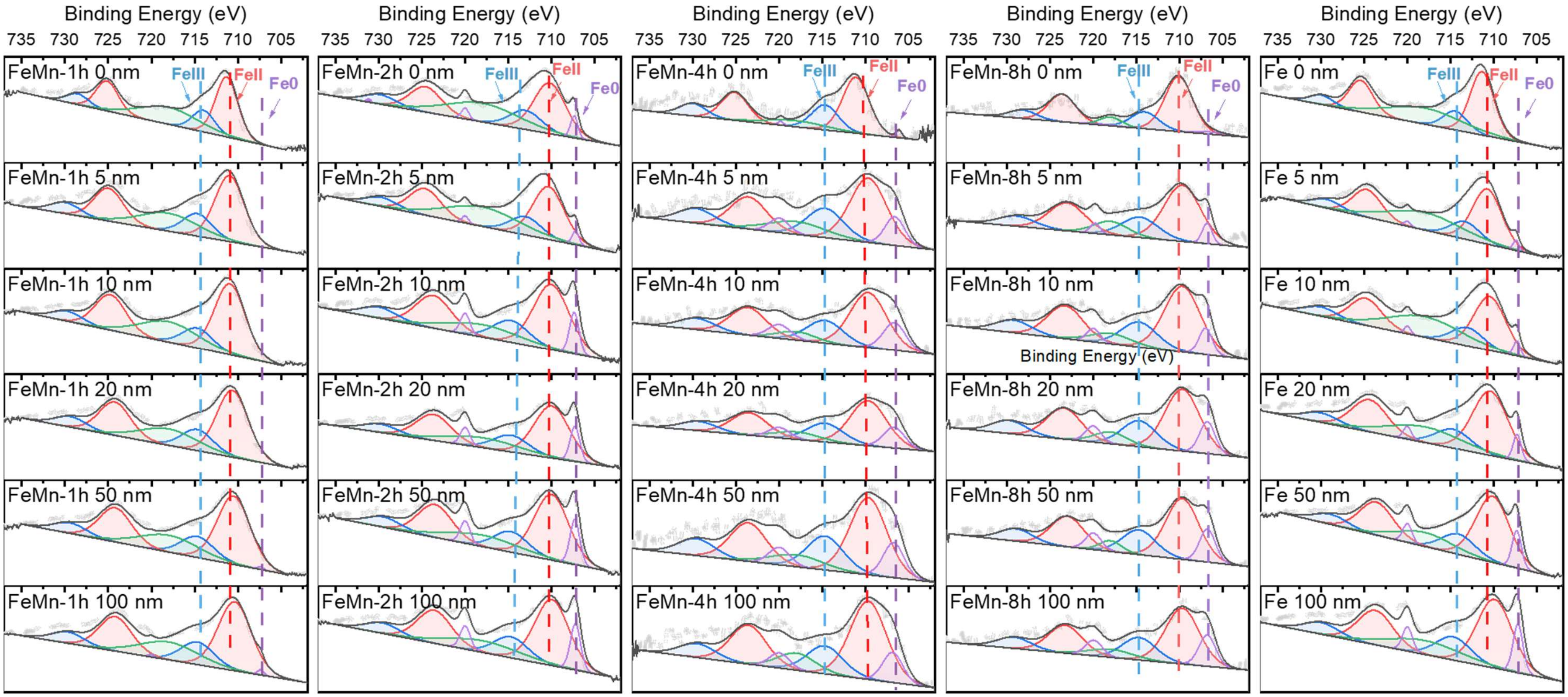

Figure F6. XPS depth profiling analysis of the Fe2p binding state in the selected biochars (Fe-Mn biochar with a hold time of 1, 2, 4, and 8 h and Fe biochar, the detailed proportion could be found in Table F1)

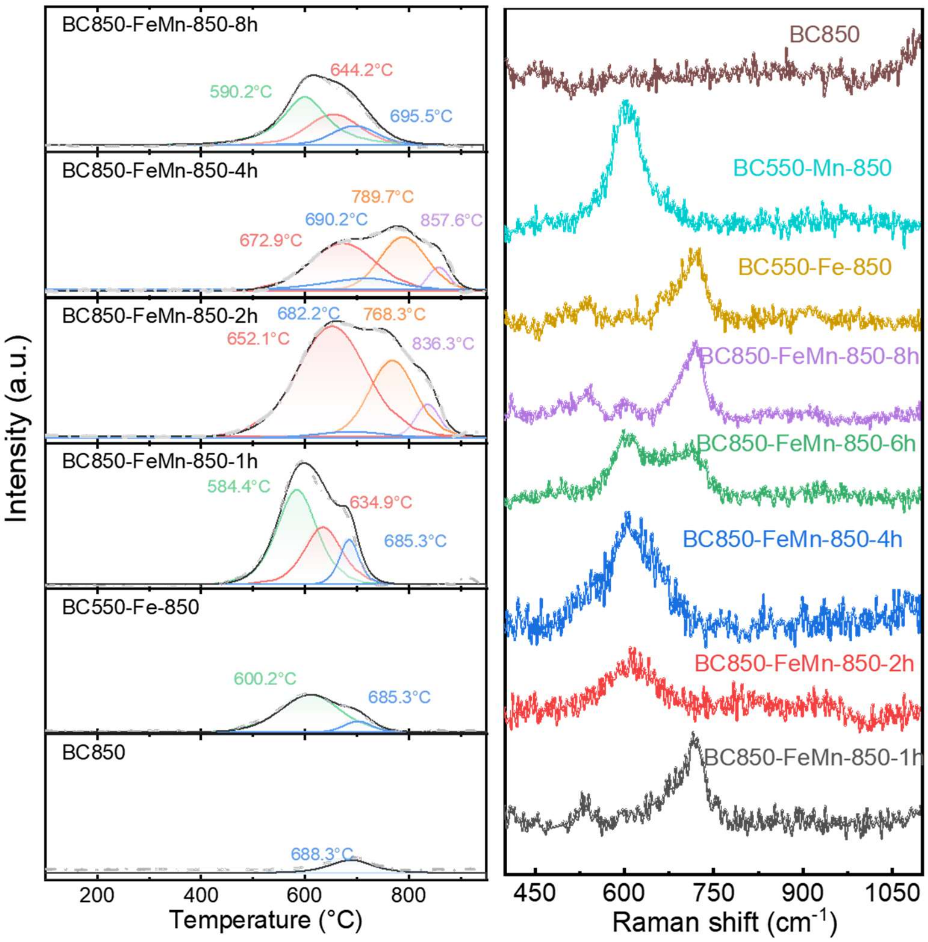

Figure F7. H_2-TRP and Raman analysis of modified biochar.

H_2-TPR analysis also revealed the transformation of Fe speciation during the pyrolysis process. BC850 only showed a peak at ~690 °C due to carbon gasification, while another peak (~600 °C) appeared in BC550-Fe-850 due to the reduction of iron oxides (mainly amorphous ferrous oxides) to metallic iron (Gai et al., 2017, Li et al., 2020c). The reduction peak of iron oxides to ZVI was only shown in the BC850-FeMn-850-1h and BC850-FeMn-850-8h, indicating the presence of similar iron species compared with BC550-Fe-850. Interestingly, several unique peaks at ~650 °C, ~770 °C, and ~840 °C appeared in BC850-FeMn-850-2h and BC850-FeMn-850-4h, which were attributed to the reduction of the Fe−O structure in the $FeMnO_2$. The Fe−O within $FeMnO_2$ (i.e., Fe−O−Mn) was more stable than that in ferrous oxides and required higher energy for reduction. A similar phenomenon was observed in the Fe−O reduction after the coordination with SiO_2 due to the formation of the Fe−O−Si structure

(Li et al., 2020c). In addition, the higher required temperature might be related to the stabilization of FeO structure by the oxide support with strong interfacial compatibility (Wang et al., 2021e, Zhou et al., 2022a). The intensity of all reduction peaks in BC850-FeMn-850-4h was lower than that in BC850-FeMn-850-2h, which corroborated the decrease of oxygen content in the Fe-Mn oxides along with the formation of ZVI clusters.

Raman spectrum further supported the in-situ formation of embedded ZVI clusters during pyrolysis. Characteristic peaks of iron oxides (~700 and 540 cm^{-1}) (Achola et al., 2020, Gong et al., 2021, López-Sánchez et al., 2022) were shown in the BC550-Fe-850, BC850-FeMn-850-1h, BC850-FeMn-850-6h, and BC850-FeMn-850-8h, indicating the surface passivation of ZVI alone due to natural oxidation or Raman scattering. By contrast, only characteristic peaks of the Mn−O bonding (~640 cm^{-1}) (Li et al., 2020b, Portillo-Vélez and Zanella 2020) could be found in BC550-Mn-850, BC850-FeMn-850-2h, and BC850-FeMn-850-4h samples, and no noticeable peaks of the iron oxides were formed. This result supported that the nature of ZVI in the BC850-FeMn-850-2h and BC850-FeMn-850-4h notably differed from the ZVI particles in the Fe biochar, and they featured greater stability against oxidation. Moreover, Fe−O bonding peaks were formed again in the BC850-FeMn-850-6h and BC850-FeMn-850-8h, evidencing the ZVI reformation under a relatively long pyrolysis period.

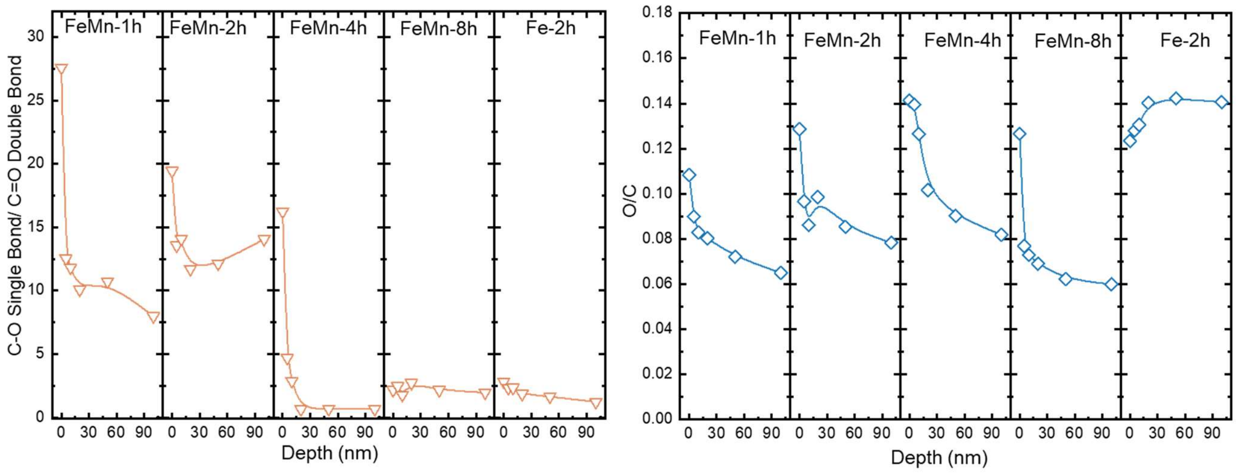

Figure F8. The ratio of C-O/C=O under the different depths of Fe-Mn/Fe biochar (left, Table F2); The O/C ratio under different depths of Fe-Mn/Fe-biochar (right, Table F3)

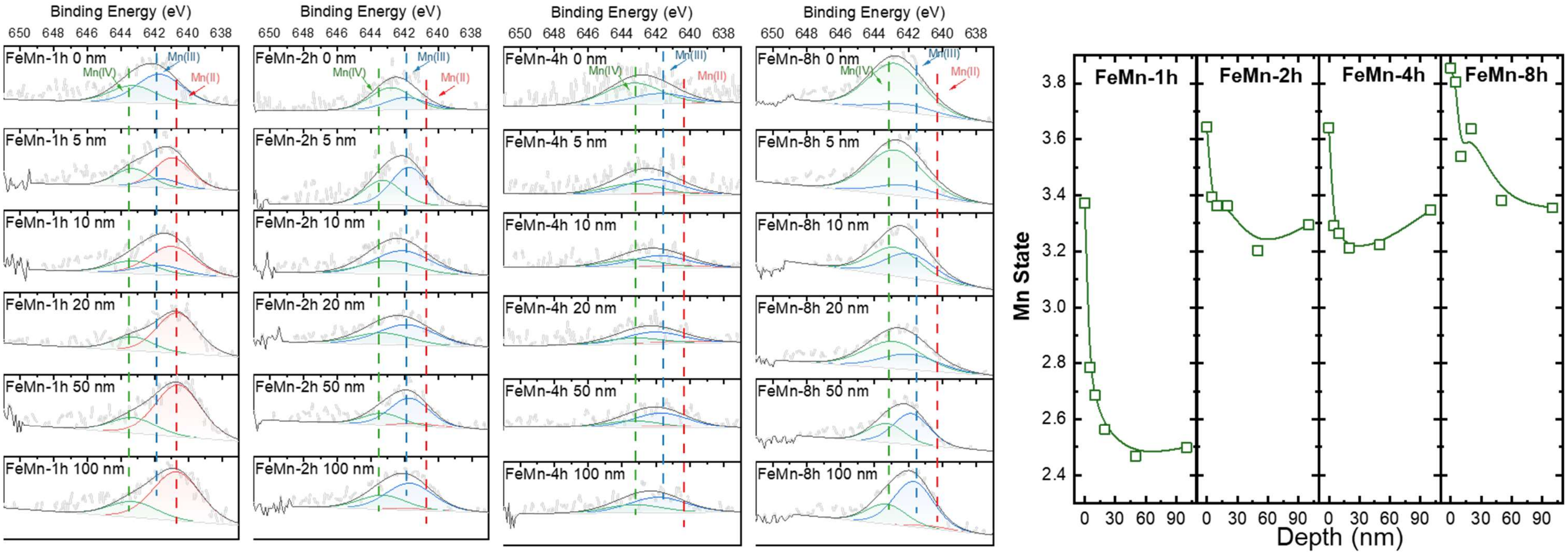

Figure F9. XPS depth profiling analysis of the Mn 2p binding state in the selected biochars (left) and average Mn valence state under the different depths of Fe-Mn biochar with different holding times (right) (detailed proportion can be found in Table F4)

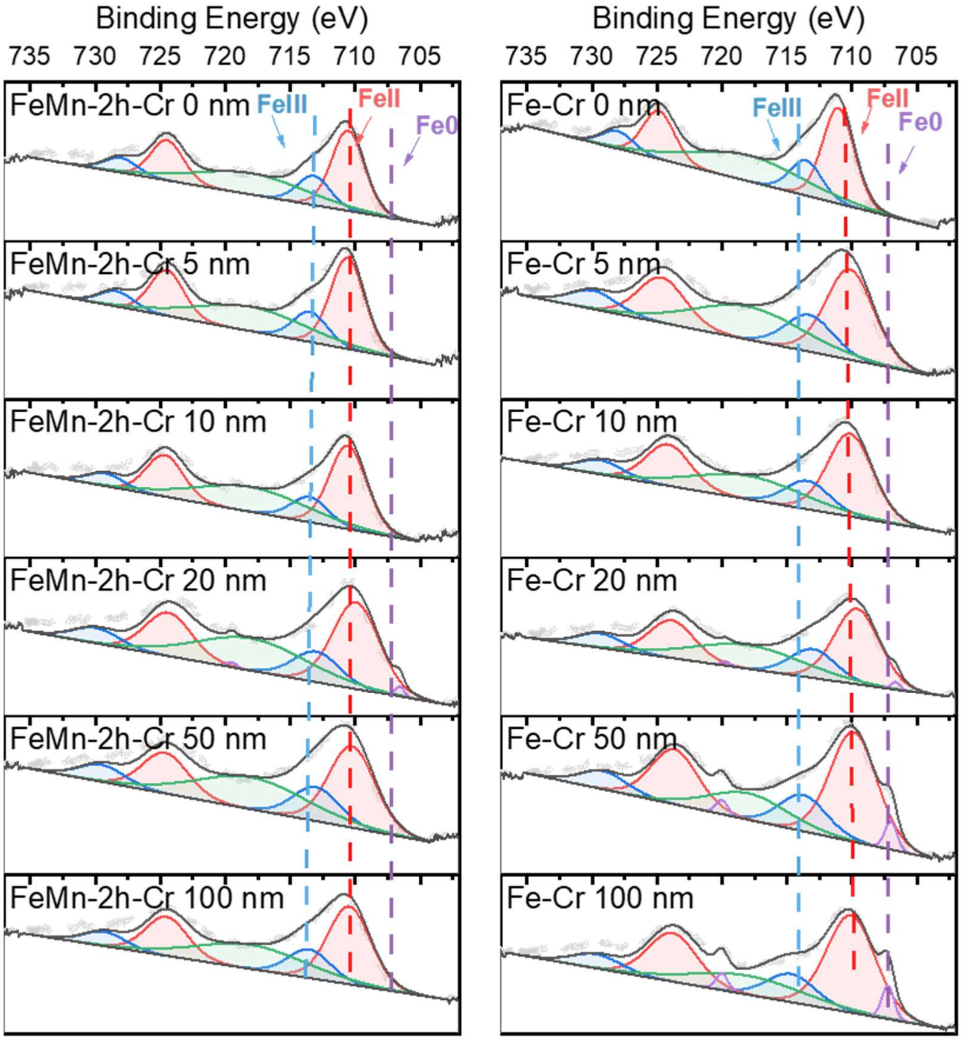

Figure F10. XPS depth profiling analysis of the Fe2p binding state in the BC850-Fe-Mn-850-2h and BC550-Fe-850-2h after Cr(VI) removal.

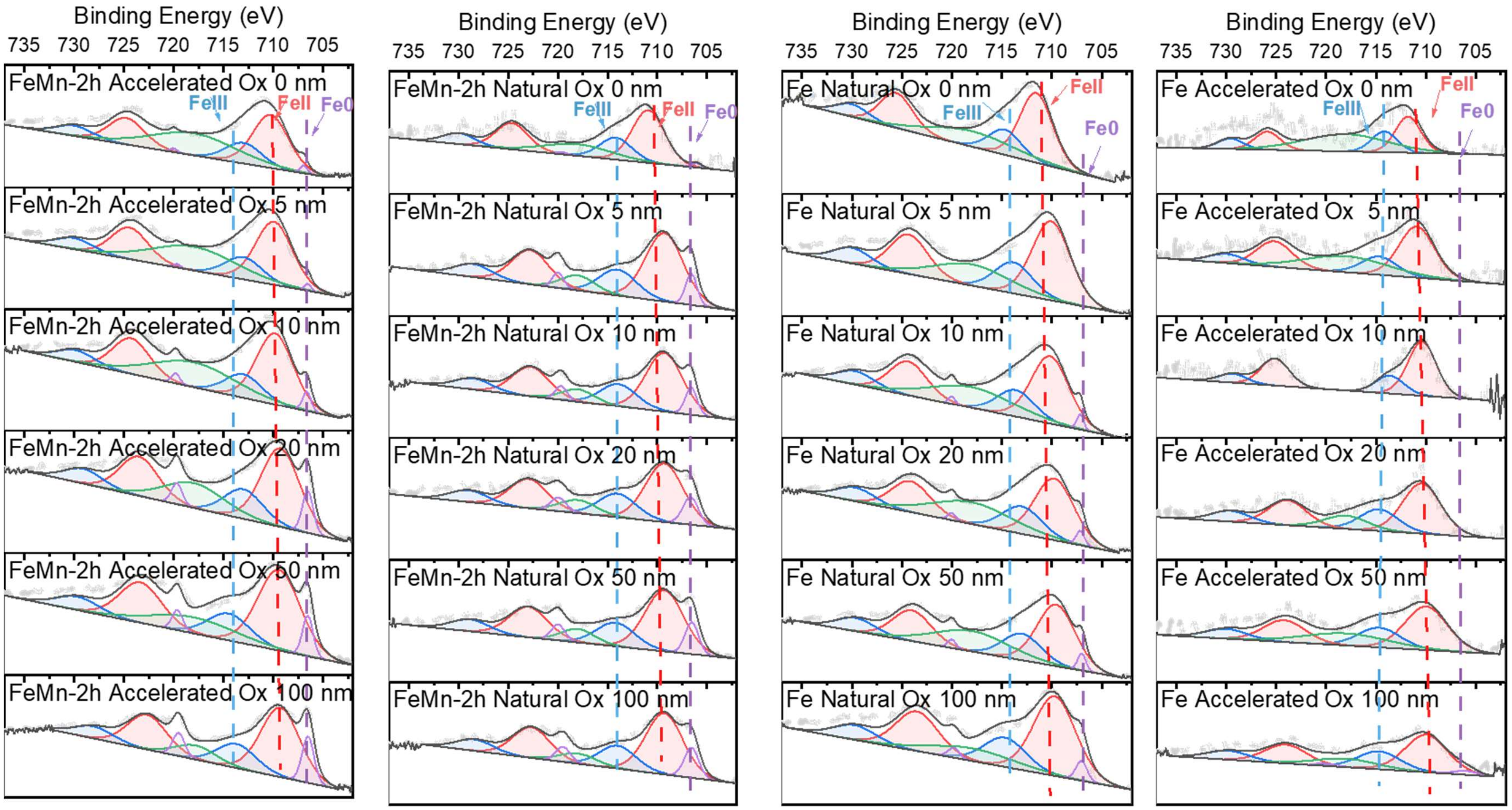

Figure F11. XPS depth profiling analysis of the Fe2p binding state in the BC850-Fe-Mn-850-2h and BC550-Fe-850-2h after accelerated oxidation with 5% H_2O_2 or natural oxidation for 2 months

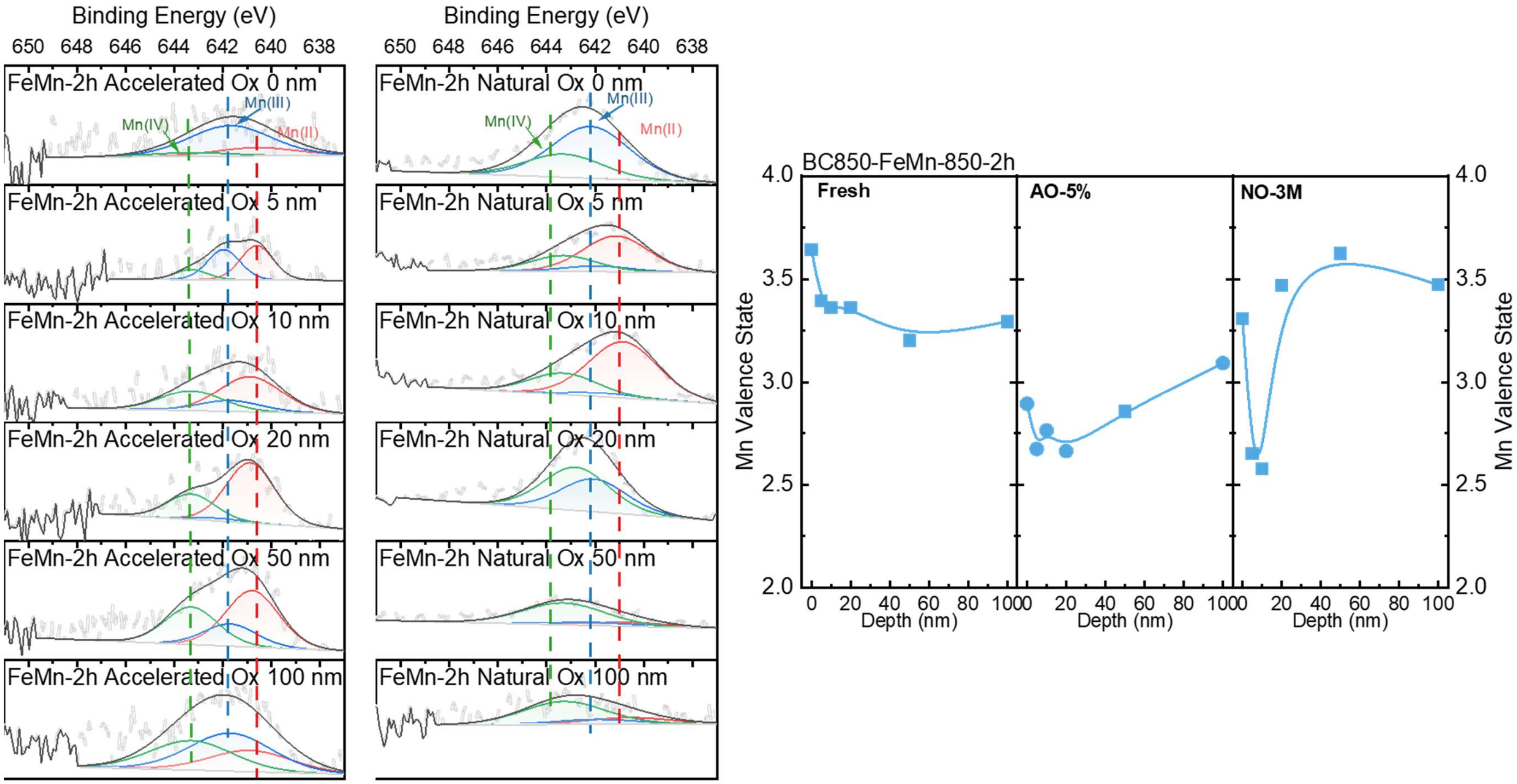

Figure F12. XPS depth profiling analysis of the Mn 2p binding state in the BC850-Fe-Mn-850-2h and BC550-Fe-850-2h after accelerated oxidation with 5% H_2O_2 or natural oxidation for two months (left) and the average Mn Valence state under different depth (right)

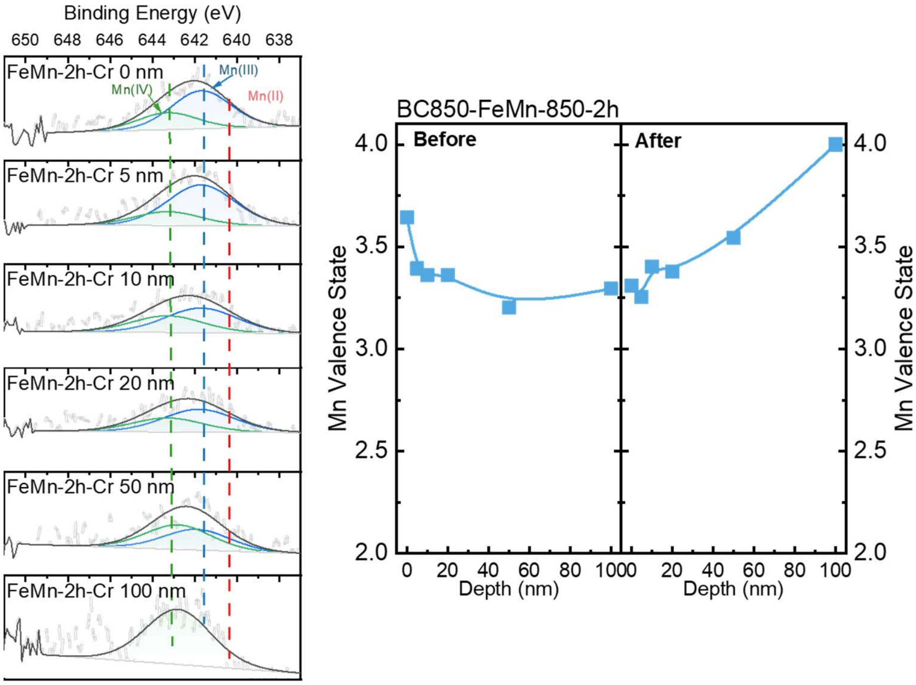

Figure F13. XPS depth profiling analysis of the Mn2p binding state in the BC850-Fe-Mn-850-2h and BC550-Fe-850-2h after Cr(VI) removal.

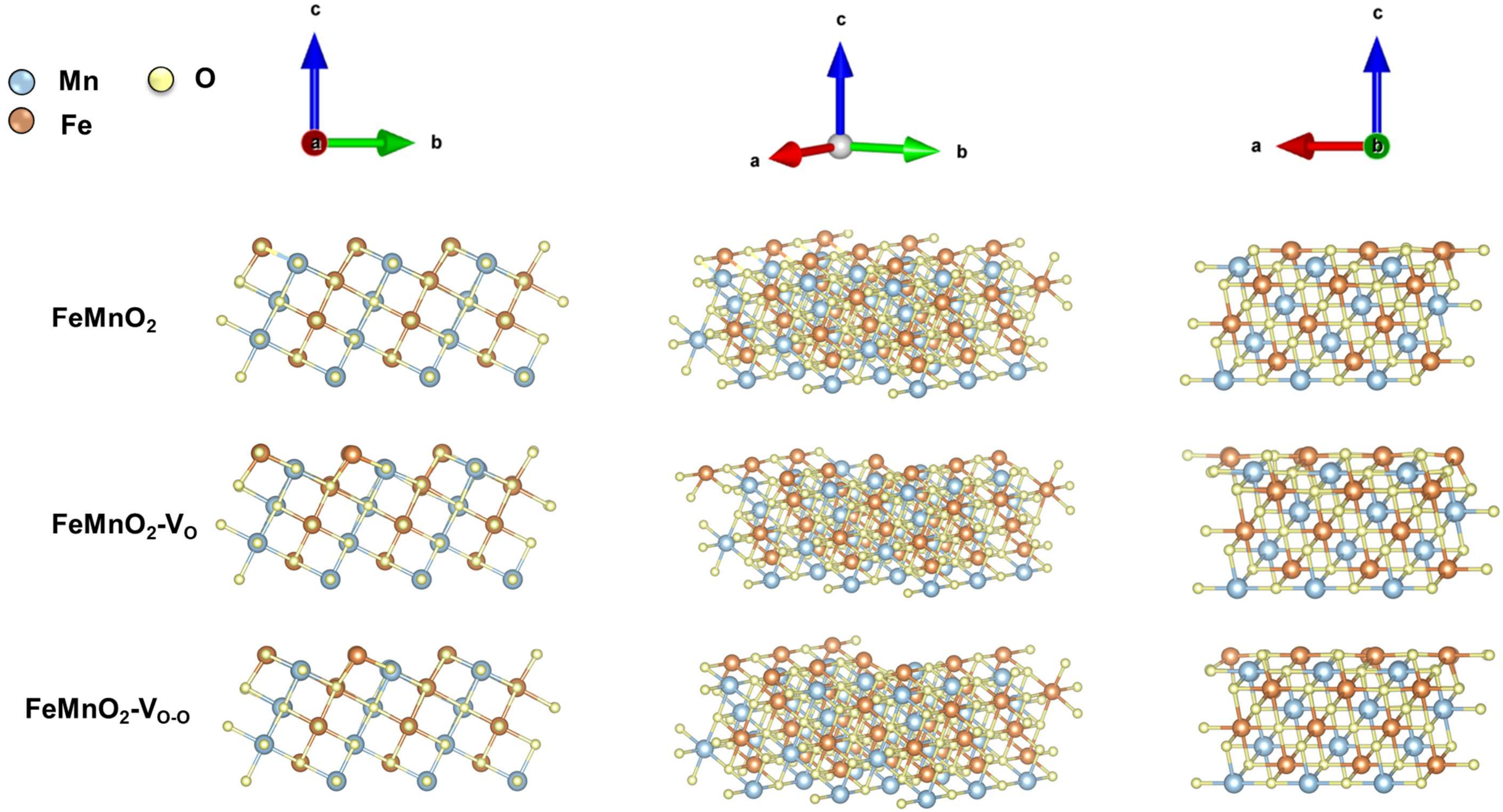

Figure F14. DFT model for the $FeMnO_2$ and $FeMnO_2$ with one or two O vacancies.

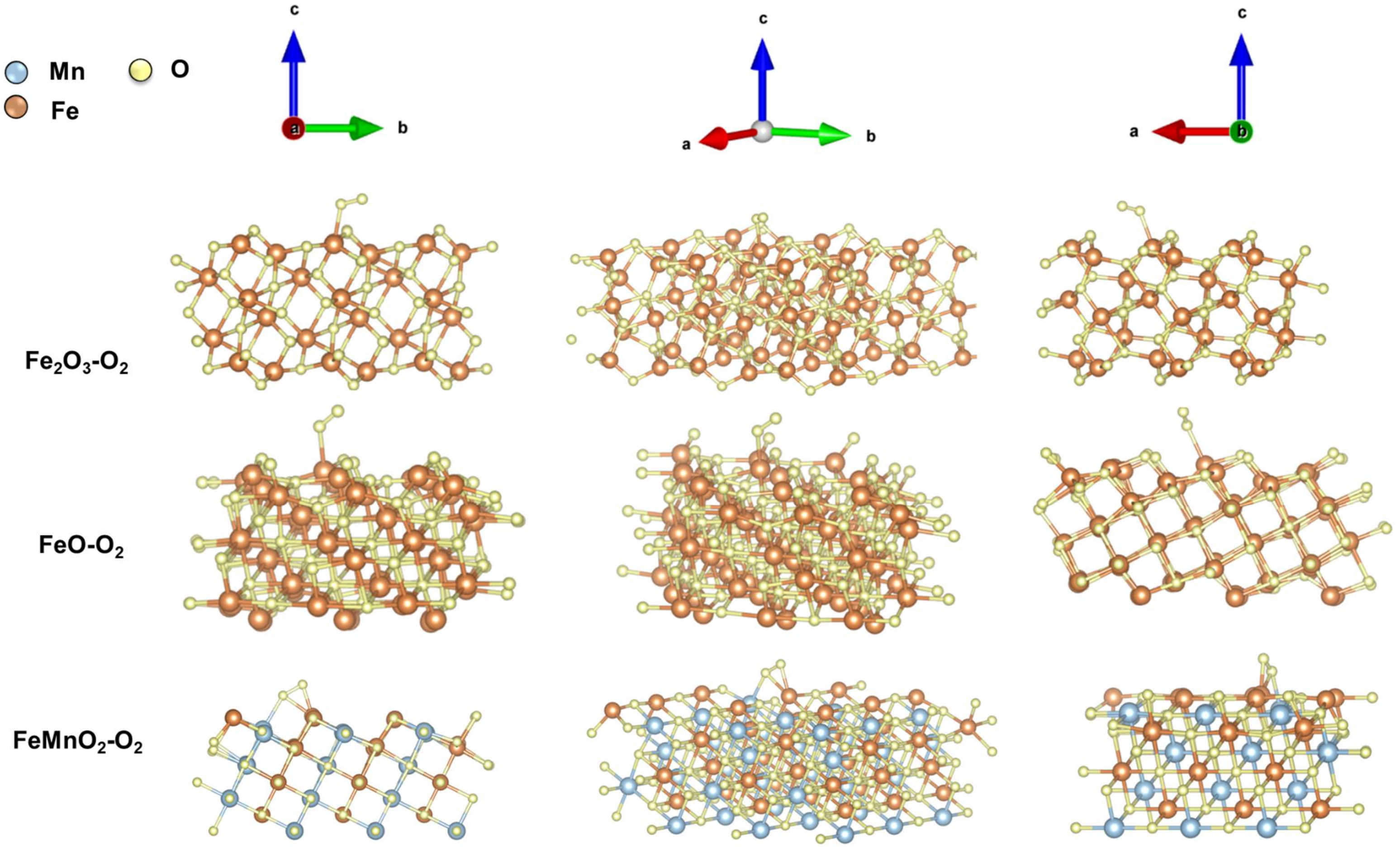

Figure F15. DFT model for the O_2 binding with $FeMnO_2$, Fe_2O_3, and FeO.

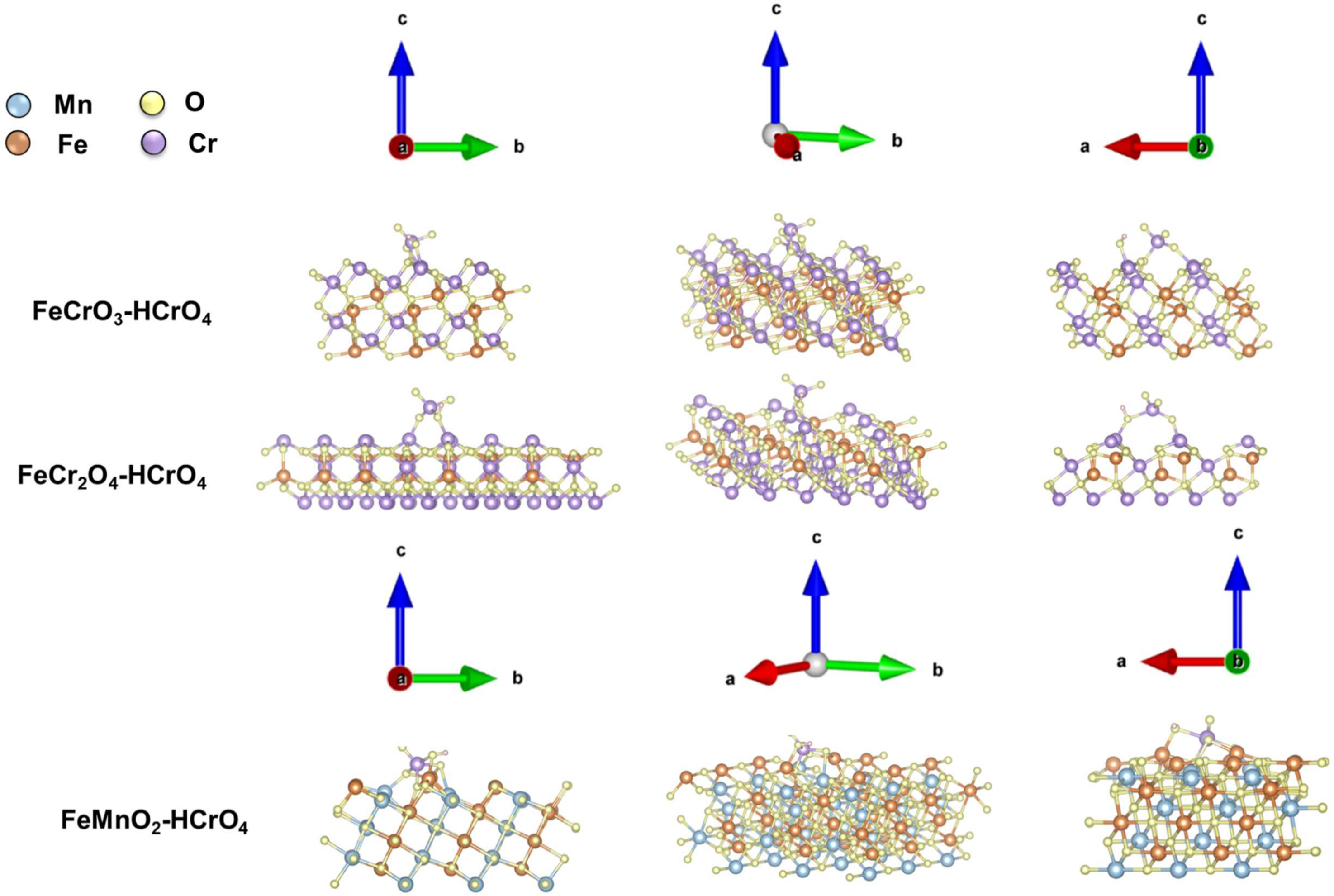

Figure F17. DFT model for the HCrO4 binding with $FeCrO_3$, $FeCr_2O_4$, and $FeMnO_2$.

Appendix G

Collected properties of Electroplating wastewater. The concentration of toxic metals, co-existed impurities, organic matters, and pH of real electroplating wastewater was collected from the following references: (Adhoum et al., 2004, Ajmal et al., 2001, Al-Shannag et al., 2015, Algarra et al., 2005, Ayalew et al., 2020, Bankole et al., 2019, Cao et al., 2013, Chang and Kim 2007, Chang and Wang 2007, Chen et al., 2020a, Chen et al., 2007, Chen et al., 2008, Chen et al., 2009, Cui et al., 2014, Deng et al., 2012, Duong et al., 2019, Ebersbach et al., 2016, Feng et al., 2007, Feng et al., 2019, Fu et al., 2021a, Guan et al., 2020, Hackbarth et al., 2016, Hamdy et al., 2019, Hu et al., 2020, Hunsom et al., 2005, Huo et al., 2021, Ithan et al., 2019, Javaid et al., 2011, John et al., 2016, Khatoon et al., 2021, Kim et al., 2017, Kim et al., 2022, Kobya et al., 2017, Kumar et al., 2008, Lan et al., 2019, Lee et al., 2017, Lee et al., 2016, Li et al., 2018, Li et al., 2022, Liu et al., 2016, Liu et al., 2014, Liu et al., 2017, Liu et al., 2018, Liu et al., 2013a, Lu et al., 2022, Malamis et al., 2012, Martin-Lara et al., 2014, Nguyen et al., 2022, Oden and Sari-Erkan 2018, Orescanin et al., 2013, Peng et al., 2020a, Peng et al., 2020b, Pereira et al., 2010, Qu et al., 2020, Rahman et al., 2020, Rahman et al., 2021, Sankararamakrishnan et al., 2007, Senthilnathan et al., 2005, Sharma et al., 2020, Shi et al., 2011, Shi et al., 2009, Sirianuntapiboon et al., 2008, Suksabye and Thiravetyan 2012, Suksabye et al., 2007, Sze and Xue 2003, Tang and Qiu 2019, Tao et al., 2022, Velazquez-Pena et al., 2012, Verma and Balomajumder 2020, Verma et al., 2020, Wang et al., 2021a, Wang et al., 2018, Wang et al., 2020a, Wei et al., 2013, Xiao et al., 2021, Xu et al., 2015, Yalcin et al., 2001, Yan et al., 2020, Zhang et al., 2015, Zhao et al., 1999, Zhao et al., 2019, Zhao et al., 2013, Zhou et al., 2020).

Based on the data, the average impurity concentration was 347.3 mg L^{-1} SO_4^{2-}, 352.8 mg L^{-1} NO_3^-, 136.6 mg L^{-1} total organic carbon, and 443.9 mg L^{-1} Cl^-, and these concentrations of impurities were used in all experiments.

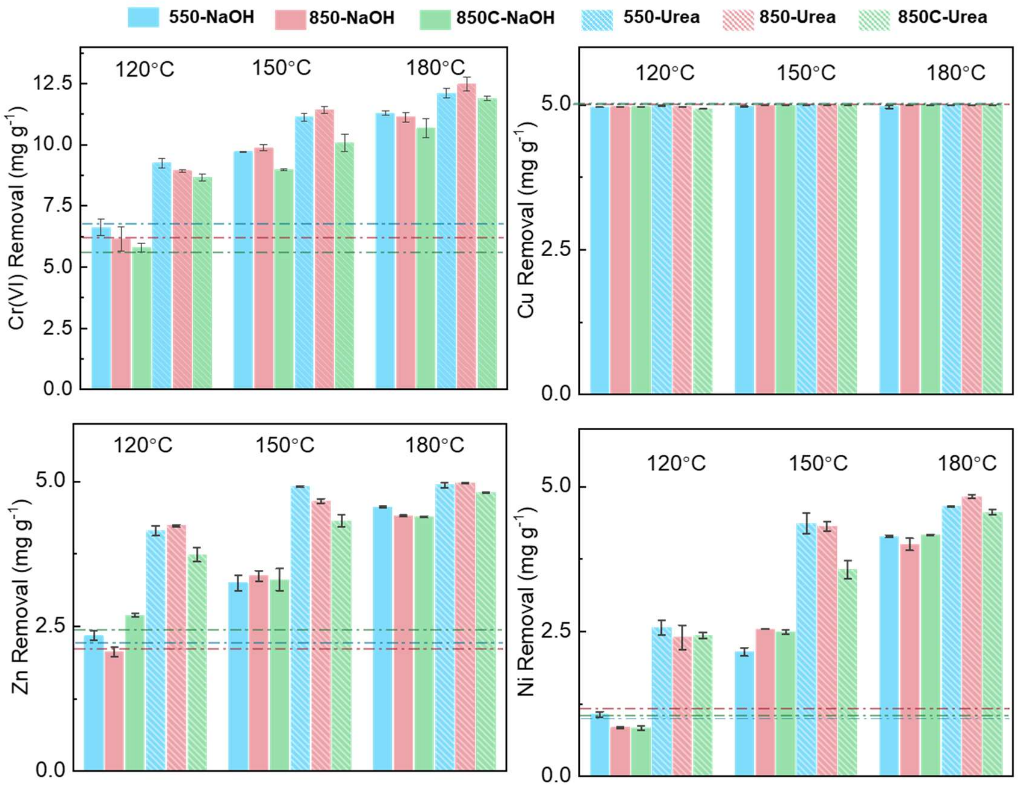

Figure G1. Removal capacities of different Fe-Mn biochars with different hydrothermal condition and carbon precursor. (line in the figure indicated the removal performance of Fe-Mn biochar without the hydrothermal treatment). pH was set as ~2.5, and the concentration of Cr(VI), Cu, Ni, and Zn was set as 25 mg L^{-1}, 10 mg L^{-1}, 10 mg L^{-1}, and 10 mg L^{-1}, respectively. The added amount of Fe-Mn biochar was 2 g L^{-1}, and the reaction time was 24h.

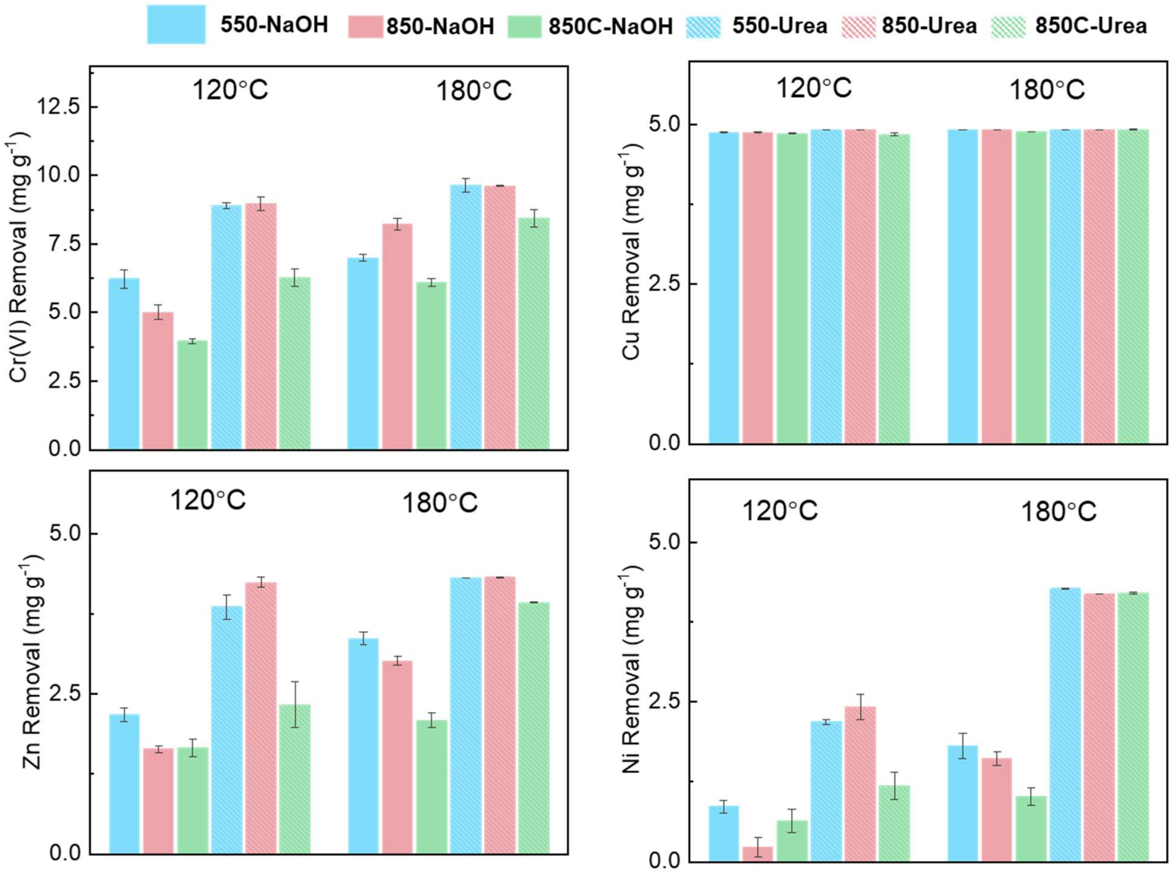

Figure G2. Removal capacities of different Fe biochars with different hydrothermal condition and carbon precursor. pH was set as ~2.5, and the concentration of Cr(VI), Cu, Ni, and Zn was set as 25 mg L^{-1}, 10 mg L^{-1}, 10 mg L^{-1}, and 10 mg L^{-1}, respectively. The added amount of Fe biochar was 2 g L^{-1}, and the reaction time was 24h.

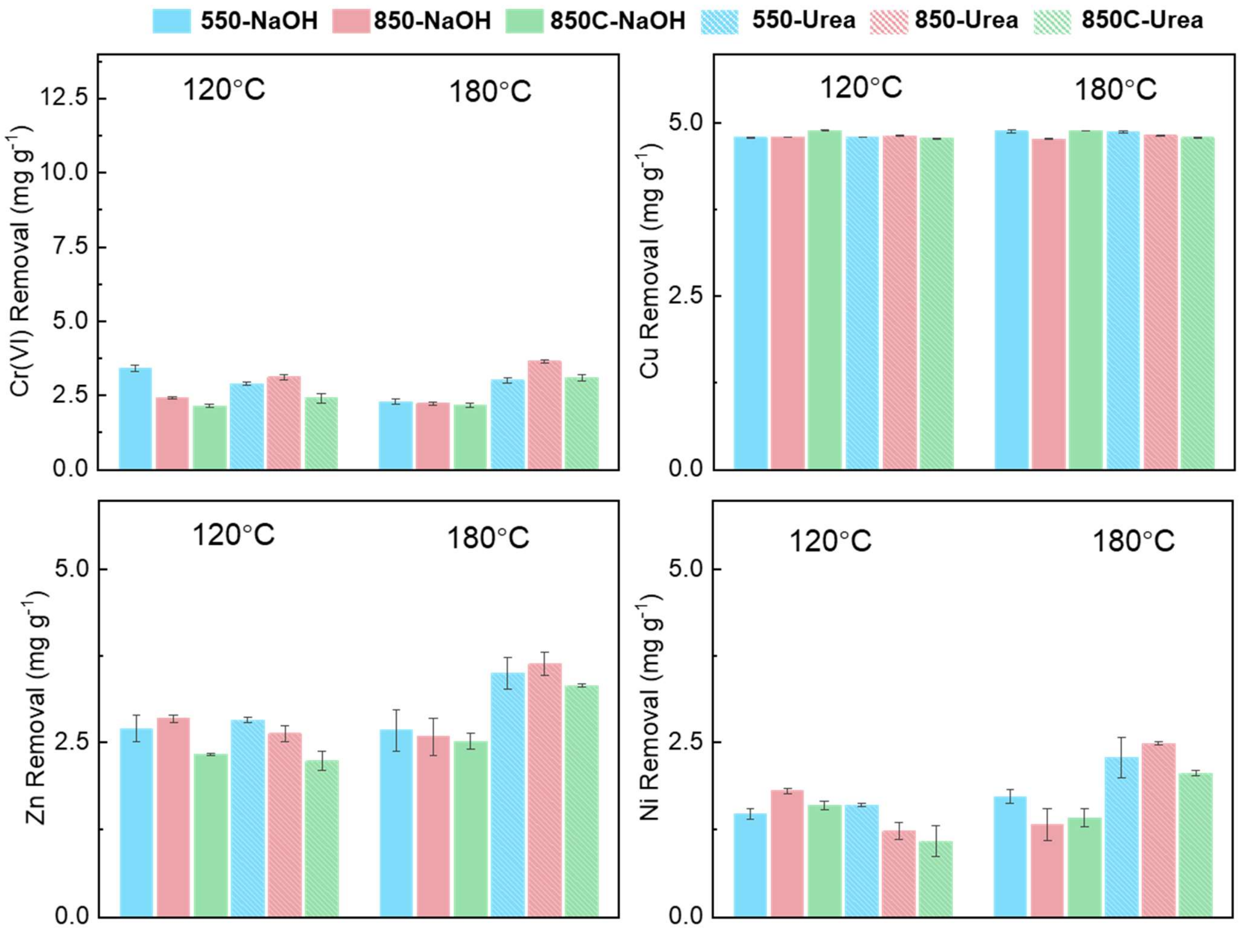

Figure G3. Removal capacities of different Mn biochars with different hydrothermal condition and carbon precursor. pH was set as ~2.5, and the concentration of Cr(VI), Cu, Ni, and Zn was set as 25 mg L^{-1}, 10 mg L^{-1}, 10 mg L^{-1}, and 10 mg L^{-1}, respectively. The added amount of Mn biochar was 2 g L^{-1}, and the reaction time was 24h.

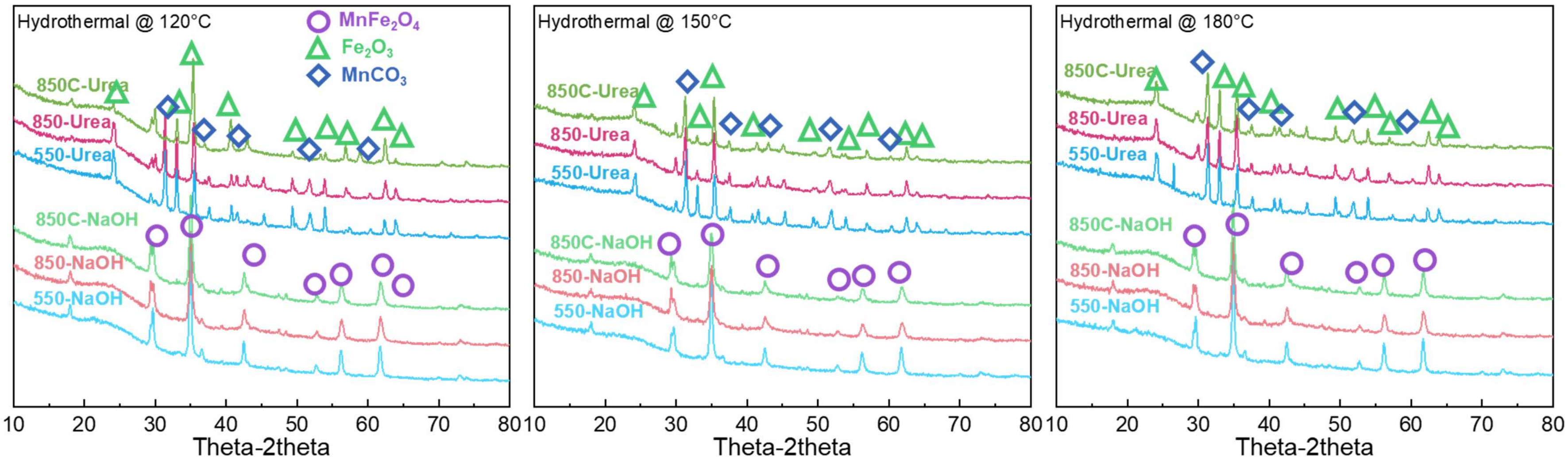

Figure G4. XRD pattern of Fe-Mn biochar after the hydrothermal process

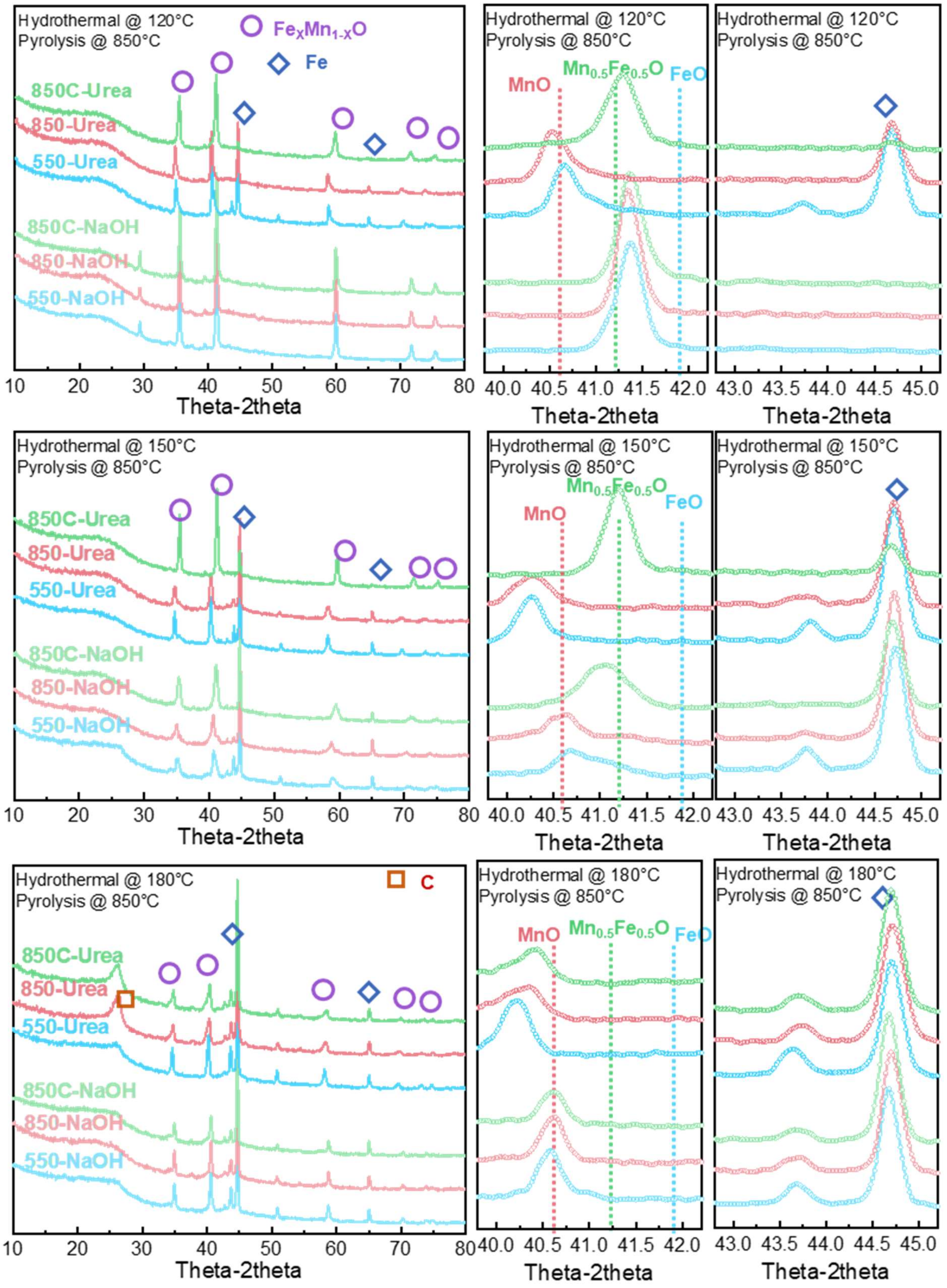

Figure G5 XRD pattern of Fe-Mn biochar after the hydrothermal and pyrolysis process. The right figure was the enlarged version of the selected area

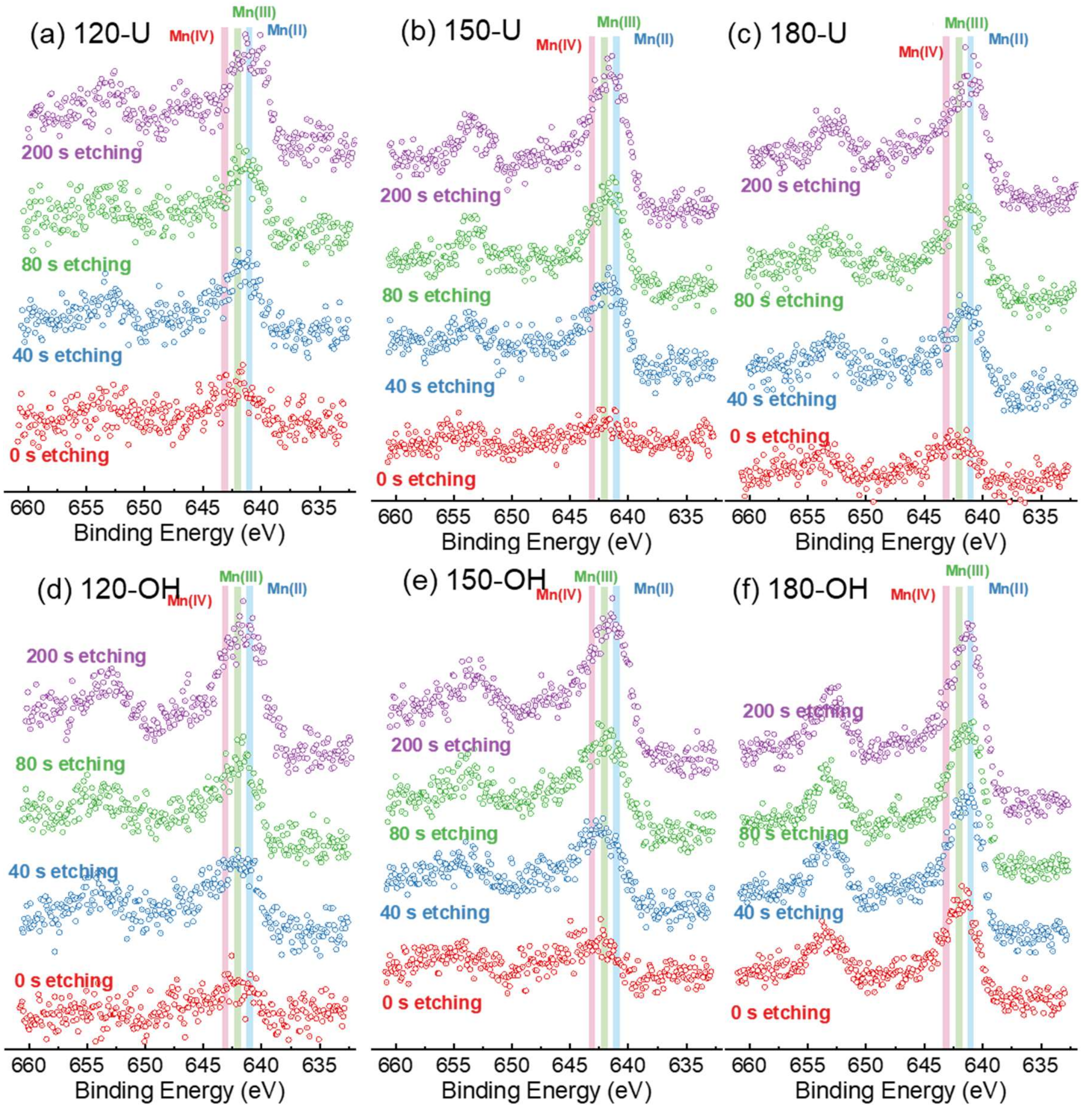

Figure G6 XPS analysis with depth profiling on the Mn2p spectrum of different Fe-Mn biochar

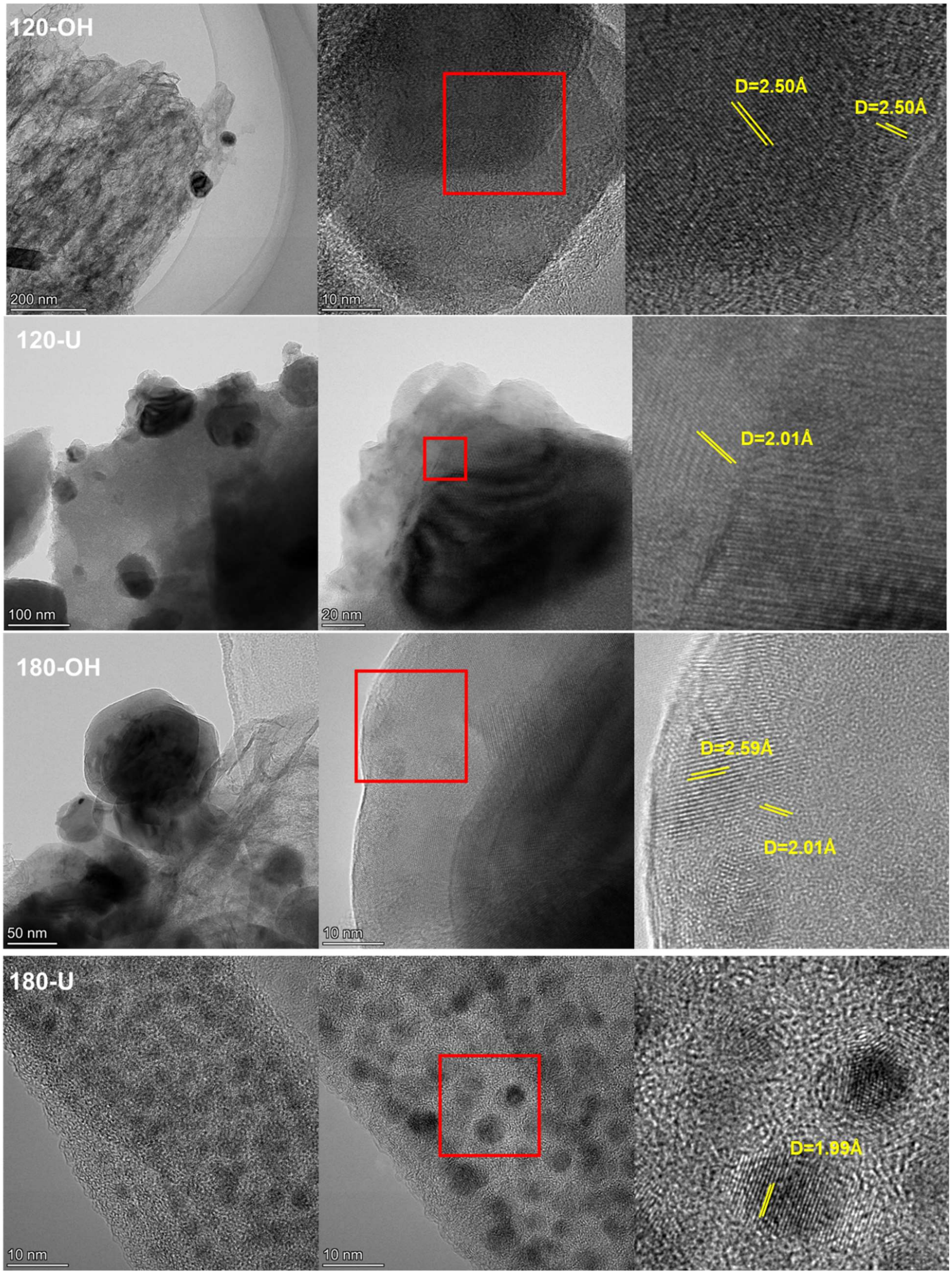

Figure G7. HR-TEM analysis of different Fe-Mn biochar

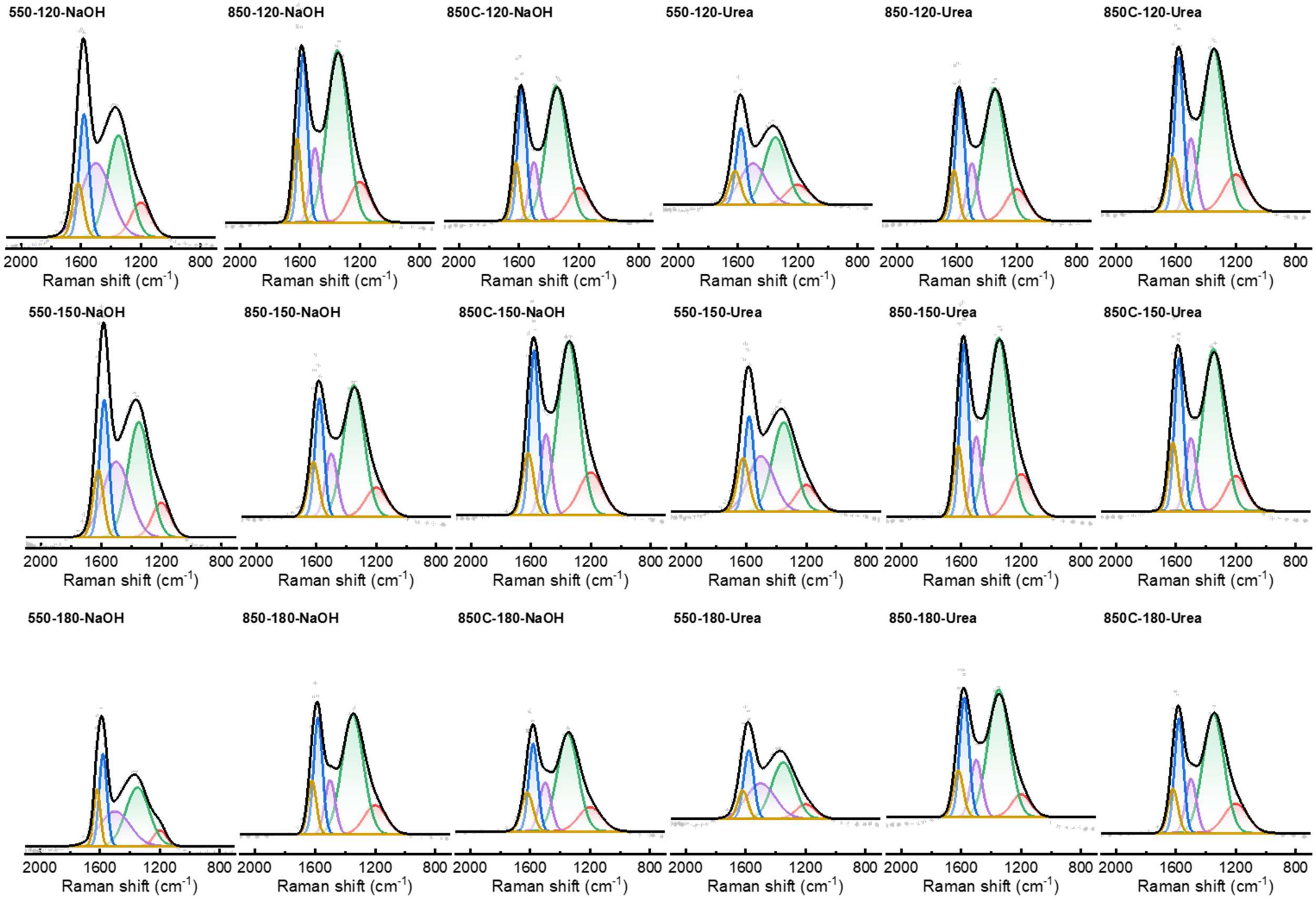

Figure G8 Raman analysis of different Fe-Mn biochars after the hydrothermal process

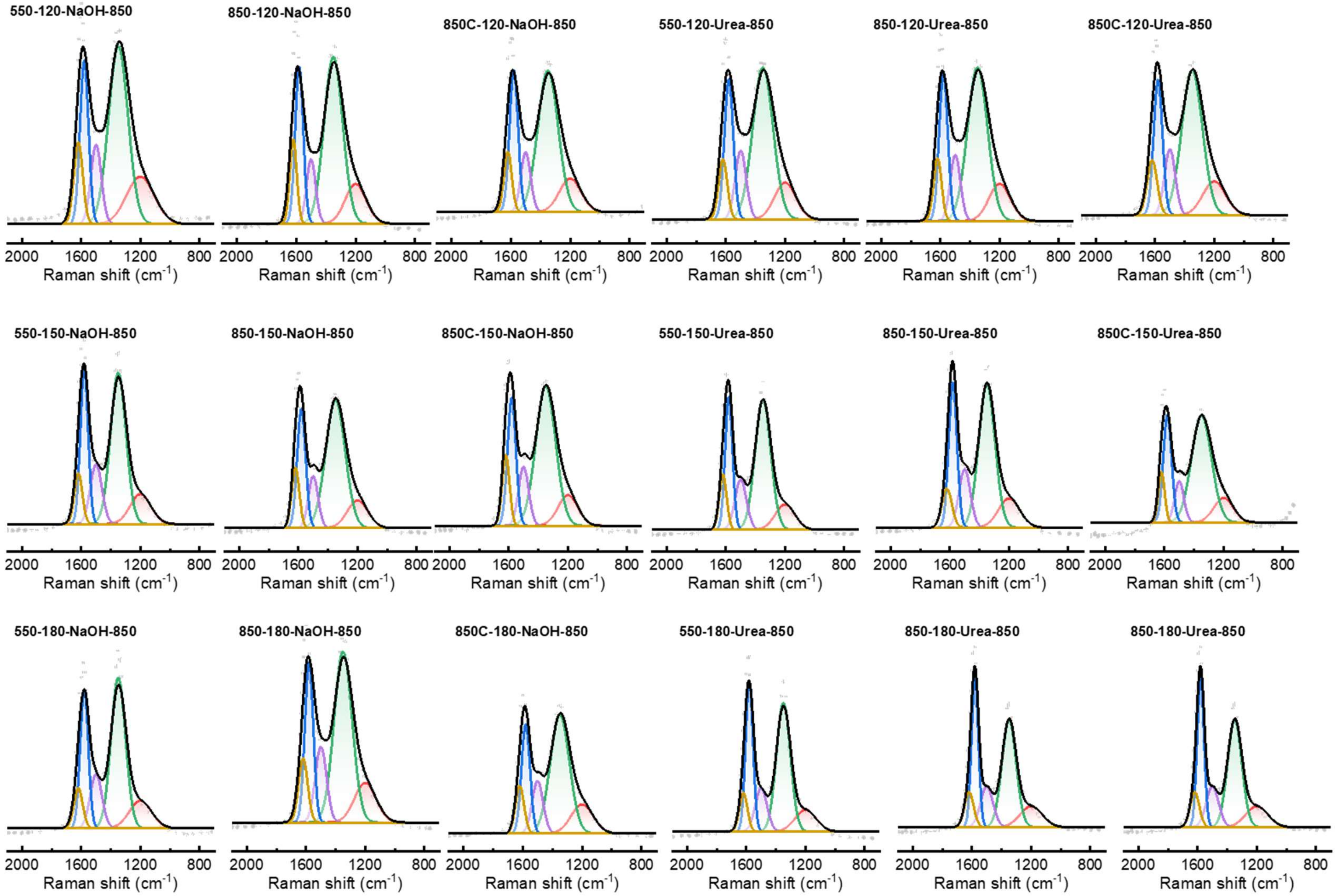

Figure G9 Raman analysis of different Fe-Mn biochars after the hydrothermal and pyrolysis process

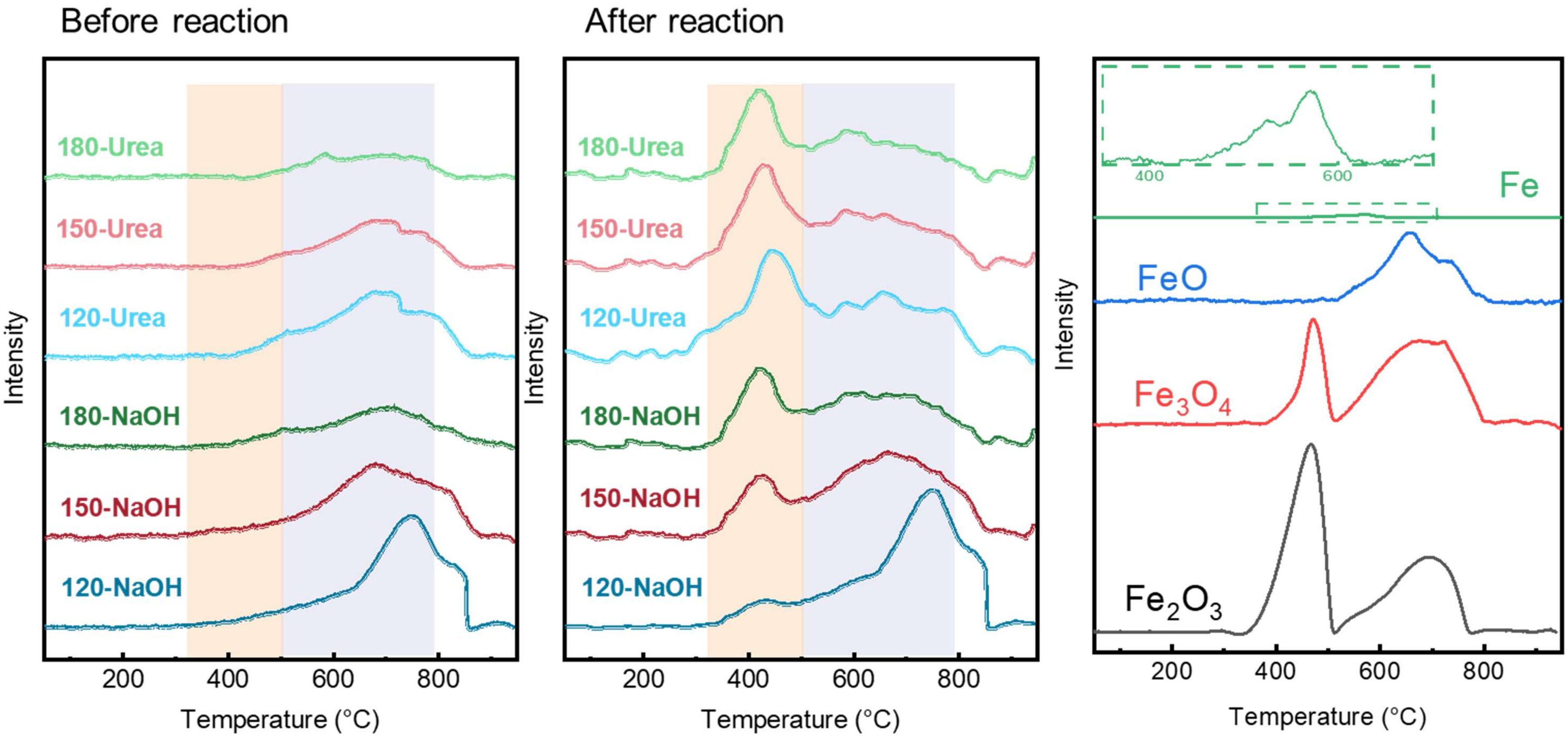

Figure G10 H_2-TPR analysis for the Fe-Mn biochar before (**left**) and after (**middle**) the toxic metals immobilization process; H_2-TPR spectrum of the standard iron minerals (**right**)

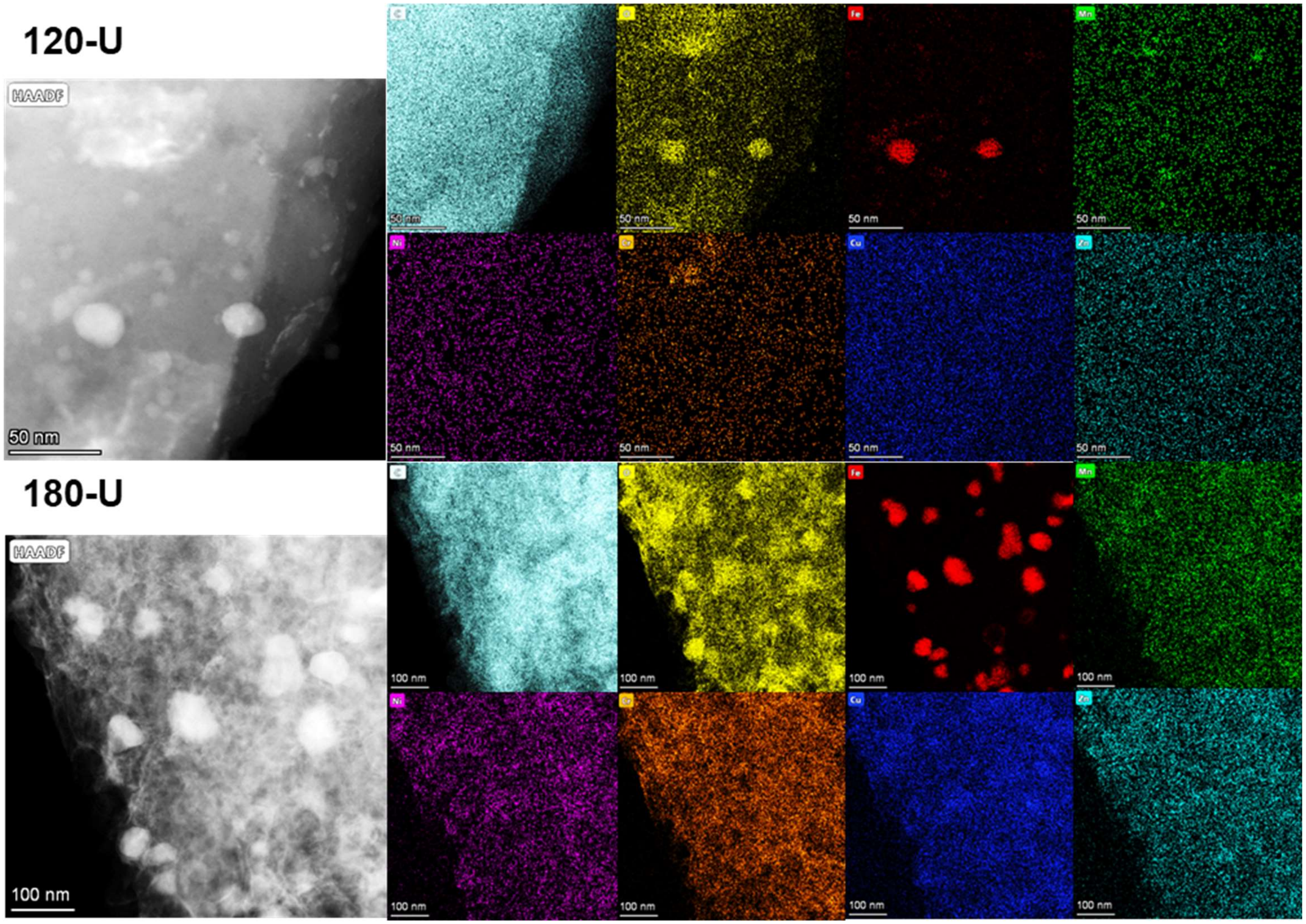

Figure G11 HR-TEM-EDX analysis of the Fe-Mn biochar after the immobilization process

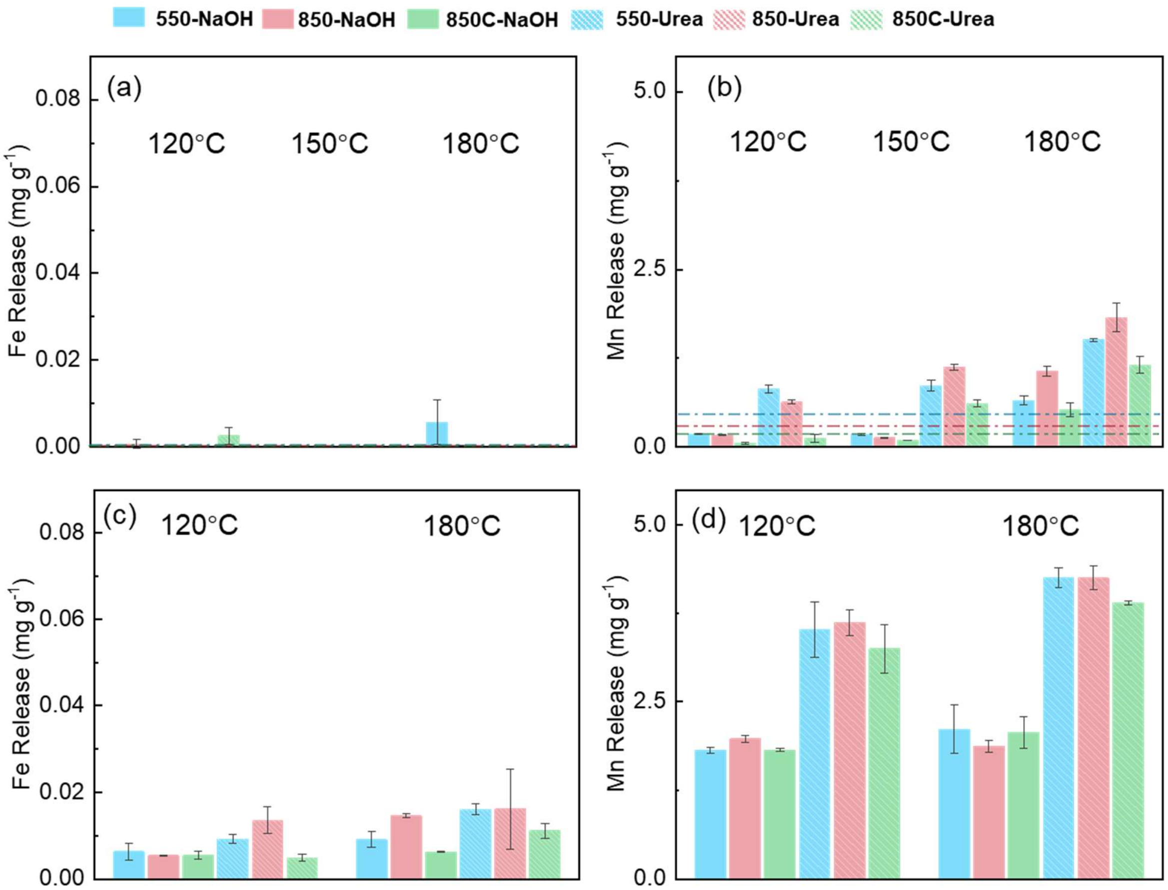

Figure G12 Release amount of Fe (**a**) and Mn (**b**) from Fe-Mn biochar after the immobilization process; Release amount of Fe from Fe-biochar (**c**) and Mn from Mn-biochar (**d**) after the immobilization process.

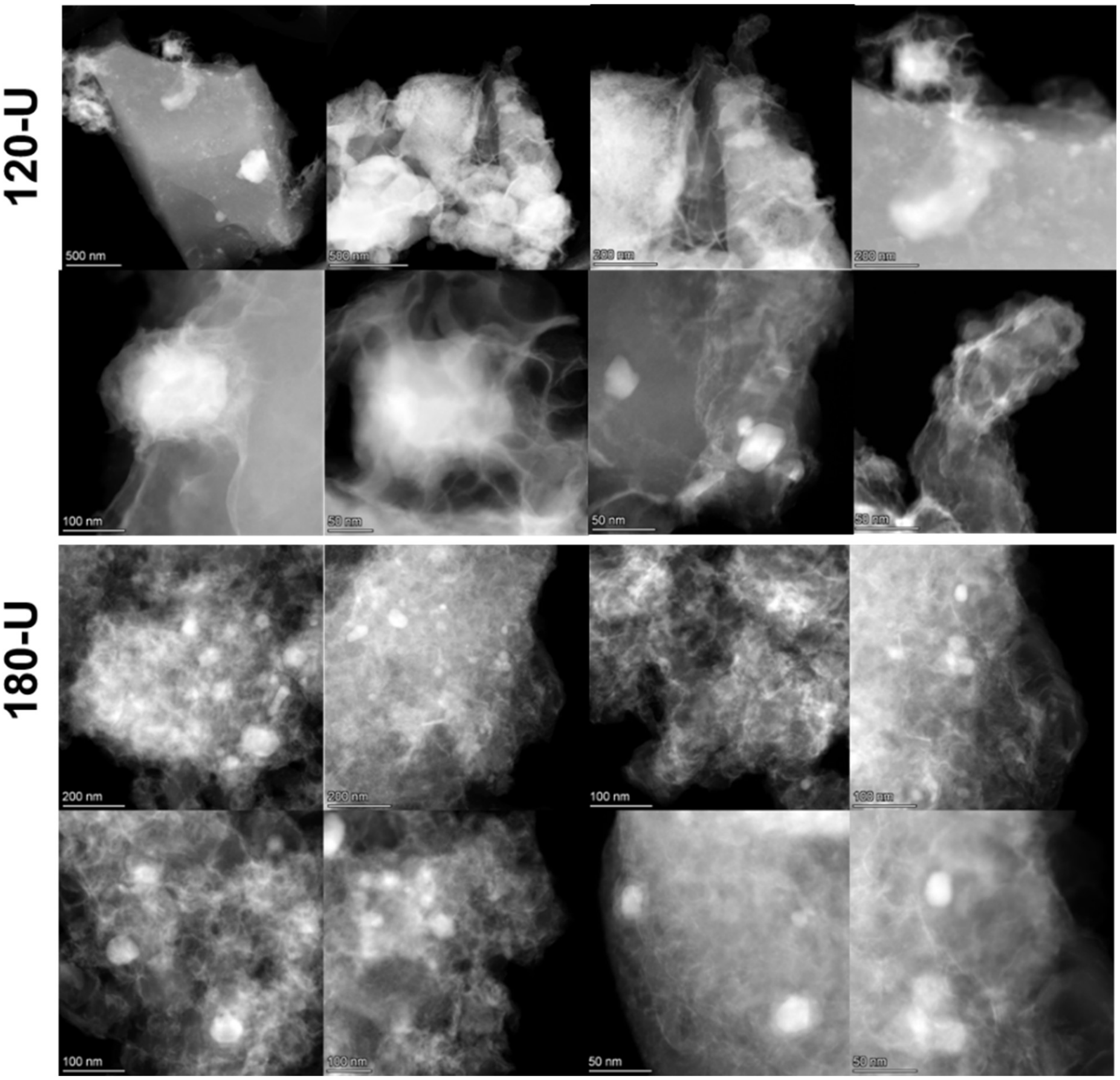

Figure G13 HR-TEM image of the Fe-Mn biochar after the toxic metals immobilization

References

Abdel-Karim, A., El-Naggar, M.E., Radwan, E.K., Mohamed, I.M., Azaam, M. and Kenawy, E.-R. (2021) High-performance mixed-matrix membranes enabled by organically/inorganic modified montmorillonite for the treatment of hazardous textile wastewater. Chemical Engineering Journal 405, 126964.

Achola, L.A., Ghebrehiwet, A., Macharia, J., Kerns, P., He, J., Fee, J., Tinson, C., Shi, J., March, S., Jain, M. and Suib, S.L. (2020) Enhanced visible-light-assisted peroxymonosulfate activation on cobalt-doped mesoporous iron oxide for orange II degradation. Applied Catalysis B: Environmental 263, 118332.

Adhoum, N., Monser, L., Bellakhal, N. and Belgaied, J.E. (2004) Treatment of electroplating wastewater containing Cu2+, Zn2+ and Cr(VI) by electrocoagulation. Journal Of Hazardous Materials 112(3), 207-213.

Aeppli, M., Kaegi, R., Kretzschmar, R., Voegelin, A., Hofstetter, T.B. and Sander, M. (2019a) Electrochemical Analysis of Changes in Iron Oxide Reducibility during Abiotic Ferrihydrite Transformation into Goethite and Magnetite. Environmental Science & Technology 53(7), 3568-3578.

Aeppli, M., Voegelin, A., Gorski, C.A., Hofstetter, T.B. and Sander, M. (2018) Mediated Electrochemical Reduction of Iron (Oxyhydr-)Oxides under Defined Thermodynamic Boundary Conditions. Environmental Science & Technology 52(2), 560-570.

Aeppli, M., Vranic, S., Kaegi, R., Kretzschmar, R., Brown, A.R., Voegelin, A., Hofstetter, T.B. and Sander, M. (2019b) Decreases in Iron Oxide Reducibility during Microbial Reductive Dissolution and Transformation of Ferrihydrite. Environmental Science & Technology 53(15), 8736-8746.

Ahmad, S., Liu, L., Zhang, S. and Tang, J. (2023) Nitrogen-doped biochar (N-doped BC) and iron/nitrogen co-doped biochar (Fe/N co-doped BC) for removal of refractory organic pollutants. Journal Of Hazardous Materials 446, 130727.

Ai, J., Ma, H., Tobler, D.J., Mangayayam, M.C., Lu, C., van den Berg, F.W.J., Yin, W. and Bruun Hansen, H.C. (2020) Bone Char Mediated Dechlorination of Trichloroethylene by Green Rust. Environmental Science & Technology 54(6), 3643-3652.

Ajmal, M., Rao, R.A.K., Ahmad, R., Ahmad, J. and Rao, L.A.K. (2001) Removal and recovery of heavy metals from electroplating wastewater by using Kyanite as an adsorbent. Journal Of Hazardous Materials 87(1-3), 127-137.

Al-Shannag, M., Al-Qodah, Z., Bani-Melhem, K., Qtaishat, M.R. and Alkasrawi, M. (2015) Heavy metal ions removal from metal plating wastewater using electrocoagulation: Kinetic study and process performance. Chemical Engineering Journal 260, 749-756.

Algarra, M., Jimenez, M.V., Rodriguez-Castellon, E., Jimenez-Lopez, A. and Jimenez-Jimenez, J. (2005) Heavy metals removal from electroplating wastewater by aminopropyl-Si MCM-41. Chemosphere 59(6), 779-786.

Alka, S., Shahir, S., Ibrahim, N., Ndejiko, M.J., Vo, D.-V.N. and Manan, F.A. (2021) Arsenic removal technologies and future trends: A mini review. Journal of Cleaner Production 278, 123805.

Alkurdi, S.S.A., Herath, I., Bundschuh, J., Al-Juboori, R.A., Vithanage, M. and Mohan, D. (2019) Biochar versus bone char for a sustainable inorganic arsenic mitigation in water: What needs to be done in future research? Environment International 127, 52-69.

Amen, R., Bashir, H., Bibi, I., Shaheen, S.M., Niazi, N.K., Shahid, M., Hussain, M.M., Antoniadis, V., Shakoor, M.B., Al-Solaimani, S.G., Wang, H., Bundschuh, J. and Rinklebe, J. (2020) A critical review on arsenic removal from water using biochar-based sorbents: The significance of modification and redox reactions. Chemical Engineering Journal 396, 125195.

Amstaetter, K., Borch, T., Larese-Casanova, P. and Kappler, A. (2010) Redox Transformation of Arsenic by Fe(II)-Activated Goethite (α-FeOOH). Environmental Science & Technology 44(1), 102-108.

Anto, S., Sudhakar, M.P., Shan Ahamed, T., Samuel, M.S., Mathimani, T., Brindhadevi, K. and Pugazhendhi, A. (2021) Activation strategies for biochar to use as an efficient catalyst in various applications. Fuel 285, 119205.

Archanjo, B.S., Baptista, D.L., Sena, L.A., Cançado, L.G., Falcão, N.P.S., Jorio, A. and Achete, C.A. (2015) Nanoscale mapping of carbon oxidation in pyrogenic black carbon from ancient Amazonian anthrosols. Environmental Science: Processes & Impacts 17(4), 775-779.

Archanjo, B.S., Mendoza, M.E., Albu, M., Mitchell, D.R.G., Hagemann, N., Mayrhofer, C., Mai, T.L.A., Weng, Z., Kappler, A., Behrens, S., Munroe, P., Achete, C.A., Donne, S., Araujo, J.R., van Zwieten, L., Horvat, J., Enders, A. and Joseph, S. (2017) Nanoscale analyses of the surface structure and composition of biochars extracted from field trials or after co-composting using advanced analytical electron microscopy. Geoderma 294, 70-79.

Arevalo-Lopez, A.M. and Alario-Franco, M.A. (2009) Reliable Method for Determining the Oxidation State in Chromium Oxides. Inorganic Chemistry 48(24), 11843-11846.

Arinchtein, A., Schmack, R., Kraffert, K., Radnik, J., Dietrich, P., Sachse, R. and Kraehnert, R. (2020) Role of Water in Phase Transformations and Crystallization of Ferrihydrite and Hematite. ACS Applied Materials & Interfaces 12(34), 38714-38722.

Arrigo, R., Haevecker, M., Wrabetz, S., Blume, R., Lerch, M., McGregor, J., Parrott, E.P.J., Zeitler, J.A., Gladden, L.F., Knop-Gericke, A., Schloegl, R. and Su, D.S. (2010) Tuning the Acid/Base Properties of Nanocarbons by Functionalization via Amination. Journal of the American Chemical Society 132(28), 9616-9630.

Ayalew, Z.M., Zhang, X.Y., Guo, X.J., Ullah, S., Leng, S., Luo, X.Y. and Ma, N. (2020) Removal of Cu, Ni and Zn directly from acidic electroplating wastewater by Oligo-Ethyleneamine dithiocarbamate (OEDTC). Separation and Purification Technology 248.

Bae, S., Collins, R.N., Waite, T.D. and Hanna, K. (2018) Advances in Surface Passivation of Nanoscale Zerovalent Iron: A Critical Review. Environmental Science & Technology 52(21), 12010-12025.

Bahureksa, W., Tfaily, M.M., Boiteau, R.M., Young, R.B., Logan, M.N., McKenna, A.M. and Borch, T. (2021) Soil Organic Matter Characterization by Fourier Transform Ion Cyclotron Resonance Mass Spectrometry (FTICR MS): A Critical Review of Sample Preparation, Analysis, and Data Interpretation. Environmental Science & Technology 55(14), 9637-9656.

Baig, S.A., Zhu, J., Muhammad, N., Sheng, T.T. and Xu, X.H. (2014) Effect of synthesis methods on magnetic Kans grass biochar for enhanced As(III, V) adsorption from aqueous solutions. Biomass & Bioenergy 71, 299-310.

Bakshi, S., Banik, C., Rathke, S.J. and Laird, D.A. (2018) Arsenic sorption on zero-valent iron-biochar complexes. Water Research 137, 153-163.

Bankole, M.T., Abdulkareem, A.S., Mohammed, I.A., Ochigbo, S.S., Tijani, J.O., Abubakre, O.K. and Roos, W.D. (2019) Selected Heavy Metals Removal From Electroplating Wastewater by Purified and Polyhydroxylbutyrate Functionalized Carbon Nanotubes Adsorbents. Scientific Reports 9.

Bishop, M.E., Dong, H., Glasser, P., Briggs, B.R., Pentrak, M., Stucki, J.W., Boyanov, M.I., Kemner, K.M. and Kovarik, L. (2019) Reactivity of redox cycled Fe-bearing subsurface sediments towards hexavalent chromium reduction. Geochimica Et Cosmochimica Acta 252, 88-106.

Bishop, M.E., Glasser, P., Dong, H., Arey, B. and Kovarik, L. (2014) Reduction and immobilization of hexavalent chromium by microbially reduced Fe-bearing clay minerals. Geochimica Et Cosmochimica Acta 133, 186-203.

Boland, D.D., Collins, R.N., Glover, C.J., Payne, T.E. and Waite, T.D. (2014) Reduction of U(VI) by Fe(II) during the Fe(II)-Accelerated Transformation of Ferrihydrite. Environmental Science & Technology 48(16), 9086-9093.

Bolisetty, S., Peydayesh, M. and Mezzenga, R.J.C.S.R. (2019) Sustainable technologies for water purification from heavy metals: review and analysis. 48(2), 463-487.

Bonneville, S., Behrends, T. and Van Cappellen, P. (2009) Solubility and dissimilatory reduction kinetics of iron(III) oxyhydroxides: A linear free energy relationship. Geochimica Et Cosmochimica Acta 73(18), 5273-5282.

Borch, T., Kretzschmar, R., Kappler, A., Cappellen, P.V., Ginder-Vogel, M., Voegelin, A. and Campbell, K. (2010) Biogeochemical Redox Processes and their Impact on Contaminant Dynamics. Environmental Science & Technology 44(1), 15-23.

Bowman, D.M., Balch, J.K., Artaxo, P., Bond, W.J., Carlson, J.M., Cochrane, M.A., D'Antonio, C.M., Defries, R.S., Doyle, J.C., Harrison, S.P., Johnston, F.H., Keeley, J.E., Krawchuk, M.A., Kull, C.A., Marston, J.B., Moritz, M.A., Prentice, I.C., Roos, C.I., Scott, A.C., Swetnam, T.W., van der Werf, G.R. and Pyne, S.J. (2009) Fire in the Earth system. Science 324(5926), 481-484.

Brockgreitens, J.W., Heidari, F. and Abbas, A. (2020) Versatile Process for the Preparation of Nanocomposite Sorbents: Phosphorus and Arsenic Removal. Environmental Science & Technology 54(14), 9034-9043.

Cai, W., Wei, J., Li, Z., Liu, Y., Zhou, J. and Han, B. (2019) Preparation of amino-functionalized magnetic biochar with excellent adsorption performance for Cr(VI) by a mild one-step hydrothermal method from peanut hull. Colloids and Surfaces A: Physicochemical and Engineering Aspects 563, 102-111.

Cai, Y.J., Ok, Y.S., Lehmann, J. and Chang, S.X. (2021) Recommendations for stronger biochar research in soil biology and fertility. Biology And Fertility Of Soils 57(3), 333-336.

Cao, W., Dang, Z., Yi, X.Y., Yang, C., Lu, G.N., Liu, Y.F., Huang, S.Y. and Zheng, L.C. (2013) Removal of chromium (VI) from electroplating wastewater using an anion exchanger derived from rice straw. Environmental Technology 34(1), 7-14.

Cao, X., Ma, L., Gao, B. and Harris, W. (2009) Dairy-Manure Derived Biochar Effectively Sorbs Lead and Atrazine. Environmental Science & Technology 43(9), 3285-3291.

Cao, X., Ma, L., Liang, Y., Gao, B. and Harris, W. (2011) Simultaneous Immobilization of Lead and Atrazine in Contaminated Soils Using Dairy-Manure Biochar. Environmental Science & Technology 45(11), 4884-4889.

Cazetta, A.L., Pezoti, O., Bedin, K.C., Silva, T.L., Paesano Junior, A., Asefa, T. and Almeida, V.C. (2016) Magnetic Activated Carbon Derived from Biomass Waste by Concurrent Synthesis: Efficient Adsorbent for Toxic Dyes. Acs Sustainable Chemistry & Engineering 4(3), 1058-1068.

Chang, I.S. and Kim, B.H. (2007) Effect of sulfate reduction activity on biological treatment of hexavalent chromium Cr(VI) contaminated electroplating wastewater under sulfate-rich condition. Chemosphere 68(2), 218-226.

Chang, Q. and Wang, G. (2007) Study on the macromolecular coagulant PEX which traps heavy metals. Chemical Engineering Science 62(17), 4636-4643.

Chen, C., Dynes, J.J., Wang, J., Karunakaran, C. and Sparks, D.L. (2014a) Soft X-ray Spectromicroscopy Study of Mineral-Organic Matter Associations in Pasture Soil Clay Fractions. Environmental Science & Technology 48(12), 6678-6686.

Chen, C., Kukkadapu, R. and Sparks, D.L. (2015a) Influence of Coprecipitated Organic Matter on Fe2+(aq)-Catalyzed Transformation of Ferrihydrite: Implications for Carbon Dynamics. Environmental Science & Technology 49(18), 10927-10936.

Chen, D., Zhang, C.S., Rong, H.W., Zhao, M.H. and Gou, S.Y. (2020a) Treatment of electroplating wastewater using the freezing method. Separation and Purification Technology 234.

Chen, L., Jiang, X., Xie, R., Zhang, Y., Jin, Y. and Jiang, W. (2020b) A novel porous biochar-supported Fe-Mn composite as a persulfate activator for the removal of acid red 88. Separation and Purification Technology 250, 117232.

Chen, M., Tao, X., Wang, D., Xu, Z., Xu, X., Hu, X., Xu, N. and Cao, X. (2019a) Facilitated transport of cadmium by biochar-Fe3O4 nanocomposites in water-saturated natural soils. Science of the Total Environment 684, 265-275.

Chen, P., Wang, L.-K., Wang, G., Gao, M.-R., Ge, J., Yuan, W.-J., Shen, Y.-H., Xie, A.-J. and Yu, S.-H. (2014b) Nitrogen-doped nanoporous carbon nanosheets derived from plant biomass: an efficient catalyst for oxygen reduction reaction. Energy & Environmental Science 7(12), 4095-4103.

Chen, S.S., Cheng, C.Y., Li, C.W., Chai, P.H. and Chang, Y.M. (2007) Reduction of chromate from electroplating wastewater from pH 1 to 2 using fluidized zero valent iron process. Journal Of Hazardous Materials 142(1-2), 362-367.

Chen, S.S., Hsu, B.C. and Hung, L.W. (2008) Chromate reduction by waste iron from electroplating wastewater using plug flow reactor. Journal Of Hazardous Materials 152(3), 1092-1097.

Chen, S.S., Li, C.W., Hsu, H.D., Lee, P.C., Chang, Y.M. and Yang, C.H. (2009) Concentration and purification of chromate from electroplating wastewater by two-stage electrodialysis processes. Journal Of Hazardous Materials 161(2-3), 1075-1080.

Chen, S.S., Sun, Y., Tsang, D.C.W., Graham, N.J.D., Ok, Y.S., Feng, Y. and Li, X.-D. (2017) Insights into the subsurface transport of As(V) and Se(VI) in produced water from hydraulic fracturing using soil samples from Qingshankou Formation, Songliao Basin, China. Environmental Pollution 223, 449-456.

Chen, S.S., Tsang, D.C.W., He, M., Sun, Y., Lau, L.S.Y., Leung, R.W.M., Lau, E.S.C., Hou, D., Liu, A. and Mohanty, S. (2021a) Designing sustainable drainage systems in subtropical cities: Challenges and opportunities. Journal of Cleaner Production 280.

Chen, W.-H., Farooq, W., Shahbaz, M., Naqvi, S.R., Ali, I., Al-Ansari, T. and Saidina Amin, N.A. (2021b) Current status of biohydrogen production from lignocellulosic biomass, technical challenges and commercial potential through pyrolysis process. Energy 226, 120433.

Chen, W., Meng, J., Han, X., Lan, Y. and Zhang, W. (2019b) Past, present, and future of biochar. Biochar 1(1), 75-87.

Chen, X., Dai, Y., Fan, J., Xu, X. and Cao, X. (2021c) Application of iron-biochar composite in topsoil for simultaneous remediation of chromium-contaminated soil and groundwater: Immobilization mechanism and long-term stability. Journal Of Hazardous Materials 405, 124226.

Chen, X., Xia, H., Lv, J., Liu, Y., Li, Y., Xu, L., Xie, C. and Wang, Y. (2023) Magnetic hydrothermal biochar for efficient enrichment of uranium(VI) by embedding Fe3O4 nanoparticles on bamboo materials from “one-can” strategy. Colloids and Surfaces A: Physicochemical and Engineering Aspects 658, 130748.

Chen, Y.-d., Wang, R., Duan, X., Wang, S., Ren, N.-q. and Ho, S.-H. (2020c) Production, properties, and catalytic applications of sludge derived biochar for environmental remediation. Water Research 187, 116390.

Chen, Z., Xiao, X., Chen, B. and Zhu, L. (2015b) Quantification of chemical states, dissociation constants and contents of oxygen-containing groups on the surface of biochars produced at different temperatures. Environ Sci Technol 49(1), 309-317.

Cho, D.W., Yoon, K., Kwon, E.E., Biswas, J.K. and Song, H. (2017) Fabrication of magnetic biochar 'as a treatment medium for As(V) via pyrolysis of FeCl3-pretreated spent coffee ground. Environmental Pollution 229, 942-949.

Chu, D., Dong, H., Li, Y., Jin, Z., Xiao, J., Xiang, S., Dong, Q. and Hou, X. (2022) Enhanced activation of sulfite by a mixture of zero-valent Fe-Mn bimetallic nanoparticles and biochar for degradation of sulfamethazine in water. Separation and Purification Technology 285, 120315.

Cismasu, A.C., Williams, K.H. and Nico, P.S. (2016) Iron and Carbon Dynamics during Aging and Reductive Transformation of Biogenic Ferrihydrite. Environmental Science & Technology 50(1), 25-35.

Clurman, A.M., Rodríguez-Narvaez, O.M., Jayarathne, A., De Silva, G., Ranasinghe, M.I., Goonetilleke,

A. and Bandala, E.R. (2020) Influence of surface hydrophobicity/hydrophilicity of biochar on the removal of emerging contaminants. Chemical Engineering Journal 402, 126277.

Cornell, R.M. and Schwertmann, U. (2003) The iron oxides: structure, properties, reactions, occurrences and uses, John Wiley & Sons.

Costa, J.M., Costa, J.G.d.R.d. and Almeida Neto, A.F.d. (2022) Techniques of nickel(II) removal from electroplating industry wastewater: Overview and trends. Journal of Water Process Engineering 46, 102593.

Cui, J.Q., Wang, X.J., Yuan, Y.L., Guo, X.W., Gu, X.Y. and Jian, L. (2014) Combined ozone oxidation and biological aerated filter processes for treatment of cyanide containing electroplating wastewater. Chemical Engineering Journal 241, 184-189.

Cuong, D.V., Wu, P.-C., Chen, L.-I. and Hou, C.-H. (2021) Active MnO2/biochar composite for efficient As(III) removal: Insight into the mechanisms of redox transformation and adsorption. Water Research 188, 116495.

Daenzer, R., Xu, L., Doerfelt, C., Jia, Y. and Demopoulos, G.P. (2014) Precipitation behaviour of As(V) during neutralization of acidic Fe(II)−As(V) solutions in batch and continuous modes. Hydrometallurgy 146, 40-47.

Das, T.K. and Bezbaruah, A.N. (2021) Comparative study of arsenic removal by iron-based nanomaterials: Potential candidates for field applications. Science of the Total Environment 764, 142914.

Daulton, T.L. and Little, B.J. (2006) Determination of chromium valence over the range Cr(0)–Cr(VI) by electron energy loss spectroscopy. Ultramicroscopy 106(7), 561-573.

Daulton, T.L., Little, B.J., Lowe, K. and Jones-Meehan, J. (2002) Electron energy loss spectroscopy techniques for the study of microbial chromium(VI) reduction. Journal of Microbiological Methods 50(1), 39-54.

De Beni, E., Giurlani, W., Fabbri, L., Emanuele, R., Santini, S., Sarti, C., Martellini, T., Piciollo, E., Cincinelli, A. and Innocenti, M. (2022) Graphene-based nanomaterials in the electroplating industry: A suitable choice for heavy metal removal from wastewater. Chemosphere 292, 133448.

Dehghani, M.H., Heibati, B., Asadi, A., Tyagi, I., Agarwal, S. and Gupta, V.K. (2016) Reduction of noxious Cr(VI) ion to Cr(III) ion in aqueous solutions using H2O2 and UV/H2O2 systems. Journal of Industrial and Engineering Chemistry 33, 197-200.

Deng, N., Li, Z.X., Zuo, X.B., Chen, J.W., Shakiba, S., Louie, S.M., Rixey, W.G. and Hu, Y.D. (2021) Coprecipitation of Fe/Cr Hydroxides with Organics: Roles of Organic Properties in Composition and Stability of the Coprecipitates. Environmental Science & Technology 55(8), 4638-4647.

Deng, Y.F., Long, T., Zhao, H., Zhu, L.L. and Chen, J. (2012) Application of Porous N-Methylimidazolium Strongly Basic Anion Exchange Resins on Cr(VI) Adsorption from Electroplating Wastewater. Separation Science and Technology 47(2), 256-263.

Dhoble, R.M., Maddigapu, P.R., Bhole, A.G. and Rayalu, S. (2018) Development of bark-based magnetic iron oxide particle (BMIOP), a bio-adsorbent for removal of arsenic (III) from water.

Environmental Science and Pollution Research 25(20), 19657-19674.

Ding, H., Zhang, Z., Li, Y., Ding, L., Sun, D. and Dong, Z. (2022) Fabrication of novel Fe/Mn/N co-doped biochar and its enhanced adsorption for bisphenol a based on π–π electron donor–acceptor interaction. Bioresource technology 364, 128018.

Duong, H.C., Pham, T.M., Luong, S.T., Nguyen, K.V., Nguyen, D.T., Ansari, A.J. and Nghiem, L.D. (2019) A novel application of membrane distillation to facilitate nickel recovery from electroplating wastewater. Environmental Science and Pollution Research 26(23), 23407-23415.

Ebersbach, I., Ludwig, S.M., Constapel, M. and Kling, H.W. (2016) An alternative treatment method for fluorosurfactant-containing wastewater by aerosol-mediated separation. Water Research 101, 333-340.

Eckmann, A., Felten, A., Mishchenko, A., Britnell, L., Krupke, R., Novoselov, K.S. and Casiraghi, C. (2012) Probing the Nature of Defects in Graphene by Raman Spectroscopy. Nano Letters 12(8), 3925-3930.

EPA, U.J.A.E., editor. Washington DC, USA (1992) Method 1311 Toxicity characteristic leaching procedure (TCLP).

Fan, J., Chen, X., Xu, Z., Xu, X., Zhao, L., Qiu, H. and Cao, X. (2020) One-pot synthesis of nZVI-embedded biochar for remediation of two mining arsenic-contaminated soils: Arsenic immobilization associated with iron transformation. Journal Of Hazardous Materials 398, 122901.

Fan, Z.-J., Kai, W., Yan, J., Wei, T., Zhi, L.-J., Feng, J., Ren, Y.-m., Song, L.-P. and Wei, F. (2011) Facile Synthesis of Graphene Nanosheets via Fe Reduction of Exfoliated Graphite Oxide. Acs Nano 5(1), 191-198.

Fang, G., Zhu, C., Dionysiou, D.D., Gao, J. and Zhou, D. (2015) Mechanism of hydroxyl radical generation from biochar suspensions: Implications to diethyl phthalate degradation. Bioresource technology 176, 210-217.

Fang, Q., Chen, B., Lin, Y. and Guan, Y. (2014) Aromatic and hydrophobic surfaces of wood-derived biochar enhance perchlorate adsorption via hydrogen bonding to oxygen-containing organic groups. Environ Sci Technol 48(1), 279-288.

Fei, Y.-h., Li, M., Ye, Z., Guan, J., Huang, Z., Xiao, T. and Zhang, P. (2022) The pH-sensitive sorption governed reduction of Cr(VI) by sludge derived biochar and the accelerating effect of organic acids. Journal Of Hazardous Materials 423, 127205.

Feng, K., Xu, Z., Gao, B., Xu, X., Zhao, L., Qiu, H. and Cao, X. (2021) Mesoporous ball-milling iron-loaded biochar for enhanced sorption of reactive red: Performance and mechanisms. Environmental Pollution 290, 117992.

Feng, X., Wu, Z.C. and Chen, X.F. (2007) Removal of metal ions from electroplating effluent by EDI process and recycle of purified water. Separation and Purification Technology 57(2), 257-263.

Feng, Y., Liu, P., Wang, Y., Finfrock, Y.Z., Xie, X., Su, C., Liu, N., Yang, Y. and Xu, Y. (2020) Distribution and speciation of iron in Fe-modified biochars and its application in removal of As(V), As(III), Cr(VI), and Hg(II): An X-ray absorption study. Journal Of Hazardous Materials 384, 121342.

Feng, Y., Yang, S.M., Xia, L., Wang, Z.W., Suo, N., Chen, H., Long, Y.Y., Zhou, B. and Yu, Y.Z. (2019) In-situ ion exchange electrocatalysis biological coupling (i-IEEBC) for simultaneously enhanced degradation of organic pollutants and heavy metals in electroplating wastewater. Journal Of Hazardous Materials 364, 562-570.

Francis, A., Ionescu, E., Fasel, C. and Riedel, R. (2009) Crystallization Behavior and Controlling Mechanism of Iron-Containing Si−C−N Ceramics. Inorganic Chemistry 48(21), 10078-10083.

Fritzsche, A., Bosch, J., Sander, M., Schröder, C., Byrne, J.M., Ritschel, T., Joshi, P., Maisch, M., Meckenstock, R.U., Kappler, A. and Totsche, K.U. (2021) Organic Matter from Redoximorphic Soils Accelerates and Sustains Microbial Fe(III) Reduction. Environmental Science & Technology 55(15), 10821-10831.

Fu, D., Kurniawan, T.A., Avtar, R., Xu, P. and Othman, M.H.D. (2021a) Recovering heavy metals from electroplating wastewater and their conversion into Zn2Cr-layered double hydroxide (LDH) for pyrophosphate removal from industrial wastewater. Chemosphere 271.

Fu, X.-Z., Wu, J., Cui, S., Wang, X.-M., Liu, H.-Q., He, R.-L., Yang, C., Deng, X., Tan, Z.-L. and Li, W.-W. (2021b) Self-regenerable bio-hybrid with biogenic ferrous sulfide nanoparticles for treating high-concentration chromium-containing wastewater. Water Research 206, 117731.

Gai, C., Zhang, F., Lang, Q., Liu, T., Peng, N. and Liu, Z. (2017) Facile one-pot synthesis of iron nanoparticles immobilized into the porous hydrochar for catalytic decomposition of phenol. Applied Catalysis B: Environmental 204, 566-576.

Gan, Q., Hou, H., Liang, S., Qiu, J., Tao, S., Yang, L., Yu, W., Xiao, K., Liu, B., Hu, J., Wang, Y. and Yang, J. (2020) Sludge-derived biochar with multivalent iron as an efficient Fenton catalyst for degradation of 4-Chlorophenol. Science of the Total Environment 725, 138299.

Gao, F., Lyu, H., Ahmad, S., Xu, S. and Tang, J. (2023) Enhanced reductive degradation of tetrabromobisphenol A by biochar supported sulfidated nanoscale zero-valent iron: Selectivity and core reactivity. Applied Catalysis B: Environmental 324, 122246.

Gao, S., Wang, Q., Nie, J., Poon, C.S., Yin, H. and Li, J.-s. (2021) Arsenate(V) removal from aqueous system by using modified incinerated sewage sludge ash (ISSA) as a novel adsorbent. Chemosphere 270, 129423.

Garcia, A.N., Zhang, Y., Ghoshal, S., He, F. and O'Carroll, D.M. (2021) Recent Advances in Sulfidated Zerovalent Iron for Contaminant Transformation. Environmental Science & Technology 55(13), 8464-8483.

Garg, N., Garg, A. and Mukherji, S. (2022) Sequential treatment of simulated textile wastewater using zero-valent aluminum under alkaline conditions and biodegradation. Journal of Cleaner Production 379, 134733.

Gholami, P., Dinpazhoh, L., Khataee, A., Hassani, A. and Bhatnagar, A. (2020) Facile hydrothermal synthesis of novel Fe-Cu layered double hydroxide/biochar nanocomposite with enhanced sonocatalytic activity for degradation of cefazolin sodium. Journal Of Hazardous Materials 381, 120742.

Ghoreishian, S.M., Ranjith, K.S., Park, B., Hwang, S.-K., Hosseini, R., Behjatmanesh-Ardakani, R., Pourmortazavi, S.M., Lee, H.U., Son, B., Mirsadeghi, S., Han, Y.-K. and Huh, Y.S. (2021) Full-spectrum-responsive Bi2S3@CdS S-scheme heterostructure with intimated ultrathin RGO toward photocatalytic Cr(VI) reduction and H2O2 production: Experimental and DFT studies. Chemical Engineering Journal 419, 129530.

Gillingham, M.D., Gomes, R.L., Ferrari, R. and West, H.M. (2022) Sorption, separation and recycling of ammonium in agricultural soils: A viable application for magnetic biochar? Science of the Total Environment 812, 151440.

Goel, R., Jha, R. and Ravikant, C. (2022) Synergistic effect of Urea and Potassium Sulphate during hydrothermal synthesis of NiO nanospheres with reduced crystallite size and enhanced electrical conductivity. Inorganic Chemistry Communications 141, 109563.

Gong, H., Zhao, L., Rui, X., Hu, J. and Zhu, N. (2022) A review of pristine and modified biochar immobilizing typical heavy metals in soil: Applications and challenges. Journal Of Hazardous Materials 432, 128668.

Gong, L., Qi, J., Lv, N., Qiu, X., Gu, Y., Zhao, J. and He, F. (2021) Mechanistic role of nitrate anion in TCE dechlorination by ball milled ZVI and sulfidated ZVI: Experimental investigation and theoretical analysis. Journal Of Hazardous Materials 403, 123844.

Gu, Y., Gong, L., Qi, J., Cai, S., Tu, W. and He, F. (2019) Sulfidation mitigates the passivation of zero valent iron at alkaline pHs: Experimental evidences and mechanism. Water Research 159, 233-241.

Guan, X.-H., Wang, J. and Chusuei, C.C. (2008) Removal of arsenic from water using granular ferric hydroxide: Macroscopic and microscopic studies. Journal Of Hazardous Materials 156(1), 178-185.

Guan, X., Sun, Y., Qin, H., Li, J., Lo, I.M.C., He, D. and Dong, H. (2015) The limitations of applying zero-valent iron technology in contaminants sequestration and the corresponding countermeasures: The development in zero-valent iron technology in the last two decades (1994–2014). Water Research 75, 224-248.

Guan, Z.J., Guo, Y.P., Li, S.P., Feng, S.Q., Deng, Y.H., Ou, X.L., Ren, J., Sun, S.Y. and Liang, J.L. (2020) Decomplexation of heterogeneous catalytic ozonation assisted with heavy metal chelation for advanced treatment of coordination complexes of Ni. Science of the Total Environment 732.

Gubler, R. and ThomasArrigo, L.K. (2021) Ferrous iron enhances arsenic sorption and oxidation by non-stoichiometric magnetite and maghemite. Journal Of Hazardous Materials 402, 123425.

Guo, X., Jia, J., Dong, H., Wang, Q., Xu, T., Fu, B., Ran, R., Liang, P., Huang, X. and Zhang, X. (2019) Hydrothermal synthesis of FeMn bimetallic nanocatalysts as high-efficiency cathode catalysts for microbial fuel cells. Journal of Power Sources 414, 444-452.

Hackbarth, F.V., Maass, D., de Souza, A.A.U., Vilar, V.J.P. and de Souza, S. (2016) Removal of hexavalent chromium from electroplating wastewaters using marine macroalga Pelvetia canaliculata as natural electron donor. Chemical Engineering Journal 290, 477-489.

Hagemann, N., Joseph, S., Schmidt, H.-P., Kammann, C.I., Harter, J., Borch, T., Young, R.B., Varga, K., Taherymoosavi, S., Elliott, K.W., McKenna, A., Albu, M., Mayrhofer, C., Obst, M., Conte, P., Dieguez-Alonso, A., Orsetti, S., Subdiaga, E., Behrens, S. and Kappler, A. (2017) Organic coating on biochar explains its nutrient retention and stimulation of soil fertility. Nature Communications 8(1), 1089.

Hajji, S., Montes-Hernandez, G., Sarret, G., Tordo, A., Morin, G., Ona-Nguema, G., Bureau, S., Turki, T. and Mzoughi, N. (2019) Arsenite and chromate sequestration onto ferrihydrite, siderite and goethite nanostructured minerals: Isotherms from flow-through reactor experiments and XAS measurements. Journal Of Hazardous Materials 362, 358-367.

Hamdy, A., Mostafa, M.K. and Nasr, M. (2019) Techno-economic estimation of electroplating wastewater treatment using zero-valent iron nanoparticles: batch optimization, continuous feed, and scaling up studies. Environmental Science and Pollution Research 26(24), 25372-25385.

Hammond, C.M., Root, R.A., Maier, R.M. and Chorover, J. (2020) Arsenic and iron speciation and mobilization during phytostabilization of pyritic mine tailings. Geochimica Et Cosmochimica Acta 286, 306-323.

Han, H., Song, P., Cai, Z., Dong, W., Khan, A., Yang, K., Fang, Y., Liu, P., Mašek, O. and Li, X. (2022) Immobilizing chromate reductase NfoR on magnetic biochar reduced Cr(VI) in copper-containing wastewater. Journal of Cleaner Production 361, 132118.

Han, Z., Sani, B., Mrozik, W., Obst, M., Beckingham, B., Karapanagioti, H.K. and Werner, D. (2015) Magnetite impregnation effects on the sorbent properties of activated carbons and biochars. Water Research 70, 394-403.

Hao, H., Zhang, Q., Qiu, Y., Meng, L., Wei, X., Sang, W. and Tao, J. (2020) Insight into the degradation of Orange G by persulfate activated with biochar modified by iron and manganese oxides: Synergism between Fe and Mn. Journal of Water Process Engineering 37, 101470.

He, M., Xu, Z., Sun, Y., Chan, P.S., Lui, I. and Tsang, D.C.W. (2021a) Critical impacts of pyrolysis conditions and activation methods on application-oriented production of wood waste-derived biochar. Bioresour Technol 341, 125811.

He, M., Xu, Z., Sun, Y., Chan, P.S., Lui, I. and Tsang, D.C.W. (2021b) Critical impacts of pyrolysis conditions and activation methods on application-oriented production of wood waste-derived biochar. Bioresource technology 341, 125811.

He, M.J., Xu, Z.B., Hou, D.Y., Gao, B., Cao, X.D., Ok, Y.S., Rinklebe, J., Bolan, N.S. and Tsang, D.C.W. (2022) Waste-derived biochar for water pollution control and sustainable development. Nature Reviews Earth & Environment 3(7), 444-460.

He, R.Z., Peng, Z.Y., Lyu, H.H., Huang, H., Nan, Q. and Tang, J.C. (2018) Synthesis and characterization of an iron-impregnated biochar for aqueous arsenic removal. Science of the Total Environment 612, 1177-1186.

He, Z., Zhang, Q., Wei, Z., Wang, S. and Pan, X. (2019) Multiple-pathway arsenic oxidation and removal from wastewater by a novel manganese-oxidizing aerobic granular sludge. Water Research 157, 83-93.

Heinrich, L., Rothe, M., Braun, B. and Hupfer, M. (2021) Transformation of redox-sensitive to redox-stable iron-bound phosphorus in anoxic lake sediments under laboratory conditions. Water Research

189, 116609.

Herndon, E., AlBashaireh, A., Singer, D., Roy Chowdhury, T., Gu, B. and Graham, D. (2017) Influence of iron redox cycling on organo-mineral associations in Arctic tundra soil. Geochimica Et Cosmochimica Acta 207, 210-231.

Hou, W., Wang, S., Li, Y., Hao, Z., Zhang, Y. and Kong, F. (2021) Influence of modified biochar supported Fe–Cu/polyvinylpyrrolidone on nitrate removal and high selectivity towards nitrogen in constructed wetlands. Environmental Pollution 289, 117812.

Hu, C., Guo, H., Mei, H. and Zhu, J. (2021) Prediction of iron content in soil based on microspectrophotometry analysis. Forensic Science International 318, 110600.

Hu, K.Q., Xu, D. and Chen, Y.C. (2020) An assessment of sulfate reducing bacteria on treating sulfate-rich metal-laden wastewater from electroplating plant. Journal Of Hazardous Materials 393.

Hu, P., Su, H., Chen, Z., Yu, C., Li, Q., Zhou, B., Alvarez, P.J.J. and Long, M. (2017) Selective Degradation of Organic Pollutants Using an Efficient Metal-Free Catalyst Derived from Carbonized Polypyrrole via Peroxymonosulfate Activation. Environmental Science & Technology 51(19), 11288-11296.

Hu, S., Lu, Y., Peng, L., Wang, P., Zhu, M., Dohnalkova, A.C., Chen, H., Lin, Z., Dang, Z. and Shi, Z. (2018) Coupled Kinetics of Ferrihydrite Transformation and As(V) Sequestration under the Effect of Humic Acids: A Mechanistic and Quantitative Study. Environmental Science & Technology 52(20), 11632-11641.

Hu, X., Ding, Z., Zimmerman, A.R., Wang, S. and Gao, B. (2015) Batch and column sorption of arsenic onto iron-impregnated biochar synthesized through hydrolysis. Water Research 68, 206-216.

Hu, Y., Peng, X., Ai, Z., Jia, F. and Zhang, L. (2019) Liquid Nitrogen Activation of Zero-Valent Iron and Its Enhanced Cr(VI) Removal Performance. Environmental Science & Technology 53(14), 8333-8341.

Huang, P., Zhang, P., Wang, C., Du, X., Jia, H. and Sun, H. (2023) P-doped Biochar Regulates nZVI Nanocracks Formation for Superefficient Persulfate Activation. Journal Of Hazardous Materials, 130999.

Huang, P., Zhang, P., Wang, C., Tang, J. and Sun, H. (2022) Enhancement of persulfate activation by Fe-biochar composites: Synergism of Fe and N-doped biochar. Applied Catalysis B: Environmental 303, 120926.

Huang, Y.-N., Qian, T.-T., Dang, F., Yin, Y.-G., Li, M. and Zhou, D.-M. (2019) Significant contribution of metastable particulate organic matter to natural formation of silver nanoparticles in soils. Nature Communications 10(1), 3775.

Hunsom, M., Pruksathorn, K., Damronglerd, S., Vergnes, H. and Duverneuil, P. (2005) Electrochemical treatment of heavy metals (Cu2+, Cr6+Ni2+) from industrial effluent and modeling of copper reduction. Water Research 39(4), 610-616.

Huo, Y., Khan, A., Liu, Y.W., Wang, Z.H., Yu, Y., Sun, T., Liang, D.X., Su, T., Ri, K., Xie, X.F., Zhu, S.Y. and Wang, Z.F. (2021) Conversion of Fe-bearing minerals in sludge to nanorod erdite for real electroplating wastewater treatment: Comparative study between ferrihydrite, hematite, magnetite, and troilite. Journal of Cleaner Production 298.

IBI (2015a) International Biochar Initiative: Standardized Product Definition and Product Testing Guidelines for Biochar that is used in Soil (Version 2.1).

IBI (2015b) State of the Biochar Industry 2015, The International Biochar Initiative (IBI).

IPCC (2019) Summary for Policymakers. In: Global Warming of 1.5°C; Chapter 4: Strengthening and Implementing the Global Response. Waterfield, T. (ed).

Ithan, F., Ulucan-Altuntas, K., Avsar, Y., Kurt, U. and Saral, A. (2019) Electrocoagulation process for the treatment of metal-plating wastewater: Kinetic modeling and energy consumption. Frontiers of Environmental Science & Engineering 13(5).

Javaid, A., Bajwa, R., Shafique, U. and Anwar, J. (2011) Removal of heavy metals by adsorption on Pleurotus ostreatus. Biomass & Bioenergy 35(5), 1675-1682.

Jiang, Z., Li, J., Jiang, D., Gao, Y., Chen, Y., Wang, W., Cao, B., Tao, Y., Wang, L. and Zhang, Y. (2020) Removal of atrazine by biochar-supported zero-valent iron catalyzed persulfate oxidation: Reactivity, radical production and transformation pathway. Environmental research 184, 109260.

John, M., Heuss-Assbichler, S., Ullrich, A. and Rettenwander, D. (2016) Purification of heavy metal loaded wastewater from electroplating industry under synthesis of delafossite (ABO(2)) by "Lt-delafossite process". Water Research 100, 98-104.

Johnston, C.P. and Chrysochoou, M. (2012) Investigation of Chromate Coordination on Ferrihydrite by in Situ ATR-FTIR Spectroscopy and Theoretical Frequency Calculations. Environmental Science & Technology 46(11), 5851-5858.

Johnston, C.P. and Chrysochoou, M. (2016) Mechanisms of Chromate, Selenate, and Sulfate Adsorption on Al-Substituted Ferrihydrite: Implications for Ferrihydrite Surface Structure and Reactivity. Environmental Science & Technology 50(7), 3589-3596.

Joseph, S.D., Camps-Arbestain, M., Lin, Y., Munroe, P., Chia, C., Hook, J., Van Zwieten, L., Kimber, S., Cowie, A. and Singh, B.J.S.R. (2010) An investigation into the reactions of biochar in soil. 48(7), 501-515.

Kamali, M., Appels, L., Kwon, E.E., Aminabhavi, T.M. and Dewil, R. (2021) Biochar in water and wastewater treatment - a sustainability assessment. Chemical Engineering Journal 420, 129946.

Kang, X., Zhang, Q., Liu, X., Song, J., Guo, H. and Wang, L. (2023) The interface mechanism of sludge biochar activating persulfate to remove tetracycline: The role of the C-O-Fe bridge at the carbon surface. Journal of Cleaner Production 384, 135514.

Kawamoto, K., Yokoo, H., Ochiai, A., Nakano, Y., Takeda, A., Oki, T., Takehara, M., Uehara, M., Fukuyama, K., Ohara, Y., Ohnuki, T., Hochella, M.F. and Utsunomiya, S. (2021) The role of nanoscale aggregation of ferrihydrite and amorphous silica in the natural attenuation of contaminant metals at mill tailings sites. Geochimica Et Cosmochimica Acta.

Keiluweit, M., Nico, P.S., Johnson, M.G. and Kleber, M. (2010) Dynamic Molecular Structure of Plant Biomass-Derived Black Carbon (Biochar). Environmental Science & Technology 44(4), 1247-1253.

Khatoon, A., Rao, R.A.K. and Nasar, A. (2021) Preparation and characterization of epichlorohydrin treated Putranjiva roxburghii seeds as a novel adsorbent: removal of Ni(II) from the artificial and real electroplating wastewaters. Separation Science and Technology 56(17), 2880-2894.

Kim, C., Lee, C.R., Song, Y.E., Heo, J., Choi, S.M., Lim, D.H., Cho, J., Park, C., Jang, M. and Kim, J.R. (2017) Hexavalent chromium as a cathodic electron acceptor in a bipolar membrane microbial fuel cell with the simultaneous treatment of electroplating wastewater. Chemical Engineering Journal 328, 703-707.

Kim, E.J. and Baek, K. (2019) Selective recovery of ferrous oxalate and removal of arsenic and other metals from soil-washing wastewater using a reduction reaction. Journal of Cleaner Production 221, 635-643.

Kim, H.-B., Kim, J.-G., Kim, T., Alessi, D.S. and Baek, K. (2020) Mobility of arsenic in soil amended with biochar derived from biomass with different lignin contents: Relationships between lignin content and dissolved organic matter leaching. Chemical Engineering Journal 393, 124687.

Kim, J., Yoon, S., Choi, M., Min, K.J., Park, K.Y., Chon, K. and Bae, S. (2022) Metal ion recovery from electrodialysis-concentrated plating wastewater via pilot-scale sequential electrowinning/chemical precipitation. Journal of Cleaner Production 330.

Kim, K., Kim, J., Bokare, A.D., Choi, W., Yoon, H.-I. and Kim, J. (2015) Enhanced Removal of Hexavalent Chromium in the Presence of H2O2 in Frozen Aqueous Solutions. Environmental Science & Technology 49(18), 10937-10944.

Kluepfel, L., Keiluweit, M., Kleber, M. and Sander, M. (2014) Redox Properties of Plant Biomass-Derived Black Carbon (Biochar). Environmental Science & Technology 48(10), 5601-5611.

Klüpfel, L., Keiluweit, M., Kleber, M. and Sander, M. (2014) Redox Properties of Plant Biomass-Derived Black Carbon (Biochar). Environmental Science & Technology 48(10), 5601-5611.

Kobya, M., Demirbas, E., Ozyonar, F., Sirtbas, G. and Gengec, E. (2017) Treatments of alkaline non-cyanide, alkaline cyanide and acidic zinc electroplating wastewaters by electrocoagulation. Process Safety and Environmental Protection 105, 373-385.

Kovtun, A., Jones, D., Dell'Elce, S., Treossi, E., Liscio, A. and Palermo, V. (2019) Accurate chemical analysis of oxygenated graphene-based materials using X-ray photoelectron spectroscopy. Carbon 143, 268-275.

Kumar, M., Xiong, X., Wan, Z., Sun, Y., Tsang, D.C.W., Gupta, J., Gao, B., Cao, X., Tang, J. and Ok, Y.S. (2020) Ball milling as a mechanochemical technology for fabrication of novel biochar nanomaterials. Bioresource technology 312, 123613.

Kumar, R., Bishnoi, N.R., Garima and Bishnoi, K. (2008) Biosorption of chromium(VI) from aqueous solution and electroplating wastewater using fungal biomass. Chemical Engineering Journal 135(3), 202-208.

Kümmerer, K., Dionysiou, D.D., Olsson, O. and Fatta-Kassinos, D. (2018) A path to clean water. 361(6399), 222-224.

Lan, J., Ren, Y.X., Lu, Y.B., Liu, G.L., Luo, H.P. and Zhang, R.D. (2019) Combined microbial desalination and chemical-production cell with Fenton process for treatment of electroplating wastewater nanofiltration concentrate. Chemical Engineering Journal 359, 1139-1149.

Lee, C.G., Lee, S., Park, J.A., Park, C., Lee, S.J., Kim, S.B., An, B., Yun, S.T., Lee, S.H. and Choi, J.W. (2017) Removal of copper, nickel and chromium mixtures from metal plating wastewater by adsorption with modified carbon foam. Chemosphere 166, 203-211.

Lee, C.G., Song, M.K., Ryu, J.C., Park, C., Choi, J.W. and Lee, S.H. (2016) Application of carbon foam for heavy metal removal from industrial plating wastewater and toxicity evaluation of the adsorbent. Chemosphere 153, 1-9.

Lehmann, J. (2007a) Bio-energy in the black. Frontiers in Ecology and the Environment 5(7), 381-387.

Lehmann, J. (2007b) A handful of carbon. Nature 447(7141), 143-144.

Lehmann, J., Cowie, A., Masiello, C.A., Kammann, C., Woolf, D., Amonette, J.E., Cayuela, M.L., Camps-Arbestain, M. and Whitman, T. (2021) Biochar in climate change mitigation. Nature Geoscience 14(12), 883-+.

Lehmann, J., Gaunt, J. and Rondon, M. (2006) Bio-char Sequestration in Terrestrial Ecosystems – A Review. Mitigation and Adaptation Strategies for Global Change 11(2), 403-427.

Lehmann, J. and Joseph, S. (2012) Biochar for environmental management: science and technology, Routledge.

Lehmann, J. and Joseph, S. (2015) Biochar for environmental management : science, technology and implementation, London ; New York : Routledge/Taylor & Francis Group, London ; New York.

Leng, L. and Huang, H. (2018) An overview of the effect of pyrolysis process parameters on biochar stability. Bioresource technology 270, 627-642.

Lewin, E., Gorgoi, M., Schäfers, F., Svensson, S. and Jansson, U. (2009) Influence of sputter damage on the XPS analysis of metastable nanocomposite coatings. Surface and Coatings Technology 204(4), 455-462.

Li, B., Yang, L., Wang, C.-q., Zhang, Q.-p., Liu, Q.-c., Li, Y.-d. and Xiao, R. (2017a) Adsorption of Cd(II) from aqueous solutions by rape straw biochar derived from different modification processes. Chemosphere 175, 332-340.

Li, H., Chen, Y., Liu, S. and Liu, Q. (2021a) Enhancement of hydrothermal synthesis of FDU-12-derived nickel phyllosilicate using double accelerators of ammonium fluoride and urea for CO2 methanation. Journal of CO2 Utilization 52, 101677.

Li, H., Dong, X., da Silva, E.B., de Oliveira, L.M., Chen, Y. and Ma, L.Q. (2017b) Mechanisms of metal sorption by biochars: Biochar characteristics and modifications. Chemosphere 178, 466-478.

Li, J., Guan, X. and Zhang, W.-x. (2021b) Architectural Genesis of Metal(loid)s with Iron Nanoparticle in Water. Environmental Science & Technology 55(19), 12801-12808.

Li, J., Xu, H., Huang, Z., Hong, Q., Qiu, Y., Yan, N. and Qu, Z. (2021c) Strengthen the Affinity of Element Mercury on the Carbon-Based Material by Adjusting the Coordination Environment of Single-Site Manganese. Environmental Science & Technology 55(20), 14126-14135.

Li, M., Shang, H., Li, H., Hong, Y., Ling, C., Wei, K., Zhou, B., Mao, C., Ai, Z. and Zhang, L. (2021d)

Kirkendall Effect Boosts Phosphorylated nZVI for Efficient Heavy Metal Wastewater Treatment. 60(31), 17115-17122.

Li, S., Harris, S., Anandhi, A. and Chen, G. (2019) Predicting biochar properties and functions based on feedstock and pyrolysis temperature: A review and data syntheses. Journal of Cleaner Production 215, 890-902.

Li, S., Shao, L., Zhang, H., He, P. and Lü, F. (2020a) Quantifying the contributions of surface area and redox-active moieties to electron exchange capacities of biochar. Journal Of Hazardous Materials 394, 122541.

Li, S.Y., Hu, Z.Q., Xie, S.B., Liu, H.Y. and Liu, J.X. (2018) Removal of Cr(VI) From Electroplating Industry Effluent via Electrochemical Reduction. International Journal of Electrochemical Science 13(1), 655-663.

Li, T., Bian, H.K., Wang, W., Fan, X.Q., Tao, L.Y., Yu, G. and Deng, S.B. (2022) Removal of low-concentration nickel in electroplating wastewater via incomplete decomplexation by ozonation and subsequent resin adsorption. Chemical Engineering Journal 435.

Li, W., Gao, X., Chen, Z., Guo, R., Zou, G., Hou, H., Deng, W., Ji, X. and Zhao, J. (2020b) Electrochemically activated MnO cathodes for high performance aqueous zinc-ion battery. Chemical Engineering Journal 402, 125509.

Li, X., Hayashi, J.-i. and Li, C.-Z. (2006) FT-Raman spectroscopic study of the evolution of char structure during the pyrolysis of a Victorian brown coal. Fuel 85(12), 1700-1707.

Li, X., Qin, Y., Jia, Y., Li, Y., Zhao, Y., Pan, Y. and Sun, J. (2021e) Preparation and application of Fe/biochar (Fe-BC) catalysts in wastewater treatment: A review. Chemosphere 274, 129766.

Li, X., Wang, L., Zhang, B., Khajeh, A. and Shahbazi, A. (2020c) Iron oxide supported on silicalite-1 as a multifunctional material for biomass chemical looping gasification and syngas upgrading. Chemical Engineering Journal 401, 125943.

Li, Y., Qi, X., Li, G. and Wang, H. (2021f) Efficient removal of arsenic from copper smelting wastewater via a synergy of steel-making slag and KMnO4. Journal of Cleaner Production 287, 125578.

Li, Y., Yang, M., Pentrak, M., He, H. and Arai, Y. (2020d) Carbonate-Enhanced Transformation of Ferrihydrite to Hematite. Environmental Science & Technology 54(21), 13701-13708.

Li, Z., Ji, S., Liu, Y., Cao, X., Tian, S., Chen, Y., Niu, Z. and Li, Y. (2020e) Well-Defined Materials for Heterogeneous Catalysis: From Nanoparticles to Isolated Single-Atom Sites. Chemical Reviews 120(2), 623-682.

Li, Z., Sun, Y., Yang, Y., Han, Y., Wang, T., Chen, J. and Tsang, D.C.W. (2020f) Biochar-supported nanoscale zero-valent iron as an efficient catalyst for organic degradation in groundwater. Journal Of Hazardous Materials 383, 121240.

Lian, F., Yu, W., Wang, Z. and Xing, B. (2019) New Insights into Black Carbon Nanoparticle-Induced Dispersibility of Goethite Colloids and Configuration-Dependent Sorption for Phenanthrene. Environmental Science & Technology 53(2), 661-670.

Liang, C., Sun, H., Ling, C., Liu, X., Li, M., Zhang, X., Guo, F., Zhang, X., Shi, Y., Cao, S., He, H., Ai,

Z. and Zhang, L. (2023) Pyrolysis temperature-switchable Fe-N sites in pharmaceutical sludge biochar toward peroxymonosulfate activation for efficient pollutants degradation. Water Research 228, 119328.

Liang, G., Yang, Z., Wang, Z., Cai, X., Zhang, X. and Xie, X. (2021a) Relying on the non-radical pathways for selective degradation organic pollutants in Fe and Cu co-doped biochar/peroxymonosulfate system: The roles of Cu, Fe, defect sites and ketonic group. Separation and Purification Technology 279, 119697.

Liang, J., Duan, X., Xu, X., Chen, K., Wu, F., Qiu, H., Liu, C., Wang, S. and Cao, X. (2021b) Biomass-derived pyrolytic carbons accelerated Fe(III)/Fe(II) redox cycle for persulfate activation: Pyrolysis temperature-depended performance and mechanisms. Applied Catalysis B: Environmental 297, 120446.

Liang, J., Duan, X., Xu, X., Chen, K., Zhang, Y., Zhao, L., Qiu, H., Wang, S. and Cao, X. (2021c) Persulfate Oxidation of Sulfamethoxazole by Magnetic Iron-Char Composites via Nonradical Pathways: Fe(IV) Versus Surface-Mediated Electron Transfer. Environmental Science & Technology 55(14), 10077-10086.

Liang, J., Duan, X., Xu, X., Chen, K., Zhang, Y., Zhao, L., Qiu, H., Wang, S. and Cao, X. (2021d) Persulfate Oxidation of Sulfamethoxazole by Magnetic Iron-Char Composites via Nonradical Pathways: Fe(IV) Versus Surface-Mediated Electron Transfer. Environmental Science & Technology.

Liang, J., Tang, D., Huang, L., Chen, Y., Ren, W. and Sun, J. (2018) High oxygen reduction reaction performance nitrogen-doped biochar cathode: A strategy for comprehensive utilizing nitrogen and carbon in water hyacinth. Bioresource technology 267, 524-531.

Liao, T., Xi, Y., Zhang, L., Li, J. and Cui, K. (2021) Removal of toxic arsenic (As(III)) from industrial wastewater by ultrasonic enhanced zero-valent lead combined with CuSO4. Journal Of Hazardous Materials 408, 124464.

Lin, L., Qiu, W., Wang, D., Huang, Q., Song, Z. and Chau, H.W. (2017) Arsenic removal in aqueous solution by a novel Fe-Mn modified biochar composite: Characterization and mechanism. Ecotoxicology and Environmental Safety 144, 514-521.

Ling, C., Wu, S., Han, J., Dong, T., Zhu, C., Li, X., Xu, L., Zhang, Y., Zhou, M. and Pan, Y. (2022) Sulfide-modified zero-valent iron activated periodate for sulfadiazine removal: Performance and dominant routine of reactive species production. Water Research 220, 118676.

Ling, L., Huang, X., Li, M. and Zhang, W.-x. (2017) Mapping the Reactions in a Single Zero-Valent Iron Nanoparticle. Environmental Science & Technology 51(24), 14293-14300.

Ling, L. and Zhang, W.-x. (2014) Sequestration of Arsenate in Zero-Valent Iron Nanoparticles: Visualization of Intraparticle Reactions at Angstrom Resolution. Environmental Science & Technology Letters 1(7), 305-309.

Ling, L. and Zhang, W.-x. (2017) Visualizing Arsenate Reactions and Encapsulation in a Single Zero-Valent Iron Nanoparticle. Environmental Science & Technology 51(4), 2288-2294.

Liu, B., Kim, K.-H., Kumar, V. and Kim, S. (2020a) A review of functional sorbents for adsorptive removal of arsenic ions in aqueous systems. Journal Of Hazardous Materials 388, 121815.

Liu, C., Fiol, N., Poch, J. and Villaescusa, I. (2016) A new technology for the treatment of chromium electroplating wastewater based on biosorption. Journal of Water Process Engineering 11, 143-151.

Liu, H.B., Zhu, M.L. and Gao, S.S. (2014) Application of three tailing-based composites in treating comprehensive electroplating wastewater. Water Science and Technology 70(1), 47-54.

Liu, J., Xu, Z. and Zhang, W. (2023) Unraveling the role of Fe in As(III & V) removal by biochar via machine learning exploration. Separation and Purification Technology 311, 123245.

Liu, K., Li, F., Cui, J., Yang, S. and Fang, L. (2020b) Simultaneous removal of Cd(II) and As(III) by graphene-like biochar-supported zero-valent iron from irrigation waters under aerobic conditions: Synergistic effects and mechanisms. Journal Of Hazardous Materials 395, 122623.

Liu, L.-L., Chen, F., Wu, J.-H., Ke, M.-K., Cui, C., Chen, J.-J. and Yu, H.-Q. (2022) Edge electronic vacancy on ultrathin carbon nitride nanosheets anchoring O2 to boost H2O2 photoproduction. Applied Catalysis B: Environmental 302, 120845.

Liu, L., Qiao, Q., Tan, W., Sun, X., Liu, C., Dang, Z. and Qiu, G. (2021a) Arsenic detoxification by iron-manganese nodules under electrochemically controlled redox: Mechanism and application. Journal Of Hazardous Materials 403, 123912.

Liu, L.H., Zhao, J.R., Liu, X., Bai, S.Y., Lin, H. and Wang, D.Q. (2021b) Reduction and removal of As(V) in aqueous solution by biochar derived from nano zero-valent-iron (nZVI) and sewage sludge. Chemosphere 277.

Liu, N., Zhang, Y., Xu, C., Liu, P., Lv, J., Liu, Y. and Wang, Q. (2020c) Removal mechanisms of aqueous Cr(VI) using apple wood biochar: a spectroscopic study. Journal Of Hazardous Materials 384, 121371.

Liu, S.Q., Mishra, S.B., Zhang, Y. and Qi, L. (2017) Uptake of Hexavalent Chromium in Electroplating Wastewater by Hydrothermally Treated and Functionalized Sand and Its Sustainable Reutilization for Glass Production. Acs Sustainable Chemistry & Engineering 5(2), 1509-1516.

Liu, S.Q., Sun, Y.Y., Wang, R.L., Mishra, S.B., Duan, H.M. and Qu, H. (2018) Modification of sand with iron and copper derived from electroplating wastewater for efficient adsorption of phosphorus from aqueous solutions: A combinatorial approach for an effective waste minimization. Journal of Cleaner Production 200, 471-477.

Liu, T.Y., Yang, X., Wang, Z.L. and Yan, X.X. (2013a) Enhanced chitosan beads-supported Fe-0-nanoparticles for removal of heavy metals from electroplating wastewater in permeable reactive barriers. Water Research 47(17), 6691-6700.

Liu, W.-J., Jiang, H., Tian, K., Ding, Y.-W. and Yu, H.-Q. (2013b) Mesoporous Carbon Stabilized MgO Nanoparticles Synthesized by Pyrolysis of MgCl2 Preloaded Waste Biomass for Highly Efficient CO2 Capture. Environmental Science & Technology 47(16), 9397-9403.

Liu, X.N., Shen, F., Smith, R.L. and Qi, X.H. (2019) Black liquor-derived calcium-activated biochar for recovery of phosphate from aqueous solutions. Bioresource technology 294, 8.

López-Sánchez, J., Serrano, A., del Campo, A., Muñoz-Noval, Á., Salas-Colera, E., Cabero, M., Varela, M., Abuín, M., Castro, G.R., Rubio-Zuazo, J., Rodríguez de la Fuente, Ó. and Carmona, N. (2022) A combined micro-Raman, X-ray absorption and magnetic study to follow the glycerol-assisted growth of epsilon-iron oxide sol-gel coatings. Journal of Alloys and Compounds 892, 162061.

Lu, Y., Yang, F.J., Chen, S.Y., Shi, W.C., Qi, C.D. and Peng, G.L. (2022) Decomplexation of Ni(II)-citrate and recovery of nickel from chelated nickel containing electroplating wastewater by peroxymonosulfate with nickel. Separation and Purification Technology 283.

Luan, F., Xie, L., Sheng, J., Li, J., Zhou, Q. and Zhai, G. (2012) Reduction of nitrobenzene by steel convert slag with Fe(II) system: The role of calcium in steel slag. Journal Of Hazardous Materials 217, 416-421.

Luo, J., Li, X., Ge, C., Müller, K., Yu, H., Huang, P., Li, J., Tsang, D.C.W., Bolan, N.S., Rinklebe, J. and Wang, H. (2018) Sorption of norfloxacin, sulfamerazine and oxytetracycline by KOH-modified biochar under single and ternary systems. Bioresource technology 263, 385-392.

Luong, V.T., Cañas Kurz, E.E., Hellriegel, U., Luu, T.L., Hoinkis, J. and Bundschuh, J. (2018) Iron-based subsurface arsenic removal technologies by aeration: A review of the current state and future prospects. Water Research 133, 110-122.

Lyu, H., Tang, J., Cui, M., Gao, B. and Shen, B. (2020) Biochar/iron (BC/Fe) composites for soil and groundwater remediation: Synthesis, applications, and mechanisms. Chemosphere 246, 125609.

Lyu, H., Tang, J., Huang, Y., Gai, L., Zeng, E.Y., Liber, K. and Gong, Y. (2017) Removal of hexavalent chromium from aqueous solutions by a novel biochar supported nanoscale iron sulfide composite. Chemical Engineering Journal 322, 516-524.

Malamis, S., Katsou, E., Kosanovic, T. and Haralambous, K.J. (2012) Combined Adsorption and Ultrafiltration Processes Employed for the Removal of Pollutants from Metal Plating Wastewater. Separation Science and Technology 47(7), 983-996.

Mamun, A.A., Morita, M., Matsuoka, M. and Tokoro, C. (2017) Sorption mechanisms of chromate with coprecipitated ferrihydrite in aqueous solution. Journal Of Hazardous Materials 334, 142-149.

Mandal, S., Sarkar, B., Bolan, N., Ok, Y.S. and Naidu, R. (2017) Enhancement of chromate reduction in soils by surface modified biochar. Journal of Environmental Management 186, 277-284.

Mao, Q., Zhou, Y., Yang, Y., Zhang, J., Liang, L., Wang, H., Luo, S., Luo, L., Jeyakumar, P., Ok, Y.S. and Rizwan, M. (2019) Experimental and theoretical aspects of biochar-supported nanoscale zero-valent iron activating H2O2 for ciprofloxacin removal from aqueous solution. Journal Of Hazardous Materials 380, 120848.

Martin-Lara, M.A., Blazquez, G., Trujillo, M.C., Perez, A. and Calero, M. (2014) New treatment of real electroplating wastewater containing heavy metal ions by adsorption onto olive stone. Journal of Cleaner Production 81, 120-129.

Martín-Lara, M.A., Blázquez, G., Trujillo, M.C., Pérez, A. and Calero, M. (2014) New treatment of real electroplating wastewater containing heavy metal ions by adsorption onto olive stone. Journal of Cleaner Production 81, 120-129.

Matta, R., Hanna, K. and Chiron, S. (2007) Fenton-like oxidation of 2,4,6-trinitrotoluene using different iron minerals. Science of the Total Environment 385(1), 242-251.

Mazarji, M., Minkina, T., Sushkova, S., Mandzhieva, S., Bidhendi, G.N., Barakhov, A. and Bhatnagar, A. (2021) Effect of nanomaterials on remediation of polycyclic aromatic hydrocarbons-contaminated soils: A review. Journal of Environmental Management 284, 112023.

McCann, C.M., Peacock, C.L., Hudson-Edwards, K.A., Shrimpton, T., Gray, N.D. and Johnson, K.L. (2018) In situ arsenic oxidation and sorption by a Fe-Mn binary oxide waste in soil. Journal Of Hazardous Materials 342, 724-731.

McDonald-Wharry, J., Manley-Harris, M. and Pickering, K. (2013) Carbonisation of biomass-derived chars and the thermal reduction of a graphene oxide sample studied using Raman spectroscopy. Carbon 59, 383-405.

Medeiros, D.C.C.d.S., Nzediegwu, C., Benally, C., Messele, S.A., Kwak, J.-H., Naeth, M.A., Ok, Y.S., Chang, S.X. and Gamal El-Din, M. (2021) Pristine and engineered biochar for the removal of contaminants co-existing in several types of industrial wastewaters: A critical review. Science of the Total Environment, 151120.

Meers, E., Samson, R., Tack, F.M.G., Ruttens, A., Vandegehuchte, M., Vangronsveld, J. and Verloo, M.G. (2007) Phytoavailability assessment of heavy metals in soils by single extractions and accumulation by Phaseolus vulgaris. Environmental and Experimental Botany 60(3), 385-396.

Meng, X., Bang, S. and Korfiatis, G.P. (2000) Effects of silicate, sulfate, and carbonate on arsenic removal by ferric chloride. Water Research 34(4), 1255-1261.

Miranda, L.S., Ayoko, G.A., Egodawatta, P. and Goonetilleke, A. (2022) Adsorption-desorption behavior of heavy metals in aquatic environments: Influence of sediment, water and metal ionic properties. Journal Of Hazardous Materials 421, 126743.

Moreira, L.J.D., da Silva, E.B., Fontes, M.P.F., Liu, X. and Ma, L.Q. (2018) Speciation, bioaccessibility and potential risk of chromium in Amazon forest soils. Environmental Pollution 239, 384-391.

Mu, Y., Jia, F., Ai, Z. and Zhang, L. (2017) Iron oxide shell mediated environmental remediation properties of nano zero-valent iron. Environmental Science: Nano 4(1), 27-45.

Mullet, M., Demoisson, F., Humbert, B., Michot, L.J. and Vantelon, D. (2007) Aqueous Cr(VI) reduction by pyrite: Speciation and characterisation of the solid phases by X-ray photoelectron, Raman and X-ray absorption spectroscopies. Geochimica Et Cosmochimica Acta 71(13), 3257-3271.

Nadejde, C., Neamtu, M., Hodoroaba, V.D., Schneider, R.J., Paul, A., Ababei, G. and Panne, U. (2015) Green Fenton-like magnetic nanocatalysts: Synthesis, characterization and catalytic application. Applied Catalysis B: Environmental 176-177, 667-677.

Nan, H., Xiao, Z., Zhao, L., Yang, F., Xu, H., Xu, X. and Qiu, H. (2020) Nitrogen Transformation during Pyrolysis of Various N-Containing Biowastes with Participation of Mineral Calcium. Acs Sustainable Chemistry & Engineering 8(32), 12197-12207.

Nandagudi, A., Nagarajarao, S.H., Santosh, M.S., Basavaraja, B.M., Malode, S.J., Mascarenhas, R.J. and Shetti, N.P. (2022) Hydrothermal synthesis of transition metal oxides, transition metal oxide/carbonaceous material nanocomposites for supercapacitor applications. Materials Today Sustainability 19, 100214.

Nguyen, Q.H., Tran, A.T.K., Hoang, N.T.T., Tran, Y.T.H., Nguyen, P.X., Pham, T.T., Nguyen, M.K. and Van der Bruggen, B. (2022) Plastic waste as a valuable resource: strategy to remove heavy metals from wastewater in bench scale application. Environmental Science and Pollution Research 29(28), 42074-42089.

Niazi, N.K., Bibi, I., Shahid, M., Ok, Y.S., Burton, E.D., Wang, H., Shaheen, S.M., Rinklebe, J. and Lüttge, A. (2018) Arsenic removal by perilla leaf biochar in aqueous solutions and groundwater: An integrated spectroscopic and microscopic examination. Environmental Pollution 232, 31-41.

Numpilai, T., Ng, K.H., Polsomboon, N., Cheng, C.K., Donphai, W., Chareonpanich, M. and Witoon, T. (2022) Hydrothermal synthesis temperature induces sponge-like loose silica structure: A potential support for Fe2O3-based adsorbent in treating As(V)-contaminated water. Chemosphere 308, 136267.

Nzediegwu, C., Naeth, M.A. and Chang, S.X. (2021) Feedstock type drives surface property, demineralization and element leaching of nitric acid-activated biochars more than pyrolysis temperature. Bioresource technology, 126316.

Oden, M.K. and Sari-Erkan, H. (2018) Treatment of metal plating wastewater using iron electrode by electrocoagulation process: Optimization and process performance. Process Safety and Environmental Protection 119, 207-217.

Ona-Nguema, G., Morin, G., Wang, Y., Foster, A.L., Juillot, F., Calas, G. and Brown, G.E. (2010) XANES Evidence for Rapid Arsenic(III) Oxidation at Magnetite and Ferrihydrite Surfaces by Dissolved O2 via Fe2+-Mediated Reactions. Environmental Science & Technology 44(14), 5416-5422.

Orescanin, V., Kollar, R., Mikelic, I.L. and Nad, K. (2013) Electroplating wastewater treatment by the combined electrochemical and ozonation methods. Journal of Environmental Science and Health Part a-Toxic/Hazardous Substances & Environmental Engineering 48(11), 1450-1455.

Otero-González, L., Mikhalovsky, S.V., Václavíková, M., Trenikhin, M.V., Cundy, A.B. and Savina, I.N. (2020) Novel nanostructured iron oxide cryogels for arsenic (As(III)) removal. Journal Of Hazardous Materials 381, 120996.

Pan, H., Yang, X., Chen, H., Sarkar, B., Bolan, N., Shaheen, S.M., Wu, F., Che, L., Ma, Y., Rinklebe, J. and Wang, H. (2021) Pristine and iron-engineered animal- and plant-derived biochars enhanced bacterial abundance and immobilized arsenic and lead in a contaminated soil. Science of the Total Environment 763, 144218.

Pandey, B., Kinrade, S.D. and Catalan, L.J.J. (2012) Effects of carbonation on the leachability and compressive strength of cement-solidified and geopolymer-solidified synthetic metal wastes. Journal of Environmental Management 101, 59-67.

Pang, H., Diao, Z., Wang, X., Ma, Y., Yu, S., Zhu, H., Chen, Z., Hu, B., Chen, J. and Wang, X. (2019) Adsorptive and reductive removal of U(VI) by Dictyophora indusiate-derived biochar supported sulfide NZVI from wastewater. Chemical Engineering Journal 366, 368-377.

Pang, S.-Y., Jiang, J. and Ma, J. (2011) Oxidation of Sulfoxides and Arsenic(III) in Corrosion of Nanoscale Zero Valent Iron by Oxygen: Evidence against Ferryl Ions (Fe(IV)) as Active Intermediates in Fenton Reaction. Environmental Science & Technology 45(1), 307-312.

Park, J.-H., Wang, J.J., Tafti, N. and Delaune, R.D. (2019) Removal of Eriochrome Black T by sulfate radical generated from Fe-impregnated biochar/persulfate in Fenton-like reaction. Journal of Industrial and Engineering Chemistry 71, 201-209.

Peng, G.L., Deng, S.B., Liu, F.L., Li, T. and Yu, G. (2020a) Superhigh adsorption of nickel from electroplating wastewater by raw and calcined electroplating sludge waste. Journal of Cleaner Production 246.

Peng, G.L., Deng, S.B., Liu, F.L., Qi, C.D., Tao, L.Y., Li, T. and Yu, G. (2020b) Calcined electroplating sludge as a novel bifunctional material for removing Ni(II)-citrate in electroplating wastewater. Journal of Cleaner Production 262.

Pereira, F.V., Gurgel, L.V.A. and Gil, L.F. (2010) Removal of Zn2+ from aqueous single metal solutions and electroplating wastewater with wood sawdust and sugarcane bagasse modified with EDTA dianhydride (EDTAD). Journal Of Hazardous Materials 176(1-3), 856-863.

Pignatello, J.J., Mitch, W.A. and Xu, W. (2017) Activity and Reactivity of Pyrogenic Carbonaceous Matter toward Organic Compounds. Environmental Science & Technology 51(16), 8893-8908.

Poggenburg, C., Mikutta, R., Schippers, A., Dohrmann, R. and Guggenberger, G. (2018) Impact of natural organic matter coatings on the microbial reduction of iron oxides. Geochimica Et Cosmochimica Acta 224, 223-248.

Pontoni, L., van Hullebusch, E.D., Fabbricino, M., Esposito, G. and Pirozzi, F. (2016) Assessment of trace heavy metals dynamics during the interaction of aqueous solutions with the artificial OECD soil: Evaluation of the effect of soil organic matter content and colloidal mobilization. Chemosphere 163, 382-391.

Portillo-Vélez, N.S. and Zanella, R. (2020) Comparative study of transition metal (Mn, Fe or Co) catalysts supported on titania: Effect of Au nanoparticles addition towards CO oxidation and soot combustion reactions. Chemical Engineering Journal 385, 123848.

Poulton, S.W. and Canfield, D.E. (2005) Development of a sequential extraction procedure for iron: implications for iron partitioning in continentally derived particulates. Chemical Geology 214(3), 209-221.

Qi, F., Xu, B., Zhao, L., Chen, Z., Zhang, L., Sun, D. and Ma, J. (2012) Comparison of the efficiency and mechanism of catalytic ozonation of 2,4,6-trichloroanisole by iron and manganese modified bauxite. Applied Catalysis B: Environmental 121-122, 171-181.

Qi, H., Pan, G., Shi, X. and Sun, Z. (2022) Cu–Fe–FeC3@nitrogen-doped biochar microsphere catalyst derived from CuFe2O4@chitosan for the efficient removal of amoxicillin through the heterogeneous electro-Fenton process. Chemical Engineering Journal 434, 134675.

Qian, L., Shang, X., Zhang, B., Zhang, W., Su, A., Chen, Y., Ouyang, D., Han, L., Yan, J. and Chen, M. (2019) Enhanced removal of Cr(VI) by silicon rich biochar-supported nanoscale zero-valent iron. Chemosphere 215, 739-745.

Qian, S., Zhou, X., Fu, Y., Song, B., Yan, H., Chen, Z., Sun, Q., Ye, H., Qin, L. and Lai, C. (2023) Biochar-compost as a new option for soil improvement: Application in various problem soils. Science of the Total Environment 870, 162024.

Qian, X.F., Ren, M., Zhu, Y., Yue, D.T., Han, Y., Jia, J.P. and Zhao, Y.X. (2017) Visible Light Assisted

Heterogeneous Fenton-Like Degradation of Organic Pollutant via alpha-FeOOH/Mesoporous Carbon Composites. Environmental Science & Technology 51(7), 3993-4000.

Qin, J., Wang, X., Deng, M., Li, H. and Lin, C. (2022) Red mud-biochar composites (co-pyrolyzed red mud-plant materials): Characteristics and improved efficacy on the treatment of acidic mine water and trace element-contaminated soils. Science of the Total Environment 844, 157062.

Qiu, Y., Xu, X., Xu, Z., Liang, J., Yu, Y. and Cao, X. (2020) Contribution of different iron species in the iron-biochar composites to sorption and degradation of two dyes with varying properties. Chemical Engineering Journal 389, 124471.

Qu, J., Che, N., Niu, G., Liu, L., Li, C. and Liu, Y. (2023) Iron/manganese binary metal oxide-biochar nano-composites with high adsorption capacities of Cd2+: Preparation and adsorption mechanisms. Journal of Water Process Engineering 51, 103332.

Qu, J.H., Tian, X., Jiang, Z., Cao, B., Akindolie, M.S., Hu, Q., Feng, C.C., Feng, Y., Meng, X.L. and Zhang, Y. (2020) Multi -component adsorption of Pb(II), Cd(II) and Ni(II) onto microwave-functionalized cellulose: Kinetics, isotherms, thermodynamics, mechanisms and application for electroplating wastewater purification. Journal Of Hazardous Materials 387.

Rahman, M.L., Fui, C.J., Sarjadi, M.S., Arshad, S.E., Musta, B., Abdullah, M.H., Sarkar, S.M. and O'Reilly, E.J. (2020) Poly(amidoxime) ligand derived from waste palm fiber for the removal of heavy metals from electroplating wastewater. Environmental Science and Pollution Research 27(27), 34541-34556.

Rahman, M.L., Wong, Z.J., Sarjadi, M.S., Abdullah, M.H., Heffernan, M.A., Sarkar, M.S. and O'Reilly, E. (2021) Poly(hydroxamic acid) ligand from palm-based waste materials for removal of heavy metals from electroplating wastewater. Journal of Applied Polymer Science 138(2).

Rajabi, H., Mosleh, M.H., Mandal, P., Lea-Langton, A. and Sedighi, M. (2021) Sorption behaviour of xylene isomers on biochar from a range of feedstock. Chemosphere 268, 129310.

Rajoria, S., Vashishtha, M. and Sangal, V.K. (2021) Review on the treatment of electroplating industry wastewater by electrochemical methods. Materials Today: Proceedings 47, 1472-1479.

Ramos, M.A.V., Yan, W., Li, X.-q., Koel, B.E. and Zhang, W.-x. (2009) Simultaneous Oxidation and Reduction of Arsenic by Zero-Valent Iron Nanoparticles: Understanding the Significance of the Core−Shell Structure. The Journal of Physical Chemistry C 113(33), 14591-14594.

Rawal, A., Joseph, S.D., Hook, J.M., Chia, C.H., Munroe, P.R., Donne, S., Lin, Y., Phelan, D., Mitchell, D.R.G., Pace, B., Horvat, J. and Webber, J.B.W. (2016) Mineral-Biochar Composites: Molecular Structure and Porosity. Environmental Science & Technology 50(14), 7706-7714.

Rong, X., Xie, M., Kong, L., Natarajan, V., Ma, L. and Zhan, J. (2019) The magnetic biochar derived from banana peels as a persulfate activator for organic contaminants degradation. Chemical Engineering Journal 372, 294-303.

Ruan, X., Sun, Y., Du, W., Tang, Y., Liu, Q., Zhang, Z., Doherty, W., Frost, R.L., Qian, G. and Tsang, D.C.W. (2019) Formation, characteristics, and applications of environmentally persistent free radicals in biochars: A review. Bioresource Technology 281, 457-468.

Sanford, J.R., Larson, R.A. and Runge, T. (2019) Nitrate sorption to biochar following chemical oxidation. Science of the Total Environment 669, 938-947.

Sankararamakrishnan, N., Sharma, A.K. and Sanghi, R. (2007) Novel chitosan derivative for the removal of cadmium in the presence of cyanide from electroplating wastewater. Journal Of Hazardous Materials 148(1-2), 353-359.

Scherrer, P. (1912) Kolloidchemie Ein Lehrbuch. Zsigmondy, R. (ed), pp. 387-409, Springer Berlin Heidelberg, Berlin, Heidelberg.

Senthilnathan, J., Mohan, S. and Palanivelu, K. (2005) Recovery of chromium from electroplating wastewater using DI 2-(ethylhexyl) phosphoric acid. Separation Science and Technology 40(10), 2125-2137.

Shaheen, S.M., Mosa, A., Natasha, Abdelrahman, H., Niazi, N.K., Antoniadis, V., Shahid, M., Song, H., Kwon, E.E. and Rinklebe, J. (2022) Removal of toxic elements from aqueous environments using nano zero-valent iron- and iron oxide-modified biochar: a review. Biochar 4(1), 24.

Shaheen, S.M., Niazi, N.K., Hassan, N.E.E., Bibi, I., Wang, H., Tsang, Daniel C.W., Ok, Y.S., Bolan, N. and Rinklebe, J. (2019a) Wood-based biochar for the removal of potentially toxic elements in water and wastewater: a critical review. INT MATER REV 64(4), 216-247.

Shaheen, S.M., Niazi, N.K., Hassan, N.E.E., Bibi, I., Wang, H.L., Tsang, D.C.W., Ok, Y.S., Bolan, N. and Rinklebe, J. (2019b) Wood-based biochar for the removal of potentially toxic elements in water and wastewater: a critical review. International Materials Reviews 64(4), 216-247.

Shan, D., Deng, S., Zhao, T., Wang, B., Wang, Y., Huang, J., Yu, G., Winglee, J. and Wiesner, M.R. (2016) Preparation of ultrafine magnetic biochar and activated carbon for pharmaceutical adsorption and subsequent degradation by ball milling. Journal Of Hazardous Materials 305, 156-163.

Shannon, M.A., Bohn, P.W., Elimelech, M., Georgiadis, J.G., Mariñas, B.J. and Mayes, A.M. (2008) Science and technology for water purification in the coming decades. Nature 452(7185), 301-310.

Sharma, D., Chaudhari, P.K. and Prajapati, A.K. (2020) Removal of chromium (VI) and lead from electroplating effluent using electrocoagulation. Separation Science and Technology 55(2), 321-331.

Shen, Y.F. (2015) Carbothermal synthesis of metal-functionalized nanostructures for energy and environmental applications. Journal of Materials Chemistry A 3(25), 13114-13188.

Shi, J., Han, H. and Xu, C. (2019) A novel enhanced anaerobic biodegradation method using biochar and Fe(OH)3@biochar for the removal of nitrogen heterocyclic compounds from coal gasification wastewater. Science of the Total Environment 697, 134052.

Shi, L.N., Zhang, X. and Chen, Z.L. (2011) Removal of Chromium (VI) from wastewater using bentonite-supported nanoscale zero-valent iron. Water Research 45(2), 886-892.

Shi, T.H., Wang, Z.C., Liu, Y., Jia, S.G. and Changming, D. (2009) Removal of hexavalent chromium from aqueous solutions by D301, D314 and D354 anion-exchange resins. Journal Of Hazardous Materials 161(2-3), 900-906.

Shi, Y.-L., Chen, W.-Q., Wu, S.-L. and Zhu, Y.-G. (2017) Anthropogenic Cycles of Arsenic in Mainland China: 1990–2010. Environmental Science & Technology 51(3), 1670-1678.

Singh, P., Pal, P., Mondal, P., Saravanan, G., Nagababu, P., Majumdar, S., Labhsetwar, N. and Bhowmick, S. (2021) Kinetics and mechanism of arsenic removal using sulfide-modified nanoscale zerovalent iron. Chemical Engineering Journal 412, 128667.

Sirianuntapiboon, S., Chairattanawan, K. and Rarunroeng, M. (2008) Biological removal of cyanide compounds from electroplating wastewater (EPWW) by sequencing batch reactor (SBR) system. Journal Of Hazardous Materials 154(1-3), 526-534.

Sizmur, T., Fresno, T., Akgül, G., Frost, H. and Moreno-Jiménez, E. (2017) Biochar modification to enhance sorption of inorganics from water. Bioresource technology 246, 34-47.

Slotznick, S.P., Eiler, J.M. and Fischer, W.W. (2018) The effects of metamorphism on iron mineralogy and the iron speciation redox proxy. Geochimica Et Cosmochimica Acta 224, 96-115.

Smedley, P.L. and Kinniburgh, D.G. (2002) A review of the source, behaviour and distribution of arsenic in natural waters. Applied Geochemistry 17(5), 517-568.

Song, Z., Garg, S., Ma, J. and Waite, T.D. (2020) Selective Arsenic Removal from Groundwaters Using Redox-Active Polyvinylferrocene-Functionalized Electrodes: Role of Oxygen. Environmental Science & Technology 54(19), 12081-12091.

Sowers, T.D., Harrington, J.M., Polizzotto, M.L. and Duckworth, O.W. (2017) Sorption of arsenic to biogenic iron (oxyhydr)oxides produced in circumneutral environments. Geochimica Et Cosmochimica Acta 198, 194-207.

Stein, S., Sivan, O., Yechieli, Y. and Kasher, R. (2021) Redox condition of saline groundwater from coastal aquifers influences reverse osmosis desalination process. Water Research 188, 116508.

Suksabye, P. and Thiravetyan, P. (2012) Cr(VI) adsorption from electroplating plating wastewater by chemically modified coir pith. Journal of Environmental Management 102, 1-8.

Suksabye, P., Thiravetyan, P., Nakbanpote, W. and Chayabutra, S. (2007) Chromium removal from electroplating wastewater by coir pith. Journal Of Hazardous Materials 141(3), 637-644.

Sun, F., Osseo-Asare, K.A., Chen, Y. and Dempsey, B.A. (2011) Reduction of As(V) to As(III) by commercial ZVI or As(0) with acid-treated ZVI. Journal Of Hazardous Materials 196, 311-317.

Sun, J., Prommer, H., Siade, A.J., Chillrud, S.N., Mailloux, B.J. and Bostick, B.C. (2018a) Model-Based Analysis of Arsenic Immobilization via Iron Mineral Transformation under Advective Flows. Environmental Science & Technology 52(16), 9243-9253.

Sun, T., Levin, B.D.A., Guzman, J.J.L., Enders, A., Muller, D.A., Angenent, L.T. and Lehmann, J. (2017) Rapid electron transfer by the carbon matrix in natural pyrogenic carbon. Nature Communications 8.

Sun, T., Levin, B.D.A., Schmidt, M.P., Guzman, J.J.L., Enders, A., Martínez, C.E., Muller, D.A., Angenent, L.T. and Lehmann, J. (2018b) Simultaneous Quantification of Electron Transfer by Carbon Matrices and Functional Groups in Pyrogenic Carbon. Environmental Science & Technology 52(15), 8538-8547.

Sun, T., Sun, Y., Xu, Y., Wang, L. and Liang, X. (2023) Effective removal of Hg2+ and Cd2+ in aqueous systems by Fe–Mn oxide modified biochar: A combined experimental and DFT calculation. Desalination 549, 116306.

Sun, Y., Yu, I.K.M., Tsang, D.C.W., Cao, X., Lin, D., Wang, L., Graham, N.J.D., Alessi, D.S., Komarek, M., Ok, Y.S., Feng, Y. and Li, X.D. (2019) Multifunctional iron-biochar composites for the removal of potentially toxic elements, inherent cations, and hetero-chloride from hydraulic fracturing wastewater. Environ Int 124, 521-532.

Sutton, C.C.R., da Silva, G. and Franks, G.V. (2015) Modeling the IR Spectra of Aqueous Metal Carboxylate Complexes: Correlation between Bonding Geometry and Stretching Mode Wavenumber Shifts. Chemistry-a European Journal 21(18), 6801-6805.

Sze, Y.K.P. and Xue, L.Z. (2003) Extraction of zinc and chromium(III) and its application to treatment of alloy electroplating wastewater. Separation Science and Technology 38(2), 405-425.

Tan, W.-T., Zhou, H., Tang, S.-F., Chen, Q., Zhou, X., Liu, X.-H., Zeng, P., Gu, J.-F. and Liao, B.-H. (2023) Simultaneous alleviation of Cd availability in contaminated soil and accumulation in rice (Oryza sativa L.) by Fe-Mn oxide-modified biochar. Science of the Total Environment 858, 159730.

Tang, L., Feng, H., Tang, J., Zeng, G., Deng, Y., Wang, J., Liu, Y. and Zhou, Y. (2017) Treatment of arsenic in acid wastewater and river sediment by Fe@Fe2O3 nanobunches: The effect of environmental conditions and reaction mechanism. Water Research 117, 175-186.

Tang, S.Y. and Qiu, Y.R. (2019) Selective separation of copper and zinc and regeneration of polymer from electroplating effluent using shear induced dissociation coupling with ultrafiltration. Korean Journal of Chemical Engineering 36(8), 1321-1327.

Tao, S., Liang, S., Chen, Y., Yu, W., Hou, H., Qiu, J., Zhu, Y., Xiao, K., Hu, J., Liu, B., Wang, Y. and Yang, J. (2020) Enhanced sludge dewaterability with sludge-derived biochar activating hydrogen peroxide: Synergism of Fe and Al elements in biochar. Water research (Oxford) 182, 115927-115927.

Tao, X., Hu, X.W., Wen, Z.P., Ming, Y., Li, J., Liu, Y.L. and Chen, R. (2022) Highly efficient Cr(VI) removal from industrial electroplating wastewater over Bi2S3 nanostructures prepared by dual sulfur-precursors: Insights on the promotion effect of sulfate ions. Journal Of Hazardous Materials 424.

Taylor, J.F., Robinson, A., Johnson, N., Marroquin-Cardona, A., Brattin, B., Taylor, R. and Phillips, T.D. (2009) In Vitro Evaluation of Ferrihydrite as an Enterosorbent for Arsenic from Contaminated Drinking Water. Environmental Science & Technology 43(14), 5501-5506.

Tian, B., Li, F., Zhang, Y., Wang, S., Zhou, Z., Han, H. and Xu, C. (2021a) Looking deeper: Decoding the core structure of a micron-sized S-ZVI particle. Chemical Engineering Journal 417, 128092.

Tian, S.-Q., Qi, J.-Y., Wang, Y.-P., Liu, Y.-L., Wang, L. and Ma, J. (2021b) Heterogeneous catalytic ozonation of atrazine with Mn-loaded and Fe-loaded biochar. Water Research 193, 116860.

Tian, S.-Q., Wang, L., Liu, Y.-L. and Ma, J. (2020) Degradation of organic pollutants by ferrate/biochar: Enhanced formation of strong intermediate oxidative iron species. Water Research 183, 116054.

Tian, S.-Q., Wang, L., Liu, Y.-L., Yang, T., Huang, Z.-S., Wang, X.-S., He, H.-Y., Jiang, J. and Ma, J. (2019) Enhanced Permanganate Oxidation of Sulfamethoxazole and Removal of Dissolved Organics with Biochar: Formation of Highly Oxidative Manganese Intermediate Species and in Situ Activation of Biochar. Environmental Science & Technology 53(9), 5282-5291.

Velazquez-Pena, S., Barrera-Diaz, C., Linares-Hernandez, I., Bilyeu, B. and Martinez-Delgadillo, S.A.

(2012) An Effective Electrochemical Cr(VI) Removal Contained in Electroplating Industry Wastewater and the Chemical Characterization of the Sludge Produced. Industrial & Engineering Chemistry Research 51(17), 5905-5910.

Verma, B. and Balomajumder, C. (2020) HEXAVALENT CHROMIUM REDUCTION FROM REAL ELECTROPLATING WASTEWATER BY CHEMICAL PRECIPITATION. Bulletin of the Chemical Society of Ethiopia 34(1), 67-74.

Verma, B., Sewani, H. and Balomajumder, C. (2020) Synthesis of carbon nanotubes via chemical vapor deposition: an advanced application in the Management of Electroplating Effluent. Environmental Science and Pollution Research 27(12), 14007-14018.

Veselská, V., Fajgar, R., Číhalová, S., Bolanz, R.M., Göttlicher, J., Steininger, R., Siddique, J.A. and Komárek, M. (2016) Chromate adsorption on selected soil minerals: Surface complexation modeling coupled with spectroscopic investigation. Journal Of Hazardous Materials 318, 433-442.

Villalobos, M. and Leckie, J.O. (2000) Carbonate adsorption on goethite under closed and open CO2 conditions. Geochimica Et Cosmochimica Acta 64(22), 3787-3802.

Vogt, C. and Weckhuysen, B.M. (2022) The concept of active site in heterogeneous catalysis. Nature Reviews Chemistry.

Wan, Z., Sun, Y., Tsang, D.C.W., Khan, E., Yip, A.C.K., Ng, Y.H., Rinklebe, J. and Ok, Y.S. (2020a) Customised fabrication of nitrogen-doped biochar for environmental and energy applications. Chemical Engineering Journal 401, 126136.

Wan, Z., Sun, Y., Tsang, D.C.W., Xu, Z., Khan, E., Liu, S.-H. and Cao, X. (2020b) Sustainable impact of tartaric acid as electron shuttle on hierarchical iron-incorporated biochar. Chemical Engineering Journal 395, 125138.

Wan, Z., Sun, Y., Tsang, D.C.W., Yu, I.K.M., Fan, J., Clark, J.H., Zhou, Y., Cao, X., Gao, B. and Ok, Y.S. (2019) A sustainable biochar catalyst synergized with copper heteroatoms and CO2 for singlet oxygenation and electron transfer routes. Green Chemistry 21(17), 4800-4814.

Wan, Z., Xu, Z., Sun, Y., He, M., Hou, D., Cao, X. and Tsang, D.C.W. (2021) Critical Impact of Nitrogen Vacancies in Nonradical Carbocatalysis on Nitrogen-Doped Graphitic Biochar. Environmental science & technology 55(10), 7004-7014.

Wan, Z.H., Cao, Y., Xu, Z.B., Duan, X.G., Xu, S.G., Hou, D.Y., Wang, S.B. and Tsang, D.C.W. (2023) Revealing Intrinsic Relations Between Cu Scales and Radical/Nonradical Oxidations to Regulate Nucleophilic/Electrophilic Catalysis. Advanced Functional Materials n/a(n/a), 2212227.

Wan, Z.H., Sun, Y.Q., Tsang, D.C.W., Hou, D.Y., Cao, X.D., Zhang, S.C., Gao, B. and Ok, Y.S. (2020c) Sustainable remediation with an electroactive biochar system: mechanisms and perspectives. Green Chemistry 22(9), 2688-2711.

Wang, C., Li, T., Yu, G. and Deng, S.B. (2021a) Removal of low concentrations of nickel ions in electroplating wastewater using capacitive deionization technology. Chemosphere 284.

Wang, D., Huang, D., Wu, S., Fang, G., Zhu, F., Chen, N., Liu, S., Zhu, C. and Zhou, D. (2021b) Pyrogenic Carbon Initiated the Generation of Hydroxyl Radicals from the Oxidation of Sulfide.

Environmental Science & Technology 55(9), 6001-6011.

Wang, D., Huang, D., Wu, S., Fang, G., Zhu, F., Chen, N., Liu, S., Zhu, C. and Zhou, D. (2021c) Pyrogenic Carbon Initiated the Generation of Hydroxyl Radicals from the Oxidation of Sulfide. Environmental Science & Technology.

Wang, F., Guo, C., Liu, X., Sun, H., Zhang, C., Sun, Y. and Zhu, H. (2022a) Revealing carbon-iron interaction characteristics in sludge-derived hydrochars under different hydrothermal conditions. Chemosphere 300, 134572.

Wang, G.R., Zhang, J., Liu, L., Zhou, J.Z., Liu, Q., Qian, G.R., Xu, Z.P. and Richards, R.M. (2018) Novel multi-metal containing MnCr catalyst made from manganese slag and chromium wastewater for effective selective catalytic reduction of nitric oxide at low temperature. Journal of Cleaner Production 183, 917-924.

Wang, H., Wang, H., Zhao, H. and Yan, Q. (2020a) Adsorption and Fenton-like removal of chelated nickel from Zn-Ni alloy electroplating wastewater using activated biochar composite derived from Taihu blue algae. Chemical Engineering Journal 379.

Wang, J., Kou, L., Zhao, L. and Duan, W. (2020b) One-pot fabrication of sludge-derived magnetic Fe,N-codoped carbon catalysts for peroxymonosulfate-induced elimination of phenolic contaminants. Chemosphere 248, 126076.

Wang, J., Liao, Z., Ifthikar, J., Shi, L., Du, Y., Zhu, J., Xi, S., Chen, Z. and Chen, Z. (2017a) Treatment of refractory contaminants by sludge-derived biochar/persulfate system via both adsorption and advanced oxidation process. Chemosphere 185, 754-763.

Wang, J. and Wang, S. (2019) Preparation, modification and environmental application of biochar: A review. Journal of Cleaner Production 227, 1002-1022.

Wang, K., Sun, Y., Tang, J., He, J. and Sun, H. (2020c) Aqueous Cr(VI) removal by a novel ball milled Fe0-biochar composite: Role of biochar electron transfer capacity under high pyrolysis temperature. Chemosphere 241, 125044.

Wang, L., Li, Z.T., Wang, Y., Brookes, P.C., Wang, F., Zhang, Q.C., Xu, J.M. and Liu, X.M. (2021d) Performance and mechanisms for remediation of Cd(II) and As(III) co-contamination by magnetic biochar-microbe biochemical composite: Competition and synergy effects. Science of the Total Environment 750.

Wang, L., O'Connor, D., Rinklebe, J., Ok, Y.S., Tsang, D.C.W., Shen, Z. and Hou, D. (2020d) Biochar Aging: Mechanisms, Physicochemical Changes, Assessment, And Implications for Field Applications. Environmental Science & Technology 54(23), 14797-14814.

Wang, S., Gao, B., Li, Y., Creamer, A.E. and He, F. (2017b) Adsorptive removal of arsenate from aqueous solutions by biochar supported zero-valent iron nanocomposite: Batch and continuous flow tests. Journal Of Hazardous Materials 322, 172-181.

Wang, S., Gao, B., Li, Y., Wan, Y. and Creamer, A.E. (2015a) Sorption of arsenate onto magnetic iron–manganese (Fe–Mn) biochar composites. Rsc Advances 5(83), 67971-67978.

Wang, S., Gao, B., Zimmerman, A.R., Li, Y., Ma, L., Harris, W.G. and Migliaccio, K.W. (2015b)

Removal of arsenic by magnetic biochar prepared from pinewood and natural hematite. Bioresource technology 175, 391-395.

Wang, X., Zhang, Y., Zhang, H., Wu, X., Ding, J., Wang, L., Chen, J., Wu, X., Xiao, J., Wang, L., Tsang, D.C.W. and Crittenden, J.C. (2022b) Insights into deep decline of As(III) leachability induced by As(III) partial oxidation during lime stabilization of As–Ca sludge. Journal Of Hazardous Materials 424, 127575.

Wang, Y., Wu, J., Wang, G., Yang, D., Ishihara, T. and Guo, L. (2021e) Oxygen vacancy engineering in Fe doped akhtenskite-type MnO2 for low-temperature toluene oxidation. Applied Catalysis B: Environmental 285, 119873.

Warren, B.E. (1941) X-Ray Diffraction in Random Layer Lattices. Physical Review 59(9), 693-698.

Weerasundara, L., Ok, Y.-S. and Bundschuh, J. (2021) Selective removal of arsenic in water: A critical review. Environmental Pollution 268, 115668.

Wei, K., Li, H., Gu, H.Y., Liu, X.F., Ling, C.C., Cao, S.Y., Li, M.Q., Liao, M.Z., Peng, X., Shi, Y.B., Shen, W.J., Liang, C., Ai, Z.H. and Zhang, L.Z. (2022) Strained Zero-Valent Iron for Highly Efficient Heavy Metal Removal. Advanced Functional Materials 32(26).

Wei, X., Li, X., Tang, L., Yu, J., Deng, J., Luo, T., Liang, J., Chen, X. and Zhou, Y. (2021) Exploring the role of Fe species from biochar-iron composites in the removal and long-term immobilization of SeO42- against competing oxyanions. Journal Of Hazardous Materials 418, 126311.

Wei, X.Z., Kong, X., Wang, S.X., Xiang, H., Wang, J.D. and Chen, J.Y. (2013) Removal of Heavy Metals from Electroplating Wastewater by Thin-Film Composite Nanofiltration Hollow-Fiber Membranes. Industrial & Engineering Chemistry Research 52(49), 17583-17590.

Wei, Y.F., Wei, S.D., Liu, C.B., Chen, T., Tang, Y.H., Ma, J.H., Yin, K. and Luo, S.L. (2019) Efficient removal of arsenic from groundwater using iron oxide nanoneedle array-decorated biochar fibers with high Fe utilization and fast adsorption kinetics. Water Research 167.

Wen, Z., Lu, J., Zhang, Y., Cheng, G., Guo, S., Wei, P., Ming, Y.-a., Wang, Y. and Chen, R. (2020) Simultaneous oxidation and immobilization of arsenite from water by nanosized magnetic mesoporous iron manganese bimetal oxides (Nanosized-MMIM): Synergistic effect and interface catalysis. Chemical Engineering Journal 391, 123578.

Wen, Z., Xi, J., Lu, J., Zhang, Y., Cheng, G., Zhang, Y. and Chen, R. (2021) Porous biochar-supported MnFe2O4 magnetic nanocomposite as an excellent adsorbent for simultaneous and effective removal of organic/inorganic arsenic from water. Journal Of Hazardous Materials 411, 124909.

Whitman, T. and Lehmann, J. (2009) Biochar—One way forward for soil carbon in offset mechanisms in Africa? Environmental Science & Policy 12(7), 1024-1027.

Woolf, D., Amonette, J.E., Street-Perrott, F.A., Lehmann, J. and Joseph, S. (2010) Sustainable biochar to mitigate global climate change. Nature Communications 1(1), 56.

Wu, L., Sun, Z., Zhen, Y., Zhu, S., Yang, C., Lu, J., Tian, Y., Zhong, D. and Ma, J. (2021) Oxygen Vacancy-Induced Nonradical Degradation of Organics: Critical Trigger of Oxygen (O2) in the Fe–Co LDH/Peroxymonosulfate System. Environmental Science & Technology 55(22), 15400-15411.

Wu, Q., Ouyang, J., Xie, K., Sun, L., Wang, M. and Lin, C. (2012) Ultrasound-assisted synthesis and visible-light-driven photocatalytic activity of Fe-incorporated TiO2 nanotube array photocatalysts. Journal Of Hazardous Materials 199-200, 410-417.

Wu, X., Lee, B. and Jun, Y.-S. (2020) Interfacial and Activation Energies of Environmentally Abundant Heterogeneously Nucleated Iron(III) (Hydr)oxide on Quartz. Environmental Science & Technology 54(19), 12119-12129.

Xi, Y., Zou, J., Luo, Y., Li, J., Li, X., Liao, T., Zhang, L., Wang, C. and Lin, G. (2019) Performance and mechanism of arsenic removal in waste acid by combination of CuSO4 and zero-valent iron. Chemical Engineering Journal 375, 121928.

Xia, H., Zhang, Z., Liu, J., Deng, Y., Zhang, D., Du, P., Zhang, S. and Lu, X. (2019) Novel Fe-Mn-O nanosheets/wood carbon hybrid with tunable surface properties as a superior catalyst for Fenton-like oxidation. Applied Catalysis B: Environmental 259, 118058.

Xiao, X. and Chen, B. (2017a) A Direct Observation of the Fine Aromatic Clusters and Molecular Structures of Biochars. Environmental Science & Technology 51(10), 5473-5482.

Xiao, X., Chen, B., Chen, Z., Zhu, L. and Schnoor, J.L. (2018a) Insight into Multiple and Multilevel Structures of Biochars and Their Potential Environmental Applications: A Critical Review. Environmental Science & Technology 52(9), 5027-5047.

Xiao, X., Chen, B. and Zhu, L. (2014) Transformation, Morphology, and Dissolution of Silicon and Carbon in Rice Straw-Derived Biochars under Different Pyrolytic Temperatures. Environmental Science & Technology 48(6), 3411-3419.

Xiao, X., Chen, B., Zhu, L. and Schnoor, J.L. (2017) Sugar Cane-Converted Graphene-like Material for the Superhigh Adsorption of Organic Pollutants from Water via Coassembly Mechanisms. Environmental Science & Technology 51(21), 12644-12652.

Xiao, X. and Chen, B.L. (2017b) A Direct Observation of the Fine Aromatic Clusters and Molecular Structures of Biochars. Environmental Science & Technology 51(10), 5473-5482.

Xiao, X., Chen, B.L., Chen, Z.M., Zhu, L.Z. and Schnoor, J.L. (2018b) Insight into Multiple and Multilevel Structures of Biochars and Their Potential Environmental Applications: A Critical Review. Environmental Science & Technology 52(9), 5027-5047.

Xiao, X.F., Sun, Y.J., Liu, J.W. and Zheng, H.L. (2021) Flocculation of heavy metal by functionalized starch-based bioflocculants: Characterization and process evaluation. Separation and Purification Technology 267.

Xie, L., Gou, L., Xu, D., Kapusta, K., Dai, L. and Wang, Y. (2023) Coupling influences of organic components and temperature on nitrogen transformation and hydrochar characterization during hydrothermal carbonization of sewage sludge. Science of the Total Environment 866, 161354.

Xie, T., Lu, S., Zeng, J., Rao, L., Wang, X., Win, M.S., Zhang, D., Lu, H., Liu, X. and Wang, Q. (2020) Soluble Fe release from iron-bearing clay mineral particles in acid environment and their oxidative potential. Science of the Total Environment 726, 138650.

Xie, X., Wang, B., Wang, Y., Ni, C., Sun, X. and Du, W. (2022) Spinel structured MFe2O4 (M = Fe, Co, Ni, Mn, Zn) and their composites for microwave absorption: A review. Chemical Engineering Journal 428, 131160.

Xing, X., Ren, X., Alharbi, N.S. and Chen, C. (2022) Biochar-supported Fe/Ni bimetallic nanoparticles for the efficient removal of Cr(VI) from aqueous solution. Journal of Molecular Liquids 359, 119257.

Xu, H., Sun, Y., Li, J., Li, F. and Guan, X. (2016) Aging of Zerovalent Iron in Synthetic Groundwater: X-ray Photoelectron Spectroscopy Depth Profiling Characterization and Depassivation with Uniform Magnetic Field. Environmental Science & Technology 50(15), 8214-8222.

Xu, J., Avellan, A., Li, H., Clark, E.A., Henkelman, G., Kaegi, R. and Lowry, G.V. (2020a) Iron and Sulfur Precursors Affect Crystalline Structure, Speciation, and Reactivity of Sulfidized Nanoscale Zerovalent Iron. Environmental Science & Technology 54(20), 13294-13303.

Xu, J., Avellan, A., Li, H., Liu, X., Noël, V., Lou, Z., Wang, Y., Kaegi, R., Henkelman, G. and Lowry, G.V. (2020b) Sulfur Loading and Speciation Control the Hydrophobicity, Electron Transfer, Reactivity, and Selectivity of Sulfidized Nanoscale Zerovalent Iron. 32(17), 1906910.

Xu, J., Liu, X., Cao, Z., Bai, W., Shi, Q. and Yang, Y. (2020c) Fast degradation, large capacity, and high electron efficiency of chloramphenicol removal by different carbon-supported nanoscale zerovalent iron. Journal Of Hazardous Materials 384, 121253.

Xu, L., Fu, B., Sun, Y., Jin, P., Bai, X., Jin, X., Shi, X., Wang, Y. and Nie, S. (2020d) Degradation of organic pollutants by Fe/N co-doped biochar via peroxymonosulfate activation: Synthesis, performance, mechanism and its potential for practical application. Chemical Engineering Journal 400, 125870.

Xu, L., He, Z., Wei, X., Shang, Y., Shi, J., Jin, X., Bai, X., Shi, X. and Jin, P. (2023a) Facile-prepared Fe/Mn co-doped biochar is an efficient catalyst for mediating the degradation of aqueous ibuprofen via catalytic ozonation. Chemical Engineering Journal, 142028.

Xu, W., Walpen, N., Keiluweit, M., Kleber, M. and Sander, M. (2021a) Redox Properties of Pyrogenic Dissolved Organic Matter (pyDOM) from Biomass-Derived Chars. Environmental Science & Technology.

Xu, X., Huang, H., Zhang, Y., Xu, Z. and Cao, X. (2018a) Biochar as both electron donor and electron shuttle for the reduction transformation of Cr(VI) during its sorption. Environmental pollution (Barking, Essex : 1987) 244, 423-430.

Xu, X., Huang, H., Zhang, Y., Xu, Z. and Cao, X. (2019a) Biochar as both electron donor and electron shuttle for the reduction transformation of Cr(VI) during its sorption. Environ Pollut 244, 423-430.

Xu, X., Zhao, Y., Sima, J., Zhao, L., Masek, O. and Cao, X. (2017) Indispensable role of biochar-inherent mineral constituents in its environmental applications: A review. Bioresource technology 241, 887-899.

Xu, Y.F., Zhang, J., Liang, Y., Zhou, J.Z., Zhao, J., Ruan, X.X., Xu, Z.P. and Qian, G.R. (2015) Synchronous cyanide purification with metals removal in the co-treatment of Zn-CN and Ni electroplating wastewaters via the Ni2+-assisted precipitation of LDH. Separation and Purification Technology 145, 92-97.

Xu, Z., He, M., Xu, X., Cao, X. and Tsang, D.C.W. (2021b) Impacts of different activation processes on the carbon stability of biochar for oxidation resistance. Bioresource technology 338, 125555.

Xu, Z., Sun, M., Xu, X., Cao, X., Ippolito, J.A., Mohanty, S.K., Ni, B.-J., Xu, S. and Tsang, D.C.W. (2023b) Electron donation of Fe-Mn biochar for chromium(VI) immobilization: Key roles of embedded zero-valent iron clusters within iron-manganese oxide. Journal Of Hazardous Materials 456, 131632.

Xu, Z., Wan, Z., Sun, Y., Cao, X., Hou, D., Alessi, D.S., Ok, Y.S. and Tsang, D.C.W. (2021c) Unraveling iron speciation on Fe-biochar with distinct arsenic removal mechanisms and depth distributions of As and Fe. Chemical Engineering Journal 425, 131489.

Xu, Z., Wan, Z., Sun, Y., Cao, X., Hou, D., Alessi, D.S., Sik Ok, Y. and Tsang, D.C.W. (2021d) Unraveling Iron Speciation on Fe-biochar with Distinct Arsenic Removal Mechanisms and Depth Distributions of As and Fe. Chemical Engineering Journal, 131489.

Xu, Z., Wan, Z., Sun, Y., Gao, B., Hou, D., Cao, X., Komarek, M., Ok, Y.S. and Tsang, D.C.W. (2022a) Electroactive Fe-biochar for redox-related remediation of arsenic and chromium: Distinct redox nature with varying iron/carbon speciation. J Hazard Mater 430, 128479.

Xu, Z., Xu, X., Tao, X., Yao, C., Tsang, D.C.W. and Cao, X. (2019b) Interaction with low molecular weight organic acids affects the electron shuttling of biochar for Cr(VI) reduction. Journal Of Hazardous Materials 378.

Xu, Z., Xu, X., Tao, X., Yao, C., Tsang, D.C.W. and Cao, X. (2019c) Interaction with low molecular weight organic acids affects the electron shuttling of biochar for Cr(VI) reduction. Journal Of Hazardous Materials 378, 120705.

Xu, Z., Xu, X., Tsang, D.C.W. and Cao, X. (2018b) Contrasting impacts of pre- and post-application aging of biochar on the immobilization of Cd in contaminated soils. Environmental Pollution.

Xu, Z., Xu, X., Tsang, D.C.W. and Cao, X. (2018c) Contrasting impacts of pre- and post-application aging of biochar on the immobilization of Cd in contaminated soils. Environmental Pollution 242, 1362-1370.

Xu, Z., Xu, X., Tsang, D.C.W., Yang, F., Zhao, L., Qiu, H. and Cao, X. (2019d) Participation of soil active components in the reduction of Cr(VI) by biochar: Differing effects of iron mineral alone and its combination with organic acid. Journal Of Hazardous Materials, 121455.

Xu, Z., Xu, X., Tsang, D.C.W., Yang, F., Zhao, L., Qiu, H. and Cao, X. (2020e) Participation of soil active components in the reduction of Cr(VI) by biochar: Differing effects of iron mineral alone and its combination with organic acid. J Hazard Mater 384, 121455.

Xu, Z., Xu, X., Yu, Y., Yao, C., Tsang, D.C.W. and Cao, X. (2021e) Evolution of redox activity of biochar during interaction with soil minerals: Effect on the electron donating and mediating capacities for Cr(VI) reduction. J Hazard Mater 414, 125483.

Xu, Z., Xu, X., Zhang, Y., Yu, Y. and Cao, X. (2019e) Pyrolysis-temperature depended electron donating and mediating mechanisms of biochar for Cr(VI) reduction. Journal Of Hazardous Materials, 121794.

Xu, Z., Xu, X., Zhang, Y., Yu, Y. and Cao, X. (2020f) Pyrolysis-temperature depended electron donating and mediating mechanisms of biochar for Cr(VI) reduction. J Hazard Mater 388, 121794.

Xu, Z., Yu, Y., Xu, X., Tsang, D.C.W., Yao, C., Fan, J., Zhao, L., Qiu, H. and Cao, X. (2022b) Direct and Indirect Electron Transfer Routes of Chromium(VI) Reduction with Different Crystalline Ferric Oxyhydroxides in the Presence of Pyrogenic Carbon. Environmental Science & Technology.

Xu, Z.B., Wan, Z.H., Sun, Y.Q., Cao, X.D., Hou, D.Y., Alessi, D.S., Ok, Y.S. and Tsang, D.C.W. (2021f) Unraveling iron speciation on Fe-biochar with distinct arsenic removal mechanisms and depth distributions of As and Fe. Chemical Engineering Journal 425, 131489.

Xue, D.P., Xia, H.C., Yan, W.F., Zhang, J.A. and Mu, S.C. (2020) Defect Engineering on Carbon-Based Catalysts for Electrocatalytic CO2 Reduction. Nano-Micro Letters 13(1), 23.

Xue, D.P., Xia, H.C., Yan, W.F., Zhang, J.A. and Mu, S.C. (2021) Defect Engineering on Carbon-Based Catalysts for Electrocatalytic CO2 Reduction. Nano-Micro Letters 13(1).

Yalcin, S., Apak, R., Hizal, J. and Afsar, H. (2001) Recovery of copper (II) and chromium (III,VI) from electroplating-industry wastewater by ion exchange. Separation Science and Technology 36(10), 2181-2196.

Yan, F.L., Wang, Y., Wang, W.H., Zhao, J.X., Feng, L.L., Li, J.J. and Zhao, J.C. (2020) Application of biochars obtained through the pyrolysis of Lemna minor in the treatment of Ni-electroplating wastewater. Journal of Water Process Engineering 37.

Yan, Q., Wan, C., Liu, J., Gao, J., Yu, F., Zhang, J. and Cai, Z. (2013) Iron nanoparticles in situ encapsulated in biochar-based carbon as an effective catalyst for the conversion of biomass-derived syngas to liquid hydrocarbons. Green Chemistry 15(6), 1631-1640.

Yan, W., Ramos, M.A.V., Koel, B.E. and Zhang, W.-x. (2012a) As(III) Sequestration by Iron Nanoparticles: Study of Solid-Phase Redox Transformations with X-ray Photoelectron Spectroscopy. The Journal of Physical Chemistry C 116(9), 5303-5311.

Yan, W., Vasic, R., Frenkel, A.I. and Koel, B.E. (2012b) Intraparticle Reduction of Arsenite (As(III)) by Nanoscale Zerovalent Iron (nZVI) Investigated with In Situ X-ray Absorption Spectroscopy. Environmental Science & Technology 46(13), 7018-7026.

Yan, X., Xu, X., Liu, Q., Guo, J., Kang, L. and Yao, J. (2018) Functionalization of multi-walled carbon nanotubes with iron phthalocyanine via a liquid chemical reaction for oxygen reduction in alkaline media. Journal of Power Sources 389, 260-266.

Yang, D., Wang, L., Li, Z., Tang, X., He, M., Yang, S., Liu, X. and Xu, J. (2020a) Simultaneous adsorption of Cd(II)andAs(III)by a novel biochar-supported nanoscale zero-valent iron in aqueous systems. Science of the Total Environment 708, 134823.

Yang, F., Jiang, Y., Dai, M., Hou, X. and Peng, C. (2022a) Active biochar-supported iron oxides for Cr(VI) removal from groundwater: Kinetics, stability and the key role of FeO in electron-transfer mechanism. Journal Of Hazardous Materials 424, 127542.

Yang, F., Xu, Z., Yu, L., Gao, B., Xu, X., Zhao, L. and Cao, X. (2018a) Kaolinite Enhances the Stability of the Dissolvable and Undissolvable Fractions of Biochar via Different Mechanisms. Environmental Science & Technology.

Yang, F., Zhao, L., Gao, B., Xu, X.Y. and Cao, X.D. (2016) The Interfacial Behavior between Biochar and Soil Minerals and Its Effect on Biochar Stability. Environmental Science & Technology 50(5), 2264-2271.

Yang, J.B., Cai, N.S. and Li, Z.S. (2008) Hydrogen production from the steam-iron process with direct reduction of iron oxide by chemical looping combustion of coal char. Energy & Fuels 22(4), 2570-2579.

Yang, Q., Chen, Y., Duan, X., Zhou, S., Niu, Y., Sun, H., Zhi, L. and Wang, S. (2020b) Unzipping carbon nanotubes to nanoribbons for revealing the mechanism of nonradical oxidation by carbocatalysis. Applied Catalysis B: Environmental 276, 119146.

Yang, Q., Li, Z., Lu, X., Duan, Q., Huang, L. and Bi, J. (2018b) A review of soil heavy metal pollution from industrial and agricultural regions in China: Pollution and risk assessment. Science of the Total Environment 642, 690-700.

Yang, Q., Zhou, H., Bartocci, P., Fantozzi, F., Mašek, O., Agblevor, F.A., Wei, Z., Yang, H., Chen, H., Lu, X., Chen, G., Zheng, C., Nielsen, C.P. and McElroy, M.B. (2021a) Prospective contributions of biomass pyrolysis to China's 2050 carbon reduction and renewable energy goals. Nat Commun 12(1), 1698-1698.

Yang, Q., Zhou, H., Bartocci, P., Fantozzi, F., Mašek, O., Agblevor, F.A., Wei, Z., Yang, H., Chen, H., Lu, X., Chen, G., Zheng, C., Nielsen, C.P. and McElroy, M.B. (2021b) Prospective contributions of biomass pyrolysis to China’s 2050 carbon reduction and renewable energy goals. Nature Communications 12(1), 1698.

Yang, T., Meng, L., Han, S., Hou, J., Wang, S. and Wang, X. (2017) Simultaneous reductive and sorptive removal of Cr(vi) by activated carbon supported β-FeOOH. Rsc Advances 7(55), 34687-34693.

Yang, T., Xu, Y., Huang, Q., Sun, Y., Liang, X. and Wang, L. (2022b) Removal mechanisms of Cd from water and soil using Fe–Mn oxides modified biochar. Environmental research 212, 113406.

Yang, Z., Zhang, X., Jiang, Z., Li, Q., Huang, P., Zheng, C., Liao, Q. and Yang, W. (2021c) Reductive materials for remediation of hexavalent chromium contaminated soil – A review. Science of the Total Environment 773, 145654.

Yao, F., Yang, Q., Yan, M., Li, X., Chen, F., Zhong, Y., Yin, H., Chen, S., Fu, J., Wang, D. and Li, X. (2020) Synergistic adsorption and electrocatalytic reduction of bromate by Pd/N-doped loofah sponge-derived biochar electrode. Journal Of Hazardous Materials 386, 121651.

Yi, Y., Tu, G., Eric Tsang, P. and Fang, Z. (2020) Insight into the influence of pyrolysis temperature on Fenton-like catalytic performance of magnetic biochar. Chemical Engineering Journal 380, 122518.

Yin, G., Song, X., Tao, L., Sarkar, B., Sarmah, A.K., Zhang, W., Lin, Q., Xiao, R., Liu, Q. and Wang, H. (2020a) Novel Fe-Mn binary oxide-biochar as an adsorbent for removing Cd(II) from aqueous solutions. Chemical Engineering Journal 389, 124465.

Yin, K., Wang, Q., Lv, M. and Chen, L. (2019) Microorganism remediation strategies towards heavy metals. Chemical Engineering Journal 360, 1553-1563.

Yin, P., Zhang, L., Jiang, Y., Zhang, Y., Wang, J., Feng, X., Dai, J. and Tang, Y. (2020b) Recycling of waste straw in sorghum for preparation of biochar/(Fe,Ni) hybrid aimed at significant electromagnetic absorbing of low-frequency band. Journal of Materials Research and Technology 9(6), 14212-14222.

Yoon, K., Cho, D.-W., Bhatnagar, A. and Song, H. (2020) Adsorption of As(V) and Ni(II) by Fe-Biochar composite fabricated by co-pyrolysis of orange peel and red mud. Environmental research 188, 109809.

Yoon, Y., Park, W.K., Hwang, T.-M., Yoon, D.H., Yang, W.S. and Kang, J.-W. (2016) Comparative evaluation of magnetite–graphene oxide and magnetite-reduced graphene oxide composite for As(III) and As(V) removal. Journal Of Hazardous Materials 304, 196-204.

Yu, C., Tang, J., Su, H., Huang, J., Liu, F., Wang, L. and Sun, H. (2022) Development of a novel biochar/iron oxide composite from green algae for bisphenol-A removal: Adsorption and Fenton-like reaction. Environmental Technology & Innovation 28, 102647.

Yu, Y.L., Xu, Z.B., Xu, X.Y., Zhao, L., Qiu, H. and Cao, X.D. (2021) Synergistic role of bulk carbon and iron minerals inherent in the sludge-derived biochar for As(V) immobilization. Chemical Engineering Journal 417, 129183.

Yuan, X., Suvarna, M., Low, S., Dissanayake, P.D., Lee, K.B., Li, J., Wang, X. and Ok, Y.S. (2021) Applied Machine Learning for Prediction of CO2 Adsorption on Biomass Waste-Derived Porous Carbons. Environmental Science & Technology.

Yuan, Y., Bolan, N., Prévoteau, A., Vithanage, M., Biswas, J.K., Ok, Y.S. and Wang, H. (2017) Applications of biochar in redox-mediated reactions. Bioresource technology 246, 271-281.

Zeng, L., Zhang, G., Huang, X., Wang, H., Zhou, T. and Xie, H. (2021) Tuning crystal structure of MnO2 during different hydrothermal synthesis temperature and its electrochemical performance as cathode material for zinc ion battery. Vacuum 192, 110398.

Zeng, Q., Wang, X., Liu, X., Huang, L., Hu, J., Chu, R., Tolic, N. and Dong, H. (2020) Mutual Interactions between Reduced Fe-Bearing Clay Minerals and Humic Acids under Dark, Oxygenated Conditions: Hydroxyl Radical Generation and Humic Acid Transformation. Environmental Science & Technology 54(23), 15013-15023.

Zhang, B., Zhou, S., Zhou, L., Wen, J. and Yuan, Y. (2019a) Pyrolysis temperature-dependent electron transfer capacities of dissolved organic matters derived from wheat straw biochar. Science of the Total Environment 696, 133895.

Zhang, C., Lu, J. and Wu, J. (2020a) One-step green preparation of magnetic seaweed biochar/sulfidated Fe0 composite with strengthen adsorptive removal of tetrabromobisphenol A through in situ reduction. Bioresource technology 307, 123170.

Zhang, F., Wang, X., Xionghui, J. and Ma, L. (2016a) Efficient arsenate removal by magnetite-modified water hyacinth biochar. Environmental Pollution 216, 575-583.

Zhang, G., Liu, F., Liu, H., Qu, J. and Liu, R. (2014) Respective Role of Fe and Mn Oxide Contents for Arsenic Sorption in Iron and Manganese Binary Oxide: An X-ray Absorption Spectroscopy Investigation. Environmental Science & Technology 48(17), 10316-10322.

Zhang, H. and Hay, A.G. (2020) Magnetic biochar derived from biosolids via hydrothermal carbonization: Enzyme immobilization, immobilized-enzyme kinetics, environmental toxicity. Journal Of Hazardous Materials 384, 121272.

Zhang, J., Liu, L., Liang, Y., Zhou, J.Z., Xu, Y.F., Ruan, X.X., Lu, Y.S., Xu, Z.P. and Qian, G.R. (2015) Enhanced precipitation of cyanide from electroplating wastewater via self-assembly of bimetal cyanide complex. Separation and Purification Technology 150, 179-185.

Zhang, L., Zhu, T., Liu, X. and Zhang, W. (2016b) Simultaneous oxidation and adsorption of As(III) from water by cerium modified chitosan ultrafine nanobiosorbent. Journal Of Hazardous Materials 308, 1-10.

Zhang, M., Chen, Q., Zhang, R., Zhang, Y., Wang, F., He, M., Guo, X., Yang, J., Zhang, X. and Mu, J. (2023) Pyrolysis of Ca/Fe-rich antibiotic fermentation residues into biochars for efficient phosphate removal/recovery from wastewater: Turning hazardous waste to phosphorous fertilizer. Science of the Total Environment 869, 161732.

Zhang, N., Bu, X., Li, Y., Zhang, Y., Yuan, S., Wen, Z., Tong, M. and Lin, L. (2020b) Water Table Fluctuations Regulate Hydrogen Peroxide Production and Distribution in Unconfined Aquifers. Environmental Science & Technology 54(8), 4942-4951.

Zhang, P., Fan, J., Xu, X., Xu, Z., Yu, Y., Zhao, L., Qiu, H. and Cao, X. (2022a) Contrasting effects of dry-wet and freeze-thaw aging on the immobilization of As in As-contaminated soils amended by zero-valent iron-embedded biochar. Journal Of Hazardous Materials 426, 128123.

Zhang, S.-H., Wu, M.-F., Tang, T.-T., Xing, Q.-J., Peng, C.-Q., Li, F., Liu, H., Luo, X.-B., Zou, J.-P., Min, X.-B. and Luo, J.-M. (2018a) Mechanism investigation of anoxic Cr(VI) removal by nano zero-valent iron based on XPS analysis in time scale. Chemical Engineering Journal 335, 945-953.

Zhang, S., Lyu, H., Tang, J., Song, B., Zhen, M. and Liu, X. (2019b) A novel biochar supported CMC stabilized nano zero-valent iron composite for hexavalent chromium removal from water. Chemosphere 217, 686-694.

Zhang, T., Liu, Y., Yang, L., Li, W., Wang, W. and Liu, P. (2020c) Ti–Sn–Ce/bamboo biochar particle electrodes for enhanced electrocatalytic treatment of coking wastewater in a three-dimensional electrochemical reaction system. Journal of Cleaner Production 258, 120273.

Zhang, T., Zhao, Y., Kang, S., Bai, H., Gu, W., Fang, D., Komarneni, S. and Zhang, Q. (2021) Mechanical activation of zero-valent iron (ZVI) in the presence of CaCO3: Improved reactivity of ZVI for enhancing As(III) removal from water. Journal of Cleaner Production 286, 124926.

Zhang, X., Sun, P., Wei, K., Huang, X. and Zhang, X. (2020d) Enhanced H2O2 activation and sulfamethoxazole degradation by Fe-impregnated biochar. Chemical Engineering Journal 385, 123921.

Zhang, Y.-J., Huang, G.-X., Winter, L.R., Chen, J.-J., Tian, L., Mei, S.-C., Zhang, Z., Chen, F., Guo, Z.-Y., Ji, R., You, Y.-Z., Li, W.-W., Liu, X.-W., Yu, H.-Q. and Elimelech, M. (2022b) Simultaneous nanocatalytic surface activation of pollutants and oxidants for highly efficient water decontamination. Nature Communications 13(1), 3005.

Zhang, Y., Jiang, Q., Xie, W., Wang, Y. and Kang, J. (2019c) Effects of temperature, time and acidity of hydrothermal carbonization on the hydrochar properties and nitrogen recovery from corn stover. Biomass and Bioenergy 122, 175-182.

Zhang, Y., Xu, X., Cao, L., Ok, Y.S. and Cao, X. (2018b) Characterization and quantification of electron donating capacity and its structure dependence in biochar derived from three waste biomasses. Chemosphere 211, 1073-1081.

Zhang, Y., Xu, X., Cao, L., Ok, Y.S. and Cao, X. (2018c) Characterization and quantification of electron donating capacity and its structure dependence in biochar derived from three waste biomasses. Chemosphere.

Zhang, Y., Xu, X., Zhang, P., Ling, Z., Qiu, H. and Cao, X. (2019d) Pyrolysis-temperature depended quinone and carbonyl groups as the electron accepting sites in barley grass derived biochar. Chemosphere 232, 273-280.

Zhang, Z., Ma, W., Hu, J., Xin, G., Chen, Z., Wan, C., Wang, S. and Zhang, Q. (2022c) A novel biochar electrode for efficient electroreduction of nitrate: Selective and regulation of halogen. Chemosphere 288, 132400.

Zhao, B., O'Connor, D., Zhang, J., Peng, T., Shen, Z., Tsang, D.C.W. and Hou, D. (2018a) Effect of pyrolysis temperature, heating rate, and residence time on rapeseed stem derived biochar. Journal of Cleaner Production 174, 977-987.

Zhao, J., Xiong, S., Chen, F., Yin, W., Gong, Y., Wu, J., Huang, L.-Z. and Dionysiou, D.D. (2022a) One-time removal of Cr(VI) and carbon tetrachloride from groundwater by silicate stabilized green rust: The slow release of reactive sites driven by Fe(III)-Cr(III) oxides formation. Chemical Engineering Journal 433, 134462.

Zhao, L., Cao, X., Zheng, W., Scott, J.W., Sharma, B.K. and Chen, X. (2016a) Copyrolysis of Biomass with Phosphate Fertilizers To Improve Biochar Carbon Retention, Slow Nutrient Release, and Stabilize Heavy Metals in Soil. Acs Sustainable Chemistry & Engineering 4(3), 1630-1636.

Zhao, L., Zhao, Y.H., Nan, H.Y., Yang, F., Qiu, H., Xu, X.Y. and Cao, X.D. (2020) Suppressed formation of polycyclic aromatic hydrocarbons (PAHs) during pyrolytic production of Fe-enriched composite biochar. Journal Of Hazardous Materials 382.

Zhao, M., Duncan, J.R. and Van Hille, R.P. (1999) Removal and recovery of zinc from solution and electroplating effluent using Azolla filiculoides. Water Research 33(6), 1516-1522.

Zhao, N., Yin, Z., Liu, F., Zhang, M., Lv, Y., Hao, Z., Pan, G. and Zhang, J. (2018b) Environmentally persistent free radicals mediated removal of Cr(VI) from highly saline water by corn straw biochars. Bioresource technology 260, 294-301.

Zhao, R.R., Zhou, Z.M., Zhao, X.D. and Jing, G.H. (2019) Enhanced Cr(VI) removal from simulated electroplating rinse wastewater by amino-functionalized vermiculite-supported nanoscale zero-valent iron. Chemosphere 218, 458-467.

Zhao, X., Liu, W., Cai, Z., Han, B., Qian, T. and Zhao, D. (2016b) An overview of preparation and applications of stabilized zero-valent iron nanoparticles for soil and groundwater remediation. Water Research 100, 245-266.

Zhao, X., Wang, H.D., Chen, F.Y., Mao, R., Liu, H.J. and Qu, J.H. (2013) Efficient treatment of an electroplating wastewater containing heavy metal ions, cyanide, and organics by H2O2 oxidation followed by the anodic Fenton process. Water Science and Technology 68(6), 1329-1335.

Zhao, X.M., Sobecky, P.A., Zhao, L.P., Crawford, P. and Li, M.T. (2016c) Chromium(VI) transport and fate in unsaturated zone and aquifer: 3D Sandbox results. Journal Of Hazardous Materials 306, 203-

209.

Zhao, Z., Wang, X., Zhu, G., Wang, F., Zhou, Y., Dong, W., Wang, H., Sun, F. and Xie, H. (2022b) Enhanced removal of Cu-EDTA in a three-dimensional electrolysis system with highly graphitic activated biochar produced via acidic and K2FeO4 treatment. Chemical Engineering Journal 430, 132661.

Zhong, D., Jiang, Y., Zhao, Z., Wang, L., Chen, J., Ren, S., Liu, Z., Zhang, Y., Tsang, D.C.W. and Crittenden, J.C. (2019) pH Dependence of Arsenic Oxidation by Rice-Husk-Derived Biochar: Roles of Redox-Active Moieties. Environ Sci Technol 53(15), 9034-9044.

Zhong, D., Ren, S., Dong, X., Yang, X., Wang, L., Chen, J., Zhao, Z., Zhang, Y., Tsang, D.C.W. and Crittenden, J.C. (2021a) Rice husk-derived biochar can aggravate arsenic mobility in ferrous-rich groundwater during oxygenation. Water Research 200, 117264.

Zhong, D., Ren, S., Dong, X., Yang, X., Wang, L., Chen, J., Zhao, Z., Zhang, Y., Tsang, D.C.W. and Crittenden, J.C. (2021b) Rice husk-derived biochar can aggravate arsenic mobility in ferrous-rich groundwater during oxygenation. Water Res 200, 117264.

Zhong, D., Zhang, Y., Wang, L., Chen, J., Jiang, Y., Tsang, D.C.W., Zhao, Z., Ren, S., Liu, Z. and Crittenden, J.C. (2018) Mechanistic insights into adsorption and reduction of hexavalent chromium from water using magnetic biochar composite: Key roles of Fe3O4 and persistent free radicals. Environmental Pollution 243, 1302-1309.

Zhong, D., Zhao, Z., Jiang, Y., Yang, X., Wang, L., Chen, J., Guan, C.-Y., Zhang, Y., Tsang, D.C.W. and Crittenden, J.C. (2020) Contrasting abiotic As(III) immobilization by undissolved and dissolved fractions of biochar in Ca2+-rich groundwater under anoxic conditions. Water Research 183, 116106.

Zhou, J.-H., Sui, Z.-J., Zhu, J., Li, P., Chen, D., Dai, Y.-C. and Yuan, W.-K. (2007) Characterization of surface oxygen complexes on carbon nanofibers by TPD, XPS and FT-IR. Carbon 45(4), 785-796.

Zhou, J., Gao, Z., Xiang, G., Zhai, T., Liu, Z., Zhao, W., Liang, X. and Wang, L. (2022a) Interfacial compatibility critically controls Ru/TiO2 metal-support interaction modes in CO2 hydrogenation. Nature Communications 13(1), 327.

Zhou, J.Z., Liu, P., Liu, Z.Y., Zhang, J. and Huang, X. (2020) Simultaneous recovery of phosphorus with nickel purification in nickel-plating wastewater via Fe/C activated H2O2 oxidation. Chemical Engineering Journal 381.

Zhou, L., Li, Z., Yi, Y., Tsang, E.P. and Fang, Z. (2022b) Increasing the electron selectivity of nanoscale zero-valent iron in environmental remediation: A review. Journal Of Hazardous Materials 421, 126709.

Zhou, Y., Leng, Y., Zhou, W., Huang, J., Zhao, M., Zhan, J., Feng, C., Tang, Z., Chen, S. and Liu, H. (2015) Sulfur and nitrogen self-doped carbon nanosheets derived from peanut root nodules as high-efficiency non-metal electrocatalyst for hydrogen evolution reaction. Nano Energy 16, 357-366.

Zhou, Y., Wu, Y., Lei, Y., Pan, Y., Cheng, S., Ouyang, G. and Yang, X. (2021) Redox-Active Moieties in Dissolved Organic Matter Accelerate the Degradation of Nitroimidazoles in SO4•–-Based Oxidation. Environmental Science & Technology 55(21), 14844-14853.

Zhu, F., Li, L., Ren, W., Deng, X. and Liu, T. (2017a) Effect of pH, temperature, humic acid and coexisting anions on reduction of Cr(VI) in the soil leachate by nZVI/Ni bimetal material. Environmental Pollution 227, 444-450.

Zhu, J., Lou, Z., Liu, Y., Fu, R., Baig, S.A. and Xu, X. (2015) Adsorption behavior and removal mechanism of arsenic on graphene modified by iron–manganese binary oxide (FeMnOx/RGO) from aqueous solutions. Rsc Advances 5(83), 67951-67961.

Zhu, L., Fu, F. and Tang, B. (2019a) Three-dimensional transfer of Cr(VI) co-precipitated with ferrihydrite containing silicate and its redistribution and retention during aging. Science of the Total Environment 696, 133966.

Zhu, Q., Gao, H., Sun, Y., Xiang, Y., Liang, X., Ivanets, A., Li, X., Su, X. and Lin, Z. (2022a) Highly efficient adsorption of chromium on N, S-codoped porous carbon materials derived from paper sludge. Science of the Total Environment 834, 155312.

Zhu, S., Ho, S.-H., Huang, X., Wang, D., Yang, F., Wang, L., Wang, C., Cao, X. and Ma, F. (2017b) Magnetic Nanoscale Zerovalent Iron Assisted Biochar: Interfacial Chemical Behaviors and Heavy Metals Remediation Performance. Acs Sustainable Chemistry & Engineering 5(11), 9673-9682.

Zhu, X., Li, Y. and Wang, X. (2019b) Machine learning prediction of biochar yield and carbon contents in biochar based on biomass characteristics and pyrolysis conditions. Bioresource technology 288, 121527.

Zhu, X., Wan, Z., Tsang, D.C.W., He, M., Hou, D., Su, Z. and Shang, J. (2021) Machine learning for the selection of carbon-based materials for tetracycline and sulfamethoxazole adsorption. Chemical Engineering Journal 406, 126782.

Zhu, X., Xu, Z., You, S., Komárek, M., Alessi, D.S., Yuan, X., Palansooriya, K.N., Ok, Y.S. and Tsang, D.C.W. (2022b) Machine learning exploration of the direct and indirect roles of Fe impregnation on Cr(VI) removal by engineered biochar. Chemical Engineering Journal 428, 131967.

Zhuang, S., Lee, E.S., Lei, L., Nunna, B.B., Kuang, L. and Zhang, W. (2016) Synthesis of nitrogen-doped graphene catalyst by high-energy wet ball milling for electrochemical systems. International Journal of Energy Research 40(15), 2136-2149.

Zoroufchi Benis, K., Soltan, J. and McPhedran, K.N. (2022) A novel method for fabrication of a binary oxide biochar composite for oxidative adsorption of arsenite: Characterization, adsorption mechanism and mass transfer modeling. Journal of Cleaner Production 356, 131832.

Zou, Y., Wang, X., Khan, A., Wang, P., Liu, Y., Alsaedi, A., Hayat, T. and Wang, X. (2016) Environmental Remediation and Application of Nanoscale Zero-Valent Iron and Its Composites for the Removal of Heavy Metal Ions: A Review. Environmental Science & Technology 50(14), 7290-7304.

Zuo, W., Yu, Y. and Huang, H. (2021) Making waves: Microbe-photocatalyst hybrids may provide new opportunities for treating heavy metal polluted wastewater. Water Research 195, 116984.